The Pb-Zn deposits in the Drau Range (Eastern Alps, Austria/Slovenia):

A multi-analytical research approach for investigation of the ore-forming mechanisms

PhD Thesis

Montanuniversitaet Leoben
Department of Applied Geosciences
Chair of Resource Mineralogy

Dipl. -Geol. Elisabeth Henjes-Kunst

Supervisors: Univ.-Prof. Dr. J. G. Raith
Univ.-Prof. Dr. F. Melcher

- April 2014 -

Herewith I affirm in the lieu of oath that I prepared this PhD thesis myself, using exclusively the references, cited in this volume.

Leoben April 2014

Acknowledgement

First of all, I would like to thank my supervisors Johann G. Raith (Chair of Resource Mineralogy, Montanuniversitaet Leoben) and Frank Melcher (Chair of Economic Geology, Montanuniveritaet Leoben) for help and support during my research and for constructive critic and discussions during the writing process!

This PhD thesis was financed from the UZAG funding of the Montanuniversitaet Leoben. I gratfully acknowledge the financial support of the UZAG funding and the connected preliminary work of Robert Scholger (Chair of Applied Geophysics, Montanuniversitatet Leoben).

For the sample (thin and thick section) preparation and for help with electron microprobe analysis I want to thank Helmut Mühlhans. Many thanks to Federica Zaccharini (MUL) and Jerzy Lodiziak (BGR Hannover) for analytical/technical support during the microprobe measurements at the Montanuniversitaet Leoben and at the BGR Hannover. Furthermore, I express my gratitude to Adrian J. Boyce and his staff members at the SUERC Glasgow for the help during the sulfur isotope analyses. For Pb and Rb-Sr isotope measurements and sample pre-treatment I thank Friedhelm Henjes-Kunst and his team (BGR Hannover). I am grateful to Wolfgang Schwinger (FEI Europe B.V.), Alan Butcher, Leonardo Salazar and Gerda Gloy for offering the possibility to have QUEMSCAN analyses done at FEI laboratories (Brisbane, Australia). For the LA ICP-MS analyses of sphalerites I would like to thank Helene Brätz (GeoZentrum Nordbayern, University Erlangen).

Preparation of this thesis would not have been possible without the help of many people, who were willing to provide samples or helped to collect own samples. In this context, I thank Michael Götzinger (Department of Mineralogy and Petrology, University Vienna) for providing samples from the collection of the institute collection; Günther Scharfe (former Chair of Economic Geology, Montanuniversitaet Leoben) for providing samples from the Walter Siegl collection; Oskar Schulz (former University Innsbruck) for providing access to his own large collection and for giving me detailed information of the former mining at Bleiberg; Frank Melcher for providing samples from the western part of the Bleiberg mine, which he and Oskar Schulz sampled during the last periods of active mining at Bleiberg. Furthermore I want to thank Helmut Prassnik, who has a great expertise on the Pb-Zn deposits within the Drau Range and helped me to collect own samples from various smaller Pb-Zn deposits within Carinthia. I also thank Suzanna Fajmuth-Strucl (and her staff members) for access to the Mezica mine and for allowing me to collect Topla samples. For providing me sketches of the mining areas of the former Bleiberg mine I thank Friedrich Kremser (GKB Bergbau GmbH, Bärnbach).

Furthermore I want to thank all the (former) staff members of the chair for Resource Mineralogy at the Montauniversitaet Leoben for their support: Judith Bergthaler, Ronald Bakker, Oskar Thalhammer, Amir Morteza Azim Zadeh, Miriam Baumgartner, Gerald Doppler, Peter Kollegger, Michael Kozlik and Kristina Stocker. Thank you for administrative, scientific and of course for moral support!

Many thanks to my family, who helped and supported me in every situation of life!

Finally: special thanks to Chris, for discussions, support, calming me down and everything he gave to me!

Abstract

The ore forming processes and the timing of ore precipitation of the Pb-Zn deposits within the Drau Range have been controversially discussed for decades. A combination of conventional analytical techniques (TIMS Pb and Rb-Sr) combined with techniques that allow a high spatial resolution (e.g. EMP, LA-combustion) was applied in order to investigate the ore forming processes.

Electromicroprobe (EMP) analyses revealed a strong heterogeneity in the trace element composition of sphalerite. From the distribution patterns and the observed inter-element relations it is concluded that only a part of the measured trace/minor elements is directly incorporated into the sphalerite lattice (Fe, Cd, Ge). The remaining trace elements (Pb, As, Tl, Cu) are possibly present in nano-inclusions rather than in solid solution within the sphalerite lattice.

High-resolution sulfur isotope analyses displayed also very variable $\delta^{34}S$ values (-30.4 to +1.8 ‰) of the investigated sulfides. More than 50% of the investigated sulfides have a very light sulfur isotope composition (< -20‰). This is interpreted as dominant input of reduced sulfur from a reservoir, where sulfate reduction was caused by bacterial metabolism (bacteriogenic sulfate reduction, BSR). In three samples from the Bleiberg deposit a temporal variability in $\delta^{34}S$ of co-occurring sulfides is documented on the cm-scale. The chronological evolution of the $\delta^{34}S$ values is not uniform within these three samples. The wide and non-uniform variation in sulfur isotope composition of the sulfides indicates that a further sulfur reservoir was involved into ore formation. Within this reservoir the reduction process caused a smaller sulfur isotope fractionation and consequently sulfides derived from this second reservoir have heavier sulfur isotope compositions. It is assumed that within the second reservoir a thermochemical process caused sulfate reduction (thermochemical sulfate reduction, TSR).

In contrast to the observed heterogeneity in trace element and sulfur isotope composition, the Pb isotope composition of sphalerite and galena from the different studied deposits is rather homogeneous and indicates a crustal origin of the ore lead. With the exception of two samples coexisting sphalerite and galena show very similar Pb isotope compositions. Therefore it is assumed that both base metals were mainly derived from the same crustal source. No systematic difference in the Pb isotope composition of chemically or sulfur isotopically distinct sphalerite was observed. Furthermore, the geological context of the individual deposits had also no influence on the Pb isotope composition of the sulfides.

Due to the missing correlation between trace element composition and $\delta^{34}S$ it is concluded that the metals and the reduced sulfur were transported in different fluids. The trace metals were presumably transported together with the base metals (Pb + Zn), which originate from a crustal reservoir. The observed trace element variations result presumably from the leaching of metals from the country rocks during the

migration of the metal bearing fluid. Furthermore, the observed trace element variations are attributed to the prevailing physico-chemical conditions (e.g. redox conditions, sulfur species) at the depositional site during the ore precipitation.

Rb-Sr isotope measurements of sphalerite were performed in order to date the age of ore formation. In addition to the data of this study, Rb-Sr data of sphalerites (+ one pyrite) from the western Bleiberg mine, determined by J. Schneider (partly published in Melcher et al., 2010) were considered for the calculation of isochron ages. Three meaningful ages, which show a small uncertainty were calculated from differently divided subsets: *(1)* 204.2±3.2 Ma (n = 5); *(2)* 195.1±2.6 Ma (n = 7); *(3)* 225±2.1 Ma (n = 3). The majority of the data indicates an epigenetic ore formation at approximately 200 Ma (and younger). However, the possibility of an earlier probably syngenetic stage of ore formation at about 225 Ma cannot be excluded.

Zusammenfassung

Die Prozesse und der Zeitraum der Pb-Zn Vererzung im Drauzug werden seit Jahrzehnten kontrovers diskutiert. Eine Kombination klassischer analytischer Methoden (z.B TIMS Pb und Rb-Sr) mit hochortsauflösenden Methoden (z.B. EMP, LA combustion) wurde genutzt um die Mechanismen der Vererzung zu untersuchen.

Elektronenstrahlmikrosonden (EMP) Analysen zeigten, dass Sphalerite eine sehr variable Spurenelementzusammensetzung aufweisen. Aufgrund der Verteilungsmuster der Spurenelemente und aufgrund ihrer Korrelationen zueinander wird gefolgert, dass nur ein Teil der gemessenen Spurenelemente direkt im Sphaleritgitter als Substitution für Zn vorkommt (Fe, Cd, Ge). Die anderen Spurenelemente (Pb, As, Tl, Cu) sind vermutlich eher an Nano-Einschlüsse gebunden und sind nicht gittergebunden.

Hochortsauflösende Schwefelisotopenuntersuchungen zeigten sehr variable $\delta^{34}S$ Werte in den untersuchten Sulfiden (-30.4 bis +1.8‰). Über 50% der untersuchten Sulfide weist eine sehr leichte Schwefelisotopensignatur auf (< -20‰). Basierend auf dieser überwiegend sehr leichten Schwefelisotopen-Zusammensetzung wird gefolgert, dass der reduzierte Schwefel überwiegend aus einem Reservoir stammte, wo bakterieller Stoffwechsel zur Sulfatreduktion geführt hat (bakteriogene Sulfatreduktion, BSR). In drei Proben aus der Lagerstätte Bleiberg sind bereits auf kleinem Maßstab (cm Maßstab) deutliche Variationen in den $\delta^{34}S$ Werten von Sulfiden vorhanden. Anhand der texturellen Beziehungen lässt sich für die Sulfide in diesen drei Proben eine Bildungschronologie ableiten. Ein Vergleich zeigt, dass die zeitliche Entwicklung der $\delta^{34}S$ Werte in diesen drei Proben nicht einheitlich ist. Die starken und uneinheitlichen Variationen in $\delta^{34}S$ zeigen, dass ein weiteres Schwefelreservoir an dem Vererzungsprozess beteiligt war. Die Fraktionierung des leichten Schwefelisotops (^{34}S) war in diesem Reservoir deutlich geringer was zu schwerer Isotopenzusammensetzung in den daraus resultierenden Sulfiden führte. Aufgrund dieser geringeren Fraktionierung ist es wahrscheinlich, dass im zweiten Reservoir thermochemische Prozesse zur Sulfatreduktion geführt haben (TSR, thermochemische Sulfatreduktion).

Die Pb-Isotopensignatur von Sphalerit und Galena ist im Gegensatz zur beobachteten Heterogenität in der Spurenelement- und Schwefelisotopenzusammensetzung sehr homogen. Die Pb-Isotopenzusammensetzung der Sulfide weist darauf hin, dass das Erzblei aus der Erdkruste stammt. Mit Ausnahme zweier Proben sind Sphalerit und Galena, die gemeinsam in einer Probe vorkommen, durch nahezu identische Pb-Isotopenzusammensetzung gekennzeichnet. Es ist daher anzunehmen, dass die Metalle für die Bildung von Sphalerit und Galena aus der gleichen Quelle stammen. Es wurden keine systematischen Unterschiede in der Pb-Isotopensignatur von chemisch oder schwefelisotopenchemisch unterschiedlichen Sphaleriten festgestellt. Des Weiteren ist kein Einfluss der Geologie der jeweiligen Lagerstätten auf die Pb-Isotopensignatur zu erkennen.

Da es keinen Zusammenhang zwischen der Spurenelementzusammensetzung und den $\delta^{34}S$ Werten der Sphalerite gibt, wird gefolgert, dass die Spurenelemente und reduzierter Schwefel unabhängig voneinander transportiert wurden. Die Spurenelemente wurden wahrscheinlich zusammen mit den Metallen Pb + Zn, die eine Krustenherkunft haben, transportiert. Die beobachteten Variationen in der Spurenelementzusammensetzung sind wahrscheinlich das Resultat von Wechselwirkungen des Fluids mit den Nebengesteinen während der Fluidzirkulation. Außerdem werden die beobachteten Variationen in der Spurenelementzusammensetzung der Sphalerite als Ergebnis der physikalisch-chemischen Bedingung (z.B. redox Bedingungen, pH, Schwefelspezies) am Ablagerungsort interpretiert.

Um den Zeitraum der Erzbildung zu datieren wurden Rb-Sr Messungen an Sphaleriten durchgeführt. Zusätzlich zu den Daten dieser Studie, wurden noch die Ergebnisse von Rb-Sr Messungen an Sphaleriten (und einem Pyrit) von J. Schneider (z.T. veröffentlich in Melcher et al., 2010) für die Isochronenberechnung berücksichtigt. Drei mögliche Isochronenalter, welche eine gering Streuung zeigen, wurden aus unterschiedlichen Datensets berechnet: *(1)* 204,2±3,2 Ma (n = 5); *(2)* 195,1±2,6 Ma (n = 7); *(3)* 225±2,1 Ma(n = 3). Ein Großteil der Rb-Sr Daten deutet eine epigenetische Erzbildung um etwas 200 Ma (und jünger) an. Allerdings kann die Möglichkeit einer jüngeren (syngenetischen) Vererzungsphase nicht vollkommen ausgeschlossen werden.

Contents

List of Figures

List of Tables

1 Introduction

Within the Drau Range (Eastern Alps, Austria/Slovenia), numerous Pb-Zn deposits are hosted by Triassic platform carbonates. Together with very similar Pb-Zn deposits within the Northern Calcareous Alps and within the Southern Alps, these deposits are summarized as “Alpine Type Pb-Zn mineralization” (*APT*). The Pb-Zn deposit Bleiberg is located in the western Drau Range (about 15 km west of Villach, Austria) and is the type locality for this group of deposits. The mineralization is primarily restricted to the Ladinian – Carnian Wetterstein Formation but smaller Pb-Zn deposits are also hosted by the Anisian Muschelkalk Formation and by the Carnian Raibl sequence. Due to their occurrence within platform carbonates, these deposits are very similar to the large Pb-Zn districts within the Mississippi valley, which are commonly referred to as Mississippi Valley Type (MVT) deposit. However, although the APT deposits are hosted by platform carbonates like the MVT deposits (platform carbonates) and although they share similar characteristics (e.g. ore mineralogy, gangue paragenesis, mineralization textures), the APT deposits are considered unique, since they show some differences to the classical MVT deposits. These comprise the sulfur isotope signature of the sulfides, the lead isotope signature and the trace element content of the sulfides (e.g. Schroll, 2008 cum lit.).

The Pb-Zn deposits within the Drau Range (and also the other APT deposits) are abandoned now. The Bleiberg mine was closed in 1993 due to a decrease in the prices for Pb and Zn and thus lower reserves (Schroll, 2008). In Mezica (Slovenia), the second biggest mine within the Drau Range, mining stopped one year later in 1994 (Recnik, 2011). The Pb-Zn deposits within the Drau Range were studied for decades using very different investigation approaches (Holler, 1936, 1953, Schroll, 1955, 1983, Siegl, 1956, Schulz, 1960, 1985, Schneider, 1964, Maucher & Schneider, 1967, Kostelka, 1972, Schulz et al., 1972, 1977, Bechstädt, 1973, 1975, 1979, Brigo et al., 1977, Drovenik et al., 1980, 1987, Schroll et al., 1983, Köppel & Schroll, 1988, Cerny, 1989, Kucha & Stumpfl, 1992, Zeeh & Staerk, 1992, Zeeh & Bechstädt, 1994, Kuhlemann et al., 1993, 1995) and are still being studied (Rantitsch et al., 1999, Spangenberg et al. 2001, Kucha et al., 2002, 2009, 2010, Schroll & Rantitsch, 2005, Schroll et al., 2006, Spangenberg & Herlec, 2006, Herlec et al., 2010, Melcher et al., 2010, Henjes-Kunst et al., 2012, 2013). The investigations of the Pb-Zn deposits include e.g. petrographic studies of ore and gangue minerals and textures, the study of different isotope systems (e.g. sulfur and lead isotopes), geochemical investigations, investigations of the host rocks. All these investigation approaches actually aimed to put forward a genetic model (epigenesis vs. syngenesis).

The Pb-Zn deposits of the Drau Range have been studied for decades, using very different investigation approaches. Although different authors obtained similar results (e.g. sulfur isotope signature of the sulfides, trace element composition of sphalerite, textural observations), the interpretation of these results is not conformable regarding the mineralization processes and the genesis of the ore deposits. Different isotopic

dating approaches (e.g. Schroll et al., 2006, Melcher et al., 2010) were carried out in order to derive an exact age of ore formation, but no genetic model could be verified or excluded. The latest Rb-Sr dating of sphalerites (+ Fe-sulfides), carried out by J. Schneider, indicate that the ore mineralization occurred at different stages (201±1.5 Ma and 225.2±2.1 Ma) during the Triassic (unpublished results; summarized in Melcher et al., 2010).

This thesis aims to evaluate if a multi-stage mineralization process occurred. For this purpose, a multi-technical approach is considered as most useful. New isotopic Rb-Sr dates of sphalerite are combined with petrographic, chemical and isotopic observations. This combined research approach should show if variable ages are related to systematic variations in mineral assemblage/chemistry and/or isotope chemistry. This procedure aims to detect if a systematic temporal variability in the ore assemblage is present or not. Furthermore, in order to derive information about the homogeneity of the metal source, Pb isotope measurements of ore minerals (sphalerite + galena) were carried out. Currently, only Pb isotope ratios for galena and host rocks are available. High-resolution Pb isotope measurements of (coexisting) galena and sphalerite should show, if the metals originate from the same source. Measurement of Pb isotope ratios is considered as source-indicative, because no fractionation occurs in response to metal leaching, transport and precipitation (Gariepy & Dupre, 1991).

2 Geology & Ore Mineralization

This thesis focuses on Pb-Zn mineralizations, which occur in the Drau Range. The Drau Range is a mountain range in the Eastern Alps (Austria/Slovenia), which extends over a distance of approximately 180 km from the spring of the river Drau in the west (in Eastern Tyrol) and extends across Carinthia towards the Bachern Mountains in Slovenia in the east. The Drau Range strikes parallel to the Periadriatic Lineament, which is a first order dextral strike slip fault and separates the Austroalpine and the Southern Alpine tectonic realms (Figure 2.1).

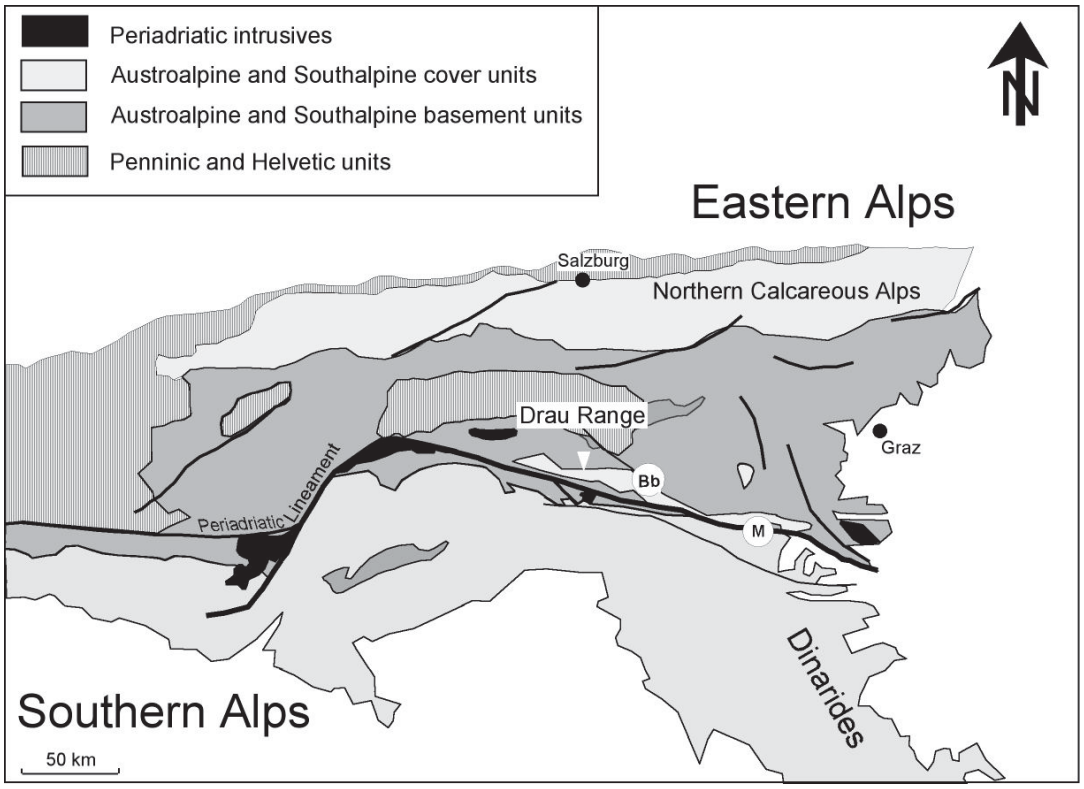

Figure 2.1: Major units of the Eastern Alps (modified after Schroll & Rantitsch, 2005) with the position of the Drau Range. The position of the major Pb-Zn deposits (Bb = Bleiberg, M = Mezica) is furthermore marked.

2.1 Geology of the Drau Range

The Drau Range is part of the Austroalpine nappe system (Schmid et al., 2004), although its position within the Austroalpine is controversially discussed. Traditionally the Drau Range has been considered as an autonomous part of the Upper Austroalpine unit (Tollmann, 1977), which remained in a southern position after detachment of the remaining Upper Austroalpine units which were transported further to the north. However, different authors have revised this traditional classification of the Drau Range more recently (Schmid et al., 2004).

According to Tollmann (1977) the Austroalpine tectonic system is separated into three major tectonic units: Lower -, Middle - and Upper Austroalpine. The Lower and Middle Austroalpine units comprise medium grade metamorphic basement nappes and relicts of Permo-Mesozoic cover sediments. The Upper Austroalpine consists of a nearly un-metamorphosed Permo-Mesozoic sedimentary cover and low-grade basement rocks of Paleozoic age (Greywacke Zone etc.). During the Mesozoic the three major units of the Austroalpine were situated at the shelf on the northern (Adriatic) microplate. The Upper Austroalpine was positioned at the southernmost part of the former shelf (= distal), the Middle Austroalpine in the middle, and the Lower Austroalpine in the northernmost (= proximal) position. In the Lower Cretaceous early Alpine compressional tectonics lead to thrusting of the southernmost Upper Austroalpine units above the Middle - and Lower Austroalpine. Thus large parts of the Upper Austroalpine nappes (e.g., Northern Calcareous Alps, Greywacke Zone) are in a northern position today and only the Drau Range remained in its former southern position. This interpretation is mostly based on similarities between the facies of the Mesozoic units in the Northern Calcareous Alps and in the Drau range and let Tollmann (1977) assume that the Drau Range represents the former southern prolongation of the Northern Calcareous, before tectonic detachment of the Northern Calcareous Alps. Hence, following Tollmann's (1977) model the Drau Range is interpreted as the root zone of the Upper Austroalpine unit from which the remaining parts of the Upper Austroalpine were detached during the Upper Cretaceous and transported towards the north.

More recent studies on the tectonic evolution of the Eastern Alps reduce the extend of the Middle Austroalpine nappes (Frank, 1987) or even avoid the term Middle Austroalpine (Schuster & Frank, 1999) and the Drau Range is not anymore correlated with the Northern Calcareous Alps (Frank 1987, Schmid et al., 2004). Schmid et al. (2004) correlate the Drau Range with the South Alpine sedimentary sequence and proposed that it rather derived from the southern Apulian plate and not from the northern Adriatic plate. According to this new tectonic concept the Drau Range does not represent the detached root zone of the Upper Austroalpine. Schmidt et al. (1991) see the Drau Range as the former western prolongation of the Northern Calcareous Alps (Adriatic microplate). This area was transported along strike-slip faults towards the east, during the Middle Jurassic to the Early Cretaceous, into its present day position. These faults formed in response to the opening of the Piedmont-Ligurian Ocean. .

2.2 Paleogeographic and tectonic evolution of the Austroalpine

According to Schmidt et al. (1991) the Alpine realm was part of the supercontinent Pangaea during the whole Paleozoic until the Early Triassic. Opening of the Neo-Tethys in the Permian to Triassic lead to increasing marine influence with time in the Alpine realm from the southeast to the northwest (Figure 2.2 A). The northwestwards propagation of the Tethyan Ocean is documented by progression of deep-water sediments, which were deposited in Turkey during the Late Permian, in the Dinarides during the Early Anisian and in the Alps during the Middle to Late Anisian. Rifting during the Permian lead to formation of a passive continental margin and the opening

of the Meliata-Hallstatt Ocean, which developed as a separate ocean basin west of the Neo-Tethys. Opening of the Meliata-Hallstatt ocean separated the Apulian from the Eurasian plate (Neubauer et al., 1999, Schmid et al., 2004; Figure 2.2 B). A second rift phase in the Early Jurassic caused the complete breakup of Pangaea and the formation of the Penninic Ocean and the Adriatic microplate (Apulian plate N' of the Meliata-Hallstatt Ocean, Schmidt et al., 1991). The Penninic Ocean was divided into the Valais (in the N) and the Piedmont-Ligurian Ocean (in the S), which were separated by the Brianconnais, a block of continental lithosphere (Schmid et al., 2004). During the Early to Middle Jurassic it came to the separation of the present day Austroalpine units on the Adriatic microplate from the Eurasian and Apulian Plates (Neubauer et al., 1999). The Meliata-Hallstatt Ocean in the southeast and the Piedmont-Ligurian Ocean in the north bordered the Adriatic microplate. Subduction of the Meliata-Hallstatt Ocean started in the Middle Jurassic. In the Early Cretaceous the ocean was completely subducted and the Adriatic microplate became incorporated into the Apulian plate (Figure 2.2 C, Neubauer et al., 1999).

The closure of the Meliata-Hallstatt Ocean led to an Early Cretaceous tectonic event ("Eoalpine"). During this Eoalpine event, W-NW directed thrusting of the Austroalpine units formed the Austroalpine nappe pile (Neubauer et al., 1999). There are contrasting ideas whether the Drau Range was situated on the passive or active margin of the Meliata-Hallstatt Ocean at that time. According to Tollmann (1977) the Drau range was situated at the most distal part of the passive margin of the Meliata-Hallstatt Ocean and the Northern Calcareous Alps were situated in a more proximal position. During the Eoalpine tectonics the Northern Calcareous Alps were detached from the Drau Range and overthrust the adjacent northern units, whereas the Drau Range remained in its position. After Schmid et al. (2004) the Drau Range was positioned at the active margin of Meliata-Hallstatt Ocean and was *not* connected to the Northern Calcareous Alps. After this phase of Eoalpine tectonics the Gosau sediments were deposited (Upper Cretaceous to Eocene), which partly unconformably overlie the Permo-Mesozoic sedimentary cover of the Austroalpine.

South-directed subduction of the Piedmont-Ligurian Ocean in the Late Cretaceous is related to the second tectonic phase, which led to the present day configuration of the Austroalpine nappes and their adjacent tectonic units (Neubauer et al., 1999). The complete closure of the Piedmont-Ligurian Ocean occurred not earlier than the late Eocene (Neubauer et al., 1999). Final continent-continent collision during the Eocene was connected to subsequent shortening until the Oligocene and then to frontal thrusting towards NNE (Neubauer et al., 1999). Back-thrusting towards the south also occurred in the Neogene after activation of the Periadriatic Lineament (Neubauer et al., 1999).

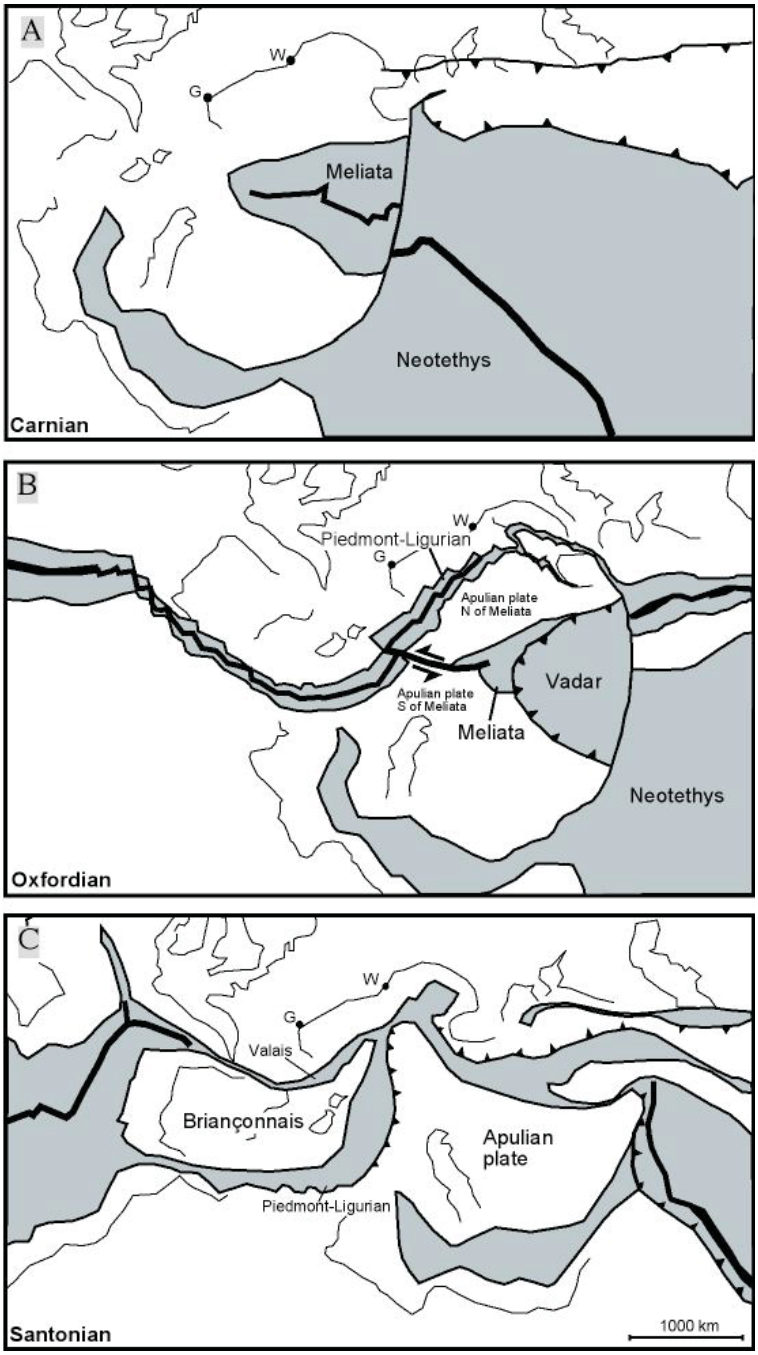

Figure 2.2: A) Position of the Tethys and Neotethys oceans during the Triassic (after Schmid et al., 2004). G = Geneva, W = Vienna.

B) Opening of the Piedmont-Ligurian Ocean during the Jurassic causes the separation of the Adriatic Microplate (= Apulian Plate N' of Meliata) from the Eurasian Plate (Schmid et al., 2004).

C) Reconstruction, showing the distribution of the plates, which were involved into formation of the Alps, during the Cretaceous (after Schmid et al., 2004). The Adriatic microplate is incorporated to the Apulian Plate after subduction of the Meliata-Hallstatt Ocean.

It is important to note that the Drau Range records a different facies evolution than the areas, which are surrounding it. The Late Permian strata in the Drau Range are composed of continental red beds, whereas the surrounding areas show already beginning marine facies (e.g. evaporates). Thus the Drau Range is interpreted as an exotic block in its present day framework (Schmidt et al., 1991).

2.3 Stratigraphy of the Drau Range

The basement rocks of the Drau Range are pre-Alpine and are separated from the Permo-Mesozoic cover by later faults (Ebner, 1997). Four different basement units are distinguished within the Drau Range based on differences in lithology and metamorphic grade: 1. Garnet micaschist – plagioclase gneiss zone; 2. Phyllonite zone; 3. Staurolite-garnet micaschist zone and 4. The Gailtal Paleozoic, which is composed of (Quartz-) Mica-schist with intercalations of greenschist and amphibolite.

The Pb-Zn deposits (occurrences) in the Drau range are hosted by a 4 – 5 km thick Permo-Mesozoic sedimentary sequence, which rests transgressively and unconformably on the weakly metamorphic basement (Rantitsch et al., 1999). Permo-Mesozoic sediments host the Pb-Zn mineralizations, therefore the sedimentary sequence is described more detailed in the following (see Ebner, 1997, cum lit.). The oldest cover sediments in the Drau Range are clastic rocks of the Laas Formation, which is probably of Lower Permian age. Middle Permian sediments are not present in the Drau Range, because of a hiatus. Thus, Permian clastic sediments (Gröden Formation) are directly deposited above the Laas Formation. Following on the Gröden Formation, the clastic Alpine Buntsandstein Formation was deposited during the Scythian. During the late Scythian the paleo-depositional environment of the Drau Range changed, which is marked by the sedimentation of the marine clastic carbonate rocks of the Werfen Formation. The marine sediments of the Drau Range were deposited on the shelf of the former Meliata-Hallstatt Ocean (chapter 2.2). During the Early Triassic limestones (Anisian Alpine Muschelkalk) were deposited. In the Middle Triassic the depositional area of the Meliata-Hallstatt shelf was subdivided into different sedimentation environments, which led to deposition of distinct carbonate facies (e.g. platform carbonates, basin carbonates) during the Upper Anisian to Lower Carnian (i.e. Zwischendolomit, Fellbacher Plattenkalk, Abfaltersbach Formation and Wetterstein Formation). The platform carbonates of the Wetterstein Formation are the main host rocks for Pb-Zn ores and will be described more in detail in chapter 2.5. With the sedimentation of the Carnian Raibl Group in the Ladinian the facies differentiation ended and a more homogenous sedimentation environment was present. The Raibl Group comprises three shale horizons, which are separated by interlayered carbonate rocks. During the Norian deposition of the Hauptdolomit occurred. The Hauptdolomit is a mighty carbonate sequence and composed of partly bituminous dolomites. The youngest sediments in the Drau Range are the Norian to Rhaetian clastic sediments of the Kössen Formation and the Upper Rhaetian carbonate rocks.

2.4 Pb-Zn deposits in the Drau Range

Numerous Pb-Zn mineralizations occur in the Triassic strata of the Drau Range. Approximately 50 Pb-Zn occurrences are listed in the IRIS database of the Geologische Bundesanstalt. However, there are numerous smaller occurrences, which are not included in this compilation, but are documented by mineral collectors (Prasnik et al., 2008). The location of the deposits investigated in the course of this study is displayed in figure 2.3.

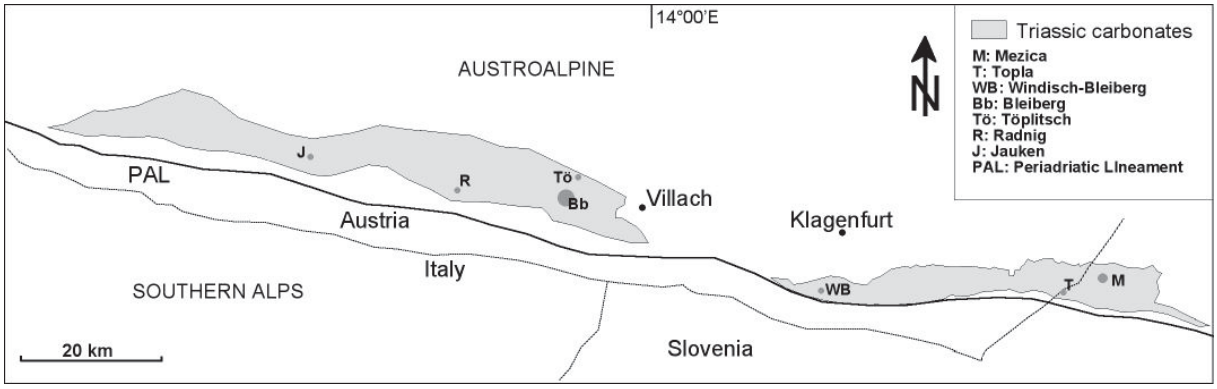

Figure 2.3: Simplified map of the Drau Range (after Schroll & Rantitsch, 2005) showing the positions of the studied Pb-Zn deposits.

2.5 Ore mineralization -the Triassic host carbonates of the Drau Range

The schematic stratigraphic profile (Figure 2.4) displays the positions of the different ore horizons, which are known in the Drau Range. Most of the Pb-Zn deposits are hosted by the Ladinian – Carnian carbonate sequences of the Wetterstein Formation occurring in a similar stratigraphic position as Pb-Zn deposits in the Southern Alps and in the Northern Calcareous Alps (Cerny 1989, cum lit.). Thus, the carbonate rocks of the Wetterstein Formation are the most important host rocks for Pb-Zn mineralizations in the Alps. However, also the Anisian (Alpine Muschelkalk) and the Carnian (Raibl sequence) are locally host rocks for Pb-Zn ore.

In the Drau Range the uppermost ±120 m of the Ladinian to Carnian Wetterstein Formation, exhibit a special facies differentiation (Bechstädt, 1975, 1979, Cerny, 1989, Zeeh & Staerk, 1992, Zeeh, 1994). The Wetterstein Formation consists of platform carbonates, which were formed on the shelf of the former Meliata-Hallstatt Ocean (Ebner, 1997). The uppermost parts of the Wetterstein Formation, which host the most important Pb-Zn mineralizations in the Drau Range, were paleogeographically elevated with respect to the rest of the carbonate platform (Bechstädt, 1975, 1979, Zeeh & Staerk, 1992). Due to cyclic sea level oscillations these high-relief areas were not permanently flooded and emerged sporadically above the sea level (Zeeh, 1994). According to Bechstädt (1975, 1979), Zeeh et al. (1992) and Zeeh (1994), cyclic repeating transgression and regression of the sea led to a special facies differentiation and deposition of characteristic sediments. During times of high sea level, sub- and intertidal sediments were deposited. During times of low sea level supratidal sediments were formed. Periodic drying out of the elevated areas furthermore facilitated synsedimentary karstification and brecciation. The three facies are distinguished as follows (Zeeh, 1994): Subtidal sediments are mainly composed of limestones and/or dolostones; intertidal depositions are characterized by a rapid alternation of packstones, wackestones, mudstones and stromatolites (Zeeh, 1994). Emersion layers

(supertidal sediments) occur above an erosional unconformity and consist of caliche crusts and pisolites.

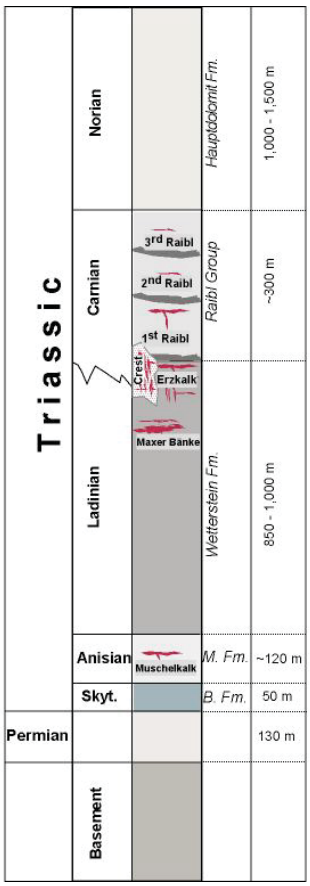

Figure 2.4: Schematic profile showing the positions of the ore-horizons in the different stratigraphic niveaus (modified after Cerny, 1989). M.Fm. = Muschelkalk Formation, B.Fm. = Buntsandstein Formation.

In Bleiberg this special facies is referred as “Erzkalk”, “Bleiberg Fazies” or “Sonderfazies”. These terms have also been used to describe the special development of the Wetterstein Formation in other Pb-Zn occurrences of the Drau Range. In Bleiberg, Schulz (1985) distinguishes nine emersion layers in the uppermost 120 m of the Wetterstein Formation. Schulz (1985) highlighted the importance of emersion layers for concordant Pb-Zn mineralization. During active mining, these emersion layers were important tracer horizons for exploration, because stratiform Pb-Zn ores are connected to them. Therefore, the former miners referred to these emersion horizons as “Edle Flächen”. According to Cerny & Hagemeister (1986), the special facies differentiation of the Wetterstein Formation can be traced over a distance of approximately 160 km from Urslja Gora (Slovenia) in the east to Jauken in the west. The ore mineralizations in the deposits Mezica, Windisch Bleiberg, Bleiberg, Radnig and Jauken are connected to this special facies type (Cerny & Hagemeister, 1986).

In addition to the Erzkalk horizon, the “Maxer Bänke” forms a further important ore horizon within the Wetterstein Formation at Bleiberg (Schroll, 2008, cum lit.). The Maxer Bänke occur in a deeper stratigraphic position with respect to the Erzkalk horizon. They are positioned 170 – 360 m below the 1st Raibl shale (Cerny, 1989). The

lithofacies from the Maxer Bänke differs from that of the Erzkalk horizon. According to Hagenguth (1984), sediments of the Maxer Bänke were deposited in a lagoon, which was characterized by a highly irregular bottom relief. Due to this irregular relief the sedimentation environment within the lagoon was subdivided into six different microfacies, which are indicative for sub- inter- and supratidal depositional environments. Hagenguth (1984) reports ore mineralization within (marly) dolomites from all three facies. Ore mineralization, which is hosted by subtidal dolostones is sphalerite rich and often shows a fine bedding of stratiform ore minerals. Ore mineralization in the intertidal facies is still sphalerite rich, but the sphalerite grains are larger and schalenblende textures are more common. Besides, anhedral galena is present in the intertidal facies. The supratidal facies often hosts discordant mineralizations, e.g. schalenblende in emersion cracks. Thus, depending on the host (micro) facies, the ore mineralization within the Maxer Bänke horizon can be concordant and discordant. However, no larger (> 100m) stratiform ore-bodies, like in the Erzkalk horizon, are present in the Maxer Bänke (Hagenguth, 1984). The Maxer Bänke horizon was mined in the western part of the Bleiberg mine. According to Hagenguth (1984), the Maxer Bänke lithofacies is also present in Mezica. However, there is no report of any ore mineralization from the Maxer Bänke in Mezica.

For the Bleiberg deposit another special facies type in the Wetterstein Formation, the crest facies ("Schwellenfazies"), is distinguished (Cerny, 1989, Schroll, 2008). The crest facies hosts a high-grade sphalerite rich breccia-type mineralization and occurs in the hanging parts of the Wetterstein Formation locally extending up to the 1st Raibl shale (Schroll, 2008, cum lit.). Crest horizons are only described from Bleiberg. Four individual ore bodies (i.e. Kalkscholle, Josefischolle, Riedhardtscholle and Revier Erlach) in the western part of the Bleiberg mine belong to the crest facies. The mechanisms, which lead to formation of the crest facies, are discussed controversially (e.g. Bechstädt 1973, Cerny, 1989, Schulz 2006) because Zn-Pb mineralization in the crest facies occurs in the breccia cement as well as in the breccia components. The latter observation requires brecciation of already existing ore mineralization. Supporters of syngenetic models suggested that synsedimentary tectonics caused brecciation and resedimentation of Pb-Zn ores (e.g. Cerny, 1989, Schulz, 2006). According to Cerny (1989), the crest facies was situated at the southern margin of the former elevated Erzkalk area. This marginal paleogeographic position in combination with synsedimentary tectonic activities caused gravitational slumping and led to the formation of massive ore breccia bodies at the margins of the former Erzkalk elevation. Schulz (2006) also favored a similar formation mechanism for the crest facies but related breccia formation and slumping to several tectonic events. In contrast, Bechstädt (1973) suggested that the brecciation, which is characteristic for the crest facies, is related to ore formation in a karst system due to collapse of earlier formed ore minerals into karst cavities and their cementation by later mineralizing fluids. According to the latter model formation of the Crest breccia ores is a purely epigenetic.

Besides the ore horizons in the Wetterstein Formation also the Anisian strata (Alpine Muschelkalk) and the carbonate interlayers between the Carnian Raibl shales host

locally Pb-Zn mineralization. However, mineralization within these stratigraphic horizons is rather rare. Hence, these ore horizons were always of less economic interest. Only about 10% of the known Pb-Zn occurrences in the Alps are hosted by the Anisian Muschelkalk Formation (Cerny, 1989 cum lit.). In the Drau Range the Topla deposit (Slovenia) was the most important Anisian Pb-Zn mineralization, which was mined economically. Additional Ansian Pb-Zn mineralizations in the Drau Range are e.g. Kolm, Kellerberg and Bleiwände. Deposition of the Alpine Muschelkalk occurred in a shallow marine environment. Pb-Zn mineralization within the Anisian is connected to dolostones in the Alpine Muschelkalk Formation, which occur 150 – 170 m above the Werfen Formation. Pb-Zn mineralization within the Anisian strata is generally stratabound and can be traced horizontally over 100 – 350 m. The easternmost (Topla) and westernmost (Kolm) Pb-Zn occurrences are rather Zn-rich. The Ansian occurrences that are located along the northern margin of the Drau Range (e.g. Kellerberg, Bleiwände), are rather Pb dominated.

Pb-Zn mineralization within the carbonate rocks of the Carnian Raibl Group was also of minor economic importance. It occurs for example at Bleiberg, Förolach and Mitterberg. The Raibl Group consists of a three times repeating schist-carbonate alternation (Bechstädt & Schweizer, 1991). Deposition of the 1st Raibl shale stopped the platform evolution of the Wetterstein Formation. Cyclic tectono-eustatic sea level oscillations were the driving mechanism for the alternating schist carbonate deposition. The carbonate layers formed at sea level lowstands whereas the three clastic shale horizons formed during sea level highstands (Bechstädt & Schweizer, 1991). Pb-Zn mineralization in the Raibl Group is stratabound and restricted to the carbonate horizons. All three Raibl carbonate horizons can be ore bearing. In Bleiberg the 1st Raibl carbonate was economically mined, but also the 3rd carbonate layer was locally mined in the Rubland Unit, which occurs about 4.5 km north of Bleiberg (Cerny, 1989). According to Cerny (1989), the three ore horizons in the Raibl Group are rather enriched in Zn and contain barite and fluorite as gangue constituents. Schulz (1958, 1960) described the ore mineralization in the 1st Raibl carbonate layer as “subparallel” to the bedding. Furthermore, Schulz (1958, 1960) reported mineralized breccia components, which formation he attributed to deformation processes, which occurred coeval to the diagenesis.

3 Analytical Methods & Samples

3.1 Petrographic investigation

The petrographic investigation of the mineral assemblages from the Pb-Zn deposits in the Drau Range and a few other Alpine occurrences includes 120 polished (thin) sections. Detailed studies of the ore-gangue assemblage were performed using standard reflected and transmitted light microcopy.

3.2 Cathodoluminescence microscopy

In order to gain first information on chemical differences of the gangue mineralogy and the sphalerites, 46 thin sections were investigated using cathodoluminescence (CL) techniques. CL microscopy was performed at the BGR Hannover, using a hot cathode (Neuser HC2-LM) coupled to an Olympus BHMJ microscope. CL observations were carried out with a beam voltage of 14 kV and a filament current of 1.7 kV. In order to avoid sample damage due to overheating, the beam current did not exceed 0.2 µA during CL observations.

Using the Neuser instrument, CL microscopy can only be carried out on polished thin sections and does only provide information on translucent minerals. Hence, sphalerite is the only ore mineral, which can be investigated using CL microscopy. In order to assure electrical conductivity of the sample surface, the polished thin sections were sputtered with carbon in advance. CL activity of a given mineral depends on (1) the chemical composition; e.g., high Fe-contents are considered as CL-inhibiting and (2) on the crystal structure; e.g., defects in the crystal lattice are considered as CL-promoting (Miller, 1989). Thus, CL is a first simple method for the characterization of sphalerites and is also helpful for distinguishing the different kinds of gangue carbonates present in a sample.

3.3 Quantitative Evaluation of Minerals by Scanning Electron Microscopy (QUEMSCAN)

The ore gangue paragenesis of two samples from the Bleiberg mine was additionally investigated using QUEMSCAN (**Q**uantitative **E**valuation of **M**inerals by **Scan**ning electron microscopy) techniques. QUEMSCAN allows the illustration of delicate differences in the ore-gangue paragenesis and is therefore a further tool in order to display differences in the sample assemblage. The analyses were carried out at the FEI laboratories in Brisbane (Australia) by L. Salazar and G. Gloy. The QUEMSCAN investigations were performed on two polished thin sections using a FEI Quanta 650F SEM instrument equipped with two Bruker EDS detectors. Data processing was done with the QUEMSCAN software. The analyses were carried out in FieldImage mode.

The two samples were scanned automatically using 10 and 5 mm spot size (=pixel size). The results of the QUEMSCAN analyses are shown in false color images in direct comparison with photographs of polished slaps of the respective sample (chapter 4.4, Figure 4.21; 4.27).

3.4 Major and trace element analyses of sphalerites

3.4.1 Electron Microprobe Analyses

Major and trace element compositions of sphalerites were mainly determined by electron microprobe (EMP) analyses using the JEOL JXA 8200 superprobe of UZAG Steiermark installed at the Chair of Resource Mineralogy, Montanuniversitaet Leoben (Austria) and a CAMECA SX 100 probe at the Federal Institute for Geosciences and Natural Resources (BGR) in Hannover (Germany). EMP techniques allow the non-destructive analyses of minerals on the micro-scale (µm) and can be performed on all solid materials, which tolerate vacuum conditions.

EMP analyses were performed on 59 polished (thin) sections, which were coated with carbon in advance, in order to ensure electrical conductivity of the surface. Sample selection and the selection of points of interest (measurement points) were previously performed using standard transmitted and reflected light microscopy.

For EMP measurements an electron beam (approximately 1 µm diameter) is focused on the sample surface, where among others element specific X-Rays are generated. X-rays of specific wavelengths are emitted for each element. The intensity) of the signal is proportional to the concentration of the given element. During EMP measurements information about the chemical composition of a mineral can be obtained in different ways:

- Visual information via backscattered electron images (BSE); textural features, like mineral zonation due to chemical differences, become visible due to the number of back scattered electrons, which depends on the atomic weight; i.e. minerals/zones composed of heavier elements display lighter colors.
- Information via energy-dispersive analyses (EDS); a solid state detector collects and counts all emitted X-rays at once. In this study the EDS was only used to obtain qualitative information about chemical composition.
- Quantitative information via wavelength dispersive analysis (WDS); the signal of the generated element-specific X-rays is counted and compared to a standard of known composition, thus allowing the quantification of the chemical element of interest.

EDS analyses are very fast, but – if carried out in standardless mode - not very precise and have comparably high detection limits. WDS measurements are much more precise, but require more time because for WDS analysis of each specific element, the

generated X-rays must be counted through a spectrometer. Modern electron microprobes are equipped with several (4-5) spectrometers and with different analyzing crystals. Selection of spectrometer and the analyzing crystal depends on the element to be measured.

$$L.O.D.[ppm] = \frac{\frac{1}{I_{netSTD}}}{mass(\%)_{STD}} \sqrt{\frac{2 * I_{back}}{t_{back}}} \qquad \textit{Formula 3.1}$$

For trace/minor element analyses of sphalerites a limit of detection as low as possible is required and thus the EMP analyses were carried out in WDS mode. The detection limit during EMP measurements is primarily a function of the intensities of the background counts in the unknown (sample) and of the peak counts in the standard (Scott & Love, 1983). A long counting-time is required to reduce the detection limit for trace element analyses with the EMP. The limits of detection were calculated automatically with the software of the respective microprobe. The JEOL software calculates the limit of detection (L.O.D.) using formula 3.1. For calculation of the detection limits the software considers *1.)* average X-ray intensities of the background (I_{back}), *2.)* counting time of the background signal (t_{back}), *3.)* intensity of the characteristic X-ray of the analyzed element on the standard (I_{netSTD}) and *4.)* mass concentration of the element in the standard sample)$mass(\%)_{STD}$).

Table 3.1: Measurement conditions and used standards for EMP analyses (LOD = limit of detection; P/BG = counting time on the peak and counting time on the background).

	CAMECA SX100 (30kV, 40nA)					JEOL JXA8200 (20 kV, 40nA)				
	Line	**Crystal**	**Time [s] P/BG**	**Standard**	**LOD [ppm]**	**Line**	**Crystal**	**Time [s] P/BG**	**Standard**	**LOD [ppm]**
S	Ka	PET	10/5	ZnS	400	Ka	PETJ	15/5	ZnS	80
Zn	Ka	LLIF	10/5	ZnS	560	Ka	LIFH	15/5	ZnS	130
Fe	Ka	LLIF	30/15	FeS	100	Ka	LIFH	20/10	CuFeS2	50
Cd	La	PET	120/60	Cd	240	La	PETH	90/40	Cd	30
Pb	Ma	PET	10/5	PbS	2000	Ma	PETJ	20/10	PbS	250
Ge	Ka	LLIF	120/60	Ge	130	La	TAP	90/40	Ge	40
As	La	TAP	140/70	AsGa	250	La	TAP	90/40	PtAs	50
Cu	Ka	LLIF	130/75	Cu	110	Ka	LIFH	90/40	CuFeS2	60
Tl	Ma	LPET	140/70	Tl	670	Ma	PETH	90/40	TlBrI	300

Besides several trace/minor elements (Table 3.1), also the major elements Zn and S were analyzed in sphalerite. For the JEOL JXA 8200 superprobe at Montanuniversitaet Leoben, best measurement results (low detection limits) were achieved using a beam current of 40 nA and an acceleration voltage of 20 kV. For trace/minor element analyses of sphalerites using the CAMECA SX 100 (BGR Hannover) an analytical routine with 30 kV and 40 nA was established. The measurement conditions and used standards for both microprobes are instrument/laboratory specific and listed in Table

3.1. The limit of detection reported for both microprobes is very different. Hence, the lowest concentrations of around 50 ppm measured with the JEOL EMP are considered carefully. However, it is assumed that the JEOL microprobe detected low concentrations of the respective elements which concentrations are in the > 50 to 100 ppm range. The results of the EMP measurements are partly presented within chapter 4.2 and 4.4. The complete EMP dataset is furthermore presented within the Appendix (Tables 4 – 13).

3.4.2 Laser Ablation ICP MS Analyses

Laser Ablation Inductively Coupled Plasma Mass Spectrometry (*LA ICP-MS)* analyses of minor/trace elements on two samples were performed by Helene Brätz at the GeoZentrum Nordbayern (Friedrich-Alexander Universität Erlangen-Nürnberg). LA ICP-MS analyses have been commissioned in order to verify the EMP results. LA ICP-MS is a powerful tool for in-situ geochemical analyses, because it can be performed on solid samples and provides a very good detection limit in the ppb range.

In the GeoZentrum Nord Bayern an UP193Fx Argon Fluoride Fast eXcimer laser ablation system (New Wave Research) is used, which is coupled to an Agilent 7500i ICP-MS. The laser has a wavelength of 193nm, this reduces mechanical spalling or thermal melting and sputtering of melt droplets during the ablation process, which may lead to a reduced fractionation of the measured elements and a more constant ablation of the material (Moenke-Blankenburg et al., 1992, Darke & Tyson, 1993, Heinrich et al., 2003). The ablated material was transported by helium (0.65 L/min) carrier gas into the mass spectrometer. In the mass spectrometer the sample was dissociated, atomized and ionized and converted into a cloud of positively charged ions by a high-temperature argon plasma and measured by mass spectrometry.

The laser ablation was operated with a pulse rate of 15 Hz. The spot size was 25µm in diameter. During LA ICP-MS analyses the concentrations of ^{29}Si, ^{33}S, ^{34}S, ^{66}Zn, ^{68}Zn, ^{51}V, ^{55}Mn, ^{57}Fe, ^{59}Co, ^{63}Cu, ^{65}Cu, ^{69}Ga, ^{71}Ga, ^{75}As, ^{109}Ag, ^{111}Cd, ^{115}In, ^{118}Sn, ^{182}W, ^{203}Tl, ^{205}Tl, ^{207}Pb, ^{208}Pb and ^{209}Bi were measured. Calibration of the measurements was performed with an external standard (MASS-1, USGS) and Zn as an internal standard. Analyses time for each measurement was 50 s, with 25 s on the background (laser switched off) and 25 s on the sample (laser switched on). To check for interferences among the elements Cu, Ga, Tl and Pb several isotopes of these elements were measured. Unfortunately, the MASS-1 standard is not doped with Ge and thus it could not be measured using LA-ICP MS. Raw data were processed using the GLITTER (van Achterbergh et al., 2000) on-line software. The uncertainties of the analyses (ppm) are reported on the 1σ level. The results of the LA-ICP MS measurements are graphically presented in chapter 4.2. The full LA-ICP MS dataset can furthermore be seen in the Appendix (Tables 14, 15).

3.5 Sulfur isotope analyses of sulfides

Sulfur isotope analyses were performed at the Scottish Universities Environmental Research Centre (SUERC) in East Kilbride (UK) at the Stable Isotope Laboratory in cooperation with Adrian Boyce. All sulfur isotope analyses are given in standard $\delta^{34}S$ notation ($^{34}S/^{32}S$) in per mill (‰) relative to the Canyon Diablo troilite (CDT).

For the sulfur isotope analyses, polished slabs (counter-pieces of sections) were prepared from selected samples. Sample selection was based on the previously performed petrographical and geochemical investigations. The samples were selected in order to analyze a representative sample set, with respect to *(1)* the different deposits of the Drau Range and *(2)* the different ore bearing stratigraphic positions/ore horizons within major deposits. Sulfur isotope analyses were carried out on the sulfides sphalerite, galena, Fe-sulfides in 18 different samples from several Pb-Zn deposits in the Drau Range (Appendix, Table 16).

Sulfur isotope analyses were carried out by conventional and *in situ* laser extraction:

1. Drilling of pre-selected (micro) areas, by using a standard dentist drill or a MICRO MILL drilling system connected to a microscope. The dentist drill affects areas of at least 2 mm^2 and is therefore only suitable for large sulfide grains or homogenous sulfide accumulations. The MICRO MILL drilling system allows much more precise sampling of spots or lines (or any pre-defined path) < 1 mm. Micro-drilled sulfide samples were combusted to SO_2 by a reaction with Cu_2O in excess at 1070°C for 25 minutes as described by Robinson & Kusakabe (1975). Subsequent to combustion, cryogenic purification in a glass extraction line was carried out.
2. For precise sampling using a laser beam, the samples were inserted into a sample chamber, which was evacuated and than filled with excess O_2. For in-situ sampling a SPECTRON LASERS 902Q CW Nd-YAG laser was used (1-W power). To gather enough material for later analyses, trenches were ablated with a width of around 25 to 50 µm and a length between 2 to 14 mm. The excess O_2-environment in the sample chamber enabled direct oxidation of the sulfides to SO_2. The resulting SO_2 gas was than carried into a miniature glass extraction line, where it was cryogenically purified.

Cryogenic purification of the SO_2 gas was necessary to remove contaminations like H_2O, N_2 and CO_2. It was carried out in a glass extraction line and includes several freezing and heating steps. In the first step H_2O is removed by an acetone/CO_2 slush ice trap. In additional freezing and heating steps in several traps, which were performed with liquid nitrogen, N_2 and CO_2 were removed.

Subsequent to purification, the SO_2 gas was analyzed in a VG SIRA II (laser) or a THERMOSCIENTIFIC MAT253 (conventional) gas-source mass spectrometer.

Conversion of the raw δ^{66}_{SO2} data to $\delta^{34}S$ values, were performed by calibration with international NBS-123 (+17.1‰) and IAEA-S-3 (-31.5‰) as well as SUERC's international lab standard CP-1 (-4.6‰). Reproducibility of the analytical results (around ±0.2‰ during these analyses) was controlled through replicate measurements of these standards. All data are presented as true $d^{34}S$, and if necessary corrected using the small mineral-dependent laser fractionation factors calculated by (Wagner et al. 2002).

3.6 Rb-Sr isotope analysis of sphalerites

Rb-Sr isotope analyses were performed in order to allow direct isotopic dating of the sphalerite formation process(es). Rb-Sr dating of sphalerite was performed on seven handpicked sphalerite separates (Table 4.12) obtained from well-characterized sample groups. The samples are grouped according to different locations, to differences in geochemistry and/or sulfur isotope chemistry. This procedure should allow a more detailed interpretation of likely Rb-Sr isochron relations of the sample groups in terms of formation and/or recrystallization processes and then, of course, of the significance of the obtained Rb-Sr ages.

3.6.1 Chemical & mechanical pre-treatment of the sphalerite separates

Rb and Sr occur in ultra-trace amounts in sphalerite. Their incorporation mechanism in sphalerite is not fully understood yet (Pettke & Diamond, 1995). As a consequence of the very small Rb and Sr concentrations, the analysis is prone to enhanced blank contaminations, which might occur during chemical processing of the samples and mass spectrometric analysis of Rb and Sr. Hence, sample preparation and analytical techniques as used for routine Rb-Sr isotope analyses are unsuitable for Rb-Sr dating of sphalerites and have to be adjusted in order to minimize blank effects. For this purpose thoroughly cleaned labware, ultra-pure reagents (i.e. sub-boiling distilled acids, Milli-Q water) have to be used. Chemical pretreatment and processing of the sphalerites were performed in a clean-air lab. Sphalerite preparation for Rb-Sr analysis and isotope measurements by thermal ionization mass spectrometry (TIMS) were done at the Federal Institute for Geosciences and Natural Resources (BGR), Hannover in collaboration with F. Henjes-Kunst (BGR Hannover). The cleanness of all reagents and tools were regularly checked by blank analysis. A further problem for the Rb-Sr isotope analysis of sphalerite is introduced by the presence of trapped fluid inclusions and/or intergrowth with other minerals with elevated Rb and/or Sr contents. Because of the very low concentrations of Rb and Sr in sphalerite itself, any solid or fluid inclusion contaminant can greatly disturb the Rb-Sr isotope system of the host sphalerite and must therefore be carefully removed prior to chemical digestion and isotope analyses. Removal of fluid inclusions and intergrowths of solids is performed in several chemical and mechanical steps, which are described in the following. We used a modified version of the crush-leach procedure, which is based on the procedure described by Nakai et al. (1990, 1993), Brannon et al. (1991, 1992) and Christensen et al. (1995a, 1995b).

Prior to grinding down, handpicked sphalerite separates with weights of 50 to 100 mg were chemically treated with different acids in order to reduce the amount of mineral intergrowths (e.g. carbonates, silicates). Firstly, the sphalerite fragments were soaked with a 3 m acetic acid on a hot plate (80°C), until all reactions stopped (no more bubbles). Afterwards the leachates were removed and the residuals were rinsed several times with H_2O. In a next step, the residuals were put with 2 – 3 n HF on a hot plate (up to 120°C) for several minutes. The leachates were again discarded and the residuals were carefully washed with H_2O. In a third step, the residuals were leached with 2 -3 n HCl on a hot plate (120°C) for several minutes. Afterwards, the leachates were removed and the residuals were again rinsed with H_2O.

Subsequent to the chemical pre-treatment, the sphalerite residuals were mechanically crushed using a boron-carbide (BC) mortar and pestle. Boron-carbide is a very hard and chemical inert material, which can be cleaned using aggressive acids. Mechanical treatment of the sphalerite residues was performed in order to open and remove any trapped fluids. In several steps the sphalerite particles were carefully crushed down to powder size in millipore water. Afterwards the powder sphalerite was separated from the H_2O (leachate) by centrifugation. The powdered sphalerite was then repeatedly rinsed with H_2O. In the case that analysis of the leachates is also required, the H_2O fractions have to be collected during the various preparation stages and have to be evaporated until dryness. We did not consider the fluid inclusion fractions for further isotope analyses, as we were not sure that the fluid inclusions are primary ones.

The powdered sphalerites were then again chemically treated, in order to remove foreign mineral components (inclusions like carbonates, silicates). The powdered sphalerite was leached in subsequent steps with 3 n HF and 2.5 n HCl, each for several minutes and followed by separation of the leachates from the residual using a centrifuge and subsequently rinsing with H_2O. Afterwards, the sphalerite residuals were transferred into a screw-top Savillex® beaker and evaporated to dryness on a hot plate at 60°C.

The sample weight of the sphalerite residuals was determined prior to chemical decomposition. In order to allow for determination of the Rb and Sr concentrations (via the isotope dilution method), a highly enriched mixed ^{87}Rb-^{84}Sr spike calibrated against a Rb-Sr shelf solution prepared from MERCK Certipur™ Rb and Sr reference solutions was added to the sample prior to digestion. In a first digestion step, the sphalerite residuals were treated with 6.1 n HCl at 130°C for several hours. If no further H_2S formation is evident the top of the beaker can be closed during this step. Afterwards, the solutions were dried on a hot plate at 90°C. The second digestion step was performed with 3 m HNO_3 at 130°C for several hours with the top of the beaker closed. Afterwards the solutions were evaporated at 90°C to dryness. The samples were taken up with 0.4 ml of a 3 m HNO_3 for chemical separation of Sr, Rb and Pb.

Chemical separation of Sr, Rb and Pb was performed on PFA columns. In a first step, the Sr fraction was separated using 200 µl of Sr resin (EICHROM®) and evaporated to dryness. This Sr fraction is ready for isotope measurements. Afterwards, for separation of the Rb fraction, the remaining solution was dried and picked up with 1.75 n HCl which was then cleaned by using 250 µl BIORAD® AG 50 W-x12 cation resin. This Rb fraction was dried and is ready for isotope measurements. The Pb fraction for isotope measurements was obtained from the remaining solution with 100 µl Pre-filter resin (EICHROM®).

3.6.2 TIMS analysis of Rb and Sr

For TIMS analysis, the Sr fractions were loaded onto single W filaments using a Ta-HF solution as activator (Birck, 1986, Charlier et al. 2006) in order to enhance Sr ionization. Isotope measurements were performed on a ThermoFinnigan Triton TIMS in static mode. Rb was checked via ^{85}Rb throughout the Sr isotope measurements. If present the ^{87}Rb interference on ^{87}Sr was corrected for using an $^{85}Rb/^{87}Rb$ of 2.6 as frequently determined at the onset of Sr ionization at c. 1250°C of the W filament. Sr isotope abundances were measured at signal intensities of > 750 mV for ^{88}Sr (10^{11} Ohm resistor) for generally 120 scans, grouped into 10 blocks. Basement registrations were performed in between the blocks. The measured Sr isotope ratios were corrected for spike contribution and normalized to $^{86}Sr/^{88}Sr = 0.1194$ in an offline calculation. Repeated measurements of the NBS SRM 987 Sr isotope standard using Sr element concentrations and preparation techniques similar to those of the sphalerite Sr fractions yielded 0.710197 ± 0.008% (2 RSD).

Rb was loaded onto a Re side filaments with the addition of 1 µl 1n $H_3PO_4$and measured in double Re filament assembly in static mode on a Finnigan MAT261 TIMS. The mass spectrometric fractionation was controlled externally by repeated measurements of Rb standard preparations using element concentrations, which are similar to those of the samples.

The Rb and Sr element concentrations were calculated from the TIMS data by standard isotope-dilution algorithms. Total procedural blank amount to c. 50 pg and 15 pg for Sr and Rb, respectively, as determined by repeated blank determinations. The $^{87}Sr/^{86}Sr$ of the chemical blank was determined to 0.70928. The element concentrations and the isotope ratios were corrected for blank contribution. The uncertainties in the Sr and Rb concentrations include the error of the blanks plus the errors in the measured isotope ratios. The uncertainties in the $^{87}Rb/^{86}Sr$ additionally include the error of the spike calibration. For the individual analyses, the uncertainties in the element concentrations range from 0.23 to 0.58% for Rb and from 0.009 to 0.83% for Sr while the uncertainties in $^{87}Rb/^{86}Sr$ range from 0.61 to 1.04%. The error of the $^{87}Sr/^{86}Sr$ recalculated to an age of 205 Ma (see chapter 5.3) varies between 0.004 and 0.12%. All errors are quoted at the 2σ level unless otherwise stated. The IUGS-recommended constants (Steiger & Jäger, 1977) were used for recalculation of the Rb-Sr isotope data. Recalculation and graphical presentation of the Rb-Sr isotope data was done using Isoplot 3.7 (Ludwig, 2009).

3.7 Pb isotope analysis of galena and sphalerite

Analysis of Pb isotope ratios was carried out on seven handpicked galena fractions, originating from five samples and furthermore on ten handpicked sphalerite separates from seven samples (Table 4.4). Pb isotope analysis was performed in order to estimate if the metal for mineralization originated from different sources.

Chemical processing of the handpicked galena and sphalerite separates and measurement of the Pb isotope ratios were carried out in collaboration with F. Henjes-Kunst at the BGR Hannover. The Pb isotope measurements were performed on a ThermoFinnigan Triton TIMS in static mode.

The galena separates were dissolved in ultra-pure hot HCL (6n) and the Pb isotope measurements were performed directly on c. 100 ng Pb aliquots of these solutions. Measurement of Pb isotope ratios and concentrations of sphalerites were performed on the element fractions, which were obtained during the separation of Rb and Sr of the sphalerite residuals (chapter 3.6).

In a first step the Pb concentrations of the samples were determined using the isotope-dilution method. Subsequently, highly precise Pb isotope ratio measurements were conducted by using the double-spike (Pb-DS) technique. We used the SBL74 double spike, which is enriched in ^{207}Pb and ^{204}Pb. The SBL74 was originally produced and calibrated against the NBS892 standard (^{208}Pb/^{206}Pb = 1.00016) jointly between the National Oceanography Centre (Southampton, UK), Ifremer (Brest, France) and the former Danish Lithosphere Centre (Copenhagen, Denmark). The SBL74 batch, which is used at the BGR Hannover, has been commercially obtained from the Ifremer. The reduction of the double-spike data uses the average baseline corrected raw data of 5 - 10 data blocks (= 50 – 100 scans with 10 integrations each) and follows the algorithm of Johnson & Beard (1999 cum lit.). Using the double-spike ratios of Ifremer (Dosso et al., 2002), values for the double-spiked NBS981 common Pb standard measured along with the samples are ^{206}Pb/^{204}Pb = 16.9418 ± 0.0011, ^{207}Pb/^{204}Pb = 15.4983 ± 0.0013, ^{208}Pb/^{204}Pb = 36.7224 ± 0.0041 (n=8). These values compare well to published double-spike and triple-spike isotope data for the NBS981 (Galer, 1999, Thirlwall, 2000, 2002, Baker et al., 2004, Timm et al., 2011). Prior to loading of Pb on rhenium single filaments with colloidal silica gel (Gerstenberger & Haase, 1997), the samples were split into a ~100 ng fraction for the unspiked measurement (IC) and a ~10 ng fraction for the spiked measurement (ID-DS), which involves the addition of 3 µl of SBL74 (~13ng) to the sample Pb in order to obtain an optimized ^{204}Pb/^{206}Pb ratio of close to 1 in the sample-spike mixture. Total Pb chemistry and TIMS preparation blanks were less than 20 pg and thus are considered as insignificant. The 2 sigma uncertainties of the isotope analyses were obtained from repeated standard (NBS981) measurements.

In order to allow comparison of our data with already published Pb isotope data from Bleiberg (Köppel & Schroll, 1978, 1988, Köppel, 1983, Schroll et al., 2006), the measured Pb isotope ratios were corrected to the NBS981 reference values as used in these older publications. The correction values reported by Cumming et al. (1987) were used. The not recalculated isotope ratios are listed in the appendix (Table 17).

3.8 Samples

Mining of carbonate-hosted Pb-Zn deposits in the Eastern and Southern Alps has ceased in the beginning of the 1990ies. Access to the largest Pb-Zn mine (Bleiberg) is restricted due to safety reasons (upper levels) or impossible (flooded lower levels). In Mezica parts of the former mining area can still be accessed, but outcropping mineralization is nearly absent. Hence, the studied samples were mostly obtained from private or university collections or were collected on dumps, with the exception of Mezica where rock fragments from the closed underground mine were recovered. Concerning the materials from collections, it was tried to obtain samples for which a detailed description of the location (stratigraphic position, position within the deposit) was available present. The disadvantage of this approach is, that information on large-scale textures (e.g. orientation on the outcrop scale) is missing.

Samples, which were investigated for this study originate from:

- Bleiberg (from various collections; material from various ore horizons, stratigraphies, locations; Appendix Table 1)
- Mezica (collected in various districts of the former mine + samples obtained from S. Fajmuth; Appendix Table 2)
- Topla (own collection of dump material)
- Jauken (own collection of dump material)
- Töplitsch (own collection of dump material)
- Windisch Bleiberg (collection of E. Schroll)
- Radnig (collection of E. Schroll),
- Zunderwand; small Anisian Pb-Zn occurrence in the Nock Mountains, Middle Austro Alpine (sensu Tollmann, 1977)
- Raibl; Pb-Zn deposit in the Southern Alps (Italy, Udine); hosted by the Wetterstein Formation (BGR collection)
- Lafatsch; Northern Calcareous Alps (Upper Austroalpine, sensu Tollmann, 1977), Karwendel Mountain Range, hosted by the Wetterstein Formation (BGR collection)

A summary on the most extensive studied samples, which shows a brief description and the carried out investigation approaches is given in the Appendix (Tables 1 - 3). The position of the samples, which originated from the Drau Range are marked within the sketch map in chapter 2 (Figure 2.3).

Some samples were obtained at a late stage of this PhD project and were therefore not studied with all different techniques. Hence, no sulfur isotope measurements of the Radnig and Windisch Bleiberg samples could be carried out.

4 Results

4.1 Ore textures

The investigations were focused on sphalerite textures, geochemistry and isotope chemistry. Compared to galena (the second major ore mineral) textural variations of the sphalerites are more prominent. Thus sphalerites are more appropriate for texture-based investigations. This chapter presents the results of the textural observations.

4.1.1 Macroscopic and microscopic mineralization textures

Ore mineralization within the Drau Range shows a considerable textural diversity on both the macroscopic and microscopic scale. Especially the Bleiberg deposit exhibits a distinct diversity in textures. A selection of characteristic textures and mineralization types for samples from the Bleiberg deposit is shown in Figure 4.1 a – d:

- Layered/bedded mineralization: ore minerals (especially sphalerite) are enriched in parallel layers (Figure 4.1 a). Such laminated ores were observed in samples from the Maxer Bänke and the Erzkalk horizon in Bleiberg.
- Massive mineralization: samples consisting nearly completely of ore minerals, which form massive aggregates (Figure 4.1 b).
- Breccia-mineralization: ore minerals form either interstitially between host-rock breccia components (Figure 4.1 c), and/or occur within the breccia components themselves (Figure 4.1 d). Ore minerals, which cement gangue clasts, form an interstitial network between the clasts. In the breccia ores, ore minerals either originated from cataclastic brecciation of an already existing mineralization or they formed by replacing the original components. Breccia mineralization was observed in samples from Bleiberg and Mezica.
- Disperse mineralization: fine-grained ore minerals (sphalerite, Galena, FeS_2) occur dispersed in the host rocks. This mineralization style is characteristic for Topla samples. It was only rarely observed in other deposits, due to the fact that the sample set was biased and more samples with higher-grade ore were available.

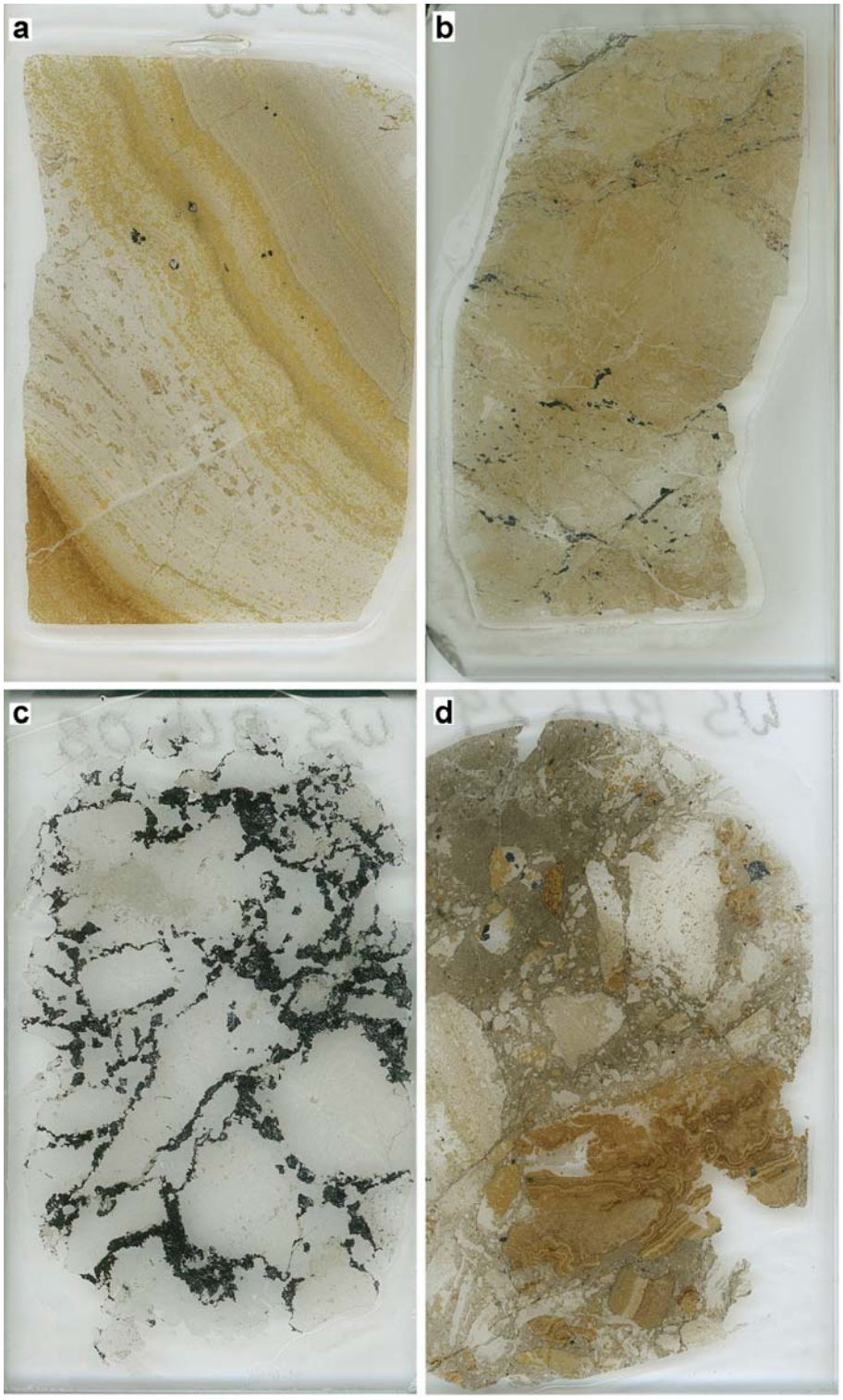

Figure 4.1 (a - d): Photographs of thin sections (size = 46 x 27 mm) showing a selection of macroscopically different mineralization types from the Bleiberg deposit. a) Fine-grained sphalerite enriched in layers, sample Blb26, Maxer Bänke horizon (Bellegarde Schachtl Läufl). b) Massive sphalerite mineralization besides smaller amounts of opaque FeS_2 in sample K2-2 from the Kalkscholle (crest horizon). c) Galena and sphalerite forming a network mineralization in the interstitials of carbonate clasts (sample WS_Blb08, unknown ore horizon, Revier Rudolf). d) Sphalerite mineralization within the components of an ore breccia, in sample WS_Blb29 from the 1st Raibl horizon. Furthermore some sphalerite is also present within the breccia cement.

The most prominent sphalerite-texture are aggregates of differently colored sphalerite layers, referred to as schalenblende or colloform sphalerite (Figure 4.2). Schalenblende consists of microcrystalline sphalerite accumulations, which form parallel bands of different color. The colors of the individual colloform layers ("schalen") range from very light beige to darkest brown (nearly black). Individual layers are approximately between < 1mm and 3 mm thick. When studying schalenblende in transmitted light, the layered structure is nicely visible and individual layers show the same color like on macroscopic scale in the hand specimen (Figure 4.2 c). Single grains, or grain boundaries cannot be determined under the microscope due to the microcrystalline texture of schalenblende. In reflected light (PPL) the layered texture of the schalenblende is not visible, i.e. the reflectivity is uniform (Figure 4.2 a). Partly the layering can be hardly traced, because of many tiny gangue and/or galena inclusions in certain layers or along the boundaries from one layer to another. Under crossed polarizers (XPL) the layering becomes visible, due to specific internal reflections of the individual layers (Figure 4.2 b). BSE images of schalenblende display the typical layered appearance only with increased contrast and a slow scan speed (Figure 4.2 d). Schalenblende occurs either as primary ore aggregates or secondary as breccia components. Schalenblende textures were observed in samples from Bleiberg (all ore horizons), Mezica and Radnig.

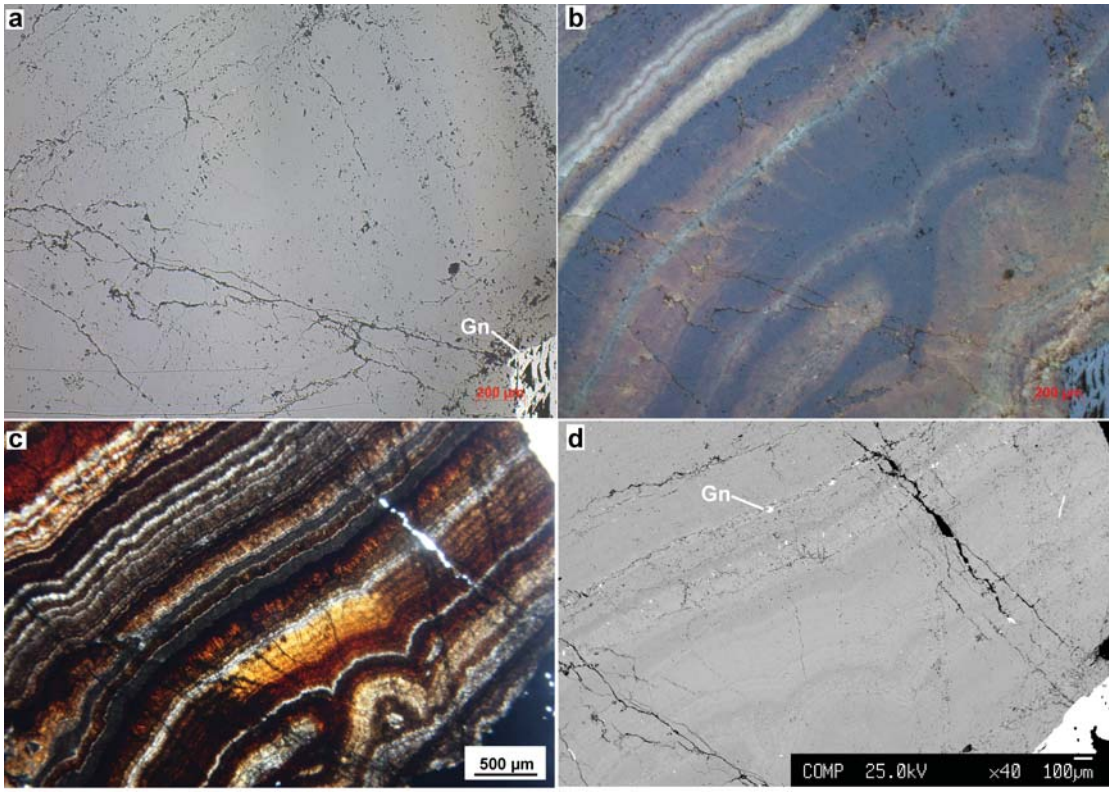

Figure 4.2 (a – d): Schalenblende aggregate in sample EHK11 from Bleiberg (unknown horizon). a – b) Microphotographs (reflected light; a = PPL/b = XPL), the characteristic layering is nearly not observable in the PPL image. c) The same micro-area of the schalenblende (but at smaller magnification) in transmitted light (PPL). d) BSE image of the same part of the schalenblende in backscattered electron image (BSE); the schalenblende texture becomes faintly visible when the contrast is increased. Furthermore BSE images show that certain layers contain many tiny inclusions (e.g. in this case galena). Mineral abbreviations according to Siivola & Schmid (2007).

Coarse-grained, crystalline sphalerite aggregates are a further common texture (Figure 4.3). The individual grains are euhedral/anhedral and range in size from a few 100 µm to > 1000 µm. Accumulations of coarse-grained sphalerite grains can form massive Zn ores. The color of coarse-grained sphalerite is variable. Common shades are e.g. uniform beige, honey-colored to brown and grayish brown. This kind of texture is not restricted to a specific stratigraphic position or deposit and occurs among others in Bleiberg, Mezica, Töplitsch and Radnig.

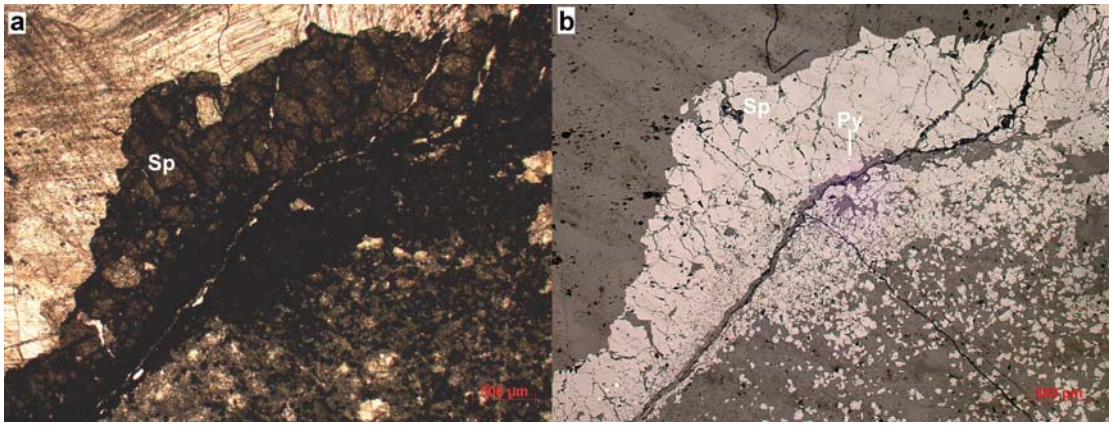

Figure 4.3 (a – b): Microphotographs of coarse-grained sphalerite accumulation in sample Mz08 (Mezica Moring mining district). a = transmitted light/ b = reflected light. Mineral abbreviations according to Siivola & Schmid (2007).

Very fine-grained and macroscopically not visible (< 100µm), often euhedral, dispersed sphalerite grains are also present in some samples (e.g. Bleiberg, Topla, Mezica). In transmitted light these grains can have a brownish-grey color or the grains are nearly colorless (Figure 4.4 b). In reflected light it is visible, that some of this fine-grained sphalerite contains tiny gangue and/or pyrite inclusions that sometimes causes the brownish color in transmitted light (Figure 4.4 a). A special case of fine-grained sphalerite is documented in samples from Topla (Figure 4.5). Some areas of the Topla samples are very rich in sphalerite, which is macroscopically nearly invisible, but becomes visible under the microscope. Under the microscope these grains often show a nearly spherical morphology and in some globules the core is composed of carbonate gangue. The margins of the grains are partly highly frayed. This sphalerite texture is referred as sphalerite peloid (e.g. Kucha et al. 2002, 2010 and Kucha, pers. comm.) and often contains bio-mineralization relicts, which resemble present day sulfate reducing bacteria.

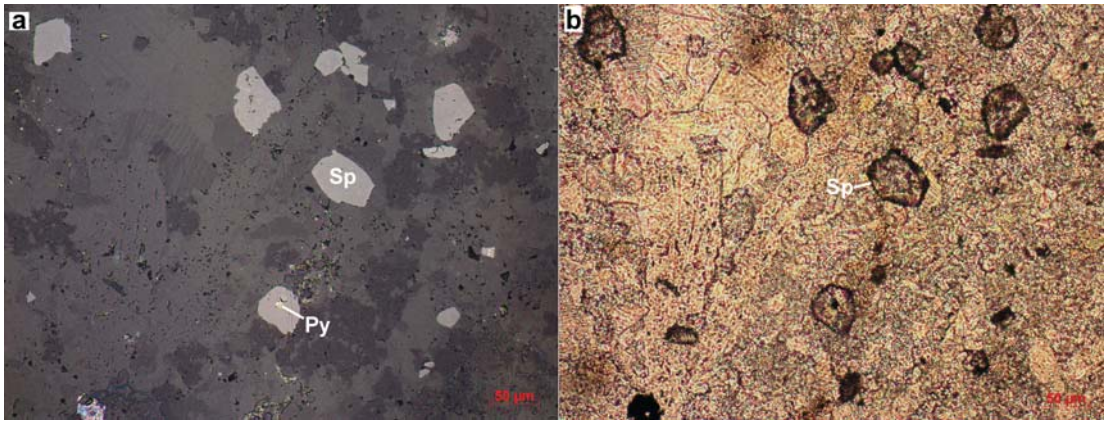

Figure 4.4 (a – b): Microphotographs of fine-grained dispersed sphalerite crystals hosted by a carbonate matrix (sample WS_Blb07, Bleiberg, Erzkalk, Rudolf). Some sphalerite grains host small pyrite inclusions, which cause the brown color in transmitted light (a = reflected light/ b = transmitted light). Mineral abbreviations according to Siivola & Schmid (2007).

Since most investigated samples were provided by university collections or from private collectors, the orientation of the sample in the outcrop (deposit) and its spatial position are not known. Textures therefore are likely to be more heterogeneous on the outcrop scale compared to the hand-specimen scale presented here.

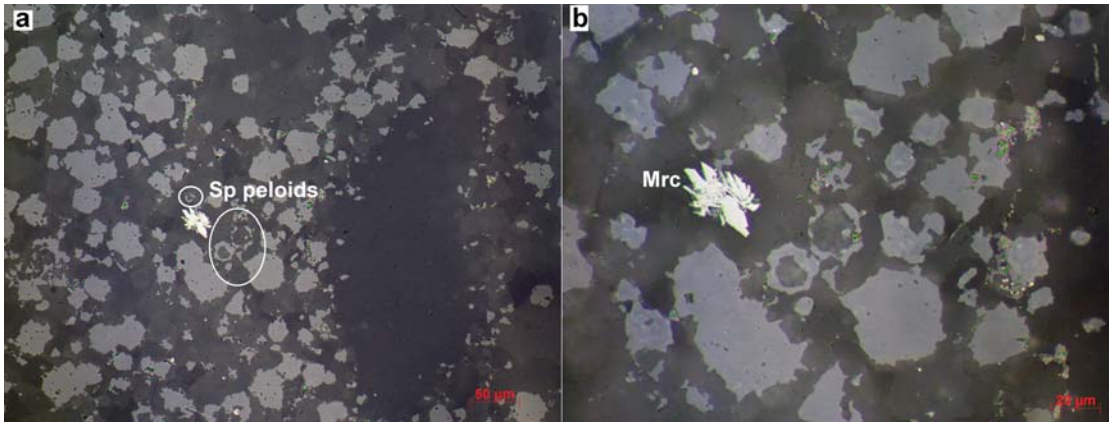

Figure 4.5 (a – b): Microphotographs of sphalerite peloids besides marcasite in a Topla sample (PPL, reflected light).

4.1.2 Cathodoluminescence

Cathodoluminescence (CL) investigations were carried out on 46 polished thin sections, in order to obtain a first chemistry-related characterization. CL behavior of a given mineral depends on its chemical composition and on defects in the crystal lattice (Miller, 1989). Hence, CL can be used as a simple tool to illustrate differences in the chemical composition of minerals.

No uniform CL behavior was observed in the investigated samples. Some sphalerites were easily activated by the cathode beam, causing in different bright colors. Other sphalerites only show dull luminescence or show no CL signal at all. Observed CL colors are blue,

green, dark-red and brownish-orange (Figure 4.6). Sphalerite grains and aggregates often show reaction on CL activation. In contrast, luminescence was only rarely visible in schalenblende (Figure 4.6 a). In some minerals CL colors indicate a zonation, which is not evident with microscopic techniques (Figure 4.6 b). Within one sample, sphalerites with different luminescence can occur, e.g. in sample Mz08 from Mezica light and dark blue as well as orange luminescent sphalerites are present, which do not show any difference in color in transmitted and reflected light (Figure 4.6 d). CL of sphalerites was observed in samples from Bleiberg, Mezica, Topla and Töplitsch (Figure 4.6; Appendix Figures 1 – 4). There is no relation between CL behavior/color and sample location.

Besides of sphalerite also the gangue minerals may exhibit various CL colors. The carbonate host rocks displayed either red, or orange to yellowish CL colors. Fluorite and quartz often show blue luminescence, which is very similar to some blue luminescent sphalerites.

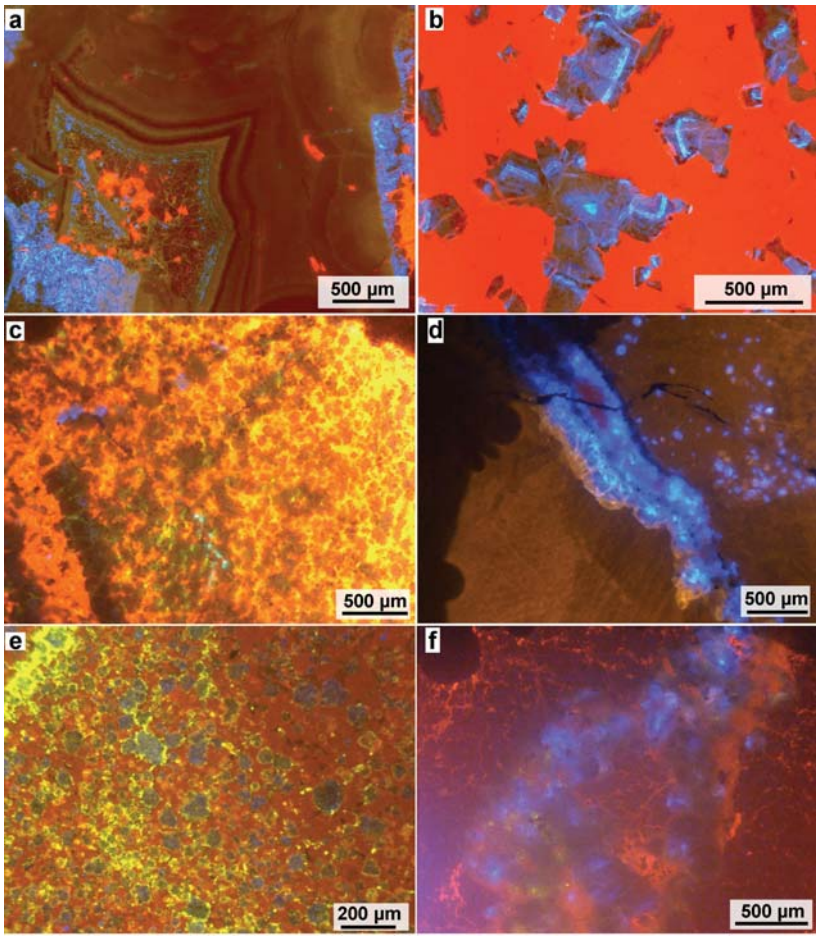

Figure 4.6 (a – f): Microphotographs showing the CL colors of different sphalerites from Pb-Zn deposits in the Drau Range. a) Brown-greenish luminescence in a schalenblende aggregate next to blue luminescent sphalerite grains (sample J10.4, Josefischolle, Bleiberg). b) Sphalerite grain, which exhibits a blue-green CL zonation, which is not evident in transmitted or reflected light; the matrix (red CL) is composed of carbonates (J10.1, crest, Josefischolle, Bleiberg). c) Dull greenish and bluish luminescence in sphalerites from the Kalkscholle (K2-2, Bleiberg). d) Different CL colors (orange and blue) in a coarse-grained sphalerite aggregate from Mezica (Mz08, Moring mining district, Mezica). e) Blue and light green CL colors evident in Topla sphalerites (Tp04). f) Blue and subordinate greenish CL color of a coarse-grained sphalerite aggregate in sample Toe01 (Töplitsch).

4.1.3 Backscattered electron imaging

Backscattered electron (BSE) images made at the electron microprobe were used to study micro-textures of ore minerals, especially sphalerite. Similar to CL, BSE can illustrate chemical heterogeneities in minerals expressed as differences in the brightness. Hence, BSE is a further tool to connect chemical data to micro-textural observations. In most investigated samples, sphalerites are mostly homogenous and only a few ones display zonation or textural heterogeneity on the micro-scale.

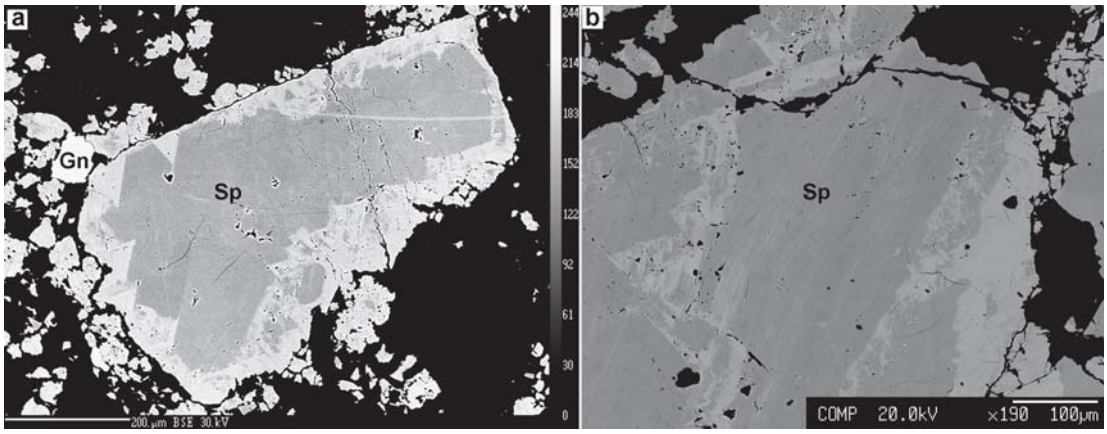

Figure 4.7 (a – b): BSE image showing the zonation of sphalerite. a) Sphalerite grain (Bleiberg, E14.3 Revier Erlach), which is composed of a darker core and a lighter rims. b) Irregularly zonation in a sphalerite grain from the Maxer Bänke horizon (Blb11, Bleiberg, Bellegarde-Schachtl Läufl).

Zonation was documented in some schalenblende aggregates. BSE images show the same banding as seen in hand specimens and in the microscope (Figure 4.2 d). No uniform relationship between macroscopic color of the individual layers and BSE brightness could be established, but in some cases the darkest (brown to black) schalenblende layers show brighter BSE zoning. Not every schalenblende aggregate displays a zonation on BSE images. Besides, some coarse-grained sphalerites in Bleiberg samples (Revier Erlach and Maxer Bänke) exhibit an irregularly grain-zonation on BSE images. Zoned sphalerite grains generally consist of a darker core and a lighter colored corona. The zonation continues along cleavage planes towards the grain gore (Figure 4.7 b). Sometimes also lighter and darker zones alternate (Figure 4.7 a, b).

Besides for the visualization of chemical heterogeneities, BSE imaging was used to illustrate the amount and the kind of the inclusions occurring within sphalerite. BSE imaging of schalenblende showed that certain schalenblende layers are characterized by numerous small (< 5µm) inclusions of solid phases (e.g. galena, carbonate, quartz, pyrite), which cannot be distinguished under the microscope (Figure 4.8). Mineral inclusions include gangue minerals such as carbonates and quartz as well as ore minerals (galena, pyrite). They were identified using EDS techniques.

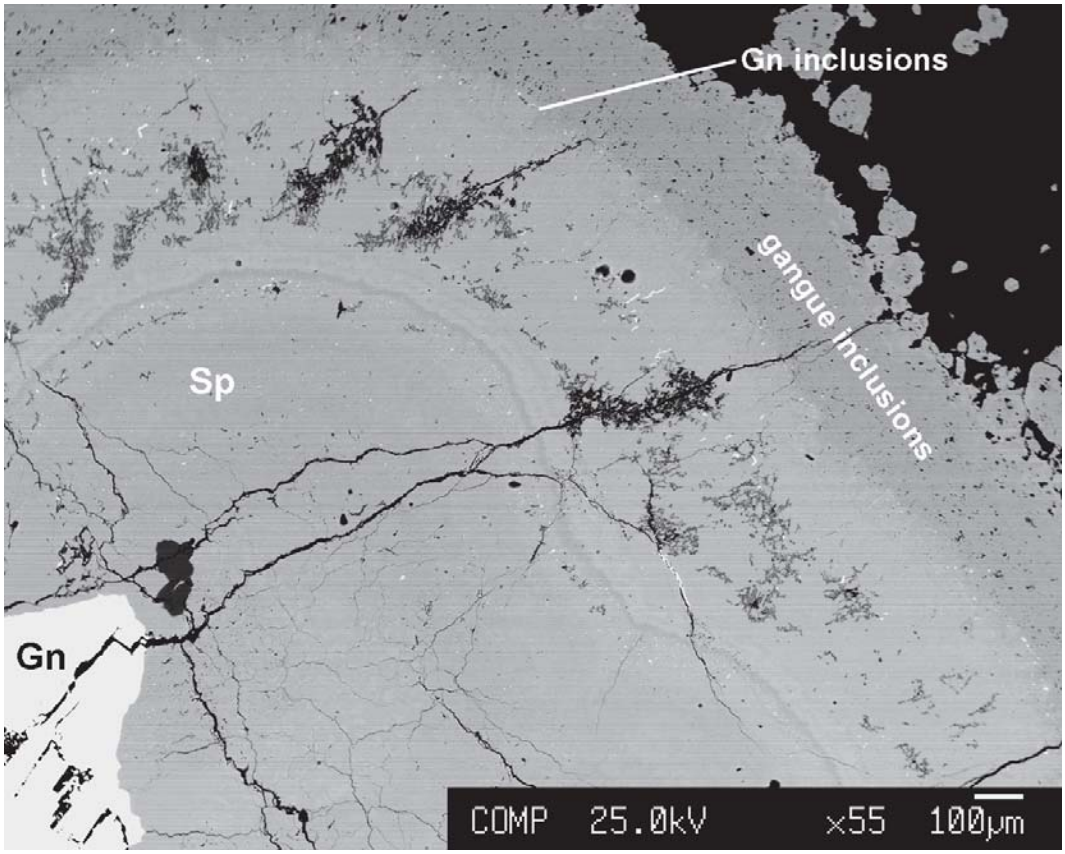

Figure 4.8: BSE image showing part of a zoned schalenblende aggregate within sample Blb17 (Bleiberg, Erzkalk). Numerous small inclusions of galena and gangue are concentrated in certain layers. Mineral abbreviations according to Siivola & Schmid (2007).

4.2 Trace Element Chemistry of Sphalerite

Information on the chemical composition of sphalerite from the Pb-Zn occurrences in the Drau Range was mainly obtained by electron microprobe analysis (EMPA). Furthermore, in two samples the trace element composition of sphalerite was measured with LA ICP-MS at the GeoZentrum Nordbayern (Erlangen). LA ICP-MS investigations were performed in order to review the results of the EMP measurements.

4.2.1 Electron microprobe analysis

The trace element concentrations of sphalerite from 53 different samples originating from seven different deposits in the Drau Range were investigated using EMP techniques. Additionally, the trace element distribution in sphalerite from three samples from other Alpine Pb-Zn deposits (not in the Drau Range) was analyzed with EMP. The locations of the investigated Drau Range deposits are marked within the schematic map within figure 2.3. The results of the EMP analyses are summarized in the following and are furthermore presented more detailed within chapter 4.4. The full EMP dataset is furthermore listed within the appendix (Tables 4 – 13). The sphalerites were analyzed for the trace elements As, Fe, Pb, Ge, Cu, Tl and Cd. Furthermore, the Zn and S concentrations were also determined, in order to obtain complete analyses. The selection of the elements is mainly based upon earlier studies and represents those elements, which may occur in concentrations in sphalerite that can be measured with EMP (summarized in Schroll, 1997).

Sphalerites from the Drau Range show a large variation in chemical compositions. Table 4.1 gives a summary of the mineral chemical analyses by listing some basic statistical parameters (minimum and maximum values, mean, median, single standard deviation) for the analyzed elements. It can be seen that Fe and Cd are the two trace elements with the highest concentrations. Besides, also Pb, As and Ge were often detectable in concentrations above the limits of detection of EMPA. Tl and Cu were only rarely found in concentrations above the limit of detection. Tl was only measured in sphalerites from Bleiberg, Cu in Bleiberg and Mezica. The calculated mean/median values only refer to analyses above the detection limit of the EMP. All analyses below the detection limit of the EMP (i.e. below the minimum value given in Table 4.1) were excluded from statistical calculations. Therefore, the calculated mean and median values are higher than they are in reality. The presented minimum values represent furthermore the limit of detection of the EMP and not the real minimum value. Hence lower concentrations of the respective element might be present, but cannot be analyzed with EMP. The standard deviations of the measurements that are also given in table 4.1 are often higher than the calculated mean values. This results from a right skewed data distribution, where the mean is strongly influenced by a few increased outlier data. Altogether, the calculated statistical parameters reflect a highly heterogeneous distribution.

The Bleiberg dataset is the most comprehensive one and therefore exhibits the largest variability in almost all trace elements (Table 4.1). However, despite this fact some regional

differences in trace element composition of sphalerites become evident. When comparing sphalerites from Bleiberg and Mezica, which are the two largest Pb-Zn deposits in the Drau Range, a pronounced Cd enrichment is indicated in Mezica sphalerites (Table 4.1). In Bleiberg Fe and Cd in sphalerites were measurable about equally often (97% of the analyses are above the limit of detection). In contrast, in Mezica, Cd was analyzed much more frequently than Fe. Furthermore, the Mezica sphalerites exhibit a larger variability in their Cu contents although the dataset is smaller than that of the Bleiberg. Other regional trends regarding trace element distribution are the high Ge contents in sphalerite from Jauken (always above the EMP detection limit) and the very low trace element contents of sphalerite from Topla and Töplitsch. However, variations in chemical composition of sphalerite is not only present on the regional scale, but can also be documented on the deposit or even within-sample scale, what will be shown more in detail in chapter 4.4.

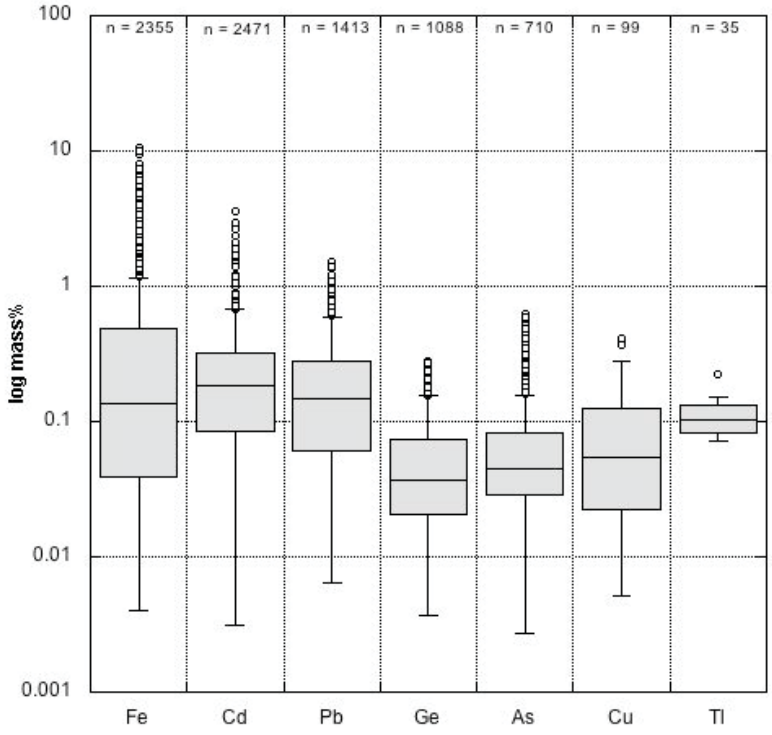

Figure 4.9: Boxplots displaying the variation of trace element concentrations in sphalerite from all studied Pb-Zn deposits in the Drau Range. Because only analyses above the detection limit of the EMP were used for the calculation, the data show a strongly skewed distribution caused by the numerous high outlier values. The number of analyses is shown above the respective boxplot for each element.

The boxplots in figure 4.9 display the variability and skewness in the sphalerite data set very well. They illustrate that for most elements there exist a lot of outlier analyses. The mean values of these trace elements are therefore generally higher than the median values (Table 4.1). The smaller number of outlier data in the Cu and Tl dataset results from the less comprehensive dataset for these two elements.

Table 4.1: Statistical parameters for trace element concentrations of sphalerites from different Pb-Zn deposits in the Drau Range determined by EMPA. Win.Blb. = Windisch Bleiberg. All elements were analyzed in all samples. The number (n) of analyses with concentrations above the limit of detection taken for statistical calculations is given in brackets. The presented minimum value results from the LOD of the EMP.

All samples (2577)	**Fe** (2355)	**Cd** (2471)	**Pb** (1413)	**Ge** (1088)	**As** (710)	**Cu** (99)	**Tl** (35)
Min [mass%]	0.004	0.003	0.007	0.004	0.003	0.005	0.071
Max [mass%]	10.69	3.62	1.53	0.28	0.62	0.41	0.23
Mean [mass%]	0.48	0.24	0.22	0.057	0.080	0.089	0.110
Median [mass%]	0.17	0.19	0.15	0.037	0.044	0.054	0.102
Std.dev. [mass%]	0.87	0.23	0.22	0.053	0.10	0.094	0.032
Bleiberg (1805)	**Fe** (1728)	**Cd** (1740)	**Pb** (1021)	**Ge** (904)	**As** (549)	**Cu** (35)	**Tl** (35)
Min [mass%]	0.005	0.003	0.012	0.004	0.003	0.008	0.071
Max [mass%]	10.69	3.62	1.53	0.28	0.62	0.39	0.23
Mean [mass%]	0.58	0.23	0.23	0.056	0.086	0.039	0.11
Median [mass%]	0.18	0.19	0.17	0.038	0.047	0.023	0.10
Std.dev. [mass%]	1.02	0.19	0.23	0.050	0.11	0.064	0.032
Mezica (311)	**Fe** (196)	**Cd** (310)	**Pb** (162)	**Ge** (51)	**As** (92)	**Cu** (64)	**Tl** (<d.l.)
Min [mass%]	0.004	0.021	0.013	0.005	0.004	0.005	
Max [mass%]	0.62	2.93	0.90	0.088	0.41	0.41	
Mean [mass%]	0.049	0.46	0.17	0.034	0.086	0.12	
Median [mass%]	0.018	0.35	0.14	0.029	0.058	0.087	
Std.dev. [mass%]	0.088	0.43	0.16	0.022	0.083	0.097	
Topla (200)	**Fe** (197)	**Cd** (199)	**Pb** (127)	**Ge** (2)	**As** (30)	**Cu**(<d.l.)	**Tl** (<d.l.)
Min [mass%]	0.008	0.004	0.007	0.005	0.003		
Max [mass%]	0.90	0.37	0.80	0.028	0.051		
Mean [mass%]	0.16	0.12	0.19		0.016		
Median [mass%]	0.082	0.10	0.11		0.016		
Std.dev. [mass%]	0.18	0.078	0.20		0.010		
Jauken (44)	**Fe** (44)	**Cd** (41)	**Pb** (13)	**Ge** (44)	**As** (5)	**Cu**(<d.l.)	**Tl** (<d.l.)
Min [mass%]	0.15	0.030	0.11	0.014	0.03		
Max [mass%]	2.17	0.098	0.23	0.27	0.05		
Mean [mass%]	0.42	0.060	0.14	0.13			
Median [mass%]	0.30	0.063	0.13	0.14			
Std.dev. [mass%]	0.36	0.017	0.032	0.065			
Radnig (49)	**Fe** (49)	**Cd** (49)	**Pb** (20)	**Ge** (41)	**As** (8)	**Cu**(<d.l.)	**Tl** (<d.l.)
Min [mass%]	0.01	0.029	0.027	0.006	0.004		
Max [mass%]	1.72	0.27	0.23	0.28	0.012		
Mean [mass%]	0.52	0.13	0.067	0.073	0.009		
Median [mass%]	0.20	0.12	0.059	0.042	0.010		
Std.dev. [mass%]	0.57	0.061	0.043	0.076	0.003		
Töplitsch (105)	**Fe** (79)	**Cd** (71)	**Pb** (25)	**Ge** (18)	**As**(<d.l.)	**Cu**(<d.l.)	**Tl** (<d.l.)
Min [mass%]	0.006	0.003	0.024	0.004			
Max [mass%]	0.24	0.14	0.15	0.067			
Mean [mass%]	0.054	0.050	0.072	0.018			
Median [mass%]	0.031	0.050	0.045	0.012			
Std.dev. [mass%]	0.056	0.033	0.047	0.015			
Win.Blb.(41)	**Fe** (41)	**Cd** (41)	**Pb** (28)	**Ge** (26)	**As** (25)	**Cu**(<d.l.)	**Tl** (<d.l.)
Min [mass%]	0.008	0.010	0.032	0.005	0.003		
Max [mass%]	0.76	0.24	0.47	0.089	0.081		
Mean [mass%]	0.22	0.10	0.14	0.034	0.019		
Median [mass%]	0.19	0.085	0.11	0.023	0.012		
Std.dev. [mass%]	0.17	0.058	0.10	0.026	0.018		

In addition to samples from the Drau Range, sphalerites from the historic Pb-Zn deposits Lafatsch (Northern Tyrol) in the Northern Calcareous Alps, Raibl (Cave I Predil, Italy) in the Southern Alps and Zunderwand in the Nock Mountains in Carinthia (Middle Austroalpine sensu Tollmann, 1977) were analyzed. The Lafatsch and Raibl samples are from the Ladinian/Carnian Wetterstein Formation. The Zunderwand ore is hosted by the Alpine Muschelkalk Formation (Anisian; pers. comm. H. Prassnik). Statistical data for these three non-Drau Range Pb-Zn mineralizations are listed in Table 4.2. The dataset is furthermore presented within the Appendix (Table 13). The trace element contents of sphalerites from these three deposits lie within the range of those from the Drau Range. The data show less variation although it must be noted that the number of analyses and samples is too small to allow a serious comparison.

Table 4.2: Statistical summary on the trace element composition of sphalerites from Pb-Zn deposits outside the Drau Range. Zunderw. = Anisian Zunderwand occurrence in the Middle Austroalpine tectonic unit (sensu Tollmann, 1977). The number of analyses that were considered for the statistics (n, number of analyses above the LOD) is given in brackets for each element.

Lafatsch (61):	**Fe (61)**	**Cd (61)**	**Pb (56)**	**As (58)**	**Ge (12)**	**Cu (1)**	**Tl (<d.l.)**
Min [mass%]	0.007	0.001	0.009	0.005	0.001	/	
Max [mass%]	0.28	0.95	0.92	0.21	0.041	0.04	
Mean [mass%]	0.14	0.28	0.43	0.10	0.009	/	
Median [mass%]	0.14	0.15	0.49	0.11	0.006	/	
Std.dev.	0.068	0.28	0.23	0.057	0.011	/	
Raibl (21)	**Fe (20)**	**Cd (21)**	**Pb (21)**	**As (21)**	**Ge (20)**	**Cu(<d.l.)**	**Tl (<d.l.)**
Min [mass%]	0.013	0.005	0.028	0.002	0.014	/	/
Max [mass%]	0.12	0.65	1.18	0.29	0.12	/	/
Mean [mass%]	0.072	0.082	0.65	0.15	0.066	/	/
Median [mass%]	0.068	0.031	0.76	0.18	0.069	/	/
Std.dev. [mass%]	0.029	0.14	0.33	0.089	0.030	/	/
Zunderw. (15)	**Fe (15)**	**Cd (9)**	**Pb (6)**	**As (1)**	**Ge (1)**	**Cu(<d.l.)**	**Tl (<d.l.)**
Min [mass%]	0.028	0.003	0.027	/	/	/	/
Max [mass%]	0.30	0.007	0.081	0.007	0.005	/	/
Mean [mass%]	0.088	0.005	0.041	/	/	/	/
Median [mass%]	0.067	0.005	0.036	/	/	/	/
Std.dev. [mass%]	0.072	0.001	0.018	/	/	/	/

4.2.2 Laser ablation ICP MS

Trace element analyses with LA-ICP MS were carried out on samples Blb26_WD (Bleiberg, Maxer Bänke) and WS_Blb29 (Bleiberg, 1st Raibl horizon) in order to crosscheck the results obtained by EMP. The LA ICP-MS analyses confirm that Cd and Fe are the most frequent and highest enriched trace elements in the sphalerites (Table 4.3; Appendix, Tables 14/15). LA ICP-MS measurements also confirmed EMP data insofar that Pb and As are the next frequent trace elements within both samples. The mean and median values for As and Pb calculated from LA-ICP MS data are smaller than those calculated from EMP, what is due to the much lower detection limits of LA-ICP MS. Hence, more data points with lower values were included in the calculations. LA-ICP MS measurements also confirmed that Cu and Tl contents were mostly well below the detection limits of the EMP (a few tens ppm). Other trace elements, like In, Ga, Mn and Ag occur in very low concentrations, normally far below the limit of detection of the EMP (< 1ppm). Unfortunately, no information on the Ge contents could be obtained, because no reference material for Ge was available and it could therefore

not be calibrated. However, Ge was measured with two different EMP instruments giving consistent results. Altogether LA ICP-MS confirmed the EMP data for the other elements. The EMP analysis is therefore suitable in order to investigate the relative enrichment and depletion of trace elements within the sphalerites.

Table 4.3: Statistical parameters of trace elements in sphalerite. Data obtained from LA-ICP-MS measurements of samples Blb26WD and WS_Blb29 from Bleiberg. Number of analysis (n) used for calculations are shown in brackets.

	Blb26WD (n =61)					
	Fe (61)	**Cd** (61)	**Pb** (61)	**As** (61)	**Cu** (33)	**Tl** (61)
Min [ppm]	105	526	119	6	0.244	3
Max [ppm]	8741	3156	1228	821	19	285
Mean [ppm]	850	1571	343	110	3	23
Median [ppm]	279	1455	258	49	1	46
Std.dev. [ppm]	1677	611	255	182	4	63

	WS_Blb29 (n=70)					
	Fe (70)	**Cd** (70)	**Pb** (70)	**As** (70)	**Cu** (67)	**Tl** (70)
Min [ppm]	453	195	78	12	0.36	6
Max [ppm]	25606	2618	1145	768	35.5	207
Mean [ppm]	4802	1095	571	290	9	69
Median [ppm]	3771	984	559	295	5	65
Std.dev. [ppm]	3761	467	219	134	9	32

4.2.3 Trace element distribution

The sphalerites from the Drau Range exhibit a large variability in their trace element concentrations (Table 4.1 and Figure 4.9). In order to investigate and understand the trace element distribution of sphalerite, it has been investigated carefully down to the micro-scale to document their regional variations (ore deposits, ore horizons) and their inter-element-correlations.

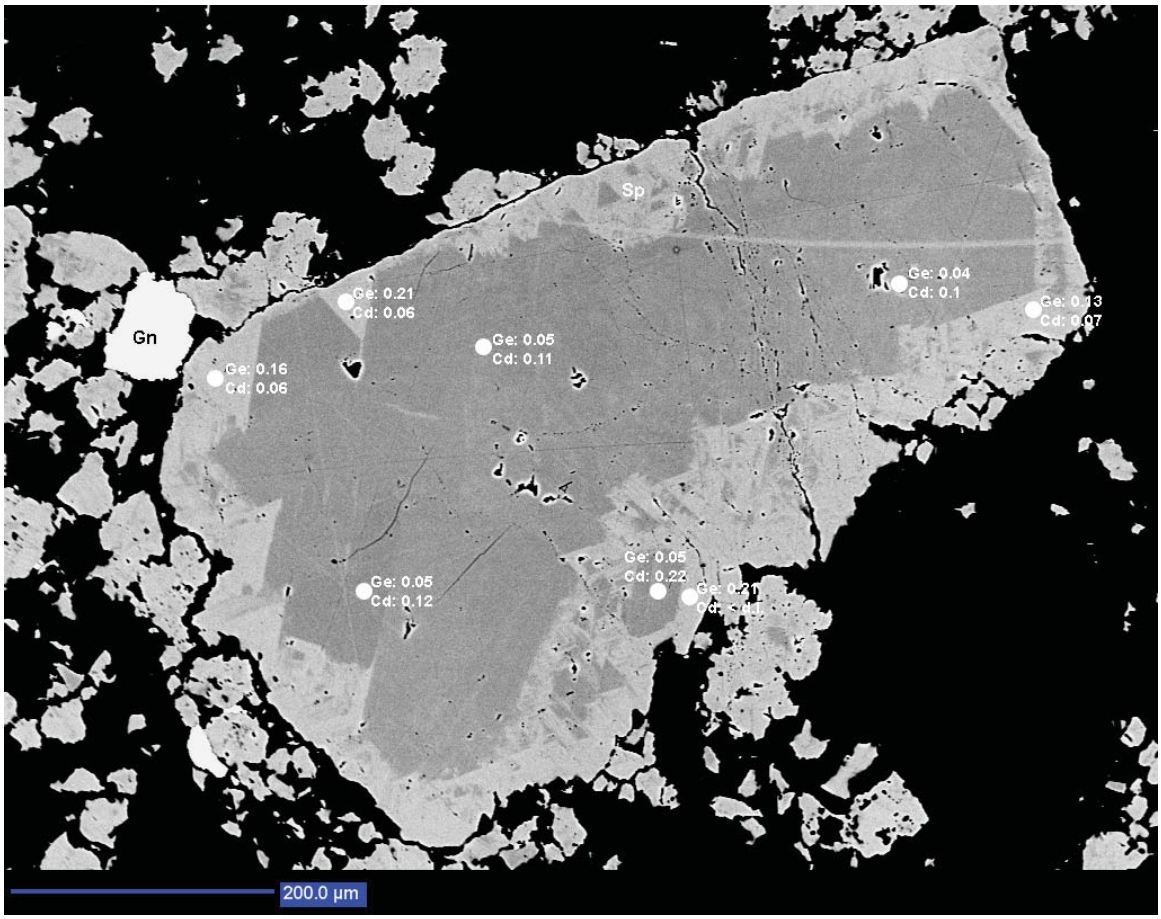

Figure 4.10: BSE image showing zoned sphalerite grain. The zonation is very irregularly. The zonation generally consists of a light colored corona and continues along cleavage planes towards the core. Differences in brightness reflect systematic variations in the Cd and Ge concentrations. Sample E14.3, Erlach, Bleiberg.

Cadmium

Cadmium was the most frequently measured trace element in sphalerites in the Drau Range. In about 96% of the analyses Cd was positively detected. Variations of Cd contents in sphalerites from the Drau Range are around factor 100 (0.03 to 3.62 mass%) when considering the whole ore district or the larger ore deposits within this district (Bleiberg and Mezica). The maximum Cd concentration of 3.62 mass% was measured in a sample from Bleiberg (unknown ore horizon, Antonishaft). However also in Mezica sphalerite Cd contents > 1 mass% were measured. The maximum Cd concentration of Mezica sphalerite is with a value of 2.93 mass also very high (Mezica Moring). In literature average Cd contents of 1860 ppm are reported for Bleiberg (Schroll, 1997).

On the scale of single ore horizons within these deposits, the Cd contents vary by a factor of >10. Cd variation becomes much smaller (maximum factor 5) on the sample scale. In a few samples a distinctive and more pronounced variation in Cd contents has been recognized, which can be linked with textural and sulfur isotopic variations (see chapter 4.4). In a few samples Cd concentrations vary by a factor 2 – 3 already on the grain scale. The BSE zonation reported in chapter 4.1.3 results from a heterogeneous element distribution. Dark zones show Cd enrichment and bright zones are enriched in Ge (Figure 4.10). The variability in Cd contents increases when a large deposit is considered (e.g. Bleiberg, Mezica). In Bleiberg and Mezica the variability in Cd contents is of a factor 100.

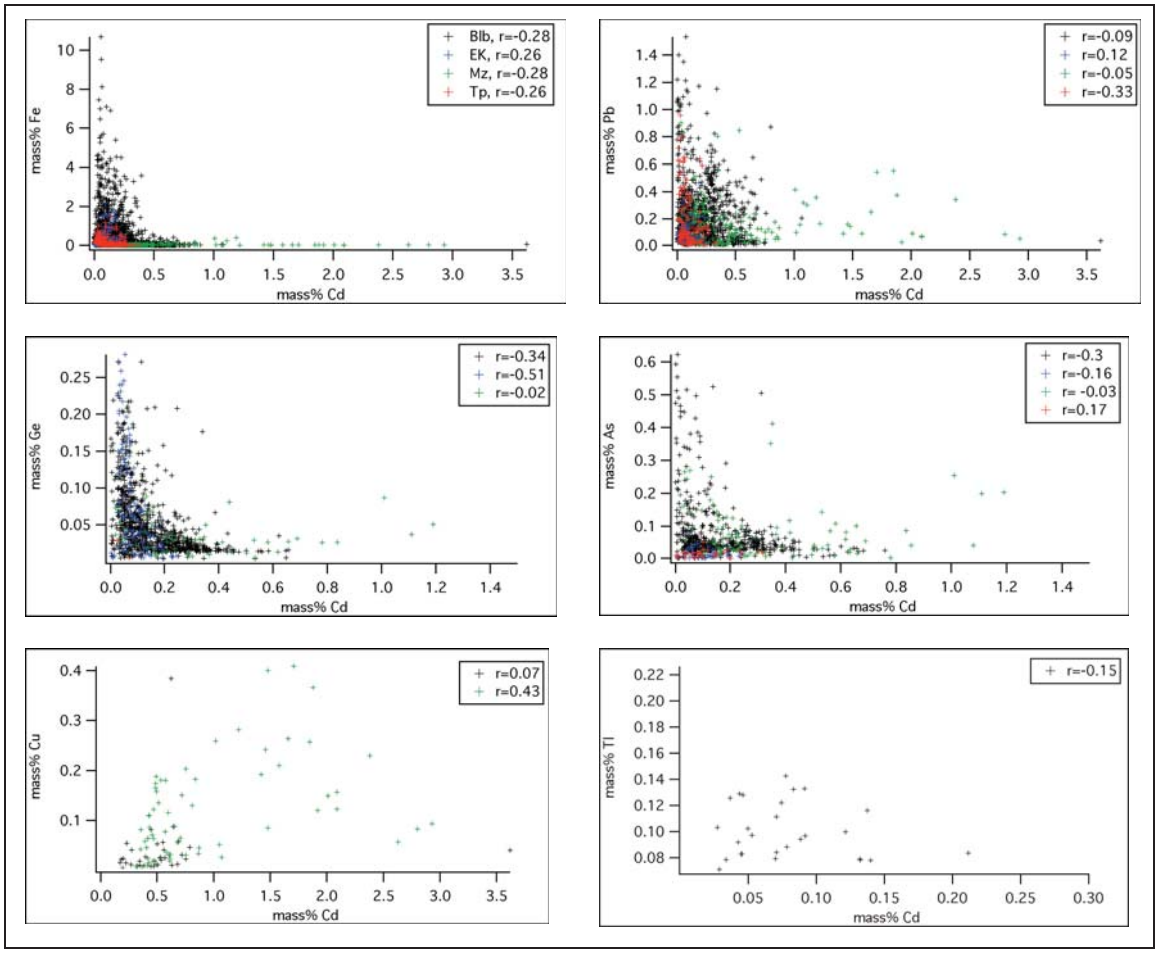

Figure 4.11: Plots displaying the relations between Cd and other trace elements measured by EMP. The dataset is sorted with respect to the sample origin from the different deposits within the Drau Range (Blb = Bleiberg, Mz = Mezica, Tp = Topla, EK = Jauken, Töplischt, Radnig, Windisch Bleiberg). Only data above the detection limits for the individual elements are displayed. Correlation coefficients (r) were calculated using the formula, which assumes a linear dependence of two variables (Pearson's correlation).

The interelement relations between Cd and the other trace elements are displayed in figure 4.11. The dataset is sorted into a Bleiberg (Blb), a Mezica (Mz), and a Topla (Tp) set. Furthermore, the remaining deposits are summarized into a Erzkalk dataset (Jauken, Töplitsch, Radnig, Windisch Bleiberg; EK). The interelement correlations are different when comparing the data of one deposit to another. Only few pronounced correlations are evident:

within the Mezica dataset there is a positive correlation with Cu (r = 0.43). Furthermore, a distinct negative relation between Cd and Ge is evident in the EK dataset (r = -0.51) and a less distinct one in the Bleiberg dataset (r = -0.34). This observation is in accordance to the compositional zonation of Cd and Ge, described above that indicates a negative correlation of these two elements on the micro-scale. No clear relation between Fe and Cd is evident within the dataset. Within the Mezica, Bleiberg and Topla set a negative relation of Fe and Cd is indicated (< -0.28). The Erzkalk dataset indicates a positive one.

Iron

Iron is the second common trace element besides Cd. It was detectable in sphalerites from all investigated deposits and Fe-bearing sphalerites were found in Pb-Zn ores from all three stratigraphic positions in the Early Triassic strata; i.e. Anisian Muschelkalk, Carnian/Ladinian Wetterstein Formation, Ladinian Raibl Group.

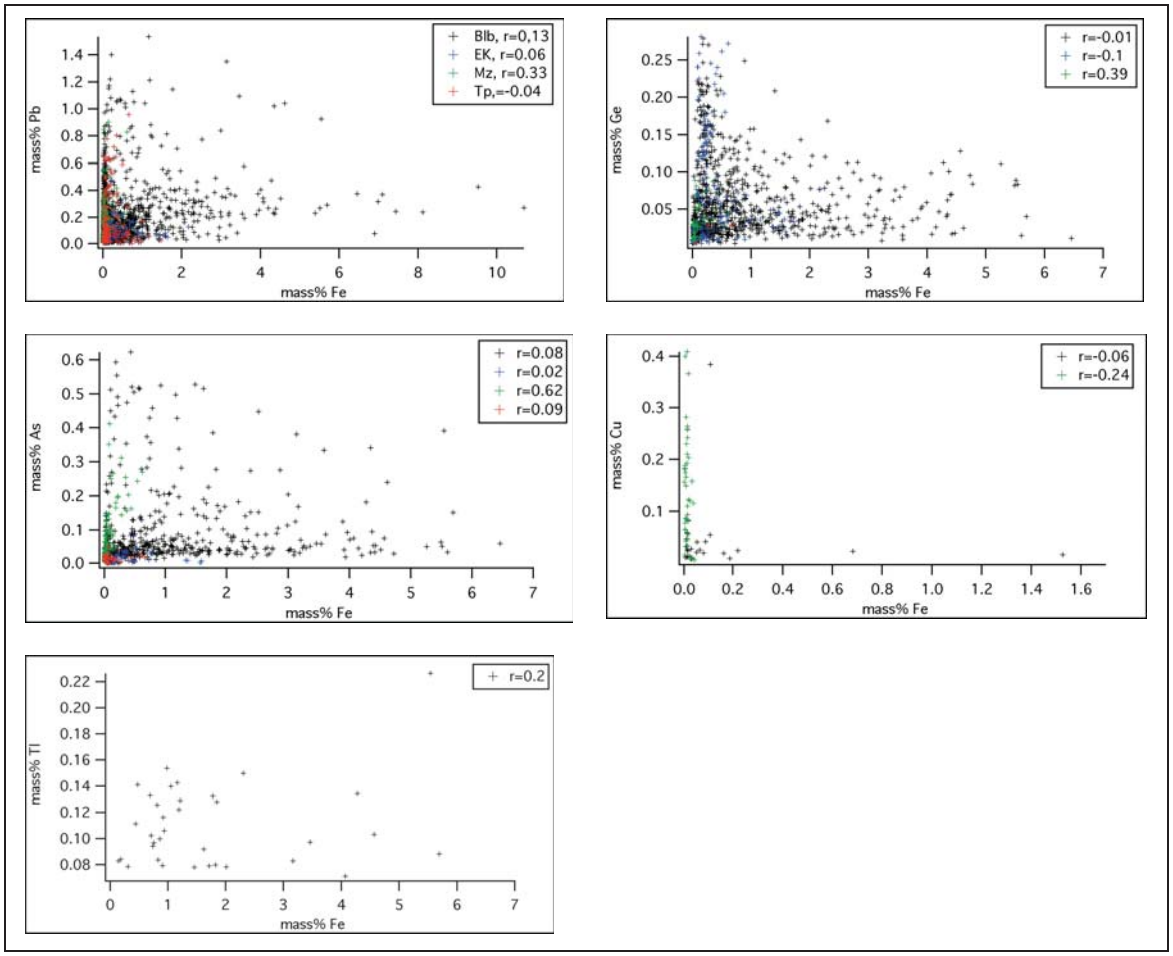

Figure 4.12: Plots showing the correlations between Fe and other trace element measured by EMP. Only data above the detection limits for the individual elements are displayed. Correlation coefficients (r) were calculated using the formula, which assumes a linear dependency of two variables (Pearson's correlation).

Sphalerite from the Mezica deposit is generally poorer in Fe than sphalerite from the Bleiberg deposit. However, the Mezica sphalerites are not really Fe poor. Only sphalerite from the

Anisian Topla deposit and from the small outcrops at Töplitsch is generally very low in Fe. Iron contents of sphalerite range between approximately 400 ppm and 10.69 mass%. Sphalerites from Bleiberg cover this whole variation range, the maximum Fe concentration of 10.69 mass% was measured in a schalenblende from an unknown ore horizon (Blb11). For Bleiberg average Fe concentrations of 4240 ppm are reported (Schroll, 1997). In Mezica the variation is smaller (400 ppm to < 6 mass%). There is a clear relation of Fe contents with the textural type of sphalerite. The highest Fe concentrations were measured in schalenblende aggregates. Iron concentrations of > 1 mass% normally occur in schalenblende and not in crystalline sphalerite. Sphalerites with more than approximately 0.5 mass% Fe do not display CL colors because iron is a CL inhibiting element (Miller, 1989).

No correlation between Fe and any other trace elements in sphalerite was detected regularly (Figure 4.12). Within the Mezica dataset a strong positive relation between high Fe and high As contents is indicated (r = 0.6). Reviewing the measurability of other trace/minor element with respect to Fe, it becomes visible, that Tl was mostly measured in sphalerites, which contain more Fe than Cd. Also Ge was more often above the detection limit in sphalerites that contain more Fe than Cd. Additionally, a negative relation between Fe and Cd was partly evident.

Lead

Pb was positively determined quite frequently in the Drau Range sphalerite. In comparison to Cd and Fe, it occurs much more heterogeneously distributed. The Pb contents, measured with EMP, vary from 700 ppm to 1.53 mass%. The highest Pb concentration of 1.53 mass% was detected within the schalenblende aggregate from the Maxer Bänke horizon (Blb17, chapter 4.4.1). Pb concentrations of > 0.1 mass% were measured sporadically in sphalerites in nearly all samples. Very high Pb contents of > 0.5 mass% were often measured in inclusion-rich layers of schalenblende aggregates, or in inclusion-rich sphalerite grains.

A positive correlation of Pb and As is evident within the Blb, Mz and EK data (r = 0.58 to 0.73, Figure 4.13). The Topla dataset indicates no relation between Pb and As concentrations. The LA-ICP MS data display also a positive correlation of Pb and As. In this dataset the correlation between Pb and As is even higher (r > 0.9). Lead also shows a positive correlation with Tl (r = 0.8 and 0.9 respectively) in sphalerites from samples Blb26 and WSBlb29 (see below). Furthermore, a positive relation between Cu and Pb is indicated by the EMP data of Mezica sphalerite (r = 0.52).

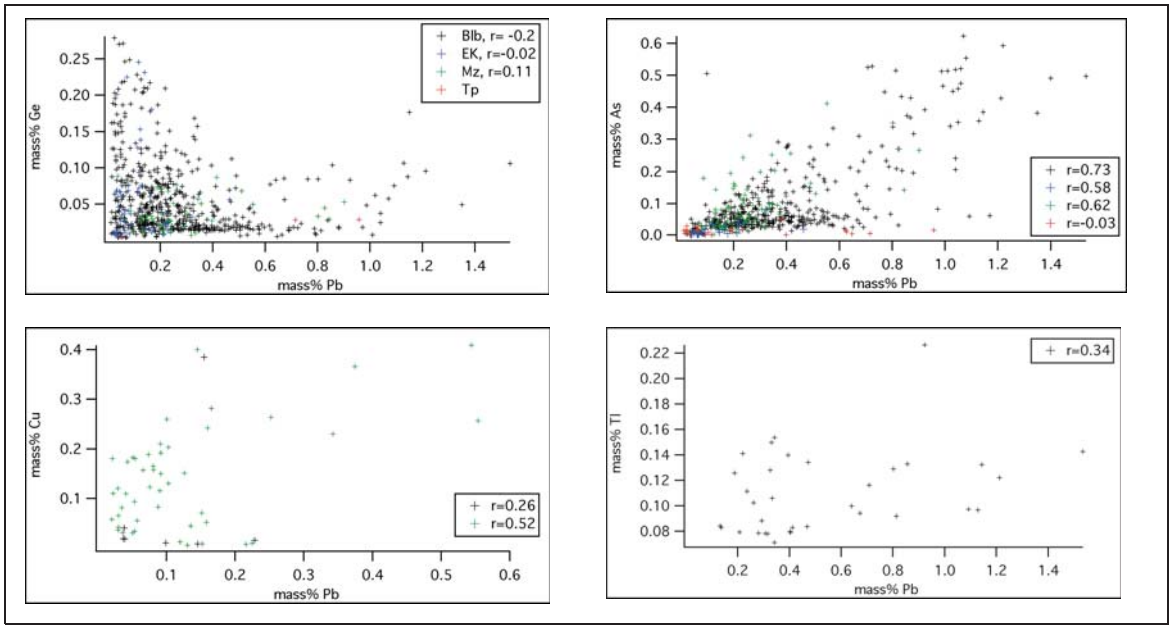

Figure 4.13: Plots, displaying the relation between Pb and the other measured trace elements. The correlation coefficients (r) were calculated using the formula, which assumes a linear dependency between two variables (Pearson's correlation). Only analysis, which were above the LOD of the EMP were considered for the plots.

Germanium

Germanium concentrations of sphalerite from all deposits in the Drau Range exhibit considerable variability (factor about 70) ranging from >50 ppm to 0.28 mass%. For Bleiberg an average Ge concentration of 59 ppm is reported (Schroll, 1997). Sphalerite with very high Ge content is present at Revier Erlach (Bleiberg) and at the Jauken deposit. Sphalerite from both locations has nearly always > 0.1 mass% Ge (maximum of 0.28 mass%). Furthermore, in some samples from the Erzkalk, Maxer Bänke and crest horizons (Bleiberg), from the Graben district (Mezica) and from the Radnig deposit increased Ge contents were measured in some sphalerites, but in these locations Ge rich sphalerites are not the norm. The measured Ge contents vary on the ore deposit and regional scale in the Drau Range in a non-systematic way. As shown in the subchapter on Cd, variations by a factor of 4 are even present on the grain scale (Figure 4.10). In samples, where crystalline sphalerite is associated with schalenblende aggregates, the crystalline variety contains more Ge.

Within the Mz and Ek data a negative correlation of Ge with Cd is evident (r = -0.34, -0.51 respectively, Figure 4.11). Furthermore, within the Mezica data a positive relation between high Ge and high As contents is visible (r = 0.6; Figure 4.14). When examining the EMP dataset critically, it can be recognized that higher Ge contents predominantly occur in samples, which contain more Fe than Cd. However, Fe concentrations of < 0.5 mass% inhibit high Ge contents of > 0.1 mass%. Thus no simple positive correlation of Ge and Fe exists.

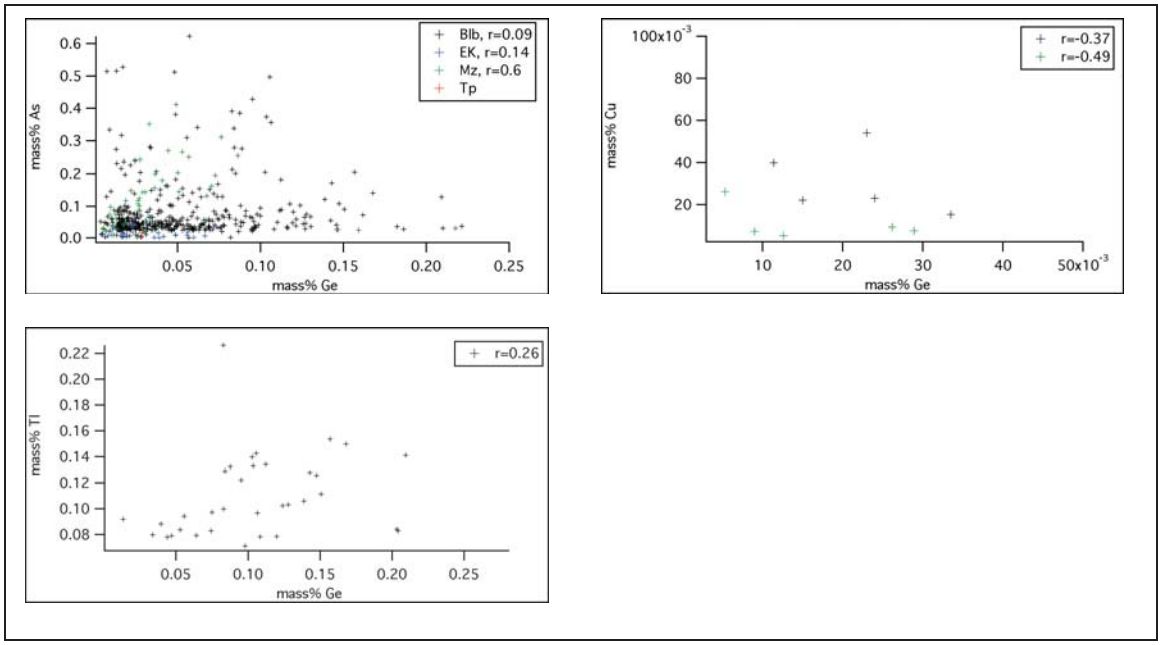

Figure 4.14: Correlation plots of Ge and As, Cu and Tl. The plots were constructed using the formula, which assumes a linear dependency between two variables (Pearson's correlation) and refer only to analyses, which were above the LOD of the microprobe. The calculated correlation coefficients (r) are furthermore displayed in each plot. EMP data indicates no positive (or negative) relation between high Ge contents and the elements Cu, As and Tl.

Arsenic

Arsenic was detectable rather sporadically, but it was enriched in certain sphalerites. It was clearly more often enriched above the limit of detection in schalenblende compared to crystalline sphalerite. A maximum As content of 0.62 mass% was measured in red schalenblende oncoids (Bleiberg, unknown ore horizon). According to Schroll (1997), the average As content of sphalerite from Bleiberg is 174 ppm.

Besides of the positive correlation with Pb, the Mezica data indicates a positive relation of As and Fe/Ge (Figures 4.12, 4.13, 4.14). In addition, in the LA–ICP MS dataset a positive relation between As and Tl is visible (Pearson's r = 0.9; Figure 4.16).

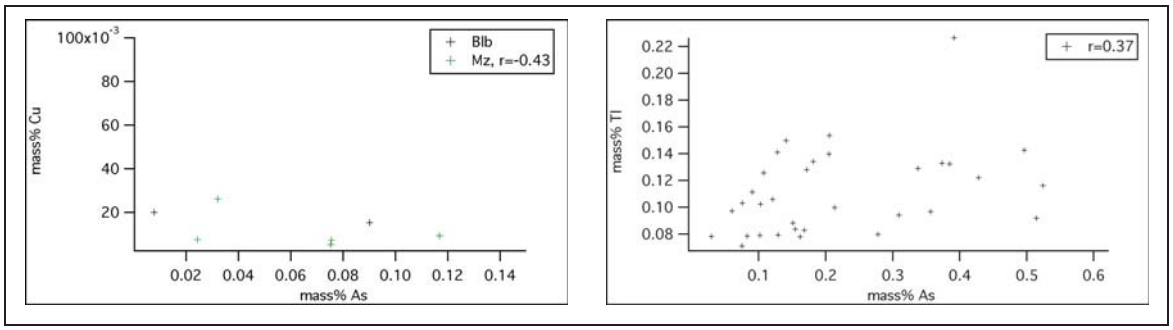

Figure 4.15: Plots showing the relation between As and Cu (right) and As and Tl (left). The calculation of the correlation coefficients (r) was performed with the formula of Pearson, which assumes a linear dependency between two variables.

Copper

Cu was only rarely detected using EMP techniques. LA–ICP MS measurements confirmed that the Cu concentrations of sphalerites in both samples are generally below 20 ppm and thus are below the detection limit of the EMP (> 50 – 110 ppm). In the few cases when Cu could be analyzed with the EMP, Cu contents range from 50 ppm to 0.41 mass%. Comparison of the EMP sphalerite data of Bleiberg and Mezica indicates that Cu concentrations are higher at Mezica. In Mezica Cu was above the detection limit in 83 out of 337 (25%) analyses, whereas at Bleiberg it was only 35 out of 1805 (2%). Within the Mezica dataset Cu was very often detected in four samples (Mz01.1, Mz02b, Mz08 and Mz09) from the Union and Moring district. The sphalerite in these samples are characterized by high Cd (> 0.1 mass%) and rather low Fe concentrations (generally in the 100 ppm range). The preferred Cu enrichment in Cd rich sphalerite is also indicated by the positive correlation between Cu and Cd within the Mezica data (r = 0.43, Figure 4.11).

LA-ICP MS data of sphalerite from samples Blb26 and WSBlb29 indicate a weak positive correlation of In and Cu. Indium was only detectable when Cu was also higher, i.e. above the LA-ICP MS detection limit (≈ 0.15 ppm). For verification of this trend more LA-ICP MS analyses are, however, necessary.

Thallium

Thallium was detected very rarely with EMP techniques. Only less than 2% of the analyses showed Tl contents above the detection limit of the microprobe (300 ppm Jeol, MUL; 670 ppm CAMECA, BGR). The maximum Tl concentration measured with EMP is 0.23 mass% (Schalenblende, Bleiberg, Maxer Bänke horizon, Blb17). However, the precision of the Tl data achieved from EMP measurements is partly dubious and must be interpreted with care. Replicate measurements of the same spots using the EMP at Montanuniversitaet Leoben (MUL) and at BGR Hannover did not match. Thallium was more often detectable with the CAMECA microprobe at BGR, although the detection limit of this microprobe was higher than that of the JEOL microprobe at MUL. Only few analyses, done at Leoben, yield values above the limit of detection. Probably the standard material, which is available in Leoben (TlBrI), is not suitable for analysis of trace amounts of Tl in a sulfide lattice, because of the different types of chemical bonding in these compounds. The LA-ICP MS measurements of samples Blb26 and WSBlb29 confirmed the presence of trace amounts of Tl (Chapter 4.2.2). In literature an average Tl concentration of 0.1 ppm is reported for Bleiberg sphalerite (Schroll, 1997). This very small value is clearly below the limit of detection of the EMP.

Thallium was only found in measurable concentrations in sphalerites from the Bleiberg deposit. It is not sure if this is a characteristic feature of Bleiberg or an analytical artifact, which is caused by the difficulties with Tl measurements. Thallium was more often detected in schalenblende than in sphalerite crystals (similar to As). Furthermore are higher Tl contents more frequent in sphalerites, which contain more Fe than Cd. However, Tl cannot be used as a discriminating element to distinguish sphalerites from Bleiberg from those of

other deposits. For this purpose the Tl data are too scarce and heterogeneous. The correlation of Tl with As and Pb was dealt with before (Figure 4.16).

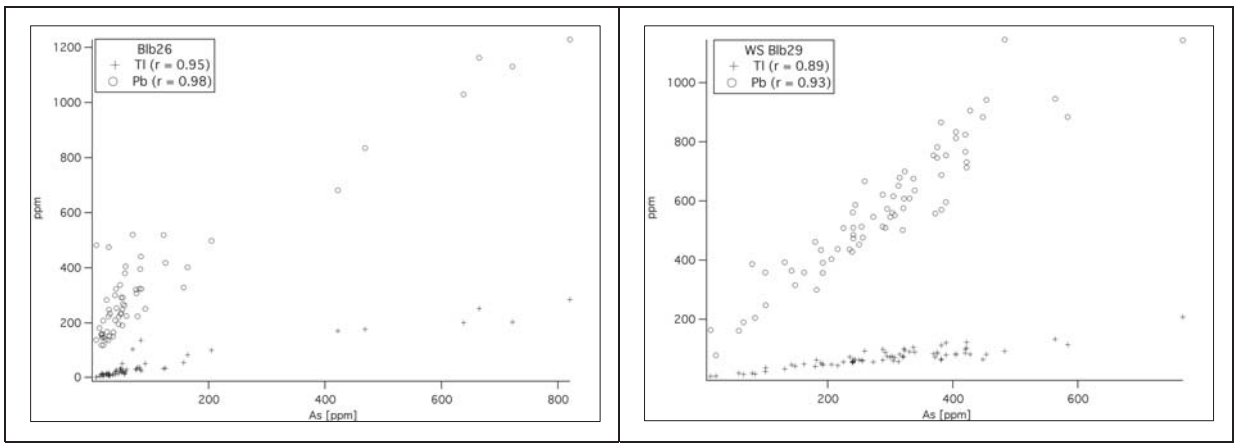

Figure 4.16: LA ICP-MS data for As, Pb and Tl for samples Blb26 (left) and WS Blb29 (right) from Bleiberg. In contrast to EMP data a clear positive correlation (Pearson's correlation coefficient, r) between As and Pb and Tl is evident within both samples.

4.3 Isotopes of Sulfur and Lead

4.3.1 Sulfur isotopes

Sulfur isotope composition ($\delta^{34}S$) of sulfides was measured in 17 samples, from 5 different Pb-Zn deposits of the Drau Range (Appendix, Table 16). Furthermore $\delta^{34}S$ in one sample from the Zunderwand occurrence, which is an Anisian Pb-Zn mineralization close to Radenthein not located in the Drau Range, was measured. The analyses were focused on the sulfur isotope composition of sphalerites, but also galena and Fe-sulfides (if present) were measured in order to test if the sulfur isotope composition of different sulfide species within one sample is similar and if the fractionation of ^{34}S in the three sulfide phases reflects isotopic equilibrium among the different sulfides or not.

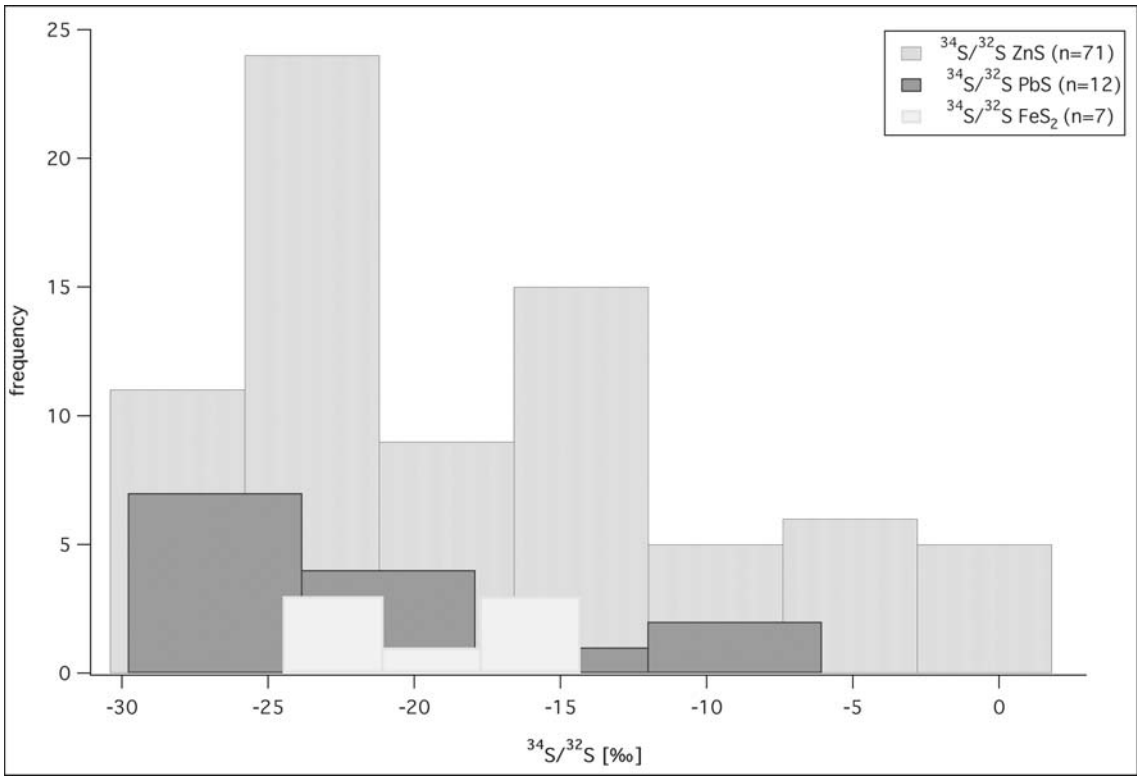

Figure 4.17: Histogram showing the frequency and distribution of $\delta^{34}S$ values in sphalerite, galena and pyrite. Two clear peaks are evident in the $\delta^{34}S$ distribution of sphalerites, one at about -25 the other at about -15 ‰. Furthermore a strong skewness towards negative (< -20‰) $\delta^{34}S$ values is present within the dataset. The number of bins displayed for each mineral depends on the number of analyses.

The investigated sulfides show a considerable range of $\delta^{34}S$ values. Sphalerites display $\delta^{34}S$ values varying from -30.4 to +1.8‰. These values are the threshold $\delta^{34}S$ values of sulfides for the whole dataset. Since sulfur isotope measurements were focused on sphalerite, the variations in $\delta^{34}S$ of galena and pyrite/marcasite are smaller compared to sphalerite (galena: -29.8 to -6.1‰/Fe-sulfides: -24.5 to -14.4‰). Figure 4.17 shows the frequency distribution of $\delta^{34}S$ values in a histogram of all three sulfides minerals in the Drau Range sample set. The dataset shows a clear tendency towards light sulfur isotope signature in sulfides. More than

50% of the investigated sulfides are characterized by $\delta^{34}S$ values < -20‰. In the $\delta^{34}S$ distribution of sphalerites two marked peaks, at about -25 and -15 ‰ are present. Furthermore, a less distinct peak at around -5 ‰ is observed. The limited $\delta^{34}S$ data for FeS_2 and PbS do not display a similar three-peak distribution of $\delta^{34}S$. Sulfur isotope composition of galena was only measured in samples from Bleiberg and Mezica. The $\delta^{34}S$ values range from -29.8 to -6.1‰. The $\delta^{34}S$ values of galena are always similar to the $\delta^{34}S$ of the sphalerite, which occur together within the sample. No strict fractionation sequence of ^{34}S in coexisting galena-sphalerite pairs in the way of $\delta^{34}S$ PbS < $\delta^{34}S$ sphalerite is visible in the whole sulfur isotope data set. The relation of $\delta^{34}S$ values in coexisting sphalerite and galena changes from one sample to another and is described in the detail in chapter 4.4. Fe-sulfides show a much smaller variation in sulfur isotope compositions, which range from -24.4 to -14.4 ‰. Also no persistent fractionation trend between coexisting ZnS-FeS_2 pairs is evident within the sample set.

Sulfides from the Bleiberg deposit display the largest variation in $\delta^{34}S$ values (-30.4 to -1.5‰) and cover nearly the complete $\delta^{34}S$ range. However, more Bleiberg samples were investigated on the sulfur isotope composition, and thus larger $\delta^{34}S$ variability in Bleiberg samples might be an analytical artifact. Sulfur isotope composition in the three investigated Mezica samples varies over approximately 10‰ (-20 to -10‰). The sphalerites in the single non-Drau Range sample have $\delta^{34}S$ values close to zero and occupy therefore an outlier position with respect to most of the Drau Range sphalerites (and other sulfides). However, the non-Drau Range sample does not mark the positive $\delta^{34}S$ threshold position. The heaviest sulfur isotope composition ($\delta^{34}S$ +1.8‰) was found in sphalerites from the Jauken deposit (western Drau Range). The most negative $\delta^{34}S$ values of -30.4‰ were measured in sphalerite from the Bleiberg deposit (Kalkscholle, crest horizon).

4.3.2 Lead isotopes

Determination of Pb isotope ratios by TIMS analysis was carried out on 7 handpicked galena separates (5 samples) and on 9 sphalerite separates (6 samples, Table 4.4). It was difficult to obtain pure mineral separates. Therefore only few sphalerite and galena separates suitable for the Pb isotope measurements were available. The results of the Pb isotope measurements of galena and sphalerite are listed in table 4.4 and displayed in figures 4.18, 4.19 and 4.20 respectively. In order to allow the direct comparison with previously published data (summarized in Schroll, 1997) the data presented here were corrected using the same Pb isotope ratios for the NBS981 standard as used in these previous studies (e.g. Köppel 1983). The original data, which have been obtained by highly precise double-spike technique, are listed in the appendix (Table 17).

Table 4.4: Results of Pb isotope measurements and the approximate Pb concentrations (c., ppm) of sphalerites from Pb-Zn deposits in the Drau Range. In order to allow a better comparison with previously published data (summarized in Schroll, 1997) the Pb isotope ratios have been corrected using the same values for reference material NBS981 as used for the comparison data set (e.g. Köppel, 1983). The values for NBS981 are given in Cumming et al. (1987). The uncertainty of the measurements (2σ) was calculated after repeated measurements (n = 8) of the NBS981 standard.

sample/origin	ID	Min.	c. [ppm]	$^{206}Pb/^{204}Pb$ ±0.004%	$^{207}Pb/^{204}Pb$ ±0.004%	$^{208}Pb/^{204}Pb$ ±0.005%
EHK02 Bleiberg, Erzkalk horizon	EHK02 ZnS-SB	Sp	18600	18.380	15.666	38.529
	EHK02 ZnS-xx	Sp	5000	18.381	15.668	38.535
	EHK02 PbS1	Gn	890000	18.379	15.667	38.529
	EHK02 PbS2	Gn	890000	18.378	15.665	38.254
J10.4 Bleiberg, Josefischolle (Crest horizon)	J10.4 ZnS-xx	Sp	700	18.371	15.667	38.536
	J10.4 ZnS-SB	Sp	7600	18.373	15.668	38.539
	J10.4 PbS	Gn	890000	18.374	15.668	38.550
E14.6 Bleiberg, Erlach	E14.6 ZnS	Sp	5200	18.386	15.665	38.524
	E14.6 PbS	Gn	890000	18.387	15.668	38.526
C6.14, Bleiberg 1st Raibl.horizon	C6.14 ZnS	Sp	500	18.385	15.669	38.540
Mz08 Mezica, Moring	Mz08 ZnS	Sp	3000	18.366	15.666	38.533
	Mz08 PbS	Gn	890000	18.363	15.666	38.532
MzH01 Mezica, Helena	MzH01 ZnS-SB	Sp	61200	18.403	15.663	38.502
	MzH01 ZnS-xx	Sp	400	18.435	15.666	38.499
	MzH01 PbS1	Gn	890000	18.401	15.665	38.506
	MzH01 PbS2	Gn	890000	18.392	15.666	38.513
JK5-9, Jauken	JK5-9 ZnS	Sp	150	18.418	15.670	38.535

Galena data are shown on $^{207}Pb/^{204}Pb$ vs. $^{206}Pb/^{204}Pb$ and $^{208}Pb/^{204}Pb$ vs. $^{206}Pb/^{204}Pb$ plots (Figure 4.18). Most of the galena separates irrespective whether they are coming from different deposits or ore horizons within one deposit define rather linear trends (within the 2-sigma uncertainties of the analyses) in the $^{207}Pb/^{204}Pb$ vs. $^{206}Pb/^{204}Pb$ and $^{208}Pb/^{204}Pb$ vs. $^{206}Pb/^{204}Pb$ plots. Only sample Mz08 from Moring district in Mezica is an exception. It occupies an outlier position in both plots (Figure 4.18).

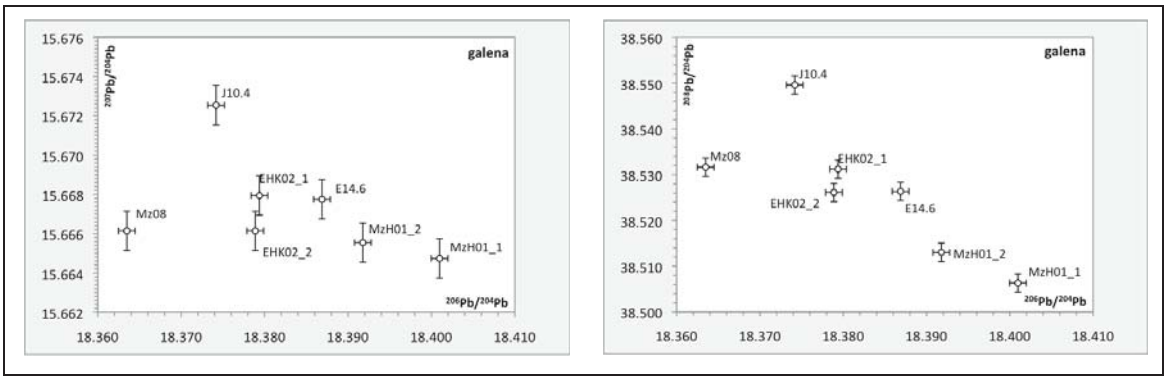

Figure 4.18: Plots of $^{207}Pb/^{204}Pb$ vs. $^{206}Pb/^{204}Pb$ (left) and $^{208}Pb/^{204}Pb$ vs. $^{206}Pb/^{204}Pb$ (right) of galena. The analytical 2σ uncertainties are shown as error bars. For sample numbers and locations see table 4.4.

Highly variable Pb concentrations were determined within the sphalerite separates. The measured Pb concentrations range from approximately 150 to 61200 ppm (Table 4.4). Very high Pb concentrations in the range of several thousands of ppm were commonly measured in schalenblende separates. These extreme values are likely due to (sub)microscopic galena inclusions. Sphalerite display similar linear trends in the Pb isotope plots like galena, except of the Jauken deposit (JK5-9) and the crystalline sphalerite in sample MzH01 (ZnS-xx) from Mezica; Figure 4.19). The sphalerites in samples JK5-9 and MzH01 are characterized by clearly more radiogenic Pb isotope ratios and occupy outlier positions in Figure 4.19.

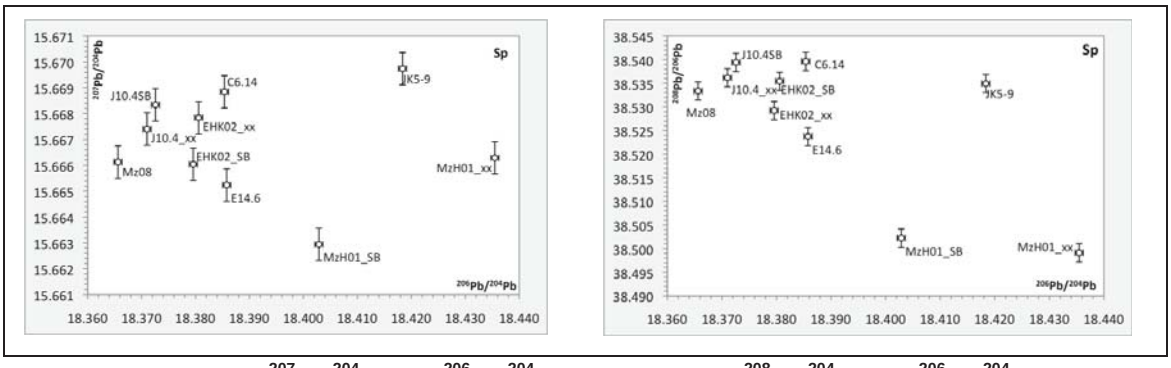

Figure 4.19: Plots of $^{207}Pb/^{204}Pb$ vs. $^{206}Pb/^{204}Pb$ plot (left) and $^{208}Pb/^{204}Pb$ vs. $^{206}Pb/^{204}Pb$ (right) of sphalerite. The 2σ uncertainty is shown in error bars. For sample numbers and locations see table 4.4.

Combined measurement of Pb isotope ratios in co-existing sphalerite and galena was only possible in five samples (Table 4.4). Comparison of the Pb isotope data of

sphalerite and galena on $^{207}Pb/^{204}Pb$ vs. $^{206}Pb/^{204}Pb$ and $^{208}Pb/^{204}Pb$ vs. $^{206}Pb/^{204}Pb$ plots shows that within most samples the two sulfides mostly have similar (considering the 2-sigma uncertainties) isotope ratios. (Figure 4.20). Sphalerite from sample MzH01 (ZnS-xx) is exceptional in that its Pb isotope signature differs clearly from the other mineral separates of this sample (Figure 4.20).

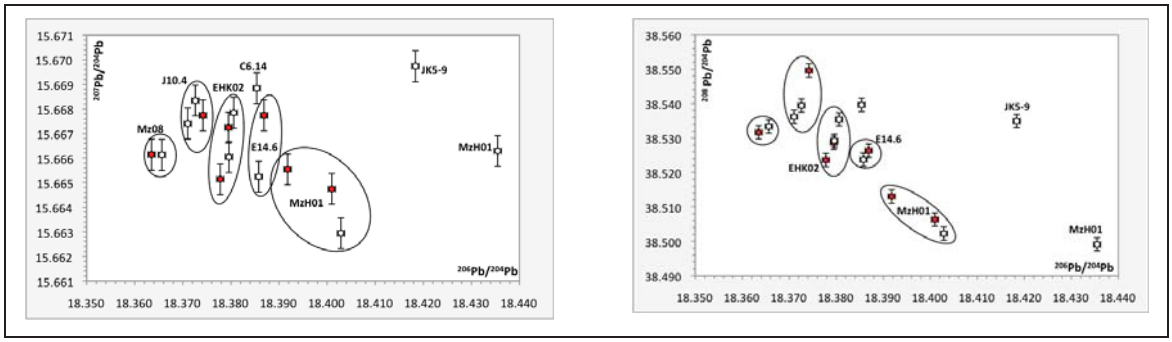

Figure 4.20: Comparison of Pb isotope ratios of galena (red circles) and sphalerite (white circles) Pb isotope ratios in $^{207}Pb/^{204}Pb$ vs. $^{206}Pb/^{204}Pb$ plot (left) and $^{208}Pb/^{204}Pb$ vs. $^{206}Pb/^{204}Pb$ (right) plots. The ellipses mark sphalerite and galena separates, which were obtained from the same sample. For sample numbers and locations see table 4.4.

4.4 Detailed Investigations of Textures, Chemistry and Isotopy

The sphalerites from the Pb-Zn district of the Drau Range are, as outlined in the chapters above, highly variable regarding their mineralogy, texture, chemical composition and sulfur isotope composition. The aim of this chapter is to combine the results, which have been obtained by petrography and chemical methods summarized in the chapters 4.1 -.4.3, in order to find out if the different parameters are linked together.

In some samples the sphalerites show distinct variations in textures, chemical composition and $\delta^{34}S$ values on a small scale (max. 3 cm). In three samples from the Bleiberg deposit (different ore horizons) systematic variations of textures, chemical composition and $\delta^{34}S$ values occurs. Combined results of these samples will be documented in detail in the following.

4.4.1 Maxer Bänke horizon, Bleiberg

Blb17

Sample Blb17 originates from the “Bellegarde Schachtl Läufl” in the western part of the Bleiberg mine. The ore assemblage within this sample consists of sphalerite and galena with a predominance of sphalerite. A main feature of this sample is a schalenblende aggregate (lower part of figure 4.21 a; b). Furthermore, sphalerite rich layers trend parallel to this schalenblende aggregate (upper 2/3 of figure 4.21). Fluorite is the main gangue constituent (approximately 40 vol% of the sample, Figure 4.21 b). Besides of fluorite, minor amounts of quartz and dolomite are present as further gangue components (Figure 4.21 b).

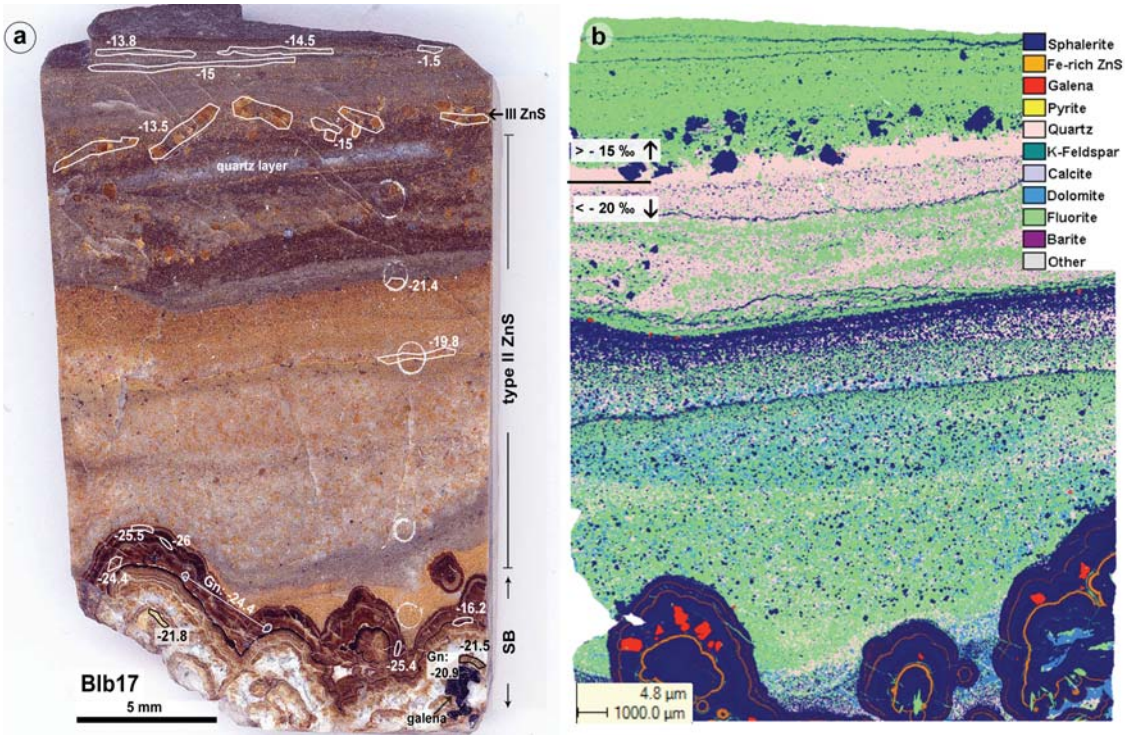

Figure 4.21: a) Polished slap of sample Blb17 showing the spatial distribution of δ34S values in relation to sulfide textures. The chronological sequence of the different mineralizing events is from the bottom to the top of the sample (see text for details). b) QUEMSCAN image of the respective thin section. The QUEMSCAN image nicely illustrates the differences within the gangue paragenesis, which are partly associated to the sphalerite textures.

Based on textural differences, three main sphalerite types are distinguished in this sample (Figure 4.22): *(1)* an approximately 0.5 cm thick microcrystalline schalenblende aggregate (SB), which exhibits typical schalenblende layering (Figure 4.22 a, b). *(2)* Fine-grained (< 100µm), mostly euhedral sphalerite crystals (ZnS II, Figure 4.22 c, d). *(3)* Rather coarse-grained (1000 µm) subhedral brownish crystalline sphalerite (ZnS III, Figure 4.22 d, e). The fine-grained sphalerite occurs dispersed and partly in discrete layers, in a gangue mixture of fluorite and quartz. Sphalerite in individual layers is characterized by certain size and color of the grains. The coarse-grained ZnS III occurs

above a quartz layer in a mono-mineralic fluorite gangue (Figure 4.21 b). Galena is only an accessory ore mineral in this sample and forms small inclusions in the schalenblende.

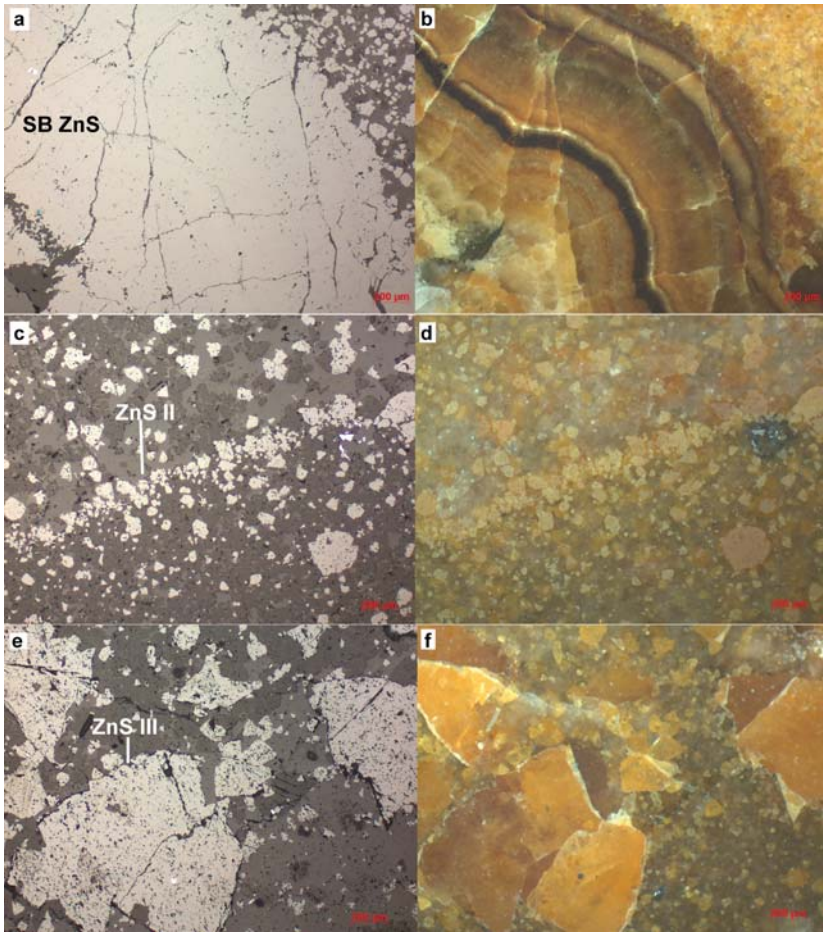

Figure 4.22: Microphotographs (reflected light) of the three different sphalerite types in sample Blb17. a, b) Schalenblende (a PPL, b XPL). c, d) Fine-grained crystalline sphalerite (ZnS II) dispersed and partly enriched in a layer (c PPL, d = XPL). e, f) Coarse-grained crystalline sphalerite (ZnS III) (e PPL, f XPL).

Directly adjacent to the schalenblende aggregate, the layering of ZnS II follows the curvature of the botryoidal surface of the schalenblende, which indicates that the schalenblende formed prior to the ZnS II. Thus the younging direction is oriented upwards in Figure 4.21.

Sphalerite chemistry and $\delta^{34}S$ of sulfides in Blb17

The boxplots in Figure 4.23 show the trace element characteristics of the three sphalerite types present in Blb17 (SB, ZnS II, ZnS III). Fe contents in the schalenblende are very variable, but on average enriched (mean approximately 1 mass%) compared to the other types of sphalerite. Individual layers of the schalenblende have up to 5.5 mass% Fe (e.g. the dark brown layer in Figure 4.22 b. The Cd contents of the schalenblende are by comparison low, ranging from 0.04 to 0.28 mass% (mean 0.14 mass%). Fe contents in the fine-grained ZnS II are varying over a smaller range (0.03 to 0.9 mass%) and are generally lower than in the schalenblende (mean 0.36 mass%). Cd contents in the fine-grained ZnS II are similar

to that of the schalenblende. The coarse-grained ZnS III and also the above following layers of fine-grained sphalerite are characterized by very low Fe concentrations (< 0.1 mass%, mean 0.035 mass%) and increased Cd contents between 0.24 and 0.44 mass% (mean 0.36 mass%). These obvious differences in the Fe and Cd contents are best evident in the Fe-Cd ratios. The schalenblende has an average Fe-Cd ratio of 8.6, the fine-grained ZnS II is characterized by Fe-Cd of 3.6 and the coarse-grained and following ZnS III by 0.1. Besides these clear differences in Fe:Cd of the different sphalerite types, also minor differences regarding the Pb, As and Tl concentrations are present. The early-formed schalenblende is also enriched in Pb and As and contains the highest measured Tl contents (0.23 mass%). Also within the ZnS II Tl concentrations (0.08 – 0.14 mass%) were above the detection limit in three analyses.

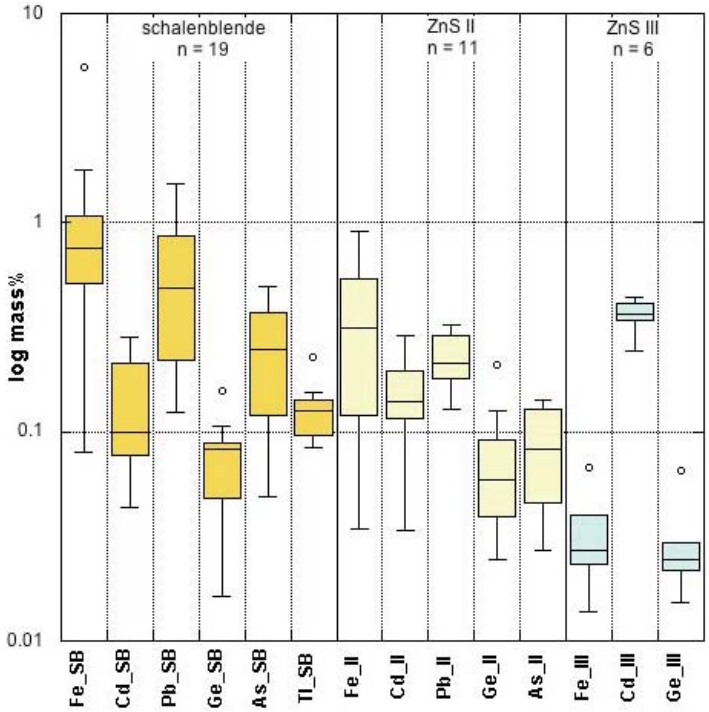

Figure 4.23: Boxplots summarizing variability of minor/trace elements in the three different sphalerite types in sample Blb17; SB = schalenblende, II = ZnS II, III = ZnS III (see text).

Besides the variations in the chemical composition, the morphologically different sphalerites are characterized by variable $\delta^{34}S$ values (-25 to -1.5‰). Figure 4.21 shows the $\delta^{34}S$ values in relation to the textural aspects in sample Blb17. The schalenblende and the ZnS II layers up to the quartz layer (upper third of Figure 4.21) have a light sulfur isotope composition ($\delta^{34}S$ values < -20‰). Some non-systematic variations in $\delta^{34}S$ (from -26 to -16‰) already occur within the schalenblende aggregate itself. The least negative $\delta^{34}S$ was measured in a thin, very Fe-rich schalenblende layer. Galena, which is included in the schalenblende, has similar negative $\delta^{34}S$ values from -24.4 to -20.9‰. The fine-grained ZnS II, deposited between the schalenblende and the quartz layer, exhibits $\delta^{34}S$ values of -21.4 and -19.8‰. Coarse-grained ZnS III mainly occurs above this quartz layer and is characterized by less negative sulfur isotope composition. The $\delta^{34}S$ values of it range between -15 and -13.5‰. The uppermost, very fine-grained (~10µm) sphalerite layer shows a dramatic change in sulfur isotope composition. In this fine-grained layer $\delta^{34}S$ is -1.5‰. Unfortunately, only very small

amounts of this layer were present in the sample. Hence, it was not possible to replicate this sulfur isotope measurement.

Combination of the different parameters shows that the textural variations of sphalerite in this sample can be related to geochemical and sulfur isotope variations. The microcrystalline schalenblende is rather Fe-rich/Cd-poor (average Fe-Cd ratio of 8.6) and additionally enriched in As, Pb and Tl. It shows, despite some internal variations in $\delta^{34}S$, a very negative sulfur isotope composition (commonly $\delta^{34}S$ < -20‰). The following fine-grained ZnS II layers show lower Fe contents than the schalenblende, but similar low Cd contents (Fe-Cd ratio of 3.6). In comparison to the schalenblende it is furthermore depleted in Pb and As. The sulfur isotope composition is with similar to the schalenblende. The textural change towards coarse-grained ZnS III is connected to a decrease in Fe, Pb and As and an increase in Cd contents (average Fe-Cd of 0.1). It is also related to a change in $\delta^{34}S$ values, towards less negative values (> -15‰).

Blb26

Sample Blb26 is from the same locality as Blb17. The sample exhibits stratiform sphalerite layers, which are interlayered with gangue material of different color. The individual sphalerite-rich layers differ in the modal amount, grain size and color of sphalerite (Figure 4.24; Figure 4.25). In addition minor amounts of very fine-grained (max. 10 µm) galena and pyrite are present.

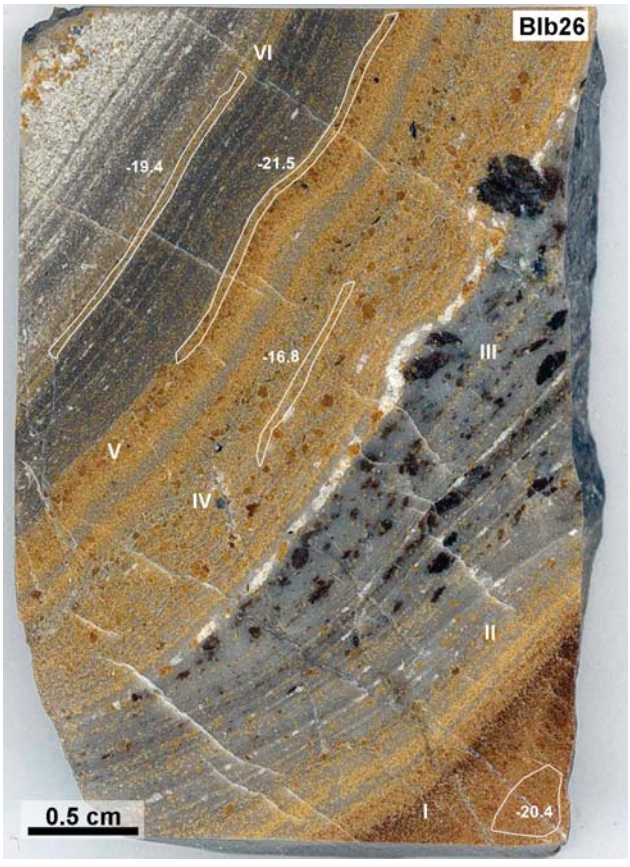

Figure 4.24: Polished slab of sample Blb26. Roman numbers I to IV refer to the sphalerite notification, which is used in the boxplots (Figure 4.26). δ34S values vary by about 5‰ within this sample although variation is not systematic.

The gangue in Blb26 is mainly composed of carbonates (calcite and/or dolomite). Further gangue constituents are fluorite and quartz. The carbonates are concentrated in layers too. The grain size of the gangue is also variable, but roughly corresponds to the grain size of sphalerite next to it: i.e. coarse sphalerite grains are usually associated to rather coarse-grained gangue. Very fine-grained (<5 µm) sphalerite and Pyrite mineralization has furthermore been observed along cleavage planes and grain boundaries of coarse-grained dolomite accumulations in the central part of the sample (Figure 4.25 b, Figure 4.24). The relative chronology of precipitation of sphalerite and carbonate layers is from bottom right to top left as shown on Figure 4.24. The relative timing of sphalerite formation can be determined, because the sphalerite mineralization follows elevations and depressions, which result from the coarse-grained dolomite accumulations underneath.

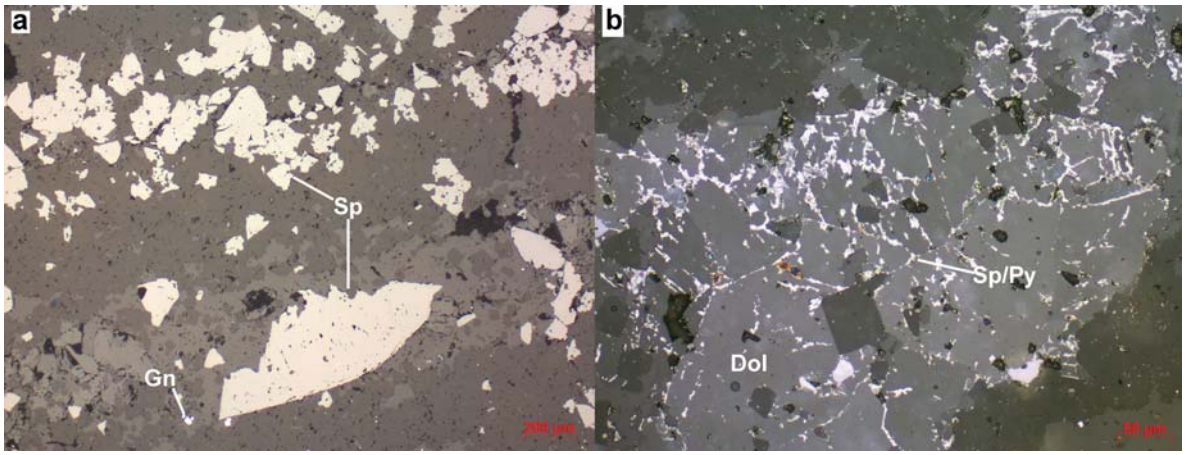

Figure 4.25: Microphotographs (reflected light) of sample Blb26. a) Coarse-grained sphalerite next to a layer of finer-grained sphalerite. b) Fine-grained sphalerite +pyrite forming along cleavage planes and grain boundaries of gangue dolomite. Furthermore, some fluorite crystals (dark grey in reflected light) are visible.

Sphalerite chemistry and $\delta^{34}S$ of sulfides in sample Blb26

The trace/minor element composition of the sphalerites shows variation from one layer to another. The boxplots (Figure 4.26 a) display the variability of Fe and Cd in six different sphalerite layers (numbered I to VI in Figure 4.24). Figure 4.26 b also displays the variability in Pb and Ge concentrations. The early-formed brown sphalerites (number I in Figure 4.24) are by comparison enriched in Fe, Pb and Ge. They contain regularly measurable (by EMP) concentrations of As and Tl (not displayed in Figure 4.26). Increased concentrations of those elements are accompanied by low Cd contents. In the later formed sphalerite layers (II to VI) a jump towards high Cd and low Fe/Ge contents is evident. Pb concentrations in the sphalerite layers II to VI are also slightly lower than in layer I, but the differences are less distinct. The change in Fe and Cd contents from layer I to layers II – VI is the most obvious one. Fe decreases by about factor 5 and Cd increases by about factor 4. In this sample a clear negative correlation between FE and Cd contents is evident.

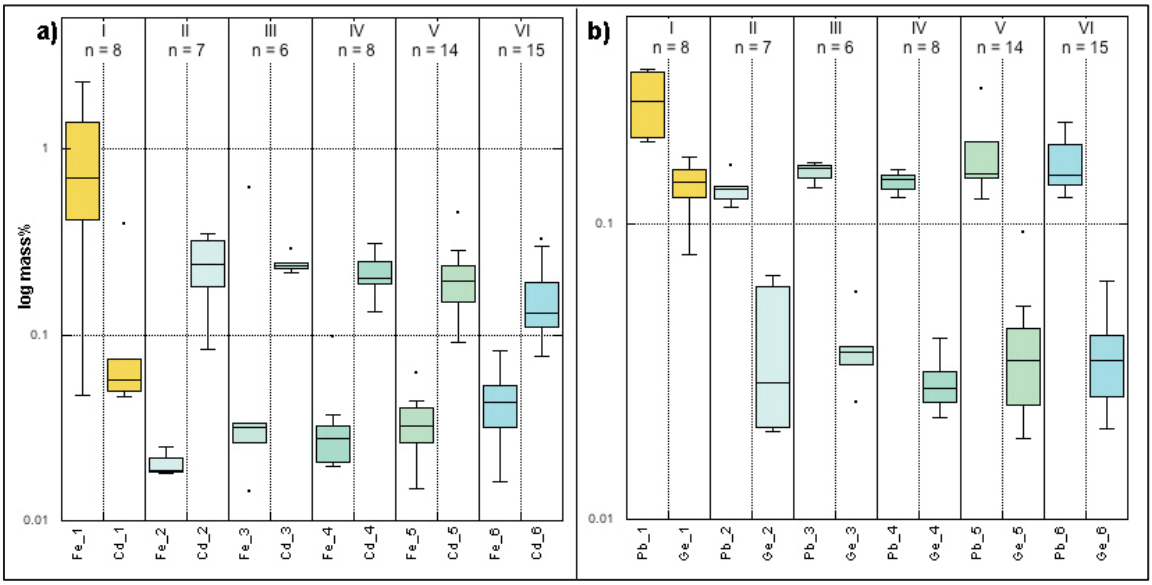

Figure 4.26: a – b) Boxplots summarizing the minor/trace element variability of sphalerites in layers I to IV in sample Blb26. a) Fe and Cd, b) Pb and Ge.

Regardless of the strong variations in the chemical composition of the sphalerites only minor and non-systematic variations in $\delta^{34}S$ were documented (Figure 4.26). In the early-formed Fe (+ Ge) rich sphalerites $\delta^{34}S$ is -20.4‰. The jump towards higher Cd and low Fe/Ge in the central part of sample Blb26, where coarse- and fine-grained sphalerites co-occur, is accompanied a shift in $\delta^{34}S$ values of about 4 ‰ units ($\delta^{34}S$ -16.8 ‰). Towards the top of the sample again very light values ($\delta^{34}S$ of -21.5 and -19.4 ‰) were measured.

4.4.2 Erzkalk horizon, Bleiberg

EHK02

Sample EHK02 originates from a western position in the Bleiberg mine (Antoni, 6th level, Pflockschachtlager). The ore assemblage consists of approximately the same amounts of galena and sphalerite (Figure 4.27; each 20 vol%). Furthermore, minor amounts of pyrite are present. The major gangue phases in EHK02 are barite (about 30 vol%) and fluorite. Carbonates and quartz are minor gangue constituents. Barite has white color and forms massive bands of tabular crystals. The top part of the sample is free of barite and is dominated by fluorite. The whole sample, especially in its lower part, shows evidence of brittle deformation, which caused formation of micro-fractures now mostly filled with dolomite.

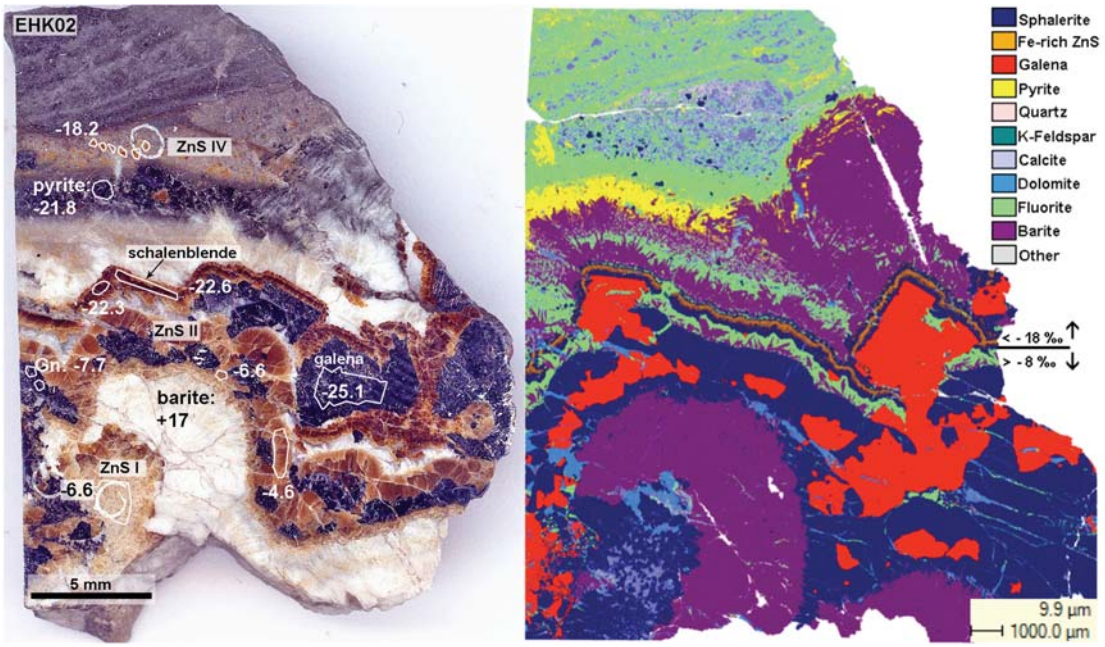

Figure 4.27: a) Photograph of the polished slap prepared from sample EHK02 for sulfur isotope analyses. Macroscopically different sphalerite textures are evident within this sample. Besides, galena is macroscopically visible within this sample. Furthermore, the results of the sulfur isotope analyses of sphalerite, galena, pyrite and barite are displayed. b) QUEMSCAN image of the respective thin section, which illustrates the differences that occur in the ore-gangue paragenesis.

Sphalerite and galena are enriched in the central part of the sample (Figure 4.27), where two texturally different sphalerite bands/aggregates overgrow up to 5 mm large (partly euhedral) galena crystals (Figure 4.27). In the lower part coarser-grained polycrystalline sphalerite (ZnS II, Figure 4.28 a & b) of uniform beige color is present. Besides an approximately 800 µm thick microcrystalline schalenblende aggregate (Figure 4.28 c & d) occurs. The schalenblende aggregate consists of three differently colored microcrystalline sphalerite-layers with a thin intercalation of a fluorite-barite band in-between. A further, approximately 800 µm thick barite-fluorite band separates the schalenblende from the coarse-grained ZnS II aggregate. Additionally, minor

amounts of crystalline sphalerite are present below (ZnS I, Figure 4.28 e) and above (ZnS IV, Figure 4.28 f) the central ore accumulation. The ZnS I (in the lower part of Figure 4.27) has pale beige color. It forms a gangue-inclusion rich accumulation and is in its morphology very similar to ZnS II. In the upper part of the sample ZnS IV forms subhedral grains of a few 100 µm size. Both, ZnS I and ZnS IV are intergrown with carbonates.

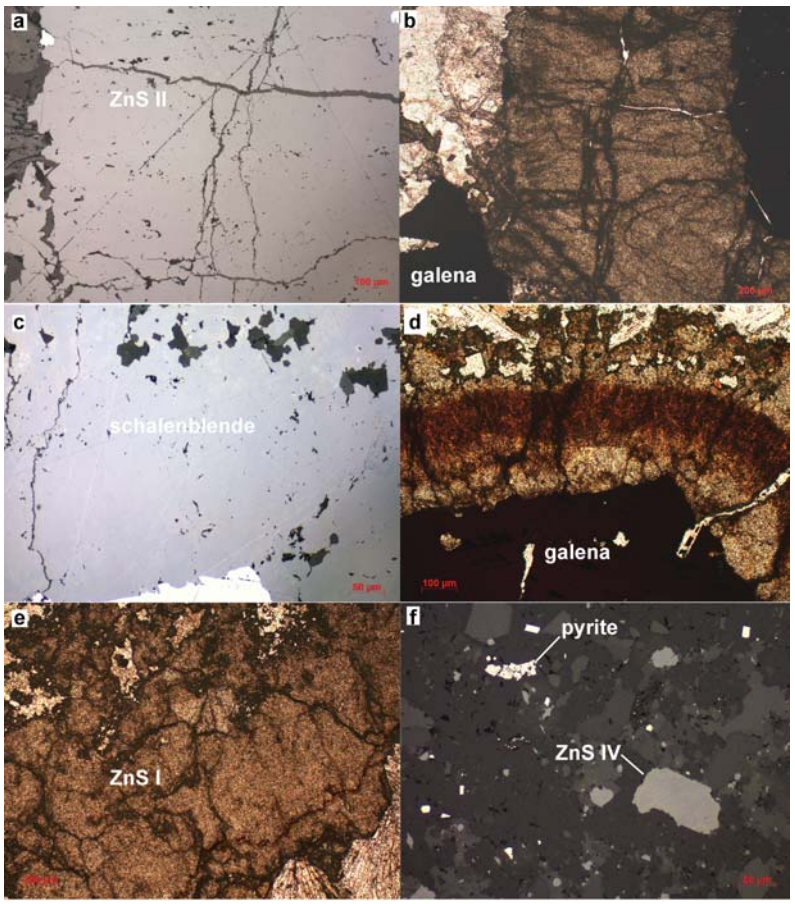

Figure 4.28: (a – f): Reflected and transmitted light microphotographs (all PPL) of sphalerites in sample EHK02. a) Coarse-grained ZnS II, reflected light. b) The same aggregate (but lower magnification) in transmitted light. c). Schalenblende next to galena, reflected light. d) Same micro-area in transmitted light. e) Crystalline coarse-grained ZnS I, transmitted light. f) Sub- to anhedral ZnS IV and pyrite, reflected light.

Textural relations of the different sphalerite types in EHK02 allow establishing of a relative growth chronology. ZnS I is overgrown by barite, which itself is overgrown by the ZnS II aggregate, which in turn is overgrown by barite/fluorite and the schalenblende. Thus it is very supposable that ZnS I formed prior to ZnS II, which formed prior to the schalenblende and ZnS IV. Formation of the ZnS II aggregate was closely connected to the formation of anhedral coarse-grained galena. Schalenblende precipitation was predated by formation of large euhedral galena crystals, which are overgrown by the schalenblende. ZnS IV is hosted by a partly different gangue paragenesis than the earlier formed sphalerites in this sample and formed at the latest stage. The formation of ZnS IV is preceded by precipitation of a pyrite band. Pyrite grains co-exist also with the ZnS IV grains. The whole texture of this sample can be best interpreted due to crystallization pulses of ore minerals and gangue minerals in an open cavity. The relative timing of the crystallization events is from the bottom to the top of the sample (as shown in Figure 4.27). Regarding the distribution of the gangue

phases, two main paragenetic stages are distinguished. In the lower part barite and carbonates are the exclusive gangue minerals, whereas in the upper part fluorite becomes a major and calcite a minor gangue mineral and barite becomes completely absent.

Sphalerite chemistry and $\delta^{34}S$ + Pb isotope signature of sulfides in EHK02

The trace element variability of the four different sphalerite types in EHK02 is summarized in boxplots (Figure 4.29). The schalenblende (blue boxes in Figure 4.29) is characterized by very variable trace/minor element contents. Especially Fe-concentrations show a large variability (0.7 – 3.2 mass%), but are mostly increased (mean 0.97 mass%). The dark brown layer in the middle of the aggregate is very Fe-rich (generally >1 mass%). Cadmium contents of the schalenblende are between 0.05 and 0.37 mass% (average 0.16 mass%) and therefore lower than Fe. The average Fe-Cd ratio of the schalenblende is 14.8 and thus very high. Within the schalenblende As was nearly permanently measurable with the microprobe (not displayed in figure 4.29) and furthermore high Pb concentrations were measured. One analysis of the schalenblende revealed 0.08 mass% Tl. The beige ZnS II aggregate shows less trace/minor element variability than the schalenblende. The Fe concentrations range from 0.06 to 0.1 mass% (mean 0.09) and are clearly lower than in the schalenblende. Cd concentrations are between 0.65 and 0.86 mass% (mean 0.3 mass%). The Fe-Cd ratio of ZnS II is 0.5 and thus, compared to the adjacent schalenblende, very small. The chemical variability of the beige ZnS II is displayed in the turquoise boxes in Figure 4.29. The early-formed ZnS I show similar trace element characteristics like the ZnS II aggregate. The Fe concentrations are low whereas Cd contents are increased (average Fe-Cd ratio 0.5). The latest formed ZnS IV grains contain more Fe than ZnS I and ZnS II, but smaller amounts than the schalenblende. The Cd contents in ZnS IV are generally low (average Fe-Cd ratio 1.6). ZnS IV contains furthermore constantly detectable As contents (not displayed in Figure 4.29).

Sample EHK02 evidences a large range in $\delta^{34}S$ values, both for sphalerite and galena. Two galena analyses yielded $\delta^{34}S$ values of -7.7 and -25.1‰, respectively. $\delta^{34}S$ values of sphalerites vary between -4.6 and -22.6‰ (Figure 4.27). One pyrite analysis yielded a $\delta^{34}S$ value of -21.8‰. The sulfur isotope composition of the sulfides in this sample shows a bimodal spatial distribution. Sulfides in the lower part of EHK02 (ZnS I and ZnS II aggregate) have distinctly less negative $\delta^{34}S$ values (> -8‰) than those in the upper part of the sample (schalenblende and ZnS IV, $\delta^{34}S$ < -18‰).

The Pb isotope signature of the early sphalerites (ZnS I, ZnS II) and the later schalenblende stage are very similar. Furthermore, both galena stages are also very similar to the sphalerite in their Pb isotope signature.

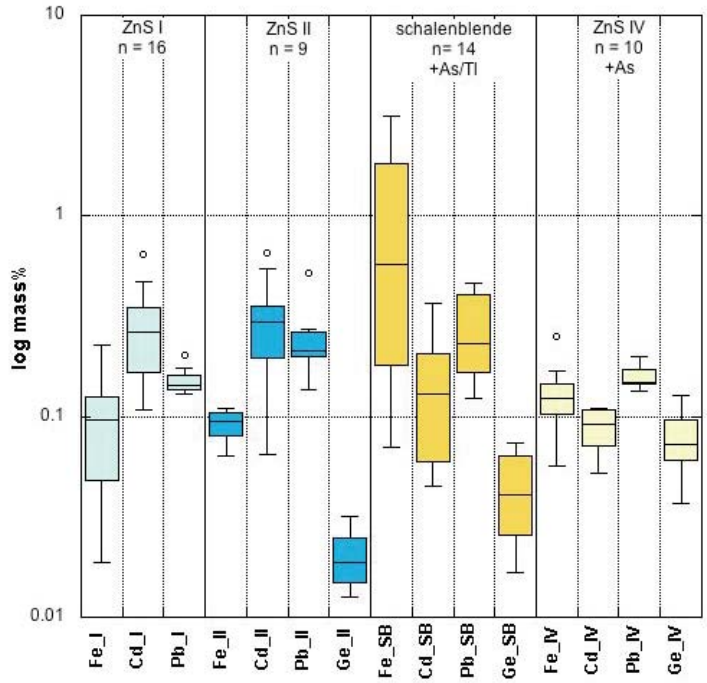

Figure 4.29: Boxplot summarizing the variability in trace/minor element composition of sphalerites in sample EHK02. Sphalerite nomenclature as used in the text (SB = schalenblende).

Sulfur isotope variations can be linked to mineralogical, chemical and textural changes (Figure 4.27). There is a dramatic change in gangue mineralogy, trace/minor element and sulfur isotope composition in the central part of the sample over a distance < 1cm. A jump of -18‰ in $\delta^{34}S$, from -4.6 to -22.6, is accompanied by sudden increase in Fe and Pb (+As) and decrease in Cd contents. Galena shows a similar jump in $\delta^{34}S$ values. The gangue mineralogy changes from a barite-dominated to a barite-free but fluorite-dominated paragenesis. Crystalline ZnS I and ZnS II are very similar regarding their heavy sulfur isotope signature and their trace element inventory (e.g., < Fe/Cd, <Ge). The $\delta^{34}S$ values of crystalline ZnS IV in the upper part of sample EHK02 are much more negative and comparable to those of the schalenblende in this respect. However, it contains less Cd and Fe than the schalenblende. Hence large variations in textures, trace element chemistry and $\delta^{34}S$, occur from the ZnS II to the schalenblende stage. These variations do not concern the Pb isotope signature of the sulfides.

WS_Blb07

Sample WS_Blb07 originates from the Erzkalk horizon in the eastern part of Bleiberg (Rudolf shaft, Pflockschachtlager). Macroscopically visible galena is enriched in layers and causes a stratiform appearance (Appendix, Figure 5). Barite is a major gangue constituent and forms macroscopically visible tabular crystals. Fine-grained euhedral sphalerite (about 10 µm) occurs disseminated in this sample (Figures 4.30 & Appendix Figure 5). Besides of barite the gangue consists of calcite, dolomite and quartz. The whole ore-gangue paragenesis is crosscut by an about 1 mm thick calcite vein.

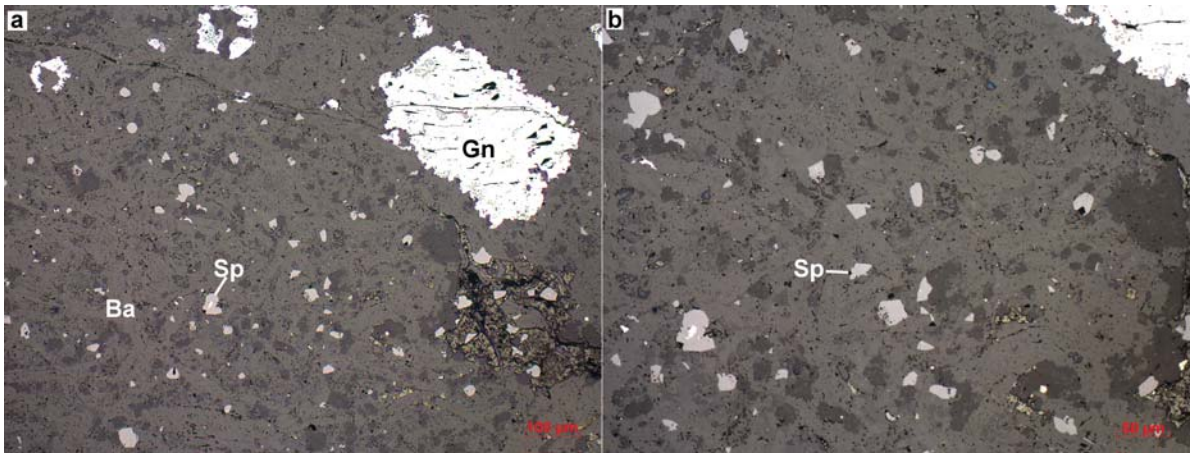

Figure 4.30: (a – b): Microphotographs (reflected light, PPL) showing disseminated fine-grained sphalerite next to larger galena in sample WS_Blb07. Furthermore, the tabular morphology of barite (medium grey) is visible.

Sphalerite chemistry and $\delta^{34}S$ of sulfides in WS_Blb07

Chemically the fine-grained sphalerite in sample WS_Blb07 are best described as trace element poor, except of high Cd contents (Table 4.5). The Cd concentrations are always >0.23 mass%. The average Cd concentration of sphalerite in this sample is 0.48 mass%. Fe concentrations are very low (max. 0.08, mean 0.03 mass%). These sphalerites are characterized by a blue luminescence color. Because of the small grain size of the sphalerite, sulfur isotope analysis could only be carried out on galena. It yielded -6.1‰ $\delta^{34}S$ (Appendix, Figure 5).

Table 4.5: Statistics summarizing trace element contents of sphalerites in sample WS-Blb07. The number of analyses above the LOD (n) is given for each element.

	WS_Blb07		
mass%	**Cd**	**Fe**	**Pb**
	n = 51	n = 38	n= 21
Min	0.23	0.01	0.01
Max	0.68	0.08	0.27
Mean	0.49	0.03	0.06
Median	0.51	0.02	0.03
Std.dev.	0.12	0.02	0.07

4.4.3 Crest horizons, Bleiberg

R8/2

Sample R8/2 originates from the Riedhardtscholle in the western part of the Bleiberg deposit. The ore assemblage in R8/2 is dominated by sphalerite (Figure 4.31). Besides small amounts of galena and pyrite are present. The gangue consists of nearly the same amounts of barite and calcite. Barite forms massive aggregates (>1000 µm) composed of tabular crystals and it also occurs dispersed/disseminated as smaller grains in the matrix (50 – 200 µm). Calcite forms accumulations, which are partly highly fragmented. Furthermore, small amounts of dolomite and quartz are present.

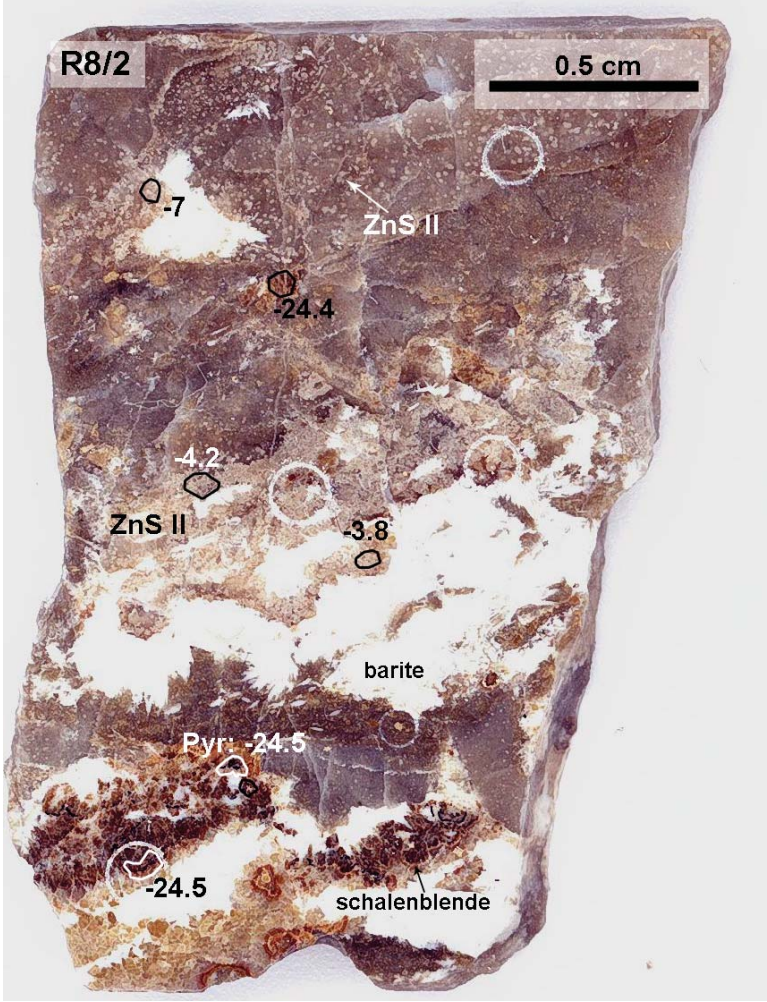

Figure 4.31: Polished slab of sample R8/2 (Riedhardtscholle, Bleiberg) showing micro-areas that were sampled for sulfur isotope analyses. The sample was affected by brittle deformation, which caused fracturing of the whole ore-gangue assemblage. The gangue is rich in barite, which has a white color. Two different sphalerite textures are macroscopically visible: schalenblende aggregates and crystalline sphalerite (ZnS II). Furthermore, the results of the sulfur isotope measurements are also shown.

In sample R8/2 two major sphalerite types can be distinguished (Figure 4.32 a - f): *(1)* botryoidal schalenblende clasts (SB), *(2)* crystalline sphalerite (ZnS II, < 100 µm to few 100 µm). The botryoidal schalenblende clasts are partly highly fragmented and recrystalized and are cemented by barite aggregates and/or ZnS II aggregates. The crystalline sphalerite either forms coarse-grained accumulations, which cement botryoidal schalenblende components. Furthermore, fine-grained (<100 µm) ZnS II is dispersed within the calcite gangue or accumulates in fissures in the calcite gangue.

Botryoidal and crystalline sphalerite in R8/2 cannot easily be distinguished in reflected light under plane-polarized light (PPL), because the partly highly fragmented and recrystallized schalenblende looks optically similar to coarse-grained ZnS II aggregates. The differences between schalenblende and crystalline ZnS II become best visible with crossed polarizers (XPL) in reflected light. In this mode, (fragmented) schalenblende displays yellowish and brownish internal reflection and the ZnS II is characterized by white (and bluish) ones (Figure 4.32 a – f).

As ZnS II aggregates cement botryoidal schalenblende (Figure 4.32 a & b), it must have formed subsequent to the schalenblende.

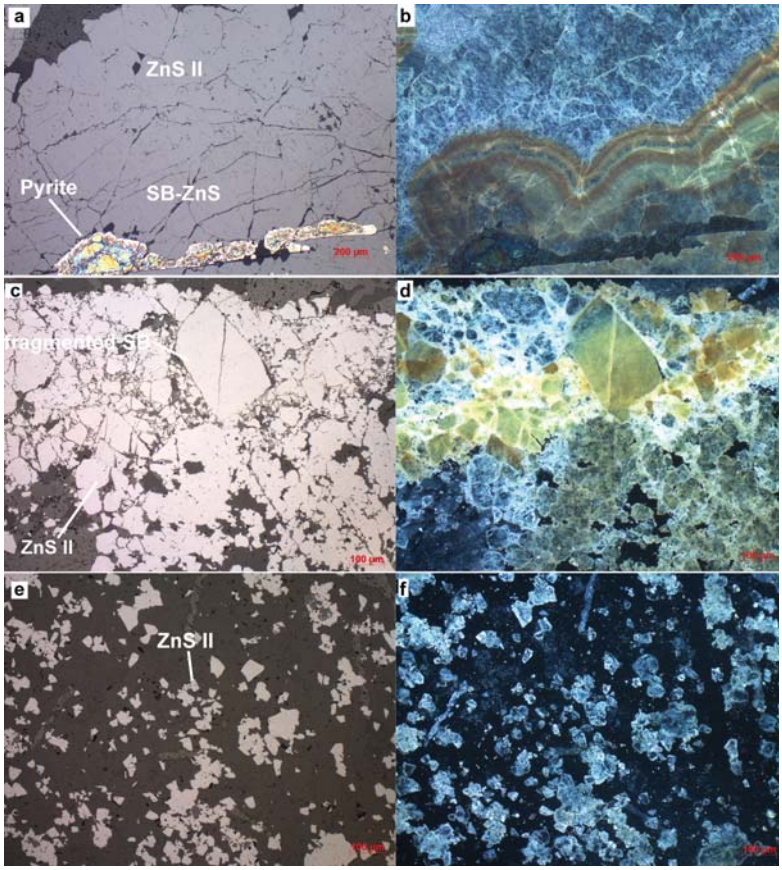

Figure 4.32 (a – f): Microscope photographs of sphalerites present in sample R8/2 (all reflected light). a & b) Botryoidal schalenblende cemented by coarse-grained ZnS II (a = PPL/b = XPL). The crystalline ZnS II is characterized by bluish-white internal reflection in XPL. c & d) Fragmented and partly recrystallized schalenblende (c = PPL/d = XPL). e & f) Dispersed, fine-grained ZnS II in calcite gangue (e = PPL/f = XPL).

Sphalerite chemistry and $\delta^{34}S$ of sulfides in sample R8/2

The trace element characteristics of the schalenblende clasts and the crystalline sphalerite are displayed in a boxplot (Figure 4.33). The schalenblende differs from the crystalline ZnS II especially in its Pb concentrations. In the crystalline ZnS II Pb was only rarely measured and concentrations were always < 0.05 mass%. In the schalenblende Pb was more frequently measured and concentrations exceed sporadically 1 mass%. Furthermore, the schalenblende is, by comparison to ZnS II, high in Fe and poor in Cd. A further difference concerns the As contents of schalenblende, which lie above the detection limit of the EMP in approximately 50% of the analyses. In the crystalline ZnS II As was nearly absent, therefore As-distribution of

crystalline ZnS II is not displayed in the boxplot (Figure 4.33). Germanium was rarely detectable in both sphalerite types and is therefore not shown on Figure 4.33.

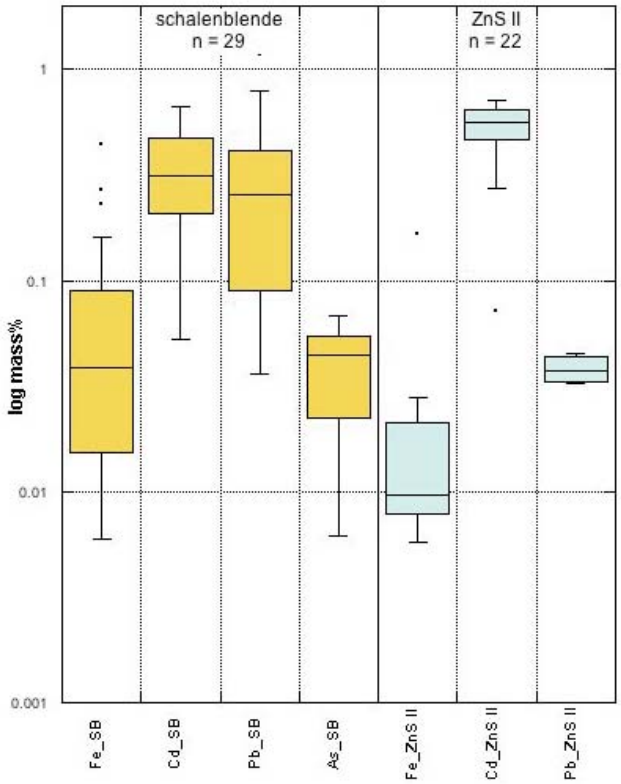

Figure 4.33: Trace element characteristics oft the schalenblende (SB) and crystalline sphalerite (ZnS II) in sample R8/2.

The textural and chemical variations of sphalerites are related to the sulfur isotope composition (Figure 4.31). The schalenblende clasts exhibit very negative $\delta^{34}S$ values of around -24‰. The crystalline ZnS II is composed of heavier sulfur isotopes with $\delta^{34}S$ values between -4 and -7‰. One sulfur isotope analysis of pyrite, which is enclosed in a schalenblende clast, gave also a strongly negative $\delta^{34}S$ value of -24.5‰. Hence, texturally and chemically different sphalerites in this sample show a $\delta^{34}S$ variation of 17‰. In summary, the older schalenblende clasts are Pb and Fe rich and Cd poor and characterized by strongly negative $\delta^{34}S$ values (-24‰). Crystalline ZnS II has high Cd but low Fe, Pb and As contents and less negative $\delta^{34}S$ values (> -7‰).

J10.4 (AS8619)

Sample J10.4 originates from the Josefischolle in the western part of the Bleiberg mine. This sample is primarily composed of sphalerite with minor galena (Figure 4.34). Dolomite is the major gangue mineral.

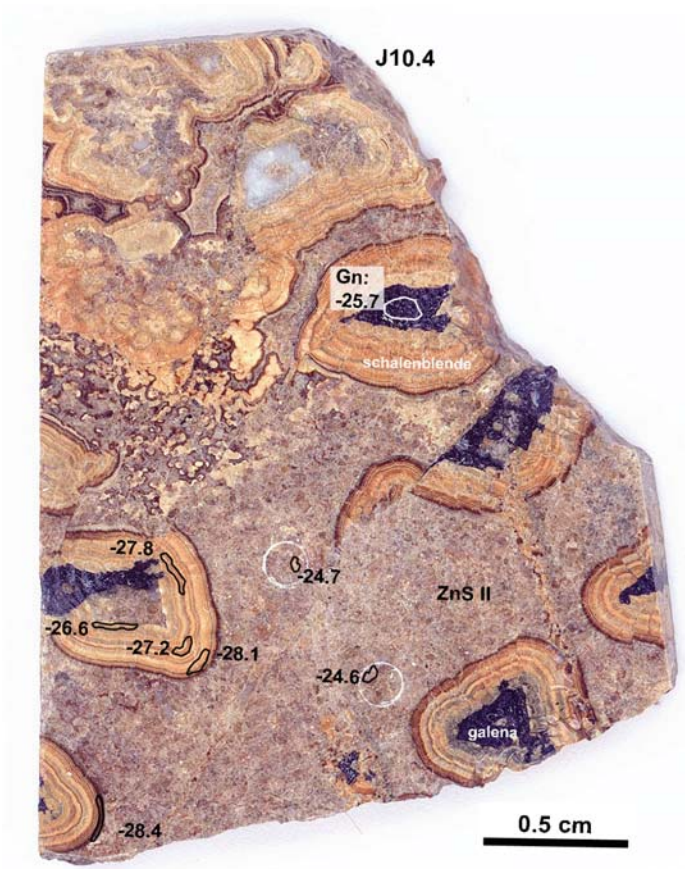

Figure 4.34: Photograph of the polished slab prepared from sample J10.4. Two different sphalerite textures are evident. Besides the δ34S values of schalenblende oncoids, massive crystalline ZnS II and galena are displayed. The sample originates from the Josefischolle (crest horizon), Bleiberg.

The sphalerites within this sample exhibit two different textures (Figures 4.34; 4.35 a - d). Microcrystalline schalenblende aggregates occur together with crystalline subhedral sphalerite grains (ZnS II, approximately 50 to 500 µm in size). The schalenblende aggregates have a spherical shape (schalenblende oncoids) and are approximately 0.5 cm in size. Intact schalenblende oncoids consist of a galena core (subhedral galena) surrounded by layers of microcrystalline sphalerite. The color the single schalenblende layers ranges from beige to dark brown. The crystalline sphalerite grains exhibit a beige-brownish color and cement the different spherical schalenblende aggregates. Furthermore, crystalline ZnS II occurs secondary in some oncoid cores, where it replaces galena. Besides crystalline sphalerite and/or galena also some dolomite occurs as secondary phase in the oncoid cores.

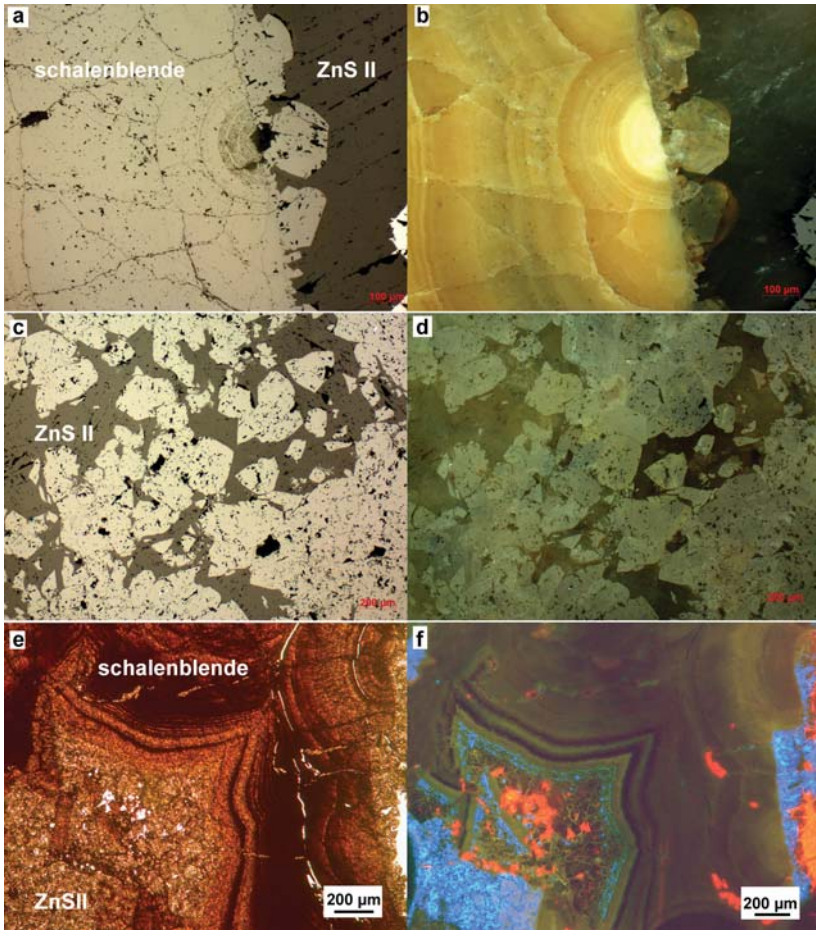

Figure 4.35 (a – f): Microphotographs of characteristic sphalerite textures within sample J10.4. a) & b) Central part of a schalenblende oncoid. Besides ZnS II is present (a PPL; b XPL). c, d) Crystalline ZnS II in dolomite matrix (c PPL; d XPL). e) Schalenblende associated with crystalline ZnS II. f) CL image of the same micro-area shown in (e). The schalenblende shows different shades of green CL. The crystalline ZnS II exhibits bright blue CL. The red CL color is characteristic for the dolomite gangue.

Sphalerites in this sample exhibit peculiar CL colors. The layers of the schalenblende oncoids luminescent in green shades. Crystalline ZnS II shows bright blue CL colors. Furthermore, sometimes a blue-greenish zonation is evident. This zonation follows prominent crystal planes (Figure 4.34 e - f). The dolomite gangue is characterized by a red (orange) CL color.

The sample was affected by late brittle deformation, what lead to local displacements of some schalenblende oncoids along micro-fractures. Galena is overgrown by sphalerite oncoids. The crystalline ZnS II replaces partly the galena within the cores of the oncoids and forms furthermore the cement of the oncoids (Figure 4.34). The textural interpretation therefore is that the crystalline ZnS II formed subsequent to the schalenblende and the galena.

Sphalerite chemistry and $\delta^{34}S$ + Pb isotope signature of sulfides in sample J10/4

Mineral chemical analysis of sphalerites in sample J10.4 were carried out in the frame of my diploma thesis (Henjes-Kunst, 2010). Comparing trace/minor element contents of schalenblende oncoids and crystalline sphalerite, shows that the schalenblende oncoids contain more Pb and Fe than the crystalline ZnS II (Figure 4.36). Furthermore, As and Ge were only detectable in the schalenblende oncoids. No differences in the Cd concentrations are present when comparing schalenblende and crystalline ZnS II.

Both sphalerite types (schalenblende and crystalline ZnS II) in this sample contain more Cd than Fe.

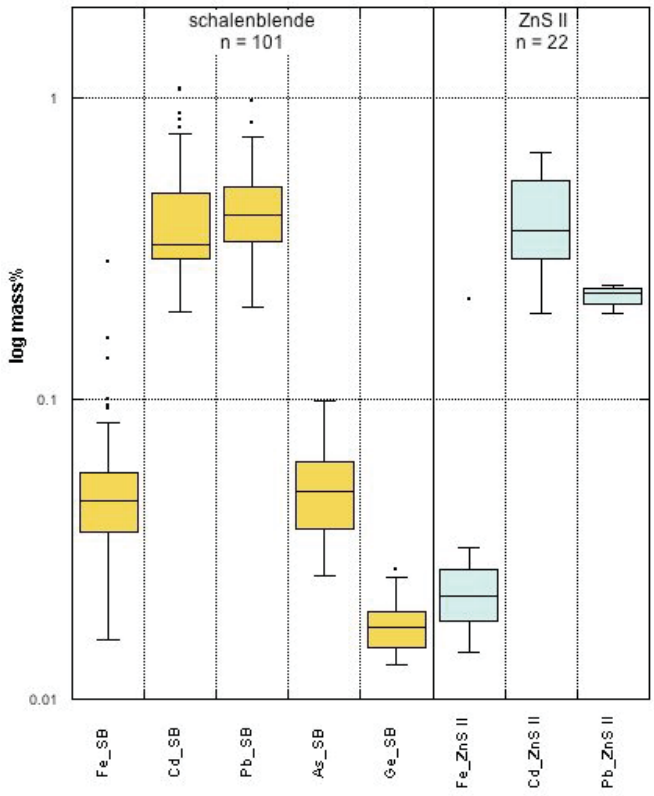

Figure 4.36: Trace element signature of the schalenblende (yellow boxes) and crystalline ZnS II (blue boxes) in sample J10.4.

Sulfur isotope measurements of schalenblende oncoids and crystalline ZnS II show despite the obvious morphological differences only small differences in sulfur isotope composition (Figure 4.34). The schalenblende is characterized by a $\delta^{34}S$ of around -27‰. Measurements of crystalline ZnS II gave values of approximately -25‰. Analysis of one galena crystal within an oncoid core gave $\delta^{34}S$ of -26, what is slightly heavier than the $\delta^{34}S$ values of the surrounding schalenblende next to it. The different layers of a single schalenblende oncoid exhibit nearly homogeneous $\delta^{34}S$ values (Figure 4.34).

The Pb isotope measurements of crystalline ZnS II, schalenblende and galena displayed also a rather homogenous Pb isotope composition. The galena, schalenblende and ZnS II plot in a very narrow area within the Pb-Pb plots (chapter 4.3.2).

The textural very different sphalerites in this sample exhibit only slight variations in their sulfur and Pb isotope composition. Geochemical variations are more prominent, but not very significant.

K2-2

K2-2 is a further sample from the Crest horizon. It is from Kalkscholle, a location in the western Bleiberg mine and represents a high-grade Zn ore, which is predominantly composed of sphalerite (Figure 4.37).

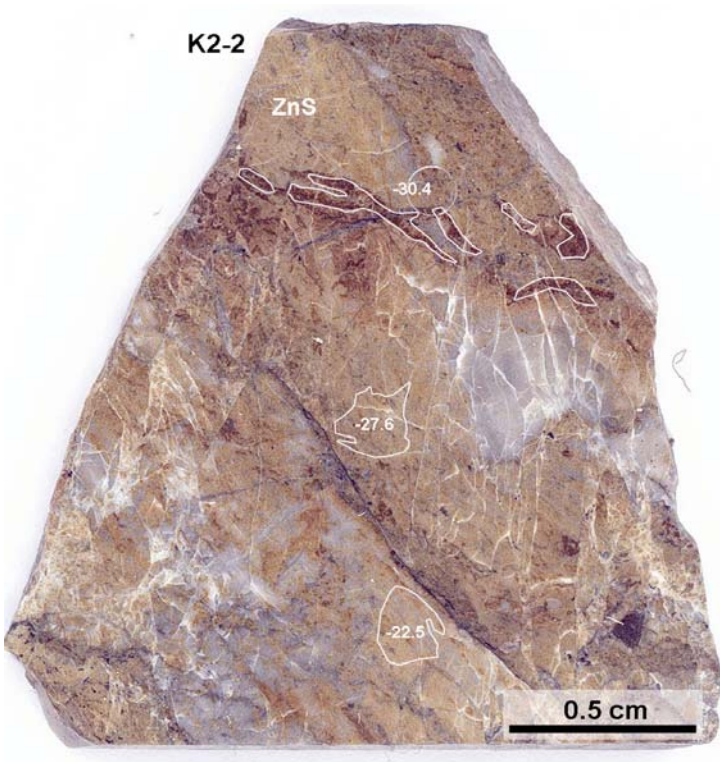

Figure 4.37: Polished slab prepared from sample K2-2. The sample comprises a massive sphalerite mineralization. Especially within the upper part of the slap are the dark brown sphalerite accumulations evident. Furthermore, the δ34S values of the sphalerites are displayed.

The paragenesis consists furthermore of carbonates as gangue and small amounts of galena and pyrite. Sphalerite forms either small subhedral grains (mostly < 100 µm, Figure 4.38 a), which have a light brown color on the macroscopic scale (Figure 4.37). Besides, sphalerite forms elongated and fragmented rather coarse-grained (anhedral) accumulations. The elongated sphalerite accumulations exhibit macroscopically a dark brown color (Figure 4.37). Anhedral galena occurs together with these elongated sphalerite accumulations (Figure 4.38 b). Furthermore, small amounts of pyrite are associated with both texturally different sphalerites. The main gangue phase in sample K2-2 is dolomite, besides small amounts of calcite, which form together with late dolomite veinlets. The whole sample is strongly affected by late fracturing, which is evident within the sample scan (Figure 4.37).

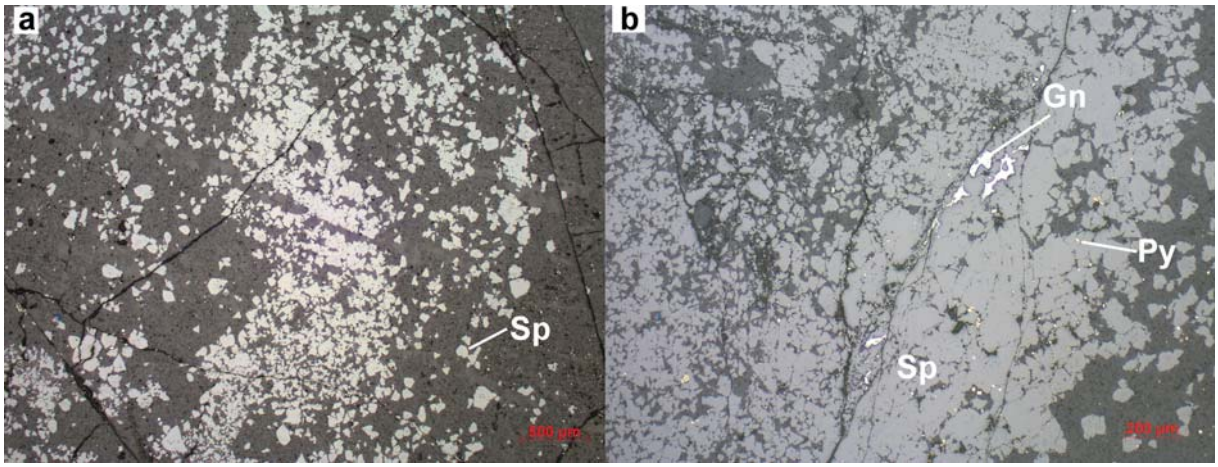

Figure 4.38 (a – b): Microphotographs showing sphalerite textures in sample K2-2, reflected light (PPL). a) Single fine-grained sphalerite crystals. b) Sphalerite grains besides an elongated sphalerite accumulation, which encloses some anhedral galena (right half of the image). Mineral abbreviations according to Siivola & Schmid (2007).

Sphalerite chemistry and $\delta^{34}S$ of sulfides in sample K2-2

Comparing the elongated sphalerite accumulations to the sphalerite grains in sample K2-2 shows that the accumulations are enriched in Fe, Pb and Cd with respect to the fined-grained sphalerite crystals (Table 4.6). Sulfur isotope measurements of elongated sphalerite aggregates in K2-2 yield the most negative $\delta^{34}S$ values of the complete dataset (-30.4‰; Figure 4.37). However, the $\delta^{34}S$ measurements in sample K2-2 were carried out on micro-drilled samples and a contamination of the sphalerite with some galena is presumable. Galena occurs as small inclusions enclosed in these sphalerite accumulations (Figure 4.38 b). Thus, this very negative $\delta^{34}S$ value likely is as mixed sulfide analysis. Two further $\delta^{34}S$ measurements of micro-drilled sphalerite grains in sample K2-2 gave values of -27.6 and -22.5‰, respectively (Figure 4.37).

Table 4.6: Comparison of EMP data for coarse-grained crystalline sphalerite and finer-grained sphalerite crystals; sample K2-2. The number of analyses above the LOD (n) is shown for each element.

	ZnS accumulations (n = 20)			ZnS grains (n = 29)		
mass%	**Fe**	**Cd**	**Pb**	**Fe**	**Cd**	**Pb**
	n = 20	n = 17	n = 17	n = 29	n = 28	n = 18
Min	0.18	0.02	.03	0.06	0.01	0.03
Max	2.75	0.55	0.33	1.1	0.26	0.16
Mean	0.85	0.19	0.15	0.31	0.11	0.06
Median	0.69	0.15	0.14	0.25	0.1	0.06
Std.dev.	0.70	0.06	0.06	0.27	0.06	0.04

4.4.4 Revier Erlach

E14.2-4

Sample E14.2-4 originates from the Revier Erlach, which is located in the westernmost part of the Bleiberg deposit. The main feature of this sample is an approximately 1.5 cm thick polycrystalline schalenblende aggregate (Figure 4.39).

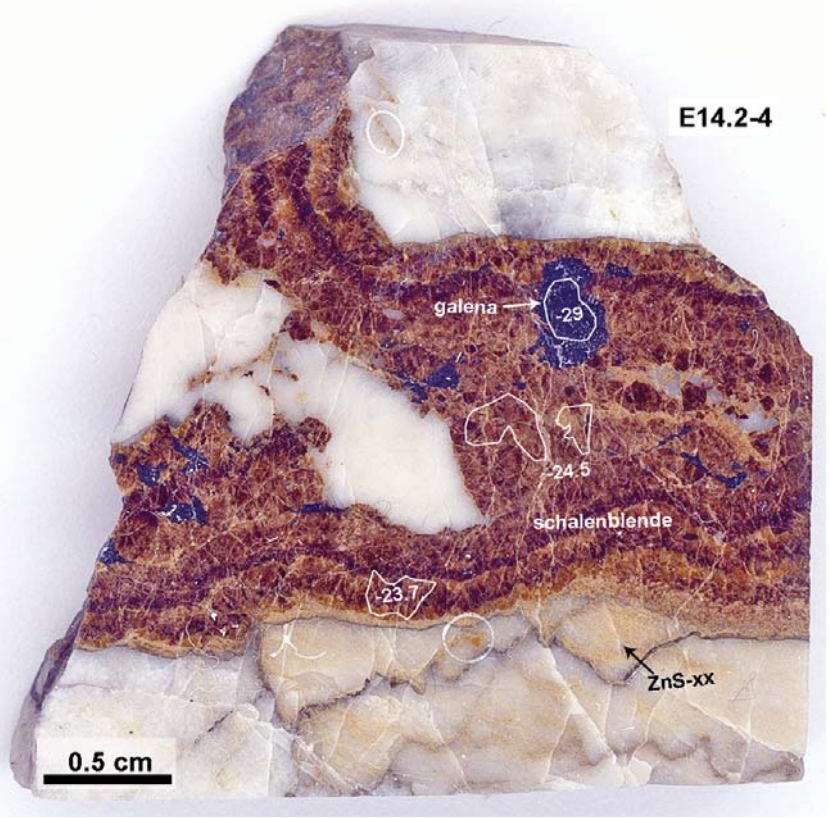

Figure 4.39: Photograph of the polished slap, prepared from sample E14.2-4 for sulfur isotope analysis. The main feature of this sample is a > 1cm schalenblende aggregate. Adjacent to the lower margin of this aggregate, some crystalline sphalerite (ZnS-xx) is accumulated. Furthermore, the results of sulfur isotope analyses of the schalenblende and enclosed galena are displayed.

The single layers of these schalenblende aggregate are up to 1 mm thick, what is best seen in transmitted light (Figure 4.40 b). Locally, numerous large (> 500 µm) anhedral galena is intergrown with schalenblende (Figure 4.39). Furthermore, fine-grained (~10 µm) micro-crystalline sphalerite accumulates at the margin of the schalenblende aggregate. It is associated with small amounts of even finer pyrite (Figure 4.40a). These small sphalerite grains contain numerous tiny inclusions of gangue. The gangue is primarily composed of dolomite. The schalenblende aggregate shows evidence of recrystallization and the whole sample was affected by brittle deformation, which caused displacement of the schalenblende layers along micro-fractures. These micro-fractures are filled with late calcite

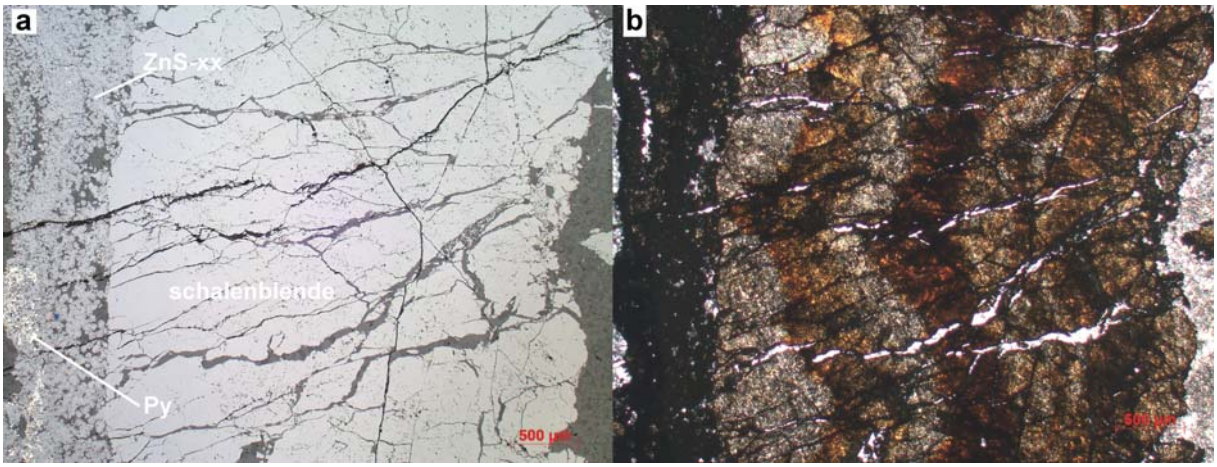

Figure 4.40: Microphotographs of sample E14.2-4. a) Accumulation of fine-grained crystalline sphalerite (ZnS-xx) adjacent to a schalenblende aggregate. Pyrite (Py) is intergrown with sphalerite (reflected light, PPL). b) Banding in schalenblende due to different colors of the individual colloform layers. Schalenblende is strongly fractured (transmitted light, PPL).

Sphalerite chemistry and $\delta^{34}S$ of sulfides in sample E14.2-4

The sphalerite chemistry in sample E14.2-4 was already analyzed in the frame of my diploma thesis (Henjes-Kunst, 2010). The schalenblende aggregate in sample E14.2-4 is very Fe-rich. Fe concentrations range from 0.08 to 5.49 mass% (mean 1.89 mass%, Figure 4.41). Furthermore, the schalenblende is rich in Ge. Other trace elements, like as Pb and As were only sporadically present in concentrations detectable with the EMP. Thallium was sometimes measured within the schalenblende, but is not displayed in the boxplots in figure 4.41. Only few analyses could be made on the fine-grained sphalerite crystals, since the grains are very small and commonly contain tiny gangue inclusions. Compared to the schalenblende, the Fe concentrations in the crystalline sphalerite show a smaller variability and the absolute concentrations are also much lower. Concentrations of Cd are similar to those in the schalenblende but the Ge contents are higher in the fine-grained sphalerite crystals. Arsenic and Pb were nearly not detected in these fine-grained sphalerites.

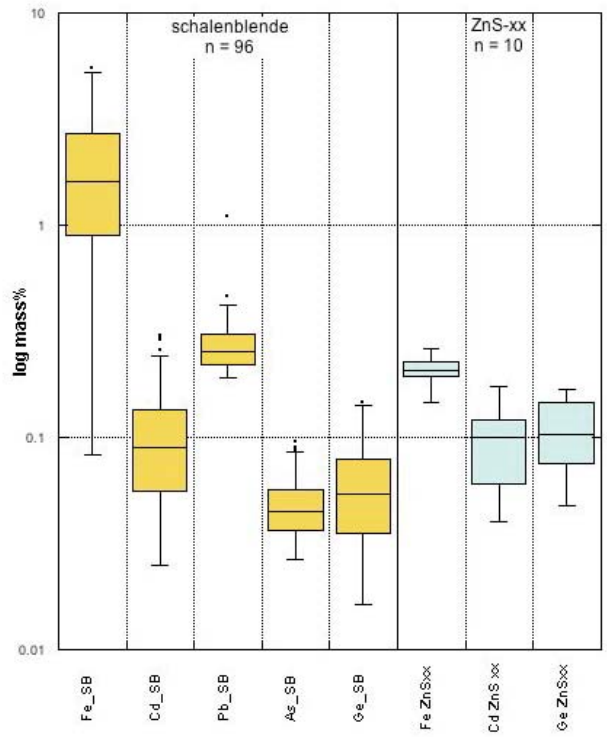

Figure 4.41: Boxplots, displaying the trace/minor element contents of schalenblende and crystalline sphalerite in E14.2-4. The schalenblende exhibits increased Fe contents, which show a large variability. The crystalline sphalerite comprises higher Ge concentrations than the schalenblende.

Sulfur isotope measurements were only possible in the schalenblende aggregate, since the crystalline sphalerite grains were to small to sample sufficient material for analysis. The schalenblende exhibits negative $\delta^{34}S$ values of -24.5 and -23.7‰, respectively (Figure 4.39). One sulfur isotope analyses of galena (inclusion in schalenblende) yielded a more negative $\delta^{34}S$ value of -29.0‰ (Figure 4.39; $\delta^{34}S$ galena < $\delta^{34}S$ sphalerite).

E14.3 (AS8604)

Sample E14.3 originates also form the Revier Erlach in the western Bleiberg mine and was already described in Henjes-Kunst (2010). The sample comprises a massive ore mineralization, consisting of sphalerite and smaller amounts of galena. This sample shows a breccia-type macro-texture (Figure 4.42). Carbonate breccia components (predominantly dolomite) approximately 0.5 cm in size are cemented by honey-colored sphalerite of variable size (< 50 µm to ~1000 µm). More coarse-grained sphalerites display a slightly darker macroscopic color (Figure 4.42). Besides, accumulations composed of small (< 50 µm) anhedral galena crystals (Figures 4.42; 4.43 a, b) are present as further ore mineral. The carbonate breccia components are partly fractured and the micro-fractures are filled with fine-grained (<100 µm) sphalerite.

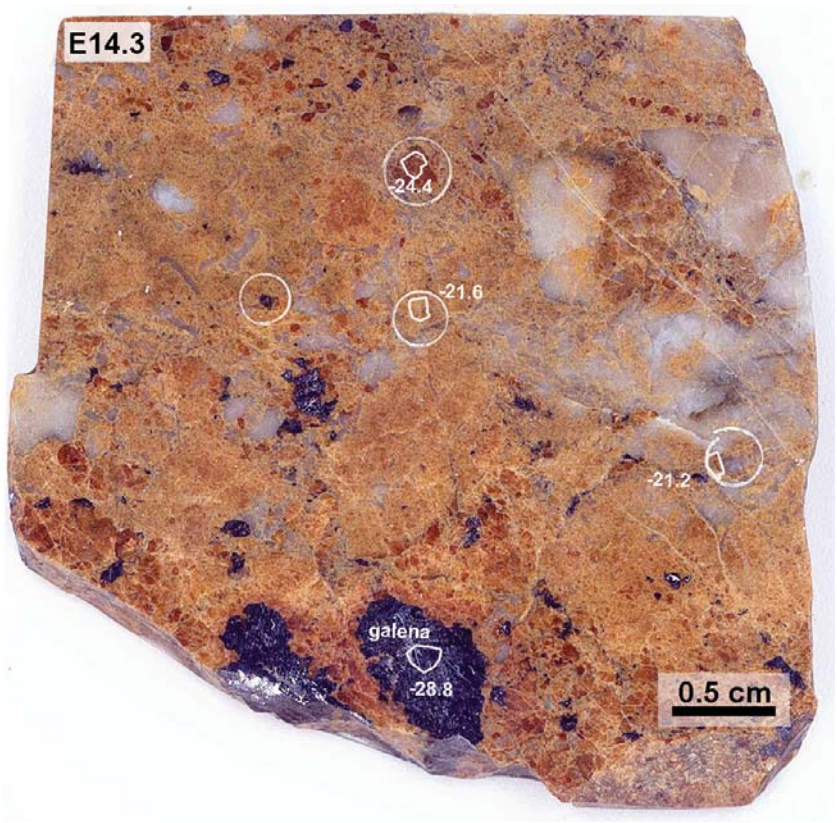

Figure 4.42: Photograph of the polished slap, prepared from sample E14.3. The sample comprises a massive sphalerite-dominated mineralization. The grain size of the sphalerites is variable. With increasing size the grains become darker. Furthermore, $\delta^{34}S$ values of sphalerites and galena are displayed.

Microprobe BSE imaging reveals a secondary light-dark zonation in larger sphalerite grains (Figure4.43 c + d). Zoned sphalerite grains generally consist of a darker colored core and a lighter colored rim. The zonation follows along cleavage planes from the rim of the grains into its centers. The BSE zonation does roughly correspond to the light brown/darker brown zonation, evident at XPL in figure 4.43 b.

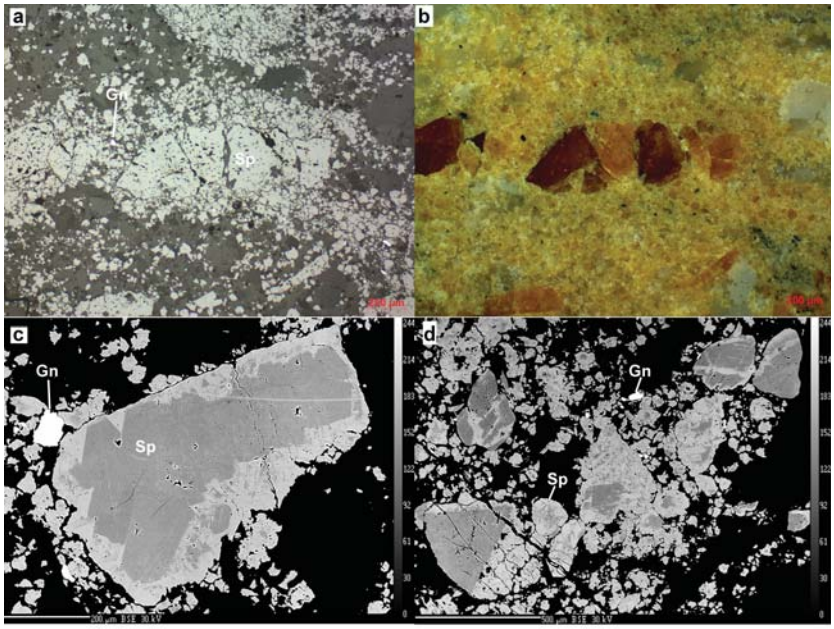

Figure 4.43: a & b) Reflected light photographs of coarse-grained and fragmented sphalerite grains besides fine-grained sphalerite accumulations in sample E14.3 (a = PPL/b = XPL). c & d) BSE images, showing zonation patterns of lager sphalerite grains.

Sphalerite chemistry and $\delta^{34}S$ of sulfides in sample E14.3

Sphalerites within sample E14.3 contain only few trace elements in detectable concentrations regardless of size or macroscopic color. Only Fe, Ge and Cd were detected regularly by EMP. Furthermore, As could be measured two times. Light-dark zonation, visible on BSE images is related to a systematic variation in chemical composition (Table 4.7, chapter 4.2.3). Light zones are enriched in Ge with respect to dark zones (about factor 4). In contrast, dark zones contain more Cd than light zones.

Table 4.7: Comparison of EMP data for dark and light sphalerite (in BSE images) grains from sample E14.3. The number of analyses above the LOD of the EMP (n) is given for each element.

	ZnS dark (n = 13)			ZnS light (n = 14)		
mass%	**Fe**	**Ge**	**Cd**	**Fe**	**Ge**	**Cd**
	n = 13	n = 13	n = 13	n = 14	n = 14	n = 13
Min	0.25	0.04	0.06	0.20	0.09	0.04
Max	1.07	0.13	0.22	0.51	0.21	0.12
Mean	0.56	0.07	0.12	0.28	0.16	0.07
Median	0.47	0.05	0.10	0.26	0.17	0.06
Std.dev.	0.28	0.03	0.05	0.08	0.04	0.03

Sulfur isotope measurements of sphalerites in sample E14.3 gave $\delta^{34}S$ values of -21.2‰ for fine-grained sphalerite accumulations and -24.4‰ for a larger brown sphalerite grains (Figure 4.42). Measurement of one galena grain in E14.3 gave a more negative $\delta^{34}S$ value of -28.8‰. Hence, galena is characterized by more negative $\delta^{34}S$ values than sphalerite ($\delta^{34}S$ galena < $\delta^{34}S$ sphalerite).

4.4.5 1st Raibl horizon, Bleiberg

C6.14 (AS8591)

Sample C6.14 originates from the carbonate layer above the 1st Raibl shale. Its sphalerite chemistry has already been described in Henjes-Kunst (2010). The sample comprises large amounts of sphalerite, which occurs in different textures. The most obvious sphalerite texture in this sample is elongated schalenblende in fragments (Figure 4.44). These schalenblende fragments are fractured and show beginning recrystallization features. Besides also more fine-grained sphalerite is macroscopically evident. The sphalerite is enriched in roughly parallel trending layers (Figure 4.44).

Figure 4.44: Photograph of the polished slap prepared from sample C6.14 (1st Raibl horizon, Bleiberg). Sphalerite is the main ore mineral in this sample. Besides some galena is present. Sphalerite is enriched in parallel trending layers. Furthermore, the results of sulfur isotope measurements of sphalerites and galena are displayed. SB = schalenblende.

The fine-grained sphalerites can microscopically be differentiated: *(I)* fine sphalerites (10 µm, Figure 4.45 a). The sphalerite grains partly have a triangular or hexagonal shape and accumulate in approximately parallel trending bands, which can be up to 1 mm wide. *(II)* Furthermore, larger sphalerite grains (*II*, approximately 100 µm in size) are present. These larger sphalerite grains are sometimes overgrown by the fine-grained sphalerite (Figure 4.45 a & b). *(III)* Additionally, relicts of colloform schalenblende textures in breccia components are present (Figure 4.45 c). The schalenblende components are fragmented (Figure 4.45 d). The gangue in C6.14 is mainly composed of dolomite. Besides sphalerite, galena is already macroscopically visible. Furthermore, very fine-grained pyrite (< 10 µm) in styolites is present as further ore minerals.

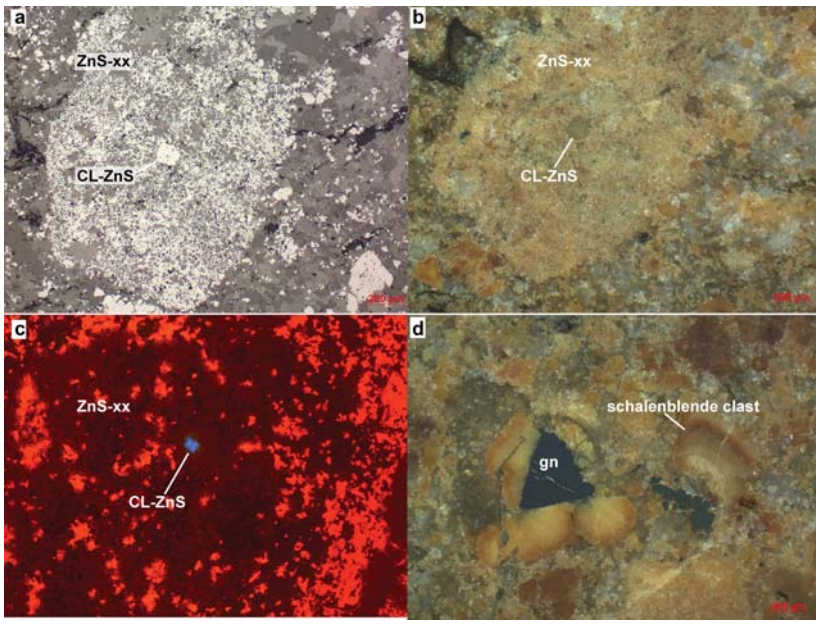

Figure 4.45: a – c) Fine-grained sphalerite (ZnS-xx) and more coarse-grained blue luminescent sphalerite (CL-ZnS); a = reflected light PPL/b = transmitted light, XPL/ c = CL image, showing the different CL colors of those two sphalerite types. d) Photograph of a fragmented schalenblende clast and galena (reflected light, XPL).

Trace element chemistry and Pb isotope signature of sphalerite + $\delta^{34}S$ of sulfides in C6.14

A summary of the chemical composition of the three sphalerite types, which are present in sample C6.14, is displayed in table 4.8. The blue luminescent sphalerite grain is trace element poor. The EMP analysis revealed only Fe (very low concentrations, maximum of 400 ppm) and Cd (up to 0.5 mass%) as trace elements. The Fe contents of the fine-grained sphalerite are, when compared to the blue luminescent sphalerite grain, elevated (mean of 0.2 mass%) whereas the Cd concentrations are lower (mean of 0.11 mass). Additionally, some Ge in the 100 ppm range was measured in the fine-grained sphalerite. The schalenblende clasts are characterized by distinctly higher Fe contents (maximum of 1.26 mass%, mean 0.52 mass%) and when compared to the other two sphalerite types, intermediate Cd contents (average of 0.16 mass%). It contains furthermore Ge in the 100 ppm range.

Table 4.8: Statistical parameters of trace element data for sphalerite with blue luminescence (CL ZnS), fine-grained crystalline ZnS and schalenblende clasts in sample C6.14.

	CL ZnS n = 4		**fine-grained ZnS** n = 4			**schalenblende clasts** n = 5		
[mass%]	**Fe**	**Cd**	**Fe**	**Cd**	**Ge**	**Fe**	**Cd**	**Ge**
Min	0.02	0.20	0.14	0.09	0.02	0.11	0.05	0.02
Max	0.04	0.50	0.27	0.13	0.03	1.46	0.26	0.04
Mean	0.03	0.38	0.2	0.11	0.02	0.52	0.16	0.03
Median	0.03	0.38	0.2	0.11	0.02	0.34	0.14	0.04
Std.dev.	0.006	0.14	0.07	0.02	0.01	0.54	0.09	0.01

The sulfides in this sample show very negative $\delta^{34}S$ values of mostly < -25‰ (Figure 4.44). Schalenblende shows the most negative $\delta^{34}S$ of the sphalerites (-29.0‰). One

galena analysis yielded a slightly more negative $\delta^{34}S$ of -29.8‰. No relationship between $\delta^{34}S$ values and chemical composition can be established for the sphalerites in this sample. Hence, no obvious relation between variations in chemical composition and sulfur isotope signature is evident. The Pb isotope composition of the sphalerite separate, which was prepared from sample C6.14 is very similar to other Bleiberg samples (chapter 4.3.2).

4.4.6 Mezica – Erzkalk equivalent Pb-Zn ore

Mz_H01

Sample Mz_H01 was collected in the Helena district in the Mezica mine (level 0). The Helena district is located in the central part of the Mezica mine. It comprises a massive galena and sphalerite ore and consists of approximately the same amounts of sphalerite and galena. One half of the sample (upper half in Figure 4.46) is dominated by galena. The lower half within figure 4.46 is dominate by sphalerite.

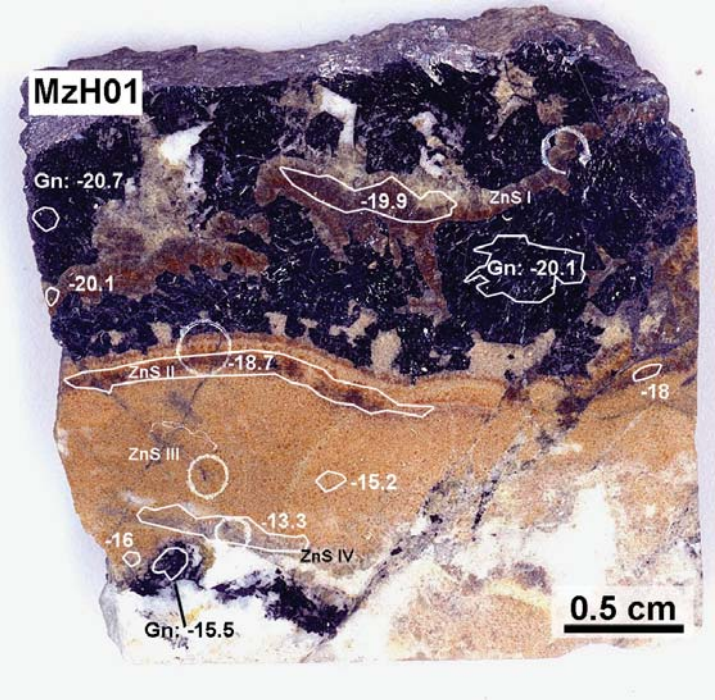

Figure 4.46: Photograph of the polished slap prepared from sample MzH01 for sulfur isotope analysis. The sample comprises approximately the same amounts of sphalerite and galena. The upper half is dominated by galena, whereas the lower half exhibits more sphalerite. The sphalerite nomenclature (ZnS I to ZnS IV) is described in the text. Furthermore the results of the sulfur isotope measurements are displayed. A gradual change in δ34S values from ZnS I to ZnS III is evident. (2007).

Within the galena dominated half (Figure 4.46) dark brown and coarse-crystalline sphalerite (*ZnS I*) occurs only in an approximately 2 mm thick veinlet. It is crosscut by numerous very fine micro-fractures, which are filled with Fe-sulfides (Figure 4.47 a). Within the sphalerite dominated half of the sample (lower half in Figure 4.46) a succession of texturally different sphalerites is evident. The direct contact to the galena dominated part is characterized by a sphalerite aggregate, which shows a vaguely developed color zonation similar to the color banding characteristic for schalenblende (*ZnS II* Figure 4.46; Figure 4.47 c, d). More distal to the galena subhedral crystalline sphalerite grains (about 100 µm in size) are accumulated (*ZnS III*, Figure 8.27 b). This sphalerite type comprises macroscopically a light brown color. Still further away from the galena even coarser (>200 µm) sphalerite is concentrated in an approximately 1000 µm big aggregate (ZnS IV in Figure 4.47 b). The gangue in MzH01 is mainly composed of coarse-grained (~500 µm) dolomite.

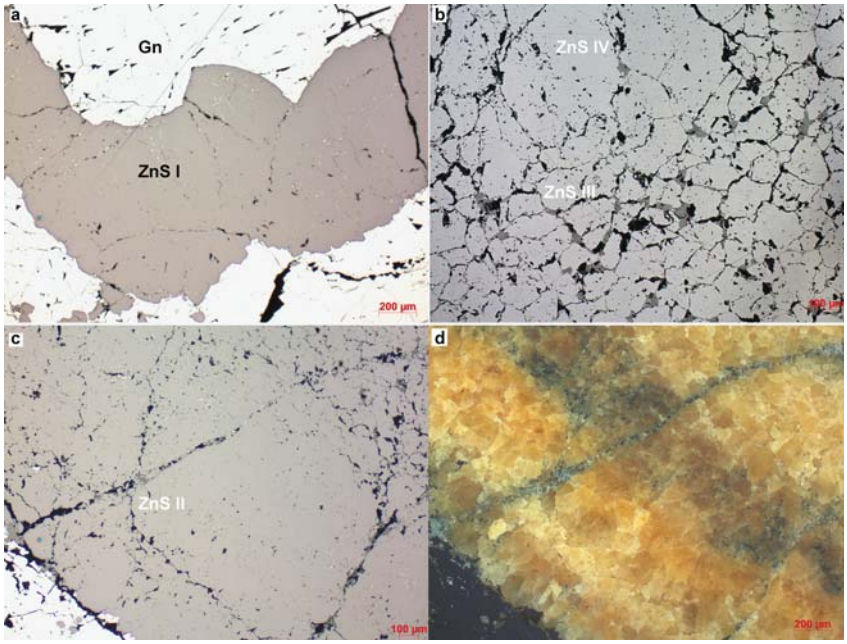

Figure 4.47: Microphotographs of sample Mz-H01 a) Sphalerite (ZnS I) in a veinlet crosscutting galena (reflected light, PPL). b) Transition between finer-grained (ZnS III) and coarser-grained sphalerite (ZnS IV) in the sphalerite-dominated half of MzH01 (reflected light, PPL). c, d) Reflected light images of zoned ZnS II in the contact zone to the galena half (c = PPL/d = XPL).

Chemistry, $\delta^{34}S$ and Pb Isotope composition of sulfides in sample MzH01

The sphalerites in sample MzH01 are very Cd rich. They contain more Cd than Fe (Figure 4.48). Moreover, the Cd contents are steadily decreasing from ZnS I to ZnS III. The ZnS IV is characterized by a similar median Cd content like as the ZnS III, but shows less variability in Cd. Iron contents in ZnS I are significantly higher than in the other types. Besides, the tendency towards lower variability in Fe contents is furthermore evident from ZnS I to ZnS IV (Figure 4.48). However, a serious comparison of the variability of the data subsets is not possible, since more data on the trace element composition of ZnS I is present. Besides of Cd and Fe, also As (0.02 to 0.28 mass%) and Pb (0.02 – 0.82 mass%) were measured with EMP (Appendix, Table 10).

The steady decrease in Cd in the sphalerites corresponds to slightly increasing $\delta^{34}S$ values from -20.1‰ in ZnS I towards -13.3‰ in ZnS IV (Figure 4.46). One sulfur isotope analysis of ZnS IV yielded furthermore a $\delta^{34}S$ of -16.0‰. Galena in the upper half of figure 4.46 has a $\delta^{34}S$ of around -20‰ and shows a similar sulfur isotope signature like ZnS I from sphalerite veinlet. In the lower half of the sample (Figure 4.46) galena has a $\delta^{34}S$ value of -15.5 ‰ what is lighter than the adjacent ZnS IV (-13.3‰).

ZnS I and PbS in both parts of the sample are, regarding their Pb isotope signature, very similar. The sphalerite within the lower part of sample MzH01 (ZnS II to IV) clearly differs in its Pb isotope signature and is characterized by a more radiogenic Pb isotope composition (Figure 4.20). Within ZnS II to IV lower Pb concentrations than in ZnS I were measured with TIMS (Table 4.4).

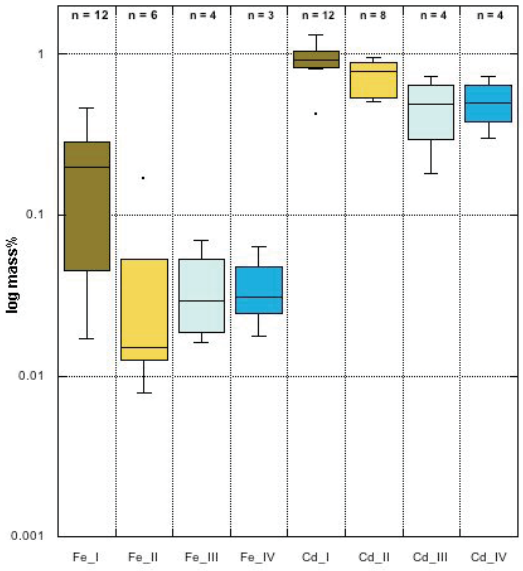

Figure 4.48: Distribution of Cd and Fe in ZnS I to IV in sample MzH01.

Mz08

Sample Mz08 was collected in the Moring district (8th level), which is in the central part of the Mezica mine. The sample comprises approximately the same amounts of galena and sphalerite. Galena forms a massive aggregate in the central part of the sample (Figure 4.49) and is surrounded by sphalerite.

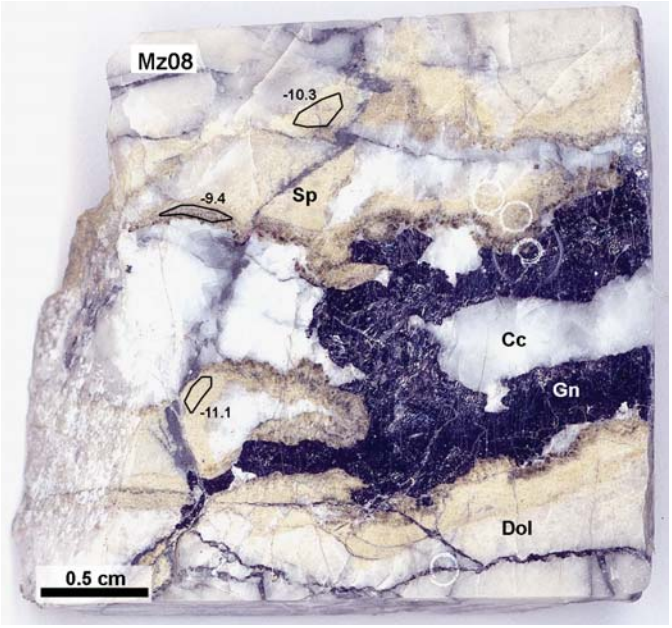

Figure 4.49: Photograph of the polished slap prepared from sample Mz08 for sulfur isotope measurements. Within the central part of the sample a massive galena aggregate is visible. This galena aggregate is surrounded by sphalerite. The color of the sphalerite, which occurs direct adjacent to the galena is grayish brown. Further distal to the galena aggregate the sphalerite exhibits a beige color. The gangue consists of carbonates, which are white in this photograph. Furthermore, the results of the sulfur isotope measurements of sphalerite are displayed.

In the contact zone to the galena aggregate the sphalerite is coarse-grained (a few 100 µm) and has a brown color (Figure 4.49; Figure 4.50 a). Further distal to the galena aggregate the sphalerite is of beige color (Figure 4.49) and much more fine-grained (max. 100 µm). Besides reduction in grain size sphalerites are getting furthermore enriched in gangue inclusions with increasing distance to the central galena aggregate

(Figure 4.50 b). Small amounts of pyrite are also present in the sample especially in late crosscutting veinlets. The gangue consists of carbonates (calcite + dolomite). Adjacent to massive sulfide accumulations coarse-grained calcite is the dominant gangue. The more fine-grained sphalerite mineralization is rather associated with dolomite.

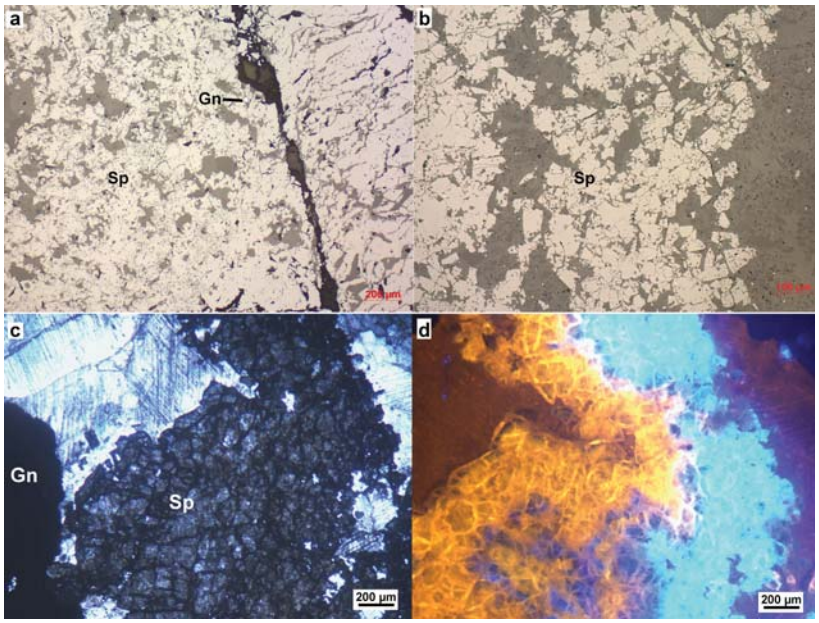

Figure 4.50 (a – d): Microphotographs of sphalerites in sample Mz08. a) Transition from a rather coarse-grained sphalerite accumulation (on the right) to less massive, partly gangue inclusion rich, sphalerite accumulation (left, reflected light, PPL). b) Detailed image of the gangue inclusion rich sphalerite grains (reflected light, PPL). c) Transmitted light image of a sphalerite accumulation and the respective CL image (d).

The sphalerites this sample are characterized by peculiarly CL behavior. In the sphalerite sequence (coarse-grained brown -, fine grained - and fine-grained + inclusion-rich sphalerite) a CL sequence from orange to dark blue to light blue (Figure 4.50 c, d) was observed. CL colors are not completely related to macroscopic and microscopic aspects. Within the coarse grained sphalerite grains itself the sequence from orange at the margins of the grains over dark blue towards light blue in the central parts of the grains can be present (Appendix, Figure 3f). The fine-grained sphalerites display only a light blue CL color.

Chemistry, $\delta^{34}S$ and Pb isotope composition of sulfides in sample Mz08

The CL colors of sphalerite in this sample can be related to trace element contents (Figure 4.51). The orange luminescent coarse-grained sphalerites always have high Cd contents (median > 1 mass%) and are low in Fe. Besides of Cd, this sphalerite is higher in Cu. Cu was detectable in more than 80% of the EMP analyses. In contrast the dark-blue luminescent sphalerites are lower in Cd than the orange ones (median of 0.75 mass%) and are also very low in Fe (concentrations generally < 0.01 mass%). The boxplot (Figure 4.51) indicates higher Cu-contents within the dark blue sphalerite with respect to the orange ones. However, this is not fully correct, because in the dark blue sphalerites Cu was not detected as regularly as in the orange sphalerite (< 50%, 6 measurements out of 14). In the light blue luminescent sphalerites the Cd contents are even lower (median of 0.45 mass%) than in the other two sphalerite types. Therefore

the Fe contents vary over a larger range. However, higher variability in Fe results from one measurement, which exhibit a Fe concentration of > 0.02 mass%. Cu was not detectable in the light blue luminescent sphalerites. The sphalerites in this sample are very Cd rich and Fe poor. Cu was often measured in this sample and occurs in higher concentrations than Fe. The Pb concentrations of the sphalerites are also higher than Fe contents. However, the Pb concentrations are similar in all three sphalerite types.

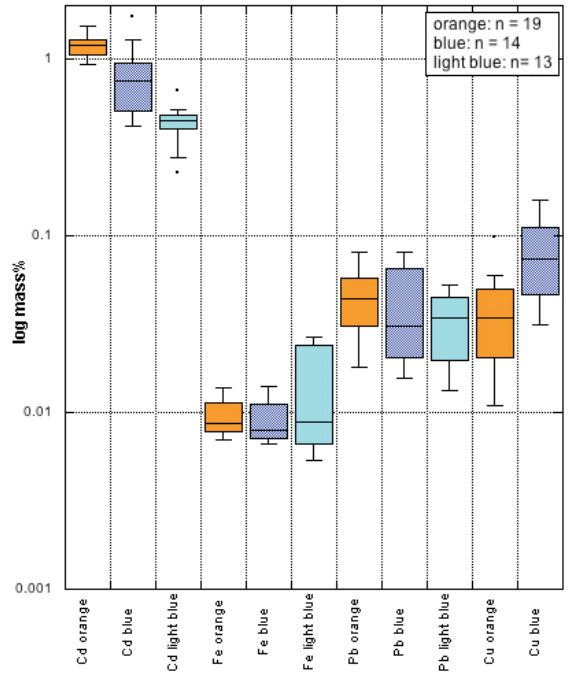

Figure 4.51: Trace element distribution of the three different sphalerite types (ordered with respect to their CL) in sample Mz08.

The sulfur isotope composition of the different sphalerites in this sample is rather uniform regardless of the obvious CL and chemical variations (Figure 4.49). The $\delta^{34}S$ values of sphalerite range between -11.1 and -9.4 ‰. The Pb isotope signature of the sulfides within sample Mz08 differs from that of the other samples, which Pb isotope signature was investigated (chapter 4.3.2).

SF03

Sample SF03 originates from the Graben district in the eastern part Mezica mine. The main feature of this sample is a strongly fractured and schalenblende accumulation (Figure 4.52). Besides, fine-grained crystalline sphalerite and furthermore pyrite are present as further ore constituents. The gangue has macroscopically a grayish-white color and is also strongly affected by brittle deformation (Figure 4.52).

Figure 4.52: Photograph of the polished slap, prepared from sample SF03 (Mezica, Graben district). The most obvious feature within this sample is a strongly fractured schalenblende accumulation. Besides, crystalline sphalerite (ZnS-xx) and pyrite are present as further ore constituents. The gangue (grayish-white) consists of a mixture of dolomite, calcite and quartz. Furthermore, the results of the sulfur isotope analyses of sphalerite and pyrite are displayed.

Under the microscope it becomes evident that the schalenblende was affected by remobilization. Remobilization of the schalenblende was facilitated by the layered texture of the schalenblende and occurs along the boundaries of the single colloform layers (Figure 4.53 a). Remobilization led to decomposition of the schalenblende into its single shells, which is nicely visible with reflected light microscopy (PPL, Figure 4.53 a).

Furthermore, small amounts of fine-grained (approximately 50 µm) sphalerite are also present within the sample (Figure 4.53 b). Pyrite occurs as a further sulfide mineral. Pyrite is either enriched within certain layers of the schalenblende, or forms accumulations adjacent to the schalenblende fragments (black in the sample photograph, Figure 4.52). Furthermore, fine-grained pyrite is associated with the crystalline sphalerite (Figure 4.53 b). The gangue is dolomite rich. Additionally small amounts of calcite and quartz are further gangue constituents. Certain layers of the schalenblende fragments host many fine-grained gangue inclusions (Figure 4.53 a).

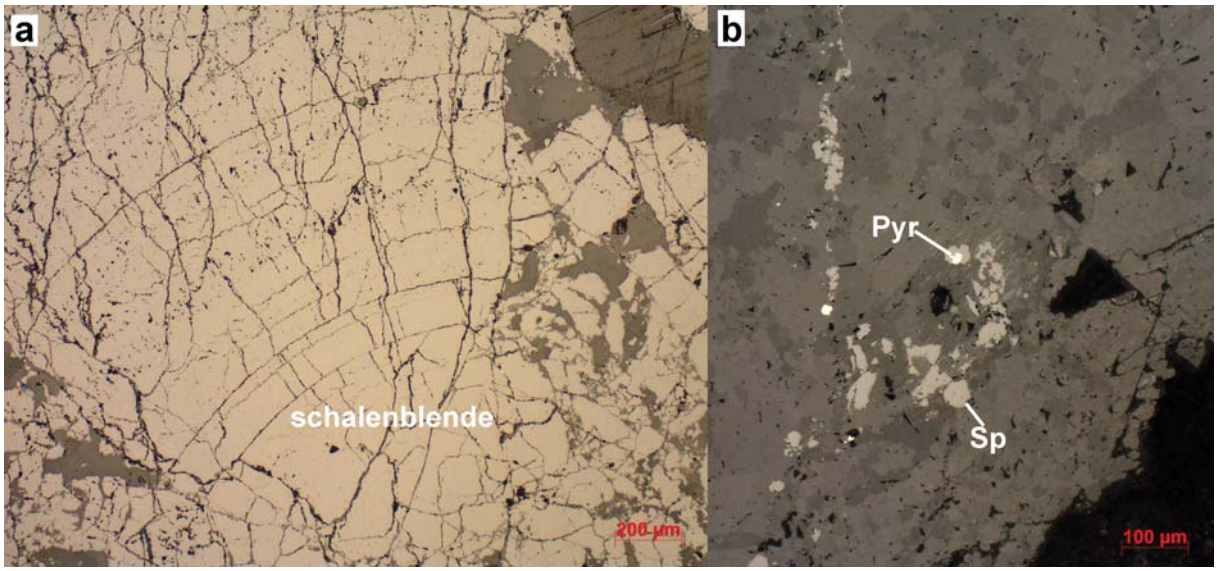

Figure 4.53: a – b) Reflected light microscopy photographs of sphalerite textures occurring in sample SF03 (PPL). a) Fractured schalenblende aggregate. The characteristic "schalenblende texture" is visible in reflected light (PPL), because remobilization occurred along the transitions between the individual colloform layers. Certain layers contain many small gangue inclusions. The aggregate is furthermore strongly fractured. b) Anhedral sphalerite (< 100 µm) associated with more fine-grained pyrite. The gangue is mainly composed of dolomite (medium grey). Furthermore, small amounts of calcite and quartz are present (dark grey).

Sphalerite chemistry and $\delta^{34}S$ of sulfides in sample SF03

The mineral chemical data of sphalerites in sample SF03 are summarized in Table 4.9. The four analyses for crystalline sphalerite display lower variability in trace element compositions when compared to the schalenblende (Table 4.9). However, the dataset of the crystalline sphalerite is more than six times smaller than that of the schalenblende. Hence the dataset allows no serious comparison of crystalline sphalerite and schalenblende. The sphalerite types in this sample (crystalline sphalerite and schalenblende) are rather Cd rich. The average and median Cd concentrations of the schalenblende are higher than the average/median Fe concentrations (Table 4.9). The maximum Fe content of the schalenblende is higher than the maximum Cd content (0.62 and 0.53 mass% respectively). However, this results presumably from a pyrite contamination. Besides, within the schalenblende Pb was measured permanently. The mean and median Pb concentrations are even higher than the Cd contents (Table 4.9). Arsenic was also measured very often and also the mean/median As contents are higher than the mean/median Fe concentrations. Germanium was only sporadically detectable with EMP.

Table 4.9: Statistical parameters for the schalenblende fragments and the crystalline sphalerite within sample SF03. The number of analyses about the LOD of the EMP is given in brackets for each element.

	ZnS-xx (n = 4)				schalenblende (n = 26)				
[mass%]	**Fe**	**Cd**	**Pb**	**As**	**Fe**	**Cd**	**Pb**	**As**	**Ge**
	(4)	(4)	(3)	(3)	(26)	(26)	(26)	(25)	(5)
Min	0.02	0.04	0.14	0.03	0.01	0.04	0.06	0.01	0.03
Max	0.09	0.18	0.26	0.06	0.62	0.53	0.9	0.27	0.07
Mean					0.07	0.2	0.35	0.09	0.04
Median					0.03	0.22	0.29	0.07	0.04
Std.dev.					0.12	0.11	0.21	0.07	0.02

The schalenblende exhibit a very narrow range in $\delta^{34}S$ values from -14.6 to -15.7‰ (Figure 4.52). Sulfur isotope analysis of crystalline sphalerite was not possible, because the laser beam did not interact with the grains and no material could be ablated. Two pyrite analyses gave $\delta^{34}S$ values of -14.4‰ and -18.8‰, respectively. Pyrite is therefore characterized by more negative and by less negative $\delta^{34}S$ values than the schalenblende.

4.4.7 Topla, Anisian Pb-Zn ores

Tp01

Sample Tp01 was collected on the dumps of the Topla deposit (right of the former main entrance of the mine). The Topla ore is hosted by the stratigraphic deepest ore horizon, the Ansian Muschelkalk Formation. On macroscopic scale large marcasite aggregates (> 1 mm) are the only ore minerals, which can be identified (Figure 4.54). The presence of sphalerite can only be assumed due to the heavy weight of the sample. Sphalerite is very fine-grained and occurs dispersed within the sample. The gangue is mostly also fine-grained and is mainly composed of dolomite, which has macroscopically a brownish color (Figure 4.54).

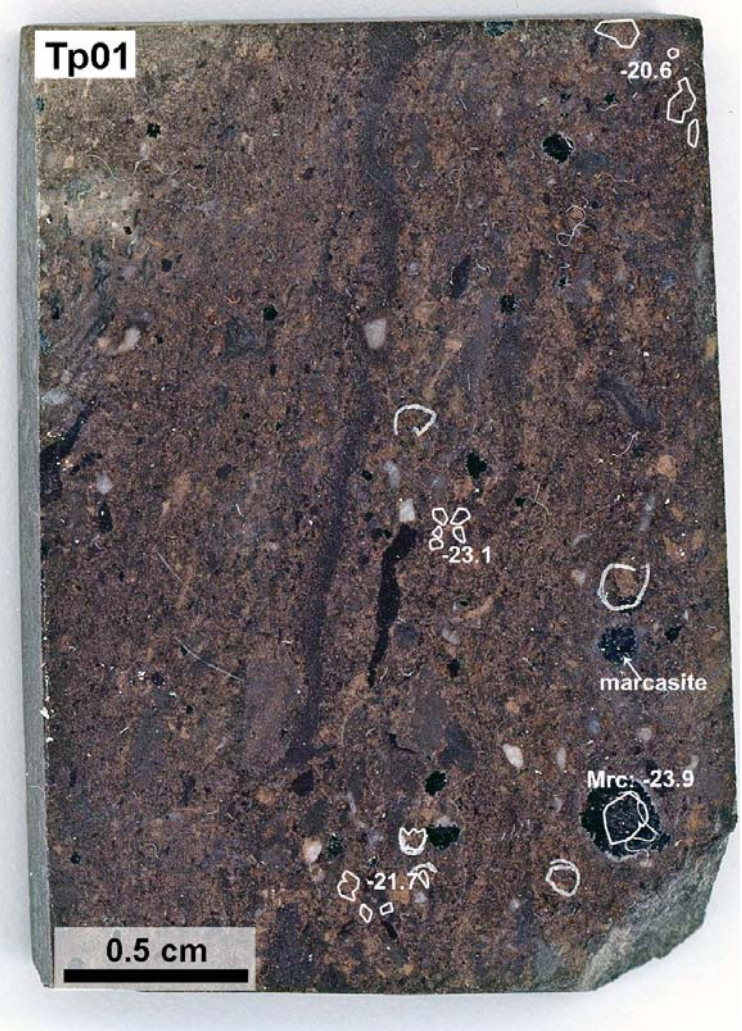

Figure 4.54: Photograph of the polished slap prepared from sample Tp01 (Topla). The sample comprises very-fine grained and often disseminated sphalerite, which can macroscopically not be identified. Some sphalerite grains form accumulations, which are macroscopically apparent, because they exhibit a slightly lighter color than the gangue. Marcasite is the only ore mineral, which can be macroscopically identified. Marcasite is present in > 1 mm aggregates. The presence of ore minerals besides marcasite can be assumed, because the sample is rather heavy. Furthermore, the result of sulfur isotope analyses of sphalerite and marcasite are displayed.

The sphalerite ore is mostly very fine-grained (< 50 µm) and occurs dispersed/disseminated all over the sample. The sphalerite grains exhibit a sub- to euhedral morphology (Figure 4.55 a; b). Besides dispersed sphalerite grains, also accumulations of fine-grained sphalerite can be observed, which replace bioclasts (Figure 4.55 b). Sphalerite peloids are another characteristic sphalerite micro-texture (see chapter 4.1.1; Figure 4.55 a; Figure 4.5). Further sulfide minerals are marcasite

and pyrite. Marcasite also occurs in larger aggregates (> 1mm, Figure 4.54). Sphalerite and marcasite are closely associated. Both minerals were observed as inclusions in each other. Pyrite is also rather fine grained (< 10µm) and sometimes exhibits framboidal textures. It forms very fine-grained inclusions in sphalerite or occurs in separate grains. Thus, we conclude that sphalerite and the Fe-sulfides formed coevally. Very fine-grained (< 10µm) galena is furthermore present in inclusions sphalerite and marcasite in accessory amounts. The ore minerals are hosted by a brownish-gray dolomite-dominated gangue. Further gangue constituents are quartz and calcite.

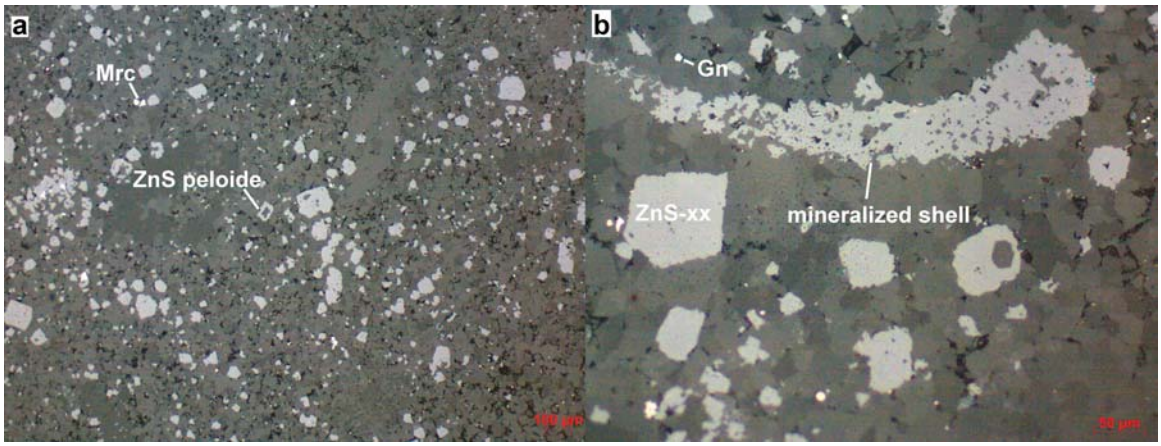

Figure 4.55: a – b) Microphotographs (reflected light, PPL) of the fine-grained sphalerites in sample Tp01. a) Dispersed sphalerite grains and marcasite. Besides a sphalerite peloid, which core consists of dolomite is visible. b) Fine-grained sphalerite accumulation in a former shell. Furthermore, a nearly euhedral sphalerite grain (ZnS-xx) is visible.

The sphalerites in Tp01 display peculiar blue and light green CL colors (Figure 4.56; Appendix Figure 5.6 f). Larger grains (> 50µm) exhibit a CL color zonation, where the cores show blue and the rims light green (yellowish) CL colors. The dolomite dominated gangue shows a red (slightly orange CL).

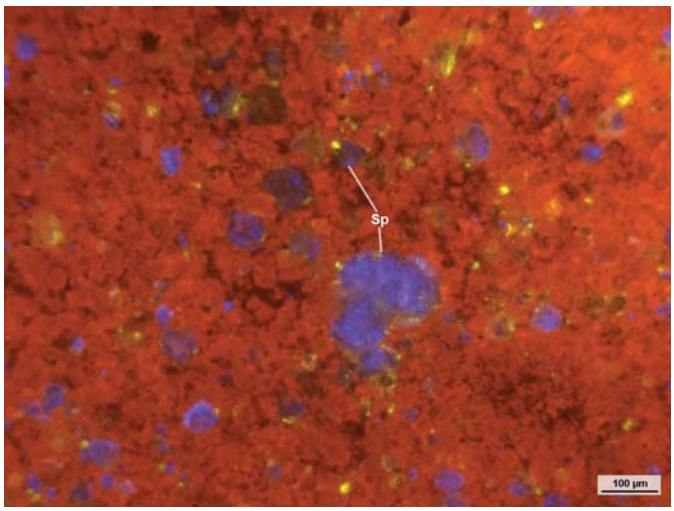

Figure 4.56: Image, showing the CL behavior of sphalerite within sample Tp01. The core of the grains exhibits a blue CL color. The rim is characterized by greenish-yellow CL. The dolomite-rich gangue shows red CL.

Sphalerite chemistry and $\delta^{34}S$ of sulfides in sample Tp01

The sphalerites in sample Tp01 are generally trace element poor (Table 4.10). Table 4.10 displays however a large range in the Fe and Pb concentrations. High Fe and Pb contents (> 0.5 mass%) were measured in a few sphalerite grains, which occur close to iron sulfides and galena, respectively. It is presumable that these high concentrations result from contamination (e.g. tiny inclusions of iron sulfides in sphalerite, small grain size of analyzed grains). The low median but high standard deviations for Fe and Pb would support this interpretation. Cadmium is also low (median 0,1 mass%). Arsenic was detectable in about 50% of the analyses. The median As concentration is 0.02 mass%.

Three sphalerite sulfur isotope measurements in sample Tp01 show a narrow range of the sulfur isotope composition. The $\delta^{34}S$ values range from -20.6 to -23.1‰ (Figure 4.54). One analysis of a marcasite aggregate (> 1mm) yielded a slightly more negative $\delta^{34}S$ value of -23.9‰. Detailed measurements of certain micro-textures (e.g. of sphalerite peloids) were not successful because not enough SO_2 gas for analysis was produced during Laser combustion of single peloids. Thus all three isotope measurements are from sphalerite accumulations where several sphalerite grains of similar textures were analyzed.

Table 4.10: Statistical parameters calculated from the trace element analyses of sphalerites within samples Tp01 and Tp04. The number of analyses (n) above the LOD of the microprobe is given for each element.

	Tp01 (n = 55)				Tp04 (n = 29)		
[mass%]	**Fe** n = 55	**Cd** n = 53	**Pb** n = 37	**As** n = 21	**Fe** n = 24	**Cd** n = 27	**Pb** n = 15
Min	0.01	0.01	0.01	0.01	0.01	0.09	0.12
Max	1.28	0.32	1.22	0.05	0.55	0.28	0.59
Mean	0.17	0.11	0.27	0.02	0.12	0.19	0.21
Median	0.07	0.10	0.11	0.02	0.05	0.19	0.14
Std.dev.	0.24	0.08	0.33	0.009	0.16	0.05	0.13

Tp04

Sample Tp04 was also collected on the dumps of the former Topla mine (same position like as sample Tp01). The mineral paragenesis and textures are very similar to those in sample Tp01. Sphalerite is very fine-grained and not visible on the macroscopic scale. It occurs dispersed/disseminated all over the sample (not visible within Figure 4.57). Marcasite sometimes occurs in larger aggregates (> 1 mm) and is macroscopically visible (Figure 4.57). Compared to sample Tp01 more marcasite is present in Tp04. The iron sulfides were partly affected by weathering, which explains the ocher-brown oxidation colors in the polished slab (Figure 4.57).

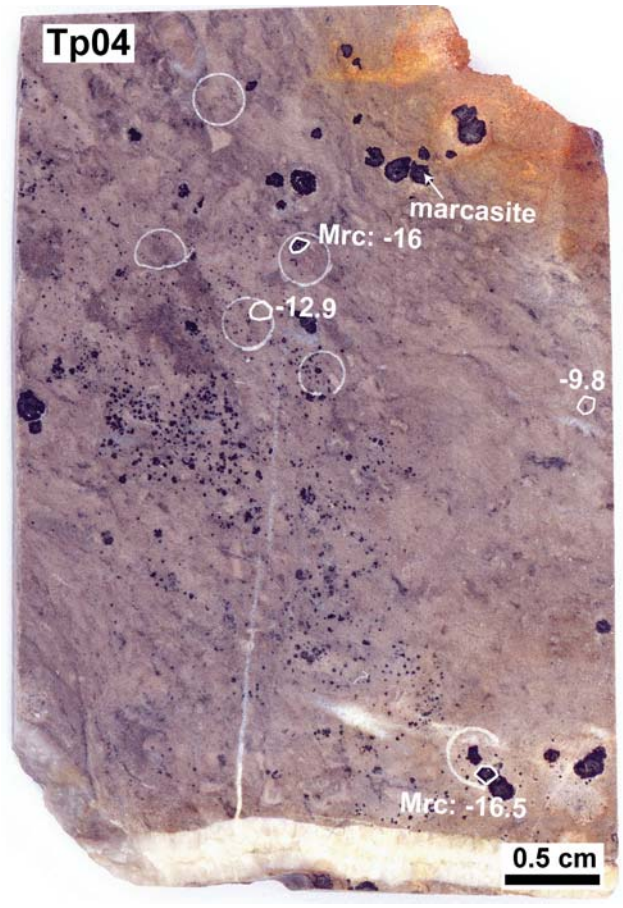

Figure 4.57: Photograph of the polished slap prepared from sample Tp01 for sulfur isotope analysis. Marcasite is the only ore mineral, which can be identified on a macroscopic scale. Sphalerite is very fine-grained and is not visible in this photograph. The sample was affected by weathering, which caused oxidation (upper right corner). The gangue is mainly composed of fine-grained, grayish dolomite. Furthermore a veinlet (5 mm), filled white (coarse-grained) dolomite is evident (lowermost part of the photograph). Furthermore the δ34Svalues of sulfides are displayed.

Sphalerite is very fine-grained and occurs dispersed within the sample (euhedral microcrystalline sphalerite, sphalerite peloids, sphalerite accumulations). Sphalerite inclusions in marcasite/pyrite or vice verse indicate coeval formation of the ore minerals. In addition to sphalerite numerous small (< 10 µm) galena inclusions occur within some marcasite aggregates (Figure 4.58). Besides, small galena inclusions occur also within sphalerite. The gangue consists primarily of dolomite and minor quartz and calcite. The sphalerites in this sample also display blue and green CL colors (Figure 5.6 e; Appendix Figure 4).

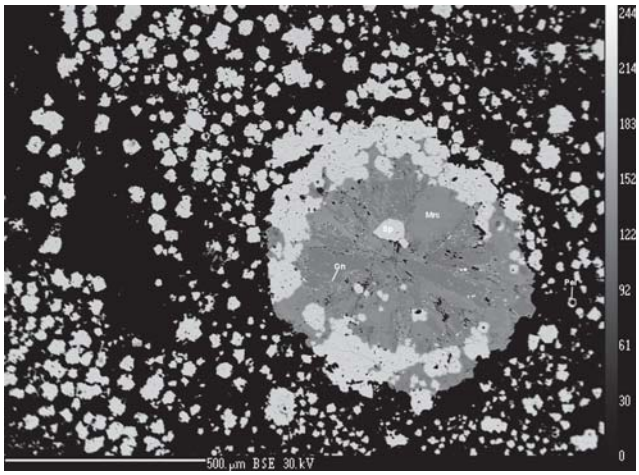

Figure 4.58: BSE image showing a marcasite aggregate (500 µm), which hosts numerous sphalerite grains and furthermore very fine-grained galena.

Sphalerite chemistry and $\delta^{34}S$ of sulfides in sample Tp04

The trace element signature of the sphalerites in Tp04 is nearly equivalent to that in sample Tp01 (Table 4.10). The mean concentrations of Cd, Fe and Pb overlap within their uncertainty. The only significant difference regards the As contents. Arsenic was more often measured in sample Tp01 and only three times within sample Tp04. As contents are not displayed within table 4.10 (Appendix, Table 11). Fe contents > 1 mass% were measured sporadically within the sphalerites, but such values were only achieved in sphalerite inclusions occurring within marcasite aggregates and values are thus most presumably affected by lacking spatial resolution of EMP. Thus, sphalerite analyses were Fe contents were > 1 mass% are not displayed in table 4.10.

The results of sulfur isotope analyses of sphalerite and marcasite and the location of the analyzed micro-areas are displayed in Figure 4.57. Due to the small grain size of sphalerite, analysis of individual micro-textures (peloids, etc.) was not achievable. Thus sphalerite sulfur isotope measurements were performed on sphalerite accumulations. Two sphalerite analyses yielded $\delta^{34}S$ values of -9.8 and -12.9 ‰. Furthermore, two marcasite analyses yielded -16 and -16.5 ‰.

4.4.8 Other Pb-Zn mineralizations in Erzkalk equivalent units

JK5-9

Sample JK5-9 originates from the Jauken deposit. It was collected on the dumps of the former mining area close to the Frauenstollen. The dumps are located on the southern side of the Jauken mountain. Its ore assemblage is sphalerite dominated. Macroscopical, coarse-grained (> 300 µm) eu- to anhedral sphalerite grains form impregnations in carbonate gangue (Figure 4.59). The color of this sphalerites ranges in between honey colored and dark brown. The sample is crosscut by late veins, which are filled with coarse-grained carbonates (Figure 4.59).

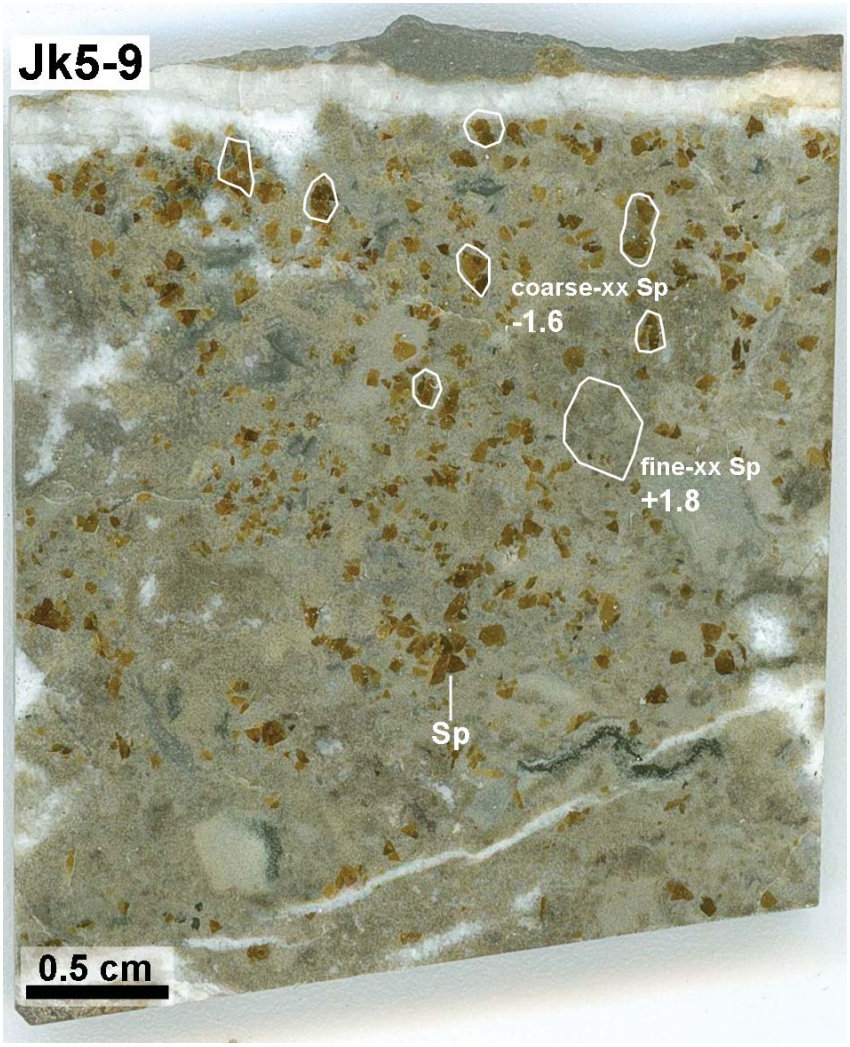

Figure 4.59: Photograph of the polished slap prepared from sample JK5-9 for the sulfur isotope analyses. This sample comprises coarse-grained sphalerite ore, which form impregnations in the carbonate gangue. Besides, more fine-grained sphalerite occurs also within this sample. Furthermore, the results of the sulfur isotope measurements of the sphalerite are displayed.

In addition to the coarse-grained sphalerite, also fine-grained sphalerite (10 – 100 µm) is present within this sample (Figure 4.60). Besides, very small galena inclusions (< 1 µm) occur in some sphalerite grains (or in their vicinity) and small amounts of pyrite are present. (Figure 4.60).

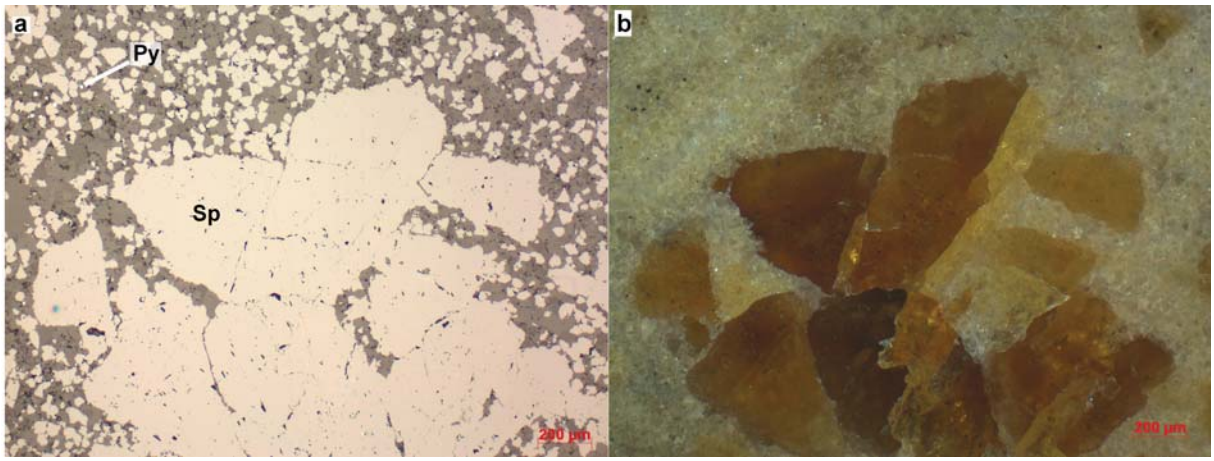

Figure 4.60: a – b) Microscopy photographs (reflected light) of coarse-grained sphalerite besides fine-grained one in sample JK5-9 (a = PPL/ b = XPL). Furthermore, very fine-grained pyrite is visible. The coarse-grained sphalerite is characterized by brown and honey colored internal reflections at XPL. The fine-grained sphalerite displays yellowish-white internal reflections at XPL (b).

Chemistry, $\delta^{34}S$ and Pb isotope composition of sphalerites in sample JK5-9

Sphalerites from the Jauken deposit are characterized by high Ge contents. The sphalerites often contain more Ge than Cd. The mean and median Ge concentrations are higher than the mean/median Cd contents and Ge was measured more often with EMP than Cd. Iron is a further important trace element, which was measured regularly in the Jauken sphalerites. However, due to the inhomogeneity in the Fe distribution and due to the presence of tiny gangue- and pyrite inclusions within the sphalerite grains, increased Fe concentrations might partly be caused by contamination of FeS_2. Pb was only measured in < 30% of the analyses. The irregularly presence of Pb could also be affected by the presence of the above-described tiny Galena inclusions in sphalerite. Figure 4.61 shows the distribution of the regularly occurring trace element contents of the fine-grained and the coarse grained sphalerites. Some differences in the Fe and Ge contents between the coarse-grained and the fine-grained sphalerites are evident. The coarse-grained sphalerites are characterized by higher Fe and therefore lower Ge contents, when compared to the fine-grained ones. However, these differences overlap within the uncertainty (Figure 4.61). Furthermore, the dataset for the fine-grained sphalerites is three times larger than that of the coarse-grained sphalerites (32 and 11, respectively). Hence, in order to estimate if the observed differences in Fe and Ge contents are systematic, further measurements would be desired.

Among all samples from the Drau Range Jauken sphalerites are not only special regarding their very high Ge contents, but also regarding their heavy sulfur isotope signature. Within the Jauken sample, $\delta^{34}S$ values of -1.6 and +1.8 ‰ were measured in the sphalerite (Figure 4.59). These values are the highest within the complete dataset. Besides, also regarding the Pb isotope signature the Jauken sphalerites are characterized by a more radiogenic Pb isotope composition (chapter 4.3.2; Figure 4.20).

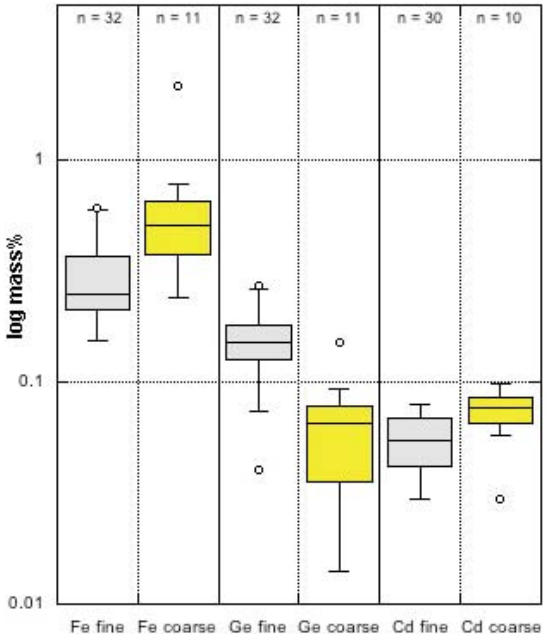

Figure 4.61: Comparison of trace element contents of fine grained (grey) and coarse-grained sphalerite (yellow), present in sample JK 5-9, in boxplot. Some differences in the trace element chemistry are evident. However, these differences overlap within the uncertainty.

Tö01

Sample Tö01 originates from the very small Pb-Zn occurrence Töplitsch. The Töplitsch occurrence is approximately 7 km NE of the Bleiberg mine and direct adjacent to the marble quarry Gummern (Figure 2.3). In Töplitsch only small surface outcrops have been mined. The sample was collected on the dumps, close to a former surface mining pit. The mineralization in Töplitsch is hosted by carbonates of the Wetterstein Formation (Bernhard et al., 2008, cum lit.).

The sample comprises a network sphalerite mineralization, which occurs in the interstitials of carbonate clasts (Figure 4.62). Besides the sphalerite ore sometimes impregnates the carbonate clasts. The sphalerite has a beige (sometimes yellowish) color. The sample was affected by brittle deformation, which caused fracturing of the mineral paragenesis. Furthermore, some late-stage processes led to the formation of veinlets, which are filled with coarse-grained carbonates (Figure 4.62).

Figure 4.62: Photograph of the polished slap prepared from sample Toe01 for sulfur isotope analyses. The sample comprises a sphalerite (+barite) network mineralization, which occurs within the interstitials of carbonate clasts. Furthermore, the results of the sulfur isotope analyses of sphalerites are displayed.

The gangue clasts are mainly composed of rather fine-grained dolomite (< 100 µm). The sphalerite network mineralization is associated with barite, which has a tabular morphology (Figure 4.63 a; b). The barite is approximately 500 µm in size. The sphalerites are sub- to anhedral and range in size from ~100 - 500 µm. The sample was affected by weathering and as a consequence some sphalerite is already transformed to Zn oxide (Figure 4.63 b). Sphalerites in sample Tö01 (and in the other Töplitsch samples) are characterized by blue CL colors, as shown in figure 4.6 f in chapter 4.1.2.

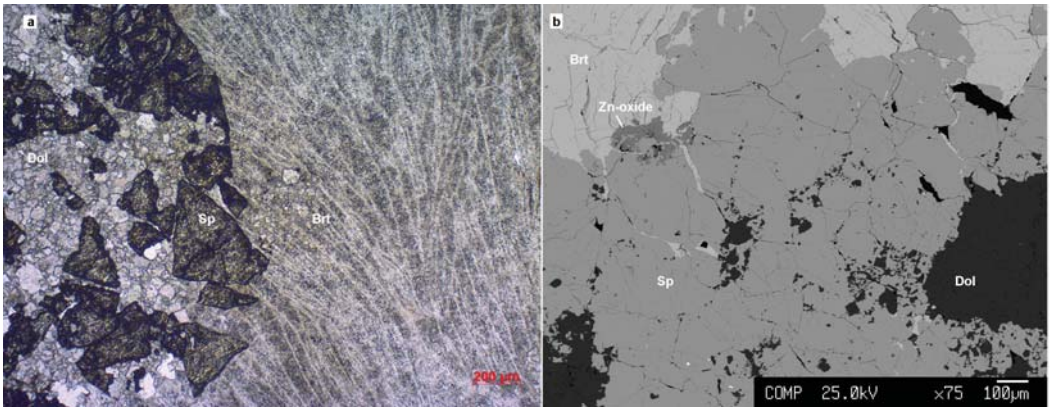

Figure 4.63: a) Photograph (Transmitted light microscopy, PPL) of subhedral sphalerite grains besides barite aggregates and dolomite. b) BSE image of sphalerite, barite and dolomite. Additionally Zn-oxide, which formed due to oxidation of the sphalerite is evident.

Sphalerite chemistry and $\delta^{34}S$ of sulfides in sample Tö01

Töplitsch sphalerites are trace element poor (Table 4.1; Appendix Table 12). Within sample Toe 01 the Pb and Ge contents are always < 0.1 mass% (Table 4.11). Only during four of 19 analyses, Fe-concentrations were > 0.1 mass% and only one Cd analysis revealed a value > 0.1 mass%. The very low Fe contents are conformable with the observed CL behavior of the Töplitsch sphalerites. Two sulfur isotope measurements gave intermediate $\delta^{34}S$ values of -11.5 and -13.2‰ (Figure 4.62). However, the analysis was performed on micro-drilled samples and a contamination from the adjacent barite crystals cannot fully be ruled out. Hence, these two values might be shifted towards higher values due to the adjacent barite crystals.

Table 4.11: Statistics, summarizing the trace element composition of sphalerites within sample Toe01. Statistics were calculated from the EMP measurements, only analyses above the LOD (shown in brackets for each element) were considered for the calculations.

Toe01 (19)	Fe (19)	Cd (10)	Pb (7)	Ge (7)
min [mass%]	0.006	0.003	0.003	0.006
max [mass%]	0.21	0.14	0.06	0.07
mean [mass%]	0.07	0.04	0.04	0.02
median [mass%]	0.06	0.02	0.03	0.01
Std.dev. [mass%]	0.07	0.04	0.07	0.02

4.4.9 Other Anisian Pb-Zn mineralization, not Drau Range

Rd01

Sample Rd01 originates from the small Anisian Pb-Zn occurrence “Zunderwand” in the Middle Austro Alpine (close to the Radenthein magnesite deposit) and belongs thus not to the Drau Range sample set. The sample was collected from a small outcrop, where some pending sphalerite (+fluorite) mineralization is present. The outcrop is in the Nock Mountains in the southwest of the Erlacher Block at an altitude of approximately 1900 m. Although the sample originates not from the Drau Range it was chemical and sulfur isotopic investigated, because it was the only further available sample, besides Topla samples, which is hosted by the Anisian strata. Furthermore, because it was taken from the outcrop itself, the mineralization textures can be interpreted more easily. The Zunderwand mineralization exhibits the typical texture of a hydrothermal breccia and is texturally very different from the Topla samples. Coarse-grained sphalerite + fluorite and calcite occur as impregnation in the interstitials between dolomite clasts (Figure 4.64).

Sphalerite chemistry and $\delta^{34}S$ of sulfides in sample Rd01.1

The chemical composition of the Zunderwand sphalerites is shown in table 4.2 (chapter 4.2.1). The sphalerites from the Zunderwand occurrence are rather trace element poor. Elevated Fe contents of > 0.1 mass% were only measured twice. Cd and Pb concentrations are always < 0.1 mass%.

Two sphalerite sulfur isotope measurements were carried out. The sphalerites are characterized by $\delta^{34}S$ values of 0.5 and 0.2 ‰ (Figure 4.64). These values are compared to the most Drau Range values exceptional high. However, these rather high values fit to the hydrothermal-breccia macrotexture.

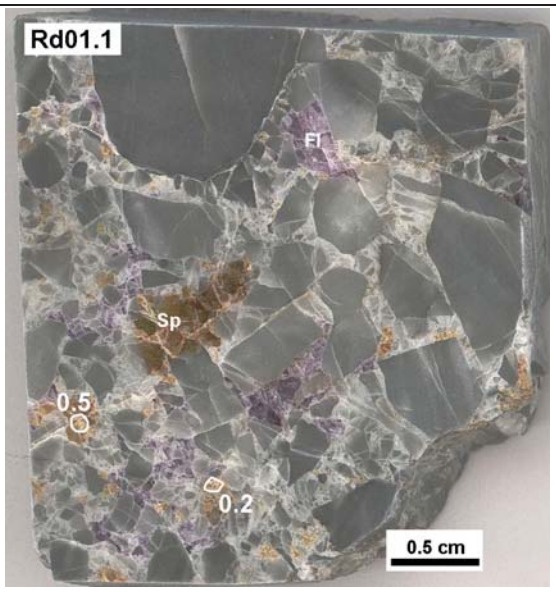

Figure 4.64: Photograph of the polished slap prepared from sample Rd01.1 for sulfur isotope analyses. A hydrothermal breccia texture is evident. The sphalerite mineralization is associated with fluorite (purple color). The breccia components consist of dark grey carbonates. Furthermore, the results of the sulfur isotope measurements of sphalerites within this sample are displayed.

4.5 Isotopic Dating of Sphalerite

It was planned to date Zn-Pb ore formation processes using the Rb-Sr isotope system applied to well-characterized sphalerites (i.e. textures, chemistry, and sulfur and lead isotope compositions). This plan was of limited success due to difficulties in obtaining sufficient quantities (at least 50 mg) of “clean” handpicked mineral fractions and the limited amount of sample material available for some samples. Often it was not possible to clearly separate texturally, chemically and/or isotopically different types of sphalerite intimately intergrown on a very small scale (e.g. sample Blb17). Especially, it was not possible to obtain any suitable sphalerite separates from samples containing very fine-grained sphalerite (e.g. Tp01, Tp04, parts of Blb17, WS_Blb07). The partly intimate intergrowth of sphalerite with gangue minerals was a further problem encountered during mineral separation (e.g. intergrowths of sphalerite with barite in sample EHK02). Gangue minerals usually contain Sr concentrations in large excess of those in sphalerite thus dominating the Sr budget of a separate even when the modal amount is relatively low. Nevertheless, sphalerite separates were prepared from 15 samples for Rb-Sr isotope analysis by conventional TIMS. So far, the isotope data for 8 sphalerite separates have been obtained in the course of the still ongoing investigations.

The measured Rb and Sr element concentrations and $^{87}Rb/^{86}Sr$ and $^{87}Sr/^{86}Sr$ values of the sphalerites analyzed so far are listed in table 4.12. All uncertainties are given at the 2σ level. Furthermore, the $^{87}Sr/^{86}Sr$ values recalculated for an age of 205 Ma, which is the first age estimate for the main stage of Pb-Zn mineralization at Bleiberg (Melcher et al., 2010), are listed. Analytical details of the applied Rb-Sr dating method are given in chapter 3.6. The Rb and Sr element concentrations and the $^{87}Rb/^{86}Sr$ and $^{87}Sr/^{86}Sr$ values show a considerable variability. Within both sphalerite separates of sample EHK02 very high Sr concentrations of > 100 ppm were determined. These high values are not realistic for sphalerite. We presently do not know which mineral caused these very high Sr concentrations. Barite, which is intimately intergrown with the two sphalerites, would be a possible Sr contaminant. However, also for barite Sr concentrations of > 1000 ppm are very high. Because of these uncertainties, the $^{87}Sr/^{86}Sr$ and $^{87}Rb/^{86}Rb$ values for these two sphalerite fractions are not reported. For the other samples, the $^{87}Sr/^{86}Sr$ values recalculated for an age of 205 Ma, average to $^{87}Sr/^{86}Sr = 0.70787$ with an 2σ uncertainty of ± 0.41%. Isochron calculations and the discussion on the reliability of the Rb-Sr data are given in chapter 5.3.

Table 4.12: Results of the Rb and Sr TIMS analyses. The concentrations of Rb and Sr are given in ppm, the uncertainty (2σ) is given in %.

Sample/ Origin	ID	Rb [ppm]	2σ [%]	Sr [ppm]	2σ [%]	$^{87}Rb/^{86}Sr$	2σ [%]	$^{87}Sr/^{86}Sr$	2σ [%]	$^{87}Sr/^{86}Sr$ t: 205 Ma	2σ [%]
E14.6 Bleiberg Erlach	E14.6 SB	0.839	0.41	0.053	0.82	46.13	1.04	0.8372	0.12	0.7027	0.25
J10.4 Bleiberg, Josefischolle (crest)	J10.4 SB	1.00	0.47	0.60	0.04	4.854	0.69	0.72260	0.006	0.70845	0.015
	J10.4 ZnS-xx	0.21	0.23	0.07	0.38	8.764	0.67	0.73464	0.015	0.70910	0.029
C6.14 Bleiberg 1st Raibl h.	C6.14 ZnS	0.595	0.36	4.423	0.01	0.3892	0.62	0.71009	0.004	0.70895	0.004
EHK02 Bleiberg Erzkalk	EHK02 SB			>3,000							
	EHK02 ZnS II			>400							
MzH01 Mezica Helena	MzH01 SB	1.335	0.58								
	MzH01 ZnS-xx	0.477	0.31	0.071	0.4	19.65	0.71	0.76845	0.031	0.71115	0.066
Mz08 Mezica Moring	Mz08 ZnS	0.244	0.24	0.113	0.48	6.236	0.73	0.72784	0.014	0.70966	0.023
JK5-9 Jauken WF	JK5-9 ZnS	0.474	0.33	0.054	0.83	25.78	1.02	0.78027	0.074	0.7051	0.14

5 Discussion

5.1 Trace Element Variations of Sphalerite

5.1.2 Lattice incorporation vs. inclusion contamination

The chemical data set of sphalerite from the Pb-Zn deposits of the Drau Range exhibits a large variability in the trace element contents (chapters 4.2 & 4.4). The trace element distribution of sphalerites from different types of Pb-Zn deposits (MVT, VMS) have been investigated and discussed by various authors (Moh & Jager, 1978, Pimminger et al., 1985, Johan, 1988, Di Benedetto et al., 2005, Cook et al., 2009, Pfaff et al., 2011). Sphalerite is famous for its ability to incorporate a wide range of trace elements (Cook et al., 2009). However, for some elements it still under debate if they are directly incorporated into the sphalerite lattice or if they form nano-inclusions (Cook et al., 2009, Pfaff et al., 2011).

Cadmium enrichment in sphalerites is well investigated and Cd is considered to be present in solid solution substituting for Zn (Cook et al., 2009 and references therein). Cook et al. (2009) reported that Cd variations are rather small (maximum of factor 5) on a deposit scale. In most samples from Drau Range the variations in Cd contents are small, except for a few samples where the chemical variations in Cd contents are related to morphological and sulfur isotopic variations (e.g. samples Blb17, EHK02, R8/2, chapters 4.4.1 – 4.4.3). Furthermore a few samples contain sphalerites with Cd varying by a factor 2 – 3 already on the grain scale (chapter 4.2.3 and 4.4.4). The BSE zonation caused by variable Cd (+Ge) contents (Figure 4.10) is in agreement with incorporation of Cd in the sphalerite lattice. The interpretation that Cd is a typically lattice-bound trace element in sphalerite is additionally supported by the frequent occurrence of Cd. The variability in Cd contents is in Bleiberg and Mezica very high (factor 100). This high value is larger than it is reported from the majority of Pb-Zn deposits (Cook et al., 2009). Variations in Cd contents of > factor 10 were already observed within the scale of an ore horizon. Compared to the data of Cook et al. (2009), these large variations are uncommonly high. The large variation in Cd contents might be a characteristic feature for the Drau Range sphalerites. As shown in chapter 4.4, the sphalerites in some samples show a negative correlation of Fe and Cd contents and sulfur isotope signature. A correlation of Fe/Cd ratios and sulfur isotope signature has also been described from other Pb-Zn deposits, e.g. the Irish Navan deposit (Gagnevin et al., 2011).

Direct substitution of *iron* (Fe^{2+}) for Zn^{2+} is the most common substitution in sphalerite (see summary in Cook et al., 2009). Iron was measurable in sphalerite from all studied deposits. The lacking correlation of Fe with other trace elements in sphalerite together with the frequent occurrence of Fe are in agreement with a direct substitution of Fe^{2+} for Zn^{2+}. However, a part of the increased Fe measurements (> 1 mass%) in

sphalerites might be furthermore influenced by accidentally measured Fe sulfide inclusions, which occur in some samples. The > 1mass% Fe analyses in the Topla sphalerites are e.g. attributed to the presence of small-sized Fe inclusions.

Lead is commonly not considered to be present in solid solution within the sphalerite lattice (e.g. Cook et al., 2009, Pfaff et al., 2011). Both authors report very heterogeneous Pb distribution, which they attribute to presence of Pb-bearing nanoinclusions (galena and/or sulfosalts). Lead concentrations in the Drau Range sphalerites vary from 70 ppm to 1.2 mass%. High Pb contents (> 0.1 mass%) were measured sporadically. This heterogeneous Pb distribution supports this hypothesis. TIMS analyses of sphalerite confirm the high variability in Pb concentrations (144 to > 18,000 ppm) of sphalerite. Lead shows a positive correlation with As (Figure 5.1). The positive correlation between Pb and As is documented for both the EMP and the LA ICP-MS dataset (Figure 5.1; 5.2). Within the LA ICP-MS data, both elements are furthermore positively correlated with Tl (Figure 5.2). Together with the heterogeneous distribution of Pb this element association might indicate that these trace elements are present as submicroscopic sulfosalt inclusions (Pfaff et al., 2011). Furthermore, increased Pb contents might partly be due to galena inclusions in sphalerite, which were not seen on BSE images. Already Pimminger et al. (1985) suggested that Pb-bearing micro-inclusions control the Pb contents of sphalerites at Bleiberg. Further analyses, which are suitable for visualization of the Pb bearing inclusions, would be required (e.g. FIB, HR-TEM).

	As	Fe	Pb	Ge	Cu	Cd	Tl
As	1						
Fe	0.14	1					
Pb	0.7	0.16	1				
Ge	0.06	0.03	-0.14	1			
Cu	-0.26	-0.25	0.15	-0.16	1		
Cd	-0.14	-0.21	-0.07	-0.34	0.50	1	
Tl	0.29	0.23	0.31	0.28	/	-0.23	1

Figure 5.1: Correlation matrix for the trace element dataset calculated from EMP data. The values were calculated using the formula, which assumes a linear dependency between two variables (Pearson's r). Nearly no significant correlations were calculated based on the EMP dataset.

Germanium is one of the elements, for which incorporation into sphalerite is still under debate. Ge is an important element, which availability was ranked as critical by the ad-hoc working group on defining critical raw material of European Commission (2010). The major primary sink of Ge is sphalerite (e.g. Cook et al., 2009). Various authors investigated mechanisms that control the incorporation of Ge in sphalerite (e.g. Johan, 1988, Cook et al., 2009). Johan (1988) proposed that Ge is incorporated into the sphalerite lattice via a coupled substitution mechanism (Equation 5.1). According to

Johan's (1988) model Ge occurs as $^{+4}$ ion and substitutes together with other monovalent and divalent cations for Zn in the sphalerite structure.

$$2M^{+1} + M^{+2} + M^{+4} \rightarrow 4Zn$$
$$2M^{+1} = Cu, Ag$$
$$M^{+2} = Cu, Fe, Cd, Hg, Zn$$
$$M^{+4} = Ge, W, Mo, Sn$$

(Equation 5.1)

Cook et al. (2009) investigated the trace element chemistry of sphalerites from different types of Pb-Zn deposits and proposed that Ge is directly incorporated into the sphalerite lattice via solid solution. They observed a weak positive relation between Ge and Ga and furthermore a weak positive correlation of Tl and Ge. They argued against a coupled substitution mechanism of Ge with monovalent cations as proposed by Johan (1988), because no combined enrichment of monovalent cations with Ge was observed. Since Saini-Eidukat et al. (2009) and Cook et al. (2009) observed a positive correlation between strongly high Ge and high Fe contents in sphalerites from Tres Marias (Mexico), they suggest for these sphalerites a coupled substitution with Fe, in the way: $2Fe^{2+} + Ge^{4+} \rightarrow 4Zn^{2+}$. However, they did not exclude the possibility that Ge directly substitutes for Zn^{2+} in its reduced Ge^{2+} state (Cook et al., 2009). Melcher et al. (2009) were able to demonstrate that Ge is divalent in sphalerite from Tres Marias. Bellisont et al. (2014) observed a positive relation between Ge and Ag in sphalerite from the Noailhac – Saint-Salvy deposit (France) and propose a coupled substitution mechanism in the way $Ge^{+4} + 2Ag^{+} \rightarrow 3Zn^{2+}$. Moh & Jager (1979) argue that the solubility of GeS in ZnS is rather low and therefore supposed that Ge is rather incorporated in microphases than in the sphalerite lattice. We assume that Ge is directly incorporated into the sphalerite lattice, since Ge is one of the elements that causes the zonation in sphalerite (chapters 4.2 & 4.4). Di Benedetto et al. (2005) investigated compositional zoning of sphalerite crystals and attributed it to element partitioning during crystal growth along non-equivalent crystallographic faces or to a fast self-organization of elements during the deposition. Belissont et al. (2014) investigated the distribution of Ge in zoned sphalerite grains (sector zonation + rhythmic zoning) from the Noailhac – Saint-Salvy deposit (France). They observed an antithetic distribtuion of Ge and Fe/Cd and attributed to enrichment of certain trace elements at special cristallographic faces during the growth of the mineral (e.g. Fe and Cd are high at the 110 plane). The core-wards continuation of the Ge rich zones along cleavage planes indicates that the compositional zonation of Ge and Cd is not primary (i.e. growth zoning). It is more presumable that the observed zonation formed due to an overgowth of Ge rich sphalerite on pre-existing Cd rich sphalerite grains. Nevertheless, this zonation indicates that Ge is directly incorporated into the sphalerite lattice, despite the fact that it partly precipitated during a later growth stage. Increased Ge contents are not always linked to a (visible) zonation (e.g. in the Jauken sphalerite). A further argument for lattice bound Ge incorporation might be the preferred enrichment of Ge in crystalline sphalerite grains rather than in coexisting schalenblende (Blb17, E14.2-4). Schalenblende is considered to form due to rapid precipitation from a relatively super-saturated fluid (Roedder, 1968). It tends to host high amounts of inclusions because of

its rapid formation. If Ge were incorporated in nano- or microinclusions it would be higher in schalenblende (with a more erratic distribution) than in the coexisting crystalline sphalerite. Exactly the opposite is the case Ge contents are higher in co-existing crystalline sphalerite. No distinct correlation (neither positive nor negative) of Ge and another trace elements is documented in our data. When examining our dataset critically, it becomes evident that Ge tends to be rather enriched in sphalerites, which contain more Fe than Cd but have Fe concentrations < 1 mass%. Thus, a simple positive correlation between Ge and Fe, as proposed by Cook et al. (2009) for the Tres Marias sphalerites, is not evident within our dataset. The coupled substitution mechanism of Ge for monovalent cations (e.g. Cu^{1+}), (Johan 1988), was also not confirmed in this study. It is supposable that the reduced Ge^{2+} ion directly substitutes for Zn^{2+}.

Arsenic is a further trace element for which incorporation in sphalerite is debated controversially (Clark, 1970, Pimminger et al., 1985, Cook et al., 2009, Pfaff et al., 2011). According to a literature review and their own LA ICP-MS data, As is regarded as a rather rare trace element in sphalerite by Cook et al. (2009) who reported maximum As contents of 0.06 mass% in sphalerites from Tres Marias. Based on this finding, Cook et al. (2009) concluded that the solubility of As in solid solution with sphalerite is low and that As is rather characteristic for low-temperature deposits. This assumption is partly in agreement with Clark et al. (1970), who stated that As enriched sphalerite is restricted to Pb-Zn deposits which formed at temperatures <200°C. The possibility that Pb-As-Tl nanoinclusions have an important control on increased As contents in sphalerites has already been discussed above. However, a direct incorporation of small amounts of As into the sphalerite lattice cannot be excluded.

Copper is not easily incorporated in significant quantities into the sphalerite lattice (Cook et al., 2009). Also Barton & Bethke (1987) stated that the solid-solution series between CuS and ZnS is very limited and proposed that Cu is often bound to submicroscopic (< 5 µm) blebs of chalcopyrite, which tend to occur along crystallographic axes of the host-sphalerite (chalcopyrite-disease). Johan (1988) proposed that Cu occurs as monovalent cation (Cu^{1+}) and substitutes together with Ge^{4+} for Zn^{2+} (see subchapter on Ge). Cook et al. (2009) found a weak positive correlation of In and Cu, which would agree to a coupled substitution of Cu^{1+} and In^{3+} for Zn^{2+}. The preferred occurrence of In together with Cu was also observed in our LA ICP-MS data of sample Blb26 (Figure 5.2). Cook et al. (2009) were not able to determine a positive relation between Cu and Ge, which has been proposed as a further possible substitution mechanism by Johan (1988). Within the Drau Range dataset also no positive correlation of Ge and Cu, which would indicate a coupled substitution mechanism of Cu^{1+} and Ge^{4+}, is evident. However, also no Cu-bearing micro-inclusion were observed under the microscope or on BSE images. In contrast, Cu was more often detectable in inclusion-poor and Cd-rich crystalline sphalerite grains, than in inclusion-rich schalenblende aggregates.

LA ICP-MS Blb26									
	As	**Fe**	**Pb**	**Cd**	**Tl**	**Cu**	**Ga**	**Ag**	**In**
As	1								
Fe	0.98	1							
Pb	0.95	0.92	1						
Cd	-0.52	-0.47	-0.61	1					
Tl	0.95	0.93	0.93	-0.61	1				
Cu	-0.17	-0.15	-0.12	0.13	-0.16	1			
Ga	0.52	0.48	0.5	-0.34	0.59	0.02	1		
Ag	0.11	0.1	0.05	0.36	0.08	0.17	0.3	1	
In	-0.15	-0.13	-0.14	0.18	-0.16	0.8	0.05	0.1	1

EMP Blb26						
	As	**Fe**	**Pb**	**Ge**	**Cd**	**Tl**
As	1					
Fe	0.88	1				
Pb	0.79	0.66	1			
Ge	0.83	0.73	0.68	1		
Cd	-0.71	-0.52	-0.57	-0.66	1	
Tl	-0.57	0.85	0.25	0.85	-0.51	1

LA ICP-MS WSBlb29								
	As	**Fe**	**Pb**	**Cd**	**Tl**	**Cu**	**Ga**	**Ag**
As	1							
Fe	0.55	1						
Pb	0.93	0.57	1					
Cd	-0.35	-0.4	-0.31	1				
Tl	0.89	0.38	0.78	-0.41	1			
Cu	-0.2	-0.38	-0.04	0.63	-0.24	1		
Ga	-0.33	-0.19	-0.27	0.33	-0.29	-0.07	1	
Ag	-0.09	-0.3	-0.06	0.48	0.01	0.71	-0.06	1

EMP WSBlb29					
	As	**Fe**	**Pb**	**Ge**	**Cd**
As	1				
Fe	0.53	1			
Pb	0.52	0.18	1		
Ge	0.29	0.34	0.06	1	
Cd	-0.29	-0.25	-0.08	-0.57	1

Figure 5.2: Correlation matrices, comparing LA ICP-MS correlation coefficients to EMP correlations. From LA ICP-MS data much more pronounced correlation coefficients were calculated.

The incorporation mechanisms for *thallium* were to some extent already discussed in the subchapters about As and Pb. In addition to the inclusion-bound Tl (Pimminger et al., 1985, Pfaff et al., 2011), Xiong (2007) suggested that Tl^{1+} might substitute together with trivalent cations such as As^{3+} for Zn^{2+} in the sphalerite lattice. Cook et al. (2009) reported that Tl concentrations in sphalerites are generally low and are either caused by sulfosalt inclusions or more rarely attributed to solid solution of Tl in sphalerite. To which extent the restriction of Tl to Bleiberg sphalerites is a characteristic feature of this

deposit cannot be said with certainty, because of the analytical problems with Tl analyses using EMP techniques.

5.1.2 Trace/minor elements in sphalerite – summary

Figure 5.1 summarizes the interelement relationships in a correlation matrix. It gives the correlation coefficients (Pearson's r) of the elements, which were measured with EMP techniques. In Figure 5.2 additional correlation matrices of individual samples, which display a comparison in the correlations calculated from the LA ICP-MS and the EMP data are shown. From the distribution patterns it is concluded that the elements Fe, Cd and Ge are mostly directly incorporated into the lattice of the sphalerites. The remaining elements are at least partly considered as nano-inclusions. The incorporation mechanisms of Pb, As, Tl and Cu remain uncertain. In order to evaluate to which extent these elements occur also within the sphalerite lattice itself further in-situ chemical analyses, which offer a better detection limit (e.g. LA ICP-MS) are required. In order to visualize the supposed nano-inclusions, further analyses that allow a high spatial resolution (e.g. HR-TEM) are desirable.

Figure 5.2 shows a comparison of the correlations calculated from the EMP and LA ICP-MS data. The correlations, calculated from the EMP data partly differ from that for the LA ICP-MS data (Figure 5.2). Compared to the EMP data, the correlations calculated from the LA ICP-MS data are more pronounced. The LA ICP-MS data of sample Blb26 indicates e.g. a very strong (≥ 0.95) positive relation between As, Fe, Pb and Tl. Within the EMP data these relations are < 0.9 (Figure 5.2). The comparison of LA ICP-MS with EMP data clearly shows, that EMP data can only be used for rough orientation. In order to fully understand incorporation mechanisms of certain trace/minor elements in sphalerite more precise data and data with better spatial resolution are desirable. When comparing the correlations calculated from the EMP data of single samples (Blb26 and WS_Blb29) with the correlations calculated from the complete EMP data (Figure 5.1; 5.2) it becomes evident that the correlations that include the whole EMP data are not fully representative for the interelement relationships of single samples. Hence, the trace element patterns of sphalerite from the Drau Range are highly heterogeneous. The interelement relationships are variable from one sample to another.

5.2 Sulfur Isotopes

5.2.1 Causes of sulfur isotope variations

The range in sulfur isotope compositions of 17 investigated samples from the Drau Range is > 30‰. A three-peak distribution can be observed in the $\delta^{34}S$ distribution of the sphalerites (Figure 4.17). Most (> 50%) sphalerites are characterized by a very light sulfur isotope composition ($\delta^{34}S$ < -20‰). A second, less distinct peak is present at a $\delta^{34}S$ of -15‰. A third even more vague peak can be seen by a less negative $\delta^{34}S$ of around -5‰. The variability in $\delta^{34}S$ values of the sphalerites from Bleiberg covers nearly the complete $\delta^{34}S$ range of the whole dataset.

The sulfur isotope composition of sulfides depends among other factors on the processes which cause the reduction of sulfate (S^{6+}) to sulfide (S^{2-}) prior tore mineralization (Ohmoto & Goldhaber, 1997, cum lit.). Particular redox mechanisms of sulfate (S^{6+}) to sulfide (S^{2-}) lead to specific fractionation trends (Figure 5.3, Warren, 2000).

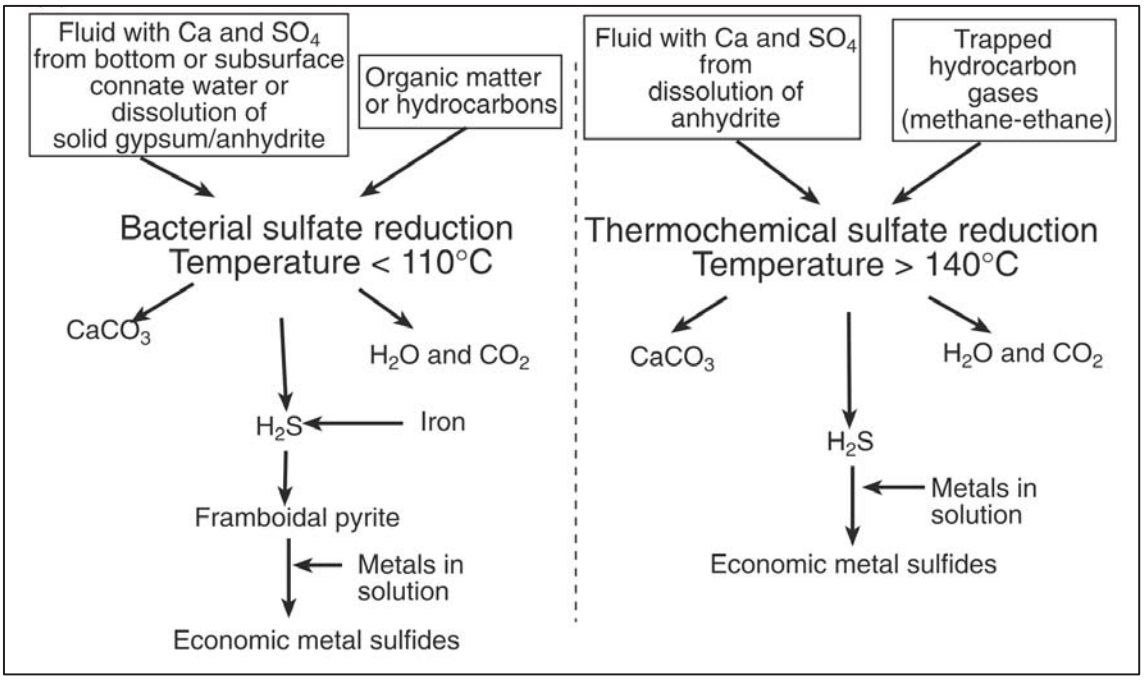

Figure 5.3: Starting material, chemical pathways and products during bacterial sulfate reduction (BSR, left) and during thermochemical sulfate reduction (TSR, right). After Warren (2000). BSR causes a strong isotopic fractionation of 20 to 30‰ lighter than the precursor sulfate. The isotopic frationation during TSR is rahater small (20 to 0‰ lighter than the precursor sulfate).

Machel et al. (1995) describe two distinct pathways of sulfate reduction: *(1)* Thermochemical sulfate reduction *(TSR)*, which is driven by increased temperatures. TSR leads only to small isotope fractionation with respect to the precursor sulfate. The fractionation factor is temperature-dependent (about 20‰ at 100°C and 10‰ at 200°C). The presence of organic compounds can catalyze TSR, which allows that TSR operates at lower temperatures (< 100°C). However, in some natural systems no

fractionation occurs at all. *(2)* Bacterial sulfate reduction *(BSR)* is considered as a low temperature process. BSR leads to a strong isotopic fractionation of ^{32}S with respect to ^{34}S, because bacteria more easily metabolize the lighter sulfur isotope. The resulting isotopic fractionation is about 20 to 30‰ lighter with respect to the $\delta^{34}S$ of the precursor sulfate. Isotope fractionation can even increase to values > 30‰ when sulfate reduction occurs stepwise and involves intermediate sulfur compounds (e.g. thiosulfates). When BSR occurs in a closed system (i.e. restricted input of "fresh" sulfates), bacteria are forced to metabolize also the heavier sulfur isotope. A closed-system BSR reservoir can be identified by gradually increasing $\delta^{34}S$ values (Seal II, 2006).

The wide variation in sulfur isotope composition of the sphalerite + galena/Fe-sulfides from the carbonate-hosted Pb-Zn deposits of the Drau Range indicates, that at least two different sulfur reservoirs were involved into ore formation. One reservoir provided light (very negative $\delta^{34}S$ values) sulfur and another reservoir contributed heavier (less negative to positive $\delta^{34}S$) sulfur for ore mineralization. In three samples from Bleiberg a temporal variability in $\delta^{34}S$ values of co-occurring sulfides is evident (samples Blb17, EHK02, R8/2, chapter 4.4). The chronological evolution of the $\delta^{34}S$ values is not uniform within these three samples. The early-formed sulfides in sample Blb17 and R8/2 are sulfur isotopically light, whereas the earliest ZnS (+ galena) generation in sample EHK02 is clearly distinctly heavier than the later formed generations. Changes in isotope composition occur over a small scale, are rather abrupt and can partly be correlated with a change in gangue mineralogy (see chapter 4.4.1/4.4.2). The non-uniform temporal evolution of $\delta^{34}S$ in these three samples contradicts the idea of a single closed-system reservoir, because in this case a continuous evolution would be evident; e.g. a systematic trend from light to heavy sulfur isotope compositions. Since fossilized relicts of bacteria (filaments of sulfate-reducing bacteria, sphalerite nanoglobules) have been reported from Bleiberg (Kucha et al., 2005, 2010) and ZnS-mineralized peloids, which are interpreted as bacterially formed were observed in the Topla deposit (Chapters 4.1 & 4.4), it is concluded that at least a part of the very light sulfur was provided from bacterial reduced seawater sulfate. The other reservoir with a heavier isotope composition ($\delta^{34}S$ > -5‰) derived its sulfur isotope signature presumably via thermochemical sulfate reduction (TSR), what may indicate a hydrothermal imprint/source. The extent of TSR contribution is not clear. The highest measured $\delta^{34}S$ values of > -5 to +1.8 are certainly relatively low for TSR, when considering Triassic seawater sulfate as precursor, which has a $\delta^{34}S$ of +15 to +18 ‰. The isotope fractionation would be about 15 to 20 ‰ with respect to the precursor sulfate, which is according to Machel et al. (1995) close to the maximum of the TSR process and would only be possible at low temperatures.

As documented for sample Rd01.1 (Zunderwand occurrence, not Drau Range) the $\delta^{34}S$ values are around -1.5‰. Texturally this Zn-fluorite mineralization is of breccia type (see chapter 4.4.9). A rather low-temperature hydrothermal fluid (c. 100°C) might explain the strong isotopic fractionation. A strong isotopic fractionation might occur within a TSR reservoir at low temperatures of around 100°C (Machel et al., 1995). It cannot be excluded, however, that the, for TSR, uncommonly light $\delta^{34}S$ values reflect admixture of sulfur from two different sulfur reservoirs. Because sulfides with light

sulfur isotope composition predominate we think that TSR was presumably of minor importance and BSR was the predominant sulfate reducing mechanism.

The variability in $\delta^{34}S$ values of sulfides from Pb-Zn deposits in the Drau Range has already been documented in previous studies (Drovenik et al., 1980, Schroll et al., 1983, Kuhlemann et al., 2001, Spangenberg et al., 2001, Kucha et al., 2002, 2004, Schroll & Rantitsch, 2005, Herlec et al., 2010) and the polymodal three-peak distribution with the strong bias towards very light values (< -20‰) has also been known from Bleiberg before (Schroll & Rantitsch, 2005, Kucha et al. 2010).

Herlec et al. (2010) document a bimodal $\delta^{34}S$ distribution for sphalerites from Mezica, but in contrast to the Bleiberg data (including the new data of this study) the main peak is at less negative values at about -15‰. The generally negative sulfur isotope signature of the Alpine Pb-Zn deposits has often been used as argument for discriminating Alpine Pb-Zn deposits from the classic MVT deposits (see Schroll & Rantitsch, 2005, cum lit.). The above-mentioned authors agree that the large variability in sulfur isotope composition is due to input of reduced sulfur from both a BSR and a TSR reservoir. Furthermore, most authors agree that seawater sulfates are the presumable sulfur source, because sulfur isotope measurements of coexisting sulfates gave $\delta^{34}S$ values of around +15‰, what is in the range of Triassic seawater (e.g. Schroll et al., 1983, Kuhlemann et al., 2001). However, the importance of TSR versus BSR derived sulfur for ore formation is controversially discussed by the above-mentioned authors. Kuhlemann et al. (2001) argue for a major TSR reservoir. They propose a chronological evolution towards heavier sulfur isotope composition with time. Contrariwise, Schroll & Rantitsch (2005) and Herlec et al. (2010) argued that the main quantity of sulfide sulfur was provided by microbial reduction of seawater sulfate.

This study confirms a clear bias towards $\delta^{34}S$ values < -20‰ and indicates a dominant BSR reservoir. More than 50% of the sulfides shows very light sulfur isotope composition (< -20‰), whereas only a small percentage is characterized by $\delta^{34}S$ values > -5‰. Very light sulfur isotope compositions predominate in sulfides at Bleiberg from where also the largest variation is documented. In contrast sulfides from Mezica are characterized by less negative values. The larger variability in $\delta^{34}S$ values in Bleiberg sulfides is at least partly due to the focus of investigations on the Bleiberg mineralization. The tendency towards more intermediate sulfur isotope composition in Mezica sulfides might however be a diagnostic feature, because it is in accordance to the $\delta^{34}S$ distribution, which is reported by Herlec et al. (2010). The $\delta^{34}S$ values of the Jauken sphalerites are in an outlier position with respect to the remaining Drau Range sphalerites. The correctness of the measurements is however not doubted, because Kuhlemann et al. (2001) report also positive $\delta^{34}S$ values (approximately +2‰) in sphalerites from Jauken.

The combination of sulfur isotope with chemical data and textural aspects (see chapter 4.4) demonstrated the small-scale (within sample) variations of Pb-Zn mineralization.

Sulfides, which have very negative $\delta^{34}S$ values (< -20‰) occur together on the mm-scale with those, having $\delta^{34}S$ values of > -5‰ in samples from different ore horizons of the Bleiberg deposit. These small-scale heterogeneities in sulfur isotope composition resulted most presumably from the interactions of local BSR reservoirs with sulfur derived from other reservoir(s) and the metal bearing fluid at the depositional site. It is presumable that both reservoirs were able to provide reduced sulfur during the whole mineralization process and no strict formation chronology of sulfur isotopically distinct sulfides is evident. A predominance of BSR-derived sulfur in most of the ore horizons at Bleiberg is present. This is similar to the Irish Navan deposit (Fallick *et al.*, 2001). In analogy to the Irish Pb-Zn district only small uneconomic occurrences (e.g. Jauken) contain TSR-dominated sulfur (Henjes-Kunst *et al.*, 2013). $\delta^{34}S$ values > -10‰ were more often measured within the deeper ore bodies in the Wetterstein Formation (Erzkalk, Maxer Bänke). Only one sample (R8/2) from a stratigraphically higher seated ore body exhibited $\delta^{34}S$ values of approximately -5‰. A trend towards heavier sulfur isotope compositions with depth could be a further analogy with the Irish Pb-Zn deposits; at Lisheen mine the $\delta^{34}S$ values of sphalerite and galena increase with increasing depth (Wilkinson *et al.*, 2005). This might be the reason for the less negative sulfur isotope signature at Mezica. The host rocks for the ore mineralization at Mezica belong to the hanging Wetterstein Formation (Erzkalk horizon equivalent). The Erzkalk horizon is also at Bleiberg more often characterized by less negative $\delta^{34}S$ values. According to Wilkinson et al. (2005) this increase in TSR derived sulfur towards the depth may serve as an indicator for the increasing influx of hydrothermal fluid from depth, which migrated along fractures into the ore system.

The coexistence of sulfides having very different isotope composition within one sample gives important information on the transport of reduced sulfur. BSR works less effective at temperatures > 80°C (Machel et al., 1995) In contrast TSR starts to produce reduced sulfur effectively at temperatures > 80 to 100°C. This circumstance proofs the presence of two different sulfur reservoirs, which are spatially separated. Furthermore, it requires transport of reduced sulfur from two reservoirs to depositional site. The meeting of two different sulfur bearing fluids at depositional site is, according to Anderson (1975) highly implausible. However, in a later publication Anderson (2008) supports the idea of fluid mixing as relevant mineralization mechanism. Another possibility to produce TSR signature sulfides in a low temperature environment (< 80°C) would be the presence of organic matter (Machel et al., 1995). Fossil bacteria filaments and ZnS nanospheres are known from certain ore horizons of Bleiberg (e.g. Kucha et al., 2010) and sphalerite peloids, which are presumable to contain also fossil sulfate-reducing bacteria are described for the Topla deposit within this study. Due to the detection of fossil sulfate reducing bacteria in some sphalerites it is plausible that a part of the ore mineralization occurred in the BSR reservoir itself (Henjes-Kunst et al., 2013). However, not all sphalerites, which are characterized by very negative $\delta^{34}S$ values, evidence fossil bacteria filaments. Therefore, also transport of BSR derived reduced sulfur to depositional site in fluids is required.

5.2.2 Sulfur isotope compositions of coexisting sulfide pairs – implications for formation temperatures?

Table 5.1 summarizes sulfur isotope data of those samples, in which the sulfur isotope composition of coexisting sulfides (ZnS, PbS and FeS_2) could be measured within a single sample micro-area. In the following it will be briefly discussed if there exists an isotopic equilibrium among the coexisting phases and if these data can be used for sulfur isotope thermometry in order to estimate the temperatures of ore formation.

For isotopic equilibrium the ^{34}S values of coexisting pyrite/marcasite, galena and sphalerite must be related in the way $\delta^{34}S$ PbS < $\delta^{34}S$ ZnS < $\delta^{34}S$ FeS_2 (Bachinski, 1969). The fractionation of ^{34}S in these sulfides is related to the relative strength of the metal-sulfur bond of the respective mineral (Bachinski, 1969). Heavier sulfur isotopes tend to fractionate in minerals which are characterized by a higher bond energy (Bachinski, 1969). Because fractionation between sphalerite and iron sulfides is controversially debated most recent studies focus on the fractionation of $\delta^{34}S$ between sphalerite and galena (Li & Liu, 2006). Table 5.1 shows that the fractionation of ^{34}S of coexisting sphalerite-galena pairs is not constant. In some samples $\delta^{34}S$ ZnS > $\delta^{34}S$ PbS, what could be indicative for sulfide precipitation under isotopic equilibrium. In contrast, in other samples (J10/4, Blb17) an opposite fractionation sequence is present. In these samples the two sulfides were certainly precipitated in isotopic disequilibrium. The $\delta^{34}S$ values of pyrite/marcasite are always smaller than those of coexisting sphalerites. Hence, in all cases iron sulfides were precipitated in isotopic disequilibrium with sphalerite.

Table 5.1: Summary of $\delta^{34}S$ values for coexisting sulfide pairs.

Sample	$\delta^{34}S$ ZnS [‰]	$\delta^{34}S$ PbS [‰]	$\delta^{34}S$ FeS_2 [‰]	fract. sequence
R8/2	> -24.5	/	-24.5	ZnS ≥ FeS_2
J10/4	< -26.6	-25.7		ZnS < PbS
EHK02	> -6.6	-7.7		ZnS > PbS
EHK02	> -22.6	-25.1		ZnS > PbS
EHK02	-18.2		-21.8	ZnS > FeS_2
E14.3	> -24.4	-28.8		ZnS > PbS
E14.2-4	> -24.5	-29		ZnS > PbS
C6.14	> -29	-29.8		ZnS > PbS
MzH01	> -20.1	-20.1 to -20.7		ZnS ≥ PbS
MzH01	-18.7 - -13.3	-15.5		ZnS ≅ PbS
SF03	-15.6 - -14.6	-18.8 to -14.4		ZnS ≅ FeS_2
Tp01	> -23.1		-23.9	ZnS > FeS_2
Tp04	> -12.9		< -16	ZnS > FeS_2
Blb17	-21.5	-20.9		ZnS < PbS
Blb17	-24.4	-24.4		ZnS ≅ PbS

Bachinski (1969) suggested that at least three different minerals should be analyzed within a single sample in order to figure out if isotopic equilibrium has been established among theses phases. Analysis of three different sulfide minerals within the same

sample could only be carried out in sample EHK02, but within this sample the enormous variation in $\delta^{34}S$ values indicates isotopic disequilibrium. As pointed out in chapter 4.4.2 this is in accordance to the interpretation that mineralization occurred in different pulses.

According to Ohmoto & Rye (1979) isotopic equilibrium between two sulfur bearing compounds (in this case sphalerite and galena) can be written as follows (Equation 5.2).

$Zn^{34}S + Pb^{32}S \Leftrightarrow Zn^{32}S + Pb^{34}S$ *(Equation 5.2)*

In Equation 11.1 one exchangeable atom is present and the isotopic fractionation factor (α) between both compounds is related to the equilibrium constant (K) of the reaction (Equation 5.3).

$$\alpha_{(ZnS,PbS)} = \frac{(^{34}S/^{32}S)_{PbS}}{(^{34}S/^{32}S)_{ZnS}} = K \qquad \textit{(Equation 5.3)}$$

The fractionation of ^{34}S between two compounds can furthermore be related to α (Equation 5.4).

$$\delta^{34}S_{(PbS)} - \delta^{34}S_{(ZnS)} = \Delta^{34}S_{(PbS-ZnS)}$$
$$= 1000(\alpha - 1) * \left[1 + \frac{\delta^{34}S_{(ZnS)}}{1000}\right] \qquad \textit{(Equation 5.4)}$$
$$1000(\alpha - 1) \approx 1000 \ln \alpha$$

Equilibrium sulfur isotope fractionation is primarily a function of temperature (Ohmoto & Goldhaber, 1997) and thus differences in $\delta^{34}S$ values between two coexisting sulfides in isotopic equilibrium can be used to estimate the formation temperature. The necessary isotopic equilibrium constants are estimated from theoretical and experimental studies; they are approximately $1/T^2$ [K] (Ohmoto & Rye, 1979). Experimentally determined fractionation factors between sphalerite and galena vary from $0.63/T^2 * 10^6$ to $0.90/T^2 * 10^6$ what results in considerable uncertainties in the calculation of formation temperatures (Goldhaber & Rye, 1979, cum lit.). The temperature dependency between the fractionation factor and differences in $\delta^{34}S$ values of ZnS and PbS is shown in equation 5.5.

$$T[K] = \sqrt{\frac{A + 10^6}{\Delta^{34} S}}$$
$$A = 1000 \ln \alpha (ZnS - PbS) \qquad \textit{(Equation 5.5)}$$
$$\Delta^{34} S = \delta^{34} S_{ZnS} - \delta^{34} S_{PbS}$$

Ohmoto & Rye (1979) give a value of 0.85 ± 0.03 for A in order to calculate the equilibrium temperature, based on the fractionation of ^{34}S between sphalerite and galena. Using this value for calculation of formation temperatures of appropriate sphalerite-galena pairs ($\delta^{34}S$ PbS < $\delta^{34}S$ ZnS) gives temperatures ranging from approximately 120°C to 917°C for a value of 0.85 (Table 5.2). The effects of the uncertainty of A on temperature calculations are also shown in this table. Even using a lower fractionation value of A = 0.63 (Grootenboer & Schwarcz, 1969), clearly results in too high temperatures.

Table 5.2: Temperature calculation (Equation 11.4) based on the relation between $\Delta^{34}S_{(ZnS\ PbS)}$ values and the isotopic fractionation factor of 0.85±0.03 (Ohmoto & Rye, 1979).

sample	$\Delta^{34}S_{(ZnS\ PbS)}$ [‰]	T [°C] A = 0.85	T [°C] A = 0.82	T [°C] A = 0.88
EHK02	1.1	605.90	590.25	621.28
EHK02	2.5	309.95	299.56	320.15
E14.3	4.4	166.37	158.55	174.06
E14.2-4	5.5	119.97	112.97	126.85
C6.14	0.8	757.63	739.27	775.69
MzH01	0.6	917.09	895.90	937.91

For most samples, the calculated temperatures are far above the maximum formation temperatures known from carbonate hosted Pb-Zn deposits, which generally range between about 50 and 200°C (Leach et al., 2010, cum lit). Formation temperatures >200°C for Pb-Zn deposits in the Drau Range are furthermore unrealistic due to the geological context (e.g., lacking high-T alteration, maximum burial temperatures). Only the results of two samples from the Revier Erlach at Bleiberg (special ore horizon; E14.3 and E14.2-4) yielded temperatures of approximately 174 - 177 and 120 - 127 °C, respectively, which are within the possible formation temperature range of carbonate-hosted Pb-Zn deposits. For obtaining geologically meaningful temperatures with this approach the following requirements must be fulfilled Ohmoto & Rye (1979):

1. isotopic equilibrium between the two considered mineral phases,
2. no isotopic exchange between the two mineral phases, or between a mineral phase and a fluid after formation and
3. analyses of sulfur isotope composition on pure mineral phases.

The elevated temperature calculation indicates, together with the non-uniform fractionation sequence of $\delta^{34}S$ values in ZnS, PbS and FeS_2 in the complete sample set and the highly variable $\delta^{34}S$ values that the ore minerals formed mainly not in

isotopic equilibrium. Isotopic disequilibrium might have different reasons. One reason for isotopic disequilibrium might be the mixing of reduced sulfur derived from different sources. A further reason might be that the ore minerals within low temperature deposits do generally not form under isotopic equilibrium (Seal II, 2006).

5.3 Isochron Constructions & Age Calculations

In addition to the Rb-Sr data, which were obtained for this thesis, the Rb-Sr isotope data of sphalerites (and one pyrite) from the western Bleiberg mine, determined by J. Schneider (Appendix Table 18; partly published in Melcher et al., 2010) were considered for the calculation of isochron ages. For the constructions of the isochrons, the individual 2σ uncertainties of the $^{87}Rb/^{86}Sr$ and $^{87}Sr/^{86}Sr$ values were considered. The results of all Rb-Sr isotope analyses on sphalerite cannot be interpreted in terms of a single formation age since the data points do not fit to a common isochron. The isochron model assumes that the samples under consideration have experience a closed system evolution in terms of their Rb-Sr system starting from t = 0 which is generally inferred as the time of formation or pervasive recrystallization until present day. In addition, the Rb-Sr isotope system of the samples should have evolved from a reservoir with homogenous initial $^{87}Sr/^{86}Sr$.

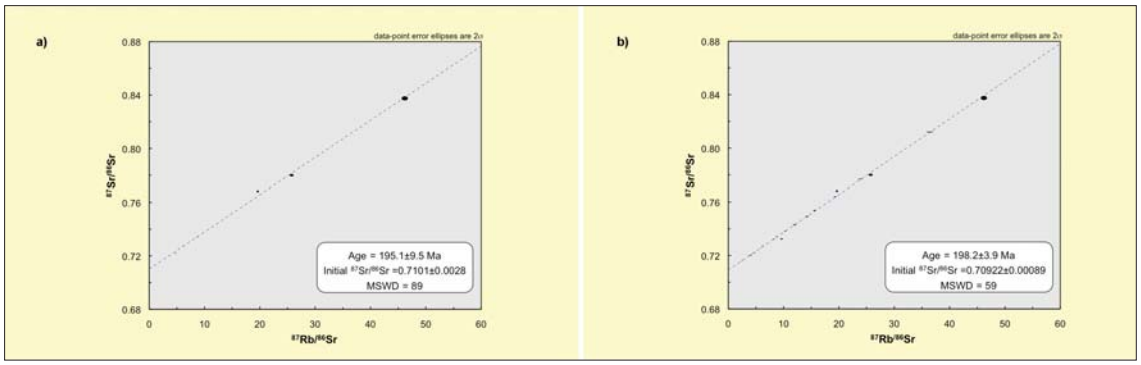

Figure 5.4: (a – b): a) a) Isochron plots from the Rb-Sr isotope data of sphalerite of this study (n = 7). This isochron includes data of sphalerite from different deposits and different ore horizons. b) Isochron calculation based on the Rb-Sr isotope data of all sphalerites (n = 23; own data + data of J. Schneider).

Construction of an isochron based only on the Rb-Sr isotope data of sphalerites obtained in the course of this study (n = 7) yields an age of 195.1±9.5 Ma (Figure 5.4 a). The very high mean square weighted deviation (MSWD) of the isotope ratios of 89, however, clearly indicates scatter of the data points off the isochron in large excess of the *a priori* (analytical) error. This age calculation is therefore geologically not very reliable. Adding the sphalerite Rb-Sr isotope data of J. Schneider (partly published in Melcher et al., 2010) to the dataset yields an isochron with a slightly higher and statistically better-defined age of 198.2±2.6 Ma (Figure 5.4 b). However, the high MSWD of 59 for this age calculation also clearly demonstrates that the data points define an errorchron without geological relevance rather than an isochron. However, reasonable isochrons with low MSWD which means without or with only a low degree of excess geological scatter, can be constructed when sorting the complete dataset into subsets (e.g. sample origin subsets):

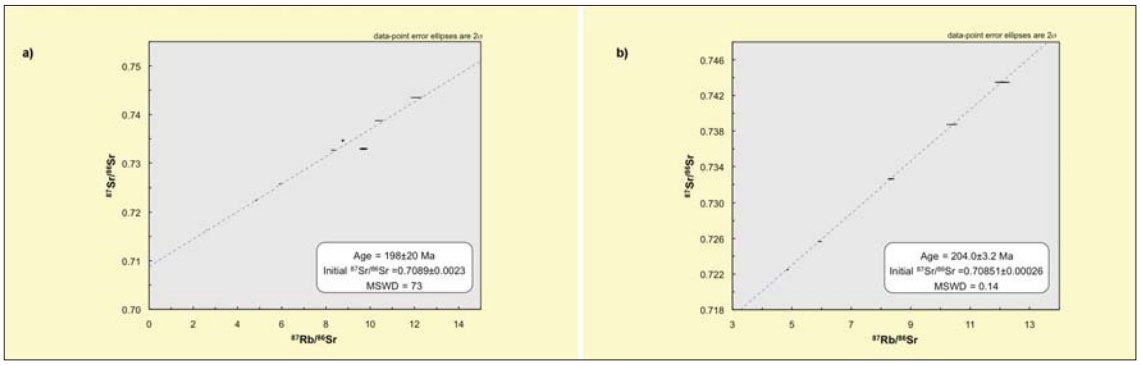

Figure 5.5: (a - b): Isochron calculations for Sphalerite separates from the crest horizon (Bleiberg). a) Isochron for the Rb-Sr isotope data of all crest sphalerites (n = 9). b) Age calculation based of Rb-Sr isotope data of five Sphalerite from the crest horizon excluding the outlier data points in figure 5.5 a).

- Isochron construction (Figure 5.5 a), which includes all sphalerite samples from the crest horizon at Bleiberg (Josefi-, Kalk- and Riedthardtscholle) results in an isochron age of 198 Ma with a high error of 20 Ma and a high MSWD 73. Exclusion of the outlier data points, evident within figure 5.5 a (Sphalerite from all three crest horizons: J10.4 ZnSxx, J10.1 ZnS hell, K2-2, R2-3), results in a well defined isochron (MSWD = 0.14) with an age of 204.0±3.2 Ma (Figure 5.5 b). The initial $^{87}Sr/^{86}Sr$ of 0.70851±0.00026 corresponds with the Sr isotope signature of Triassic seawater 200 Ma ago (Burke et al., 1982). This isochron age of 204±3.2 Ma may thus date formation of the crest sphalerite and based on statistical considerations appears as geologically reliable. However, the sphalerite outlier within figure 5.5 a have a very similar trace element chemistry and sulfur isotope composition as the crest sphalerite samples defining the isochron in figure 5.5 b.
- A further isochron was constructed based on the Rb-Sr isotope analyses of Revier Erlach (Ge-rich ore, special ore horizon, Bleiberg) sphalerites. The sphalerites from the Revier Erlach have been discussed earlier as a special case due to the heterogeneous distribution of Ge and Cd on the grain scale (secondary zonation of sphalerite crystals). The isochron obtained on seven Revier Erlach samples indicates an ore formation at 195.1±2.6 Ma (Figure 5.6). The MSWD of this isochron of 1.9 indicates a low and acceptable degree of geological scatter of the data points. However, the initial $^{87}Sr/^{86}Sr$ of 0.71051±0.00068 is considerably higher as compared to Triassic seawater (Burke et al., 1982). The zonation of the Revier Erlach sphalerites strongly indicates that an overprint of preexisting sphalerite grains occurred. The well-defined Rb-Sr isochron may thus be interpreted to date the overprint event. In this case, the elevated initial Sr isotope ratio indicates a new Sr isotope component of nonmarine origin introduced during the secondary overprint.

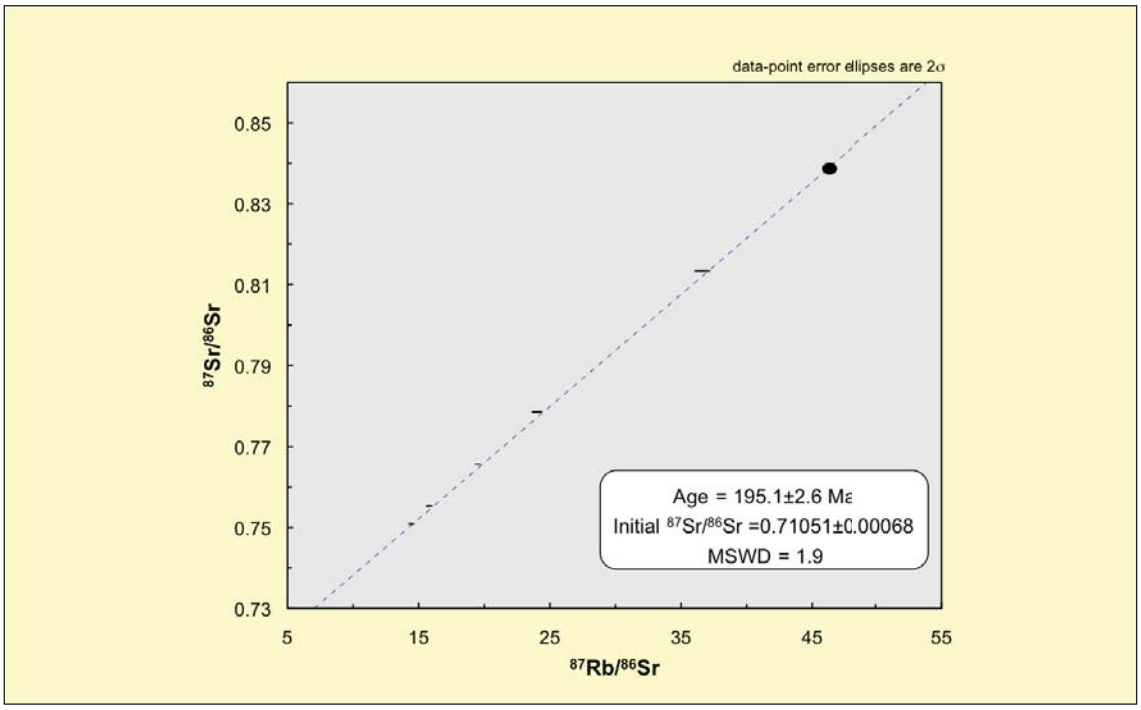

Figure 5.6: Isochron construction based on Rb-Sr measurements of Erlach sphalerites (n = 7).

- An earlier formation event at 225±2.2 Ma, which would correspond to a syngenetic ore formation, was suspected from a 3-point isochron of mineral separates from the 1st Raibl horizon at Bleiberg (Melcher et al., 2010). This calculation combines the results of two sphalerite and a single pyrite Rb-Sr analyses upon one isochron. One of the targets of this study was testing if this early mineralization event can be supported with further data in order to test if a multi-stage ore formation did occur. When adding the Rb-Sr data of sphalerite from a further 1st Raibl horizon samples for isochron construction the age is shifted towards 215 Ma (Figure 5.7 a). The uncertainty of this age calculation is with a value of 56 Ma very high and also the MSWD of 1245 indicates an enormous scatter. Due to the large scatter and the very high MSWD this age calculation is not reliable. When excluding the Rb-Sr analysis of the pyrite from the isochron construction, the variability of the isochron increases even more (204±150 Ma; Figure 5.7 b). It was not possible to support the early mineralization event suspected on the base of a 3-point isochron (Melcher et al., 2010) with further data. When adding an additional sphalerite data point the age calculation is characterized by an enormous scatter and is therefore no suitable to support an earlier ore formation. The 3-point isochron published in Melcher et al. (2010) is very precise and has also a low MSWD of 2.5. The low uncertainty and the low MSWD of this isochron might indicate that this age calculation is reliable but it is not known if the sphalerite and the pyrite considered for isochron construction, formed at the same time. Figures 5.7 a; b demonstrate that the calculations are shifted towards older ages when considering the pyrite Rb-Sr analysis for the isochron constructions.

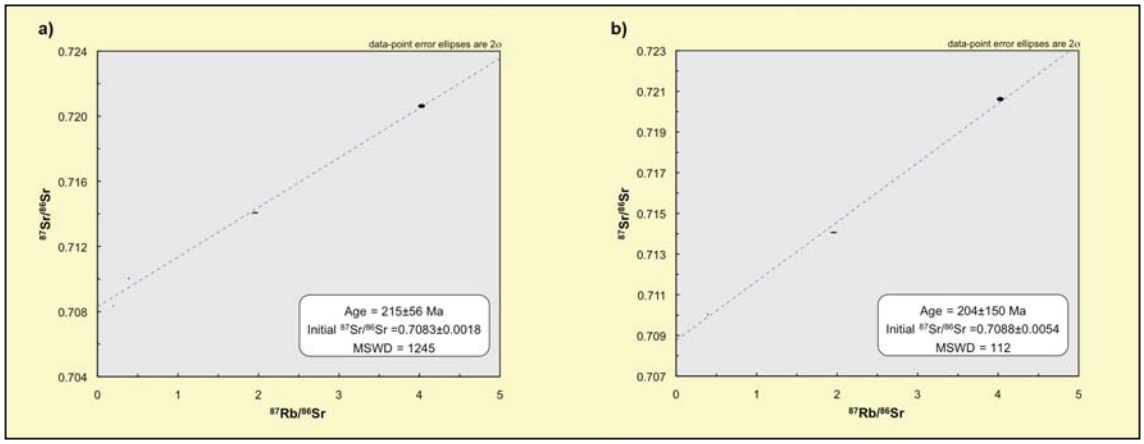

Figure 5.7 (a-b): Isochron constructions based on Rb-Sr analyses of ore minerals from the 1st Raibl horizon. a) Isochron including the Rb-Sr data of three sphalerites and one pyrite from the 1st Raibl horizon. The age calculation has an enormous uncertainty and MSWD. b) 3-point isochron (3 ZnS), which excludes the Rb-Sr measurement of pyrite. The uncertainty of this isochron is even larger.

Further isochron calculations of a differently subdivided datasets, e.g. according to sample origin (e.g. Mezica samples, or Erzkalk samples), or according to the chemical composition (Ge rich, Fe rich, Cd rich), or according to the sulfur isotope signature (> -15‰), give no reasonable results as indicated by high uncertainties in age and/or high MSWD values.

Further sphalerite samples are presently investigated for their Rb-Sr isotope composition. In addition, gangue minerals will be analyzed in order to check their influence as likely contaminants of the sphalerites with Sr isotope compositions not directly related to the pristine Sphalerite formation. The results of these analyses are still pending.

The incorporation mechanisms of Rb and Sr into the Sphalerite lattice are not understood yet (Pettke & Diamond, 1995). It is not evident if or how the Rb-Sr budget of sphalerite is affected by remobilization and recrystallization. As long as is not known, how these factors influence the Rb-Sr budget of sphalerite, the isotopic dating approach should be always considered with caution and thoroughly tested for its reliability. Methodical shortcomings as for instance the difficult and in part not successful removal of intergrowths of gangue minerals with Sr isotope compositions unrelated to sphalerite formation further complicate the dating approach. We assume that at least those sphalerites which show elevated Sr concentrations but low Rb/Sr and Sr isotope ratios are contaminated by carbonate intergrowths, which “survived” the mechanical and chemical pre-treatment. In order to review the reliability of the Rb-Sr data, Rb-Sr isotope analysis of co-genetic (sensu-stricto) carbonates or barites is very desirable. It would furthermore allow understanding if the ore formed under truly marine influence, since analyses of low-Rb minerals like carbonate and barite would enable the calculation of a well-defined initial $^{87}Sr/^{86}Sr$.

The discussion of the Rb-Sr data clearly shows that not one single isochron age can be obtained from the Rb-Sr isotope data. The crest isochron age of 204±3.2 Ma seems to be geologically reliable. But it should be kept in mind that the sphalerite separates, which were excluded from this isochron, are very similar in terms of chemistry and sulfur isotopes to those that considered for isochron calculation. The Revier Erlach isochron, which yields the youngest age of 195.1±2.6 Ma might also be realistic. However, this age calculation presumably dates the timing of remobilization and not necessarily the time of first ore formation at the Revier Erlach. The older age of 225±2.2 Ma based on an isochron of three samples from the likely syngenetic 1st Raibl horizon (Melcher et al., 2010) could not be supported by new data. However, only a part of the considered samples turned out to be appropriate for Rb-Sr dating. Especially the very fine-grained sphalerites, which most likely can be interpreted as “synsedimentary” (e.g. Topla mineralization), could not be separated from a secondary coarse-grained Sphalerite generation, which precludes a reliable Rb-Sr isotope determination. Based on the recent state of work three different formation ages might be indicated based on the Rb-Sr dating. The Rb-Sr dating implies that the main quantity of ore minerals formed at an epigenetic event at about 200 Ma. Furthermore a syngenetic ore formation at about 225 Ma might be suspected from a 3-point isochron, which includes different mineral phases from the 1st Raibl horizon. The youngest age of 195 Ma calculated from Revier Erlach sphalerites presumably dates a later secondary event.

5.4 Lead Isotopes

Coexisting sphalerite and galena in most samples from the Bleiberg district and from Mezica show very similar Pb isotope compositions (chapter 4.3.2; Figure 4.20). The Pb concentrations of the sphalerites as determined by isotope-dilution techniques are highly variable (150 to 61200 ppm). High to very high Pb values e.g. as found in sphalerites within sample EHK02, Mz08, E14.6, MzH01 (SB), and J10.4 (SB) are likely due to variable amounts of galena as nano-inclusions within the mineral. On the opposite, low Pb concentrations as found in sphalerite JK5-9, J10.4 (ZnS-xx), MzH01 (ZnS-xx) and C6.14 probably represent real lattice-bound Pb (chapter 5.1). Since, however, the PbS nano-inclusions have formed at the same time as the host sphalerite, it is very likely that sphalerite and PbS obtained Pb from identical source(s). Thus, it can be assumed that both would be characterized by a within-error identical initial Pb isotope composition. As stated in chapter 4.5 (Rb-Sr dating of sphalerite), the analyzed sphalerite separates may in addition be contaminated by unknown amounts of gangue. Based on Pb abundance and isotope ratio considerations, gangue contamination will not affect the Pb isotope signature of galena. Due to the similarity in the Pb isotope compositions of most coexisting galena and sphalerite, we further conclude that the influence of gangue contamination onto the Pb isotope signature of the sphalerite is mostly also negligible.

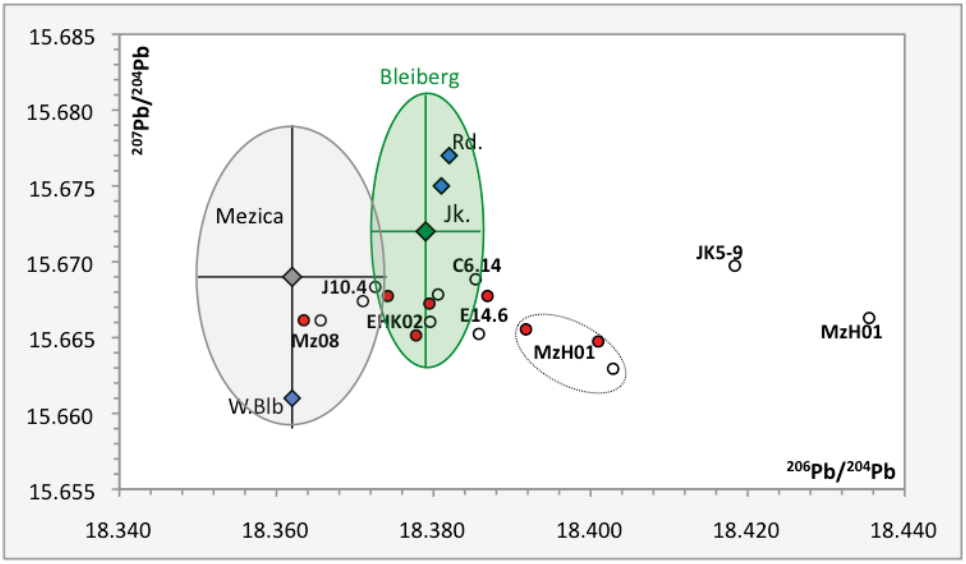

Figure 5.8: Comparison of our Pb isotope ratios ($^{207}Pb/^{204}Pb$ vs. $^{206}Pb/^{204}Pb$) of sphalerite (white circles) and galena (red circles) with previously published data (summarized in Schroll, 1997). Blue diamonds = previously published single data points (no errors given; Rd. = Radnig, Jk. = Jauken, W.Blb. = Windisch Bleiberg). The grey shaded area marks the Pb signature, which is published for Mezica (n = 4), the green shaded area indicates the published Bleiberg data (n = 22).

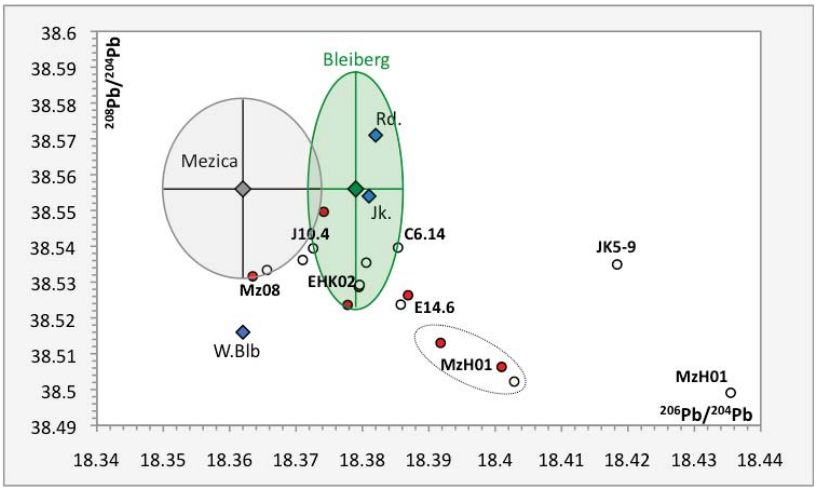

Figure 5.9: Comparison of previously published data (summarized in Schroll, 1997) with the data obtained in this study in a $^{208}Pb/^{204}Pb$ vs. $^{206}Pb/^{204}Pb$ diagram. The markers and abbreviations, which were used within this diagram, are equivalent to those in Figure 5.8.

Published Pb isotope data for the Bleiberg district on the one hand and for Mezica on the other overlap only to a small degree (Figure 5.8, Figure 5.9; summarized in Schroll, 1997). Compared to Bleiberg, data for Mezica indicate on average somewhat less radiogenic ^{206}Pb and ^{207}Pb isotope compositions. The Pb isotope data of this study only partly plot into the Pb isotope variation fields of the respective occurrences. While data points for galena and sphalerite of one Mezica sample (Mz08) fall into the range of Pb isotope fields of Mezica (Figure 5.8; 5.9), two galena separates and one sphalerite fraction of the second Mezica sample (MzH01) plot outside the fields and are considerably offset to more radiogenic $^{206}Pb/^{204}Pb$ compositions (Figure 5.8; 5.9). The second sphalerite separate of MzH01 is offset to even higher $^{206}Pb/^{204}Pb$ values. Pb isotope data for the Bleiberg samples E14.6, J10.4, EHK02 are largely consistent with previously published galena data from this deposit. They plot into the respective variation fields or close by (Figure 5.8; 5.9). The Jauken sphalerite (JK5-9) is characterized by more radiogenic ^{206}Pb and occupies an outlier position within the isotope plots with respect to the Bleiberg samples and also the published data for galena from Jauken (Figures 5.8 and 5.9). This might reflect the fact, that in this case Pb isotope data of different minerals are compared. Unfortunately, no galena from Jauken sample was available for analysis.

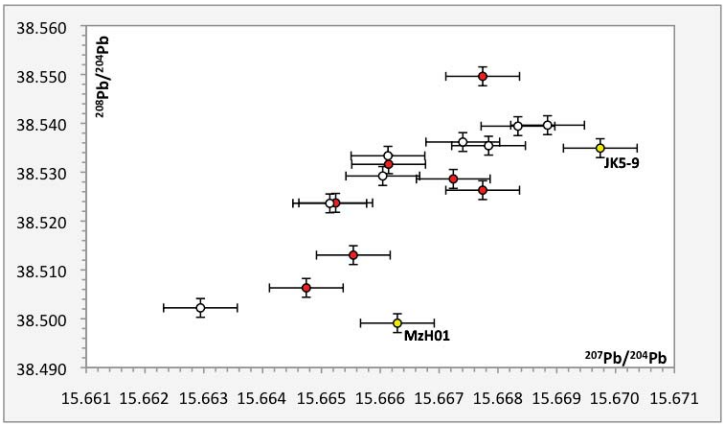

Figure 5.10: Results of Pb isotope measurements of sphalerite and galena within a $^{208}Pb/^{204}Pb$ vs. $^{207}Pb/^{204}Pb$ plot. The positions of sphalerite from samples JK5-9 and MzH01 (ZnS-xx) are highlighted (yellow circles). The other data are not labeled any more (sphalerite = white, galena = red).

In a $^{208}Pb/^{204}Pb$ vs. $^{207}Pb/^{204}Pb$ diagram (Figure 5.10), the data points of the present study indicate a general trend of increasing ^{208}Pb and ^{207}Pb. While the two galena and one sphalerite (PbS1, PbS2, SB-ZnS) data points of MzH01 are in line with this trend, the two other outliers (JK5-9, MzH01-ZnS-xx) in the $^{208}Pb/^{204}Pb$ vs. $^{206}Pb/^{204}Pb$ and $^{207}Pb/^{204}Pb$ vs. $^{206}Pb/^{204}Pb$ diagrams are again offset to somewhat more radiogenic ^{207}Pb. This effect is more evident for MzH01 as compared to JK-5. There is no indication for elevated ^{208}Pb in these sphalerites as compared to the other samples. Both outlier sphalerite samples have low Pb contents (MzH01 c. 400 ppm; JK5-9 c. 150 ppm). These low element contents suggest that the Pb is here bound in the sphalerite lattice. Various reasons can be discussed for the distinctly more radiogenic ^{206}Pb and ^{207}Pb isotope signatures of these two sphalerite samples:

- The metals were leached from a source with more radiogenic ^{206}Pb and ^{207}Pb isotope signature.
- The more radiogenic Pb isotope signature results from in-situ decay of U to Pb within the sphalerite itself.
- Contamination of the sphalerite separates by gangue minerals with more radiogenic ^{206}Pb and ^{207}Pb isotopic compositions.

Variations in the Pb isotope composition of the metal source(s) in excess to those indicated by the literature data are evident from the $^{208}Pb/^{204}Pb$ vs. $^{206}Pb/^{204}Pb$ and $^{207}Pb/^{204}Pb$ vs. $^{206}Pb/^{204}Pb$ diagrams (Figures 5.8 and 5.9). These are largely restricted to the ^{206}Pb and ^{207}Pb isotopes (U decay series). Systematic differences in the ^{208}Pb (Th decay series) are not evident. Especially the results for the two galena and one sphalerite fractions of MzH01 indicate a source component which contained a somewhat more radiogenic ^{206}Pb and ^{207}Pb composition compared to the other Mezica samples. In this respect, the even more radiogenic ^{206}Pb and ^{207}Pb compositions of the second sphalerite separate of MzH01 (ZnS-xx) may be a fingerprint of a source component that experienced a time-integrated gain of radiogenic ^{206}Pb and ^{207}Pb due to an elevated U/Th.

Only few literature data about U concentrations in sphalerite are available. Gulson (1984) reports that the U concentrations in sphalerites from the Broken Hill deposit (Australia) are generally < 1 ppm, except for one samples where a U content of 18.7 ppm was measured. We calculated the amounts of U that would be required in order to achieve the elevated radiogenic Pb isotope composition analyzed in the ZnS-xx from sample MzH01. For this calculation an age of ore formation of 200 Ma was assumed. In order to generate the offset from typical Mezica Pb isotope ratios to the analyzed $^{206}Pb/^{204}Pb$ by in-situ decay of U, 10 ppm U are required within the sphalerite lattice. ICP-MS measurements are required to test the hypothesis that both sphalerite outliers MzH01 and JK-5-9 contain elevated U abundances. The obvious difference in the Pb isotope ratios between MzH01 (ZnS-xx) and JK-5-9 and the other minerals separates obtained from this sample might as well be caused by a contamination by gangue minerals. The influence of carbonate contaminations on the Pb isotope composition of contaminated sphalerite may be envisaged by the present-day Pb isotope data of carbonates from the Wettersteinkalk (Köppel & Schroll, 1985, Schroll et al., 2006). In a $^{207}Pb/^{204}Pb$ vs. $^{206}Pb/^{204}Pb$ diagram (Fig. 5.12 a), the data points for Wettersteinkalk

samples are offset from the Bleiberg and Mezica Pb isotope variation fields to variable degrees to more radiogenic Pb compositions. So far, however, we have not analyzed gangue minerals for their Pb element concentration and isotope composition. At the present state of knowledge, the contamination hypothesis cannot be verified. Based on the very homogeneous Pb isotope compositions of the two galena fractions from MzH01, however, we do not consider the first hypothesis (different source component) likely. Instead, the second (elevated U content) or the third hypothesis (contamination by gangue) seems a likely explanation for the offset of the Pb isotope data of one sphalerite fraction of MzH01 to more radiogenic Pb isotope compositions. Identical considerations probably hold true for the offset of the Jauken sphalerite data point (JK5-9) to more radiogenic ^{206}Pb compositions (see above).

With the exception of the two sphalerites discussed above (MzH01, JK5-9), the Pb isotope compositions of galena and sphalerites of samples investigated in the course of this study show no systematic differences. There is no systematic variation in the Pb isotope ratios related to the origin of the samples, to their stratigraphic position, or to their chemical, sulfur or strontium isotopic compositions.

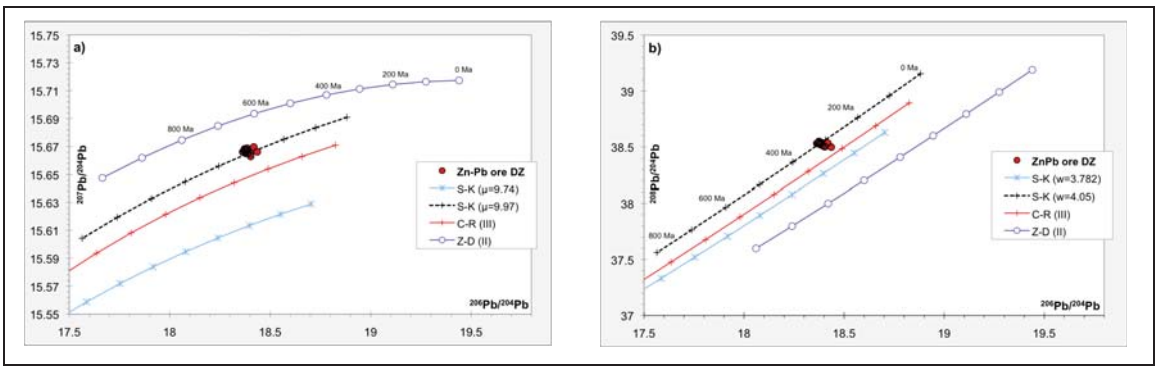

Figure 5.11 (a - b): Plots showing the Pb isotope data of the sphalerite and galena of this study together with the Pb evolution curves for the crust after Cumming & Richards (*C-R;* Model III; 1975), Stacey & Kramers (*S-K;* 1975) and Zartman & Doe (*Z-D;* Version II; 1981). a) ^{207}Pb/^{204}Pb vs. ^{206}Pb/^{204}Pb; b) ^{208}Pb/^{204}Pb vs. ^{206}Pb/^{204}Pb. The distance between the markers represents time periods of 100 Ma (0 Ma on the right). The samples investigated in the course of this study plot close to the evolution curves of Cumming & Richards (1975) and Zartman & Doe (1981).

Köppel & Schroll (1985, 1988) and Schroll et al. (2006) interpreted the Pb isotope data of samples from Zn-Pb mineralizations in the Drau Range in terms of an origin of the Pb from a Paleozoic crustal source. The Pb isotope data obtained in the course of this study largely confirm the results of the previous studies. Several publications have tried to model the Pb isotopic evolution of crustal reservoirs in time assuming different chemical and isotopic fractionation processes. In Figures 5.11 a; b, our Pb isotope data on sphalerite and galena are plotted in addition to Pb isotope evolution curves for crustal reservoirs calculated according to Cummings & Richard (1975), Stacey & Kramers (1975) and Zartman & Doe (1981; version II). Only those evolution lines are considered which run close to the Pb isotope data points of the Zn-Pb ores from the Drau Range. In the ^{206}Pb/^{204}Pb vs. ^{207}Pb/^{204}Pb diagram (Figure 5.11 a), the data points fall in between the Pb model evolution curves for upper crust according to Zartman &

Doe (1981, version II) and upper crust evolution curve based on Cumming & Richards (1975, model III). In the $^{208}Pb/^{204}Pb$ vs. $^{206}Pb/^{204}Pb$ diagram (Figure 5.11 b), the data points plot close to the crustal evolution lines according to Cumming & Richards (1975, model III) and Stacey and Kramers (1975). Interestingly, the Pb isotope data of this study in most cases closely match compositions calculated for late Paleozoic and younger model compositions. Only from the Zartman & Doe (1975) evolution line in the $^{207}Pb/^{204}Pb$ vs. $^{206}Pb/^{204}Pb$ diagram a somewhat higher age of c. 600 Ma is indicated. By a slight increase of the $^{238}U/^{204}Pb$ (“μ”) and $^{232}Th/^{204}Pb$ (“w”) values, the Stacey and Kramers (1975) growth curve was adjusted to run through the data points for galena and sphalerite from the Drau Range district. In this case, the model composition corresponds to an age of c. 300 Ma.

Köppel & Schroll (1985, 1988) and Schroll et al. (2006) identified various lithologies as the most likely sources of the ore lead based on the Pb isotope compositions of feldspars. The Pb isotope data of the respective feldspars which originate from underlying Gröden Sandstone, Werfen Formation, and a Permian Gneiss and from different Triassic magmatic rocks (unspecified) are plotted together with the data points for galena and sphalerites from the Mezica and Bleiberg districts in figures 5.12 a, b. Additionally, the Pb isotope data of various carbonate rocks, both ore free Wetterstein Formation carbonates (from the Dobratsch area) and ore bearing Wettersteinkalk and carbonates from the 1st Raibl horizon (Köppel & Schroll, 1985, 1988, Schroll et al. 2006) are shown. The Pb isotope data of all carbonate samples, however, are modified to various degrees by in-situ decay of U and Th since the time of the their formation. This cannot be corrected because the respective element abundances have not been determined. However, the least radiogenic Pb isotopic compositions for ore-free Wetterstein carbonates closely match the Pb isotopic compositions of galena and sphalerite from the Mezica and Bleiberg districts. This may indicate that the Pb of the Pb-Zn mineralizations can directly be related to the primary marine Pb signature of the Wetterstein Formation. However, comparison of the present-day Pb isotope data for the carbonate samples clearly shows that the ore bearing samples of the Wettersteinkalk and 1st Raibl horizon experienced different radiogenic Pb growths as compared to the ore-free Wetterstein Formation. The ore-free Wetterstein Formation samples follow well-defined linear trends of increasing $^{207}Pb/^{204}Pb$ but almost constant $^{208}Pb/^{204}Pb$ with increasing $^{206}Pb/^{204}Pb$. This is indicative of an isotope evolution in an environment with very high U/Th. The isotopic composition of ore-bearing carbonates especially from the 1st Raibl horizon, however, evolves towards high $^{208}Pb/^{204}Pb$ at almost constant $^{206}Pb/^{204}Pb$. This indicates that the chemical composition of the Wetterstein Formation was modified during ore formation to considerably higher Th/U. Since the data points of Bleiberg and Mezica ore samples (without radiogenic Pb increase) plot close to the least radiogenic Pb isotopic composition for the ore-free Wetterstein Formation, there is no indication for a foreign Pb isotopic component added to the Wetterstein Formation during Pb-Zn ore formation.

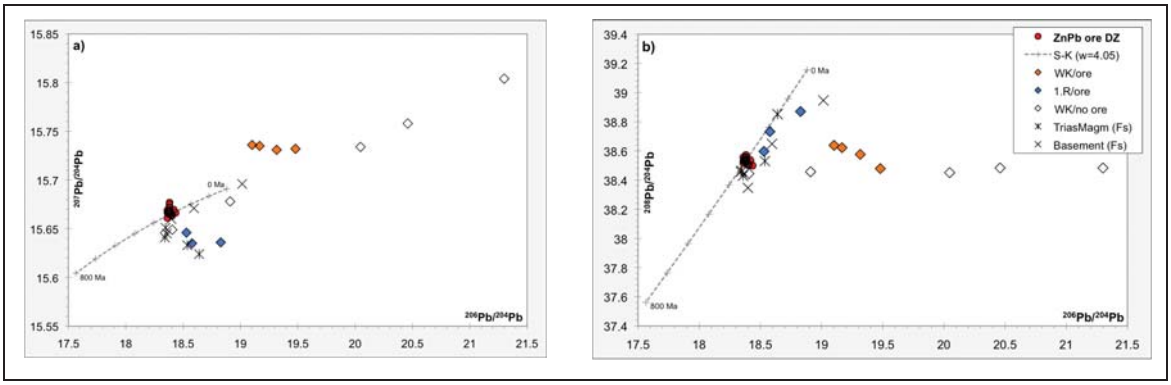

Figure 5.12 (a - b): Comparison of the Pb isotope data for the samples investigated in the course of this study (ZnPb ore DZ) to Pb isotope data from previous studies (Köppel & Schroll, 1985, 1988, Schroll et al. 2006). a) $^{207}Pb/^{204}Pb$ vs. $^{206}Pb/^{204}Pb$; b) $^{208}Pb/^{204}Pb$ vs. $^{206}Pb/^{204}Pb$. WK/ore = whole rock data of mineralized Wetterstein Formation carbonates (Bleiberg); 1.R/ore = whole rock Pb isotope data of ore bearing carbonates from the 1st Raibl horizon (Bleiberg). WK/no ore = whole rock Pb isotope data of not mineralized carbonates from the Wetterstein Formation (Dobratsch area). TriasMagm (Fs) = Pb isotope data for feldspars from Triassic magmatic rocks (unspecified); Basement (Fs) = Pb isotope data of feldspars from different underlying units. Additionally, a modified Pb evolution curve after Stacey & Kramer (1975) is displayed. The distances between the marker positions of this Pb evolution curve represent time periods of 100 Ma.

The role of individual crustal lithologies as sources for the ore Pb as suggested by Köppel & Schroll (1985, 1988) and Schroll et al. (2006) cannot be discussed in greater depth here. Most data points of feldspars from Triassic magmatic rocks and underlying metasediments plot very close to the data points of galena and sphalerites from the Mezica and Bleiberg districts. But they plot also very close to the least radiogenic Pb isotopic composition for the ore-free Wetterstein Formation. This may indicate that the Pb in the Wetterstein formation was largely derived from these Triassic magmatic and older metasedimentary lithologies. However, the role of source rocks with elevated $^{208}Pb/^{204}Pb$ (Permian gneiss) has to be reinvestigated since the Mezica and Bleiberg ore samples do not match the trend in Pb isotopic composition of ore-bearing carbonates from the 1st Raibl horizon towards high $^{208}Pb/^{204}Pb$. In conclusion, as stated earlier, our data for the ore samples strengthen the interpretation of Köppel & Schroll (1985, 1988) and Schroll et al. (2006) that the ore Pb may well originate indirectly from preexisting basement rocks. However, we find no evidence for a Pb component in the ore, which is isotopically significantly different from the Pb of the Wetterstein Formation. Instead, chemical fractionation processes, e.g., strong increase of Th relative to U, during ore formation may as well explain the trends in Pb isotopic composition of ore-bearing carbonate samples away from the respective data points for the Wetterstein Formation.

The interpretation of the Pb isotope signature of the Mezica and Bleiberg ore in terms of a crustal origin seems at first glance in contrast to the mostly marine Sr isotope signature of the sphalerites (Schroll et al., 2006; Melcher et al., 2010, own data). One should, however, bear in mind that the mean residence time for Sr in the oceans is high enough to enable effective isotopic mixing on a worldwide scale. The mean residence time for Pb is considerable smaller (Rollinson, 1996) and will not allow for a comparable mixing in the oceans. Instead, influences due to sedimentary influx of local sources for instance will dominate the Pb isotopic composition.

5.5 Small Scale Investigations – Systematic Relations?

In a selected set of samples the sphalerites (+co-existing sulfides) were investigated using different (high-resolution) investigation techniques. In the previous chapters were shown that strong variations in the trace element and the sulfur isotope signatures of sphalerites are present. The sulfur isotope variations were interpreted as input of reduced sulfur from two distinct sulfur reservoirs (BSR and TSR, chapter 5.2.1). This chapter aims to investigate if the different 'systems' are linked together in a uniform or somehow systematic way. Besides, based on the connection of textural with chemical and/or isotopic aspects, information on the ore forming processes can be drawn (e.g. physico-chemical conditions at depositional site, fluids involved into ore formation).

5.5.1 Interpretation of samples with strong $\delta^{34}S$ variations

In three samples from Bleiberg, small-scale $\delta^{34}S$ variations in co-existing sulfides were documented in detail (Blb17, EHK02 and R8/2, chapter 4.4.1 – 4.4.3). From textural relations a temporal sequence of sulfide and gangue mineralogy was established for theses samples. This helps to reconstruct the ore-forming processes based on the temporal variability of the sulfur isotope and chemical compositions.

Sample Blb17 (Bleiberg, Maxer Bänke)

Based on textural aspects a formation chronology of sphalerite was derived for sample Blb17. The distinct sphalerite stages show differences in textures, gangue mineralogy, trace element composition and sulfur isotope signature. The relation between textural, mineralogical, chemical and sulfur isotopic aspects is displayed in table 5.3.

Table 5.3: Textures, -chemistry and -sulfur isotope composition of sphalerite in Blb17 combined with mineralogical aspects. Listing according to the relative formation sequence established for this sample (chapter 4.4.1). The arrows indicate the trace element distribution of the sphalerite stages (↑ very high contents; ↗ intermediate high contents; ↓ low contents).

Blb17, Bleiberg Maxer Bänke					
time	**ZnS**	**texture**	**ore + gangue**	**$\delta^{34}S$**	**trace/minor elements**
old	SB	colloform schalenblende	fluorite, dolomite, quartz + galena	-26 to -16.2	↑Fe, Pb, As + ↗Tl, Ge ↓Cd
	II	fine-grained ZnS, partly enriched in II layers	fluorite, quartz, dolomite	~ -20	↗Fe, Pb, As, Ge ↓Cd
young	III	coarse-grained ZnS +fine-grained ZnS	quartz, fluorite	-14 to -1.5	↑Cd ↓Fe, Ge

The variations in the trace element composition of sphalerite are related to variations in the sulfur isotope signature and the gangue mineralogy (Table 5.3). The sulfur isotope variations that are present within this sample are interpreted as a change in the dominant sulfur reservoir because they occur rather suddenly and not gradually. Gradual changes in $\delta^{34}S$ could be interpreted as closed system sulfur isotope fractionations. In the lower part of the sample a dominant BSR reservoir caused the very negative $\delta^{34}S$ values (< -20‰) in the early-formed schalenblende and the ZnS II stage. It is assumed that the BSR sulfur was not generated at the deposital site, because no textural evidence for sulfate reducing bacteria (peloids) was observed. Therefore, transport of reduced sulfur from a BSR reservoir towards the depositional site is presumable. In the upper third of the sample a sudden shift in $\delta^{34}S$ (+ 6‰) indicates that a further reservoir (TSR) was able to contribute considerable amounts of reduced sulfur that mixed at depositional site with the BSR sulfur. The mixing of BSR and TSR sulfur led to deposition of sphalerite with intermediate $\delta^{34}S$ values (-14‰). In the last formed sphalerite layer a $\delta^{34}S$ value of -1.5‰ indicates that the TSR reservoir became dominant. The change in sulfur isotope composition in the upper third of the sample correlates with a change in trace element composition and gangue mineralogy (Table 5.3). The sphalerite grains in the upper part of the sample are rich in Cd and poor in Fe, when compared to the previously formed schalenblende and ZnS II grains. This obvious increase in Cd and decrease in Fe contents either was caused by fading input of Fe or increasing input of Cd. Fe might have competed with Cd for its incorporation into the sphalerite lattice (Sims et al., 1961). Besides, this correlation might indicate that the two sulfur-bearing fluids contained also some trace metals (i.e. Fe, Cd).

The base metals (Zn + Pb) must have been transported in an own fluid not together with reduced sulfur (BSR and TSR derived) because sphalerite ore occurs independenly from the dominant sulfur reservoir. Furthermore it is implausible that the base metals and the reduced sulfur were transported together, because the co-transport of reduced sulfur and base metals requires unrealistic acidic conditions (e.g. Anderson, 1975), which can be precluded, because dolomite is present as a gangue constituent. It is commonly assumed that the hydrothermal transport of the base metals occurs in chloride complexes (e.g. Leach et al., 2005). The solubility of the chloride-base metal complexes is primarly controlled by the activity of reduced sulfur within the hydrothermal fluid. Furthermore, the solubility of Pb and Zn within hydrothermal fluids is controlled by the pH and the salinity of the fluid (Leach et al., 2005). A fluid that has a low activiy of reduced sulfur has a greater potential to transport base metals (Leach et al., 2005), because a high activity of reduced sulfur would cause precipitation of sulfide minerals. It is therefore concluded that the base metals and the reduced sulfur were not transported in the same brine.

The gangue in the upper part of the sample is dolomite-free (Table 5.3, Figure 4.21). The solubility of dolomite decreases with increasing pH and increasing temperature (Rimstidt, 1997). The solubility of dolomite is furthermore controlled by the salinity and the CO_2 content of the fluid (increase in salinity or CO_2 result in increasing solubility).

Also the solubility of fluorite increases with temperature and with an increase in the salinity but decreases with increasing pH (Rimstidt, 1997). The quartz solubility in a hydrothermal brine is controlled by its salinity (Rimstidt, 1997). Nearly no changes in the solubility of quartz occur at a pH <8 and also cooling at constant pH and a temperature below 200°C will not dramatically affect the solubility of quartz (Rimstidt, 1997). Hence, the solubility/precipitation of the gangue minerals results from a complex interaction of parameters like salinity, pH and temperature at the depositional site what is not yet fully understood. Fading (or missing) input of reduced sulfur from a BSR fluid might have caused changes in the physico-chemical conditions at depositional site what is now evident as differences in the gangue mineralogy.

Based on the combination of textural, chemical and isotopic aspects following mineralization scenario is assumed for sample Blb17:

1. Formation of the schalenblende: caused by a sudden oversaturation of the metal-bearing brine with respect to Zn (Roedder, 1968). A very effective way to generate a sudden Zn oversaturation at depositional site is mixing of a metal bearing brine with a sulfur transporting fluid (very negative $\delta^{34}S$ of <-20‰ indicate a BSR reservoir).
2. The subsequent formation of crystalline sphalerite (ZnS II) in descrete layers indicates that either the amount of metal, or the amount of reduced sulfur that was transported to depositional site decreased, because the formation of crystalline sphalerite indicates a lower degree of metal saturation (Roedder, 1968). However, during formation of ZnS II the BSR reservoir was still dominant ($\delta^{34}S$ about -20‰).
3. The formation of ZnS III correlates with the influx of TSR derived sulfur (sudden change in $\delta^{34}S$, Table 5.3). It is furthermore connected to a major change in the gangue paragenesis and the trace element composition of the sphalerite. The obvious change in the gangue paragenesis indicates a sudden change in the physico-chemical conditions at the depositional site. This change in the physico-chemical conditions can be related to the influx of the TSR sulfur carrying fluid.
4. The $\delta^{34}S$ value of -1.5‰ measured in the last very fine-grained sphalerite layer implies that input of BSR derived sulfur ceased.

Sample EHK02 (Bleiberg, Erzkalk)

The relative formation sequence of the sphalerite stages in sample EHK02 and their relation to the gangue mineralogy, chemical and sulfur isotopic composition is summarized in table 5.4. The different paragenetic sphalerite stages in EHK02 are partly characterized by changes in the gangue assemblage. Additionally, a relation between between the four paragenetic sphalerite stages and the trace element composition and the $\delta^{34}S$ values is evident (Table 5.4).

Table 5.4: Textures, chemical and sulfur isotopic composition of sphalerite in sample EHK02 combined with mineralogical aspects. Listing of the sphalerite stages according to the formation chronology established for this sample (chapter 4.2.2, trace element signatures are indicated with arrows like as described for table 5.3).

EHK02, Bleiberg Erzkalk					
time	**ZnS**	**texture**	**ore + gangue**	**$\delta^{34}S$**	**trace/minor elements**
old	I	coarse-grained ZnS accumulations	barite, calcite	-6.6	↑Cd ↓Fe
	II	coarse-grained ZnS accumulations	barite, secondary dolomite, anhedral galena	-7.7 to -4.6	↑Cd ↓Fe, Ge
	SB	colloform schalenblende	fluorite, barite, euhedral galena	-22.6	↑Fe, Pb + ↗As, Tl, Ge ↓Cd
young	IV	anhedral and fine-grained ZnS	fluorite, dolomite, pyrite	-18.6	↗Fe, Pb; ↑Ge ↓Cd

Both early-formed sphalerite stages (ZnS I & ZnS II, $\delta^{34}S > -6$) are Cd rich/Fe poor and very low in other trace elements (Table 5.4). ZnS I and ZnS II are hosted by a barite-dominated gangue. Furthermore, minor amounts of calcite are intergrown with these sphalerites. The formation of isotopically light schalenblende in EHK02 is preceded by the first appearance of fluorite as a further gangue constituent. Fluorite precipitation started just before the schalenblende precipitation. The schalenblende is rich in Fe, Pb and As. Besides it contains with EMP detectable Ge and Tl and is poor in Cd, compared to the earlier ZnS I and ZnS II stages. The latest ZnS IV stage is associated with pyrite and hosted by a gangue consisting of fluorite and calcite. ZnS IV has a $\delta^{34}S$ value of -18.6. The ZnS IV stage contains lower Fe, Pb and As concentrations than the schalenblende but is compared to the early ZnS I and ZnS II stages, enriched in Fe. The ZnS IV stage contains the highest Ge contents and is poor in Cd.

The changes in texture, trace element and, sulfur isotope composition and gangue mineralogy are abrupt and occur over very small distances (e.g. the change from coarse-grained ZnS to schalenblende occurs within about 1 cm, Figure 4.27). These abrupt changes can be explained with episodic mineralization phases and supply of reduced sulfur from two distinct reservoirs. It is presumable that a TSR (= heavy sulfur isotopes) and a BSR (= light sulfur isotopes) provided reduced sulfur for ore precipitation. The variations in $\delta^{34}S$ values are related to changes in the trace element composition (Table 5.4).

One sulfur isotope measurement of a coarse-grained barite aggregate in the lower part of the sample yielded a $\delta^{34}S$ of +17‰. This is in the range of Triassic seawater (Kampschulte & Strauss, 2004) and makes a seawater-origin of the sulfate very presumable. Direct sulfate reduction at the depositional site would explain the close interfingering between barite and sulfides in the lower part of sample EHK02. Reaction of a hot (> 100°C) metal bearing brine with sulfate of marine provenance (evaporites like gypsum, SO_4-bearing pore water), would cause thermochemical reduction of the sulfate species and provide reduced sulfur (H_2S), which is necessary for base metal precipitation. It is likely that the Ba for barite precipitation was transported together with the base metals towards the depositional site, because the solubility of Ba in seawater is low (Wilkinson et al., 2005). Alternatively, sulfate could have been generated at the depositional site via oxidation of a sulfide species. Anaerobic oxidation of a reduced sulfur species due to bacterial disproportionation is another possible mechanism that could explain the observed close inter-fingering of sulfates and sulfides (Böttcher and Thamdrup, 2001). Disproportionation of a reduced sulfur species to sulfate is generally an endogen process, but might energetically be favorable, if the simultaneously produced H_2S is removed from the system, which can be achieved by precipitation of base metal sulfides (Böttcher & Thamdrup, 2001). The isotope fractionation obtained through disproportional sulfur oxidation depends on base metals involved, but no data for Pb and Zn are available. However, this process is highly unlikely for EHK02, because of the very large fractionation (> 20‰) documented for this sample (Machel et al. 1995). Hence, Triassic seawater sulfate available at the depositional site is assumed as the dominant sulfur source. This assumption is in accordance with previous authors (e.g. Schroll & Rantisch, 2005, Kuhlemann et al. 2001), who also suggest Triassic seawater sulfate as a major sulfur source. The difference in $\delta^{34}S$ between barite (+17‰) and early sulfides (around -6‰) is 23‰. Such a high fractionation of ^{34}S is uncommon for TSR (Machel et al. 1995) but could be obtained if the temperature of the metal carrying fluid was low (i.e. close to 100°C).

In comparison to the ZnS I and ZnS II stages, the later-formed schalenblende stage is very different in textures, trace element composition and $\delta^{34}S$. It presumably precipitated from a rather cool (< 100°C) and Zn supersaturated fluid (Roedder, 1968). The very negative $\delta^{34}S$ of the schalenblende is indicative for a BSR sulfur reservoir. Precipitation of the schalenblende (+ coexisting galena) was most presumably due to mixing of a BSR sulfur-rich fluid with the metal bearing brine. The corresponding change in the gangue paragenesis, which is marked by the appearance of fluorite, also indicates that a further fluid became involved in the mineralization process. Fluorite precipitation can be initiated by lowering the salinity of a fluid (Rimstidt, 1997). An effective way to lower the salinity of a fluid is mixing with another fluid. Hence, the crystallization of fluorite together with the sudden decrease in $\delta^{34}S$ values are also indicative for influx of a BSR fluid, which mixed with the metal bearing brine.

Prior to the formation of the latest ZnS IV stage pyrite formed. Precipitation of pyrite indicates that the sulfur fugacity at the depositional site increased (Sims et al., 1961, Barton & Toulmin, 1966, Bethke & Barton, 1971). The increase in the sulfur fugacity

allows crystallization of FeS_2 and consequently lowers the Fe concentration of the co-precipitating sphalerite. The gangue of this ZnS IV-pyrite assemblage consists of fluorite and calcite without any barite what is interpreted as changing redox conditions. Calcite is present as gangue constituent in the complete sample. Thus, Ca was permanently present and reduced sulfur and base metals were not transported within the same fluid, because simultaneous transport of metals and reduced sulfur requires acidic conditions (Anderson, 1975, Leach et al., 2005).

Pb isotope ratios ($^{206}Pb/^{204}Pb$, $^{207}Pb/^{204}Pb$ and $^{2078}Pb/^{204}Pb$) of both galena generations and ZnS II and the schalenblende (SB) stage revealed a nearly homogenous Pb isotope composition (Figure 4.20). This indicates that the base metal source did not undergo a significant modification during the mineralization process. It is therefore assumed that the variations in the trace element composition are rather due to variations in the physico-chemical conditions at depositional site and not due to input of trace metals from variable sources.

A presumable scenario of the mineralization events in sample EHK02 is:

1. Availability of a sulfate bearing fluid (of seawater origin) within cavities in the carbonate host rocks. Alternatively, pre-existing sulfate minerals (e.g. gypsum from evaporites) were present within or nearby the cavity.
2. Influx of a hot reduced Pb, Zn and Ba bearing brine into this cavity. Mixing of the metal rich brine with the sulfate caused TSR of the seawater sulfate. Repeated changes in redox conditions were caused by an episodic input of the metal rich brine and led to the alternating formation of barite and sulfides.
3. Sudden influx of BSR derived sulfur (+ possibly Fe). The influx of this BSR sulfur fluid lowers the salinity of the metal bearing fluid, what initiates fluorite precipitation. Besides, input of further reduced sulfur caused a sudden oversaturation of the metal bearing brine with respect to Zn and results in the formation of schalenblende.
4. The latest ZnS IV stage was preceded by a rise in the sulfur fugacity causing the formation of pyrite. The absence of barite indicates furthermore that the redox conditions changed towards a permanently reducing conditions, which presumably was caused by increased input of reduced (BSR) sulfur.

Sample R8/2 (Bleiberg, Crest Horizon)

For sample R8/2 two texturally, chemically and sulfur isotopically distinct sphalerite types were described (chapter 4.4.3). A summary on textures, trace element composition and $\delta^{34}S$ is presented in table 5.5.

Table 5.5: Textures, chemical and sulfur isotopic composition of sphalerite in sample R8/2. Listing of the sphalerite stages according to the formation chronology established for this sample (chapter 4.4.3, trace element signatures are indicated with arrows like as described for table 5.3).

R8/2, Bleiberg Crest Horizon				
time	**ZnS**	**texture**	**trace elements**	**$\delta^{34}S$**
old	SB	schalenblende clasts	↑Cd, Pb ↗Fe, As	< -24‰
young	ZnS II	crystalline sphalerite grains/aggregates	↑Cd, ↗Pb ↓Fe, As	-7 to -3.8‰

The schalenblende clasts are partly cemented by the crystalline sphalerite. Thus, the schalenblende did form prior to the crystalline sphalerite. In contrast to the previously discussed samples (Blb17, EHK02), the schalenblende components did not form necessarily in-situ at the depositional site. The schalenblende occurs in fragmented components and that formed at another place. Thus, in this sample the simultaneous availbility of two different fluids (one transporting TSR and another transporting BSR sulfur) is not necessary. Both sphalerite types in this sample exhibit a clearly different sulfur isotope signature ($\delta^{34}S$ of <-24‰ and > -7‰; Table 5.5). Recrystallization does not result in isotope fractionation (Boyce et al., 1983, Anderson et al., 1989, Blakeman et al., 2002). Hence, it is implausible that the crystalline sphalerite in sample R8/2 formed due to remobilization and recrystallizaton of the schalenblende. Therefore, the sphalerite types present in this sample formed from two distict sulfur reservoirs: *1.)* BSR reservoir, which was involved in the formation of the schalenblende (now present as clasts, $\delta^{34}S$ of < -20‰) and *2.)* TSR reservoir that was involved in the precipitation of the crystalline ZnS ($\delta^{34}S$ of > -7‰).

Interestingly, the schalenblende components contain more Cd than Fe (chapter 4.4.3), what is the opposing trend to the trace element composition of the schalenblende aggregates in the samples Blb17 and EHK02. The EMP measurements of the schalenblende clasts indicated furthermore increased Pb and As contents. The sphalerite grains are also Cd rich. The Fe concentrations of the sphalerite grains are even lower than that of the schalenblende. The high Cd content of the schalenblende in this sample contradicts the trend of BSR-sulfur and Fe enrichment indicated from the two previously discussed samples (Blb17, EHK02).

Calcite and barite are associated with the sulfur isotopic heavier sphalerite and form the cement of the schalenblende clasts in sample R8/2. As for sample EHK02 it is argued that the gangue and ore minerals formed by interaction of a metal bearing brine and a TSR sulfur fluid. The timing and exact formation process of the schalenblende clasts is unclear, mostly because the geological context of this sample is unknown. Brecciation could be the product of gravitational cavity collapse with fragmentation of earlier precipitated schalenblende (e.g. on the cavity walls), or hydrothermal breccition due to fluid over-pressure, or due to exogenic sedimentary processes. In either case the angularity of the clasts indicates that the schalenblende was formed at or very close to the depositional site.

In summary, it is concluded that even on the hand specimen scale more than one mineralization event is recorded at Bleiberg. The sulfur isotope and chemical data show that the paragenetic late sphaelrite stages in all three samples did not simply form by local remobilization of earlier sphalerite. Variations can only be explained if different fluids / reservoirs did contribute to ore formation.

5.5.2 Interpretation of samples with little $\delta^{34}S$ variation

The other 15 samples that were studied using the same multi-technical approach (chapter 4.4) show only little variation in $\delta^{34}S$. In order to reduce the extent of this thesis, the data and interpretations of these samples are summarized.

Germanium rich samples

Sphalerite from Revier Erlach (E14.2-4, E14.3, Bleiberg) and the Jauken deposit (JK5-9) is regularly enriched in Ge (> 0.1 mass%). In the Erlach samples the sphalerites are often higher in Ge than in Cd. The Jauken sphalerites contain nearly always more Ge than Cd. The Fe contents of these Ge rich sphalerites are intermediate (between > 0.2 to < 1 mass). High Ge contents are sometimes related to a zonation of sphalerite grains (irregular distribution of Ge and Cd) visible in BSE images (chapter 4.2.3). This zonation is not a primary growth zonation but results from a later hydrothermal overprint. However, high Ge contents are not always linked to a zonation of sphalerite (e.g. in the case of Jauken no zonation was observed).

Sphalerite from Revier Erlach is characterized by a light sulfur isotopic composition (< -20‰). In contrast, $\delta^{34}S$ values of Jauken sphalerite are much higher (-1.6 and +1.8 ‰). These values are the heaviest sulfur isotope signatures analyzed in the Drau Range sulfides. Hence, no relation between Ge concentration and sulfur isotope composition is evident. It is therefore assumed that reduced sulfur and Ge originate not from the same source (Henjes-Kunst *et al.*, 2012). Possibly, the source rock, from which the metals for the mineralization have been leached have a controlling factor for Ge enrichment (Henjes-Kunst et al., 2012). Sicree & Barnes (1996) discussed the role of organic compounds in the leaching of metals and as complexing ligands for trace elements in the metal-carrying fluids. They state that the trace element variations of

sphalerite from a certain distric/depost are rather controlled by the presence of organic compounds that are present in the metal-bearing brine. They state that trace element variations in sphalerite from a certain district/deposit are rather caused by the presence of organic ligands, which favor the formation of organic complexes, than to differences in the metal sources. It is not evident how far organic compounds control Ge distribution within sphalerite from the Drau Range. Based on mineralogical aspects no enrichment of organic matter (i.e. organic compounds, or dark-colored carbonate host rocks) was observed in the Ge rich samples.

The variations in Ge concentrations might furthermore reflect the evolution of the metal bearing fluid, from which already some ore was precipitated. Some grains evidence a sector zonation. It is assumed that this zonation formed due to a secondary overprint of already existing Cd rich sphalerite. It might indicate that Ge incorporation in the ZnS structure is less favorable compared to other trace metals (e.g. Cd, Fe). Hence, Ge rich sphalerites might represent a younger ore stage, which formed from a residual fluid. Höll et al. (2007) already stated that Ge tends to be enriched in late hydrothermal fluids. The isochron that was constructed from the Rb-Sr measurements of Revier Erlach sphalerite supports the idea that Ge rich sphalerites in the Drau Range formed at a late stage, because an age of 195.1±2.6 Ma was calculated based on the data.

A further question concerns the source of Ge. According to Höll et al. (2007), Ge is not so scarce, but rarely enriched (Clarke value = approximately 1.6 ppm). Ge^{4+} occurs in many silicate minerals where it substitutes for Si^{4+} (Höll et al., 2007). Germanium can be enriched in coals and lignites from certain deposits, because it forms relative stable organo-complexes (e.g., lignin and humic acid, Höll et al., 2007). The carbonate host rocks of Pb-Zn ores can be excluded as Ge source, because of the very low Ge contents in carbonates (Höll et al., 2007). Seawater also is not a possible source for Ge, because it contains only low Ge contents (Höll et al., 2007). Thermal waters can clearly contain higher Ge contents and the solubility of Ge increases with increasing temperature (Melcher et al., 2006 cum lit). Increased Ge contents of sphalerite might reflect the fluid pathways, since the fluid will become enriched in Ge, if it had passed through organic-rich (and thus also Ge pre-enriched) sedimentary rocks (Bernstein, 1985).

Möller (1985, 1987) and Möller et al. (1983) estimated the leaching temperature of the metals from the basement. This approach is based on the similar geochemical behavior of Ge and Ga with Si and Al respectively. A high Ga/Ge correlates with a high leaching temperature. The Ga/Ge of sphalerite from the Drau Range is < 1 due to the very low Ga contents. Hence, a very low leaching temperature must be assumed. Möller et al. (1983) assumed that the Ga/Ge ratio of a sphalerite represents the last equilibrium of the ore forming fluid with the silicate country rocks. However, the applicability of the Ga-Ge thermometer is questionable. It is based on the assumption that during sphalerite precipitation only an insignificant fractionation of Ga and Ge occurs (Möller & Dulski, 1993), which is yet proven. Melcher et al. (2006) state that the Ge content of a hydrothermal fluid will rather increase with increasing temperature.

This contradicts the low metal-leaching temperature, which Möller (1983) derived from the low Ga/Ge ratios (=increased Ge contents). It seems more reasonable that Ge was leached during the fluid-country rock interaction along the fluid pathway.

The Ge rich Jauken sample occupies an outlier position within the Pb-Pb plots and is characterized by a slightly more radiogenic Pb component (chapter 5.4). However, Ge poor sphalerites from a Mezica sample occupy a similar outlier position like as the Ge rich ones from Jauken. Furthermore, the Pb isotope signatures of the sphalerite from Revier Erlach are very similar to the isotopic composition of rather Ge poor ones from the Bleiberg deposit. Therefore, no difference in the crustal source between Ge rich and Ge poor sphalerite was determined by the use of Pb isotope analyses.

Schalenblende samples

$\delta^{34}S$ measurements of schalenblende were carried out on various samples from Bleiberg (E14.2-4, R8/2, Blb17, EHK02, J10.4, C6.14) and on one sample from Mezica (SF03). Schalenblende in all these samples is characterized by a generally light sulfur isotope composition. They are furthermore similar regarding their very high trace element contents. This becomes obvious, when the element contents of schalenblende and coexisting crystalline sphalerite are compared (e.g. J10.4, Blb17, EHK02, see chapter 4.4.1 – 4.4.3). Schalenblende is mostly very rich in Fe, but some exceptions were observed. The spherical schalenblende (schalenblende oncoids) in sample J10.4 (Bleiberg, Crest Horizon, chapter 4.4.3) clearly contain more Cd than Fe. Schalenblende clasts in the breccia sample R8/2 (Crest Horizon Bleiberg, chapter 4.4.3, 5.5.1) is also higher in Cd than in Fe. Also in the schalenblende accumulation in sample SF03 (Mezica, Graben; chapter 4.4.6) the Cd contents exceed the Fe concentrations. Thus, no uniform trend can be deduced for the trace element contents of schalenblende.

For all analyzed schalenblende samples a BSR sulfur reservoir is indicated by the strongly negative $\delta^{34}S$ values. A BSR reservoir would be in agreement with the proposed precipitation from a cool fluid (e.g. Roedder, 1968). There is no uniform correlation trend between sulfur isotope composition and Fe and Cd contents of schalenblende in the Drau Range samples. This is unlike to the Irish Pb-Zn district in which a correlation between high Cd contents and positive $\delta^{34}S$ values and high Fe and very negative $\delta^{34}S$ was determined (Gagnevin et al., 2011). The schalenblende in sample J10.4 has nearly the most negative $\delta^{34}S$ composition but is very rich in Cd (chapter 4.4.3). A common source of BSR sulfur + Fe and TSR sulfur + Cd, as suggested from the preferred fractionation of Fe in the sulfur isotopic light schalenblende and Cd in the heavier coexisting crystalline sphalerite (as evident in samples Blb17, EHK02, chapters 4.4.1; 4.4.2; 5.5.1), is thus not always apparent.

To explain small-scale variations in sulfur isotope composition of schalenblende from the Irish Lisheen mine Barrie et al. (2009) attributed schalenblende formation to

interaction of two fluids carrying sulfur from two different reservoirs. Similarly, isotope variations of schalenblende in sample Blb17 can be explained ($\delta^{34}S$ ranging between -26 and -16.2 ‰, chapter 4.4.1). However, schalenblende layers in sample J10.4 (chapter 4.4.3) have nearly identical sulfur isotope compositions (-28.4 to -.26.6‰). Hence, formation of schalenblende requires not necessarily more than one sulfur reservoir.

Remobilization

In sample C6.14 (Bleiberg, 1st Raibl horizon) three texturally different sphalerite types are present (blue CL; schalenblende relicts; fine-grained crystalline sphalerite, chapter 4.4.5). No significant differences in the $\delta^{34}S$ values were found between the schalenblende and the fine-grained sphalerite. The sulfur isotope composition of the blue luminescent sphalerite could not be measured, due to its close intergrowth with the fine-grained sphalerite and insignificant spatial resolution of the sulfur isotope measurements. Although no significant differences in the $\delta^{34}S$ values are present, some systematic variations in the trace element contents are obvious: in the blue luminescent sphalerites only Cd and Fe could be analyzed with EMP. The blue luminescent sphalerite clearly contains more Cd than Fe. The schalenblende relicts are characterized by high Fe concentrations and low Cd contents. The fine-grained sphalerite occupies an intermediate position regarding its trace element contents (chapter 4.4.5). Based on the information obtained from trace element and sulfur isotope analyses in combination with textural aspects, it seems probable that the fine-grained Sphalerite formed due to local remobilization of the schalenblende fragments and the blue luminescent sphalerites. The mixture of both endmember chemical compositions (*1.* blue CL = high Cd/low Fe and *2.* schalenblende = low Cd/high Fe) led to the intermediated trace element composition of the fine-grained sphalerite. Remobilization does not cause fractionation of sulfur isotopes (Boyce et al., 1983, Anderson et al., 1989, Blakeman et al., 2002) but does affect the trace element distribution (Kuhlemann & Zeeh, 1995). Our findings confirm those of Kuhlemann & Zeeh (1995) who also found out that remobilized sphalerite is characterized by intermediate trace element contents.

Ore mineralization from a closed system sulfur reservoir

In sample MzH01 (Mezica, Helena district) four sphalerite “types” (ZnS I, II, III, IV) can be distinguished (chapter 4.4.6). They formed in a chronological sequence, i.e. ZnSI is the oldest, ZnSIV the youngest sphalerite. The trace element contents show a steady decrease from ZnS I to ZnS III (Table 5.6; Figure 4.48). The $\delta^{34}S$ signatures increase steadily from ZnS I (-20 ‰) to ZnS III (-13‰; Figure 4.46). These negative $\delta^{34}S$ values indicate that the sulfides derived their sulfur from a BSR reservoir. The increase in $\delta^{34}S$ with time indicates that the sulfides formed from a closed BSR reservoir (i.e. no input of fresh sulfate). In a closed reservoir the bacteria are forced to metabolize also the heavier sulfur isotope (^{34}S), which causes steadily increasing $\delta^{34}S$ values (Machel et al., 1995). In sample MzH01 increasing $\delta^{34}S$ values are related to decreasing trace

element contents. Already Herlec et al. (2010) explained the variability in $\delta^{34}S$ of sulfides from Mezica with closed-system fractionation of BSR derived sulfur.

Table 5.6: Trace element composition of ZnS I to IV in sample MzH01. The number in brackets denotes the calculated mean concentrations.

	ZnS I	ZnS II	ZnS III	ZnS IV
Fe	n = 12	n = 6	n = 4	n = 3
	0.02 – 0.46 (0.19)	0.01 – 0.17 (0.05)	0.02 – 0.07 (0.04)	0.02 – 0.06 (0.04)
Cd	n = 12	n = 8	n = 4	n = 4
	0.43 – 1.33 (0.93)	0.51 – 0.96 (0.74)	0.18 – 0.73 (0.47)	0.3 – 0.73 (0.51)
Pb	n = 12	n = 6	n = 4	n = 4
	0.03 – 0.82 (0.17)	0.02 – 0-18 (0.09)	0.07 – 0.13 (0.1)	0.06 – 0.17 (0.11)
As	n = 10	n = 3	n = 1	n= 4
	0.03 – 0.28 (0.1)	0.04	0.02	0.02 – 0.03 (0.026)

Cathodoluminscence

Sphaleriten displays cathodoluminescence in the visible light range behavior in all ore horizons. Most frequently a blue CL color was observed, but also sphalerites of greenish or orange (brownish) CL color are present. Crystalline sphalerite more often displayed CL reaction than schalenblende. However, also some schalenblende are CL active. Very low Fe contents (< 0.2 mass%) are the single common feature of all luminescent sphalerite. This observation is in agreement with the CL quenching effect of Fe (Miller, 1989). Based on the EMP data the reasons for the different CL colors of sphalerite, e.g. like seen in sample Mz08 from Moring horizon (Mezica, chapter 4.4.6; Figure 4.50), could not be determined unequivocally. The formation sequence of different luminescent sphalerites (from orange to dark blue and then to light blue) in this sample can be best explained by a restricted trace element reservoir. The trace elements contents of Cd, Fe and Cu steadily decrease from the orange luminescent sphalerites to the light blue luminescent ones (Figure 4.51). A similar CL behavior was already described by Kuhlemann & Zeeh (1995) for a sample from Mezica. According to these authors the orange luminescent sphalerites is richer in Cu and both varieties of blue luminescent sphalerite are depleted in all trace elements. This statement must be modified, because the dark blue luminescent sphalerite in this study is higher in Cu than the orange one. Moreover, Kuhlemann & Zeeh (1995) suggested that Ag acts as activator for blue and Cu for orange and green luminescence colors. Also, the possibility of self-activation of relative pure ZnS has been discussed. The EMP data obtained in this study is too inaccurate to determine if (or which) small trace elements cause the specific CL colors of sphalerite. Nevertheless CL is a useful technique to discriminate different types of sphalerite. In order to determine the reasons for different CL colors another more precise techniques for trace element analysis (e.g. LA ICP-MS) or quantitative CL spectroscopy would be desirable.

In-situ mineralization within the BSR reservoir

Sulfur isotope analyses of sphalerite and Fe-sulfides were carried out in two samples from Topla (Tp01, Tp04; chapter 4.4.7). Sphalerite peloids in the samples are

interpreted as direct in-situ mineralization by bacteria, because they often contain fossil bacteria filaments (e.g. Kucha et al., 2010 and personal communication). Such fossil bacteria resemble recent sulfate-reducing bacteria that most commonly occur in low-temperature environments (Machel et al., 1995), but are also described in higher temperature (> 100°C) environments (Jørgensen et al., 1992). Sulfate-reducing bacteria occur in a wide variety of environments (e.g. hydrosphere, sea floor, unconsolidated sediments, in pores and cavities down to several hundreds of meters below the surface) and are thus not restricted to surface or near-surface environments (Kucha et al., 2010, cum lit.). Subsurface aquifers have e.g. a high microbe density (Kucha et al., 2010).

Due to their small size sulfur isotope measurements of single sphalerite peloids were not possible. However, analysis of microareas containing peloids in sample Tp01 yielded $\delta^{34}S$ values < -20‰ (Figure 4.54, which is in accordance with BSR. Sphalerites in sample Tp04 display less negative $\delta^{34}S$ values of -10 to -13‰ (Figure 4.57). The spatial association of both samples on the deposit scale is not known, because the samples were collected on the dumps close to the former mine entrance. Hence an interpretation of the sulfur isotope data with respect to their spatial relation is not possible. The trace element chemistry of sphalerite within both samples is very similar; both are very poor in trace elements. The sulfur isotope signature of associated marcasite confirm the $\delta^{34}S$ values in each sample. Drovenik et al. (1980) reported $\delta^{34}S$ values between -24 and +8‰ for sulfides from the Topla deposit and already emphasized the dominance of isotopically light sulfides. In analogy with Bleiberg, the light sulfur isotope signature of the sulfides in combination with textural evidence for fossil sulfate reducing bacteria (e.g. Kucha et al., 2005, 2010) suggests that Zn-(Pb) mineralization at Topla occurred partly in-situ, i.e. within the BSR reservoir itself. The variation in $\delta^{34}S$ of the otherwise texturally and chemically similar sphalerite samples was possibly caused by restricted input of fresh sulfate (i.e. closed system mineralization). Spangenberg & Herlec (2006) interpreted these fine-grained (partly globular) ore minerals as the earliest formation stage, which formed in a shallow depth during the Anisian – Ladinian. The negative sulfur isotope signature is in accordance with the carbon isotope signature, which is indicative of the presence of cyanobacteria living symbiotically with sulfate reducing bacteria (Spangenberg & Herlec, 2006).

In both samples sphalerite is intimately associate with marcasite and the two minerals formed coevally (see chapter 4.4.7). The precipitation of marcasite from a Zn-enriched ore fluid requires a high sulfur fugacity (Barton & Toulmin, 1966). Marcasite may form from a relatively cool (<150°C) and acidic fluid, which contains high amounts of elemental sulfur and/or thiosulfates and polysulfides (Deer et al., 1992). According to Schoonen & Barnes (1991) the formation of marcasite and pyrite from a fluid below temperatures of 300°C requires FeS as precursor. This FeS species reacts progressively to mackinawite, hexagonal pyrrhotite/greigite before forming pyrite or marcasite (Schoonen & Barnes, 1991). The rate of reaction is extremely fast (within minutes) when elemental sulfur and/or intermediate sulfur compounds are available (Schoonen & Barnes, 1991). Kucha & Stumpfl (1992) confirmed the presence of

intermediate sulfur compounds in pyrite from Bleiberg supporting stepwise BSR of sulfate to sulfide. The in Topla samples frequently occurring peloids are interpreted as evidence for direct sulfate reduction by bacteria. BSR processes are often associated with stepwise sulfate reduction (Machel et al., 1995). Hence, it is assumed that the transformation of a FeS-species into marcasite was possible, because intermediate sulfur compounds were present.

The ore textures within the Topla samples are very different from those observed in the samples from other deposits investigated in the course of this study where peloids were not identified (although for Bleiberg peloids are described; e.g. Kucha et al., 2010).

Findings from the multi-technical approach

The multi-analytical approach, i.e. combining in-situ (small-scale) information obtained from sulfur isotopes, Pb isotopes, mineral chemical and textural investigations, provides important information on the ore forming processes. Combination of these techniques demonstrates that the Pb-Zn mineralization in the Drau Range is highly heterogeneous regarding textures, chemical composition of sphalerite and sulfur isotope composition of sulfides, but rather homogenous with repsect to the Pb isotope signature. No simple relation of textures and geochemistry and/or sulfur isotope composition is evident within the studied samples. The main information obtained from this study is:

1. Sphalerite textures are not controlled by sphalerite chemistry. For examble schalenblende is indeed often Fe rich but not always Fe rich. The formation of certain textures is primarily controlled by physico-chemical conditions (temperature, pH, degree of metal saturation) at the depositional site.
2. $\delta^{34}S$ variations result from at least two different sulfur reservoirs and not solely from closed-system fractionation. More than 50% of the analyzed sulfides are isotopically light ($\delta^{34}S$ < -20‰) and less than 10% show $\delta^{34}S$ values > -5‰. Hence, a dominant BSR reservoir is presumed. The second source could have been TSR sulfur. Clear variations in $\delta^{34}S$ occur already on a small scale (< 1cm).
3. The formation of sulfur isotopically distinct sphalerite (sulfide) was not restricted to certain time periods. The formation sulfur isotopically light sphalerite is followed by the formation of heavier ones, and vice verse (see chapters 4.4.1 to 4.4.3; 5.2.1). Both reservoirs provided reduced sulfur (simultaneously) during the mineralization.
4. There is no clear relation between $\delta^{34}S$ of the sulfides and host rock stratigraphy.
5. Within three samples small-scale $\delta^{34}S$ variations are related to chemical and textural changes, but textural/chemical variations are not always expressed in sulfur isotope variations.
6. No simple relationship between trace element contents and sulfur isotope signature (e.g. Fe, Ge, Cd) of sphalerite is present. Thus, reduced sulfur and metals did not originate from the same reservoir and were not transported by the same fluid.
7. The variable trace element contents of the sphalerites are not related to variable Pb isotope signatures.
8. Sulfur and Pb isotope compositions are not correlated. Contrary to the sulfur isotope reservoir, the Pb reservoir (base metal reservoir) was well homogenized.
9. The presence of mineralized peloids in the Topla samples provides evidence for direct in-situ mineralization within the BSR reservoir.

5.6 Genesis of carbonate-hosted Pb-Zn deposits

This study deals with the debate on the genesis of carbonate-hosted Pb-Zn deposits in the Alps. In order to explain why this genetic controversy exists since more than 150 years some background information is given on: *1.)* general aspects of carbonate-hosted Pb-Zn deposits and *2.)* Alpine Type Pb-Zn deposits (*APT*) in comparison with other carbonate-hosted Pb-Zn deposits. Then, a summary about previously proposed genetic models for Pb-Zn deposits in the Drau Range is followed by a discussion of these models in the light of the new data of this thesis.

5.6.1 Carbonate-hosted Pb-Zn deposits

Carbonate-hosted Pb-Zn deposits contain a substantial proportion of the world's Pb-Zn reserves. This class of deposits is often collectively referred to as Mississippi Valley Type (MVT) deposits (e.g. Anderson & Macqueen, 1982, Leach & Sangster, 1993, Leach et al., 2010), although the term MVT originally only referred to the large carbonate-hosted Pb-Zn districts in the Paleozoic Midcontinent Basin of the USA. Thus, today the term MVT generally implies a genetic model, which is not necessarily applicable to other carbonate-hosted Pb-Zn deposits all over the world.

Misra (2000) summarizes carbonate-hosted Pb-Zn deposits as low temperature Pb-Zn ± barite ± fluorite mineralizations. Formation temperatures range from 50 to 200°C. Carbonate-hosted Pb-Zn deposits show a great diversity in features and possibly also in origin. However, they share also some characteristic features, which set them apart from other Pb-Zn deposits in sedimentary environments (e.g. sediment-hosted massive sulfide deposits) as summarized as follows (Misra, 2000):

- commonly host rocks are carbonate rocks (often dolostones);
- strata-bound mineralization, some ore-bodies may be stratiform, but the majority is discordant (i.e. podiform, breccia ore bodies, cavity/karst fillings);
- simple ore-gangue paragenesis, which consists of low-Fe sphalerite, low-Ag galena, fluorite, barite, dolomite, calcite (± quartz and chert);
- mineralization is mostly epigenetic and formed at moderate tempartures (mostly 100 – 150°C) due to precipitation from moderately saline fluids (15 to 30 wt% NaCl equivalent) and
- no genetic relation to igneous rocks.

Several Pb-Zn deposits, which share some common features (e.g. host strata, mineralogy, geochemistry, S- and Pb isotopic composition), form up to several hundred km^2 large ore districts (Leach & Sangster, 1993). The average ore grades of a single deposit amounts to approximately 3 to 10% of combined Pb + Zn (Misra, 2000). Typical byproducts, which are won during the processing of the Pb and Zn ores are Cd, Ge, In, Ag, barite and fluorite (Misra, 2000).

Mostly the ore gangue paragenesis in carbonate-hosted Pb-Zn deposits is rather coarse grained and massive, but also disseminated ore minerals can be present (Leach & Sangster, 1993). The typical coarse-grained mineral assemblage indicates a slow precipitation process with slow crystal growth rates (Leach & Sangster, 1993). However, very fine-grained sphalerite, which forms botryoidal (colloform) aggregates (schalenblende) is also a common sphalerite texture in several Pb-Zn deposits (Misra, 2000). Such botryoidal textures are commonly interpreted as products of rapid precipitation from a highly saturated fluid (e.g. Roedder, 1968). A further characteristic ore texture of carbonate-hosted Pb-Zn deposits are ore-bearing breccia components, which might be cemented by ore minerals. To explain such ore textures a two stage mineralization process is required (Misra, 2000).

Some aspects on the genesis of carbonate-hosted Pb-Zn deposits are still controversially discussed (e.g. Leach & Sangster, 1993, Misra 2000, Leach et al., 2003, 2010, Schroll, 2008). Fluid inclusion studies indicate that the ore-gangue paragenesis is precipitated from approximately 80 – 220°C hot and moderately saline (> 15 mass% NaCl equivalent) brines. Higher temperatures are for example reported from the Irish deposits but large uncertainties exist about the temperatures of ore formation for many other deposits, among others for those in the Drau Range. Other debates concern the relative and absolute age of the mineralization, the sources of metals and reduced sulfur, the sources and evolution of the involved fluid, fluid pathways and driving mechanisms for fluid flow, mixing of fluids, ore precipitation mechanisms and many more (see Anderson, 1975, 2008, Leach & Sangster, 1993, Misra 2000, Leach et al., 2003, 2010, Schroll, 2008). Because of this controversy some authors proposed genetic subgroups (e.g. the Alpine -, Irish -, Appalachian subgroup) of carbonate-hosted Pb-Zn deposits in order to highlite regional and eventually genetic differences among individual Pb-Zn districts. Since this thesis deals with Pb-Zn deposits in the Eastern Alps the special characteristics of these deposits, referred to as Alpin Type (APT, Houtermans, 1946) are described in more detail and compared to the ‘classical MVT’ and to the ‘Irish’ subgroups.

5.6.2 Alpin Type Pb-Zn deposits

Textural features have been one reason for the differentiation of the APT subgroup. At Bleiberg, which is the type locality for the APT deposits, exhibits “sedimentary” ore textures were described from several ore horizons (especially for the Erzkalk horizon). Such sedimentary ore textures are e.g. graded bedding of fine-grained ore minerals, which are arranged in layers concordant to the bedding of the host rocks. Schulz (1968, 1985, 2006) assumed that such textures result from exhalative precipitation and external sedimentation of ore minerals on the sea floor and thus repeatedly proposed a model of syngenetic (synsedimentary) ore formation. However, the external ore formation, as proposed by Schulz (1968, 1985, 2006) is not the unique possibility to explain these “sedimentary textures”. As an alternative some authors (e.g. Siegl, 1957, Bechstädt, 1975, Zeeh & Bechstädt, 1994) suggested precipitation of finely bedded ores within karst cavities (“internal sediments”).

Cerny (1989, cum lit.) emphasized that the ore minerals from the Alpine Pb-Zn deposits are poor in Ni, Cu, Co and Ag. Ore assemblages in other Pb-Zn districts are in contrast often enriched in these elements.

A further distinct feature of the APT deposits is the sulfur isotope composition of the ore minerals. Sulfides in the APT deposits are dominated by a very light sulfur isotope composition ($\delta^{34}S < -20‰$) and only few sulfides have positive $\delta^{34}S$ values (Drovenik et al., 1980, Schroll et al., 1983, Kuhlemann et al., 2001, Spangenberg et al., 2001, Schroll & Rantitsch, 2005, Herlec et al., 2010, Kucha et al., 2010). In contrast, sulfides from the classical MVT provinces in northern America are characterized by positive $\delta^{34}S$ values (Misra, 2000, cum lit.). The sulfur isotope signature of the APT deposits is very similar to the Irish Pb-Zn district (IRT), which are also characterized by a predominance of very light sulfur isotopes (Fallick et al., 2001, Wilkinson et al., 2005).

Pb isotope measurements of ore minerals gave an additional reason for definition of the APT group (Stanton & Russel, 1959, cum lit., Köppel & Schroll, 1988, Schroll et al., 2006). The Pb isotope composition of galena from the APT deposits is different from that of the classical MVT deposits. In the APT deposits the Pb isotope composition of the ore minerals yields ages which are older than the stratigraphic age of the host rocks (Stanton & Russel, 1959, cum lit., Köppel & Schroll 1988, Schroll et al., 2006). This older model age is referred to as “Bleiberg type” (*B-type*) Pb isotope composition. The Pb isotope signature of galena correlates with that of feldspar from basement units, from which the Pb for the mineralization was leached (Schroll, 2008, cum lit.) In contrast, ore lead from many other MVT deposits shows “Joplin-type” (*J-type*) Pb isotope signature. The J-Type signature yields a younger model age of the ore minerals when compared to the age of the host rocks (Köppel & Schroll, 1988). Moreover, also the Irish Pb-Zn district differs in its Pb isotope signature from the MVT deposits (Schroll, 2008, cum lit.). The Irish Pb-Zn district shows a N-type (“Normal”) Pb isotope signature with a Pb model age of galena, which is identical to the age of the host rocks (Schroll, 2008, cum lit.). The Pb isotope composition of deposits in the Irish Pb-Zn district is very heterogeneous and directly corresponds to the respective geological framework of the different deposits (LeHuray et al., 1987).

A comparison of some distinguishing aspects of the APT deposits to other subgroups (IRT, MVT) shows that each type has its special characteristics (Table 5.7). However, for several authors (e.g. Zeeh & Bechstädt, 1994, Leach et al., 2003) this has been no reason for separating the APT deposits from the other carbonate-hosted Pb-Zn deposits.

Table 5.7: Comparison of some characteristic aspects of APT (Alpine Type), IRT (Irish Type) and MVT (Mississippi Valley Type) Pb-Zn deposits. Furthermore the different genetic models, which have been proposed for each subgroup are named (see text for further explanations).

	APT	IRT	MVT
Element association	Zn-Pb-(Ba-F-Ag-Cu) Schroll, 2008	Zn-Pb-Ag-Cu-Ba Schroll, 2008	Zn-Pb-Ba-(Ag-Cu) Schroll, 2008
Sulfur isotopes $\delta^{34}S$	**-30 to 0 ‰** dominant BSR reservoir (+TSR) Schroll, 2008, this study	**-44 to +10‰** dominant BSR reservoir (+TSR) Fallick et al., 1992; Wilkinson et al., 2005	**0 to + 20‰** dominant TSR reservoir Leach et al., 2005
Pb isotopes	**B-type** = older than host rocks homogeneous Köppel & Schroll, 1985; 1988, Schroll et al., 2006, this study	**N-type** = contemporaneous to rocks heterogeneous LeHuray et al., 1987, Fallick et al., 1992	**J-type** = younger than host rocks homogenoues Leach et al., 2005
Fluid driving mechanism	convective vs. gravity driven fluid circulation Zeeh et al., 1994, this study	small **convection** cells Hitzmann et al., 2002, Fallick et al., 1992	**gravity driven** fluid circulation Leach et al., 2005; Bethke & Marshak, 1990
Genetic models	syngenetic vs. epigenetic (external sediments vs. karst fillings) Schulz, 1968; Bechstädt, 1975	**contemporaneous** (subseafloor mineralization) Fallick et al., 1992, Hitzmann et al., 2002	**epigenetic** (mineralization in karst cavities) Leach et al., 2005

The various genetic models proposed for the APT, MVT and IRT deposits are summarized in table 5.7. For the Irish Pb-Zn it is commonly accepted that the ore mineralization occurred in a sub-seafloor environment and was finished in a time period of 10 Ma after deposition of the host rocks (Hitzmann et al., 2002). Fluid circulation and metal transport within the IRT district was driven by small convection cells, which caused the heterogeneous Pb isotope signature (LeHuray et al., 1987).

For the MVT deposits in northern America an epigenetic ore formation model is widely accepted (e.g. Leach et al., 2005). Fluid flow and metal transport in the MVT districts was triggered by topographic differences that caused gravity-driven fluid flow from an evolving orogenic front to a foreland basin (Bethke & Marshak, 1990). Pb-Zn mineralization is much younger (> 100 million years) than the carbonate host rocks.

5.6.3 Previous genetic models for carbonate hosted Pb-Zn deposits in the Drau Range

The genesis of the Pb-Zn mineralization within the Drau Range has been controversially discussed for decades. A compilation of the genetic ideas for the ore mineralization within the Drau Range (Eastern Alps), which were proposed during the last two centuries, is presented in table 5.8. Until today two contrasting genetic models - syngenetic vs. epigenetic ones – are debated.

Table 5.8: Development of the genetic ideas for the Pb-Zn mineralization in Bleiberg during the past two centuries (after Schroll, 2008).

Age/Model	Supporters
Mineralization has same age as the host rocks	Mohs (1807); Fuchs (1846); Lipold (1863); Peters (1856); Suess (1869)
Epigenetic	Cotta (1863); Potiorek (1863); Posepny (1873; 1894; 1895); Hupfeld (1897)
Syngenetic + later remobilization	Brunlechner (1899)
Cenozoic	Granigg & Koritschoner (1914)
Oligocene/Miocene	Tornquist (1927)
Sarmat	Holler (1953)
Syngenetic + later remobilization	Hegemann (1949); Taupitz (1953); Schneider (1953); Schulz (1954); Maucher & Schneider (1957); Brigo et al. (1977)
Jurassic – Cretaceous	Zeeh et al. (1994)
Upper Norian – Lower Liassic	Kuhlemann (1995)
Jurassic	Leach et al. (2003)
Same age as host rocks (= synchronous)	Schroll (1996); Schroll (2006)

Syngenesis

Geological features such as the stratabound to stratiform nature of the ores (e.g. the lateral extension of ores within the Erzkalk horizon at Bleiberg) were interpreted to reflect syngenetic ore deposition coeval with sediment deposition in the Upper Triassic (Carnian, about 220 Ma). In this context funnel-like textures were interpreted as a depositional feature; i.e. loading of the heavy ore minerals onto the non-consolidated sea floor. Discordant mineralization that is also present in the Erzkalk horizon was explained with synsedimentary tectonics, which caused the formation of fractures on the sea floor and deposition of ore within these fractures (Schulz, 1968).

The dominantly light sulfur isotopic composition of the sulfides, which is indicative for a low temperature BSR sulfur was thought to be inconsistent with epigenetic mineralization during deep burial of the host rocks (Schroll & Wedepohl, 1972, Cerny,

1989). Besides, supporters of the syngenetic ore mineralization emphasized the differences in the trace element chemistry of the sphalerites and in the Pb isotope composition of the galena, to the classical carbonate hosted Pb-Zn deposits within the Mississippi Valley district (Misra, 2000, cum lit.). These differences were used to support the syngenetic formation model.

In order to overcome the need of an exhalative synsedimentary metal input that could not be proven but is required following the Model of Schulz (e.g. 1968), Schroll (1996) and Schroll et al. (2006) suggested the term synchronous in order to describe the timing of ore formation (Table 5.8). This term does not necessarily imply external (sedimentary exhalative?) ore deposition, but implies ore precipitation within the unconsolidated sediment but close to the sediment/seawater surface. This model is similar to that proposed for the Irish deposits by Hitzman et al. (2002). According to this model, the ore formation was finished before onset of deep burial and late diagenesis. This “synchronous” model would be in accordance with the frequent occurrence of sulfides with very light sulfur isotope composition.

Epigenesis

Several authors favored an epigenetic MVT mineralization model for the Drau Range and proposed that ore mineralization occurred not before 200 Ma and subsequent to the deposition of the host rock lithologies (e.g. Kuhlemann, 1995, Zeeh et al., 1998, Leach et al., 2003). Supporters of the epigenetic model propose that carbonate-hosted Pb-Zn deposits all over the world cannot be identical regarding their ore geochemistry or Pb isotope signature, because these features are caused by complex interactions between ore forming fluids and wall rocks (e.g. Leach et al., 2003); hence, these authors classify all these deposits as carbonate-hosted MVT deposits. Furthermore, an external ore accumulation is questioned by some authors, since stratiform ore could have also formed in an already existing karst environment (e.g. Bechstädt, 1975, Leach et al., 2003).

Kuhlemann (1995) favored an epigenetic ore formation that occurred during the intermediate to deep burial of the host rocks (Upper Norian to Lower Jurassic). His epigenetic model is based on the paragenetic sequence of chemically and texturally different sphalerite generations (Table 5.9). The base metals were leached by highly saline formation waters from the Triassic carbonate host rocks , Permo-Triassic clastic units and from the Paleozoic basement and transported as chloride complexes. Fluid ascent was initiated by the opening of the Tethys ocean and occurred along large-scale fault systems. Mixing of the metal bearing brine with a fluid containing reduced sulfur caused ore precipitation. The mixing of the two fluids was most effective in geological units characterized by a high porosity (e.g. the Erzkalk). The ore formation started at the southern margin of the Northern Karawanken mountain range. The first ore minerals were trace element poor sphalerites and Fe-Tl-As-Ge-rich schalenblende (Table 5.9). The brine for this early schalenblende generation obtained its (trace) metal content from the Ladinian platform carbonates itself. Galena formation started only

after the first three stages of sphalerite were precipitated. Ore precipitation occurred preferentially close to sealing strata (e.g. below the Raibl shale horizons, or emersion layers within the Wetterstein Formation). Subsequent to the main mineralization event minor tectonically driven remobilization and recrystallization occurred.

Table 5.9: Sphalerite generations and characteristics distinguished by Kuhlemann (1995). The sphalerite generations are listed according to the proposed formation sequence (sorted from older to younger from top to bottom.

Type	CL color	Trace elements
small	same as the host rock	↑Cu, As, Cd, Tl, Ge ↓Ag
schalenblende	brown - black	↑Fe, As, Tl, Ge
light blue	light blue	↓ all trace elements
orange	orange - red	↑Cd, Cu, Ag
dark-blue	dark blue	↓ all trace elements
brown	dark brown	↑Fe, Cd, Tl, Ge
yellow	yellow	intermediate Fe, Cd, Tl, Ge

Zeeh et al. (1998) proposed two major epigenetic phases of ore formation during the Late Triassic to Early Jurassic. This model was also based on the sphalerite “chronology” presented in table 5.9 and the relation of the ore minerals to diagenetic carbonate cements. They suggested that ore mineralization started immediately after shallow burial of the Triassic host rocks. In this model the metals were leached from the crystalline basement by descending meteoric waters, which migrated from the Vindelizian-Bohemian massif in the north towards the south (Figure 5.13). The salinity of these meteoric waters increased with increasing depth. The topographic difference between the Vindelizian-Bohemian massif and the Drau Range area was thought to be the driving mechanism for fluid migration. Mixing of the metal bearing brine with sulfide-sulfur caused ore precipitation. Zeeh at al. (1998) argued for a two-stage ore formation. The early stage was sphalerite rich, the late one rather galena-rich. The ore forming fluids successively migrated through all ore horizons and caused there ore precipitation. The chemistry of the sphalerites is controlled by the trace element composition of the fluid (according to this model the trace element content of the fluid resulted from the time period of leaching) and from the Eh-pH conditions at the depositional site.

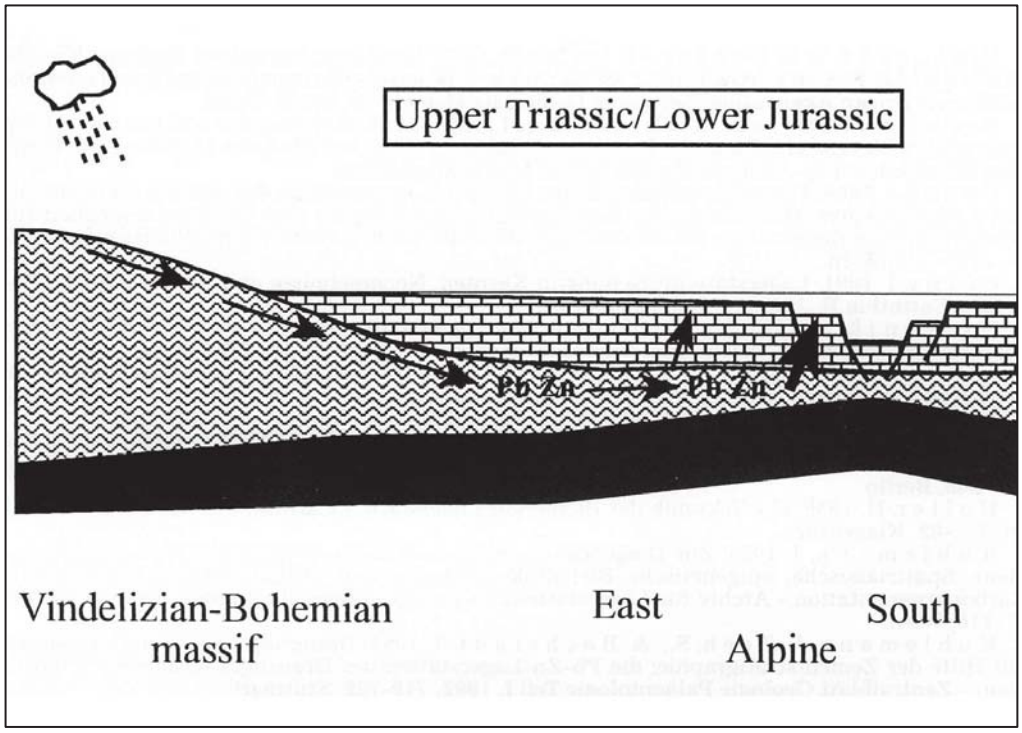

Figure 5.13: Model for Triassic/Jurassic fluid flow, which caused the formation of Pb-Zn deposits in the Alps (Zeeh et al., 1998).

The discussed epigenetic MVT models are presumably not applicable to the Topla deposit. Many researchers realized the pecularities of this deposit and separated it from the formation of the other Pb-Zn deposits within the Drau Range (e.g. Strucl, 1974, Drovenik & Pungartnik, 1987, Spangenberg & Herlec, 2006, Herlec et al., 2010). Strucl (1974) favored a strictly syngenetic-synsedimentary origin, because of the presence of sedimentary textures (e.g. load cast, ripple structures) associated with the ore minerals. Drovenik & Pungartnik (1987), Spangenberg & Herlec (2006) and Herlec et al. (2010) argue that Topla formed individually during the early diagenesis of the Anisian host rocks due to interaction of a MVT brine with fluids containing reduced sulfur from a BSR reservoir.

5.6.5 Discussion of genetic models in the light of new data

The in this study presented data show that the formation of texturally, chemically or isotopically distinct sphalerite is neither restricted to certain times nor paragenetic stages (chapters 4.4 and 5.5.1). Thus, the epigenetic model of Kuhlemann (1995) and Zeeh et al. (1998), which is based on the assumption that a uniform paragenetic sequence of ore mineals and carbonate cements can be established throughout the whole Drau Range cannot be affirmed. For example Kuhlemann (1995) suggested that the early-formed sphalerites are Ge rich and obtained their trace element contents from the Ladinian platform carbonates. The author's opinion of a carbonate source of Ge is highly unlikely, because carbonates are depleted in Ge (Höll et al., 2007). Moreover, the results of this study do not support early formation of Ge rich schalenblende but rather point to a late formation (chapters 5.1.2, 5.3 and 5.5.2). However, the previous age estimations of Pb-Zn mineralization proposed by these authors on geological

reasons (Kuhlemann, 1995, Zeeh et al., 1998) have been confirmed by the Rb-Sr dating of sphalerite. The data confirm that a major stage of Pb-Zn mineralization occurred at about 200 Ma in the Upper Triassic/Lower Jurassic (see chapter 5.3).

The model that ore formation at Bleiberg is syngenetic (synsedimentary exhalative or "synchronous" in a sub-seafloor environment) has not been confirmed by this study. A few Bleiberg samples exhibit very fine-grained ore minerals and laminated textures (e.g. Blb17, Blb26 from Maxer Bänke horizon, see chapter 4.4.1), which could be interpreted in terms of a sedimentary origin. However, precipitatoion of sulfides within an open cavity ("internal sedimentation") rather than on the seafloor ("external sedimentation") is the preferred explanation of these textures. This interpretation is based on the observation that in sample Blb17 the laminated sphalerite crystallized *after* early schalenblende what indicates a high degree of metal oversaturation. Metal oversaturation can be achieved best within a partly closed space.

The argumentation that the very light sulfur isotope composition of sulfides support syngenetic ore mineralization, because they indicate low temperature BSR, is also invalid. Although the data of this study confirm the predominance of very light sulfur isotope compositions ($\delta^{34}S$ < -20‰, chapters 4.3.1 and 5.2.1), this does not allow to draw any conclusions on the temperatures at the sites of ore deposition. As outlined in this study the base metals and the reduced sulfur were transported in different fluids (chapter 5.5). Therefore, a clear distinction must be made between the temperature of the sulfur bearing fluid(s) and the temperature of the metal bearing fluid. Warren (2000) argued that BSR can occur also in subsurface environments down to depths of 2 – 2.5 km (e.g. in enclosed pore waters) as long as the temperatures do not exceed 110°C. The burial depth of the Wetterstein Formation and the Raibl Group was less than 3 km until the beginning of the Late Cretaceous (100 Ma, Rantitsch, 2001). Temperature estimates, based on the vitrinite reflectance and thermal modeling demonstrate, that the burial temperatures of the Wetterstein Formation never exceeded 120°C (Rantitsch, 2001). BSR could therefore have been operative during most of the geological history of these deposits.

The ore textures within the Erzkalk horizon were often used to support the syngenetic model (e.g. Schulz, 1968) although within the Erzkalk horizon a heavier sulfur isotope signature was documented more frequently (Schroll & Rantitsch, 2005), what was also confirmed in this study (samples EHK02, WS_Blb07, chapter 4.4.2). Within both samples uncommonly heavy sulfur isotope values ($\delta^{34}S$ > -10‰), interpreted as input of TSR reduced sulfur (chapter 5.2), were measured. In sample EHK02 this stage clearly pre-dates sphalerie mineralization dominated by BSR sulfur.

The fact that the Pb isotope signature of the ore minerals is different from that in the classical carbonate-hosted Pb-Zn deposits in the MVT district is useful to describe the characteristics of the Alpine Pb-Zn mineralization. However, the Pb isotope signature only constraints the metal sources but not the mechanisms and timing of ore formation.

5.6.6 Genetic model for the Pb-Zn deposits in the Drau Range

This study shows that the sphalerite ore from the Pb-Zn deposits in the Drau Range is very heterogenously in textures, trace element and sulfur isotope composition but rather homogenous in its Pb isotope composition.

As pointed out the reduced sulfur was derived from at least two different reservoirs. Two different mechanisms caused reduction of sulfate – TSR as well as BSR. Most of the reduced sulfur originated from a low temperature BSR reservoir. Minor amounts of reduced sulfur originated from a TSR reservoir. Both sulfur reservoirs were able to provide reduced sulfur for ore formation to different ore horizons in a variable degree. Sulfur from these two reservoirs might also have been mixed. There is no clear evolution in time in the sulfur isotope data and there is no unique sulfur isotope signature for individual ore deposits or ore horizons within the larger Bleiberg deposit. Interestingly, the TSR component was mostly detected in deeper-seated ore bodies within the Wetterstein Formation; i.e. Erzkalk, Maxer Bänke horizons. Actually, only in a single sample from a stratigraphically higher ore body (Crest horizon, R8/2), a $\delta^{34}S$ of > -5‰ was measured. This trend could indicate that TSR was more important at the deeper levels and the BSR reservoir contributed more reduced sulfur at shallower depth. It can be speculated that hotter ascending hydrothermal brines linked with TSR were more important at deeper levels of the mineralizing system.

There is no systematic relationship of the sulfur isotope and the trace element composition of sphalerite. Hence, combined transport of trace metals and reduced sulfur is unlikely. It is rather assumed that trace metals were mainly transported together with Pb and Zn and that certain trace/minor element signatures of sphalerite result from leaching of different lithologies during the brine migration and from gradual enrichment of for sphalerite “incompatible” elements within the fluid. As further controlling factor for the trace element signature of the sphalerite, the physico-chemical conditions (pH, redox conditions) at the depositional site presumably were of great importance.

The Pb isotope signature of the investigated sphalerite and galena samples is rather homogeneous and indicates that the base metals originate from a source in the upper crust (chapter 5.4). There is no systematic difference in the Pb isotope composition of individual deposits unlike to the Pb-Zn deposits in Ireland (LeHuray et al., 1987). The rather homogeneous Pb isotope composition of the sulfides is indicative for a well-homogenized metal transporting fluid system. This may indicate a large-scale fluid circulation and is in contrast to the smaller convection cells proposed for the IRT deposits.

The Rb-Sr dating of the sphalerite indicates that the main stage of ore formation was at ~200 Ma, at the Upper Triassic / Lower Jurassic boundary. This age is consistent with

an epigenetic ore formation during early diagenetic burial of the host rocks (Rantitsch, 2001); the maximum burial of the Triassic carboante platform did not occur before the Eocene (50 Ma). It was not possible to support the suspected syngenetic mineralization event that was suggested from a 3-point isochron of samples from the 1st Raibl horizon (Melcher et al., 2010) with further data because sphalerite samples with "synsedimentary" ore textures were not suitable for the Rb-Sr dating. A slightly younger age of ore formation at 195 Ma is indicated for a few sphalerites from Revier Erlach in Bleiberg. This age calculation possibly dates a younger mineralization event. This could indicate that Pb-Zn mineralization at Bleiberg is poly-phase. Repeated mineralization events may have occurred over a longer time period. One good-defined Rb-Sr isochron age of 204± 3.2 Ma combines texturally and chemically different sphalerites onto one isochron. This supports the idea, that no clear formation sequence of texturally, chemically and sulfur isotopically distinct sphalerite generations exist.

The exact driving mechanisms of fluid migration and the origin of the metal-bearing fluids for Pb-Zn mineralization in the Drau Range are unclear. Several models were proposed: (1) Muchez et al. (2005) proposed that the formation of most European Pb-Zn deposits is related to extensional tectonics during the Mesozoic. Extensional tectonics at that time occurred in response to the incipient opening of the North and Central Atlantic Ocean and the Tethys. According to this model extensional structures facilitated downward migration of highly saline seawater (e.g. evaporated seawater). The downwards-migration of the saline water allows leaching of metals from the surrounding lithologies and a gradual metal enrichment in the fluid. The residence time of the seawater and the depth to which it migrates is regionally different. The modified seawater will become more and more enriched in base and trace metals in response to interaction with the lithologies, through which it migrates. During times of extension (rifting), expulsion of these metal rich fluids along faults occurs. Extensional tectonics caused a high geothermal gradient in the crust, which allows convective heat flow and connected brine migration in sedimentary basins. (2) Zeeh et al (1998) and Leach et al. (2001) argued for gravity-driven brine migration in the forefront of an orogen in response to tectonic activity as main causes for fluid migration. According to this model, which is largely based on Graven et al. (1993), the mineralizing brines evolved from descending meteoric waters, which migrated from the Vindelizian-Bohemian massif in the north towards the Austroalpine platform sediments in the south (Leach et al., 2003). Topographic differences caused southwards directed fluid flow. In connection with the migration, an increase in the salinity of the fluid enabled metal leaching. The ascent of the metal rich brines was facilitated by the onset of rifting in the Alpine realm (Leach et al., 2003). In a very similar model Zeeh et al. (1998) also proposed also that gravity-driven fluid flow from the Vindelician-Bohemian massif in the north during the Late Triassic/Early Jurassic caused the migration of metal rich brines (Figure 5.13). At present it is not possible to preclude any driving mechanism for fluid flow. The Vindelizian-Bohemian massif was not positioned on the same continental plate like as the Triassic carbonate platform. It is therefore not likely that metal bearing fluids from this area were important for the ore genesis in the Drau Range. Preliminary crush-leach analyses of gangue and ore minerals (Prochaska, pers. comm.) indicate that highly saline and evaporitiy fluids were involved into ore genesis. Therefore, a

seawater fluid source seems to be more realistic. The 200 Ma Rb-Sr age of sphalerite obtained in this study supports the idea that fluid circulation occurred in response to extensional tectonics. This age coincides with the incipient rifting of the Penninic ocean (chapter 2.2, Schmidt, 1991, Ebner, 1997) what caused high regional heat flow and could have initiated a large convection system in the affected sedimentary basins.

Based on the complexity, which was encountered during this study, the following mineralization model is proposed for the formation of the Pb-Zn deposits in the Drau Range:

- Synsedimentary processes (Figure 5.14): Storage of fluids containing sulfate reducing bacteria within pore space and cavities of the Wetterstein Formation, which exhibitee cavities since it was affected by synsedimentary karstification (Bechstädt, 1979). Presumably, also storage of reduced BSR sulfur in cavities. Syngenetic reduced sulfur might have been incorporated into diagentic pyrite or into organic matter. According to Herlec et al. (2010), ore samples from Mezica contain high amounts of heptanes, squalanes and sulfur-aromatic compounds, which are capable for fixation of reduced sulfur. Furthermore, storage of sulfates (seawater) within pore space/cavities and/or evaporates (gypsum, anhydrite) present in the platform carbonates (future second sulfur reservoir; Figure 5.14).

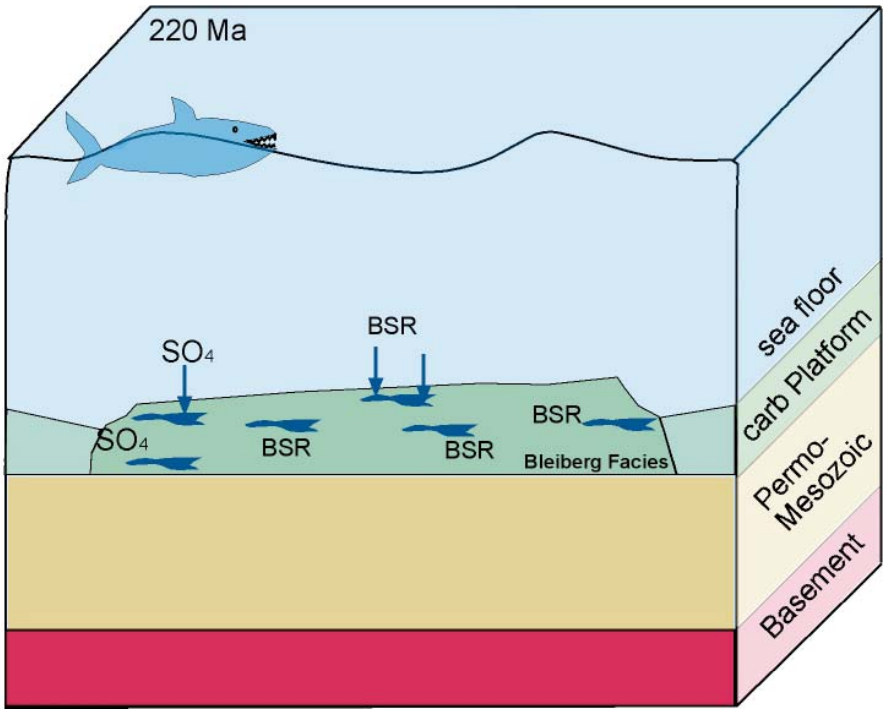

Figure 5.14: Synsedimentary processes (220 Ma): storage of fluids containing sulfate-reducing bacteria in karst cavities, which were already present due to the facies differentitation within the carbonate platform. Furthermore, storage (and incorporation into organic matter/diagenetical pyrite) of BSR sulfide-sulfur in cavities. Furthermore storage of sulfates in pore fluids and fixing of sulfate in evaporatite minerals.

- Epigenetic processes during the burial at about 200 Ma (Figure 5.15): Ongoing BSR during the beginning burial of the Wetterstein Formation, which is possible down to depth of approximately 2.5 km (Warren, 2000). Downward migration of seawater (evaporated seawater) in response to extensional tectonics. Leaching of base metals from the basement by warm - hot Cl-rich fluids/brines. The high regional geothermal gradients due to incipient rifting of the Penninic Ocean furthermore causes the evolution of a large convection cell, which facilitates ascent of the metal-enriched fluid along faults. During the further fluid circulation trace metals are also

leached from the passed sedimentary lithologies. The hot, reduced and metal-bearing fluid (>100°C) interacts with sulfatic sulfur (seawater sulfate, sulfate from evaporites) in the carbonate host rocks. This causes TSR due to the heat rise and precipitation of sulfides with a TSR sulfur isotope signature. Mixing of the metal-bearing fluid with BSR sulfur causes precipitation of sulfides with a much lighter sulfur isotope composition.

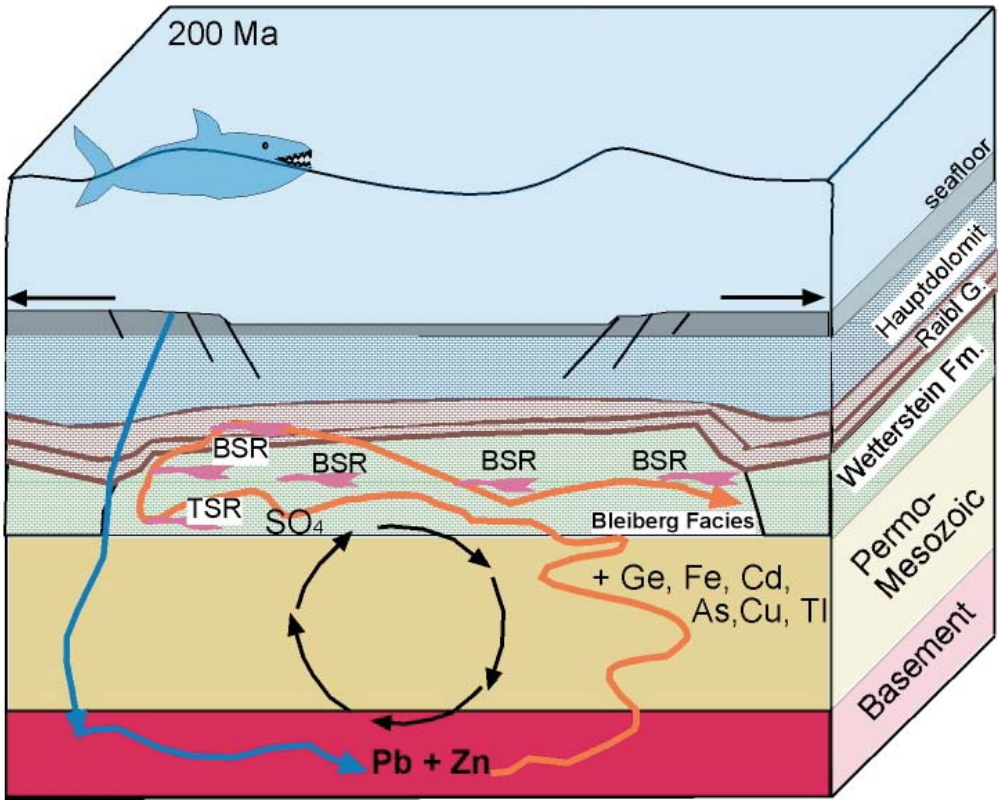

Figure 5.15: Epigenetic processes at about 220 Ma: Seawater migrates downward and leaches metals from the basement. Extensional tectonics causes high heat flow and the evolution of a larger convection cell allowing ascent and circulation of metal-rich brines, which interacted with the basement and Permomesozoic sediments. At the depositional sites, these hot (>150°C) brines react with the stored sulfates to produce TSR reduced sulfur necessary for precipitation of base metals. Reaction of the metal transporting fluid with reduced sulfur from a BSR reservoir causes further precipitation of sulfides. The Raibl shales act presumably as sealing layers and prevent further ascent of the metal rich fluids.

It is dubious, if this model is also applicable to the formation of the Anisian Topla deposit. Though the chemical composition and the sulfur isotope signature of the sphalerites from Topla is similar to that of the other Pb-Zn deposits in the Drau Range the texture of these fine-grained and dispersed sphalerite ores are very different to deposits in the Wetterstein Formation. In accordance with previous investigations it is assumed that the Topla deposit was formed independently from the other Pb-Zn mineralizations within the Drau Range. It likely represents an older stage of Pb-Zn mineralization. In order to verify this assumption a provenance analysis of the metals (e.g. Pb isotopes) would be highly desireable.

6 Summary & Outlook

The chosen multi-analytical high-resolution approach (i.e. ore textures, trace elements, sulfur isotope and Pb isotope compositions) focussing on sphalerite provided some new information on the formation of the Pb-Zn mineralization in the Drau Range. This approach showed that the studied Zn ores are highly heterogeneous in texture, trace element and sulfur isotope composition but nearly homogenous in their Pb isotope composition.

6.1 Trace elements

Sphalerite from the Drau Range may incorporate variable amounts of different trace elements as documented by EMPA analysis. Iron and Cd are the most important and occur in the highest concentrations. Both elements were detected in sphalerite from all deposits and all ore horizons. There is a tendency of Cd > Fe (mass%) at Mezica deposit. At Bleiberg the Cd and Fe contents (and the Fe/Cd) vary from one location to another and even on the sample scale large variations in the Fe/Cd of sphalerite were observed. Besides, also Pb, As and Ge were regularly above the limit of detection of the EMPA at various locations/deposits. The trace elements Cu and Tl were detectable only very sporadically. Thallium concentrations above the limit of detection are exclusively found in Bleiberg samples (from all ore horizons). Copper was detected in sphalerites from Bleiberg and more commonly Mezica. It is assumed that Pb, As and Tl are not present in solid solution within the sphalerite lattice but occur in nano-inclusions, which are too small to be identified with standard reflected light microscopy or on BSE images. This assumption is supported by the highly heterogeneous distribution of Pb, As and Tl and by a positive inter-element relation. Germanium is strongest enriched in sphalerite from Revier Erlach (western Bleiberg mine) and in sphalerite from the Jauken deposit. Germanium is present in solid solution within the sphalerite lattice. In Bleiberg (Revier Erlach) the observed zonation of sphalerite indicates that Ge-rich sphalerite formed after a first phase of ore deposition due to the hydrothermal overprint of already existing Ge-poor sphalerite. At Jauken, the other Ge rich locality, no zonation with respect to Ge was observed. Therefore it is assumed that Ge rich sphalerite was also formed as primary precipitate.

6.2 Sulfur Isotopes

The sulfur isotope composition of the investigated sulfides (sphalerite, galena, pyrite/marcasite, n = 90) varies from -30.4 to + 1.8‰. Sphalerite covers the full $\delta^{34}S$ variation range of the sulfides. The variations of $\delta^{34}S$ of galena and pyrite/marcasite are smaller compared to sphalerite (galena: -29.8 to -6.1‰; Fe-sulfides: -24.5 to -14.4‰) though less analyses were made from these minerals. Sphalerite and galena did not form under isotopic equilibrium conditions. The sulfur isotope dataset shows a clear bias towards light sulfur isotope composition; more than 50% of the analyzed sulfides are characterized by $\delta^{34}S$ values < -20‰. Only a small percentage of the sulfides (< 10%) is characterized by clearly heavier sulfur isotope composition of > -10‰. In three

samples from the Bleiberg deposit, large small-scale (cm) variations were documented in the sulfur isotope composition (> 15‰) between coexisting sulfides. Using textural observations, it was possible to establish a formation chronology of isotopically different sphalerite (sulfide) types. In two samples, the early-formed sulfides are sulfur isotopically light and followed by the formation of clearly heavier sulfides. Contrariwise, in the third sample the heavier sulfides were formed before the lighter ones. The observed sulfur isotope variations are interpreted as the result of input of reduced sulfur from at least two different reservoirs. The predominance of very light sulfur isotope compositions indicates that a BSR reservoir was most important for the ore precipitation. In addition, a second reservoir (TSR) was responsible for heavier sulfur isotope compositions. It is assumed that the BSR reservoir was located in a position close to the sea floor and that reduced sulfur derived from this reservoir was mainly transported via descending fluids towards the places of ore deposition. Various sources of sulfate for the TSR process are possible; ultimately they all derived from marine seawater. These include evaporites (anhydrite, gypsum) that are intercalated in the Triassic host carbonates or the underlying Permomesozoic sediments (e.g. Permian Haselgebirgs), but also SO_4 from connate waters entrapped in pores and cavities as well as evaporated seawater. The possibility that the sulfur isotope variations were caused by isotope fractionation within a single reservoir is excluded, because in this case a more gradual evolution of $\delta^{34}S$ values should be present.

6.3 Pb Isotopes

Coexisting sphalerite and galena in most samples from Bleiberg and Mezica have very similar Pb isotope compositions. The Pb concentrations of sphalerite as determined with the isotope dilution method are highly variable (150 to > 60,000 ppm). High Pb concentrations (in the 1000 ppm range) in sphalerite are attributed to the presence of Pb-bearing nano-inclusions. Lower Pb concentrations probably represent real lattice bound Pb. It is very likely that sphalerite and galena obtained their Pb from identical sources, because in most cases they are characterized by a very similar Pb isotope composition. Two sphalerite samples from Mezica and Jauken plot offset to more radiogenic $^{206}Pb/^{204}Pb$ and $^{207}Pb/^{204}Pb$ values. In both samples Pb concentrations are low. Three reasons are possible for the more radiogenic Pb isotope composition of these two samples: *(1)* metals were leached from a different source with more radiogenic ^{267}Pb and ^{207}Pb signature. *(2)* The more radiogenic Pb isotope signature results from in-situ decay of U to Pb within the sphalerite itself; *(3)* Contamination of the sphalerite separates with a gangue phase with a more radiogenic ^{267}Pb and ^{207}Pb signature. Plotting the Pb isotope data of this study together with the Pb isotope evolution curves for crustal reservoirs according to different authors (Cumming & Richards, 1975, Stacey & Kramers, 1975 and Zartman & Doe, 1981) the Pb isotope data of this study in most cases closely match compositions calculated for late Paleozoic and younger model compositions. Therefore, it is assumed that the ore lead was derived from a crustal reservoir, e.g. the basement. A comparison of our data with previously published Pb isotope data of galena, whole rock samples and feldspars (Köppel & Schroll, 1985, 1988, Schroll et al., 2006) strengthen previous interpretations that the ores originated indirectly from pre-exiting basement rocks. However, we find no evidence for a Pb component in the ore, which is isotopically significantly different from the Pb of the Wetterstein Formation. Instead, chemical fractionation processes,

e.g., strong increase of Th relative to U, during ore formation may as well explain the trends in Pb isotopic composition of ore-bearing carbonate samples away from the respective data points for the Wetterstein Formation.

6.4 Rb-Sr dating of sphalerite

Different subsets of the Rb-Sr data (this study + data determined by J. Schneider; partly published in Melcher et al., 2010) were used for the calculation of isochron ages. One well-defined isochron was calculated for sphalerite from the Crest horizon (Bleiberg, n = 5). This isochron indicates an ore formation age of 204±3.2 Ma and has a very low MSWD of 0.14. The initial $^{87}Sr/^{86}Sr$ of 0.70851±0.00026 corresponds with the Sr isotope signature of Triassic seawater 200 Ma ago (Burke et al., 1982). A further isochron was contructed based on the results of the Rb-Sr analyses of Revier Erlach (Bleiberg, n = 7) sphalerite. This isochron indicates a somewhat younger age of ore formation at 195.1±2.6 Ma. The MSWD of this isochron of 1.9 indicates a low and acceptable degree of geological scatter of the data points. However, the initial $^{87}Sr/^{86}Sr$ of 0.71051±0.00068 is considerably higher as compared to Triassic seawater (Burke et al., 1982). Based on a three-point isochron for samples from the 1st Raibl horizon at Bleiberg (2 sphalerite + 1 pyrite) Melcher et al. (2010) suspected an earlier ore formation stage at 225±2.2 Ma. It was not possible to support this postulated early mineralization event with further data. When adding an additional sphalerite data point from the 1st Raibl horizon the calculated isochron age has an enormous uncertainty and very high MSWD value.

6.5 Concluding remarks & outlook

Sphalerite shows a great heterogeneity in texture as well as in trace element and sulfur isotope composition; this is in contrast to the nearly homogenous Pb isotope composition. Based on a combination of the information obtained in the course of this study it is stated that *1.)* Base metals and reduced sulfur were transported in different brines. *2.)* Reduced sulfur and trace metals were transported in different brines. *3.)* The base metal source of Bleiberg, Mezica and Jauken was homogenous. *4.)* Trace element variations of sphalerite are likely the result of a complex interplay at the depositional site between the metals and sulfur bearing fluids due to the prevailing physico-chemical conditions (e.g. pH, sulfur species, redox conditions). Furthermore, trace element variations might have been caused by interaction of the base metal bearing fluid with the surrounding lithologies and from gradual enrichment of “incompatible” elements in the fluid.

Variations in textures, trace element and sulfur isotope composition have been documented on a small (within-sample) scale. This study clearly demonstrates that the ore mineralization in the Drau Range occurred during several distinct stages. However, characteristic sphalerite ‘types’ (e.g. schalenblende, sphalerite with very light sulfur isotope composition) formed repeatedly at different times/stages of ore formation. The uniform paragenetic position of specific sphalerite types throughout the whole Drau Range (or even within a larger deposit) as postulated by previous researchers was not

confirmed. Based on the data of this PhD study it is proposed that the Pb-Zn deposits in the Drau Range are mainly of epigenetic origin. The main stage of Pb-Zn deposition was at about 200 Ma.

In order to establish a comprehensive genetic model, other aspects have also to be investigated and considered. Additional research on the relations between the ore and gangue minerals in combination with stable and radiogenic isotope analyses are desired, because it is an interesting question whether sulfides with BSR signature occur in paragenesis with gangue minerals that have a marine Sr isotope signature. It would be interesting to compare the Sr isotope signature of co-existing sphalerite and gangue, in order to understand from where the sphalerite obtained its Sr isotope signature (seawater vs. crustal Sr reservoir). A further very interesting point concerns the question whether the Permian evaporites were involved in providing sulfate for (TSR) sulfate reduction and chlorine for making of chloride-rich brines necessary for base metal transport. The latter question can possibly be answered with further crush-leach-analyses of fluid inclusions in gangue minerals that coexist with TSR sulfides. In order to better constrain the temperatures of ore formation, fluid inclusion analyses of sphalerite and coexisting gangue minerals would be of vital interest. However, this approach has been hampered by the scarcity of fluid inclusions of adequate size. Also in this study no suitable fluid inclusions were observed in the investigated sphalerites. These data should be cross-checked with the burial history and the regional geological evolution of the Drau Range. Obtaining suitable and geologially well-defined specimens is one of the most important crucial points for studies aiming to establish correct genetic models. This pre-requisite was a major challenge of this project due to nowadays inaccessibility of most mines. There are still enough open scientific questions to be solved in the future in this respect.

References

Anderson, G. M. (1975). Precipitation of Mississippi Valley-type ores. *Economic Geology* **70**, 937-942.

Anderson, G. M. (2008). The mixing hypothesis and the origin of Mississippi Valley-type ore deposits. *Economic Geology* **103**, 1683-1690.

Anderson, G. M. & Macqueen, R. W. (1982). Ore Deposit Models - 6. Mississippi Valley-Type Lead-Zinc Deposits. *Geoscience Canada* **9**, 108 - 117.

Anderson, I. K., Andrew, C. J., Ashton, J. H., Boyce, A. J., Caulfield, J. B. D., Fallick, A. E. & Russell, M. J. (1989). Preliminary sulphur isotope data of diagenetic and vein sulphides in the Lower Palaeozoic strata of Ireland and southern Scotland: implications for Zn+ Pb+ Ba mineralization. *Journal of the Geological Society* **146**, 715-720.

Bachinski, D. J. (1969). Bond strength and sulfur isotopic fractionation in coexisting sulfides. *Economic Geology* **64**, 56-65.

Baker, J., Peate, D., Waight, T. & Meyzen, C. (2004). Pb isotopic analysis of standards and samples using a ^{207}Pb- ^{204}Pb double spike and thallium to correct for mass bias with a double-focusing MC-ICP-MS. *Chemical Geology* **211**, 275-303.

Barrie, C. D., Boyce, A. J., Boyle, A. P., Williams, P. J., Blake, K., Wilkinson, J. J., Lowther, M., McDermott, P. & Prior, D. J. (2009). On the growth of colloform textures: a case study of sphalerite from the Galmoy ore body, Ireland. *Journal of the Geological Society* **166**, 563-582.

Barton, P. B. & Bethke, P. M. (1987). Chalcopyrite disease in sphalerite; pathology and epidemiology. *American Mineralogist* **72**, 451-467.

Barton, P. B. & Toulmin, P. (1966). Phase relations involving sphalerite in the Fe-Zn-S system. *Economic Geology* **61**, 815-849.

Bechstädt, T. (1973). Zyklotheme im hangenden Wettersteinkalk von Bleiberg-Kreuth (Kärnten, Österreich). *Veröffentlichungen der Universität Innsbruck* **86**, 25-55.

Bechstädt, T. (1975). Lead-zinc ores dependent on cyclic sedimentation. *Mineralium Deposita* **10**, 234-248.

Bechstädt, T. (1979). The Lead-Zinc Deposit of Bleiberg-Kreuth (Carinthia, Austria): Palinspastic situation, Paleogeography and Ore Mineralisation. *Verhandlungen der Geologischen Bundesanstalt* **3**, 221 235.

Bechstädt, T. & Schweizer, T. (1991). The carbonate-clastic cycles of the East-Alpine Raibl group: Result of third-order sea-level fluctuations in the Carnian. *Sedimentary Geology* **70**, 241-270.

Belissont, R., Boiron, M.-C., Luais, B. & Cathelineau, M. (2014). LA-ICP-MS analyses of minor and trace elements and bulk Ge isotopes in zoned Ge-rich sphalerites from the Noailhac Saint-Salvy deposit (France): Insights into incorporation mechanisms and ore deposition processes. *Geochimica et Cosmochimica Acta* **126**, 518-540.

Bernstein, L. R. (1985). Germanium geochemistry and mineralogy. *Geochimica et Cosmochimica Acta* **49**, 2409-2422.

Bethke, C. M. & Marshak, S. (1990). Brine migrations across North America-The plate tectonics of groundwater. *Annual Review of Earth and Planetary Sciences* **18**, 287.

Bethke, P. M. & Barton, P. B. (1971). Distribution of some minor elements between coexisting sulfide minerals. *Economic Geology* **66**, 140-163.

Birck, J. L. (1986). Precision K-Rb-Sr isotopic analysis: application to Rb-Sr chronology. *Chemical Geology* **56**, 73-83.

Blakeman, R. J., Ashton, J. H., Boyce, A. J., Fallick, A. E. & Russell, M. J. (2002). Timing of interplay between hydrothermal and surface fluids in the Navan Zn+ Pb Orebody, Ireland: evidence from metal distribution trends, mineral textures, andδ^{34}S analyses. *Economic Geology* **97**, 73-91.

Böttcher, M. E. & Thamdrup, B. (2001). Anaerobic sulfide oxidation and stable isotope fractionation associated with bacterial sulfur disproportionation in the presence of MnO2. *Geochimica et Cosmochimica Acta* **65**, 1573-1581.

Boyce, A. J., Coleman, M. L. & Russell, M. J. (1983). Formation of fossil hydrothermal chimneys and mounds from Silvermines, Ireland. *Nature* **306**, 545-550.

Brannon, J. C., Podosek, F. A. & McLimans, R. K. (1992). Alleghenian age of the Upper Mississippi Valley zinc -lead deposit determined by Rb - Sr dating of sphalerite. *Nature* **356**, 509-511.

Brannon, J. C., Podosek, F. A., Viets, J. G., Leach, D. L., Goldhabe, M. & Rowan, E. L. (1991). Strontium isotopic constraints on the origin of ore-forming fluids of the Viburnum Trend, southeast Missouri. *Geochimica et Cosmochimica Acta* **55**, 1407-1419.

Brigo, L., Kostelka, L., Omenetto, P., Schneider, H. J., Schroll, E., Schulz, O. & Strucl, I. (1977). Comparative reflections on four Alpine Pb-Zn deposits. In: Klemm, D. D. (ed.) *Time-and strata-bound ore deposits*. Berlin: Springer, 273-293.

Brunlechner, A. (1899). Die Entstehung und Bildungsfolge der Bleiberger Erze und ihrer Begleiter. *Jahrbuch des Naturgeschichtlichen Museums von Kärnten* **25**.

Burke, W. H., Denison, R. E., Hetherington, E. A., Koepnick, R. B., Nelson, H. F. & Otto, J. B. (1982). Variation of seawater ^{87}Sr/^{86}Sr throughout Phanerozoic time. *Geology* **10**, 516-519.

Cerny, I. (1989). Die karbonatgebundenen Blei-Zink-Lagerstaetten des alpinen und ausser-alpinen Mesozoikums; Die Bedeutung ihrer Geologie, Stratigraphie und Faziesgebundenheit fuer Prospektion und Bewertung. Carbonate-bound lead-zinc deposits of the Alpine and extra-Alpine Mesozoic; implications for prospecting and evaluation of their stratigraphy and facies relationships. *Archiv für Lagerstättenforschung der Geologischen Bundesanstalt* **11**, 5-125.

Cerny, I. & Hagemeister, A. (1986). Fluoritmineralisation in mitteltriadischen Karbonatgesteinen am Jauken (Gailtaler Alpen, Kaernten, Oesterreich). Fluorite mineralization in the Middle Triassic carbonate rocks in Jauken, Gailtal Alps, Carinthia, Austria. *Carinthia II* **96**, 407-417.

Charlier, B. L. A., Ginibre, C., Morgan, D., Nowell, G. M., Pearson, D. G., Davidson, J. P. & Ottley, C. J. (2006). Methods for the microsampling and high-precision analysis of strontium and rubidium isotopes at single crystal scale for petrological and geochronological applications. *Chemical Geology* **232**, 114-133.

Christensen, J. N., Halliday, A. N., Leigh, K. E., Randell, R. N. & Kesler, S. E. (1995a). Direct dating of sulfides by Rb-Sr: A critical test using the Polaris Mississippi Valley-type Zn- Pb deposit. *Geochimica et Cosmochimica Acta* **59**, 5191-5197.

Christensen, J. N., Halliday, A. N., Vearncombe, J. R. & Kesler, S. E. (1995b). Testing models of large-scale crustal fluid flow using direct dating of sulfides; Rb-Sr evidence for early dewatering and formation of mississippi valley-type deposits, Canning Basin, Australia. *Economic Geology* **90**, 877-884.

Clark, A. H. (1970). Arsenian sphalerite from Mina Alcáran, Pampa Larga, Copiapó, Chile. *The American Mineralogist, Mineralogical Notes* **55**, 1794 - 1797.

Cook, N. J., Ciobanu, C. L., Pring, A., Skinner, W., Shimizu, M., Danyushevsky, L., Saini-Eidukat, B. & Melcher, F. (2009). Trace and minor elements in sphalerite: A LA-ICPMS study. *Geochimica et Cosmochimica Acta* **73**, 4761-4791.

Cotta, B. v. (1863). Über die Blei-und Zinklagerstätten Kärntens. *Freiberger Berg-und Hüttenmännische Zeitung*, 9 - 12.

Cumming, G. L., Köppel, V. & Ferrario, A. (1987). A lead isotope study of the northeastern Ivrea Zone and the adjoining Ceneri zone (N-Italy): evidence for a contaminated subcontinental mantle. *Contributions to Mineralogy and Petrology* **97**, 19-30.

Cumming, G. L. & Richards, J. R. (1975). Ore lead isotope ratios in a continuously changing earth. *Earth and Planetary Science Letters* **28**, 155-171.

Darke, S. A. & Tyson, J. F. (1993). Interaction of laser radiation with solid materials and its significance to analytical spectrometry. A review. *Journal of Analytical Atomic Spectrometry* **8**, 145-209.

Deer, W. A., Howie, R. A. & Zussman, J. (1992). *Rock-forming minerals*. London: Longmans.

Di Benedetto, F., Bernardini, G. P., Costagliola, P., Plant, D. & Vaughan, D. J. (2005). Compositional zoning in sphalerite crystals. *American Mineralogist* **90**, 1384-1392.

Dosso, L., Taylor, R. N. & Ishizuka, O. (2002). Interlab comparison of double spike lead isotope ratios for basaltic standards. *Geochimica et Cosmochimica Acta* **66**, A194.

Drovenik, M. & Pungartnik, M. (1987). Origin of the zinc-lead ore deposit Topla and its particluarities. *Geologija* **30**, 245-313.

Drovenik, M., Strucl, I. & Pezdic, J. (1980). Sulfur isotope composition in the lead-zinc ore deposits of the Northern Karavanke. *Mining Metallurgy Quarterly, Ljubljana* **27**, 413–436.

Dzulynski, S. & Sass-Gustkiewicz, M. (1977). Comments on the genesis of the Eastern-Alpine Zn-Pb deposits. *Mineralium Deposita* **12**, 219-233.

Ebner, F. (1997). Die geologischen Einheiten Österreichs und ihre Rohstoffe. *Handbuch der Lagerstätten der Erze, Industrieminerale und Energierohstoffe Österreichs*. Wien: Archiv für Lagerstättenforschung der Geologischen Bundesanstalt, 49 - 229.

EC. (2010). Critical raw materials for the EU: report of the ad-hoc Working group defining critical raw materials. *European Commision*.

Fallick, A. E., Ashton, J. H., Boyce, A. J., Ellam, R. M. & Russell, M. J. (2001). Bacteria were responsible for the magnitude of the worl-class hydrothermal base metal sulfide orebody at Navan, Ireland. *Economic Geology* **96**, 885-890.

Frank, W. (1987). Evolution of the Austroalpine elements in the Cretaceous. In: Flügel, H. W. & Faupl, P. (eds.) *Geodynamics of the Eastern Alps*: Deuticke, Vienna, 379 - 406.

Fuchs, W. (1846). *Beiträge zur Lehre von den Erzlagerstätten mir besonderer Berücksichtigung der vorzüglichen Bergbaureviere der k.k. Österreichischen Monarchie*. Wien: Carol Gerold.

Gagnevin, D., Menuge, J. F., Kronz, A., Barrie, C. D. & Boyce, A. J. (2011). Minor Elements in Layered Sphalerite Record Fluid Origin in the Giant Navan Zn-Pb Orebody, Ireland. *Mineralogical Magazine* **75**, 398 - 2355.

Galer, S. J. G. (1999). Optimal double and triple spiking for high precision lead isotopic measurement. *Chemical Geology* **157**, 255-274.

Gariepy, C. & Dupre, B. (1991). Pb isotopes and crust-mantle evolution. *Short course handbook on applications of radiogenic isotope systems to problems in geology* **19**, 216-217.

Gerstenberger, H. & Haase, G. (1997). A highly effective emitter substance for mass spectrometric Pb isotope ratio determinations. *Chemical Geology* **136**, 309-312.

Granigg, B. & Koritschoner, J. H. (1914). Die geologischen Verhältnisse des Bergbaugebietes von Mieß in Kärnten. *Zeitschrift für praktische Geologie*, 171-193.

Grootenboer, J. & Schwarcz, H. P. (1969). Experimentally determined sulfur isotope fractionations between sulfide minerals. *Earth and Planetary Science Letters* **7**, 162-166.

Gulson, B. L. (1984). Uranium-lead and lead-lead investigations of minerals from the Broken Hill lodes and mine sequence rocks. *Economic Geology* **79**, 476-490.

Hagenguth, G. (1984). Geochemische und fazielle Untersuchungen an den Maxerbaenken im Pb-Zn-Bergbau von Bleiberg-Kreuth/Kaernten. Geochemical and facies studies of the main horizon of lead-zinc deposits of Bleiburg-Kreuth, Carinthia. *Mitteilungen der Gesellschaft der Geologie- und Bergbaustudenten in Österreich. Sonderheft* **1**, 110.

Hegemann, F. (1949). Die Herkunft des Mo, V, As und Cr im Wulfenit der alpinen Blei-Zinklagerstdtten. *Heidelberger Beiträge zur Mineralogie und Petrographie* **1**, 690-715.

Heinrich, C. A., Pettke, T., Halter, W. E., Aigner-Torres, M., Audétat, A., Günther, D., Hattendorf, B., Bleiner, D., Guillong, M. & Horn, I. (2003). Quantitative multi-element analysis of minerals, fluid and melt inclusions by laser-ablation inductively-coupled-plasma mass-spectrometry. *Geochimica et Cosmochimica Acta* **67**, 3473-3497.

Henjes-Kunst, E. (2010). Petrographical and Geochemical Investigations on Sphalerites from Bleiberg (Austria). *Unpublished diploma thesis, Albert-Ludwigs Universität Freiburg im Brsg.*

Henjes-Kunst, E., Boyce, A. J., Melcher, F. & Raith, J. G. (2013). High-resolution sulfur isotope and trace element measurements of sphalerites from the Pb-Zn deposits of the Drau Range (Eastern Alps, Austria/Slovenia). *Conference abstracts: 12th SGA Biennial Meeting, Uppsala Sweden* **1**, 319 - 322.

Henjes-Kunst, E., Raith, J. G., Boyce, A. J. & Melcher, F. (2012). Distribution of Ge-enriched sphalerites in the Pb-Zn deposits of the Drau Range (Eastern Alps, Austria/Slovenia). *Conference abstracts: EMC2012 planent earth from core to surface*.

Herlec, U., Spangenberg, J. & Lavrič, J. (2010). Sulfur isotope variations from orebody to hand-specimen scale at the Mežica lead–zinc deposit, Slovenia: a predominantly biogenic pattern. *Mineralium Deposita* **45**, 531-547.

Hitzman, M. W., Redmond, P. B. & Beaty, D. W. (2002). The Carbonate-Hosted Lisheen Zn-Pb-Ag Deposit, County Tipperary, Ireland. *Economic Geology* **97**, 1627-1655.

Höll, R., Kling, M. & Schroll, E. (2007). Metallogenesis of germanium -A review. *Ore Geology Reviews* **30**, 145-180.

Holler, H. (1936). Die Tektonik der Bleiberger Lagerstätte. *Carinthia II* **Sonderheft 7**, 1-82.

Holler, H. (1953). Der Blei-Zinkerzbergbau Bleiberg, seine Entwicklung, Geologie und Tektonik. *Carinthia II* **143**, 35-46.

Houtermans, F. G. (1946). The isotope abundances in natural lead and the age of uranium. *Naturwissenschaften* **33**, 185 - 186.

Hupfeld, W. (1897). Der Bleiberger Erzberg. *Zeitschrift für praktische Geologie* **5**, 233.

Johan, Z. (1988). Indium and germanium in the structure of sphalerite; an example of coupled substitution with copper. *Mineralogy and Petrology* **39**, 211-229.

Johnson, C. M. & Beard, B. L. (1999). Correction of instrumentally produced mass fractionation during isotopic analysis of fe by thermal ionization mass spectrometry. *International Journal of Mass Spectrometry* **193**, 87-99.

Jørgensen, B. B., Isaksen, M. F. & Jannasch, H. W. (1992). Bacterial Sulfate Reduction Above 100°C in Deep-Sea Hydrothermal Vent Sediments. *Science* **258**, 1756-1757.

Kampschulte, A. & Strauss, H. (2004). The sulfur isotopic evolution of Phanerozoic seawater based on the analysis of structurally substituted sulfate in carbonates. *Chemical Geology* **204**, 255-286.

Köppel, V. (1983). Summary of lead isotope data from ore deposits of the Eastern and Southern Alps: some metallogenetic and geotectonic implications. In: Schneider, H. J. (ed.) *Mineral deposits of the Alps and of the Alpine Epoch in Europe*. Berlin: Springer, 162-168.

Köppel, V. & Schroll, E. (1978). Bleiisotopenzusammensetzung von Bleierzen aus dem Mesozoikum der Ostalpen. Lead isotope composition of lead ore deposits from the Mesozoic of the Eastern Alps. In: Holzer, H. F. & Stumpfl, E. F. (eds.) *Verhandlungen der Geologischen Bundesanstalt (Wien), no.3*. Vienna: Geologische Bundesanstalt, 403-409.

Köppel, V. & Schroll, E. (1985). Herkunft des Pb der triassischen Pb-Zn-Vererzungen in den Ost-und Südalpen. *Archiv für Lagerstättenforschung der Geologischen Bundesanstalt* **6**, 215-222.

Köppel, V. & Schroll, E. (1988). Pb-isotope evidence for the origin of lead in strata-bound Pb-Zn deposits in triassic carbonates of the Eastern and Southern Alps. *Mineralium Deposita* **23**, 96-103.

Kostelka, L., Bouvier, M., Enzfelder, W., Glantschnig, N., Niedermayr, G., Rainer, H. & Schulz, O. (1972). Die Blei-Zinklagerstaette Bleiberg-Kreuth in Zeit und Raum. The lead-zinc deposits in the Bleiberg-Kreuth area in time and space. *Veröffentlichungen aus dem Naturhistorischen Museum in Wien, Neue Folge* **6**, 8-14.

Kucha, H., Raith, J. G. & Anonymous. (2009). Fossil sulfide bacterial mats from Bleiberg Zn-Pb deposit, Austria. *Geochimica et Cosmochimica Acta*. New York: Elsevier, A701.

Kucha, H., Schroll, E., Raith, J. G. & Halas, S. (2010). Microbial sphalerite formation in carbonate-hosted Zn-Pb ores, Bleiberg, Austria; micro- to nanotextural and sulfur isotope evidence. *Economic Geology* **105**, 1005-1023.

Kucha, H., Schroll, E. & Stumpfl, E. F. (2001). Direct evidence for bacterial sulphur reduction in bleiberg-type deposits. In: Piestrzynski, A. (ed.) *Proceedings of the 6th Biennial SGA Meeting, vol.6*, 149-152.

Kucha, H., Schroll, E. & Stumpfl, E. F. (2002). Bacteriogenic lead-zinc mineralization in the Bleiberg Deposit, Austria. *Geochimica et Cosmochimica Acta*. Oxford: Pergamon, 688.

Kucha, H., Schroll, E. & Stumpfl, E. F. (2004). Bacteriogenic zinc-lead mineralisation in the Bleiberg Deposit; Austria. *International Geological Congress, Abstracts = Congres Geologique International, Resumes, vol.32, Part 1*. location varies: International Geological Congress, 329-330.

Kucha, H., Schroll, E. & Stumpfl, E. F. (2005). Fossil sulphate-reducing bacteria in the Bleiberg lead-zinc deposit, Austria. *Mineralium Deposita* **40**, 123-126.

Kucha, H. & Stumpfl, E. F. (1992). Thiosulphates as precursors of banded sphalerite and pyrite at Bleiberg, Austria. *Mineralogical Magazine* **56**, 165 - 172.

Kuhlemann, J. (1995). Zur Diagenese des Karwanken-Nordstammes (Österreich/Slowenien): Spättriassische, epigenetische Blei-Zink-Vererzung und mitteltertiäre, hydrothermale Karbonatzementation. *Archiv für Lagerstättenforschung der Geologischen Bundesanstalt* **18**, 57-116.

Kuhlemann, J., Vennemann, T., Herlec, U., Zeeh, S. & Bechstaedt, T. (2001). Variations of sulfur isotopes, trace element compositions, and cathodoluminescence of mississippi valley-type Pb-Zn ores from the Drau Range, Eastern Alps (Slovenia-Austria); implications for ore deposition on a regional versus microscale. *Economic Geology and the Bulletin of the Society of Economic Geologists* **96**, 1931-1941.

Kuhlemann, J. & Zeeh, S. (1995). Sphalerite stratigraphy and trace element composition of East Alpine Pb-Zn deposits (Drau Range, Austria-Slovenia). *Economic Geology and the Bulletin of the Society of Economic Geologists* **90**, 2073-2080.

Kuhlemann, J., Zeeh, S. & Bechstädt, T. (1993). The alpine lead-zinc deposits of the Drau Range (Austria/Slovenia); relative dating of ore emplacement by cement stratigraphy. In: Ibbeken, H. (ed.) *SedimentL92*: International Association of Sedimentologists, 381.

Leach, D., Bradley, D., Lewchuk, M., Symons, D., de Marsily, G. & Brannon, J. (2001). Mississippi Valley-type lead-zinc deposits through geological time: implications from recent age-dating research. *Mineralium Deposita* **36**, 711-740.

Leach, D., Sangster, D., Kelley, K., Large, R. R., Garven, G., Allen, C., Gutzmer, J. & Walters, S. G. (2005). Sediment-hosted lead-zinc deposits: A global perspective. In: Hedenquist, J. W., Thompson, J. F. H., Goldfarb, R. J. & Richards, J. P. (eds.) *Economic Geology -One Hundreth Anniversary Volume*: Society of Economic Geologists, 561-607.

Leach, D. L., Bechstadt, T., Boni, M. & Zeeh, S. (2003). Triassic-hosted MVT Zn-Pb ores of Poland, Austria, Slovenia and Italy. In: Kelly, J. G. & Irish Association for Economic, G. (eds.) *Europe's major base metal deposits*. Dublin: IAEG, 552 S.

Leach, D. L., Bradley, D. C., Huston, D., Pisarevsky, S. A., Taylor, R. D. & Gardoll, S. J. (2010). Sediment-Hosted Lead-Zinc Deposits in Earth History. *Economic Geology* **105**, 593-625.

Leach, D. L. & Sangster, D. F. (1993). Mississippi Valley-type lead-zinc deposits. *Mineral Deposit Modeling: Geological Association of Canada, Special Paper* **40**, 289-314.

LeHuray, A. P., Caulfield, J. B. D., Rye, D. M. & Dixon, P. R. (1987). Basement controls on sediment-hosted Zn-Pb deposits; a Pb isotope study of Carboniferous mineralization in central Ireland. *Economic Geology* **82**, 1695-1709.

Li, Y. & Liu, J. (2006). Calculation of sulfur isotope fractionation in sulfides. *Geochimica et Cosmochimica Acta* **70**, 1789-1795.

Lipold, J. (1863). Über die Blei-Zink Lagerstätten Kärntens. *Österreichische Zeitschrift für Berg- und Hüttenwesen*, 173 - 174.

Ludwig, K. (2009). Isoplot 3.7; a geochronology toolkit for Microsoft Excel. A User´s Manual.

Machel, H. G., Krouse, H. R. & Sassen, R. (1995). Products and distinguishing criteria of bacterial and thermochemical sulfate reduction. *Applied Geochemistry* **10**, 373-389.

Maucher, A. & Schneider, H. J. (1957). Entstehung von Blei-Zinkerzlagerstatten in Karbonatgesteinen *Berg-und Hüttenmännisches Monatsheft der Montanistischen Hochschule Leoben* **102**, 225-256.

Melcher, F., Henjes-Kunst, F., Henjes-Kunst, E., Schneider, J. & Thöni, M. (2010). Erste Rb-Sr Isotopendatierung an Sphalerit der Zn-Pb Lagerstätte Bleiberg (Kärnten), sowie Sr- und Sm-Nd-Isotopendaten von kogenetischen Karbonat und Fluorit. *Journal of Alpine Geology* **52**.

Melcher, F., Oberthür, T. & Rammlmair, D. (2006). Geochemical and mineralogical distribution of germanium in the Khusib Springs Cu, Zn, Pb, Ag sulfide deposit, Otavi Mountain Land, Namibia. *Ore Geology Reviews* **28**, 32-56.

Melcher, F., Saini-Eidukat, B., Göttlicher, J., Steininger, R., Cook, N. & Ciobanu, C. (2009). Germanium in sphalerite and willemite at the Tres Marias mine, Mexico: An EMPA, CL, LA-ICP-MS and synchrotron study. *Hallisches Jahrbuch für Geowissenschaften*

Miller, J. (1989). Cathodoluminescence Microscopy. In: Tucker, M. E. (ed.) *Techniques in sedimentology*. Oxford Blackwell, 174 - 190.

Misra, K. (2000). *Understanding mineral deposits*: Springer.

Moenke-Blankenburg, L., Schumann, T., Gunther, D., Kuss, H.-M. & Paul, M. (1992). Quantitative analysis of glass using inductively coupled plasma atomic emission and mass spectrometry, laser micro-analysis inductively coupled plasma atomic emission spectrometry and laser ablation inductively coupled plasma mass spectrometry. *Journal of Analytical Atomic Spectrometry* **7**, 251-254.

Moh, G. H. & Jager, A. (1978). Phasengleichgewicht des Systems Ge-Pb-Zn-S in Relation zu Germaniumgehalten alpiner Pb-Zn-Lagerstätten. *Verhandlungen der Geologischen Bundesanstalt*, 437 - 440.

Mohs, F. (1807). Die Villacher Alpe und die dieselbe zunächst umgebenden Gegenden; eine geognostische Skizze. *Efemeriden der Berg u. Hüttenkunde (CE Freih. v. Moll)* **3 Bd., 2. Lieferung,** , 161-228.

Möller, P. (1985). Development and application of the Ga/Ge geothermometer for sphalerite from sediment-hosted deposits. *Monograph Series on Mineral Deposits* **25**, 15-30.

Möller, P. (1987). Correlation of homogenization temperatures of accessory minerals from sphalerite-bearing deposits and Ga/Ge model temperatures. *Chemical Geology* **61**, 153-159.

Möller, P. & Dulski, P. (1993). Germanium and gallium distribution in sphalerite. In: Möller, P. & Lüders, V. (eds.) *Formation of Hydrothermal Vein Deposits-Case study of the Pb-Zn Barite and Fluorite Deposits in the Harz Mountains*. Berlin: Bornträger, 189-196.

Möller, P., Dulski, P. & Schneider, H. J. (1983). Interpretation of Ga and Ge content in sphalerite from the Triassic Pb-Zn deposits of the Alps. In: Schneider, H. J. (ed.) *Mineral Deposits of the Alps and of the Alpine Epoch in Europe*. Berlin: Springer, 213-222.

Muchez, P., Heijlen, W., Banks, D., Blundell, D., Boni, M. & Grandia, F. (2005). 7: Extensional tectonics and the timing and formation of basin-hosted deposits in Europe. *Ore Geology Reviews* **27**, 241-267.

Nakai, S., Halliday, A. N., Kesler, S. E., Jones, H. D. & Compston, W. (1990). Rb-Sr dating of sphalerites from mississippi valley type (MVT) deposits. *Abstracts - Geological Society of Australia, vol.27*, 69.

Nakai, S. i., Halliday, A. N., Kesler, S. E., Jones, H. D., Kyle, J. R. & Lane, T. E. (1993). Rb-Sr dating of sphalerites from mississippi valley-type (MVT) ore deposits. *Geochimica et Cosmochimica Acta* **57**, 417-427.

Neubauer, F., Genser, J. & Handler, R. (1999). The Eastern Alps: Result of a two-stage collison process. *Mitteilungen der Österreichischen Geologischen Gesellschaft* **92**, 117 - 134.

Ohmoto, H. & Goldhaber, M. B. (1997). Sulfur and carbon isotopes. In: Barnes, H. L. (ed.) *Geochemistry of hydrothermal ore deposits*. New York, NY Wiley, XX, 972 S.

Ohmoto, H. & Rye, R. O. (1979). Isotopes of Sulfur and Carbon. In: Barnes, H. L. (ed.) *Geochemistry of hydrothermal ore deposits*. New York, NY Wiley, XVI, 798 S.

Peters, K. (1856). Die Umgebung von Deutsch-Bleiberg in Kärnten. *Jahrbuch der Geologischen Reichsanstalt* **7**, 67-89.

Pettke, T. & Diamond, L. W. (1995). Rb-Sr isotopic analysis of fluid inclusions in quartz: Evaluation of bulk extraction procedures and geochronometer systematics using synthetic fluid inclusions. *Geochimica et Cosmochimica Acta* **59**, 4009-4027.

Pfaff, K., Koenig, A., Wenzel, T., Ridley, I., Hildebrandt, L. H., Leach, D. L. & Markl, G. (2011). Trace and minor element variations and sulfur isotopes in crystalline and colloform ZnS: Incorporation mechanisms and implications for their genesis. *Chemical Geology* **286**, 118-134.

Pimminger, M., Grasserbauer, M., Schroll, E. & Cerny, I. (1985). Trace element distribution in sphalerites from Pb−Zn-ore occurrences of the Eastern Alps. *Mineralogy and Petrology* **34**, 131-141.

Posepny, F. (1873). Die Blei-und Galmei-Erzlagerstätten von Raibl in Kärnten. *Jahrbuch der Geologischen Reichsanstalt* **23**, 317-424.

Posepny, F. (1894). Über die Entstehung der Blei-und Zinklagerstäten in auflöslichen Gesteinen. *Berg- und Hüttenmännisches Monatsheft* **42**, 77-130.

Posepny, F. (1895). The genesis of ore deposits. New York: American Institute of Mining Ingeneering.

Potiorek, P. (1863). Über die Erzlagerstätte des Bleiberger Erzberges. *Österreichische Zeitung für Berg- und Hüttenwesen* **11**, 373-375.

Prasnik, H., Niedermayr, G. & Brandstätter, F. (2008). Neue Mineralfunde aus Österreich LVII. 1519) Baryt, Cerrusit, Dolomit, Galenit, Hydrozinkit, Pyrit, Smithonit und Wulfenit von "Töplitsch" bei Stadelbach, Kärnten. *Carinthia II* **198./118**, 226 - 227.

Rantitsch, G. (2001). Thermal history of the Drau Range (Eastern Alps). *Schweizerische Mineralogische und Petrographische Mitteilungen* **81**, 181-196.

Rantitsch, G., Jochum, J., Sachsenhofer, R. F., Russegger, B. & Schroll, E. (1999). Hydrocarbon-bearing fluid inclusions in the Drau Range (Eastern Alps, Austria); implications for the genesis of bleiberg-type Pb-Zn deposits. *Mineralogy and Petrology* **65**, 141-159.

Recnik, A. (2011). *Die Mineralien der Blei-und Zinklagerstätte Mezica*: Bode Verlag.

Rimstidt, J. D. (1997). Gangue mineral transport and deposition. In: Barnes, H. L. (ed.) *Geochemistry of hydrothermal ore deposits*. New York: John Wiley and Sons Ico, 487-515.

Robinson, B. W. & Kusakabe, M. (1975). Quantitative preparation of sulfur dioxide, for sulfur-34/sulfur-32 analyses, from sulfides by combustion with cuprous oxide. *Analytical Chemistry* **47**, 1179-1181.

Roedder, E. (1968). The non-colloidal origin of 'colloform' textures in sphalerite ores. *Economic Geology* **63**, 451-471.

Rollinson, H. R. (1996). *Using geochemical data -evaluation, presentation, interpretation*. Harlow: Longman Group.

Saini-Eidukat, B., Melcher, F. & Lodziak, J. (2009). Zinc-germanium ores of the Tres Marias Mine, Chihuahua, Mexico. *Mineralium Deposita* **44**, 363-370.

Schmid, S. M., Fügenschuh, B., Kissling, E. & Schuster, R. (2004). Tectonic map and overall architecture of the Alpine orogen. *Eclogae Geologicae Helvetiae* **97**, 93-117.

Schmidt, T., Blau, J. & Kazmer, M. (1991). Large-scale strike-slip displacement of the Drauzug and the Transdanubian Mountains in early Alpine history: Evidence from permo-mesozoic facies belts. *Tectonophysics* **200**, 213-232.

Schneider, H.-J. (1964). Facies Differentiation and Controlling Factors for the Depositional Lead-Zinc Concentration in the Ladinian Geosyncline of the Eastern Alps. In: Amstutz, G. C. (ed.) *Developments in Sedimentology*: Elsevier, 29-45.

Schneider, H. J. (1953). Neue Ergebnisse zur Stoffkonzentration und Stoffwanderung in Blei-Zink-Lagerstätten der nördlichen Kalkalpen. *Fortschritte der Mineralogie* **32**, 26-30.

Schoonen, M. A. A. & Barnes, H. L. (1991). Reactions forming pyrite and marcasite from solution: II. Via FeS precursors below 100° C. *Geochimica et Cosmochimica Acta* **55**, 1505-1514.

Schroll, E. (1955). Über das Vorkommen einiger Spurenmetalle in Blei-Zink-Erzen der ostalpinen Metallprovinz. *Tschermaks mineralogische und petrographische Mitteilungen* **5**, 183-208.

Schroll, E. (1983). Geochemical characterization of the Bleiberg type and other carbonate hosted lead-zinc mineralizations. *Mineral Deposits of the Alps and of the Alpine Epoch in Europe*: Springer, 189-197.

Schroll, E. (1996). The Triassic carbonate-hosted Pb-Zn mineralization in the Alps (Europe): The genetic position of Bleiberg type deposits. *Carbonate-hosted lead-zinc deposits, Special Pub*.

Schroll, E. (1997). Geochemische und geochronologische Daten und Erläuterungen. In: Weber, L. (ed.) *Handbuch der Lagerstätten der Erze, Industrieminerale und Energierohstoffe Österreichs*. Wien: Archiv für Lagerstättenforschung der Geologischen Bundesanstalt, 395 - 537.

Schroll, E. (2006). Neues zur Genese der Blei-Zink-Lagerstaette Bleiberg. New results on the genesis of the Bleiberg lead-zinc deposit. *Carinthia II* **116**, 483-500.

Schroll, E. (2008). *Die Blei-Zink-Lagerstätte Bleiberg - die Geschichte ihrer Erforschung*. Klagenfurt: Carinthia II.

Schroll, E., Köppel, V. & Cerny, I. (2006). Pb and Sr isotope and geochemical data from the Pb-Zn deposit Bleiberg (Austria); constraints on the age of mineralization. *Mineralogy and Petrology* **86**, 129-156.

Schroll, E. & Rantitsch, G. (2005). Sulphur isotope patterns from the Bleiberg deposit (Eastern Alps) and their implications for genetically affiliated lead-zinc deposits. *Mineralogy and Petrology* **84**, 18.

Schroll, E., Schulz, O. & Pak, E. (1983). Sulphur isotope distribution in the Pb-Zn-deposit Bleiberg (Carinthia;Austria). *Mineralium Deposita* **18**, 17-25.

Schroll, E. & Wedepohl, K. H. (1972). Schwefelisotopenuntersuchungen an einigen Sulfid- und Sulfatmineralen der Blei-Zink-Erzlagerstätte Bleiberg/Kreuth, Kärnten. *Tschermaks mineralogische und petrographische Mitteilungen* **17**, 286-290.

Schulz, O. (1954). Gefügekundlich-tektonische Analyse des Blei-Zink-Bergbaugebietes Lafatsch (Karwendelgebirge, Tirol). *Berg und Hüttenmännisches Montatsheft* **100**, 259 - 269.

Schulz, O. (1958). Die Pb-Zn Vererzungen der Raibler Schichten im Bergbau Bleiberg-Kreuth (Grube Max) als Beispiel submariner Lagerstättenbildung. *Carinthia II* **37**.

Schulz, O. (1960). Die Pb-Zn Vererzung der Raibler Schichten im Bergbau Bleiberg-Kreuth (Grube Max) als BEispiel submariner Lagerstättenbildung. *Carinthia II* **Sh. 22**, 93.

Schulz, O. (1964). Lead-Zinc Deposits in the Calcareous Alps as an Example of Submarine-Hydrothermal Formation of Mineral Deposits. In: Amstutz, G. C. (ed.) *Developments in Sedimentology*: Elsevier, 47-52.

Schulz, O. (1968). Die synsedimentaere Mineralparagenese im oberen Wettersteinkalk der Pb-Zn-Lagerstaette Bleiberg-Kreuth (Kaernten). The syngenetic mineral paragenesis in the upper Wetterstein limestone of the Bleiberg-Kreuth lead-zinc deposit, Carinthia. *Tschermaks mineralogische und petrographische Mitteilungen* **12**, 230-289.

Schulz, O. (1985). Ausgewaehlte Gefuegebefunde in der kalkalpinen Pb-Zn-Lagerstaette Bleiberg-Kreuth (Gailtaler Alpen, Kaernten). Structural conditions of the Limestone Alps lead-zinc deposits of Bleiberg-Kreuth; Gailtal Alps, Carinthia. *Archiv für Lagerstättenforschung der Geologischen Bundesanstalt* **6**, 91-99.

Schulz, O. (2006). Die Entstehung der Bleiberger Lagerstätte. *Res Montanerum* **39**, 3 - 11.

Schulz, O., Niedermayr, G., Bouvier, M., Enzfelder, W., Glantschnig, N., Kostelka, L. & Rainer, H. (1972). Zur mineralogie Bleibergs. The mineralogy of Bleiberg. *Veröffentlichungen aus dem Naturhistorischen Museum in Wien, Neue Folge* **6**, 15-20.

Schulz, O. & Schroll, E. (1977). Die Pb-Zn Lagerstaette Bleiberg-Kreuth; Stand der geowissenschaftlichen Forschung 1976, Projekt 2437, 2776 S. The Bleiberg-Kreuth lead-zinc deposit; state of geologic research 1976, Project 2437, 2776 S. *Verhandlungen der Geologischen Bundesanstalt* **1977**, 375-386.

Schuster, R. & Frank, W. (1999). Metamorphic evolution of the Austroalpine units east of the Tauern window: indications for Jurrasic strike slip tectonics. *Mitteilungen der Gesellschaft der Geologie- und Bergbaustudenten Österreich* **42**, 37 - 58.

Scott, V. D. & Love, G. (1983). *Quantitative electron-probe microanalysis*: Halsted Press.

Seal, R. R., II. (2006). Sulfur isotope geochemistry of sulfide minerals. *Reviews in Mineralogy and Geochemistry* **61**, 633-677.

Sicree, A. A. & Barnes, H. L. (1996). Upper Mississippi Valley district ore fluid model: the role of organic complexes. *Ore Geology Reviews* **11**, 105-131.

Siegl, W. (1956). Bilder zur Syngenese der Bleiberger Vererzung. *Verhandlungen der Geologischen Bundesanstalt* **6**, 179 - 182.

Siegl, W. (1957). Diskussionsbemerkung zum Thema: Entstehung von Blei-Zinklagerstätten in Karbonatgesteinen. *Berg- und Hüttenmännisches Montatsheft* **9**, 237 - 238.

Siivola, J. & Schmid, R. (2007). List of mineral abbreviations. Cambridge University Press: New York, 93-110.

Sims, P. K., Barton, P. B. & Barnett, P. R. (1961). Some aspects of the geochemistry of sphalerite, Central City District, Colorado. *Economic Geology* **56**, 1211-1237.

Spangenberg, J. E. & Herlec, U. (2006). Hydrocarbon biomarkers in the Topla-Mezica zinc-lead deposits, northern Karavanke/Drau Range, Slovenia; paleoenvironment at the site of ore formation. *Economic Geology and the Bulletin of the Society of Economic Geologists* **101**, 997-1021.

Spangenberg, J. E., Lavric, J. V. & Herlec, U. (2001). Sulfur-isotope study of the Mezica mississippi valley-type lead-zinc ore deposits, Slovenia. In: Piestrzynski, A. (ed.) *Proceedings of the 6th Biennial SGA Meeting, vol.6*, 181-184.

Stacey, J. S. t. & Kramers, J. D. (1975). Approximation of terrestrial lead isotope evolution by a two-stage model. *Earth and Planetary Science Letters* **26**, 207-221.

Stanton, R. L. & Russell, R. D. (1959). Anomalous leads and the emplacement of lead sulfide ores. *Economic Geology* **54**, 588-607.

Steiger, R. H. & Jäger, E. (1977). Subcommission on geochronology: convention on the use of decay constants in geo-and cosmochronology. *Earth and Planetary Science Letters* **36**, 359-362.

Strucl, I. (1974). Die Entstehungsbedingungen der Karbonatgesteine und Blei-Zinkvererzungen in den Anisschichten von Topla. *Geologija* **17**, 299-397.

Suess, E. (1869). Geognostisch-bergmännische Skizze von Bleiberg. *Österreichische Zeitung für Berg- und Hüttenwesen*, 259 - 262, 266- 267.

Taupitz, K. C. (1953). Die verschiedene Deutbarkeit von ‚metasomatischen" Gefügen auf "telethermalen" Blei-Zink-Lagerstätten. *Fortschritte der Mineralogie* **32**, 30-31.

Thirlwall, M. F. (2000). Inter-laboratory and other errors in Pb isotope analyses investigated using a ^{207}Pb- ^{204}Pb double spike. *Chemical Geology* **163**, 299-322.

Thirlwall, M. F. (2002). Multicollector ICP-MS analysis of Pb isotopes using a ^{207}Pb-^{204}Pb double spike demonstrates up to 400 ppm/amu systematic errors in Tl-normalization. *Chemical Geology* **184**, 255-279.

Timm, C., Hoernle, K., Werner, R., Hauff, F., den Bogaard, P. v., Michael, P., Coffin, M. F. & Koppers, A. (2011). Age and geochemistry of the oceanic Manihiki Plateau, SW Pacific: New evidence for a plume origin. *Earth and Planetary Science Letters* **304**, 135-146.

Tollmann, A. (1977). *Die Zentralalpen, Geologie von Österreich mit 25 Tabellen*. Wien: Deuticke.

Tornquist, A. (1927). *Die Blei-Zinkerzlagerstatte von Bleiberg-Kreuth in Kärnten*: Springer.

van Achterbergh, E., Ryan, C. G. & Griffin, W. L. (2000). GLITTER (Version 3.0, On-line Interactive Data Reduction for LA-ICPMS, Macquarie Research Ltd.).

Wagner, T., Boyce, A. J. & Fallick, A. E. (2002). Laser combustion analysis of δ^{34}S of sulfosalt minerals: determination of the fractionation systematics and some crystal-chemical considerations. *Geochimica et Cosmochimica Acta* **66**, 2855-2863.

Warren, J. K. (2000). Evaporites, brines and base metals: Low-temperature ore emplacement controlled by evaporite diagenesis. *Australian Journal of Earth Sciences* **47**, 179-208.

Weber, L. (1997). Die metallogenetischen Einheiten Österreichs. *Handbuch der Lagerstätten der Erze, Industrieminerale und Energierohstoffe Österreichs*. Wien: Archiv fur Lagerstättenforschung der Geologischen Bundesanstalt, 230 - 394.

Wilkinson, J. J., Eyre, S. L. & Boyce, A. J. (2005). Ore-Forming Processes in Irish-Type Carbonate-Hosted Zn-Pb Deposits: Evidence from Mineralogy, Chemistry, and Isotopic Composition of Sulfides at the Lisheen Mine. *Economic Geology* **100**, 63-86.

Xiong, Y. (2007). Hydrothermal thallium mineralization up to 300°C: A thermodynamic approach. *Ore Geology Reviews* **32**, 291-313.

Zartman, R. E. & Doe, B. R. (1981). Plumbotectonics -the model. *Tectonophysics* **75**, 135-162.

Zeeh, S. (1994). The unusual cyclicity of the Triassic (Carnian) Bleiberg facies of the Wetterstein Formation (Drau Range, Austria). *Geologische Rundschau* **83**, 130-142.

Zeeh, S. & Bechstädt, T. (1994). Carbonate-Hosted Pb-Zn Mineralization at Bleiberg-Kreuth (Austria): Compilation of Data and New Aspects. In: Fontbote, L. & Boni, M. (eds.) *Sediment-Hosted Zn-Pb Ores*: Springer Berlin Heidelberg, 271-296.

Zeeh, S., Kuhlemann, J. & Bechstädt, T. (1998). The classical Pb-Zn deposits of the eastern Alps (Austria/Slovenia) revisited: MVT deposits resulting from gravity driven fluid flow in the Alpine realm. *Geologija* **41**, 257-273.

Zeeh, S. & Staerk, A. (1992). Cyclicity of the Triassic (Carnian) "Bleiberg Facies" of the Wetterstein Formation (Drau Range/Austria). *International Association of Sedimentologists Regional Meeting, vol.13*. location varies: International Association of Sedimentologists, 169.

Web Resources

iris – Online: Interaktives RohstoffInformationsSystem Metallogenetische Karte von Österreich. Geololgische Bundesanstalt

http://geomap.geolba.ac.at/IRIS/IRIS_main.cfm?Init=false

APPENDIX

Table 1: Investigated Bleiberg samples.
Besides a detailed describtion of the origin (ore horizon, shaft) the collection from which it was obtained and a macroscopic describtion of the sample is given. M. B. = Maxer Bänke, Ek. = Erzkalk, Js. =Josefischolle (crest), Rs. = Riedhardtscholle (crest), Ks. = Kalkscholle (crest), ? = unknown ore horizon.

Bleiberg					
sample ID	section ID	ore horizon	origin	collection	macroscopic description
EHK01	EHK01	M. B.	Antoni, 12. Lauf	Uni Wien	Young calcareous spar
Blb20	Blb20	M. B.	Bellegarde-Schachtl Läufl	O. Schulz	Ore Breccia
Blb11	Blb11	M. B.	Bellegarde-Schachtl Läufl	O. Schulz	Coarse-grained ZnS accumulation
Blb17	Blb17	M. B.	Bellegarde-Schachtl Läufl	O. Schulz	Schalenblende + in layers enriched ZnS
Blb26	Blb26	M. B.	Bellegarde-Schachtl Läufl	O. Schulz	Layered ZnSxx
EHK05	EHK05	Ek.	Antoni, Pflockschachtlager	Uni Wien	Fine-grained ore accumulations
EHK10	EHK10	Ek.	Antoni, 8. Lauf Pflockschachtlager	Uni Wien	ZnS accumulations
WS_Blb01	WS_Blb01	Ek.	Stephanie, 12. Lauf	W. Siegl (MUL)	Weakly mineralizaed breccia
WS_Blb07	WS_Blb07	Ek.	Rudolf, Pflockschachtlager	W. Siegl (MUL)	Calcareous bottom ore
WS_Blb25	WS_Blb25	Ek.	Antoni, 3er Lager	W. Siegl (MUL)	Nearly free of ZnS
WS_Blb06	WS_Blb06	Ek.	Stefanie, 12. Lauf	W. Siegl (MUL)	Ore breccia, ZnS, PbS, FeS2
EHK02	EHK02	Ek.	Antoni, 6. Lauf Pflockschachtlager	Uni Wien	Cockade Ore: ZnSxx-PbSxx, PbSxx-schalenblende
J10.1	AS8616a	Js.	Westschachtlauf	BGR (Melcher, Schulz)	Network ZnS mineralization
J10.4	AS8619a	Js.	Westschachtlauf	BGR (Melcher, Schulz)	Schalenblende Oncoids + galena
R6.1	AS8608a	Rs.	Westschachtlauf	BGR (Melcher, Schulz)	Massive ZnS mineralization
R11.1	AS8612b	Rs.	Westschachtlauf	BGR (Melcher, Schulz)	Massive ZnS mineralization
R8/2	R8/2	Rs.	Westschachtlauf	BGR (Melcher, Schulz)	Breccia Ore
K2-2	K2-2	Ks.	Westschachtlauf	BGR (Melcher, Schulz)	Massive mineralization
E14.6	E14.6	Erl.	Westschachtlauf	BGR (Melcher, Schulz)	Massive mineralization (schalenblende, ZnSxx, PbS)
E14.2-4	AS8602a	Erl.	Westschachtlauf	BGR (Melcher, Schulz)	Schalenblende + PbS
E14.3	AS8604a	Erl.	Westschachtlauf	BGR (Melcher, Schulz)	Massive breccia mineralization
C6.12	AS8589	1st R.	Westschachtlauf	BGR (Melcher, Schulz)	Breccia ore+ZnSxx
C6.14	AS8591a	1st R.	Westschachtlauf	BGR (Melcher, Schulz)	Breccia ore+ZnSxx
WS_Blb29	WS_Blb29	1st R.	Bleiberg Kreuth	W. Siegl (MUL)	Massive breccia mineralization
EHK11	EHK11	?	Max, Georgistollen	Uni Wien	Schalenblende mineralization
EHK23	EHK23	?	3. Lauf, Neujahrigang, 6.2 m	Uni Wien	Network mineralization
Blb122	Blb122	?	Rublandstollen	O. Schulz	Schalenblende mineralization
Blb26AS	Blb26AS	?	Antoni, 6. Lauf Unterbau	O. Schulz	Fine-grained disseminated ore + barite
WS_Blb24	WS_Blb24	?	Hauptwestschlag, 11. Lauf	W. Siegl (MUL)	Massive Ore (partly oolitic): PbS, ZnS, FeS2

Table 1: Continued Bleiberg sample list, showing which investigation approaches were performed in order to get information on the ore minerals. * = samples were prepared for analysis, but results are pending due to preparation difficulties (not known if results will be obtained).

Bleiberg						
sample ID	**EMP**	**CL**	**$\delta^{34}S$**	**Pb Isotopes**	**Rb-Sr ZnS**	**gangue**
EHK01	MUL	x	-	-	-	-
Blb20	MUL	-	-	-	-	-
Blb11	MUL	-	-	-	-	-
Blb17	BGR/MUL	x	x	*	*	*
Blb26	BGR/MUL	x	x	-	-	-
EHK05	MUL	x	-	-	-	-
EHK10	MUL	x	-	-	-	-
WS_Blb01	MUL	-	-	-	-	-
WS_Blb07	MUL	-	PbS	-	-	-
WS_Blb25	MUL	x	-	-	-	-
WS_Blb06	BGR/MUL	-	-	-	-	-
EHK02	BGR/MUL	x	-	ZnS/PbS	*	*
			$PbS/ZnS/FeS_2$			
			-		x	
J10.1	BGR (diploma thesis)	x (diploma)			J. Schneider	-
J10.4	BGR (diploma thesis)	x (diploma)	ZnS/PbS	x	x	*
			-		x	
R6.1	BGR (diploma thesis)	-		-	J. Schneider	-
			-		x	
R11.1	BGR (diploma thesis)	-		-	J. Schneider	-
R8/2	MUL		ZnS/FeS_2	*	*	*
K2-2	MUL	x	ZnS	*	*	*
E14.6	MUL	-	-	ZnS/PbS	x	-
			ZnS/PbS		x	
E14.2-4	BGR (diploma thesis)	x (diploma)		*	J. Schneider	*
			ZnS		x	
E14.3	BGR (diploma thesis)	x (diploma)		*	J. Schneider	*
C6.12	BGR (diploma thesis)	-	-	-	-	-
C6.14	BGR (diploma thesis)	x (diploma)	ZnS	ZnS	x	
WS_Blb29	MUL/BGR	x	-	-	-	-
EHK11	MUL	x	-	-	-	-
EHK23	MUL	x	-	-	-	-
Blb122	MUL	x	-	-	-	-
Blb26AS	MUL	x	-	-	-	-
WS_Blb24	MUL	-	-	-	-	-

Table 2: List of the investigated Mezica and Topla samples.
Furthermore, information on sample origin and a macroscopic description are given. Ek* = Erzkalk equivalent ore horizon, Anis. = Anisian (Muschelkalk Formation).

Mezica					
sample ID	**section ID**	**ore horizon**	**origin**	**collection**	**macroscopic description**
Mz02b	Mz02b	Ek.*	Moring 8. Lauf	Sampling Nov. 10	ZnS-PbS (dissemminated)
Mz01.1	Mz01.1	Ek.*	Moring 8. Lauf	Sampling Nov. 10	Fine-grained ZnS + gangue breccia
Mz08	Mz08	Ek.*	Moring 8. Lauf	Sampling Nov. 10	Massive PbS + ZnS
Mz09	Mz09	Ek.*	Union, 9. Lauf	Sampling Nov. 10	ZnS + PbS
MzH01	MzH01	Ek.*	Helena, 0. Lauf	Sampling May 11	Massive ZnS + PbS
SF04	SF04	Ek.*	Graben	S. Fajmuth	Irregular schalenblende mineralization
SF03	SF03	Ek.*	Graben	S. Fajmuth	Irregular schalenblende mineralization
Topla					
sample ID	**section ID**	**ore horizon**	**origin**	**collection**	**macroscopic description**
Tp01	Tp01	Anis.	Topla dumps	Sampling Nov. 10	very fine grained ZnS, Macroscopic FeS_2
Tp04	Tp04	Anis.	Topla dumps	Sampling Nov. 10	very fine grained ZnS, Macroscopic FeS_2
Tp05	Tp05	Anis.	Topla dumps	Sampling Nov. 10	very fine grained ZnS, Macroscopic FeS_2
Tp06	Tp06	Anis.	Topla dumps	Sampling Nov. 10	very fine grained ZnS, Macroscopic FeS_2
BGR_Tp01	BGR_Tp01	Anis.	1043 NN, Versuchsstollen	BGR collection	very fine grained ZnS, Macroscopic FeS_2

Table 2: Continued. Investigation approaches, carried out on the ore minerals in order to determine the formation mechanisms. * = samples were prepared for analysis, but results are pending due to preparation difficulties (not known if results will be obtained).

Mezica						
sample ID	**EMP**	**CL**	**$\delta^{34}S$**	**Pb Isotopes**	**Rb-Sr ZnS**	**gangue**
Mz02b	MUL	x	-	-	-	-
Mz01.1	MUL	x	-	-	-	-
Mz08	MUL/BGR	x	ZnS/PbS	ZnS/PbS	x	-
Mz09	MUL	x	-	-	-	-
MzH01	MUL	-	Zn/PbS	ZnS/PbS	x	-
SF04	MUL	-	-	-	-	-
SF03	MUL	-	ZnS/FeS2	*	*	*
Topla						
sample ID	**EMP**	**CL**	**$\delta^{34}S$**	**Pb Isotopes**	**Rb-Sr ZnS**	**gangue**
Tp01	MUL	x	ZnS/FeS2	*	*	*
Tp04	BGR/MUL	x	ZnS/FeS2	*	*	*
Tp05	MUL	x	-	-	-	-
Tp06	MUL	x	-	-	-	-
BGR_Tp01	MUL	-	-	-	-	-

Table 3: Investigated samples from other small Pb-Zn Drau Range deposits and samples from other occurrences in the Alps (not Drau Range).

Ek* = Erzkalk equivalent units, Anis. = Anisian (Muschelkalk).

other Pb-Zn occurrences, Drau Range					
sample ID	**section ID**	**ore horizon**	**origin**	**collection**	**macroscopic description**
EHK16	EHK16	Ek.*	Radnig	MUL (Schroll, Stumpfl)	Massive ore, partly fractured
EHK17	EHK17	Ek.*	Windisch Bleiberg	MUL (Schroll, Stumpfl)	ZnS accumulations
JK5-9	JK5-9	Ek.*	Jauken	Sampling June 11	ZnS impregnation
Toe01	Toe01	Ek.*	Töplitsch	Sampling June 11	ZnSxx + gangue brecia
Toe02	Toe02	Ek.*	Töplitsch	Sampling June 11	ZnSxx + gangue brecia
Pb-Zn occurrences, not Drau Range					
sample ID	**section ID**	**ore horizon**	**origin**	**collection**	**macroscopic description**
Rd01.1	Rd01.1	Anis.	Zunderwandt, Middle Austroalpine	Sampling, Aug. 12	Hydrothermal Breccia, ZnS; Fluorite
BGR_Ra1	BGR_Ra1	Ek.*	Raibl, Southern Alps	BGR collection	Red Schalenblende
BGR_La1	BGR_La1	Ek.*	Lafatsch, Northern CA	BGR collection	Massive ZnS + PbS

Table 3: Continued. List showing the analysis, which were performed in order to investigate the ore forming mechanisms. * = samples were prepared for analysis, but results are pending due to preparation difficulties (not known if results will be obtained).

other Pb-Zn occurrences, Drau Range						
sample ID	**EMP**	**CL**	**$\delta^{34}S$**	**Pb Isotopes**	**Rb-Sr ZnS**	**gangue**
EHK16	MUL	-	-	-	-	-
EHK17	MUL	-	-	-	-	-
JK5-9	BGR/MUL	x	ZnS	ZnS	x	*
Toe01	BGR/MUL	x	ZnS	*	*	*
Toe02	MUL	-	-	-	-	-
Pb-Zn occurrences not Drau Range						
sample ID	**EMP**	**CL**	**$\delta^{34}S$**	**Pb Isotopes**	**Rb-Sr ZnS**	**gangue**
Rd01.1	MUL	-	ZnS	*	*	*
BGR_Ra1	MUL	-	-	-	-	-
BGR_La1	MUL	-	-	-	-	-

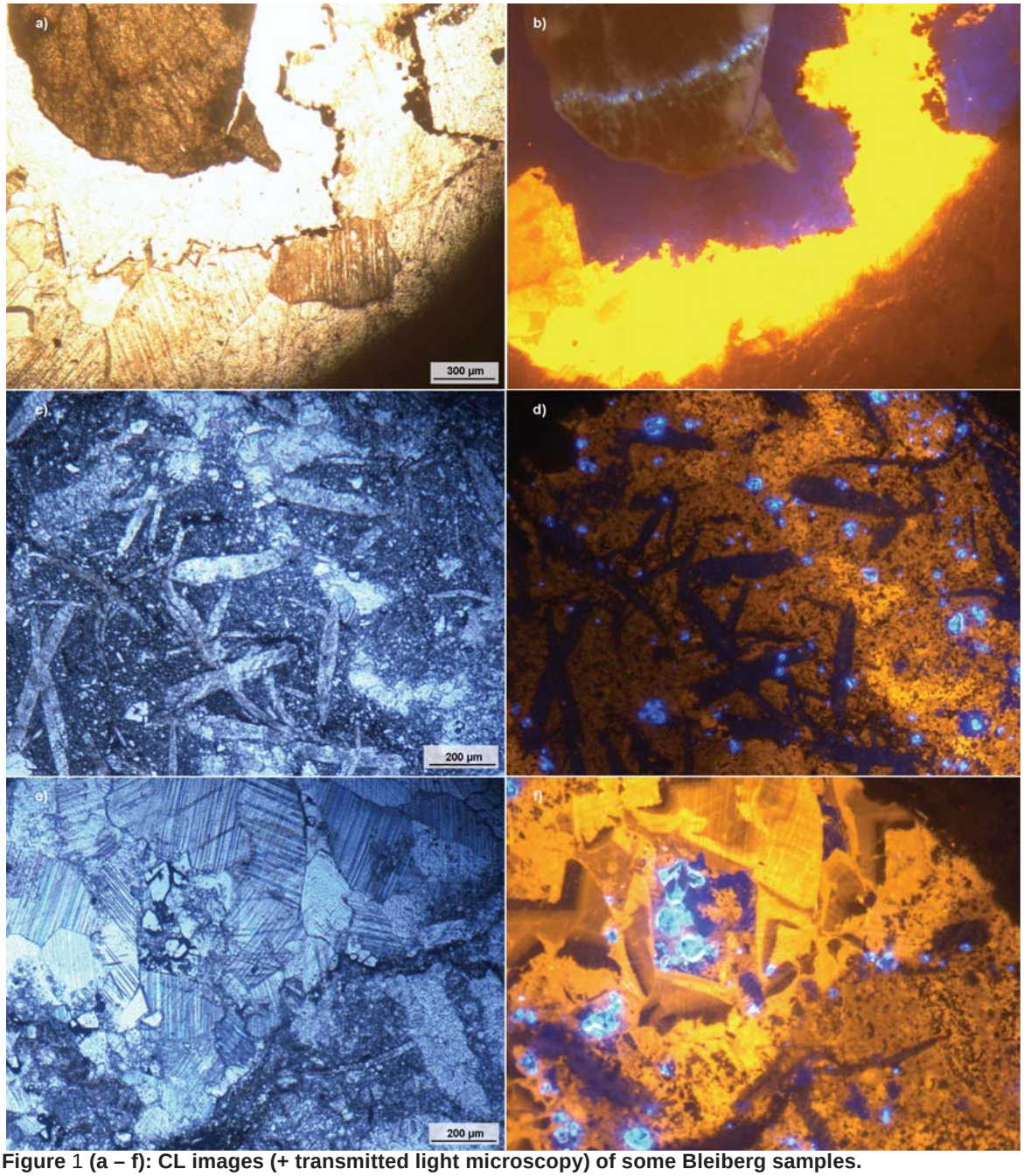

Figure 1 (a – f): CL images (+ transmitted light microscopy) of some Bleiberg samples. a & b) Sample EHK01, Maxer Bänke (Bleiberg). Brown sphalerite aggregate (upper left corner), which exhibits nearly no CL. It is surrounded by dark blue luminescent fluorite. The gangue consists of dolomite, which shows partly a yellow luminescence. The yellow CL of the dolomite results from a slight overexposure. c &d) Sample WS_Blb38, Bleiberg unknown ore horizon. Elongated barite crystals (dark blue CL) besides bright blue luminescent ZnS in a dolomite gangue (orange CL). e & f) Sample WS_Blb38, unknown ore horizon (Bleiberg). Orange luminescent dolomite, showing partly a zonation. Furthermore, fine-grained sphalerite (bright blue CL), which occurs within the interstitials of the coarse-grained dolomite.

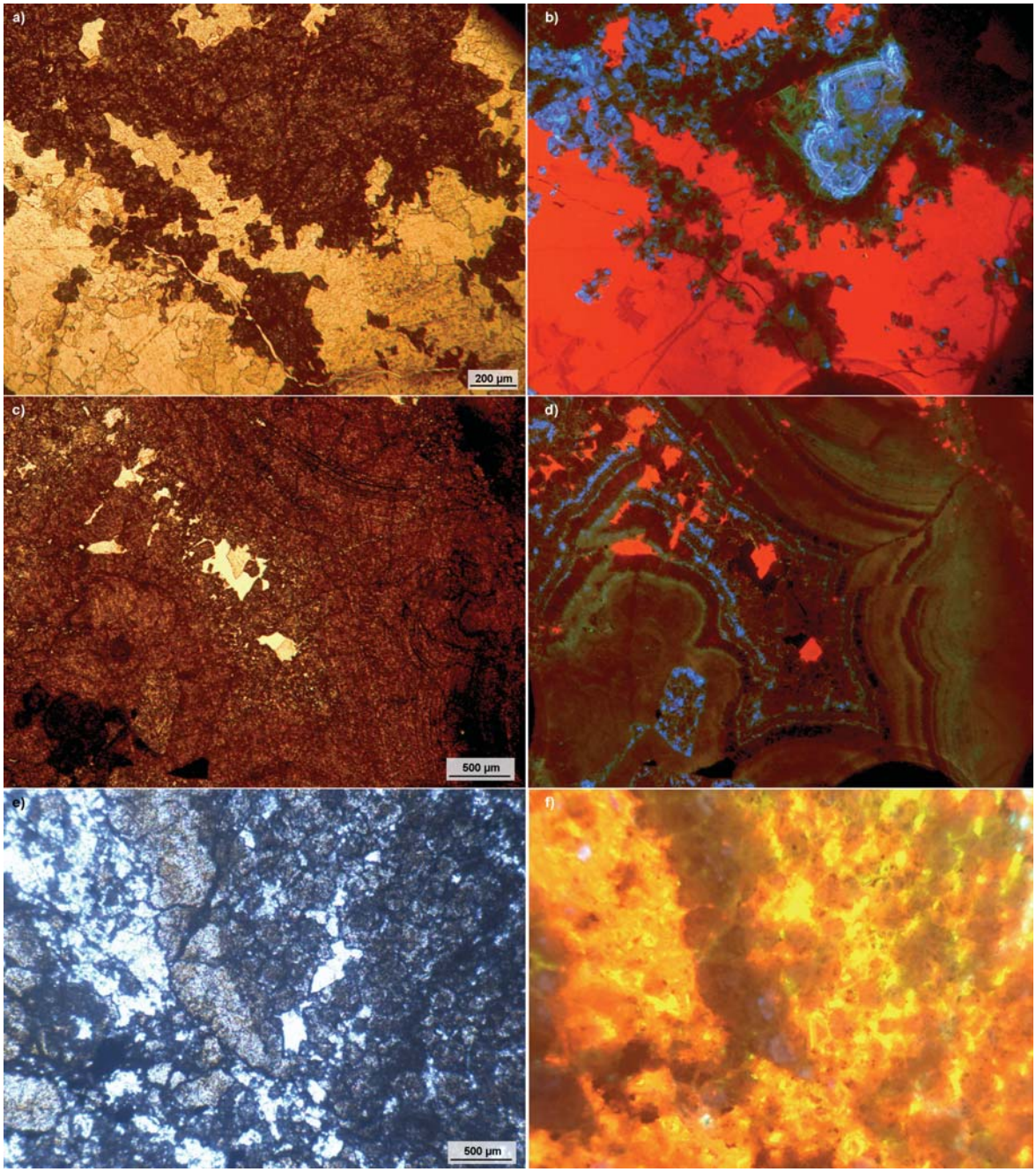

Figure 2 (a - f): CL images (+ trasnmitted light microscopy -) of some crest horizon samples (Bleiberg). a & b) Sample J10.1, Josefischolle (Bleiberg). Brown sphalerite aggregate, which exhibits blue and green CL colors. The gangue is composed of carbonates and shows red CL. c & d) Sample J10.4, Josefischolle (Bleiberg). Green, blue and brownish luminescent schalenblende. The carbonate gangue shows a red CL color. e & f) Sample K2-2, Kalkscholle (Bleiberg). Coarse-grained sphalerite aggregate (central upper part of the photograph), which shows dull brown-bluish-greenish CL colors. The sphalerites in this sample show generally only dull CL colors. The dolomite gangue has a orange CL, the yellow parts result from a overexposure, which was necessary in order to display the CL behavior of the sphalerite.

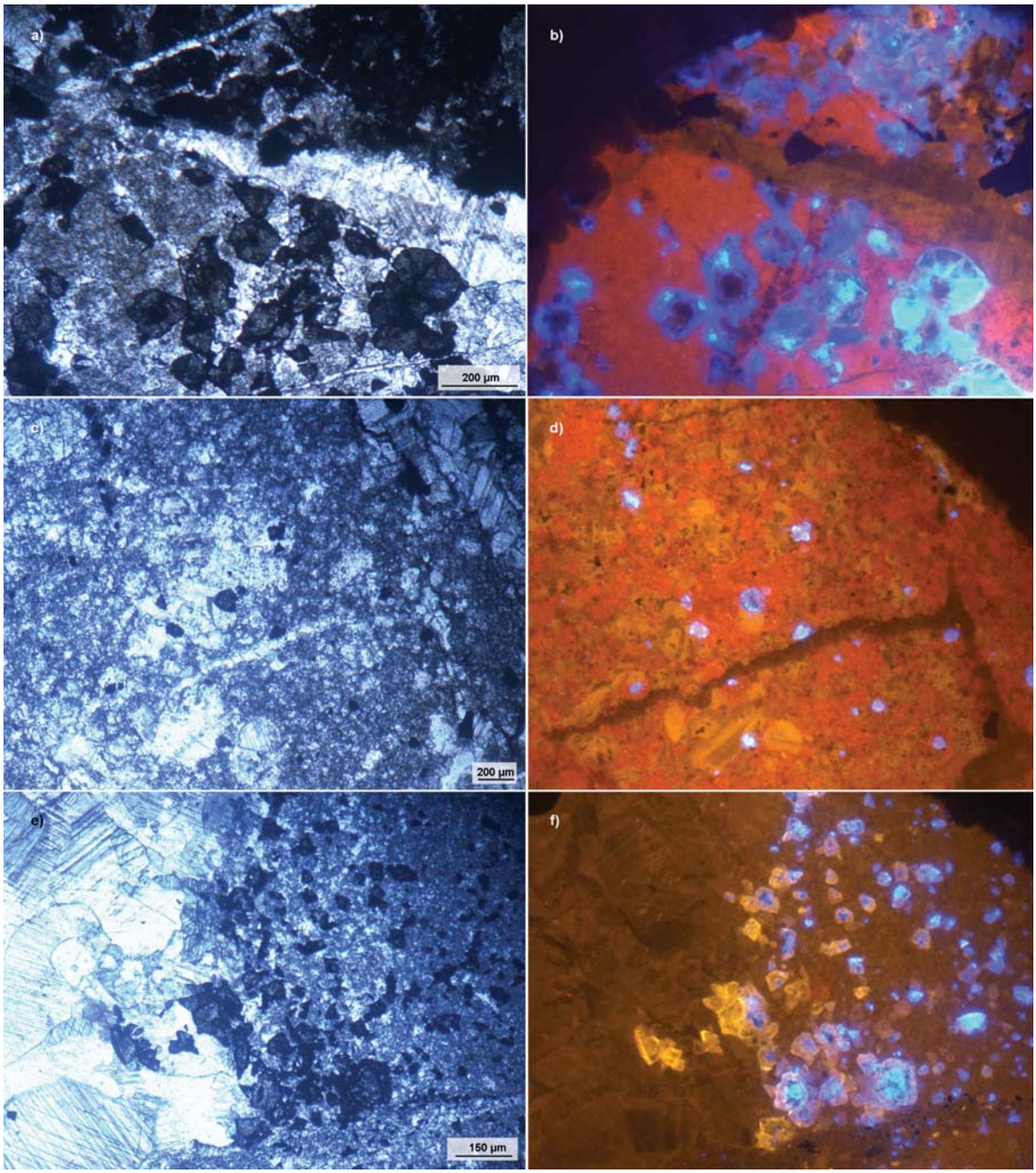

Figure 3 (a – f): CL images (+ transmitted light microscopy) of some Mezica samples. a & b) Sample Mz05, Moring (8th level). Sphalerite grains, which are characterized by blue CL color. Within larger (> 200 µm) grains a zonation is evident. The cores of larger grains have a dark brown color (transmitted light microscopy). This zonation is also evident within the CL behavior. The core of the larger grains shows a dark blue CL. c & d) Sample Mz07a, Union (10th level). Bright blue luminescent sphalerite, hosted by dolomite. The dolomite displays orange CL colors. e & f) Sample Mz08, Moring (8th level). Sphalerite grains, which exhibit partly already the zonation (bright blue-dark blue-orange) that is described in chapter 8.6.

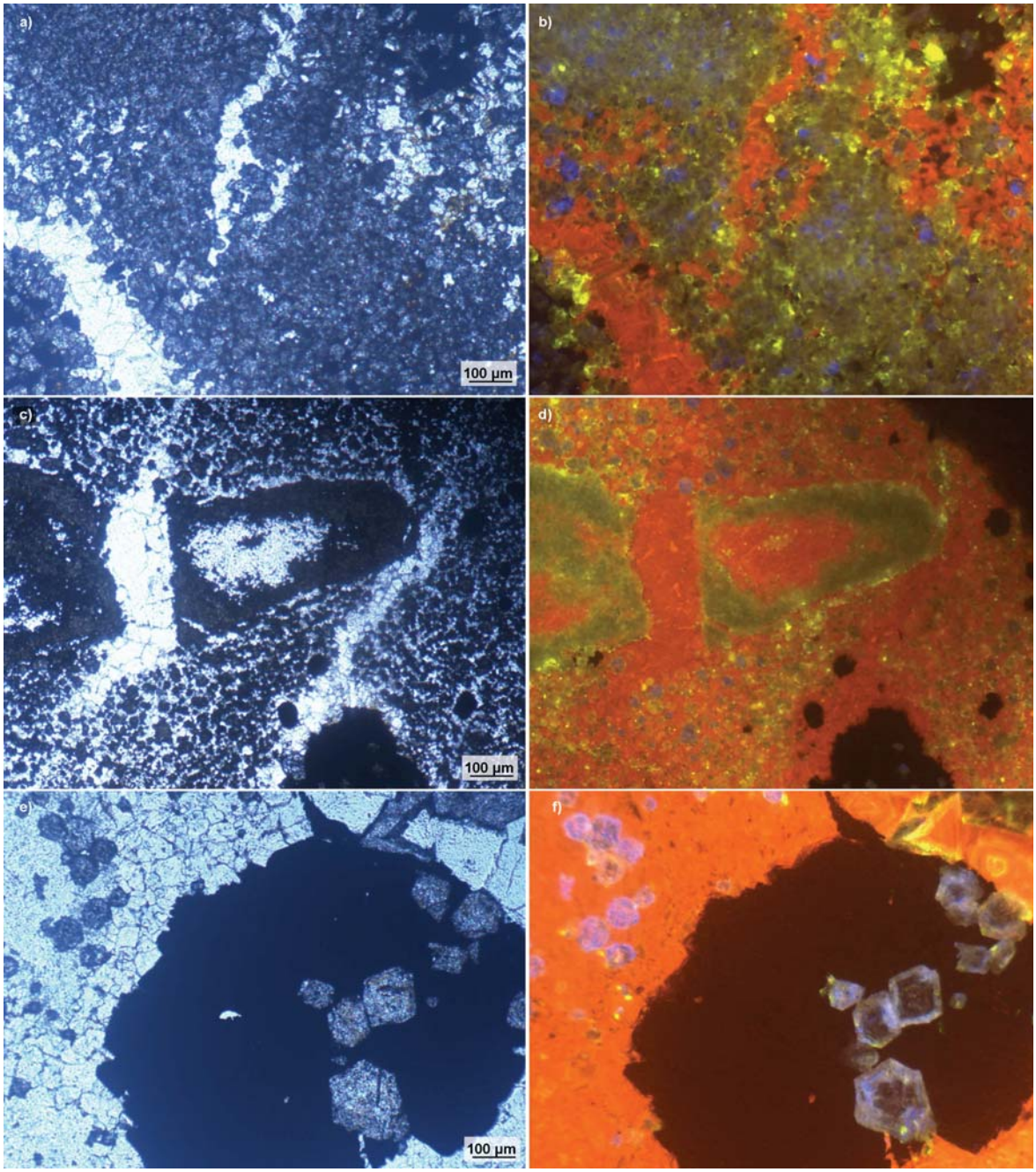

Figure 4 (a – f): CL images of some Topla samples (+ microscopy images).
a & b) Sample Tp01, dumps. Greenish CL colors (sometimes also blue) of fine-grained sphalerite grains. The gangue consists predominantly of dolomite (red CL). c & d) Sample Tp04, dumps. Very fine-grained ZnS (about 10 µm) was precipitated in a former shell. The very fine-grained sphalerites display green (yellowish) CL, whereas larger grains show partly blue CL color. The gangue consists of red luminescent dolomite. e & f) Sample Tp06, dumps. Sphalerite grains (≥ 100 µm, blue CL), which are included in a large (> 1000 µm) marcasite aggregate (opaque). Furthermore, some smaller (< 100 µm, blue CL) ZnS grains, occurring dispersed within the dolomite gangue (red CL).

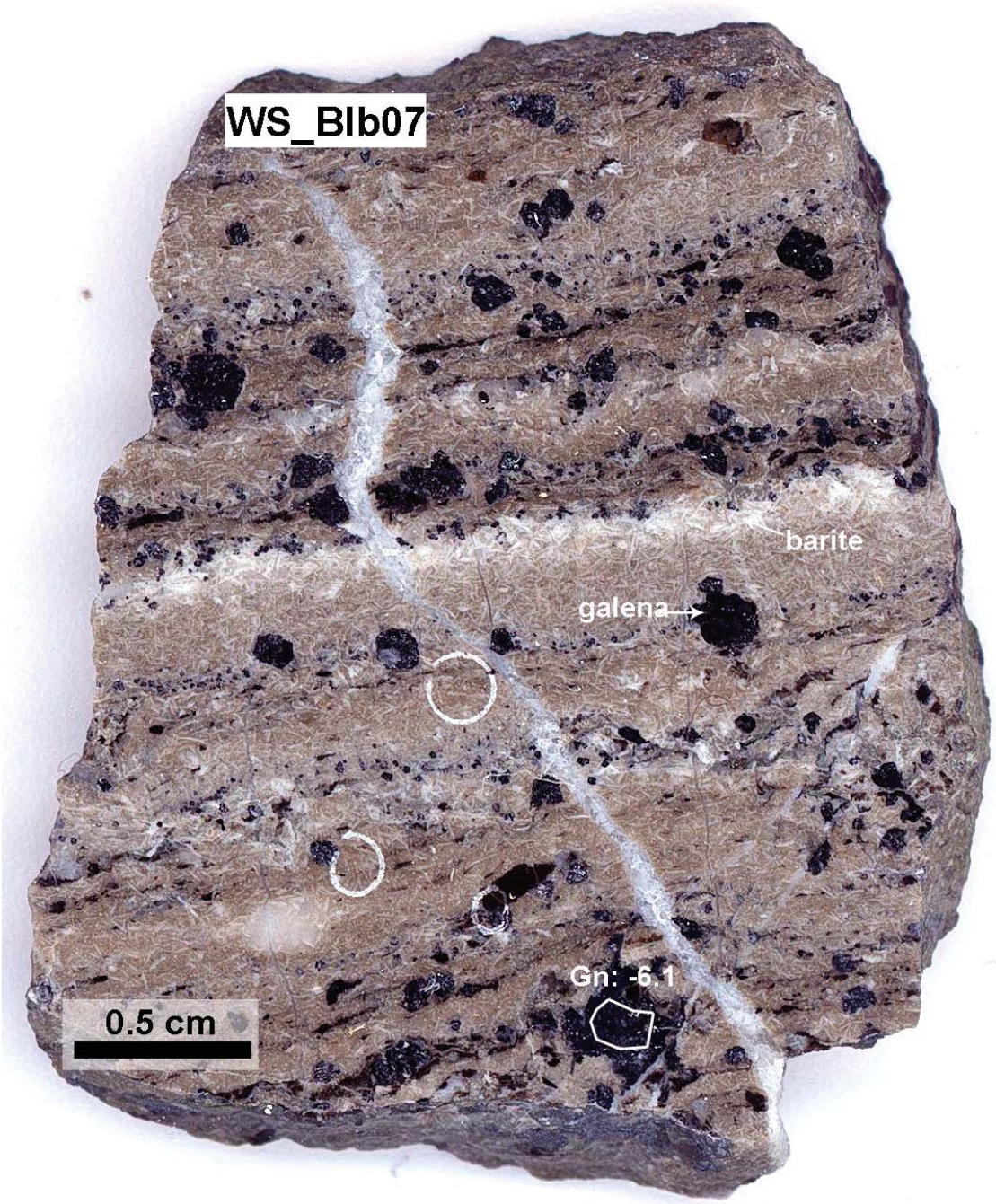

Figure 5: Photograph of sample WS_Blb07, Bleiberg, Erzkalk (Stefanie, 12th level).
The sphalerite is very fine-grained (< 100 µm) and thus not visible. Galena (Gn) forms large aggregates (> 1 mm) and is already on macroscopical scale visible. The sample is furthermore, very rich in barite (elongated white crystals).

Table 4: EMP data of sphalerites from the Maxer Bänke (Bleiberg).

	EMPA Bleiberg, Maxer Bänke [mass%]									
sample/analyses	**As**	**S**	**Zn**	**Fe**	**Pb**	**Ge**	**Cu**	**Cd**	**Tl**	**total**
EHK01_ZnS2	NA	33.55	65.22	0.20	0.019	0.127	NA	0.05	NA	99.17
EHK01_ZnS3	NA	33.09	65.55	0.38	0.024	NA	NA	0.09	NA	99.13
EHK01_ZnS4	NA	33.24	66.36	0.08	NA	NA	NA	0.15	NA	99.84
EHK01_ZnS5	NA	33.58	64.47	1.36	0.102	0.036	NA	0.04	NA	99.59
EHK01_ZnS6	NA	33.29	65.41	0.10	0.048	0.125	NA	0.06	NA	99.04
EHK01_ZnS7	NA	33.26	65.84	0.06	NA	NA	NA	0.28	NA	99.44
EHK01_ZnS8	NA	33.17	66.36	0.12	NA	NA	NA	0.28	NA	99.94
EHK01_ZnS9	NA	33.13	65.77	0.76	NA	NA	NA	0.18	NA	99.84
EHK01_ZnS10	0.051	33.07	63.77	2.44	0.321	0.025	NA	0.01	NA	99.68
EHK01_ZnS11	NA	33.15	66.47	0.10	0.055	NA	NA	0.24	NA	100.01
EHK01_ZnS12	NA	33.10	66.95	0.13	NA	NA	NA	0.37	NA	100.54
EHK01_ZnS13	NA	30.83	67.52	0.25	0.041	NA	NA	0.25	NA	98.90
EHK01_ZnS14	NA	33.19	66.99	0.20	0.031	0.054	NA	0.04	NA	100.51
EHK01_ZnS15	NA	33.18	67.05	0.04	0.016	NA	NA	0.29	NA	100.57
EHK01_ZnS16	0.152	33.36	64.05	2.52	0.315	NA	NA	0.05	NA	100.46
EHK01_ZnS17	NA	33.24	67.92	0.04	NA	NA	NA	0.10	NA	101.30
EHK01_ZnS18	NA	33.03	67.65	0.01	NA	NA	NA	0.05	NA	100.74
EHK01_ZnS19	NA	31.06	67.37	0.07	0.040	NA	NA	0.27	NA	98.81
EHK01_ZnS20	NA	32.62	67.15	0.19	0.090	NA	NA	0.30	NA	100.35
EHK01_ZnS21	NA	33.00	66.76	0.11	0.061	NA	NA	0.14	NA	100.08
EHK01_ZnS22	NA	32.89	66.60	0.17	0.101	NA	NA	0.31	NA	100.07
EHK01_ZnS23	NA	33.21	67.40	0.17	NA	NA	NA	0.15	NA	100.93
EHK01_ZnS24	NA	33.17	67.12	0.25	0.046	NA	NA	0.18	NA	100.77
EHK01_ZnS25	NA	33.22	66.74	0.11	NA	NA	NA	0.39	NA	100.46
EHK01_ZnS27	NA	33.13	66.70	0.17	NA	NA	NA	0.46	NA	100.45
EHK01_ZnS28	NA	33.24	67.18	0.09	NA	NA	NA	0.12	NA	100.63
EHK01_ZnS29	NA	32.79	66.76	0.28	0.099	0.013	NA	0.04	NA	100.01
EHK01_ZnS30	NA	33.36	67.47	0.32	NA	NA	NA	0.06	NA	101.22
EHK01_ZnS31	NA	33.20	67.62	0.12	NA	NA	NA	0.08	NA	101.02
EHK01_ZnS32	NA	33.59	66.41	0.33	NA	0.127	NA	0.06	NA	100.51
EHK01_ZnS33	NA	33.20	66.92	0.71	0.022	NA	NA	0.06	NA	100.91
EHK01_ZnS34	NA	33.16	67.35	0.27	0.049	0.020	NA	0.09	NA	100.94
EHK01_ZnS35	NA	32.95	67.31	0.67	0.031	0.038	NA	0.06	NA	101.06
EHK01_ZnS36	NA	33.76	67.52	0.25	NA	NA	NA	0.09	NA	101.62
EHK01_ZnS37	NA	33.50	67.42	0.44	0.046	NA	NA	0.05	NA	101.47
EHK01_ZnS38	NA	33.44	65.73	0.38	0.066	0.175	NA	0.03	NA	99.82
EHK01_ZnS39	NA	33.10	67.07	0.07	0.060	NA	NA	0.26	NA	100.56
EHK01_ZnS40	NA	32.99	67.37	0.06	0.059	NA	NA	0.32	NA	100.80
EHK01_ZnS41	NA	32.93	67.16	0.05	NA	NA	NA	0.29	NA	100.43
EHK01_ZnS42	NA	32.89	67.44	0.07	0.041	NA	NA	0.22	NA	100.67
EHK01_ZnS43	NA	33.35	67.67	0.13	0.014	NA	NA	0.07	NA	101.24
EHK01_ZnS44	NA	33.29	67.31	0.64	NA	0.023	NA	0.14	NA	101.42
EHK01_ZnS45	NA	33.23	67.32	0.47	0.072	0.025	NA	0.09	NA	101.20
EHK01_ZnS46	NA	29.70	64.52	0.45	0.110	NA	NA	0.30	NA	95.08
EHK01_ZnS47	NA	33.27	66.78	1.14	0.072	NA	NA	0.05	NA	101.31
EHK01_ZnS48	NA	33.50	67.43	0.43	0.016	NA	NA	0.09	NA	101.47
EHK01_ZnS49	NA	33.40	66.91	0.87	0.065	NA	NA	0.08	NA	101.33
EHK01_ZnS50	NA	33.25	67.34	0.56	0.054	NA	NA	0.09	NA	101.29

Table 4: Continued.

	EMPA Bleiberg, Maxer Bänke [mass%]									
sample/analyses	**As**	**S**	**Zn**	**Fe**	**Pb**	**Ge**	**Cu**	**Cd**	**Tl**	**total**
EHK01_ZnS51	NA	33.41	67.96	0.14	0.015	NA	NA	0.08	NA	101.61
EHK01_ZnS52	NA	33.41	67.85	0.28	NA	0.019	NA	0.09	NA	101.65
EHK01_ZnS53	NA	33.27	67.38	1.06	0.050	0.047	NA	0.09	NA	101.90
EHK01_ZnS54	NA	32.86	67.79	0.09	0.189	NA	NA	0.27	NA	101.20
EHK01_ZnS55	NA	32.97	67.50	0.27	0.078	NA	NA	0.31	NA	101.13
EHK01_ZnS56	NA	32.63	67.70	0.13	NA	NA	NA	0.30	NA	100.76
EHK01_ZnS57	NA	33.12	66.63	0.95	0.160	NA	NA	0.16	NA	101.02
EHK01_ZnS58	NA	33.29	67.06	0.26	0.127	NA	NA	0.21	NA	100.95
EHK01_ZnS59	NA	31.87	68.20	0.09	NA	NA	NA	0.19	NA	100.35
EHK01_ZnS60	NA	33.15	68.12	0.17	NA	NA	NA	0.13	NA	101.57
EHK01_ZnS61	NA	33.37	66.67	1.04	0.044	0.030	NA	0.07	NA	101.23
EHK01_ZnS62	NA	33.30	67.87	0.26	NA	NA	NA	0.08	NA	101.53
EHK01_ZnS63	NA	33.85	68.18	0.11	NA	0.020	NA	0.11	NA	102.26
EHK01_ZnS64	NA	32.70	67.50	0.16	0.182	NA	NA	0.30	NA	100.84
EHK01_ZnS65	NA	32.85	67.84	0.21	0.108	NA	NA	0.29	NA	101.30
EHK01_ZnS66	NA	32.42	67.39	0.17	0.096	NA	NA	0.28	NA	100.36
EHK01_ZnS67	NA	33.08	67.87	0.05	0.019	NA	NA	0.19	NA	101.21
EHK01_ZnS68	NA	33.04	67.60	0.05	0.045	NA	NA	0.24	NA	100.98
EHK01_ZnS69	NA	30.27	67.76	0.09	0.170	NA	NA	0.38	NA	98.67
EHK01_ZnS70	NA	32.53	67.58	0.14	0.215	NA	NA	0.26	NA	100.72
Blb20_1	NA	32.91	66.67	0.90	0.031	NA	NA	0.12	NA	100.63
Blb20_2	NA	32.91	67.12	0.47	0.020	NA	NA	0.11	NA	100.63
Blb20_3	NA	32.86	66.74	0.87	0.048	0.047	NA	0.06	NA	100.63
Blb20_4	NA	32.69	66.78	0.60	NA	NA	NA	0.15	NA	100.22
Blb20_5	NA	33.01	66.83	0.53	0.070	0.075	NA	0.11	NA	100.63
Blb20_6	NA	32.83	66.68	0.79	0.072	NA	NA	0.09	NA	100.47
Blb20_7	NA	33.06	67.57	0.12	NA	NA	NA	0.14	NA	100.89
Blb20_8	NA	33.21	67.12	0.14	NA	NA	NA	0.16	NA	100.64
Blb20_9	NA	32.69	67.37	0.04	NA	NA	NA	0.35	NA	100.45
Blb20_10	NA	32.78	67.45	0.06	NA	NA	NA	0.37	NA	100.66
Blb20_11	NA	32.98	67.57	0.03	NA	NA	NA	0.31	NA	100.89
Blb20_12	NA	32.81	67.55	0.01	NA	NA	NA	0.54	NA	100.91
Blb20_13	NA	32.74	67.74	0.03	NA	NA	NA	0.30	NA	100.81
Blb20_14	NA	30.88	65.39	0.04	0.160	NA	NA	0.18	NA	96.65
Blb20_15	NA	32.59	67.34	0.03	NA	NA	NA	0.35	NA	100.31
Blb20_16	NA	32.81	67.51	0.02	NA	NA	NA	0.25	NA	100.59
Blb20_17	NA	32.78	67.52	0.05	NA	NA	NA	0.22	NA	100.57
Blb20_18	NA	32.74	67.10	0.01	NA	NA	NA	0.55	NA	100.40
Blb20_19	NA	35.00	66.28	0.37	0.014	0.009	NA	0.08	NA	101.78
Blb20_20	NA	33.82	66.84	0.18	NA	0.091	NA	0.06	NA	100.99
Blb20_21	NA	32.45	67.38	0.23	0.016	0.162	NA	0.06	NA	100.32
Blb20_22	NA	33.02	66.83	0.17	NA	0.134	NA	0.10	NA	100.25
Blb20_23	NA	32.94	66.39	0.26	0.057	0.135	NA	0.03	NA	99.82
Blb20_24	NA	32.92	66.95	0.25	NA	0.226	NA	0.03	NA	100.37
Blb20_25	NA	32.79	66.94	0.25	NA	0.007	NA	0.07	NA	100.06
Blb20_26	NA	32.67	67.13	0.30	NA	NA	NA	0.20	NA	100.30
Blb20_27	NA	32.80	66.32	0.97	0.019	NA	NA	0.09	NA	100.19

Table 4: Continued.

EMPA Bleiberg, Maxer Bänke [mass%]										
sample/analyses	**As**	**S**	**Zn**	**Fe**	**Pb**	**Ge**	**Cu**	**Cd**	**Tl**	**total**
Blb20_28	NA	32.90	65.73	1.01	0.037	NA	NA	0.07	NA	99.75
Blb20_29	NA	32.86	66.83	0.63	0.042	0.100	NA	0.06	NA	100.53
Blb20_30	NA	32.88	66.93	0.50	0.051	0.119	NA	0.08	NA	100.56
Blb20_31	NA	32.53	67.14	0.51	0.015	NA	NA	0.20	NA	100.39
Blb20_32	NA	32.53	67.20	0.41	0.026	NA	NA	0.29	NA	100.45
Blb20_33	NA	32.71	67.70	0.04	0.065	NA	NA	0.10	NA	100.61
Blb20_34	NA	32.82	66.00	1.54	0.068	0.111	NA	0.02	NA	100.56
Blb20_35	NA	32.66	67.49	0.10	NA	NA	NA	0.08	NA	100.33
Blb20_36	NA	32.75	67.58	0.24	NA	NA	NA	0.16	NA	100.76
Blb20_37	NA	33.10	67.12	0.25	0.041	NA	NA	0.19	NA	100.70
Blb20_38	NA	32.58	66.44	0.70	NA	NA	NA	0.19	NA	99.91
Blb20_39	NA	32.66	67.31	0.15	NA	NA	NA	0.27	NA	100.39
Blb20_40	NA	32.87	67.04	0.60	NA	0.087	NA	0.08	NA	100.68
Blb20_41	NA	32.64	67.55	0.12	0.029	NA	NA	0.16	NA	100.51
Blb20_42	NA	32.95	67.06	0.50	0.048	NA	NA	0.09	NA	100.65
Blb20_43	NA	32.44	67.36	0.15	0.038	NA	NA	0.14	NA	100.14
Blb20_44	NA	32.69	67.47	0.14	0.013	0.024	NA	0.10	NA	100.43
Blb20_45	NA	32.75	67.57	0.09	NA	NA	NA	0.23	NA	100.67
Blb20_46	NA	32.47	67.28	0.34	NA	NA	NA	0.27	NA	100.36
Blb20_47	NA	32.57	67.41	0.23	0.031	NA	NA	0.23	NA	100.49
Blb20_48	NA	33.30	66.73	0.51	NA	NA	NA	0.35	NA	100.89
Blb20_49	NA	32.64	66.65	0.90	0.016	0.039	NA	0.13	NA	100.38
Blb20_50	NA	32.42	63.52	3.23	0.144	0.008	NA	0.12	NA	99.44
Blb20_51	0.207	32.37	64.78	1.07	1.040	0.037	NA	0.11	NA	99.61
Blb20_52	0.341	32.61	62.13	4.35	1.020	0.062	NA	0.03	NA	100.55
Blb20_53	0.334	32.79	62.91	3.59	0.577	0.009	NA	0.05	NA	100.26
Blb20_54	0.197	32.22	64.77	1.22	0.880	0.019	NA	0.12	NA	99.42
Blb20_55	0.015	32.16	66.08	0.73	0.420	NA	NA	0.25	NA	99.65
Blb20_56	NA	32.61	66.29	1.13	0.118	NA	NA	0.16	NA	100.31
Blb20_57	NA	32.34	66.71	0.64	0.087	NA	NA	0.28	NA	100.06
Blb20_58	NA	32.19	66.36	0.68	0.164	NA	NA	0.20	NA	99.60
Blb20_59	NA	32.19	66.06	1.11	0.137	NA	NA	0.30	NA	99.79
Blb20_60	NA	32.44	67.90	0.19	0.054	NA	NA	0.18	NA	100.76
Blb20_61	0.146	32.48	64.87	1.25	0.791	0.010	NA	0.11	NA	99.66
Blb20_62	0.144	32.28	64.71	1.52	0.556	NA	NA	0.11	NA	99.32
Blb20_63	0.382	32.16	62.38	3.14	1.350	0.049	NA	0.06	NA	99.52
Blb20_64	NA	32.54	66.57	0.72	0.041	NA	NA	0.20	NA	100.07
Blb20_65	0.141	32.56	65.33	1.62	0.348	NA	NA	0.02	NA	100.02
Blb20_66	NA	32.36	65.83	0.71	0.358	NA	NA	0.24	NA	99.50
Blb20_67	0.240	32.21	61.22	4.62	1.040	0.024	NA	0.04	NA	99.39
Blb20_68	NA	32.67	65.77	1.17	0.247	NA	NA	0.18	NA	100.04
Blb20_69	0.204	32.54	63.30	3.00	0.838	0.028	NA	0.04	NA	99.95
Blb20_70	NA	32.31	65.81	1.45	NA	NA	NA	0.20	NA	99.77
Blb20_71	NA	32.53	67.06	0.27	NA	NA	NA	0.32	NA	100.19
Blb20_72	NA	32.67	67.54	0.10	0.184	NA	NA	0.09	NA	100.58
Blb20_73	NA	32.17	67.36	0.05	NA	NA	NA	0.24	NA	99.81
Blb20_74	NA	32.63	67.85	0.11	NA	NA	NA	0.35	NA	100.94
Blb20_75	NA	32.76	66.94	0.15	NA	NA	NA	0.63	NA	100.48

Table 4: Continued.

	EMPA Bleiberg, Maxer Bänke [mass%]									
sample/analyses	**As**	**S**	**Zn**	**Fe**	**Pb**	**Ge**	**Cu**	**Cd**	**Tl**	**total**
Blb20_76	NA	32.17	67.13	0.01	NA	NA	NA	0.57	NA	99.88
Blb20_77	0.042	32.16	65.72	1.06	0.466	NA	NA	0.16	NA	99.61
Blb20_78	0.042	32.36	65.25	1.20	0.411	NA	NA	0.08	NA	99.34
Blb20_79	0.050	32.72	66.16	0.82	0.253	NA	NA	0.08	NA	100.08
Blb20_80	NA	32.49	67.44	0.01	0.017	NA	NA	0.31	NA	100.27
Blb20_81	NA	32.55	65.51	1.70	0.197	NA	NA	0.11	NA	100.07
Blb20_82	NA	32.80	67.00	0.36	0.032	NA	NA	0.20	NA	100.39
Blb20_83	NA	32.74	67.19	0.03	NA	NA	NA	0.28	NA	100.25
Blb20_84	NA	32.38	66.12	0.13	NA	0.064	NA	0.05	NA	98.75
Blb20_86	NA	32.66	67.23	0.03	NA	0.040	NA	0.14	NA	100.10
Blb20_87	NA	32.80	66.99	0.05	0.066	0.170	NA	0.05	NA	100.13
Blb20_88	NA	32.57	67.47	0.15	NA	NA	NA	0.02	NA	100.21
Blb20_89	NA	32.46	67.46	0.16	NA	NA	NA	0.02	NA	100.10
Blb11neu_ZnS1	NA	32.69	67.19	0.77	NA	0.020	NA	0.12	NA	100.78
Blb11neu_ZnS2	NA	32.90	67.17	0.74	NA	0.027	NA	0.13	NA	100.97
Blb11neu_ZnS3	NA	33.01	67.21	0.59	0.040	0.054	NA	0.18	NA	101.08
Blb11neu_ZnS4	NA	32.61	67.09	0.51	0.051	0.030	NA	0.29	NA	100.57
Blb11neu_ZnS5	NA	32.76	67.42	0.07	0.076	NA	NA	0.07	NA	100.40
Blb11neu_ZnS6	NA	32.86	66.97	0.41	NA	0.063	NA	0.15	NA	100.45
Blb11neu_ZnS7	NA	32.64	66.85	0.47	0.045	0.046	NA	0.19	NA	100.24
Blb11neu_ZnS8	NA	32.60	67.35	0.24	NA	0.067	NA	0.11	NA	100.37
Blb11neu_ZnS9	NA	32.73	67.98	0.23	NA	0.081	NA	0.07	NA	101.10
Blb11neu_ZnS10	NA	33.08	67.74	0.17	0.066	0.030	NA	0.28	NA	101.37
Blb11neu_ZnS11	NA	33.23	67.74	0.41	0.079	0.088	NA	0.06	NA	101.60
Blb11neu_ZnS12	NA	33.24	67.69	0.27	0.041	0.041	NA	0.05	NA	101.33
Blb11neu_ZnS13	NA	33.15	67.45	0.33	0.107	0.134	NA	0.07	NA	101.24
Blb11neu_ZnS14	NA	33.27	67.65	0.41	0.033	0.098	NA	0.13	NA	101.59
Blb11neu_ZnS15	NA	33.09	67.73	0.24	NA	0.061	NA	0.18	NA	101.31
Blb11neu_ZnS16	NA	33.05	67.56	0.27	0.033	0.024	NA	0.21	NA	101.14
Blb11neu_ZnS17	NA	33.08	66.60	1.27	NA	0.078	NA	0.07	NA	101.09
Blb11neu_ZnS18	NA	33.01	67.70	0.20	NA	0.011	NA	0.13	NA	101.05
Blb11neu_ZnS19	NA	33.01	67.27	0.27	0.088	0.188	NA	0.03	NA	100.86
Blb11neu_ZnS20	NA	33.02	67.23	0.28	0.043	0.270	NA	0.03	NA	100.87
Blb11neu_ZnS21	NA	33.49	67.38	0.50	0.036	0.173	NA	0.03	NA	101.61
Blb11neu_ZnS22	NA	33.37	67.75	0.14	0.030	0.030	NA	0.22	NA	101.54
Blb11neu_ZnS23	NA	32.60	67.16	0.48	0.112	0.228	NA	0.03	NA	100.61
Blb11neu_ZnS24	NA	32.78	67.74	0.26	NA	0.066	NA	0.09	NA	100.93
Blb11neu_ZnS25	NA	32.62	67.32	0.79	NA	0.044	NA	0.15	NA	100.92
Blb11neu_ZnS26	NA	32.57	66.02	1.41	0.041	0.209	NA	NA	NA	100.25
Blb11neu_ZnS27	NA	32.51	66.59	1.09	0.183	0.082	NA	0.04	NA	100.49
Blb11neu_ZnS28	NA	32.72	67.89	0.19	NA	0.030	NA	0.18	NA	101.00
Blb11neu_ZnS29	NA	33.02	66.75	0.89	0.084	0.249	NA	NA	NA	100.99
Blb11neu_ZnS30	NA	32.74	67.38	0.49	NA	0.151	NA	0.01	NA	100.78
Blb11_WH_31	NA	33.44	66.90	0.33	0.040	0.161	NA	0.01	NA	100.88
Blb11_WH_32	NA	33.22	66.38	0.54	NA	0.132	NA	NA	NA	100.27
Blb11_WH_33	0.003	33.43	67.02	0.22	0.034	0.057	NA	0.01	NA	100.77
Blb11_WH_34	0.004	33.03	67.05	0.13	NA	0.028	NA	0.11	NA	100.35

Table 4: Continued.

EMPA Bleiberg, Maxer Bänke [mass%]										
sample/analyses	**As**	**S**	**Zn**	**Fe**	**Pb**	**Ge**	**Cu**	**Cd**	**Tl**	**total**
Blb11_WH_35	NA	33.16	67.07	0.38	NA	0.039	NA	0.08	NA	100.73
Blb11_WH_36	0.004	33.30	67.27	0.11	0.041	0.006	NA	0.08	NA	100.82
Blb11_WH_38	NA	33.08	66.77	0.17	0.027	0.064	NA	0.05	NA	100.16
Blb11_WH_39	0.004	33.02	66.87	0.25	0.091	0.082	NA	0.01	NA	100.33
Blb11_WH_40	NA	33.52	65.74	0.26	NA	0.216	NA	NA	NA	99.73
Blb11_WH_41	NA	33.30	65.22	0.19	0.026	0.279	NA	NA	NA	99.01
Blb11_WH_42	NA	33.55	66.03	0.12	0.063	0.219	NA	0.01	NA	99.99
Blb11_WH_43	NA	33.17	65.70	0.12	NA	0.121	NA	0.01	NA	99.12
Blb11_WH_44	NA	33.44	65.55	0.19	NA	0.180	NA	NA	NA	99.36
Blb11_WH_45	NA	33.55	67.41	0.08	NA	0.115	NA	0.05	NA	101.21
Blb11_WH_46	NA	33.44	67.19	0.17	0.054	0.083	NA	0.07	NA	101.01
Blb11_WH_47	NA	33.51	66.97	0.32	0.032	0.112	NA	0.02	NA	100.96
Blb11_WH_49	NA	33.54	67.09	0.40	NA	0.114	NA	NA	NA	101.14
Blb11_WH_50	NA	33.37	67.04	0.24	0.072	0.083	NA	0.03	NA	100.84
Blb11_WH_51	NA	33.39	66.86	0.45	0.032	0.109	NA	NA	NA	100.84
Blb11_WH_52	NA	33.34	66.49	0.44	0.054	0.150	NA	0.00	NA	100.48
Blb11_WH_53	NA	33.16	67.18	0.04	NA	0.017	NA	0.18	NA	100.57
Blb11_WH_54	NA	33.03	67.47	0.08	0.031	0.010	NA	0.07	NA	100.68
Blb11_WH_55	0.016	33.22	67.01	0.35	0.046	0.018	NA	0.07	NA	100.73
Blb11_WH_56	NA	33.61	66.14	0.12	0.028	0.195	NA	NA	NA	100.09
Blb11_WH_57	NA	33.40	66.07	0.13	0.030	0.146	NA	NA	NA	99.77
Blb11_WH_58	NA	33.51	65.89	0.13	NA	0.167	NA	0.00	NA	99.70
Blb11_WH_59	NA	33.61	66.22	0.18	0.066	0.246	NA	NA	NA	100.33
Blb11_WH_60	NA	33.33	66.78	0.13	0.030	0.187	NA	NA	NA	100.46
1_Blb17_BSE7_1	NA	32.90	66.90	0.07	NA	NA	NA	0.14	NA	100.13
2_Blb17_BSE7_1	0.066	32.64	65.52	0.79	0.154	0.127	NA	0.07	NA	99.41
3_Blb17_BSE7_1	0.037	31.65	65.20	0.44	NA	0.116	NA	0.03	NA	97.56
4_Blb17_BSE7_1	NA	32.68	65.98	0.37	NA	0.062	NA	0.03	NA	99.28
5_Blb17_BSE7_1	0.104	32.61	64.30	2.32	0.172	0.045	NA	0.13	NA	99.72
6_Blb17_BSE7_1	0.053	32.44	65.87	0.31	0.542	0.045	NA	0.14	NA	99.40
7_Blb17_BSE7_1	0.052	30.57	66.29	0.62	0.287	0.023	NA	0.21	NA	98.06
8_Blb17_BSE7_1	NA	32.41	65.47	0.73	0.228	0.024	NA	0.40	NA	99.31
9_Blb17_BSE7_1	0.201	32.51	64.63	0.90	0.673	0.085	NA	0.09	NA	99.14
10_Blb17_BSE7_1	0.374	32.28	64.10	0.70	0.857	0.104	NA	0.09	0.133	98.63
11_Blb17_BSE7_1	0.310	31.68	64.85	0.74	0.674	0.056	NA	0.09	0.094	98.50
12_Blb17_BSE7_1	0.279	32.44	65.12	0.61	0.762	0.084	NA	0.10	NA	99.46
13_Blb17_BSE7_1	0.139	31.61	65.73	0.60	0.488	0.072	NA	0.14	NA	98.79
14_Blb17_BSE7_1	0.052	32.72	66.19	0.23	0.276	0.043	NA	0.28	NA	99.78
15_Blb17_BSE7_1	0.213	32.22	64.61	0.86	0.641	0.083	NA	0.12	0.100	98.85
16_Blb17_BSE7_1	0.392	32.42	60.36	5.55	0.923	0.083	NA	NA	0.227	99.97
17_Blb17_BSE7_1	0.338	32.60	63.80	1.22	0.802	0.084	NA	0.04	0.129	99.02
18_Blb17_BSE7_3	NA	32.82	66.03	0.38	0.145	0.020	NA	0.28	NA	99.70
19_Blb17_BSE7_3	0.497	32.21	63.03	1.17	1.534	0.106	NA	0.08	0.143	98.77
20_Blb17_BSE7_3	0.385	32.42	62.89	1.78	1.144	0.088	NA	0.08	0.132	98.92
21_Blb17_BSE7_3	0.084	32.52	65.19	0.44	0.327	0.040	NA	0.26	NA	98.87
22_Blb17_BSE7_3	0.155	32.07	64.57	0.84	0.469	0.053	NA	0.21	0.084	98.44
23_Blb17_BSE7_3	0.357	32.23	63.62	0.76	1.129	0.107	NA	0.09	0.097	98.39

Table 4: Continued.

EMPA Bleiberg, Maxer Bänke [mass%]										
sample/analyses	**As**	**S**	**Zn**	**Fe**	**Pb**	**Ge**	**Cu**	**Cd**	**Tl**	**total**
24_Blb17_BSE7_3	0.049	32.57	65.68	0.65	0.125	0.090	NA	0.07	NA	99.25
25_Blb17_BSE7_3	NA	32.21	65.89	0.32	0.126	0.016	NA	0.23	NA	98.81
26_Blb17_BSE7_3	0.428	32.21	63.00	1.19	1.213	0.095	NA	0.07	0.122	98.33
27_Blb17_BSE7_3	NA	33.18	66.27	0.08	0.125	0.027	NA	0.11	NA	99.79
28_Blb17_BSE7_3	0.206	32.80	64.49	0.98	0.343	0.157	NA	NA	0.154	99.16
29_Blb17_BSE7_3	0.101	32.58	64.05	0.77	0.164	0.088	NA	0.06	NA	97.85
30_Blb17_BSE7_5	NA	32.69	66.39	0.02	NA	0.022	NA	0.30	NA	99.43
31_Blb17_BSE7_5	NA	31.46	63.44	0.18	0.285	0.064	NA	0.08	NA	95.51
32_Blb17_BSE7_5	NA	32.78	66.32	0.08	NA	0.063	NA	0.16	NA	99.53
33_Blb17_BSE7_5	0.027	32.49	66.11	0.10	NA	0.070	NA	0.14	NA	99.07
34_Blb17_BSE7_5	0.205	32.79	64.66	1.05	0.395	0.103	NA	NA	0.140	99.37
35_Blb17_BSE7_9	NA	32.98	66.59	0.07	NA	0.040	NA	0.12	NA	99.88
36_Blb17_BSE7_9	0.129	32.85	65.44	0.91	0.207	0.064	NA	0.07	0.079	99.74
37_Blb17_BSE7_9	0.040	32.71	66.69	0.04	NA	0.036	NA	0.19	NA	99.79
38_Blb17_BSE7_9	NA	32.73	66.37	0.03	NA	0.025	NA	0.29	NA	99.56
40_Blb17_BSE7_9	0.083	32.71	65.86	0.17	0.127	0.126	NA	0.13	NA	99.21
41_Blb17_BSE7_9	0.046	32.90	65.26	0.48	0.220	0.209	NA	NA	0.141	99.36
42_Blb17_BSE7_9	0.128	32.42	65.72	0.09	0.126	0.222	NA	0.04	NA	98.70
43_Blb17_BSE7_11	0.039	32.64	65.85	0.75	0.327	0.059	NA	0.14	NA	99.95
44_Blb17_BSE7_11	0.142	32.66	66.61	0.41	0.191	0.039	NA	0.24	NA	100.20
45_Blb17_BSE7_11	0.051	32.85	66.01	0.59	0.297	0.062	NA	0.14	NA	100.11
46_Blb17_BSE7_11	0.098	32.79	66.82	0.17	0.171	0.047	NA	0.20	NA	100.22
47_Blb17_BSE7_11	0.027	32.65	66.32	0.19	0.133	0.203	NA	0.07	0.084	99.67
48_Blb17_BSE7_11	NA	32.56	66.72	0.08	NA	0.032	NA	0.18	NA	99.64
49_Blb17_BSE7_11	NA	32.55	66.27	0.12	NA	0.075	NA	0.10	NA	99.28
50_Blb17_BSE7_11	NA	32.87	66.01	0.12	NA	0.051	NA	0.19	NA	99.31
51_Blb17_BSE7_11	NA	32.76	65.44	0.12	NA	0.076	NA	0.18	NA	98.67
52_Blb17_BSE7_11	NA	32.89	65.94	0.16	0.119	0.106	NA	0.08	NA	99.34
53_Blb17_BSE7_11	NA	32.98	65.56	0.09	0.130	0.182	NA	0.09	NA	99.11
54_Blb17_BSE7_11	0.037	33.03	65.64	0.17	NA	0.043	NA	0.19	NA	99.17
55_Blb17_BSE7_11	NA	32.91	65.18	0.14	0.140	0.210	NA	0.07	NA	98.70
56_Blb17_BSE7_11	0.033	32.61	65.00	0.15	0.137	0.204	NA	0.05	0.083	98.24
57_Blb17_BSE7_13	NA	32.79	66.30	0.07	NA	0.013	NA	0.28	NA	99.51
58_Blb17_BSE7_13	NA	32.67	65.96	0.11	0.162	0.217	NA	0.07	NA	99.25
59_Blb17_BSE7_13	NA	32.84	66.28	0.16	NA	0.043	NA	0.12	NA	99.61
60_Blb17_BSE7_13	NA	32.95	65.89	0.20	0.241	0.097	NA	0.04	NA	99.52
61_Blb17_BSE7_13	0.035	32.94	66.53	0.06	0.148	0.048	NA	0.14	NA	99.91
62_Blb17_BSE7_13	0.030	32.79	66.37	0.13	0.191	0.187	NA	0.05	NA	99.75
63_Blb17_BSE7_15	0.029	32.78	66.71	NA	0.115	0.029	NA	0.34	NA	99.99
64_Blb17_BSE7_15	NA	32.84	66.67	0.01	NA	0.015	NA	0.41	NA	100.06
65_Blb17_BSE7_17	NA	32.83	66.38	0.03	NA	0.024	NA	0.39	NA	99.71
66_Blb17_BSE7_17	NA	32.75	66.09	0.02	NA	0.065	NA	0.24	NA	99.24
67_Blb17_BSE7_17	NA	32.69	65.92	0.07	NA	NA	NA	0.44	NA	99.23
68_Blb17_BSE7_17	NA	32.90	66.13	0.04	NA	0.022	NA	0.34	NA	99.56
69_Blb17_BSE7_17	NA	32.70	66.09	0.06	NA	0.030	NA	0.25	NA	99.22
70_Blb17_BSE7_17	NA	32.94	65.84	0.06	NA	0.038	NA	0.32	NA	99.30
1_Blb26_BSE2_2	NA	32.76	65.69	0.09	NA	0.110	NA	0.12	NA	98.82

Table 4: Continued.

EMPA Bleiberg, Maxer Bänke [mass%]										
sample/analyses	**As**	**S**	**Zn**	**Fe**	**Pb**	**Ge**	**Cu**	**Cd**	**Tl**	**total**
2_Blb26_BSE2_2	0.033	32.72	65.72	0.11	0.187	0.059	NA	0.25	NA	99.08
3_Blb26_BSE2_2	0.064	32.41	65.40	0.44	0.322	0.095	NA	0.06	NA	98.86
4_Blb26_BSE2_2	NA	32.71	65.74	0.08	NA	0.106	NA	0.16	NA	98.88
5_Blb26_BSE2_2	0.091	32.58	65.49	0.45	0.236	0.151	NA	0.07	0.111	99.18
6_Blb26_BSE2_2	0.108	32.77	64.91	0.82	0.188	0.147	NA	0.04	0.126	99.11
7_Blb26_BSE2_2	0.067	32.81	64.56	1.30	0.158	0.094	NA	0.05	NA	99.10
8_Blb26_BSE2_2	NA	33.16	65.98	0.09	NA	0.061	NA	0.26	NA	99.62
9_Blb26_BSE2_2	0.107	32.52	64.71	0.65	0.295	0.118	NA	0.05	NA	98.53
10_Blb26_BSE2_2	0.069	32.79	65.85	0.64	0.220	0.130	NA	0.04	NA	99.80
11_Blb26_BSE3_3	0.172	32.64	64.50	1.85	0.327	0.143	NA	0.05	0.128	99.81
12_Blb26_BSE3_3	0.074	32.68	65.88	0.32	0.190	0.162	NA	0.07	NA	99.44
13_Blb26_BSE3_3	0.121	32.86	65.37	0.94	0.333	0.139	NA	NA	0.106	99.89
15_Blb26_BSE3_3	0.141	32.97	63.69	2.31	0.331	0.168	NA	NA	0.150	99.78
16_Blb26_BSE3_3	NA	32.55	66.23	0.05	NA	NA	NA	0.40	NA	99.30
17_Blb26_BSE3_3	0.060	32.81	65.80	0.51	0.202	0.122	NA	NA	NA	99.56
18_Blb26_BSE3_3	0.103	32.73	65.09	0.71	0.261	0.124	NA	0.05	0.102	99.18
19_Blb26_BSE3_3	0.088	32.61	65.28	0.68	0.191	0.079	NA	0.06	NA	99.03
20_Blb26_BSE5_4	NA	32.74	66.66	NA	NA	0.020	NA	0.33	NA	99.79
22_Blb26_BSE5_4	NA	32.41	66.68	0.02	0.114	0.067	NA	0.24	NA	99.55
23_Blb26_BSE5_4	NA	32.83	65.90	0.02	NA	0.020	NA	0.32	NA	99.15
24_Blb26_BSE5_4	NA	32.90	66.61	NA	0.132	0.062	NA	0.24	NA	99.96
25_Blb26_BSE5_4	NA	33.23	67.04	0.02	0.158	0.036	NA	0.08	NA	100.58
26_Blb26_BSE5_4	NA	32.83	66.63	NA	0.122	0.022	NA	0.35	NA	99.99
27_Blb26_BSE6_8	NA	32.93	67.04	0.01	NA	0.025	NA	0.24	NA	100.36
28_Blb26_BSE6_8	NA	32.94	66.83	0.03	NA	0.037	NA	0.23	NA	100.14
29_Blb26_BSE6_8	NA	33.07	66.61	0.03	0.161	0.037	NA	0.24	NA	100.17
30_Blb26_BSE6_8	0.029	33.01	66.45	0.03	NA	0.059	NA	0.29	NA	99.93
31_Blb26_BSE6_8	NA	32.85	65.91	0.62	0.132	0.033	NA	0.23	NA	99.81
32_Blb26_BSE6_8	NA	33.10	66.48	0.03	0.154	0.038	NA	0.22	NA	100.04
33_Blb26_BSE11_10	NA	32.87	66.85	0.03	NA	0.036	NA	0.15	NA	100.03
34_Blb26_BSE11_10	0.037	33.01	66.56	0.10	0.141	0.032	NA	0.19	NA	100.05
35_Blb26_BSE11_10	NA	32.68	66.72	0.04	NA	0.025	NA	0.24	NA	99.82
36_Blb26_BSE11_10	0.029	32.67	66.29	0.03	NA	0.025	NA	0.20	NA	99.28
37_Blb26_BSE11_10	NA	33.15	67.05	0.02	NA	0.028	NA	0.13	NA	100.49
38_Blb26_BSE11_10	NA	32.72	67.31	0.02	0.153	0.022	NA	0.25	NA	100.48
39_Blb26_BSE11_10	NA	33.09	67.12	0.03	0.123	0.030	NA	0.30	NA	100.70
40_Blb26_BSE11_10	NA	33.09	67.02	0.02	NA	0.041	NA	0.20	NA	100.49
41_Blb26_BSE11_10	NA	33.03	66.83	NA	NA	0.023	NA	0.31	NA	100.28
42_Blb26_BSE13_10	NA	32.76	67.06	0.04	NA	0.045	NA	0.14	NA	100.10
43_Blb26_BSE13_10	NA	32.79	67.15	0.04	NA	0.035	NA	0.23	NA	100.36
44_Blb26_BSE13_10	NA	33.11	66.71	0.03	NA	0.019	NA	0.24	NA	100.20
45_Blb26_BSE13_10	NA	32.61	66.80	0.03	0.289	0.024	NA	0.09	NA	99.85
46_Blb26_BSE13_10	NA	32.96	66.88	0.02	NA	0.027	NA	0.28	NA	100.26
47_Blb26_BSE13_10	0.033	32.81	66.42	0.01	NA	NA	NA	0.46	NA	99.80
48_Blb26_BSE13_10	NA	32.67	66.58	0.03	0.145	0.045	NA	0.17	NA	99.65
49_Blb26_BSE13_10	NA	32.84	66.67	0.04	NA	0.037	NA	0.19	NA	99.83
50_Blb26_BSE13_10	NA	32.84	66.30	0.04	0.150	0.022	NA	0.21	NA	99.59
51_Blb26_BSE13_10	NA	32.96	66.03	0.06	0.121	0.044	NA	0.15	NA	99.39

Table 4: Continued.

	EMPA Bleiberg, Maxer Bänke [mass%]									
sample/analyses	**As**	**S**	**Zn**	**Fe**	**Pb**	**Ge**	**Cu**	**Cd**	**Tl**	**total**
52_Blb26_BSE13_10	NA	33.01	66.46	0.04	NA	0.053	NA	0.14	NA	99.80
53_Blb26_BSE13_10	NA	32.87	66.11	0.02	NA	0.025	NA	0.26	NA	99.33
54_Blb26_BSE13_10	NA	32.88	66.99	0.03	0.190	0.094	NA	0.15	NA	100.35
55_Blb26_BSE13_10	NA	32.76	66.49	0.03	0.143	0.025	NA	0.20	NA	99.65
56_Blb26_BSE16_11	NA	32.98	66.98	0.06	0.125	0.042	NA	0.11	NA	100.30
57_Blb26_BSE16_11	NA	32.59	65.45	0.04	NA	0.026	NA	0.22	NA	98.43
58_Blb26_BSE16_11	NA	32.84	66.24	0.06	0.123	0.064	NA	0.08	NA	99.42
59_Blb26_BSE16_11	NA	32.87	66.29	0.05	0.196	0.049	NA	0.13	NA	99.60
60_Blb26_BSE16_11	NA	32.54	65.05	0.05	0.182	0.060	NA	0.11	NA	98.02
61_Blb26_BSE16_11	NA	33.21	65.72	0.02	0.139	0.020	NA	0.14	NA	99.26
62_Blb26_BSE16_11	NA	32.84	66.09	0.03	0.185	0.022	NA	0.17	NA	99.36
63_Blb26_BSE16_11	0.030	32.96	65.95	0.04	0.186	NA	NA	0.33	NA	99.51
64_Blb26_BSE16_17	NA	32.88	66.06	0.04	NA	0.036	NA	0.11	NA	99.28
65_Blb26_BSE16_17	0.036	32.91	66.25	0.05	NA	0.042	NA	0.12	NA	99.51
66_Blb26_BSE16_17	0.035	32.75	66.24	0.03	0.143	0.026	NA	0.17	NA	99.40
67_Blb26_BSE16_17	NA	32.78	66.74	NA	0.221	NA	NA	0.08	NA	99.86
68_Blb26_BSE16_17	0.034	32.62	66.60	0.02	0.132	0.024	NA	0.21	NA	99.64
69_Blb26_BSE16_17	0.026	32.67	66.70	0.08	0.142	0.035	NA	0.13	NA	99.80
70_Blb26_BSE16_17	NA	32.29	65.10	0.02	0.150	0.027	NA	0.30	NA	97.89

Table 5: EMP data of sphalerites from the Erzkalk (Bleiberg).

	EMPA Bleiberg, Erzkalk [mass%]									
sample/analyses	**As**	**S**	**Zn**	**Fe**	**Pb**	**Ge**	**Cu**	**Cd**	**Tl**	**total**
EHK05_ZnS1	NA	32.81	66.60	0.33	0.048	NA	NA	0.34	NA	100.15
EHK05_ZnS2	NA	32.23	66.62	0.70	0.188	NA	NA	0.30	NA	100.07
EHK05_ZnS3	NA	32.24	66.65	0.27	0.106	NA	NA	0.32	NA	99.62
EHK05_ZnS4	NA	32.45	66.86	0.32	0.035	NA	NA	0.33	NA	100.01
EHK05_ZnS5	NA	32.31	67.08	0.35	0.053	NA	NA	0.30	NA	100.10
EHK05_ZnS6	NA	32.50	67.51	0.03	0.017	NA	NA	0.48	NA	100.54
EHK05_ZnS7	NA	31.87	66.98	0.12	0.040	NA	NA	0.40	NA	99.41
EHK05_ZnS8	NA	30.77	67.16	0.08	0.042	NA	NA	0.26	NA	98.31
EHK05_ZnS9	NA	32.46	67.18	0.13	NA	NA	NA	0.47	NA	100.24
EHK05_ZnS10	NA	32.44	66.93	0.28	NA	NA	NA	0.61	NA	100.26
EHK05_ZnS11	NA	32.26	67.32	0.11	0.035	NA	NA	0.21	NA	99.93
EHK05_ZnS12	NA	32.33	67.56	0.19	0.029	NA	NA	0.36	NA	100.47
EHK05_ZnS13	NA	32.33	66.89	0.23	0.019	NA	NA	0.36	NA	99.83
EHK05_ZnS14	NA	32.34	67.58	0.04	0.030	NA	NA	0.34	NA	100.34
EHK05_ZnS15	NA	32.34	67.61	0.09	NA	NA	NA	0.42	NA	100.46
EHK05_ZnS16	NA	32.03	67.16	0.06	NA	NA	NA	0.63	NA	99.88
EHK05_ZnS17	NA	32.55	67.58	0.14	NA	NA	NA	0.58	NA	100.85
EHK05_ZnS18	NA	32.25	67.36	0.06	NA	NA	NA	0.37	NA	100.04
EHK05_ZnS19	NA	32.56	67.78	0.08	NA	NA	NA	0.52	NA	100.94
EHK05_ZnS20	NA	32.61	67.78	0.05	NA	NA	NA	0.33	NA	100.77
EHK05_ZnS21	NA	32.75	66.79	0.20	0.023	NA	NA	0.36	NA	100.13
EHK05_ZnS22	NA	32.58	66.86	0.18	0.025	NA	NA	0.37	NA	100.01
EHK05_ZnS23	NA	32.38	66.53	0.18	NA	NA	NA	0.44	NA	99.53
EHK05_ZnS24	NA	32.33	67.80	0.11	NA	NA	NA	0.45	NA	100.69
EHK05_ZnS25	NA	32.44	67.71	0.12	0.037	NA	NA	0.41	NA	100.72
EHK05_ZnS26	NA	32.20	67.23	0.12	0.050	NA	NA	0.43	NA	100.03
EHK05_ZnS27	NA	32.27	67.66	0.12	0.023	NA	NA	0.40	NA	100.47
EHK05_ZnS28	NA	32.46	67.75	0.12	NA	NA	NA	0.45	NA	100.78
EHK05_ZnS29	NA	32.31	67.77	0.04	NA	NA	NA	0.45	NA	100.58
EHK05_ZnS30	NA	32.36	68.17	0.04	0.020	0.010	NA	0.29	NA	100.90
EHK05_ZnS31	NA	32.48	67.50	0.13	NA	NA	NA	0.49	NA	100.60
EHK05_ZnS32	NA	32.49	67.60	0.06	NA	NA	NA	0.42	NA	100.57
EHK05_ZnS33	NA	32.24	66.18	0.19	0.071	NA	NA	0.31	NA	99.01
EHK05_ZnS34	NA	32.60	66.76	0.24	0.015	NA	NA	0.28	NA	99.90
EHK05_ZnS35	NA	32.08	66.25	0.27	0.018	NA	NA	0.29	NA	98.91
EHK05_ZnS36	NA	32.15	66.64	0.21	0.057	NA	NA	0.56	NA	99.62
EHK05_ZnS37	NA	32.13	67.03	0.31	0.051	NA	NA	0.33	NA	99.85
EHK05_ZnS38	NA	32.48	67.20	0.24	0.082	NA	NA	0.30	NA	100.30
EHK05_ZnS39	NA	32.44	67.63	0.23	0.030	NA	NA	0.29	NA	100.63
EHK10_ZnS1	NA	33.20	67.97	0.06	NA	NA	NA	0.69	NA	101.92
EHK10_ZnS2	NA	33.29	68.41	0.01	0.014	NA	NA	0.31	NA	102.03
EHK10_ZnS3	NA	33.46	68.44	NA	NA	NA	NA	0.25	NA	102.15
EHK10_ZnS4	NA	33.23	68.18	0.02	NA	NA	NA	0.44	NA	101.87
EHK10_ZnS5	NA	33.61	67.69	0.02	NA	NA	NA	0.23	NA	101.55
EHK10_ZnS6	NA	33.27	68.05	NA	NA	NA	NA	0.43	NA	101.75
EHK10_ZnS7	NA	33.29	68.55	0.01	NA	NA	NA	0.17	NA	102.01
EHK10_ZnS8	NA	32.90	67.91	0.01	0.071	NA	NA	0.53	NA	101.42

Table 5: Continued.

	EMPA Bleiberg, Erzkalk [mass%]									
sample/analyses	**As**	**S**	**Zn**	**Fe**	**Pb**	**Ge**	**Cu**	**Cd**	**Tl**	**total**
EHK10_ZnS9	NA	33.29	67.50	0.01	0.0706	NA	NA	0.37	NA	101.23
EHK10_ZnS10	NA	33.10	67.70	0.05	0.0129	NA	NA	0.54	NA	101.36
EHK10_ZnS11	NA	33.21	67.64	NA	0.0129	NA	NA	0.43	NA	101.35
EHK10_ZnS12	NA	33.29	67.42	0.06	NA	NA	NA	0.41	NA	101.13
EHK10_ZnS13	NA	33.35	68.23	0.01	NA	NA	NA	0.27	NA	101.86
EHK10_ZnS14	NA	33.41	69.05	0.01	NA	NA	NA	0.22	NA	102.68
EHK10_ZnS15	NA	33.04	67.30	NA	NA	NA	NA	0.61	NA	100.97
EHK10_ZnS16	NA	33.00	67.41	0.02	NA	NA	NA	0.30	NA	100.71
EHK10_ZnS17	NA	33.23	67.89	NA	NA	NA	NA	0.35	NA	101.50
EHK10_ZnS18	NA	33.45	68.31	0.02	NA	NA	NA	0.28	NA	102.05
EHK10_ZnS19	NA	33.17	68.07	0.01	NA	NA	NA	0.35	NA	101.59
EHK10_ZnS20	NA	33.27	68.43	NA	NA	NA	NA	0.21	NA	101.92
EHK10_ZnS21	NA	33.26	68.34	NA	NA	NA	NA	0.33	NA	101.93
EHK10_ZnS22	NA	33.12	68.41	NA	NA	NA	NA	0.29	NA	101.82
EHK10_ZnS23	NA	33.31	68.38	NA	NA	NA	NA	0.24	NA	102.00
EHK10_ZnS24	NA	33.32	68.38	0.01	0.0561	NA	NA	0.15	NA	101.86
EHK10_ZnS25	NA	33.17	68.37	NA	NA	NA	NA	0.49	NA	102.04
EHK10_ZnS26	NA	33.37	68.17	0.01	NA	NA	NA	0.25	NA	101.79
EHK10_ZnS27	NA	33.26	68.10	NA	NA	NA	NA	0.40	NA	101.76
EHK10_ZnS28	NA	33.40	67.65	0.01	NA	NA	NA	0.47	NA	101.54
EHK10_ZnS29	NA	33.22	67.64	0.02	NA	NA	NA	0.48	NA	101.34
EHK10_ZnS30	NA	33.55	67.94	NA	NA	NA	NA	0.40	NA	101.89
EHK10_ZnS31	NA	33.24	67.60	NA	NA	NA	NA	0.71	NA	101.55
EHK10_ZnS32	NA	33.21	67.80	NA	NA	NA	NA	0.58	NA	101.59
EHK10_ZnS33	NA	33.32	68.03	0.01	NA	NA	NA	0.24	NA	101.62
EHK10_ZnS34	NA	32.66	67.62	0.01	0.0179	NA	NA	0.24	NA	100.54
EHK10_ZnS35	NA	33.39	67.67	NA	0.0173	NA	NA	0.33	NA	101.40
EHK10_ZnS36	NA	33.07	67.41	NA	NA	NA	NA	0.67	NA	101.16
EHK10_ZnS37	NA	33.29	67.50	0.01	0.0706	NA	NA	0.37	NA	101.23
WS_Blb1_ZnS1	NA	31.58	68.54	NA	NA	0.061	NA	0.06	NA	100.89
WS_Blb1_ZnS2	NA	29.22	63.93	0.59	0.061	NA	NA	0.23	NA	93.48
WS_Blb1_ZnS3	NA	32.46	67.20	0.10	NA	0.046	NA	NA	NA	100.26
WS_Blb1_ZnS4	NA	32.03	68.59	0.35	0.2042	NA	NA	0.09	NA	100.76
WS_Blb1_ZnS5	NA	31.84	69.16	0.04	NA	NA	NA	0.19	NA	101.51
WS_Blb1_ZnS6	NA	32.47	68.71	0.27	0.0568	NA	NA	0.11	NA	101.48
WS_Blb1_ZnS7	NA	31.85	67.15	0.13	0.0612	NA	NA	NA	NA	100.36
WS_Blb1_ZnS8	NA	31.77	68.26	1.18	0.1846	NA	NA	0.13	NA	100.28
WS_Blb1_ZnS9	NA	31.62	68.15	0.09	0.0204	NA	NA	0.01	NA	100.28
WS_Blb1_ZnS10	NA	31.54	68.41	0.31	0.1853	NA	NA	0.19	NA	100.48
WS_Blb1_ZnS11	NA	32.05	66.62	0.27	0.0656	0.116	NA	0.02	NA	100.27
WS_Blb1_ZnS12	0.021	32.50	63.95	1.43	0.0323	NA	NA	0.34	NA	99.31
WS_Blb1_ZnS13	NA	31.88	67.42	2.43	0.0557	NA	NA	0.14	NA	99.88
WS_Blb1_ZnS14	NA	29.30	67.95	0.41	0.0326	NA	NA	0.04	NA	97.95
WS_Blb1_ZnS15	NA	32.02	67.91	0.55	0.123	NA	NA	0.01	NA	100.39
WS_Blb1_ZnS16	0.031	31.69	67.30	0.35	0.0996	NA	NA	NA	NA	100.11
WS_Blb1_ZnS17	NA	32.00	68.08	0.95	0.1326	NA	NA	0.18	NA	100.67
WS_Blb1_ZnS18	NA	31.32	67.91	0.33	0.0834	NA	NA	0.01	NA	99.71

Table 5: Continued.

EMPA Bleiberg, Erzkalk [mass%]										
sample/analyses	**As**	**S**	**Zn**	**Fe**	**Pb**	**Ge**	**Cu**	**Cd**	**Tl**	**total**
WS_Blb1_ZnS19	NA	30.07	63.16	0.35	0.1072	0.010	NA	0.02	NA	94.09
WS_Blb1_ZnS20	NA	31.94	67.13	0.63	0.1956	0.127	NA	0.07	NA	99.93
WS_Blb1_ZnS21	NA	32.01	66.31	0.57	0.0864	NA	NA	0.02	NA	99.20
WS_Blb1_ZnS22	NA	32.01	66.23	0.78	0.0795	NA	NA	0.04	NA	98.88
WS_Blb1_ZnS23	NA	31.90	67.25	0.50	0.0978	NA	NA	0.14	NA	99.59
WS_Blb1_ZnS24	NA	32.07	67.94	0.11	0.1905	NA	NA	0.09	NA	100.25
WS_Blb1_ZnS25	NA	32.05	67.27	0.08	0.0791	0.017	NA	0.04	NA	100.07
WS_Blb1_ZnS26	NA	31.92	67.29	0.61	0.0886	NA	NA	0.12	NA	99.82
WS_Blb1_ZnS27	0.051	31.72	64.34	0.33	0.1563	NA	NA	0.01	NA	97.46
WS_Blb1_ZnS28	NA	31.78	67.80	1.11	0.2234	NA	NA	0.22	NA	100.00
WS_Blb1_ZnS29	NA	32.54	67.12	0.09	0.1028	0.090	NA	0.04	NA	100.73
WS_Blb1_ZnS30	NA	32.98	65.90	0.86	0.0791	0.061	NA	0.03	NA	99.63
WS_Blb1_ZnS31	NA	31.82	66.33	0.60	0.0569	NA	NA	NA	NA	98.84
WS_Blb1_ZnS32	NA	30.18	62.67	0.57	0.1227	NA	NA	0.10	NA	93.27
WS_Blb1_ZnS33	NA	31.98	69.08	0.13	0.1837	NA	NA	0.26	NA	101.52
WS_Blb1_ZnS34	NA	31.82	67.53	0.17	0.0288	NA	NA	0.01	NA	101.22
WS_Blb1_ZnS35	NA	32.20	68.34	1.78	0.0803	NA	NA	0.02	NA	101.47
WS_Blb1_ZnS36	NA	31.91	67.85	0.67	0.2377	NA	NA	0.04	NA	100.54
WS_Blb1_ZnS37	NA	31.89	68.72	0.51	0.2242	NA	NA	0.04	NA	101.19
WS_Blb1_ZnS38	NA	32.17	69.95	0.26	0.2859	NA	NA	0.10	NA	102.35
WS_Blb1_ZnS39	NA	31.98	70.04	0.11	0.0221	NA	NA	0.08	NA	102.45
WS_Blb1_ZnS40	NA	32.07	68.97	0.35	NA	NA	NA	0.40	NA	101.53
WS_Blb1_ZnS41	NA	31.57	67.32	0.07	0.0122	NA	NA	0.03	NA	99.51
WS_Blb1_ZnS42	NA	31.96	67.11	0.33	0.2599	0.049	NA	0.02	NA	100.06
WS_Blb1_ZnS43	NA	32.39	69.92	0.77	0.1506	NA	NA	0.15	NA	102.64
WS_Blb1_ZnS44	NA	32.10	69.12	0.17	0.0151	NA	NA	0.07	NA	101.37
WS_Blb1_ZnS45	NA	32.08	68.36	0.08	NA	NA	NA	0.42	NA	100.91
WS_Blb1_ZnS46	NA	31.31	68.72	0.04	0.0139	NA	NA	0.12	NA	100.48
WS_Blb1_ZnS47	NA	28.56	65.28	0.20	0.1336	NA	NA	0.11	NA	94.56
WS_Blb1_ZnS48	NA	30.43	69.69	0.54	0.074	NA	NA	0.14	NA	100.53
WS_Blb07_ZnS1	NA	32.21	69.06	0.27	NA	NA	NA	0.57	NA	101.84
WS_Blb07_ZnS2	NA	31.94	69.23	NA	NA	NA	NA	0.23	NA	101.42
WS_Blb07_ZnS4	NA	32.12	68.20	NA	0.0202	NA	NA	0.67	NA	101.01
WS_Blb07_ZnS5	NA	32.09	67.37	0.01	NA	NA	NA	0.57	NA	100.07
WS_Blb07_ZnS6	NA	32.07	68.17	0.02	0.0292	NA	NA	0.64	NA	100.88
WS_Blb07_ZnS7	NA	32.02	67.48	0.01	NA	NA	NA	0.31	NA	99.87
WS_Blb07_ZnS8	NA	32.05	67.81	0.01	0.0369	NA	NA	0.63	NA	100.56
WS_Blb07_ZnS9	NA	32.04	67.48	0.07	NA	NA	NA	0.49	NA	100.01
WS_Blb07_ZnS10	NA	32.41	67.94	NA	NA	NA	NA	0.43	NA	100.80
WS_Blb07_ZnS11	NA	32.01	68.87	0.02	NA	NA	NA	0.66	NA	101.59
WS_Blb07_ZnS12	NA	32.74	69.06	0.02	0.0263	NA	NA	0.60	NA	102.42
WS_Blb07_ZnS13	NA	31.99	68.71	0.02	NA	NA	NA	0.55	NA	101.30
WS_Blb07_ZnS14	NA	31.67	66.68	0.02	0.0324	NA	NA	0.56	NA	98.93
WS_Blb07_ZnS15	NA	32.09	68.59	0.01	NA	NA	NA	0.46	NA	101.19
WS_Blb07_ZnS16	NA	32.02	69.58	0.05	NA	NA	NA	0.26	NA	101.87
WS_Blb07_ZnS17	NA	32.28	68.47	0.01	NA	NA	NA	0.52	NA	101.35

Table 5: Continued.

EMPA Bleiberg, Erzkalk [mass%]										
sample/analyses	**As**	**S**	**Zn**	**Fe**	**Pb**	**Ge**	**Cu**	**Cd**	**Tl**	**total**
WS_Blb07_ZnS18	NA	32.11	67.12	0.08	NA	NA	NA	0.50	NA	99.80
WS_Blb07_ZnS19	NA	32.03	67.29	0.07	NA	NA	NA	0.56	NA	99.88
WS_Blb07_ZnS20	NA	32.73	61.74	NA	NA	NA	NA	0.45	NA	94.98
WS_Blb07_ZnS21	NA	32.02	68.84	0.03	0.0292	NA	NA	0.26	NA	101.18
WS_Blb07_ZnS22	NA	32.01	68.06	0.06	NA	NA	NA	0.51	NA	100.62
WS_Blb07_ZnS23	NA	31.92	68.46	0.03	NA	NA	NA	0.54	NA	100.98
WS_Blb07_ZnS24	NA	31.69	67.54	0.04	0.021	NA	NA	0.51	NA	99.74
WS_Blb07_ZnS25	NA	31.88	68.85	NA	NA	NA	NA	0.41	NA	101.15
WS_Blb07_ZnS26	NA	31.98	68.94	0.01	NA	NA	NA	0.30	NA	101.22
WS_Blb07_ZnS27	NA	31.92	68.10	NA	NA	NA	NA	0.56	NA	100.62
WS_Blb07_ZnS28	NA	31.89	67.77	NA	0.0358	NA	NA	0.52	NA	100.22
WS_Blb07_ZnS29	NA	32.07	67.20	NA	0.0453	NA	NA	0.48	NA	99.76
WS_Blb07_ZnS30	NA	32.26	68.11	0.01	NA	NA	NA	0.44	NA	100.81
WS_Blb07_ZnS32	NA	31.90	68.36	NA	NA	NA	NA	0.37	NA	100.63
WS_Blb07_ZnS33	NA	28.69	60.93	NA	NA	NA	NA	0.40	NA	90.04
WS_Blb07_ZnS36	NA	31.84	68.54	0.02	NA	NA	NA	0.54	NA	100.95
WS_Blb07_ZnS37	NA	32.22	67.68	NA	0.0209	NA	NA	0.43	NA	100.35
WS_Blb07_ZnS38	NA	31.98	67.61	0.01	NA	NA	NA	0.35	NA	99.95
WS_Blb07_ZnS39	NA	32.01	68.18	0.01	NA	NA	NA	0.68	NA	100.91
WS_Blb07_ZnS40	NA	31.91	68.97	0.01	0.0281	NA	NA	0.64	NA	101.56
WS_Blb07_ZnS41	NA	33.14	68.05	0.03	0.0119	NA	NA	0.55	NA	102.04
WS_Blb07_ZnS42	NA	32.01	68.49	0.04	0.2673	NA	NA	0.59	NA	101.13
WS_Blb07_ZnS43	NA	31.81	68.06	0.04	NA	NA	NA	0.56	NA	100.50
WS_Blb07_ZnS44	NA	31.81	68.72	0.01	0.0582	NA	NA	0.56	NA	101.11
WS_Blb07_ZnS46	NA	31.90	68.37	0.02	NA	NA	NA	0.53	NA	100.83
WS_Blb07_ZnS48	NA	28.79	68.25	0.03	NA	NA	NA	0.53	NA	97.83
WS_Blb07_ZnS49	NA	32.40	68.17	0.03	0.2263	NA	NA	0.64	NA	101.33
WS_Blb07_ZnS50	NA	31.66	68.59	0.03	0.0797	NA	NA	0.45	NA	100.78
WS_Blb07_ZnS51	NA	31.80	68.81	0.04	0.045	NA	NA	0.24	NA	100.85
WS_Blb07_ZnS52	NA	31.90	67.37	NA	NA	NA	NA	0.59	NA	99.90
WS_Blb07_ZnS53	NA	32.18	68.37	0.01	0.0234	NA	NA	0.42	NA	100.97
WS_Blb07_ZnS55	0.162	33.12	60.36	NA	NA	NA	NA	0.24	NA	94.00
WS_Blb07_ZnS57	NA	32.03	67.32	0.05	0.061	NA	NA	0.47	NA	99.83
WS_Blb07_ZnS58	NA	31.50	58.79	0.01	NA	NA	NA	0.42	NA	90.85
WS_Blb07_ZnS59	NA	31.64	68.44	0.06	0.0753	NA	NA	0.35	NA	100.46
WS_Blb25_ZnS1	NA	31.91	67.41	0.01	0.0197	NA	NA	0.71	NA	101.25
WS_Blb25_ZnS6	NA	32.68	67.53	1.17	0.05	NA	0.015	0.53	NA	101.58
1_MS391_WS-Blb06_BSE1	NA	32.42	66.42	0.76	0.0632	0.025	NA	0.12	NA	99.23
2_MS391_WS-Blb06_BSE1	NA	32.60	65.14	0.25	NA	0.061	NA	0.10	NA	99.44
3_MS391_WS-Blb06_BSE1	NA	32.57	65.95	1.41	0.1309	0.046	NA	0.10	NA	99.39
4_MS391_WS-Blb06_BSE1	NA	32.61	65.53	0.58	0.1499	NA	NA	0.42	NA	99.34
5_MS391_WS-Blb06_BSE1	NA	32.69	65.50	0.78	NA	0.027	NA	0.13	NA	98.63
6_MS391_WS-Blb06_BSE1	NA	32.77	65.68	0.28	NA	NA	NA	0.11	NA	99.19
7_MS391_WS-Blb06_BSE1	NA	32.42	65.70	0.63	NA	NA	NA	0.28	NA	98.92
8_MS391_WS-Blb06_BSE1	NA	32.73	66.54	0.52	NA	0.014	NA	0.18	NA	99.46
9_MS391_WS-Blb06_BSE1	NA	32.69	66.60	NA	NA	0.018	NA	0.19	NA	99.52
10_MS391_WS-Blb06_BSE1	NA	32.85	66.55	0.02	NA	NA	NA	0.54	NA	100.08

Table 5: Continued.

EMPA Bleiberg, Erzkalk [mass%]										
sample/analyses	**As**	**S**	**Zn**	**Fe**	**Pb**	**Ge**	**Cu**	**Cd**	**Tl**	**total**
12_MS391_WS-Blb06_BSE1	NA	32.74	66.67	0.01	0.1276	NA	NA	0.25	NA	99.70
13_MS391_WS-Blb06_BSE1	NA	32.87	66.94	0.03	NA	NA	NA	0.20	NA	100.04
14_MS391_WS-Blb06_BSE1	NA	32.60	66.47	0.02	NA	NA	NA	0.39	NA	99.51
15_MS391_WS-Blb06_BSE1	NA	32.93	66.94	0.06	NA	NA	NA	0.21	NA	100.25
16_MS391_WS-Blb06_BSE1	NA	32.53	66.20	0.05	0.128	0.015	NA	0.18	NA	98.96
17_MS391_WS-Blb06_BSE3	NA	32.59	66.83	0.04	NA	NA	NA	0.26	NA	99.71
18_MS391_WS-Blb06_BSE3	NA	32.46	66.74	0.02	NA	0.014	NA	0.16	NA	99.62
19_MS391_WS-Blb06_BSE3	NA	32.65	67.10	0.24	NA	NA	NA	0.09	NA	99.84
20_MS391_WS-Blb06_BSE3	NA	32.71	66.61	NA	NA	NA	NA	0.15	NA	99.48
21_MS391_WS-Blb06_BSE3	NA	32.83	66.46	NA	NA	NA	NA	0.40	NA	99.83
22_MS391_WS-Blb06_BSE3	NA	32.28	66.05	0.02	0.1206	NA	NA	0.33	NA	98.68
23_MS391_WS-Blb06_BSE3	NA	32.22	66.55	0.03	NA	NA	NA	0.13	NA	98.91
24_MS391_WS-Blb06_BSE3	NA	32.61	66.52	NA	NA	NA	NA	0.09	NA	99.22
25_MS391_WS-Blb06_BSE4	NA	32.91	66.15	NA	NA	0.074	NA	0.03	NA	99.55
26_MS391_WS-Blb06_BSE4	NA	32.94	66.75	0.25	0.133	NA	NA	0.12	NA	99.83
27_MS391_WS-Blb06_BSE4	NA	32.81	66.81	0.02	NA	0.013	NA	0.20	NA	99.86
28_MS391_WS-Blb06_BSE4	NA	32.99	67.16	0.02	NA	NA	NA	0.20	NA	100.37
29_MS391_WS-Blb06_BSE4	NA	32.67	66.72	0.01	NA	NA	NA	0.34	NA	99.76
30_MS391_WS-Blb06_BSE4	NA	32.66	66.99	0.03	NA	0.029	NA	0.12	NA	99.82
31_MS391_WS-Blb06_BSE5	NA	32.92	66.44	0.02	NA	NA	NA	0.19	NA	99.64
32_MS391_WS-Blb06_BSE5	NA	32.60	65.29	0.09	NA	0.014	NA	0.19	NA	98.34
34_MS391_WS-Blb06_BSE5	NA	31.24	63.38	0.11	0.1331	0.073	NA	0.06	NA	95.20
35_MS391_WS-Blb06_BSE5	NA	32.79	66.51	0.23	0.2282	NA	NA	0.26	NA	99.74
37_MS391_WS-Blb06_BSE6	NA	32.70	66.40	0.04	0.1344	NA	NA	0.21	NA	99.46
38_MS391_WS-Blb06_BSE6	NA	32.35	66.10	0.03	0.1196	0.018	NA	0.14	NA	98.62
39_MS391_WS-Blb06_BSE6	NA	32.92	66.19	0.02	NA	NA	NA	0.38	NA	99.53
40_MS391_WS-Blb06_BSE6	NA	32.89	66.23	0.04	NA	0.013	NA	0.18	NA	99.37
41_MS391_WS-Blb06_BSE6	NA	32.63	66.71	0.06	NA	0.019	NA	0.13	NA	99.61
42_MS391_WS-Blb06_BSE6	NA	32.71	66.90	0.12	NA	NA	NA	0.15	NA	99.93
43_MS391_WS-Blb06_BSE6	NA	32.75	67.24	0.04	0.1312	0.022	NA	0.11	NA	100.41
44_MS391_WS-Blb06_BSE6	NA	33.06	67.26	0.14	0.1442	NA	NA	0.17	NA	100.64
1_EHK02_BSE3_5b	NA	32.85	66.43	0.01	0.1436	0.037	NA	0.11	NA	99.59
2_EHK02_BSE3_5b	0.026	32.55	66.54	0.06	NA	0.059	NA	0.11	NA	99.61
3_EHK02_BSE3_5b_hell	0.036	32.83	66.55	0.13	0.1339	0.060	NA	0.05	NA	99.75
4_EHK02_BSE3_5b_hell	NA	32.73	66.25	0.11	NA	0.065	NA	0.10	NA	99.42
5_EHK02_BSE3_5b_hell	0.046	32.64	65.43	0.08	0.1651	0.127	NA	0.06	NA	98.62
6_EHK02_BSE3_5b_hell	0.029	33.06	66.50	0.11	0.147	0.096	NA	0.08	NA	99.96
7_EHK02_BSE3_5b_hell	0.034	32.74	66.27	0.10	NA	0.097	NA	0.07	NA	99.55
8_EHK02_BSE3_5b_	0.061	33.00	66.60	0.14	0.1771	0.074	NA	0.08	NA	100.33
9_EHK02_BSE3_5b_	0.042	32.89	66.42	0.25	0.1992	0.072	NA	0.11	NA	99.87
10_EHK02_BSE3_5b_	0.036	32.70	65.99	0.17	0.1492	0.074	NA	0.11	NA	99.23
11_EHK02_BSE5_6b_	NA	32.72	66.42	0.14	0.1434	0.054	NA	0.07	NA	99.95
12_EHK02_BSE5_6b_	0.151	33.19	61.32	0.54	NA	0.040	NA	0.08	0.088	100.85
13_EHK02_BSE5_6b	NA	33.10	66.21	5.70	0.2926	NA	NA	0.31	NA	100.27
14_EHK02_BSE5_7	0.076	32.92	65.85	0.56	NA	0.073	NA	NA	NA	100.21
15_EHK02_BSE5_7	0.154	32.90	65.01	1.09	0.1682	0.063	NA	0.12	NA	99.48
16_EHK02_BSE5_7	0.026	33.03	65.93	0.90	0.2564	0.053	NA	0.05	NA	99.79

Table 5: Continued.

EMPA Bleiberg, Erzkalk [mass%]										
sample/analyses	**As**	**S**	**Zn**	**Fe**	**Pb**	**Ge**	**Cu**	**Cd**	**Tl**	**total**
17_EHK02_BSE5_7	0.168	33.15	62.82	0.53	0.1617	0.074	NA	0.05	0.083	99.93
19_EHK02_BSE5_7	0.032	32.88	66.51	0.62	0.1506	0.032	NA	0.13	NA	99.99
20_EHK02_BSE5_7	NA	32.84	66.74	0.29	0.1229	0.032	NA	0.28	NA	100.10
21_EHK02_BSE5_8	NA	32.87	66.13	0.07	NA	NA	NA	0.37	NA	99.52
22_EHK02_BSE5_8	NA	32.65	66.23	0.02	NA	NA	NA	0.38	NA	99.47
23_EHK02_BSE5_8	NA	32.59	66.91	0.03	0.1584	NA	NA	0.19	NA	99.86
24_EHK02_BSE5_8	0.030	32.05	66.31	NA	0.1338	0.015	NA	0.50	NA	99.28
25_EHK02_BSE5_8	NA	32.78	66.59	0.08	0.2906	NA	NA	0.32	NA	100.07
26_EHK02_BSE5_8	NA	32.63	66.44	0.10	0.2681	0.013	NA	0.35	NA	99.76
27_EHK02_BSE5_8	NA	32.56	66.62	0.10	0.1988	0.032	NA	0.20	NA	100.04
28_EHK02_BSE5_8	NA	32.58	66.29	0.10	0.5161	0.023	NA	0.30	NA	99.59
29_EHK02_BSE5_8	0.028	32.44	66.51	0.11	0.2647	0.022	NA	0.26	NA	99.56
30_EHK02_BSE5_9	0.026	32.16	65.78	0.09	0.2116	0.020	NA	0.24	NA	98.55
31_EHK02_BSE5_9	NA	32.67	66.31	0.08	0.2449	NA	NA	0.20	NA	99.35
32_EHK02_BSE5_9	0.033	32.46	65.58	0.04	NA	0.016	NA	0.66	NA	99.07
33_EHK02_BSE5_9	NA	32.71	65.72	0.09	0.2088	0.014	NA	0.55	NA	99.22
34_EHK02_BSE5_9	NA	32.63	65.97	0.07	0.1357	0.027	NA	0.13	NA	99.12
35_EHK02_BSE5_9	0.028	31.81	66.05	0.08	0.2747	0.016	NA	0.32	NA	98.52
36_EHK02_BSE5_9	NA	32.72	66.28	0.06	0.2406	NA	NA	0.06	NA	99.38
37_EHK02_BSE5_9	0.028	32.55	66.21	0.11	0.1949	NA	NA	0.15	NA	99.20
38_EHK02_BSE4_12	NA	32.74	66.72	0.07	0.1828	NA	NA	0.19	NA	99.86
39_EHK02_BSE4_12	NA	32.43	66.40	0.04	0.1495	0.016	NA	0.42	NA	99.50
40_EHK02_BSE4_12	NA	32.78	66.53	0.07	0.1405	0.013	NA	0.45	NA	99.98
41_EHK02_BSE4_12	0.028	32.80	66.83	0.05	0.1265	NA	NA	0.32	NA	100.18
42_EHK02_BSE4_12	NA	32.85	66.59	0.05	0.1398	0.013	NA	0.33	NA	100.00
43_EHK02_BSE4_12	NA	32.68	66.35	0.07	0.1328	NA	NA	0.22	NA	99.56
44_EHK02_BSE4_12	NA	32.94	66.57	0.16	0.137	NA	0.008	0.47	NA	100.16
45_EHK02_BSE4_12	NA	32.77	66.48	0.03	0.1457	NA	NA	0.30	NA	99.84
46_EHK02_BSE4_12	NA	32.51	66.38	0.05	0.2039	NA	NA	0.17	NA	99.13
47_EHK02_BSE4_12	NA	32.76	65.86	NA	NA	NA	NA	0.64	NA	99.41
48_EHK02_BSE3_12b_dunkel	NA	32.54	66.45	0.02	NA	NA	NA	0.16	NA	99.41
49_EHK02_BSE3_12b_dunkel	NA	32.68	65.97	0.12	0.1307	0.015	NA	0.26	NA	99.26
50_EHK02_BSE3_12b_dunkel	NA	32.87	66.55	0.19	0.1455	NA	NA	0.11	NA	99.71
51_EHK02_BSE3_12b_dunkel	NA	32.75	66.40	0.09	NA	NA	NA	0.12	NA	99.40
52_EHK02_BSE3_12b_dunkel	NA	32.66	65.88	0.03	NA	NA	NA	0.23	NA	99.09
53_EHK02_BSE3_12b_dunkel	NA	32.82	66.09	0.13	0.1735	NA	NA	0.14	NA	99.40
54_EHK02_BSE3_12b_Band	0.124	32.92	62.50	0.23	NA	0.050	NA	NA	NA	99.77
55_EHK02_BSE3_12b_Band	0.035	33.07	66.23	3.90	0.2214	0.024	NA	0.14	NA	99.96
56_EHK02_BSE3_12b_Band	0.032	32.96	65.17	0.30	0.1694	0.021	NA	0.13	NA	99.95
57_EHK02_BSE3_12b_hell	NA	32.67	66.41	1.46	0.1678	NA	NA	0.27	NA	99.57
58_EHK02_BSE3_12b_hell	NA	32.77	66.28	0.11	NA	0.014	NA	0.37	NA	99.71
59_EHK02_BSE3_12b_hell	NA	32.53	66.16	0.11	0.1597	NA	NA	0.37	NA	99.30
60_EHK02_BSE3_12b_hell	NA	32.56	66.10	0.10	0.1371	NA	NA	0.43	NA	99.47
61_EHK02_BSE3_12b	NA	32.49	66.17	0.14	0.199	NA	NA	0.20	NA	99.23
62_EHK02_BSE3_7b	0.032	32.72	65.05	0.26	NA	0.041	NA	0.21	NA	99.27
62_EHK02_BSE3_7b	NA	32.65	65.69	1.02	0.1722	0.015	NA	0.20	NA	99.02
63_EHK02_BSE3_7b	NA	32.90	66.24	0.32	0.1303	0.028	NA	0.09	NA	99.67
65_EHK02_BSE3_7b	NA	32.83	66.33	0.25	0.1459	0.023	NA	0.16	NA	99.57

Table 5: Continued.

	EMPA Bleiberg, Erzkalk [mass%]									
sample/analyses	**As**	**S**	**Zn**	**Fe**	**Pb**	**Ge**	**Cu**	**Cd**	**Tl**	**total**
66_EHK02_BSE3_7b	0.152	32.80	63.53	0.13	NA	0.069	NA	0.05	NA	99.52
67_EHK02_BSE3_7b	0.133	32.66	64.05	2.39	0.4637	0.053	NA	0.06	NA	99.23
68_EHK02_BSE3_7b	0.102	32.16	64.26	1.83	0.3977	0.046	NA	0.10	NA	99.08
69_EHK02_BSE3_7b	NA	32.73	66.53	1.94	0.4115	0.026	NA	0.13	NA	99.85
70_EHK02_BSE3_7b	NA	33.32	66.28	0.18	0.2325	0.018	NA	0.32	NA	100.48
71_EHK02_BSE3_7b	NA	32.78	66.61	0.33	0.1751	0.017	NA	0.37	NA	100.06
72_EHK02_BSE3_7b	0.034	32.56	65.84	0.16	NA	0.030	NA	0.30	NA	99.47

Table 6: EMP data of sphalerites from the Crest (Bleiberg).

	EMPA Bleiberg, Josefischolle [mass%]									
sample/analyses	**As**	**S**	**Zn**	**Fe**	**Pb**	**Ge**	**Cu**	**Cd**	**Tl**	**total**
1-100_AS8616a_BSE3	NA	32.85	68.01	0.02	NA	NA	NA	0.30	NA	101.18
1-100_AS8616a_BSE3	NA	32.66	68.13	0.03	NA	NA	NA	0.39	NA	101.21
1-100_AS8616a_BSE3	NA	34.08	67.07	0.03	NA	NA	0.026	0.40	NA	101.61
1-100_AS8616a_BSE3	NA	32.20	67.58	0.16	0.336	NA	NA	0.12	NA	100.40
1-100_AS8616a_BSE3	NA	32.10	67.18	0.26	NA	NA	NA	0.14	NA	99.69
1-100_AS8616a_BSE3	0.032	33.04	67.10	0.33	NA	0.021	NA	0.11	NA	100.63
1-100_AS8616a_BSE3	NA	32.67	67.32	0.03	NA	0.014	NA	0.39	NA	100.42
1-100_AS8616a_BSE3	NA	32.72	67.09	0.07	NA	NA	0.025	0.57	NA	100.47
1-100_AS8616a_BSE3	NA	32.80	67.21	0.01	NA	NA	0.046	0.79	NA	100.85
1-100_AS8616a_BSE3	NA	32.40	67.04	0.02	NA	NA	0.058	0.69	NA	100.20
1-100_AS8616a_BSE3	NA	32.71	67.30	NA	NA	NA	0.087	0.64	NA	100.74
1-100_AS8616a_BSE3	NA	32.83	67.84	NA	NA	NA	NA	0.45	NA	101.12
1-100_AS8616a_BSE3	NA	32.62	67.37	0.01	NA	NA	NA	0.48	NA	100.48
1-100_AS8616a_BSE3	NA	32.84	67.85	NA	NA	NA	0.024	0.52	NA	101.23
1-100_AS8616a_BSE3	NA	32.63	67.70	NA	NA	NA	0.031	0.61	NA	100.96
1-100_AS8616a_BSE3	NA	32.66	67.80	0.02	NA	NA	NA	0.41	NA	100.89
1-100_AS8616a_BSE3	NA	32.48	67.50	0.08	NA	NA	NA	0.19	NA	100.24
1-100_AS8616a_BSE3	NA	32.65	67.87	0.11	NA	NA	NA	0.32	NA	100.94
1-100_AS8616a_BSE3	NA	32.84	67.65	0.68	NA	0.015	0.022	0.18	NA	101.40
1-100_AS8616a_BSE3	NA	32.79	67.59	0.04	NA	NA	NA	0.39	NA	100.81
1-100_AS8616a_BSE3	0.051	32.79	66.48	0.97	NA	NA	NA	0.29	NA	100.59
1-100_AS8616a_BSE3	NA	33.18	66.91	0.08	NA	NA	NA	0.36	NA	100.52
1-100_AS8616a_BSE3	NA	32.49	67.33	0.01	NA	NA	NA	0.19	NA	100.02
1-100_AS8616a_BSE3	NA	32.60	67.57	0.01	NA	NA	NA	0.14	NA	100.32
1-100_AS8616a_BSE3	NA	32.61	67.03	0.03	NA	NA	NA	0.53	NA	100.20
1-100_AS8616a_BSE3	NA	33.87	66.60	0.03	NA	NA	NA	0.53	NA	101.03
1-100_AS8616a_BSE3	NA	33.12	67.66	0.04	NA	NA	NA	0.39	NA	101.21
1-100_AS8616a_BSE3	NA	32.48	66.76	0.98	0.281	0.013	NA	0.18	NA	100.70
1-100_AS8616a_BSE3	NA	32.83	68.02	0.42	NA	0.024	NA	0.09	NA	101.38
1-100_AS8616a_BSE3	NA	32.71	68.35	0.05	NA	NA	NA	0.19	NA	101.29
1-100_AS8616a_BSE3	NA	32.59	68.02	0.13	NA	NA	NA	0.30	NA	101.04
1-100_AS8616a_BSE3	NA	32.93	67.04	0.53	0.366	0.016	NA	0.07	NA	100.95
1-100_AS8616a_BSE3	NA	32.56	66.47	0.78	0.236	NA	NA	0.23	NA	100.27
1-100_AS8616a_BSE3	NA	32.84	67.41	0.09	0.264	0.017	NA	0.21	NA	100.84
1-100_AS8616a_BSE3	NA	32.61	67.45	0.02	NA	NA	NA	0.36	NA	100.44
1-100_AS8616a_BSE3	NA	32.99	66.60	0.02	NA	NA	NA	0.48	NA	100.10
1-100_AS8616a_BSE3	NA	32.55	67.13	0.07	NA	NA	NA	0.42	NA	100.16
1-100_AS8616a_BSE3	NA	32.85	67.37	0.02	NA	NA	NA	0.34	NA	100.58
1-100_AS8616a_BSE3	NA	32.42	66.50	0.61	NA	0.015	NA	0.11	NA	99.66
1-100_AS8616a_BSE3	NA	32.43	67.83	0.03	NA	NA	NA	0.37	NA	100.65
1-100_AS8616a_BSE3	NA	32.50	65.59	0.11	0.338	0.024	NA	0.22	NA	98.78
1-100_AS8616a_BSE3	NA	32.28	67.54	0.03	NA	NA	NA	0.73	NA	100.58
1-100_AS8616a_BSE3	NA	32.44	67.68	0.03	0.271	NA	NA	0.57	NA	101.00
1-100_AS8616a_BSE3	NA	32.91	68.20	0.04	NA	NA	NA	0.30	NA	101.45
1-100_AS8616a_BSE3	NA	32.86	67.85	0.09	NA	NA	NA	0.29	NA	101.10
1-100_AS8616a_BSE3	NA	32.20	67.34	0.07	0.248	0.016	NA	0.32	NA	100.19
1-100_AS8616a_BSE3	0.054	32.74	63.32	4.43	NA	0.017	NA	0.14	NA	100.68

Table 6: Continued.

	EMPA Bleiberg, Josefischolle [mass%]									
sample/analyses	**As**	**S**	**Zn**	**Fe**	**Pb**	**Ge**	**Cu**	**Cd**	**Tl**	**total**
1-100_AS8616a_BSE3	NA	32.68	65.60	0.05	NA	NA	NA	0.41	NA	98.75
1-100_AS8616a_BSE3	NA	32.50	67.44	0.11	0.325	0.020	NA	0.27	NA	100.67
1-100_AS8616a_BSE3	NA	32.80	67.20	0.03	NA	NA	NA	0.54	NA	100.58
1-100_AS8616a_BSE3	NA	32.42	67.13	0.10	0.265	0.016	NA	0.25	NA	100.18
1-100_AS8616a_BSE3	NA	31.87	66.21	0.08	NA	0.014	NA	0.22	NA	98.40
1-100_AS8616a_BSE3	NA	31.48	65.18	0.05	NA	NA	NA	0.35	NA	97.07
1-100_AS8616a_BSE3	NA	32.81	67.52	0.35	NA	NA	NA	0.26	NA	100.95
1-100_AS8616a_BSE3	NA	31.98	67.91	0.03	NA	NA	NA	0.66	NA	100.59
1-100_AS8616a_BSE3	NA	32.27	67.05	0.11	0.424	0.014	NA	0.33	NA	100.20
1-100_AS8616a_BSE3	NA	31.94	67.48	0.05	NA	NA	NA	0.30	NA	99.77
1-100_AS8616a_BSE3	NA	32.48	67.63	0.08	0.271	0.020	NA	0.29	NA	100.77
1-100_AS8616a_BSE3	NA	32.41	67.35	0.03	NA	NA	NA	0.34	NA	100.13
1-100_AS8616a_BSE3	NA	32.47	67.96	0.07	0.360	NA	NA	0.28	NA	101.14
1-100_AS8616a_BSE3	NA	32.19	67.16	0.04	NA	NA	NA	0.27	NA	99.66
1-100_AS8616a_BSE3	NA	32.42	67.59	0.08	0.180	NA	NA	0.54	NA	100.82
1-100_AS8616a_BSE3	NA	30.71	61.87	0.07	NA	0.016	NA	0.23	NA	92.89
1-100_AS8616a_BSE3	0.028	32.20	66.41	1.11	NA	0.017	NA	0.25	NA	100.01
1-100_AS8616a_BSE3	NA	32.30	67.02	0.51	NA	0.026	NA	0.08	NA	99.94
1-100_AS8616a_BSE3	NA	32.10	66.47	0.02	NA	NA	0.081	0.45	NA	99.13
1-100_AS8616a_BSE3	NA	32.28	67.31	NA	NA	NA	0.053	0.50	NA	100.15
1-100_AS8616a_BSE3	NA	32.36	67.37	NA	NA	NA	NA	0.46	NA	100.19
1-100_AS8616a_BSE3	NA	32.17	67.15	0.02	NA	NA	NA	0.49	NA	99.83
1-100_AS8616a_BSE3	NA	32.47	67.54	0.31	NA	NA	NA	0.15	NA	100.47
1-100_AS8616a_BSE3	NA	31.81	67.03	0.02	NA	NA	NA	0.30	NA	99.16
1-100_AS8616a_BSE3	NA	31.72	66.53	0.01	NA	NA	NA	0.29	NA	98.55
1-100_AS8616a_BSE3	NA	32.18	68.06	0.02	NA	NA	NA	0.21	NA	100.48
1-100_AS8616a_BSE3	NA	33.35	67.74	0.02	NA	NA	NA	0.29	NA	101.40
1-100_AS8616a_BSE3	NA	32.42	68.03	0.01	NA	NA	NA	0.21	NA	100.66
1-100_AS8616a_BSE3	NA	32.38	67.66	0.02	NA	NA	NA	0.42	NA	100.48
1-100_AS8616a_BSE3	NA	32.46	67.88	0.06	NA	NA	NA	0.27	NA	100.67
1-100_AS8616a_BSE3	NA	32.32	67.54	0.32	NA	NA	NA	0.14	NA	100.32
1-100_AS8616a_BSE3	NA	31.71	65.40	0.21	0.188	NA	NA	0.23	NA	97.74
1-100_AS8616a_BSE3	0.027	29.89	66.48	0.43	NA	NA	NA	0.19	NA	97.02
1-100_AS8616a_BSE3	NA	31.24	67.21	0.22	NA	NA	NA	0.25	NA	98.92
1-100_AS8616a_BSE3	0.035	32.50	67.79	0.19	NA	0.015	NA	0.21	NA	100.73
1-100_AS8616a_BSE3	NA	32.42	67.62	0.26	NA	0.018	NA	0.32	NA	100.64
1-100_AS8616a_BSE3	NA	32.50	67.29	0.32	NA	0.014	NA	0.23	NA	100.35
1-100_AS8616a_BSE3	NA	32.82	67.79	0.13	0.202	NA	NA	0.20	NA	101.15
1-100_AS8616a_BSE3	NA	31.50	68.04	0.46	NA	NA	NA	0.25	NA	100.24
1-100_AS8616a_BSE3	NA	32.17	67.99	0.06	NA	NA	NA	0.11	NA	100.33
101_AS8616a_BSE3a	NA	32.66	67.19	0.02	NA	NA	NA	0.30	NA	100.16
1_AS8619a_BSE1a	NA	32.94	67.80	NA	NA	NA	NA	0.28	NA	101.01
2-101_AS8619a_Profil	NA	32.86	66.70	0.02	NA	NA	NA	0.33	NA	99.92
2-101_AS8619a_Profil	NA	33.19	67.01	0.02	NA	NA	NA	0.32	NA	100.54
2-101_AS8619a_Profil	NA	33.48	67.01	0.01	NA	NA	NA	0.19	NA	100.69
2-101_AS8619a_Profil	NA	33.04	67.12	0.02	NA	NA	NA	0.52	NA	100.71

Table 6: Continued.

	EMPA Bleiberg, Josefischolle [mass%]									
sample/analyses	**As**	**S**	**Zn**	**Fe**	**Pb**	**Ge**	**Cu**	**Cd**	**Tl**	**total**
2-101_AS8619a_Profil	0.042	33.17	66.23	0.04	0.543	0.016	NA	0.32	NA	100.36
2-101_AS8619a_Profil	0.047	32.68	65.91	0.03	0.480	0.017	NA	0.30	NA	99.47
2-101_AS8619a_Profil	0.038	33.01	65.81	0.03	0.296	0.019	NA	0.32	NA	99.52
2-101_AS8619a_Profil	0.047	32.85	66.12	0.03	0.407	0.018	NA	0.34	NA	99.81
2-101_AS8619a_Profil	0.027	32.41	65.77	0.04	0.691	0.017	NA	0.33	NA	99.28
2-101_AS8619a_Profil	0.030	32.39	65.35	0.04	0.333	0.020	NA	0.32	NA	98.48
2-101_AS8619a_Profil	0.033	33.80	64.50	0.04	0.562	NA	NA	0.35	NA	99.27
2-101_AS8619a_Profil	0.053	32.33	65.31	0.05	0.556	NA	NA	0.32	NA	98.61
2-101_AS8619a_Profil	0.032	32.16	64.56	0.04	0.824	NA	NA	0.32	NA	97.94
2-101_AS8619a_Profil	0.045	31.88	65.12	0.03	0.452	NA	NA	0.30	NA	97.84
2-101_AS8619a_Profil	NA	33.08	65.44	0.03	0.505	0.014	NA	0.58	NA	99.65
2-101_AS8619a_Profil	0.056	32.51	65.23	0.04	0.597	0.018	NA	0.36	NA	98.81
2-101_AS8619a_Profil	NA	32.70	65.91	0.04	0.378	0.018	NA	0.43	NA	99.48
2-101_AS8619a_Profil	0.053	33.01	65.65	0.03	0.467	0.016	NA	0.45	NA	99.67
2-101_AS8619a_Profil	NA	32.73	65.96	0.04	0.474	NA	NA	0.54	NA	99.75
2-101_AS8619a_Profil	0.043	32.56	65.65	0.04	0.418	0.019	NA	0.39	NA	99.12
2-101_AS8619a_Profil	NA	32.74	66.59	0.03	0.430	NA	NA	0.56	NA	100.35
2-101_AS8619a_Profil	0.057	32.51	65.87	0.04	0.382	NA	NA	0.43	NA	99.29
2-101_AS8619a_Profil	0.029	31.89	65.22	0.04	0.430	0.015	NA	0.39	NA	98.01
2-101_AS8619a_Profil	0.048	32.87	66.30	0.03	0.410	0.015	NA	0.43	NA	100.10
2-101_AS8619a_Profil	0.029	32.84	65.66	0.05	0.443	NA	NA	0.51	NA	99.53
2-101_AS8619a_Profil	0.061	32.66	66.41	0.06	0.410	NA	NA	0.37	NA	99.97
2-101_AS8619a_Profil	NA	32.76	66.54	0.16	0.379	0.016	NA	0.46	NA	100.31
2-101_AS8619a_Profil	0.033	32.66	66.43	0.08	0.447	0.013	NA	0.43	NA	100.10
2-101_AS8619a_Profil	0.034	32.86	66.16	0.05	0.386	0.015	NA	0.65	NA	100.16
2-101_AS8619a_Profil	NA	32.49	66.10	0.06	0.398	NA	NA	0.63	NA	99.67
2-101_AS8619a_Profil	0.029	33.05	65.77	0.03	0.318	0.014	NA	0.55	NA	99.76
2-101_AS8619a_Profil	NA	33.23	66.10	0.03	0.240	NA	NA	0.57	NA	100.18
2-101_AS8619a_Profil	NA	32.88	66.11	0.03	0.322	NA	NA	0.61	NA	99.94
2-101_AS8619a_Profil	NA	32.79	66.05	0.02	0.201	NA	NA	0.66	NA	99.72
2-101_AS8619a_Profil	NA	32.60	65.75	0.04	NA	NA	NA	1.08	NA	99.47
2-101_AS8619a_Profil	NA	32.97	66.16	0.02	NA	NA	NA	0.89	NA	100.03
2-101_AS8619a_Profil	NA	32.83	66.45	0.02	NA	NA	NA	0.80	NA	100.10
2-101_AS8619a_Profil	0.026	33.01	65.97	0.04	0.271	NA	NA	0.68	NA	100.00
2-101_AS8619a_Profil	NA	32.88	66.88	0.03	0.235	NA	NA	0.67	NA	100.69
2-101_AS8619a_Profil	NA	32.77	66.67	0.03	0.274	0.013	NA	0.56	NA	100.32
2-101_AS8619a_Profil	NA	32.65	66.78	0.03	0.266	NA	NA	0.54	NA	100.27
2-101_AS8619a_Profil	NA	32.78	66.61	0.05	0.337	NA	NA	0.48	NA	100.26
2-101_AS8619a_Profil	0.026	32.63	66.80	0.04	0.301	NA	NA	0.43	NA	100.22
2-101_AS8619a_Profil	0.036	32.94	66.44	0.04	0.252	0.016	NA	0.40	NA	100.12
2-101_AS8619a_Profil	0.031	32.64	66.35	0.05	0.577	0.015	NA	0.32	NA	99.99
2-101_AS8619a_Profil	0.047	32.96	66.21	0.04	0.334	NA	NA	0.30	NA	99.90
2-101_AS8619a_Profil	0.066	32.91	66.00	0.04	0.503	0.020	NA	0.29	NA	99.83
2-101_AS8619a_Profil	0.099	32.80	66.04	0.04	0.348	0.020	NA	0.35	NA	99.68
2-101_AS8619a_Profil	0.075	32.65	65.28	0.04	0.539	0.025	NA	0.31	NA	98.93
2-101_AS8619a_Profil	0.036	32.12	63.89	0.04	0.516	NA	NA	0.33	NA	96.94
2-101_AS8619a_Profil	0.086	31.78	64.36	0.05	0.345	0.016	NA	0.32	NA	96.96

Table 6: Continued.

EMPA Bleiberg, Josefischolle [mass%]										
sample/analyses	**As**	**S**	**Zn**	**Fe**	**Pb**	**Ge**	**Cu**	**Cd**	**Tl**	**total**
2-101_AS8619a_Profil	0.039	32.01	65.69	0.04	0.493	0.022	NA	0.30	NA	98.60
2-101_AS8619a_Profil	0.059	33.01	65.68	0.05	0.460	0.015	NA	0.29	NA	99.57
2-101_AS8619a_Profil	0.056	32.68	66.00	0.05	0.281	0.017	NA	0.30	NA	99.39
2-101_AS8619a_Profil	0.080	32.58	66.33	0.06	0.533	0.021	NA	0.29	NA	99.90
2-101_AS8619a_Profil	0.062	32.69	65.89	0.06	0.586	0.022	NA	0.32	NA	99.62
2-101_AS8619a_Profil	0.059	32.94	65.43	0.05	0.419	NA	NA	0.32	NA	99.22
2-101_AS8619a_Profil	0.063	33.04	66.54	0.05	0.397	0.020	NA	0.32	NA	100.43
2-101_AS8619a_Profil	0.047	32.88	66.28	0.05	0.352	0.018	NA	0.30	NA	99.93
2-101_AS8619a_Profil	0.045	33.56	65.03	0.05	0.408	0.014	NA	0.32	NA	99.43
2-101_AS8619a_Profil	0.053	32.93	65.90	0.06	0.458	NA	NA	0.31	NA	99.70
2-101_AS8619a_Profil	0.057	32.05	66.05	0.05	0.737	0.023	NA	0.29	NA	99.25
2-101_AS8619a_Profil	0.062	30.92	66.41	0.06	0.577	0.015	NA	0.27	NA	98.32
2-101_AS8619a_Profil	0.086	32.51	65.14	0.05	0.396	0.017	NA	0.27	NA	98.47
2-101_AS8619a_Profil	0.060	32.91	65.62	0.05	0.536	0.016	NA	0.27	NA	99.46
2-101_AS8619a_Profil	0.064	32.87	66.12	0.04	0.314	0.027	NA	0.28	NA	99.71
2-101_AS8619a_Profil	0.047	33.25	64.97	0.04	0.487	0.025	NA	0.29	NA	99.11
2-101_AS8619a_Profil	0.085	31.79	64.71	0.05	0.692	0.014	NA	0.26	NA	97.60
2-101_AS8619a_Profil	0.084	31.03	64.86	0.05	0.972	0.018	NA	0.26	NA	97.27
2-101_AS8619a_Profil	0.061	31.94	65.04	0.04	0.448	0.019	NA	0.30	NA	97.85
2-101_AS8619a_Profil	0.054	32.00	64.70	0.06	0.479	0.020	NA	0.29	NA	97.59
2-101_AS8619a_Profil	0.053	31.47	64.94	0.07	0.393	NA	NA	0.27	NA	97.20
2-101_AS8619a_Profil	0.042	32.41	63.97	0.06	0.525	0.018	NA	0.30	NA	97.32
2-101_AS8619a_Profil	0.043	31.68	64.67	0.06	0.460	0.019	NA	0.29	NA	97.22
2-101_AS8619a_Profil	0.052	31.49	64.56	0.07	0.361	0.015	NA	0.28	NA	96.83
2-101_AS8619a_Profil	0.053	31.07	64.51	0.06	0.617	0.020	NA	0.29	NA	96.62
2-101_AS8619a_Profil	0.080	32.65	64.92	0.06	0.447	0.022	NA	0.30	NA	98.47
2-101_AS8619a_Profil	0.039	31.85	64.28	0.07	0.677	NA	NA	0.29	NA	97.21
2-101_AS8619a_Profil	0.047	31.84	64.13	0.06	0.493	0.018	NA	0.28	NA	96.86
2-101_AS8619a_Profil	0.035	32.23	62.86	0.06	0.572	0.019	NA	0.25	NA	96.03
2-101_AS8619a_Profil	0.073	30.70	63.95	0.07	0.556	0.015	NA	0.26	NA	95.62
2-101_AS8619a_Profil	0.042	32.01	63.93	0.06	0.461	NA	NA	0.28	NA	96.78
2-101_AS8619a_Profil	0.086	32.30	64.65	0.10	0.513	0.019	NA	0.27	NA	97.94
2-101_AS8619a_Profil	0.081	33.88	64.76	0.10	0.489	0.014	NA	0.26	NA	99.57
2-101_AS8619a_Profil	0.102	33.27	65.32	0.10	0.418	0.018	NA	0.26	NA	99.49
2-101_AS8619a_Profil	0.092	32.55	64.55	0.07	0.435	0.015	NA	0.24	NA	97.95
2-101_AS8619a_Profil	0.291	33.02	65.97	0.26	0.368	NA	NA	0.19	NA	100.09
2-101_AS8619a_Profil	0.225	33.07	64.67	1.70	0.485	NA	NA	0.13	NA	100.28
2-101_AS8619a_Profil	0.216	32.19	65.39	0.77	0.788	0.016	NA	0.18	NA	99.54
2-101_AS8619a_Profil	0.084	31.43	66.36	0.10	0.337	NA	NA	0.22	NA	98.53
2-101_AS8619a_Profil	0.232	32.99	65.80	0.36	0.691	0.014	NA	0.13	NA	100.21
2-101_AS8619a_Profil	0.525	33.02	65.32	0.92	0.708	NA	NA	0.14	0.116	100.75
2-101_AS8619a_Profil	0.274	32.73	64.64	2.39	0.399	0.013	NA	NA	NA	100.44
2-101_AS8619a_Profil	0.035	32.50	66.14	0.22	0.472	NA	NA	0.50	NA	99.87
2-101_AS8619a_Profil	0.064	32.67	66.06	0.17	0.625	0.015	NA	0.40	NA	100.01
103-122_AS8619a_BSE4a	NA	32.84	67.75	0.02	NA	NA	NA	0.53	NA	101.14
103-122_AS8619a_BSE4a	NA	32.51	67.59	0.02	NA	NA	NA	0.29	NA	100.42
103-122_AS8619a_BSE4a	0.031	33.22	67.56	0.06	NA	NA	NA	0.40	NA	101.27

Table 6: Continued.

EMPA Bleiberg, Josefischolle [mass%]										
sample/analyses	**As**	**S**	**Zn**	**Fe**	**Pb**	**Ge**	**Cu**	**Cd**	**Tl**	**total**
103-122_AS8619a_BSE4a	NA	32.63	66.38	0.04	0.335	0.014	NA	0.45	NA	99.86
103-122_AS8619a_BSE4a	0.028	32.44	65.38	0.04	0.323	NA	NA	0.45	NA	98.65
103-122_AS8619a_BSE4a	0.044	32.69	66.91	0.05	0.290	0.016	NA	0.37	NA	100.37
103-122_AS8619a_BSE4a	0.028	32.66	66.50	0.10	0.347	0.014	NA	0.32	NA	99.97
103-122_AS8619a_BSE4a	NA	34.22	65.86	0.06	0.368	NA	NA	0.43	NA	100.94
103-122_AS8619a_BSE4a	NA	32.56	66.38	0.03	NA	NA	NA	0.58	NA	99.54
103-122_AS8619a_BSE4a	NA	32.19	66.40	0.03	0.284	NA	NA	0.58	NA	99.49
103-122_AS8619a_BSE4a	NA	32.70	66.95	0.03	0.213	NA	NA	0.54	NA	100.44
103-122_AS8619a_BSE4a	NA	32.59	67.02	0.04	0.383	NA	NA	0.66	NA	100.70
103-122_AS8619a_BSE4a	NA	32.93	67.22	0.02	0.284	NA	NA	0.68	NA	101.13
103-122_AS8619a_BSE4a	NA	32.69	67.06	0.02	0.318	NA	NA	0.55	NA	100.64
103-122_AS8619a_BSE4a	NA	32.96	67.42	0.03	0.307	NA	NA	0.39	NA	101.12
103-122_AS8619a_BSE4a	0.027	31.43	66.67	0.02	0.651	NA	NA	0.30	NA	99.10
103-122_AS8619a_BSE4a	0.040	32.98	67.04	0.04	0.330	0.014	NA	0.23	NA	100.66
103-122_AS8619a_BSE4a	0.050	32.83	67.09	0.04	0.307	0.015	NA	0.21	NA	100.54
103-122_AS8619a_BSE4a	0.062	32.79	66.78	0.04	0.429	0.025	NA	0.19	NA	100.32
123_AS8619a_BSE4b	NA	33.18	68.04	0.02	NA	NA	NA	0.19	NA	101.43
123b_AS8619a_BSE4b	NA	32.51	66.24	0.01	NA	NA	NA	0.20	NA	98.96
124_AS8619a_BSE4b	NA	33.11	67.94	0.02	NA	NA	NA	0.34	NA	101.41
125_AS8619a_BSE4b	NA	33.09	67.81	0.02	NA	NA	NA	0.32	NA	101.24
126_AS8619a_BSE4b	NA	33.19	67.76	0.02	NA	NA	NA	0.56	NA	101.53
127_AS8619a_BSE4b	NA	33.21	67.52	0.02	NA	NA	NA	0.61	NA	101.36
128-147_AS8619a_BSE5a	NA	33.46	67.27	0.02	NA	NA	NA	0.60	NA	101.34
128-147_AS8619a_BSE5a	NA	33.25	66.67	0.03	0.192	NA	NA	0.66	NA	100.79
128-147_AS8619a_BSE5a	NA	33.52	66.74	0.03	0.237	NA	NA	0.24	NA	100.77
128-147_AS8619a_BSE5a	NA	32.98	66.91	0.03	0.226	NA	NA	0.53	NA	100.67
128-147_AS8619a_BSE5a	NA	33.08	67.02	0.02	NA	NA	NA	0.52	NA	100.64
128-147_AS8619a_BSE5a	NA	33.02	66.66	0.03	NA	NA	NA	0.38	NA	100.09
128-147_AS8619a_BSE5a	NA	33.10	66.59	0.03	NA	NA	NA	0.28	NA	100.00
128-147_AS8619a_BSE5a	NA	32.66	66.36	0.08	0.351	0.015	NA	0.23	NA	99.70
128-147_AS8619a_BSE5a	NA	33.14	66.37	0.08	NA	NA	NA	0.30	NA	99.90
128-147_AS8619a_BSE5a	NA	32.88	64.47	0.28	0.391	0.014	NA	0.28	NA	98.31
128-147_AS8619a_BSE5a	NA	32.57	63.79	0.05	0.234	NA	NA	0.45	NA	97.10
128-147_AS8619a_BSE5a	0.038	32.60	65.06	0.06	0.243	NA	NA	0.39	NA	98.39
128-147_AS8619a_BSE5a	0.027	32.04	64.41	0.14	0.370	NA	NA	0.42	NA	97.40
128-147_AS8619a_BSE5a	0.038	32.53	64.91	0.05	0.333	NA	NA	0.42	NA	98.27
128-147_AS8619a_BSE5a	NA	32.94	65.66	0.05	0.336	0.015	NA	0.45	NA	99.45
128-147_AS8619a_BSE5a	NA	32.84	65.50	0.05	0.251	NA	NA	0.56	NA	99.20
128-147_AS8619a_BSE5a	0.026	32.71	65.89	0.06	0.240	NA	NA	0.76	NA	99.70
128-147_AS8619a_BSE5a	NA	32.87	66.08	0.09	NA	NA	NA	0.84	NA	99.88
128-147_AS8619a_BSE5a	NA	32.91	66.02	0.05	0.206	NA	NA	1.07	NA	100.26
128-147_AS8619a_BSE5a	NA	32.77	66.30	0.03	NA	NA	NA	0.58	NA	99.68
148_AS8619a_BSE5a	NA	33.01	66.19	0.03	NA	NA	NA	0.49	NA	99.73
149_AS8619a_BSE2d	NA	31.10	60.23	0.21	0.222	NA	NA	0.35	NA	92.11

Table 6: Continued.

EMPA Bleiberg, Riedhardtscholle [mass%]										
sample/analyses	**As**	**S**	**Zn**	**Fe**	**Pb**	**Ge**	**Cu**	**Cd**	**Tl**	**total**
1_AS8608a_BSE1b	0.528	32.67	63.95	1.49	0.725	0.017	NA	NA	NA	99.38
2_AS8608a_BSE1b	0.062	32.84	65.58	0.27	0.317	0.017	NA	0.14	NA	99.22
3_AS8608a_BSE1b	NA	33.02	66.25	0.08	NA	NA	NA	0.18	NA	99.54
4_AS8608a_BSE1b	0.515	32.23	62.64	1.63	0.814	0.013	NA	0.04	0.092	97.97
5_AS8608a_BSE1c	NA	33.03	65.70	0.16	0.221	0.019	NA	0.13	NA	99.25
6_AS8608a_BSE1c	0.049	32.74	65.13	0.44	0.668	NA	NA	0.14	NA	99.16
7_AS8608a_BSE1c	NA	33.03	65.83	0.16	NA	0.013	NA	0.21	NA	99.24
8_AS8608a_BSE1c	NA	33.03	64.85	0.37	NA	NA	NA	0.40	NA	98.66
9_AS8608a_BSE1c	0.135	32.73	64.30	0.59	0.343	NA	NA	0.16	NA	98.26
10_AS8608a_BSE2b	0.178	32.96	64.32	1.02	0.272	0.027	NA	0.04	NA	98.82
11_AS8608a_BSE2b	0.282	32.80	64.00	1.26	0.407	0.033	NA	0.04	NA	98.82
11_AS8608a_BSE2b	0.278	32.91	62.45	1.83	0.404	0.034	NA	NA	0.080	97.99
13_AS8608a_BSE2b	0.227	32.97	64.25	1.14	0.366	0.022	NA	NA	NA	98.98
14_AS8608a_BSE2b	NA	32.87	65.41	0.08	NA	NA	NA	0.22	NA	98.58
15_AS8608a_BSE2b	NA	33.11	65.11	0.12	NA	0.023	NA	0.13	NA	98.49
16_AS8608a_BSE2b	0.138	33.08	64.84	0.98	NA	0.024	NA	0.05	NA	99.11
17_AS8608a_BSE3b	NA	33.02	65.47	0.07	NA	NA	NA	0.42	NA	98.99
18_AS8608a_BSE3b	NA	32.93	65.50	0.05	NA	NA	NA	0.47	NA	98.95
19_AS8608a_BSE3b	0.067	33.08	65.02	0.79	0.258	0.033	NA	0.08	NA	99.32
20_AS8608a_BSE3b	NA	33.33	65.32	0.25	0.263	0.022	NA	0.16	NA	99.35
21_AS8608a_BSE3b	0.027	33.57	65.99	0.38	NA	0.016	NA	0.13	NA	100.11
22_AS8608a_BSE3b	NA	33.27	66.38	0.06	NA	NA	NA	0.35	NA	100.05
23_AS8608a_BSE3a	NA	33.28	66.02	0.07	NA	NA	NA	0.46	NA	99.84
24_AS8608a_BSE3a	NA	33.18	66.16	0.25	NA	NA	NA	0.22	NA	99.81
25_AS8608a_BSE3a	0.103	33.01	65.67	0.46	0.333	NA	NA	0.10	NA	99.67
26_AS8608a_BSE3a	NA	33.40	65.77	0.09	0.199	0.015	NA	0.20	NA	99.68
27_AS8608a_BSE3a	0.039	33.03	66.12	0.27	NA	0.021	NA	0.13	NA	99.60
1_AS8612b_BSE1c	NA	33.04	66.74	0.02	NA	NA	0.022	0.76	NA	100.59
2_AS8612b_BSE1c	NA	32.93	66.75	NA	NA	NA	NA	0.38	NA	100.05
3_AS8612b_BSE1c	NA	33.07	66.82	NA	NA	NA	0.056	0.55	NA	100.50
4_AS8612b_BSE1c	NA	33.28	66.96	NA	NA	NA	0.009	0.39	NA	100.63
5_AS8612b_BSE1c	NA	32.73	66.45	0.01	NA	NA	0.031	0.72	NA	99.94
6_AS8612b_BSE1c	0.135	32.44	64.83	1.67	0.270	0.040	NA	0.12	NA	99.50
7_AS8612b_BSE1c	0.119	33.09	65.62	0.82	0.273	0.038	NA	0.24	NA	100.21
8_AS8612b_BSE1c	NA	33.00	67.07	0.03	NA	NA	NA	0.17	NA	100.27
9_AS8612b_BSE1d	NA	32.91	66.64	0.04	NA	NA	0.008	0.33	NA	99.92
10_AS8612b_BSE1d	NA	32.47	66.24	0.02	NA	NA	NA	0.19	NA	98.93
11_AS8612b_BSE1d	NA	33.13	67.00	0.03	NA	NA	NA	0.19	NA	100.35
12_AS8612b_BSE1d	NA	32.67	66.85	NA	NA	NA	0.015	0.23	NA	99.76
13_AS8612b_BSE1d	0.095	32.57	65.48	0.59	NA	0.019	NA	0.19	NA	98.94
14_AS8612b_BSE1d	0.076	32.57	64.77	1.17	0.271	0.024	NA	0.21	NA	99.09
15_AS8612b_BSE2c	0.028	32.94	66.09	0.39	NA	NA	NA	0.22	NA	99.67
16_AS8612b_BSE2c	NA	33.02	67.08	0.02	NA	NA	NA	0.22	NA	100.34
17_AS8612b_BSE2c	NA	32.67	66.95	0.02	NA	NA	NA	0.33	NA	99.97
18_AS8612b_BSE2c	NA	32.91	66.60	0.04	NA	NA	NA	0.33	NA	99.89
19_AS8612b_BSE2c	0.027	32.88	66.60	0.26	NA	0.015	NA	0.19	NA	99.96

Table 6: Continued.

EMPA Bleiberg, Riedhardtscholle [mass%]										
sample/analyses	**As**	**S**	**Zn**	**Fe**	**Pb**	**Ge**	**Cu**	**Cd**	**Tl**	**total**
20_AS8612b_BSE2c	NA	32.89	66.16	0.08	NA	NA	NA	0.37	NA	99.51
21_AS8612b_BSE3c	NA	33.07	67.43	NA	NA	NA	NA	0.39	NA	100.89
22_AS8612b_BSE2c	NA	32.78	67.04	0.02	NA	NA	NA	0.33	NA	100.16
23_AS8612b_BSE2c	NA	33.08	67.08	0.01	NA	NA	0.011	0.49	NA	100.68
24_AS8612b_BSE2c	NA	32.85	67.26	0.01	NA	NA	NA	0.30	NA	100.42
25_AS8612b_BSE2c	NA	33.07	67.14	0.06	NA	NA	NA	0.35	NA	100.63
26_AS8612b_BSE3b	NA	33.02	66.96	0.16	NA	0.014	NA	0.18	NA	100.33
27_AS8612b_BSE3d	NA	33.23	67.42	0.01	NA	NA	NA	0.14	NA	100.80
28_AS8612b_BSE3d	NA	32.74	67.01	0.02	NA	NA	0.012	0.27	NA	100.06
29_AS8612b_BSE3d	0.052	32.22	66.29	0.18	0.558	0.038	NA	0.43	NA	99.77
30_AS8612b_BSE3d	0.044	32.90	67.38	0.04	NA	NA	NA	0.36	NA	100.73
31_AS8612b_BSE3d	NA	32.85	67.50	0.08	NA	NA	NA	0.26	NA	100.69
32_AS8612b_BSE4b	NA	32.83	66.66	0.02	NA	0.035	NA	0.62	NA	100.17
33_AS8612b_BSE4b	NA	32.70	66.77	NA	NA	NA	0.011	0.51	NA	99.99
34_AS8612b_BSE4b	NA	32.85	66.72	NA	NA	NA	0.041	0.56	NA	100.17
35_AS8612b_BSE4b	NA	32.64	66.64	0.03	NA	NA	0.012	0.68	NA	100.00
36_AS8612b_BSE4b	NA	32.40	66.55	0.02	NA	NA	NA	0.48	NA	99.46
37_AS8612b_BSE5b	NA	32.94	66.91	0.09	NA	NA	NA	0.21	NA	100.15
38_AS8612b_BSE5b	NA	32.89	67.39	0.02	NA	NA	NA	0.08	NA	100.38
39_AS8612b_BSE5b	NA	32.54	66.78	0.07	NA	NA	NA	0.53	NA	99.91
40_AS8612b_BSE5b	NA	32.46	66.63	0.08	0.247	NA	NA	0.45	NA	99.85
41-60_AS8612b_BSE5b	NA	32.58	66.61	0.21	NA	NA	NA	0.21	NA	99.61
41-60_AS8612b_BSE5b	NA	32.78	67.31	0.02	0.195	NA	NA	0.05	NA	100.35
41-60_AS8612b_BSE5b	NA	32.74	67.43	0.02	NA	NA	NA	0.10	NA	100.29
41-60_AS8612b_BSE5b	NA	32.74	67.33	0.02	NA	NA	NA	0.09	NA	100.18
41-60_AS8612b_BSE5b	NA	32.56	67.06	0.06	NA	NA	NA	0.19	NA	99.87
41-60_AS8612b_BSE5b	NA	32.59	67.09	0.03	NA	NA	NA	0.17	NA	99.88
41-60_AS8612b_BSE5b	NA	32.98	66.99	0.12	NA	NA	NA	0.55	NA	100.64
41-60_AS8612b_BSE5b	NA	31.45	66.90	0.06	NA	NA	NA	0.54	NA	98.96
41-60_AS8612b_BSE5b	NA	32.59	67.08	0.12	NA	NA	NA	0.47	NA	100.27
41-60_AS8612b_BSE5b	NA	32.70	67.14	0.13	NA	NA	NA	0.27	NA	100.24
41-60_AS8612b_BSE5b	NA	32.87	67.07	0.14	NA	NA	NA	0.44	NA	100.51
41-60_AS8612b_BSE5b	NA	32.84	67.07	0.19	NA	NA	0.008	0.45	NA	100.55
41-60_AS8612b_BSE5b	NA	32.19	66.55	0.14	NA	0.023	NA	0.06	NA	98.96
41-60_AS8612b_BSE5b	NA	32.80	67.29	0.05	NA	NA	NA	0.19	NA	100.33
41-60_AS8612b_BSE5b	NA	32.84	67.58	0.01	NA	NA	NA	0.09	NA	100.53
41-60_AS8612b_BSE5b	NA	32.54	67.62	NA	NA	NA	NA	0.08	NA	100.25
41-60_AS8612b_BSE5b	NA	32.53	67.39	0.04	NA	NA	NA	0.17	NA	100.13
41-60_AS8612b_BSE5b	NA	32.52	67.32	NA	NA	NA	NA	0.07	NA	99.91
41-60_AS8612b_BSE5b	NA	32.66	67.56	0.02	NA	NA	NA	0.07	NA	100.30
41-60_AS8612b_BSE5b	NA	32.53	67.49	0.01	NA	NA	NA	0.07	NA	100.10
Rh1_ZnS1	NA	33.63	67.49	0.07	0.045	NA	NA	0.12	NA	101.35
Rh1_ZnS2	0.009	33.25	67.62	0.06	NA	NA	NA	0.20	NA	101.14
Rh1_ZnS3	NA	33.11	67.60	0.06	NA	NA	NA	0.21	NA	100.98
Rh1_ZnS4	NA	33.05	67.52	0.04	0.029	NA	NA	0.12	NA	100.75
Rh1_ZnS5	NA	33.13	67.40	0.09	NA	NA	NA	0.21	NA	100.83

Table 6: Continued.

EMPA Bleiberg, Riedhardtscholle [mass%]										
sample/analyses	**As**	**S**	**Zn**	**Fe**	**Pb**	**Ge**	**Cu**	**Cd**	**Tl**	**total**
Rh1_ZnS6	NA	33.27	67.14	0.08	0.085	NA	NA	0.15	NA	100.73
Rh1_ZnS8	NA	33.19	67.06	0.47	NA	0.012	NA	0.05	NA	100.78
Rh1_ZnS9	0.005	33.72	66.95	0.47	NA	NA	NA	0.03	NA	101.17
Rh1_ZnS10	0.013	33.44	66.35	0.84	NA	0.031	NA	NA	NA	100.68
Rh1_ZnS11	0.013	33.38	67.68	0.04	NA	NA	NA	0.10	NA	101.21
Rh1_ZnS12	NA	33.22	67.34	0.11	NA	NA	NA	0.26	NA	100.93
Rh1_ZnS13	NA	33.11	67.50	0.07	NA	NA	NA	0.29	NA	100.97
Rh1_ZnS14	NA	33.39	67.58	0.02	NA	NA	NA	0.04	NA	101.03
Rh1_ZnS15	0.012	33.55	67.49	0.13	NA	NA	NA	0.16	NA	101.35
Rh1_ZnS16	NA	33.15	67.30	0.08	0.036	NA	NA	0.15	NA	100.71
Rh1_ZnS17	NA	33.24	66.87	0.12	NA	NA	NA	0.19	NA	100.42
Rh1_ZnS18	NA	33.24	67.31	0.03	0.027	NA	NA	0.07	NA	100.68
Rh1_ZnS19	NA	33.20	67.43	0.03	NA	0.037	NA	0.06	NA	100.76
Rh1_ZnS20	NA	33.02	67.18	0.08	0.052	0.004	NA	0.18	NA	100.51
WHR8/2_1	0.044	32.95	66.34	0.09	0.311	NA	NA	0.21	NA	99.95
WHR8/2_2	0.059	32.52	65.36	0.27	0.633	NA	NA	0.17	NA	99.01
WHR8/2_3	0.068	32.42	65.05	0.44	0.794	0.008	NA	0.05	NA	98.83
WHR8/2_4	NA	32.96	66.56	0.07	0.244	NA	NA	0.21	NA	100.05
WHR8/2_5	0.029	32.87	66.73	0.05	0.232	NA	NA	0.13	NA	100.03
WHR8/2_6	NA	33.24	66.82	0.04	0.111	NA	NA	0.20	NA	100.41
WHR8/2_7	NA	33.21	67.04	NA	NA	NA	NA	0.53	NA	100.78
WHR8/2_8	NA	33.12	66.52	0.03	0.060	NA	NA	0.49	NA	100.22
WHR8/2_9	NA	32.99	66.79	0.01	0.036	NA	NA	0.53	NA	100.36
WHR8/2_10	0.006	32.93	66.60	0.04	0.082	NA	NA	0.48	NA	100.14
WHR8/2_11	NA	32.56	65.54	0.03	0.646	0.005	NA	0.65	NA	99.43
WHR8/2_12	NA	32.51	65.53	0.04	0.872	NA	NA	0.80	NA	99.76
WHR8/2_13	0.065	32.95	65.88	0.23	0.396	NA	NA	0.11	NA	99.63
WHR8/2_14	0.063	32.56	65.30	0.16	1.170	NA	NA	0.19	NA	99.44
WHR8/2_1	0.044	32.95	66.34	0.09	0.311	NA	NA	0.21	NA	99.95
WHR8/2_2	0.059	32.52	65.36	0.27	0.633	NA	NA	0.17	NA	99.01
WHR8/2_3	0.068	32.42	65.05	0.44	0.794	0.008	NA	0.05	NA	98.83
WHR8/2_4	NA	32.96	66.56	0.07	0.244	NA	NA	0.21	NA	100.05
WHR8/2_5	0.029	32.87	66.73	0.05	0.232	NA	NA	0.13	NA	100.03
WHR8/2_6	NA	33.24	66.82	0.04	0.111	NA	NA	0.20	NA	100.41
WHR8/2_7	NA	33.21	67.04	NA	NA	NA	NA	0.53	NA	100.78
WHR8/2_8	NA	33.12	66.52	0.03	0.060	NA	NA	0.49	NA	100.22
WHR8/2_9	NA	32.99	66.79	0.01	0.036	NA	NA	0.53	NA	100.36
WHR8/2_10	0.006	32.93	66.60	0.04	0.082	NA	NA	0.48	NA	100.14
WHR8/2_11	NA	32.56	65.54	0.03	0.646	0.005	NA	0.65	NA	99.43
WHR8/2_12	NA	32.51	65.53	0.04	0.872	NA	NA	0.80	NA	99.76
WHR8/2_13	0.065	32.95	65.88	0.23	0.396	NA	NA	0.11	NA	99.63
WHR8/2_14	0.063	32.56	65.30	0.16	1.170	NA	NA	0.19	NA	99.44
WHR8/2_1	0.044	32.95	66.34	0.09	0.311	NA	NA	0.21	NA	99.95
WHR8/2_2	0.059	32.52	65.36	0.27	0.633	NA	NA	0.17	NA	99.01
WHR8/2_3	0.068	32.42	65.05	0.44	0.794	0.008	NA	0.05	NA	98.83
WHR8/2_4	NA	32.96	66.56	0.07	0.244	NA	NA	0.21	NA	100.05

Table 6: Continued.

	EMPA Bleiberg, Riedhardtscholle [mass%]									
sample/analyses	**As**	**S**	**Zn**	**Fe**	**Pb**	**Ge**	**Cu**	**Cd**	**Tl**	**total**
WHR8/2_15	0.014	33.07	66.51	0.15	0.256	NA	NA	0.07	NA	100.07
WHR8/2_16	NA	33.13	66.71	0.01	0.069	0.004	NA	0.53	NA	100.45
WHR8/2_17	NA	33.13	67.12	0.01	NA	NA	NA	0.25	NA	100.51
WHR8/2_18	0.013	33.21	66.57	0.02	0.072	0.004	NA	0.35	NA	100.23
WHR8/2_19	0.022	32.89	66.37	0.01	NA	NA	NA	0.62	NA	99.92
WHR8/2_20	0.023	32.91	66.27	NA	NA	NA	NA	0.66	NA	99.87
WHR8/2_21	0.050	32.82	65.99	0.04	0.506	0.006	NA	0.29	NA	99.70
WHR8/2_22	0.048	32.82	66.06	0.06	0.532	0.007	NA	0.25	NA	99.78
WHR8/2_23	0.045	32.82	66.40	0.02	0.416	NA	NA	0.36	NA	100.06
WHR8/2_24	NA	32.82	66.35	0.03	0.322	NA	NA	0.33	NA	99.85
WHR8/2_25	NA	32.90	66.39	0.02	0.239	NA	NA	0.32	NA	99.87
WHR8/2_26	NA	33.30	66.94	0.01	NA	NA	NA	0.35	NA	100.59
WHR8/2_27	0.038	32.53	66.01	0.11	0.295	NA	NA	0.37	NA	99.35
WHR8/2_28	NA	32.98	66.65	0.01	NA	NA	NA	0.59	NA	100.23
WHR8/2_29	NA	33.02	66.97	NA	NA	NA	NA	0.36	NA	100.35
WHR8/2_30	NA	32.99	66.94	NA	NA	NA	NA	0.29	NA	100.22
WHR8/2_31	NA	32.95	66.76	0.04	0.090	NA	NA	0.29	NA	100.13
WHR8/2_32	NA	33.25	66.56	0.02	NA	NA	NA	0.47	NA	100.31
WHR8/2_33	NA	32.84	66.55	NA	NA	NA	NA	0.69	NA	100.08
WHR8/2_34	NA	32.90	66.86	NA	NA	NA	NA	0.43	NA	100.19
WHR8/2_35	0.039	32.68	66.77	NA	0.045	NA	NA	0.60	NA	100.13
WHR8/2_36	NA	32.81	66.65	0.01	NA	NA	NA	0.57	NA	100.04
WHR8/2_37	NA	32.97	66.55	NA	NA	NA	NA	0.49	NA	100.01
WHR8/2_38	NA	32.63	66.24	0.01	NA	NA	NA	0.57	NA	99.44
WHR8/2_39	NA	32.95	66.89	NA	0.032	NA	NA	0.47	NA	100.34
WHR8/2_40	NA	33.03	66.86	0.01	NA	NA	NA	0.55	NA	100.45
WHR8/2_41	NA	32.13	65.20	0.01	NA	NA	NA	0.65	NA	97.99
WHR8/2_42	NA	32.91	66.73	0.01	0.042	NA	NA	0.54	NA	100.23
WHR8/2_43	NA	33.17	66.85	0.17	NA	0.009	NA	0.07	NA	100.27
WHR8/2_44	0.024	33.08	66.72	NA	NA	NA	NA	0.39	NA	100.22
WHR8/2_45	0.011	32.89	66.41	0.01	NA	0.013	NA	0.56	NA	99.89
WHR8/2_46	NA	32.77	66.79	NA	NA	NA	NA	0.48	NA	100.04
WHR8/2_47	0.013	32.64	66.58	NA	0.034	NA	NA	0.58	NA	99.84
WHR8/2_48	NA	32.73	66.56	NA	NA	NA	NA	0.56	NA	99.85
WHR8/2_49	NA	32.96	66.49	0.01	NA	NA	NA	0.71	NA	100.18
WHR8/2_50	0.031	32.73	65.42	0.85	0.113	NA	NA	0.25	NA	99.40
WHR8/2_51	0.008	32.99	66.42	0.05	NA	NA	0.020	0.54	NA	100.03
WHR8/2_52	0.010	32.98	66.87	0.08	0.067	NA	NA	0.43	NA	100.44
WHR8/2_53	NA	32.93	66.70	0.02	NA	NA	NA	0.37	NA	100.02
WHR8/2_54	NA	32.97	66.81	0.02	NA	NA	0.025	0.53	NA	100.35
WHR8/2_55	NA	33.10	67.01	NA	NA	NA	NA	0.40	NA	100.51
WHR8/2_56	NA	32.95	66.53	0.03	NA	NA	NA	0.71	NA	100.22
WHR8/2_57	NA	33.09	67.00	NA	NA	NA	NA	0.27	NA	100.36
WHR8/2_58	NA	33.14	66.68	0.01	NA	NA	NA	0.67	NA	100.50
WHR8/2_59	NA	33.12	66.55	0.02	NA	NA	NA	0.71	NA	100.41
WHR8/2_60	0.012	32.81	66.66	0.02	NA	NA	NA	0.45	NA	99.95

Table 6: Continued.

EMPA Bleiberg, Kalkscholle [mass%]										
sample/analyses	**As**	**S**	**Zn**	**Fe**	**Pb**	**Ge**	**Cu**	**Cd**	**Tl**	**total**
K2-2neu_ZnS1	0.063	31.31	66.77	0.60	0.146	0.011	NA	0.06	NA	98.96
K2-2neu_ZnS2	NA	31.58	66.82	0.47	NA	0.050	NA	NA	NA	98.92
K2-2neu_ZnS3	NA	31.33	67.05	0.08	NA	NA	NA	0.11	NA	98.57
K2-2neu_ZnS4	0.015	31.72	66.46	0.27	NA	NA	NA	0.07	NA	98.54
K2-2neu_ZnS5	0.023	31.62	66.79	0.36	0.048	0.009	NA	0.06	NA	98.91
K2-2neu_ZnS6	0.087	30.99	66.15	0.51	0.183	0.012	NA	0.05	NA	97.98
K2-2neu_ZnS7	0.009	31.18	66.41	0.40	0.078	0.021	NA	0.10	NA	98.20
K2-2neu_ZnS8	0.015	31.44	65.92	0.49	0.187	0.004	NA	0.04	NA	98.09
K2-2neu_ZnS9	NA	31.35	66.60	0.40	NA	0.024	NA	0.01	NA	98.38
K2-2neu_ZnS10	0.008	30.89	64.68	0.50	NA	NA	NA	0.10	NA	96.17
K2-2neu_ZnS11	NA	31.34	66.94	0.13	0.037	0.012	NA	0.16	NA	98.62
K2-2neu_ZnS12	0.036	31.14	66.72	0.36	0.056	NA	NA	0.15	NA	98.47
K2-2neu_ZnS13	0.057	31.05	66.32	0.44	0.105	NA	NA	0.14	NA	98.11
K2-2neu_ZnS14	0.029	31.55	66.81	0.38	0.078	NA	NA	0.13	NA	98.97
K2-2neu_ZnS15	0.067	31.16	64.56	2.08	0.188	0.045	NA	NA	NA	98.10
K2-2neu_ZnS16	0.049	31.39	66.25	0.72	0.093	NA	NA	0.10	NA	98.60
K2-2neu_ZnS17	0.053	31.66	66.14	0.73	0.039	0.004	NA	0.20	NA	98.82
K2-2neu_ZnS18	0.051	31.22	66.29	0.76	0.135	0.021	NA	NA	NA	98.47
K2-2neu_ZnS19	0.021	31.33	65.87	0.71	0.063	0.031	NA	0.04	NA	98.06
K2-2neu_ZnS20	0.005	31.74	66.90	0.17	0.035	0.017	NA	0.24	NA	99.11
K2-2neu_ZnS21	0.044	31.61	66.25	0.35	0.109	0.008	NA	0.12	NA	98.49
K2-2neu_ZnS22	0.011	31.05	65.28	0.49	0.066	0.025	NA	0.08	NA	97.00
K2-2neu_ZnS23	0.075	31.74	65.57	1.38	0.109	0.026	NA	NA	NA	98.90
K2-2neu_ZnS24	NA	31.77	67.00	0.07	NA	NA	NA	0.07	NA	98.91
K2-2neu_ZnS25	0.051	31.51	66.66	0.30	0.097	0.011	NA	0.03	NA	98.66
K2-2neu_ZnS26	0.013	31.56	66.17	0.08	0.041	NA	NA	0.20	NA	98.07
K2-2neu_ZnS27	0.016	31.98	66.72	0.10	NA	NA	NA	0.17	NA	98.99
K2-2neu_ZnS28	0.276	32.01	63.21	2.87	0.490	0.089	NA	NA	NA	98.94
K2-2neu_ZnS29	0.022	31.61	65.43	0.44	0.092	0.087	NA	0.08	NA	97.77
K2-2neu_ZnS30	0.024	31.80	65.77	0.20	0.115	NA	NA	0.23	NA	98.14
K2-2neu_ZnS31	NA	31.71	66.79	0.08	0.185	0.005	NA	0.11	NA	98.88
K2-2neu_ZnS32	0.008	31.72	66.27	0.11	0.083	NA	NA	0.14	NA	98.33
K2-2neu_ZnS33	NA	32.00	66.76	0.42	0.057	0.046	NA	0.04	NA	99.33
K2-2neu_ZnS34	0.031	31.52	65.18	0.45	0.139	0.005	NA	0.06	NA	97.38
K2-2neu_ZnS35	0.030	31.51	65.75	0.38	0.079	0.017	NA	0.08	NA	97.84
K2-2neu_ZnS36	NA	31.93	66.31	0.25	0.088	NA	NA	0.09	NA	98.67
K2-2neu_ZnS37	NA	31.79	66.62	0.02	NA	NA	NA	0.07	NA	98.51
K2-2neu_ZnS38	0.097	32.29	65.57	0.49	0.094	0.016	NA	0.10	NA	98.66
K2-2neu_ZnS39	NA	32.32	65.78	1.69	NA	0.039	NA	NA	NA	99.83
K2-2neu_ZnS40	NA	32.03	67.02	0.42	0.029	0.029	NA	0.01	NA	99.54
K2-2neu_ZnS41	NA	31.82	67.07	0.25	NA	0.045	NA	0.04	NA	99.23
K2-2neu_ZnS42	NA	31.99	67.12	0.16	0.058	NA	NA	0.08	NA	99.41
K2-2neu_ZnS43	NA	31.88	67.24	0.06	0.041	0.020	NA	0.14	NA	99.38
K2-2neu_ZnS44	NA	32.03	67.31	0.17	NA	NA	NA	0.11	NA	99.62
K2-2neu_ZnS45	0.023	32.42	66.78	0.58	0.134	0.095	NA	0.01	NA	100.04
K2-2neu_ZnS46	NA	31.72	67.15	0.17	NA	0.019	NA	0.14	NA	99.20
K2-2neu_ZnS47	NA	32.39	66.92	0.29	NA	0.036	NA	0.05	NA	99.69

Table 6: Continued.

	EMPA Bleiberg, Kalkscholle [mass%]									
sample/analyses	**As**	**S**	**Zn**	**Fe**	**Pb**	**Ge**	**Cu**	**Cd**	**Tl**	**total**
K2-2neu_ZnS48	NA	33.23	67.01	0.32	NA	0.031	NA	0.10	NA	100.68
K2-2neu_ZnS49	0.025	32.01	66.83	0.45	0.054	NA	NA	0.06	NA	99.43
K2-2neu_ZnS50	0.031	32.20	66.64	0.42	0.096	0.019	NA	0.10	NA	99.51
K2-2neu_ZnS51	0.019	32.16	66.71	0.58	NA	NA	NA	0.15	NA	99.62
K2-2neu_ZnS52	0.010	32.08	66.39	0.40	0.075	NA	NA	0.29	NA	99.25
K2-2neu_ZnS53	0.068	31.85	65.39	1.09	0.229	NA	NA	0.25	NA	98.88
K2-2neu_ZnS54	NA	32.33	66.69	0.26	NA	NA	NA	0.40	NA	99.68
K2-2neu_ZnS55	0.042	31.96	66.94	0.21	0.119	0.019	NA	0.15	NA	99.44
K2-2neu_ZnS56	0.036	31.57	65.13	0.78	0.065	0.014	NA	0.05	NA	97.65
K2-2neu_ZnS57	NA	32.47	66.42	0.70	NA	0.072	NA	NA	NA	99.66
K2-2neu_ZnS58	0.005	32.21	67.35	0.09	0.024	NA	NA	0.17	NA	99.85
K2-2neu_ZnS59	0.030	32.18	66.83	0.20	0.217	NA	NA	0.13	NA	99.59
K2-2neu_ZnS60	0.183	32.06	64.52	2.19	0.326	0.049	NA	NA	NA	99.33

Table 7: EMP data of sphalerites from the Erlach horizon (Bleiberg).

	EMPA Bleiberg, Erlach [mass%]									
sample/analyses	**As**	**S**	**Zn**	**Fe**	**Pb**	**Ge**	**Cu**	**Cd**	**Tl**	**total**
E14-6_ZnS1	NA	32.07	66.87	0.21	0.024	0.162	NA	0.09	NA	99.43
E14-6_ZnS2	NA	32.48	64.06	1.96	0.123	0.041	NA	0.23	NA	98.90
E14-6_ZnS3	NA	32.06	65.04	0.19	0.105	0.208	NA	0.14	NA	97.74
E14-6_ZnS4	NA	32.36	64.95	1.35	0.081	NA	NA	0.07	NA	98.81
E14-6_ZnS5	NA	32.22	66.14	0.41	0.151	0.209	NA	0.17	NA	99.30
E14-6_ZnS6	NA	32.18	65.97	0.79	0.158	NA	NA	0.03	NA	99.13
E14-6_ZnS7	NA	32.98	64.92	0.81	0.095	0.056	NA	0.05	NA	98.91
E14-6_ZnS8	NA	32.40	64.94	0.20	0.021	0.189	NA	0.05	NA	97.80
E14-6_ZnS9	NA	32.57	66.17	0.25	0.025	0.126	NA	0.03	NA	99.18
E14-6_ZnS10	NA	32.50	66.70	0.27	NA	0.163	NA	0.08	NA	99.71
E14-6_ZnS11	NA	32.54	66.67	0.15	NA	0.208	NA	0.25	NA	99.81
E14-6_ZnS12	NA	32.59	65.49	0.25	0.028	0.150	NA	0.06	NA	98.56
E14-6_ZnS13	NA	32.54	65.52	0.30	0.050	0.163	NA	0.05	NA	98.63
E14-6_ZnS14	NA	32.41	65.92	0.28	0.057	0.186	NA	0.09	NA	98.94
E14-6_ZnS15	NA	32.51	66.51	0.43	0.027	0.203	NA	0.05	NA	99.73
E14-6_ZnS16	NA	32.32	65.23	1.96	0.095	NA	NA	0.24	NA	99.84
E14-6_ZnS17	0.105	32.19	62.79	2.84	0.385	NA	NA	0.19	NA	98.49
E14-6_ZnS18	0.041	31.91	61.66	4.51	0.340	NA	NA	0.19	NA	98.65
E14-6_ZnS19	NA	32.33	66.86	0.71	0.105	NA	NA	0.11	NA	100.11
E14-6_ZnS20	NA	32.28	61.32	5.39	0.232	NA	NA	0.18	NA	99.40
E14-6_ZnS21	0.124	31.89	62.59	3.12	0.347	NA	NA	0.17	NA	98.25
E14-6_ZnS22	NA	32.35	66.61	0.36	0.062	0.104	NA	0.11	NA	99.60
E14-6_ZnS23	0.020	32.05	62.38	3.94	0.374	NA	NA	0.12	NA	98.89
E14-6_ZnS24	NA	32.44	66.98	0.43	0.156	NA	NA	0.29	NA	100.30
E14-6_ZnS25	NA	32.85	66.06	0.75	0.056	0.075	NA	0.08	NA	99.87
E14-6_ZnS26	NA	32.70	64.02	2.04	0.049	0.010	NA	0.08	NA	98.90
E14-6_ZnS27	NA	32.51	64.44	2.04	0.097	NA	NA	0.11	NA	99.19
E14-6_ZnS28	NA	32.49	64.32	2.94	0.062	0.042	NA	0.14	NA	99.99
E14-6_ZnS29	NA	32.61	68.25	0.29	0.021	0.031	NA	0.08	NA	101.29
E14-6_ZnS30	NA	32.35	64.31	2.67	0.076	NA	NA	0.12	NA	99.53
E14-6_ZnS31	NA	31.59	66.03	0.88	0.120	0.016	NA	0.05	NA	98.69
E14-6_ZnS32	NA	32.45	65.21	1.67	0.110	0.034	NA	0.07	NA	99.54
E14-6_ZnS33	NA	32.23	66.12	1.59	0.110	0.079	NA	0.05	NA	100.18
E14-6_ZnS34	NA	32.26	67.20	0.24	NA	0.111	NA	0.12	NA	99.92
E14-6_ZnS35	NA	32.43	67.18	0.15	0.032	0.033	NA	0.27	NA	100.09
E14-6_ZnS36	NA	32.16	65.65	0.63	0.139	0.022	NA	0.06	NA	98.66
E14-6_ZnS37	NA	32.23	64.68	0.15	1.150	0.176	NA	0.34	NA	98.73
E14-6_ZnS38	NA	32.71	66.95	0.25	0.163	0.178	NA	0.04	NA	100.30
E14-6_ZnS39	NA	32.27	67.65	0.25	0.050	0.115	NA	0.03	NA	100.36
E14-6_ZnS40	NA	32.43	67.07	0.18	0.058	0.271	NA	0.12	NA	100.12
E14-6_ZnS41	NA	31.84	66.76	0.18	0.041	0.148	NA	0.07	NA	99.04
E14-6_ZnS42	NA	32.60	66.80	0.20	0.057	0.100	NA	0.03	NA	99.79
E14-6_ZnS43	NA	32.58	67.85	0.18	NA	0.151	NA	0.14	NA	100.90
E14-6_ZnS44	NA	32.22	65.41	1.18	0.209	0.078	NA	0.04	NA	99.14
E14-6_ZnS45	NA	32.49	66.27	0.14	0.098	0.096	NA	0.07	NA	99.16
E14-6_ZnS46	NA	32.60	64.12	1.59	0.063	0.079	NA	0.05	NA	98.50
E14-6_ZnS47	NA	32.75	64.98	0.12	0.016	0.087	NA	0.09	NA	98.05

Table 7: Continued.

	EMPA Bleiberg, Erlach [mass%]									
sample/analyses	**As**	**S**	**Zn**	**Fe**	**Pb**	**Ge**	**Cu**	**Cd**	**Tl**	**total**
E14-6_ZnS48	NA	32.52	66.68	0.16	0.053	0.218	NA	0.08	NA	99.70
E14-6_ZnS49	NA	32.38	65.79	0.73	0.140	0.103	NA	0.06	NA	99.20
E14-6_ZnS50	NA	32.37	64.81	0.76	0.146	0.049	NA	0.05	NA	98.19
1_MS357_AS8602a_BSE2a	0.054	33.42	63.57	4.40	0.264	0.069	NA	0.06	NA	101.82
2-101_AS8602a_Mosaic 6X8	0.042	33.06	64.60	3.05	NA	0.028	NA	0.10	NA	100.88
2-101_AS8602a_Mosaic 6X8	0.057	33.51	65.91	1.34	0.421	0.043	NA	0.09	NA	101.37
2-101_AS8602a_Mosaic 6X8	0.037	32.66	66.04	1.35	0.347	0.063	NA	0.09	NA	100.58
2-101_AS8602a_Mosaic 6X8	0.081	33.10	66.05	1.27	0.290	0.059	NA	0.10	NA	100.95
2-101_AS8602a_Mosaic 6X8	0.041	32.70	65.69	1.70	NA	0.044	NA	0.11	NA	100.28
2-101_AS8602a_Mosaic 6X8	NA	32.92	65.80	1.41	NA	0.045	NA	0.11	NA	100.29
2-101_AS8602a_Mosaic 6X8	0.028	33.76	65.92	1.12	NA	0.045	NA	0.10	NA	100.97
2-101_AS8602a_Mosaic 6X8	NA	33.39	65.50	1.10	NA	0.053	NA	0.10	NA	100.14
2-101_AS8602a_Mosaic 6X8	NA	32.03	65.42	1.48	NA	0.052	NA	0.09	NA	99.07
2-101_AS8602a_Mosaic 6X8	0.043	32.94	65.29	1.88	NA	0.044	NA	0.11	NA	100.31
2-101_AS8602a_Mosaic 6X8	0.058	32.96	66.20	1.01	0.265	0.048	NA	0.08	NA	100.63
2-101_AS8602a_Mosaic 6X8	NA	32.70	66.33	1.17	0.266	0.046	NA	0.08	NA	100.59
2-101_AS8602a_Mosaic 6X8	0.047	33.18	65.29	2.01	0.233	0.041	NA	0.09	NA	100.89
2-101_AS8602a_Mosaic 6X8	0.069	33.20	65.95	1.61	NA	0.059	NA	0.08	NA	100.95
2-101_AS8602a_Mosaic 6X8	0.033	33.12	66.07	1.72	0.259	0.064	NA	0.07	NA	101.33
2-101_AS8602a_Mosaic 6X8	0.047	32.84	65.10	2.32	0.307	0.050	NA	0.07	NA	100.74
2-101_AS8602a_Mosaic 6X8	NA	32.95	65.21	1.64	0.205	0.046	NA	0.06	NA	100.11
2-101_AS8602a_Mosaic 6X8	0.037	32.40	64.92	1.69	NA	0.069	NA	0.06	NA	99.19
2-101_AS8602a_Mosaic 6X8	0.046	33.32	63.45	4.15	NA	0.026	NA	0.11	NA	101.10
2-101_AS8602a_Mosaic 6X8	NA	33.21	63.89	3.75	NA	0.035	NA	0.11	NA	100.99
2-101_AS8602a_Mosaic 6X8	0.036	32.98	64.41	3.11	NA	0.040	NA	0.22	NA	100.79
2-101_AS8602a_Mosaic 6X8	NA	33.16	66.94	0.67	NA	0.034	NA	0.18	NA	100.97
2-101_AS8602a_Mosaic 6X8	0.066	33.20	65.48	2.26	NA	0.078	NA	0.06	NA	101.14
2-101_AS8602a_Mosaic 6X8	0.030	33.18	65.46	2.01	0.307	0.108	NA	0.13	0.078	101.31
2-101_AS8602a_Mosaic 6X8	0.040	33.23	65.59	2.04	0.220	0.122	NA	0.08	NA	101.32
2-101_AS8602a_Mosaic 6X8	0.049	33.12	66.05	1.66	NA	0.119	NA	0.08	NA	101.08
2-101_AS8602a_Mosaic 6X8	0.035	33.18	66.75	0.91	0.271	0.096	NA	0.05	NA	101.29
2-101_AS8602a_Mosaic 6X8	0.031	33.24	66.08	1.22	NA	0.127	NA	0.05	NA	100.76
2-101_AS8602a_Mosaic 6X8	0.055	33.14	65.73	1.38	NA	0.049	NA	0.11	NA	100.46
2-101_AS8602a_Mosaic 6X8	0.029	33.48	66.44	0.86	NA	0.022	NA	0.02	NA	100.86
2-101_AS8602a_Mosaic 6X8	0.056	32.94	65.24	0.76	NA	0.142	NA	0.03	NA	99.17
2-101_AS8602a_Mosaic 6X8	0.045	32.96	65.19	2.30	0.236	0.085	NA	0.12	NA	100.94
2-101_AS8602a_Mosaic 6X8	0.046	33.07	66.13	1.31	NA	0.065	NA	0.09	NA	100.71
2-101_AS8602a_Mosaic 6X8	0.060	33.14	65.82	0.88	NA	0.069	NA	0.06	NA	100.03
2-101_AS8602a_Mosaic 6X8	0.043	33.31	64.95	2.74	0.231	0.099	NA	0.05	NA	101.42
2-101_AS8602a_Mosaic 6X8	0.071	33.18	64.55	3.20	0.233	0.091	NA	NA	NA	101.32
2-101_AS8602a_Mosaic 6X8	0.075	33.05	63.85	4.07	0.342	0.098	NA	0.03	0.071	101.58
2-101_AS8602a_Mosaic 6X8	0.095	33.33	63.55	4.37	0.227	0.100	NA	0.03	NA	101.70
2-101_AS8602a_Mosaic 6X8	0.064	33.31	62.44	5.49	NA	0.082	NA	0.05	NA	101.44
2-101_AS8602a_Mosaic 6X8	0.087	33.10	64.69	2.64	0.349	0.112	NA	0.04	NA	101.02
2-101_AS8602a_Mosaic 6X8	0.087	33.20	63.76	3.61	NA	0.079	NA	0.03	NA	100.77
2-101_AS8602a_Mosaic 6X8	0.051	33.34	62.47	5.26	NA	0.110	NA	0.05	NA	101.29

Table 7: Continued.

	EMPA Bleiberg, Erlach [mass%]									
sample/analyses	**As**	**S**	**Zn**	**Fe**	**Pb**	**Ge**	**Cu**	**Cd**	**Tl**	**total**
2-101_AS8602a_Mosaic 6X8	0.060	34.60	62.49	3.46	1.092	0.075	NA	0.05	0.097	101.93
2-101_AS8602a_Mosaic 6X8	NA	31.62	65.74	1.12	NA	0.025	NA	0.04	NA	98.54
2-101_AS8602a_Mosaic 6X8	0.085	33.14	65.04	2.50	0.281	0.091	NA	0.04	NA	101.18
2-101_AS8602a_Mosaic 6X8	0.090	32.32	64.28	2.81	0.203	0.113	NA	0.03	NA	99.86
2-101_AS8602a_Mosaic 6X8	0.042	32.52	64.46	2.01	0.251	0.078	NA	0.04	NA	99.40
2-101_AS8602a_Mosaic 6X8	NA	33.05	66.20	1.73	NA	0.092	NA	0.06	NA	101.13
2-101_AS8602a_Mosaic 6X8	0.043	32.73	67.16	0.65	NA	0.146	NA	NA	NA	100.73
2-101_AS8602a_Mosaic 6X8	NA	32.92	68.04	0.10	NA	0.025	NA	0.26	NA	101.35
2-101_AS8602a_Mosaic 6X8	0.030	33.19	67.51	0.56	NA	0.025	NA	0.30	NA	101.61
2-101_AS8602a_Mosaic 6X8	0.041	35.15	66.64	0.43	NA	0.036	NA	0.30	NA	102.59
2-101_AS8602a_Mosaic 6X8	0.047	33.12	67.56	0.16	0.346	0.033	NA	0.12	NA	101.39
2-101_AS8602a_Mosaic 6X8	0.031	32.81	67.41	0.27	0.462	0.029	NA	0.07	NA	101.09
2-101_AS8602a_Mosaic 6X8	0.035	33.13	66.10	1.52	NA	0.022	NA	0.29	NA	101.10
2-101_AS8602a_Mosaic 6X8	0.056	32.87	66.48	1.00	0.190	0.031	NA	0.21	NA	100.83
2-101_AS8602a_Mosaic 6X8	0.048	33.03	65.90	1.41	NA	0.024	NA	0.24	NA	100.67
2-101_AS8602a_Mosaic 6X8	NA	32.60	67.73	0.21	NA	0.023	NA	0.10	NA	100.68
2-101_AS8602a_Mosaic 6X8	0.039	31.93	66.03	1.72	NA	0.027	NA	0.18	NA	99.92
2-101_AS8602a_Mosaic 6X8	0.047	32.97	65.01	3.29	NA	0.030	NA	0.22	NA	101.57
2-101_AS8602a_Mosaic 6X8	NA	33.00	64.33	3.84	NA	0.038	NA	0.19	NA	101.40
2-101_AS8602a_Mosaic 6X8	0.039	33.08	65.17	3.01	0.206	0.039	NA	0.17	NA	101.70
2-101_AS8602a_Mosaic 6X8	0.053	33.23	64.74	3.26	NA	0.035	NA	0.16	NA	101.48
2-101_AS8602a_Mosaic 6X8	0.049	32.80	65.60	1.44	0.274	0.066	NA	0.11	NA	100.34
2-101_AS8602a_Mosaic 6X8	0.051	30.73	62.66	0.83	0.207	NA	NA	0.09	NA	94.57
2-101_AS8602a_Mosaic 6X8	0.040	33.48	65.26	2.06	NA	0.057	NA	0.11	NA	101.00
2-101_AS8602a_Mosaic 6X8	NA	32.99	65.12	2.34	NA	0.054	NA	0.11	NA	100.60
2-101_AS8602a_Mosaic 6X8	0.031	32.89	64.93	2.14	NA	0.054	NA	0.08	NA	100.12
2-101_AS8602a_Mosaic 6X8	0.042	32.98	65.02	3.03	0.353	0.066	NA	0.07	NA	101.56
2-101_AS8602a_Mosaic 6X8	0.045	32.90	65.66	2.46	0.221	0.056	NA	0.08	NA	101.42
2-101_AS8602a_Mosaic 6X8	NA	32.90	67.28	1.10	NA	0.030	NA	0.11	NA	101.42
2-101_AS8602a_Mosaic 6X8	0.040	33.07	66.64	1.60	0.190	0.078	NA	0.06	NA	101.69
2-101_AS8602a_Mosaic 6X8	0.036	32.06	64.29	2.17	NA	0.077	NA	0.05	NA	98.68
2-101_AS8602a_Mosaic 6X8	NA	33.12	64.28	4.00	NA	0.059	NA	0.05	NA	101.50
2-101_AS8602a_Mosaic 6X8	0.033	33.32	63.72	4.35	NA	0.043	NA	0.04	NA	101.50
2-101_AS8602a_Mosaic 6X8	0.076	33.14	63.37	4.57	NA	0.128	NA	0.03	0.103	101.41
2-101_AS8602a_Mosaic 6X8	0.035	32.92	63.04	4.42	NA	0.070	NA	0.07	NA	100.55
2-101_AS8602a_Mosaic 6X8	NA	32.88	63.06	4.78	NA	0.084	NA	0.08	NA	100.88
2-101_AS8602a_Mosaic 6X8	0.027	32.66	64.86	3.10	NA	0.095	NA	0.05	NA	100.79
2-101_AS8602a_Mosaic 6X8	NA	32.89	65.86	2.54	NA	0.078	NA	0.05	NA	101.42
2-101_AS8602a_Mosaic 6X8	NA	32.71	67.56	0.70	NA	0.049	NA	0.18	NA	101.21
2-101_AS8602a_Mosaic 6X8	NA	32.56	67.93	0.48	NA	0.040	NA	0.15	NA	101.17
2-101_AS8602a_Mosaic 6X8	NA	32.99	67.66	0.82	0.205	0.043	NA	0.20	NA	101.92
2-101_AS8602a_Mosaic 6X8	NA	32.97	68.16	0.18	NA	0.065	NA	0.14	NA	101.51
2-101_AS8602a_Mosaic 6X8	NA	33.06	67.43	0.44	0.230	0.077	NA	0.14	NA	101.37
2-101_AS8602a_Mosaic 6X8	NA	32.31	64.97	0.18	NA	0.117	NA	0.08	NA	97.66
2-101_AS8602a_Mosaic 6X8	NA	31.31	60.52	0.31	NA	0.111	NA	0.03	NA	92.28
2-101_AS8602a_Mosaic 6X8	NA	30.85	61.21	0.59	NA	0.030	NA	0.18	NA	92.86
2-101_AS8602a_Mosaic 6X8	NA	32.74	67.78	0.08	NA	0.018	NA	0.06	NA	100.68

Table 7: Continued.

	EMPA Bleiberg, Erlach [mass%]									
sample/analyses	**As**	**S**	**Zn**	**Fe**	**Pb**	**Ge**	**Cu**	**Cd**	**Tl**	**total**
2-101_AS8602a_Mosaic 6X8	NA	33.11	67.81	0.09	NA	NA	NA	0.08	NA	101.09
2-101_AS8602a_Mosaic 6X8	0.029	32.60	67.27	0.49	NA	0.016	NA	0.11	NA	100.51
2-101_AS8602a_Mosaic 6X8	NA	33.66	66.98	1.29	0.223	0.033	NA	0.19	NA	102.39
2-101_AS8602a_Mosaic 6X8	NA	32.71	67.21	1.14	NA	0.048	NA	0.17	NA	101.27
2-101_AS8602a_Mosaic 6X8	NA	32.82	67.17	1.31	NA	0.032	NA	0.24	NA	101.57
2-101_AS8602a_Mosaic 6X8	NA	32.97	67.48	1.00	NA	0.036	NA	0.14	NA	101.63
2-101_AS8602a_Mosaic 6X8	NA	32.96	68.31	0.23	NA	0.051	NA	0.14	NA	101.68
102_AS8602a_BSE1b	NA	32.93	67.55	0.22	NA	0.147	NA	0.10	NA	100.95
103_AS8602a_BSE1b	NA	33.27	67.95	0.21	NA	0.168	NA	0.06	NA	101.66
104_AS8602a_BSE1b	NA	32.87	67.83	0.26	NA	0.060	NA	0.10	NA	101.12
105_AS8602a_BSE1b	0.040	32.41	65.25	0.15	NA	0.097	NA	0.04	NA	97.98
106_AS8602a_BSE1b	NA	32.51	67.51	0.23	0.204	0.116	NA	0.12	NA	100.69
107_AS8602a_BSE1b	NA	32.99	68.02	0.19	NA	0.084	NA	0.06	NA	101.34
108_AS8602a_BSE1b	NA	32.76	68.60	0.17	NA	0.075	NA	0.14	NA	101.75
109_AS8602a_BSE7a	0.042	33.13	64.49	3.92	NA	0.053	NA	0.17	NA	101.80
110_AS8602a_BSE7a	NA	32.90	68.01	0.38	NA	0.108	NA	0.10	NA	101.50
111_AS8602a_BSE7a	NA	33.06	67.64	0.41	NA	0.052	NA	0.12	NA	101.28
112_AS8602a_BSE7a	NA	33.02	65.44	0.34	NA	0.147	NA	0.12	NA	99.07
113_AS8602a_BSE7a	NA	33.44	67.21	1.36	NA	0.139	NA	NA	NA	102.15
114_AS8602a_BSE7a	NA	33.00	66.59	1.57	NA	0.124	NA	0.21	NA	101.49
115_AS8602a_BSE3a	0.030	33.15	67.61	0.20	NA	0.048	NA	0.12	NA	101.16
116_AS8602a_BSE3a	NA	33.14	67.84	0.19	NA	0.020	NA	0.08	NA	101.27
117_AS8602a_BSE3a	NA	33.66	66.83	1.39	NA	0.029	NA	0.21	NA	102.12
118_AS8602a_BSE3a	0.030	33.45	63.50	4.73	NA	0.095	NA	NA	NA	101.80
119_AS8602a_BSE3a	NA	33.25	67.00	1.11	NA	0.074	NA	0.16	NA	101.59
120_AS8602a_BSE3b	NA	32.93	67.16	0.88	NA	0.033	NA	0.24	NA	101.23
121_AS8602a_BSE3b	NA	33.24	67.45	0.73	NA	0.141	NA	NA	NA	101.55
122_AS8602a_BSE3b	0.032	33.34	67.16	0.94	NA	0.117	NA	0.05	NA	101.63
123_AS8602a_BSE3b	0.052	33.38	62.46	5.51	0.270	0.088	NA	0.05	NA	101.81
124_AS8602a_BSE3b	NA	33.73	64.22	3.54	NA	0.066	NA	0.18	NA	101.73
125_AS8602a_BSE3b	0.037	33.32	65.52	0.97	NA	0.130	NA	0.18	NA	100.15
126_AS8602a_BSE3c	NA	33.47	65.13	2.39	NA	0.025	NA	0.25	NA	101.27
127_AS8602a_BSE3c	NA	33.30	64.26	3.41	NA	0.025	NA	0.27	NA	101.27
128_AS8602a_BSE3c	NA	33.21	66.66	0.92	NA	0.035	NA	0.26	NA	101.09
129_AS8602a_BSE5a	NA	33.14	65.85	0.20	NA	0.152	NA	0.06	NA	99.41
130_AS8602a_BSE5a	NA	33.18	65.97	0.26	NA	0.111	NA	0.17	NA	99.70
132_AS8602a_BSE5a py	NA	33.20	66.05	2.06	NA	0.015	NA	0.06	NA	101.39
135_AS8602a_BSE5a sph	NA	33.29	66.76	1.05	NA	0.158	NA	0.20	NA	101.45
1_AS8604a_BSE1c	NA	32.85	67.03	0.26	NA	0.052	NA	0.11	NA	100.30
2_AS8604a_BSE1c	NA	33.14	66.61	0.24	NA	0.207	NA	0.06	NA	100.27
3_AS8604a_BSE1c	0.036	32.94	66.07	1.05	NA	0.050	NA	0.12	NA	100.26
4_AS8604a_BSE1c	NA	33.00	66.62	0.20	NA	0.156	NA	0.06	NA	100.04
5_AS8604a_BSE1c	NA	32.80	67.22	0.39	NA	0.045	NA	0.10	NA	100.55
6_AS8604a_BSE1c	NA	33.02	66.92	0.29	NA	0.126	NA	0.07	NA	100.42
7_AS8604a_BSE1c	NA	32.80	67.13	0.25	NA	0.054	NA	0.22	NA	100.44
8_AS8604a_BSE1c	NA	33.09	66.88	0.24	NA	0.207	NA	NA	NA	100.41

Table 7: Continued.

	EMPA Bleiberg, Erlach [mass%]									
sample/analyses	**As**	**S**	**Zn**	**Fe**	**Pb**	**Ge**	**Cu**	**Cd**	**Tl**	**total**
9_AS8604a_BSE1b	NA	33.03	66.89	0.18	NA	0.207	NA	NA	NA	100.31
10_AS8604a_BSE1b	NA	32.97	66.94	0.15	NA	0.176	NA	NA	NA	100.23
11_AS8604a_BSE1b	NA	33.14	67.04	0.14	NA	0.166	NA	0.05	NA	100.53
12_AS8604a_BSE1b	NA	33.15	66.80	0.38	NA	0.129	NA	0.05	NA	100.51
13_AS8604a_BSE2c	0.026	32.87	66.71	0.86	NA	0.063	NA	0.10	NA	100.63
14_AS8604a_BSE2c	NA	33.09	67.26	0.25	NA	0.092	NA	0.12	NA	100.82
15_AS8604a_BSE2c	NA	32.76	67.16	0.47	NA	0.039	NA	0.17	NA	100.60
16_AS8604a_BSE2c	NA	33.00	67.05	0.27	NA	0.214	NA	NA	NA	100.54
17_AS8604a_BSE2d	NA	32.89	67.16	0.34	NA	0.052	NA	0.13	NA	100.57
18_AS8604a_BSE2d	NA	32.92	67.01	0.35	NA	0.056	NA	0.20	NA	100.53
19_AS8604a_BSE2d	NA	33.50	67.16	0.20	NA	0.175	NA	NA	NA	101.04
20_AS8604a_BSE2d	NA	32.94	67.00	0.23	NA	0.179	NA	0.05	NA	100.39
21_AS8604a_BSE2b	NA	32.98	66.92	0.65	NA	0.085	NA	0.08	NA	100.71
22_AS8604a_BSE2b	NA	32.92	66.39	0.51	NA	0.123	NA	0.05	NA	99.99
23_AS8604a_BSE2b	NA	32.93	66.43	0.30	NA	0.139	NA	0.04	NA	99.84
24_AS8604a_BSE2b	NA	32.90	66.43	0.52	NA	0.054	NA	0.09	NA	99.99
25_AS8604a_BSE3c	NA	32.93	66.82	0.38	NA	0.081	NA	0.08	NA	100.29
26_AS8604a_BSE3c	NA	33.27	66.80	0.23	NA	0.156	NA	NA	NA	100.45
27_AS8604a_BSE3c	NA	33.01	66.54	0.26	NA	0.187	NA	0.05	NA	100.05
28_AS8604a_BSE3d	NA	32.83	66.69	0.31	NA	0.119	NA	0.12	NA	100.07
29_AS8604a_BSE3d	NA	32.92	65.82	1.07	NA	0.107	NA	0.09	NA	100.00
30_AS8604a_BSE3d	NA	32.69	66.85	0.71	NA	0.131	NA	0.06	NA	100.43
31_AS8604a_BSE3d	NA	32.93	66.80	0.38	NA	0.182	NA	0.04	NA	100.33
32_AS8604a_BSE3b	NA	32.92	67.23	0.16	NA	0.182	NA	0.03	NA	100.52
33_AS8604a_BSE3b	NA	33.00	66.99	0.17	NA	0.217	NA	NA	NA	100.37
1-100_AS8607a_BSE6	NA	33.48	68.15	0.20	NA	0.027	NA	0.13	NA	101.98
1-100_AS8607a_BSE6	NA	33.73	67.88	0.14	NA	0.027	NA	0.15	NA	101.93
1-100_AS8607a_BSE6	0.028	33.62	67.19	0.53	NA	0.146	NA	0.06	NA	101.57
1-100_AS8607a_BSE6	NA	33.47	67.59	0.17	0.347	0.021	NA	0.09	NA	101.68
1-100_AS8607a_BSE6	0.042	33.52	67.19	0.54	0.268	0.049	NA	0.04	NA	101.65
1-100_AS8607a_BSE6	NA	33.48	66.93	0.60	NA	0.016	NA	0.15	NA	101.19
1-100_AS8607a_BSE6	NA	33.20	66.81	0.50	NA	0.020	NA	0.09	NA	100.62
1-100_AS8607a_BSE6	0.032	33.47	65.84	1.29	NA	0.034	NA	0.10	NA	100.76
1-100_AS8607a_BSE6	0.052	33.45	63.71	3.36	0.360	0.037	NA	0.12	NA	101.09
1-100_AS8607a_BSE6	0.032	33.46	64.86	2.49	NA	0.037	NA	NA	NA	100.88
1-100_AS8607a_BSE6	NA	33.35	67.46	0.09	NA	NA	NA	0.47	NA	101.36
1-100_AS8607a_BSE6	NA	33.60	67.52	0.09	NA	0.017	NA	0.35	NA	101.57
1-100_AS8607a_BSE6	NA	32.61	66.40	0.13	NA	0.038	NA	0.26	NA	99.44
1-100_AS8607a_BSE6	NA	33.35	68.10	0.45	NA	NA	NA	0.33	NA	102.23
1-100_AS8607a_BSE6	NA	33.60	66.95	1.28	NA	0.024	NA	0.19	NA	102.04
1-100_AS8607a_BSE6	NA	33.56	67.89	0.22	NA	0.020	NA	0.24	NA	101.93
1-100_AS8607a_BSE6	NA	33.66	67.69	0.32	NA	0.013	NA	0.40	NA	102.08
1-100_AS8607a_BSE6	NA	33.57	67.83	0.25	NA	0.016	NA	0.44	NA	102.12
1-100_AS8607a_BSE6	NA	34.04	67.92	0.19	NA	0.032	NA	0.35	NA	102.54
1-100_AS8607a_BSE6	NA	33.91	66.94	1.10	NA	0.020	NA	0.31	NA	102.29
1-100_AS8607a_BSE6	0.052	33.60	66.11	1.93	0.301	0.027	NA	0.15	NA	102.18

Table 7: Continued.

	EMPA Bleiberg, Erlach									
sample/analyses	**As**	**S**	**Zn**	**Fe**	**Pb**	**Ge**	**Cu**	**Cd**	**Tl**	**total**
1-100_AS8607a_BSE6	0.075	34.17	66.36	1.63	NA	0.039	NA	0.14	NA	102.41
1-100_AS8607a_BSE6	NA	34.33	65.14	2.77	0.254	0.030	NA	0.10	NA	102.63
1-100_AS8607a_BSE6	NA	30.63	66.56	0.38	NA	NA	NA	0.18	NA	97.75
1-100_AS8607a_BSE6	NA	33.46	66.96	0.70	0.214	0.029	NA	0.32	NA	101.69
1-100_AS8607a_BSE6	NA	33.65	65.94	1.81	NA	0.027	NA	0.20	NA	101.62
1-100_AS8607a_BSE6	0.026	33.45	67.33	0.29	0.440	0.029	NA	0.11	NA	101.68
1-100_AS8607a_BSE6	0.031	33.51	65.00	2.70	0.193	0.021	NA	0.20	NA	101.65
1-100_AS8607a_BSE6	NA	33.51	64.99	2.89	NA	0.019	NA	0.17	NA	101.58
1-100_AS8607a_BSE6	NA	33.70	63.98	3.59	0.193	0.026	NA	0.17	NA	101.67
1-100_AS8607a_BSE6	NA	33.06	64.40	0.83	NA	0.021	NA	0.11	NA	98.43
1-100_AS8607a_BSE6	NA	33.62	67.21	0.44	NA	0.034	NA	0.08	NA	101.39
1-100_AS8607a_BSE6	0.045	33.33	66.41	1.32	NA	0.039	NA	0.11	NA	101.26
1-100_AS8607a_BSE6	NA	32.73	64.41	1.81	NA	0.034	NA	0.21	NA	99.20
1-100_AS8607a_BSE6	NA	33.27	66.35	1.87	NA	0.022	NA	0.22	NA	101.73
1-100_AS8607a_BSE6	NA	33.22	66.36	1.75	NA	0.028	NA	0.23	NA	101.59
1-100_AS8607a_BSE6	NA	33.69	66.67	1.17	0.231	0.048	NA	0.18	NA	101.99
1-100_AS8607a_BSE6	NA	33.57	63.41	4.47	NA	0.018	NA	0.23	NA	101.70
1-100_AS8607a_BSE6	0.037	33.54	66.99	1.29	NA	0.038	NA	0.16	NA	102.04
1-100_AS8607a_BSE6	0.026	33.70	64.02	4.09	0.212	NA	NA	0.26	NA	102.31
1-100_AS8607a_BSE6	0.045	33.49	66.39	1.44	0.417	0.041	NA	0.12	NA	101.95
1-100_AS8607a_BSE6	NA	33.34	64.89	3.24	0.236	NA	NA	0.35	NA	102.06
1-100_AS8607a_BSE6	0.048	33.47	65.21	2.66	NA	0.027	NA	0.20	NA	101.62
1-100_AS8607a_BSE6	0.028	33.48	65.40	2.17	0.241	0.014	NA	0.34	NA	101.68
1-100_AS8607a_BSE6	0.044	33.57	65.83	1.55	0.230	0.027	NA	0.25	NA	101.51
1-100_AS8607a_BSE6	NA	33.30	67.22	0.62	0.268	0.014	NA	0.19	NA	101.61
1-100_AS8607a_BSE6	NA	33.39	66.69	0.89	0.335	0.028	NA	0.19	NA	101.52
1-100_AS8607a_BSE6	0.029	33.28	65.37	2.24	NA	0.016	NA	0.22	NA	101.16
1-100_AS8607a_BSE6	NA	33.42	67.29	0.35	NA	0.026	NA	0.29	NA	101.38
1-100_AS8607a_BSE6	NA	33.31	66.50	1.03	0.245	NA	NA	0.33	NA	101.42
1-100_AS8607a_BSE6	NA	33.38	64.46	3.28	NA	0.038	NA	0.13	NA	101.28
1-100_AS8607a_BSE6	0.026	33.59	64.73	2.66	0.278	0.067	NA	0.04	NA	101.39
1-100_AS8607a_BSE6	0.032	33.47	64.71	3.19	0.216	0.076	NA	NA	NA	101.70
1-100_AS8607a_BSE6	NA	34.07	61.33	6.95	NA	0.041	NA	0.05	NA	102.45
1-100_AS8607a_BSE6	NA	33.54	64.80	3.42	NA	0.062	NA	0.07	NA	101.90
1-100_AS8607a_BSE6	NA	33.20	63.63	4.33	0.233	0.040	NA	0.14	NA	101.56
1-100_AS8607a_BSE6	NA	32.99	65.37	2.21	NA	0.048	NA	0.11	NA	100.73
1-100_AS8607a_BSE6	0.026	33.53	63.73	4.20	0.269	0.046	NA	0.10	NA	101.91
1-100_AS8607a_BSE6	0.037	33.70	66.31	1.60	0.302	0.037	NA	0.10	NA	102.10
1-100_AS8607a_BSE6	0.067	31.77	64.87	2.36	0.312	0.035	NA	0.10	NA	99.51
1-100_AS8607a_BSE6	0.077	33.26	64.69	2.12	0.399	0.038	NA	0.17	NA	100.75
1-100_AS8607a_BSE6	NA	33.20	66.98	0.59	0.297	0.045	NA	0.19	NA	101.30
1-100_AS8607a_BSE6	NA	33.27	63.99	3.58	NA	0.015	NA	0.40	NA	101.26
1-100_AS8607a_BSE6	NA	33.30	66.60	0.74	NA	NA	NA	0.37	NA	101.01
1-100_AS8607a_BSE6	NA	33.38	67.18	0.35	NA	0.021	NA	0.32	NA	101.25
1-100_AS8607a_BSE6	0.062	33.13	65.84	1.74	0.330	0.018	NA	0.31	NA	101.43
1-100_AS8607a_BSE6	0.046	33.42	66.65	0.88	NA	0.026	NA	0.24	NA	101.27
1-100_AS8607a_BSE6	0.035	33.17	66.47	0.90	0.288	0.027	NA	0.25	NA	101.14

Table 7: Continued.

	EMPA Bleiberg, Erlach [mass%]									
sample/analyses	**As**	**S**	**Zn**	**Fe**	**Pb**	**Ge**	**Cu**	**Cd**	**Tl**	**total**
1-100_AS8607a_BSE6	0.027	32.68	64.39	1.71	NA	NA	NA	0.30	NA	99.10
1-100_AS8607a_BSE6	0.040	33.01	66.34	1.13	0.337	0.018	NA	0.23	NA	101.11
1-100_AS8607a_BSE6	0.027	32.69	63.92	2.00	NA	0.015	NA	0.36	NA	99.00
1-100_AS8607a_BSE6	NA	33.31	65.59	2.27	NA	0.019	NA	0.36	NA	101.55
1-100_AS8607a_BSE6	0.047	33.20	65.26	2.75	0.251	0.016	NA	0.26	NA	101.78
1-100_AS8607a_BSE6	0.039	33.33	65.96	1.61	NA	0.016	NA	0.21	NA	101.16
1-100_AS8607a_BSE6	NA	33.30	67.80	0.28	NA	0.030	NA	0.24	NA	101.64
1-100_AS8607a_BSE6	0.043	33.41	67.10	0.86	NA	0.032	NA	0.23	NA	101.68
1-100_AS8607a_BSE6	0.090	33.28	65.02	1.53	0.229	0.034	0.015	0.17	NA	100.37
1-100_AS8607a_BSE6	0.039	33.22	65.65	1.88	0.212	0.036	NA	0.15	NA	101.19
1-100_AS8607a_BSE6	0.041	33.30	63.51	1.89	0.227	0.036	NA	0.12	NA	99.12
1-100_AS8607a_BSE6	0.052	33.41	64.80	2.28	0.276	0.047	NA	0.12	NA	100.98
1-100_AS8607a_BSE6	0.043	33.49	64.78	2.63	0.205	0.038	NA	0.16	NA	101.34
1-100_AS8607a_BSE6	NA	33.20	64.20	3.28	NA	0.024	NA	0.33	NA	101.04
1-100_AS8607a_BSE6	0.037	33.30	65.83	1.56	NA	0.025	NA	0.27	NA	101.03
1-100_AS8607a_BSE6	NA	33.34	67.08	0.82	NA	0.029	NA	0.29	NA	101.56
1-100_AS8607a_BSE6	0.087	33.20	64.34	2.01	NA	0.027	NA	0.22	NA	99.89
1-100_AS8607a_BSE6	0.048	33.21	66.32	1.18	0.379	0.029	NA	0.20	NA	101.37
1-100_AS8607a_BSE6	0.049	32.36	66.20	1.12	0.448	0.029	NA	0.21	NA	100.41
1-100_AS8607a_BSE6	NA	33.12	65.55	2.10	0.299	0.027	NA	0.23	NA	101.32
1-100_AS8607a_BSE6	NA	33.05	65.57	2.49	NA	0.016	NA	0.26	NA	101.39
1-100_AS8607a_BSE6	NA	32.92	65.29	1.80	NA	0.015	NA	0.24	NA	100.27
1-100_AS8607a_BSE6	NA	32.96	67.35	0.68	NA	0.028	NA	0.19	NA	101.21
1-100_AS8607a_BSE6	NA	33.22	65.93	2.25	0.221	0.024	NA	0.24	NA	101.88
1-100_AS8607a_BSE6	NA	32.73	65.49	2.32	0.227	0.025	NA	0.18	NA	100.96
1-100_AS8607a_BSE6	NA	33.28	67.05	1.06	NA	0.035	NA	0.13	NA	101.55
1-100_AS8607a_BSE6	0.027	32.48	65.52	1.52	NA	0.027	NA	0.12	NA	99.69
1-100_AS8607a_BSE6	NA	33.01	65.55	1.39	NA	0.020	NA	0.17	NA	100.14
1-100_AS8607a_BSE6	NA	33.39	64.93	2.63	NA	0.024	NA	0.20	NA	101.18
1-100_AS8607a_BSE6	NA	33.00	66.55	1.10	0.207	0.028	NA	0.21	NA	101.09
1-100_AS8607a_BSE6	NA	33.28	67.56	0.34	NA	0.037	NA	0.20	NA	101.42
101-120_AS8607a_BSE3a	NA	33.41	67.48	0.22	NA	0.049	NA	0.23	NA	101.40
101-120_AS8607a_BSE3a	NA	33.26	67.34	0.57	NA	0.024	NA	0.07	NA	101.25
101-120_AS8607a_BSE3a	NA	32.14	67.08	0.06	0.230	NA	NA	0.22	NA	99.73
101-120_AS8607a_BSE3a	NA	33.09	67.86	0.11	NA	0.023	NA	0.08	NA	101.17
101-120_AS8607a_BSE3a	NA	33.28	67.56	0.18	NA	0.044	NA	0.33	NA	101.40
101-120_AS8607a_BSE3a	NA	33.25	67.81	0.27	NA	0.059	NA	0.06	NA	101.44
101-120_AS8607a_BSE3a	NA	33.02	68.39	0.13	NA	0.030	NA	0.09	NA	101.66
101-120_AS8607a_BSE3a	NA	33.29	68.14	0.03	NA	NA	NA	0.22	NA	101.69
101-120_AS8607a_BSE3a	NA	33.21	68.24	0.03	NA	NA	NA	0.44	NA	101.92
101-120_AS8607a_BSE3a	NA	33.24	68.00	0.03	NA	0.017	NA	0.32	NA	101.61
101-120_AS8607a_BSE3a	NA	33.23	68.06	0.04	NA	0.013	NA	0.47	NA	101.82
101-120_AS8607a_BSE3a	NA	33.30	68.03	0.05	NA	0.013	NA	0.36	NA	101.75
101-120_AS8607a_BSE3a	NA	33.12	67.89	0.04	0.222	NA	NA	0.33	NA	101.60
101-120_AS8607a_BSE3a	NA	33.31	67.79	0.28	NA	0.014	NA	0.19	NA	101.59
101-120_AS8607a_BSE3a	0.182	33.57	63.24	4.28	0.473	0.112	NA	NA	0.134	101.98
101-120_AS8607a_BSE3a	NA	33.15	67.57	0.16	NA	0.021	NA	0.44	NA	101.33

Table 7: Continued.

	EMPA Bleiberg, Erlach [mass%]									
sample/analyses	**As**	**S**	**Zn**	**Fe**	**Pb**	**Ge**	**Cu**	**Cd**	**Tl**	**total**
101-120_AS8607a_BSE3a	NA	33.13	67.53	0.35	0.190	0.059	NA	0.06	NA	101.31
101-120_AS8607a_BSE3a	NA	33.24	67.21	0.11	NA	0.016	NA	0.34	NA	100.92
101-120_AS8607a_BSE3a	NA	33.16	67.60	0.12	NA	NA	NA	0.14	NA	101.01
101-120_AS8607a_BSE3a	NA	33.23	66.84	0.58	NA	0.016	NA	0.40	NA	101.07
121_AS8607a_BSE5a hell	NA	33.15	67.12	0.29	NA	0.044	NA	0.31	NA	100.91
122_AS8607a_BSE5a dunkel	0.034	33.56	62.48	5.61	NA	0.014	NA	0.06	NA	101.75
123_AS8607a_BSE5a	NA	33.02	67.36	0.67	NA	0.015	NA	0.18	NA	101.25
124_AS8607a_BSE5a	0.031	33.65	61.57	6.77	NA	NA	NA	0.15	NA	102.17
125_AS8607a_BSE5a hell	NA	33.48	67.46	0.79	0.188	0.072	NA	0.11	NA	102.10

Table 8: EMP data of sphalerites from the 1st Raibl horizon (Bleiberg).

	EMPA Bleiberg, 1st Raibl horizon									
sample/analyses	**As**	**S**	**Zn**	**Fe**	**Pb**	**Ge**	**Cu**	**Cd**	**Tl**	**total**
1_AS8589_BSE1b	NA	33.23	67.09	0.07	NA	NA	NA	0.21	NA	100.60
2_AS8589_BSE1b	NA	33.09	67.01	0.10	NA	0.021	NA	0.23	NA	100.45
3_AS8589_BSE1b	NA	33.20	67.00	0.10	NA	NA	NA	0.19	NA	100.49
4_AS8589_BSE1b	NA	33.01	67.08	0.08	NA	NA	NA	0.32	NA	100.49
5_AS8589_BSE1b	NA	33.20	67.08	0.17	NA	0.015	NA	0.20	NA	100.65
6_AS8589_BSE1b	0.034	33.11	66.58	0.27	NA	0.015	NA	0.15	NA	100.16
7_AS8589_BSE2b	0.088	33.09	65.17	1.21	0.283	0.039	NA	0.13	NA	100.01
8_AS8589_BSE2b	NA	33.09	66.92	0.08	0.208	0.015	NA	0.10	NA	100.41
9_AS8589_BSE2b	NA	32.81	66.53	0.46	NA	NA	NA	0.06	NA	99.87
10_AS8589_BSE2b	0.102	32.46	63.48	1.71	0.404	0.047	NA	0.13	0.079	98.42
11_AS8589_BSE2b	0.083	32.93	65.25	0.97	NA	0.032	NA	0.25	NA	99.52
12_AS8589_BSE3a	0.039	32.83	66.34	0.34	NA	0.056	NA	0.11	NA	99.71
13_AS8589_BSE3a	NA	32.86	66.57	0.22	NA	0.024	0.023	0.20	NA	99.90
14_AS8589_BSE3a	0.049	33.08	65.93	0.40	NA	0.029	NA	0.12	NA	99.60
15_AS8589_BSE3a	0.045	33.19	66.47	0.47	NA	0.052	NA	0.08	NA	100.31
16_AS8589_BSE4b	NA	32.75	65.58	0.29	NA	0.059	NA	0.15	NA	98.83
17_AS8589_BSE4b	0.058	32.97	65.78	0.30	NA	0.056	NA	0.14	NA	99.29
18_AS8589_BSE4b	NA	32.99	65.66	0.37	0.306	0.031	NA	0.09	NA	99.44
19_AS8589_BSE4b	NA	32.73	66.68	0.14	NA	0.027	NA	0.19	NA	99.76
20_AS8589_BSE5c	0.046	32.70	65.48	0.81	NA	0.033	NA	0.25	NA	99.33
21_AS8589_BSE5c	0.037	32.99	66.04	0.31	NA	0.035	NA	0.13	NA	99.55
22_AS8589_BSE5c	0.030	32.60	66.06	0.44	NA	0.017	NA	0.25	NA	99.40
23_AS8589_BSE5c	0.040	32.71	64.74	1.25	NA	0.032	NA	0.28	NA	99.05
24_AS8589_BSE5b	0.066	32.89	64.98	0.97	0.294	0.034	NA	0.22	NA	99.46
25_AS8589_BSE5b	0.053	32.95	65.23	1.09	0.212	0.024	NA	0.24	NA	99.79
26_AS8589_BSE5b	NA	32.99	66.38	0.26	NA	0.018	NA	0.22	NA	99.87
27_AS8589_BSE5b	0.049	32.38	64.72	0.33	NA	0.050	NA	0.13	NA	97.66
28_AS8589_BSE5b	NA	32.80	63.88	0.15	NA	0.016	NA	0.08	NA	96.93
1_AS8591a_BSE1d	NA	32.50	66.21	0.04	NA	NA	NA	0.46	NA	99.21
2_AS8591a_BSE1d	NA	33.03	66.05	0.02	NA	NA	NA	0.53	NA	99.63
3_AS8591a_BSE1d	NA	32.77	66.23	0.03	NA	NA	NA	0.30	NA	99.32
4_AS8591a_BSE1d	NA	33.11	66.24	0.03	NA	NA	NA	0.22	NA	99.60
5_AS8591a_BSE1d	NA	32.91	66.81	0.08	NA	NA	NA	0.21	NA	100.01
6_AS8591a_BSE1d	NA	32.74	64.84	1.86	0.238	0.036	NA	0.10	NA	99.82
7_AS8591a_BSE1d	NA	33.05	66.01	0.62	NA	0.019	NA	0.16	NA	99.86
8_AS8591a_BSE1d	NA	32.74	65.62	0.10	NA	0.016	NA	0.12	NA	98.60
9_AS8591a_BSE1b	NA	32.86	66.02	0.27	NA	0.015	NA	0.13	NA	99.29
10_AS8591a_BSE1b	NA	32.70	64.24	1.69	0.274	0.024	NA	0.20	NA	99.13
11_AS8591a_BSE1a	NA	32.74	65.45	0.14	NA	0.032	NA	0.09	NA	98.46
12_AS8591a_BSE3b	NA	31.92	65.81	0.11	NA	NA	NA	0.20	NA	98.02
13_AS8591a_BSE3b	NA	32.69	65.36	0.41	NA	0.072	NA	0.06	NA	98.59
14_AS8591a_BSE3b	NA	32.62	64.35	1.46	NA	0.025	NA	0.18	NA	98.63
15_AS8591a_BSE3b	0.067	32.50	62.65	0.48	NA	0.046	NA	0.07	NA	95.81
16_AS8591a_BSE3a	NA	32.82	65.76	0.10	0.206	0.017	NA	0.29	NA	99.19
17_AS8591a_BSE3a	NA	32.79	65.75	0.40	NA	NA	NA	0.29	NA	99.24
18_AS8591a_BSE4b	NA	33.06	65.53	0.11	NA	0.023	0.054	0.23	NA	99.00

Table 8: Continued.

	EMPA Bleiberg, 1st Raibl horizon [mass%]									
sample/analyses	**As**	**S**	**Zn**	**Fe**	**Pb**	**Ge**	**Cu**	**Cd**	**Tl**	**total**
19_AS8591a_BSE4b	NA	32.57	65.33	0.24	NA	0.039	NA	0.12	NA	98.29
20_AS8591a_BSE4b	0.090	32.56	65.62	0.46	NA	0.018	NA	0.26	NA	98.99
21_AS8591a_BSE4b	0.162	32.66	64.44	1.46	0.316	0.044	NA	0.14	0.078	99.31
22_AS8591a_BSE4b	NA	32.84	66.30	0.13	0.253	0.015	NA	0.14	NA	99.68
23_AS8591a_BSE4b	NA	32.83	66.30	0.05	NA	0.039	NA	0.26	NA	99.48
24_AS8591a_BSE4a	0.163	32.77	65.57	0.34	NA	0.043	NA	0.05	NA	98.92
25_AS8591a_BSE3c	NA	31.64	58.97	0.90	NA	0.021	NA	0.17	NA	91.71
1_MS391_WS_Blb29_BSE10_1	0.033	32.40	65.49	0.82	0.169	0.025	NA	0.15	NA	99.10
2_MS391_WS_Blb29_BSE10_2	0.076	32.19	65.68	0.59	0.171	0.024	NA	0.09	NA	98.83
3_MS391_WS_Blb29_BSE10_1	NA	32.61	66.21	0.18	0.153	NA	NA	0.17	NA	99.34
4_MS391_WS_Blb29_BSE10_1	0.032	32.49	66.11	0.79	NA	0.058	NA	NA	NA	99.57
5_MS391_WS_Blb29_BSE10_1	0.071	32.15	64.85	1.14	0.204	0.028	NA	0.27	NA	98.73
6_MS391_WS_Blb29_BSE10_1	NA	32.61	65.89	0.59	NA	0.060	NA	0.05	NA	99.30
7_MS391_WS_Blb29_BSE10_1	0.038	32.41	65.80	0.70	NA	0.049	NA	0.07	NA	99.14
8_MS391_WS_Blb29_BSE10_2	0.033	32.11	66.18	0.53	0.177	0.058	NA	0.09	NA	99.18
9_MS391_WS_Blb29_BSE10_2	0.064	32.32	65.54	0.70	0.169	0.053	NA	0.08	NA	98.92
10_MS391_WS_Blb29_BSE10_2	NA	32.07	65.98	0.10	NA	0.019	NA	0.10	NA	98.37
11_MS391_WS_Blb29_BSE10_2	NA	32.29	65.72	0.39	NA	0.027	NA	0.10	NA	98.64
12_MS391_WS_Blb29_BSE10_2	0.042	32.39	65.31	0.90	NA	0.045	NA	0.08	NA	98.83
13_MS391_WS_Blb29_BSE10_2	NA	31.91	64.69	0.16	NA	0.029	NA	0.08	NA	96.96
14_MS391_WS_Blb29_BSE10_2	0.028	32.41	65.34	0.33	0.231	0.046	NA	0.07	NA	98.46
15_MS391_WS_Blb29_BSE10_2	0.073	32.39	64.96	0.94	0.241	0.081	NA	0.05	NA	98.80
16_MS391_WS_Blb29_BSE10_2	0.053	32.42	65.49	0.50	0.155	0.040	NA	0.07	NA	98.73
17_MS391_WS_Blb29_BSE10_3	0.043	32.45	65.57	0.39	0.129	0.050	NA	0.05	NA	98.68
18_MS391_WS_Blb29_BSE10_3	0.055	32.52	65.71	0.46	0.205	0.071	NA	0.05	NA	99.07
19_MS391_WS_Blb29_BSE10_3	0.061	32.41	65.63	0.68	NA	0.047	NA	0.07	NA	99.02
20_MS391_WS_Blb29_BSE10_3	0.056	32.56	66.16	0.67	0.225	0.051	NA	0.05	NA	99.80
21_MS391_WS_Blb29_BSE10_3	NA	32.15	66.31	0.18	0.124	0.021	NA	0.10	NA	98.90
22_MS391_WS_Blb29_BSE10_3	0.055	32.49	65.93	0.69	0.201	0.052	NA	0.07	NA	99.50
23_MS391_WS_Blb29_BSE10_3	NA	32.16	64.29	0.37	0.168	0.043	NA	0.07	NA	97.12
24_MS391_WS_Blb29_BSE10_3	NA	32.58	66.01	0.28	0.146	0.046	NA	0.08	NA	99.17
25_MS391_WS_Blb29_BSE10_3	NA	32.51	65.82	0.14	NA	0.022	NA	0.13	NA	98.74
26_MS391_WS_Blb29_BSE10_3	0.047	32.39	65.56	0.31	0.140	0.045	NA	0.08	NA	98.63
27_MS391_WS_Blb29_BSE12_6	NA	32.57	65.84	0.08	NA	0.014	NA	0.17	NA	98.80
28_MS391_WS_Blb29_BSE12_6	0.039	32.32	65.21	0.40	0.241	0.058	NA	0.08	NA	98.38
29_MS391_WS_Blb29_BSE12_6	0.029	32.56	65.51	0.36	NA	0.059	NA	0.07	NA	98.69
31_MS391_WS_Blb29_BSE12_6	0.053	32.27	65.04	0.66	0.126	0.096	NA	0.09	NA	98.35
32_MS391_WS_Blb29_BSE12_6	0.029	32.30	65.20	0.20	0.143	0.032	NA	0.14	NA	98.05
33_MS391_WS_Blb29_BSE12_6	0.113	32.49	62.76	2.99	0.238	0.057	NA	NA	NA	98.69
34_MS391_WS_Blb29_BSE9_7	0.039	32.52	66.51	0.14	NA	NA	NA	0.15	NA	99.41
35_MS391_WS_Blb29_BSE9_7	0.058	32.59	65.96	0.72	0.166	0.066	NA	0.08	NA	99.63
36_MS391_WS_Blb29_BSE9_7	NA	31.60	64.91	0.72	0.186	0.022	NA	0.14	NA	97.63
37_MS391_WS_Blb29_BSE9_7	0.041	32.42	66.03	0.37	0.168	0.023	NA	0.14	NA	99.20
38_MS391_WS_Blb29_BSE9_7	NA	32.69	66.12	0.30	NA	0.022	NA	0.18	NA	99.44
39_MS391_WS_Blb29_BSE9_7	0.037	32.23	66.02	0.33	NA	0.044	NA	0.11	NA	98.87
40_MS391_WS_Blb29_BSE9_7	0.130	32.44	65.55	0.46	0.220	0.077	NA	0.03	NA	98.93

Table 8: Continued.

EMPA Bleiberg, 1st Raibl horizon [mass%]										
sample/analyses	**As**	**S**	**Zn**	**Fe**	**Pb**	**Ge**	**Cu**	**Cd**	**Tl**	**total**
41_MS391_WS_Blb29_BSE9_7	0.059	32.63	64.54	0.73	0.210	0.085	NA	0.09	NA	98.35
42_MS391_WS_Blb29_BSE9_7	0.028	32.43	65.53	0.15	NA	0.056	NA	0.10	NA	98.38
43_MS391_WS_Blb29_BSE9_7	0.044	32.47	65.73	0.29	0.140	0.064	NA	0.10	NA	98.84
44_MS391_WS_Blb29_BSE6_10	0.035	32.59	65.77	0.31	0.131	0.026	NA	0.11	NA	98.97
45_MS391_WS_Blb29_BSE6_10	NA	32.28	65.89	0.30	0.179	0.014	NA	0.08	NA	98.74
46_MS391_WS_Blb29_BSE6_10	NA	32.76	64.06	2.42	0.174	0.023	NA	0.10	NA	99.55
47_MS391_WS_Blb29_BSE6_10	0.029	32.71	66.13	0.13	NA	NA	NA	0.21	NA	99.31
48_MS391_WS_Blb29_BSE6_10	NA	32.62	66.23	0.04	NA	NA	NA	0.15	NA	99.12
49_MS391_WS_Blb29_BSE6_10	NA	32.47	65.95	0.21	NA	NA	NA	0.14	NA	98.91
50_MS391_WS_Blb29_BSE6_10	0.070	32.61	64.70	1.13	0.131	0.100	NA	0.08	NA	98.86
51_MS391_WS_Blb29_BSE3_2	NA	32.73	65.66	0.15	NA	NA	NA	0.18	NA	98.84
52_MS391_WS_Blb29_BSE3_2	0.084	32.55	64.79	0.47	0.232	0.072	NA	0.06	NA	98.29
53_MS391_WS_Blb29_BSE3_2	NA	32.69	65.79	0.04	NA	0.016	NA	0.28	NA	98.90
54_MS391_WS_Blb29_BSE3_2	0.032	32.74	66.05	0.17	NA	0.020	NA	0.23	NA	99.34
55_MS391_WS_Blb29_BSE3_2	0.029	32.49	65.29	0.28	NA	0.057	NA	0.12	NA	98.36
56_MS391_WS_Blb29_BSE3_2	NA	32.48	65.69	0.11	NA	0.025	NA	0.18	NA	98.58
57_MS391_WS_Blb29_BSE3_4	0.037	32.59	64.85	0.46	0.171	0.069	NA	0.12	NA	98.30
58_MS391_WS_Blb29_BSE3_4	0.129	31.89	64.52	0.61	0.284	0.074	NA	NA	NA	97.60
59_MS391_WS_Blb29_BSE3_4	0.033	32.41	64.85	0.64	0.196	0.045	NA	0.14	NA	98.32
60_MS391_WS_Blb29_BSE3_4	0.027	32.48	65.39	0.05	NA	NA	NA	0.19	NA	98.27
61_MS391_WS_Blb29_BSE3_4	0.028	32.31	64.78	0.32	0.169	0.071	NA	0.10	NA	97.77
62_MS391_WS_Blb29_BSE3_4	0.063	32.65	64.16	1.51	NA	0.062	NA	0.11	NA	98.70
63_MS391_WS_Blb29_BSE15_10	0.030	32.69	65.31	0.65	0.205	0.067	NA	0.03	NA	98.99
65_MS391_WS_Blb29_BSE15_10	0.071	32.13	64.62	0.85	0.198	0.077	NA	0.04	NA	98.02
66_MS391_WS_Blb29_BSE15_10	0.039	31.96	64.68	0.38	0.125	0.088	NA	0.08	NA	97.38
67_MS391_WS_Blb29_BSE15_10	NA	32.79	65.88	0.26	0.157	0.021	NA	0.14	NA	99.26
68_MS391_WS_Blb29_BSE15_10	0.065	32.33	65.52	0.79	0.217	0.025	NA	0.20	NA	99.15
69_MS391_WS_Blb29_BSE15_10	NA	32.40	64.13	2.27	0.128	0.120	NA	0.06	NA	99.11

Table 9: EMP data of sphalerites from unknown horizons (Bleiberg).

	EMPA Bleiberg, unknown horizon [mass%]									
sample/analyses	**As**	**S**	**Zn**	**Fe**	**Pb**	**Ge**	**Cu**	**Cd**	**Tl**	**total**
EHK11_ZnS1	0.093	33.59	62.56	3.97	0.254	NA	NA	0.07	NA	100.53
EHK11_ZnS2	NA	33.33	63.18	4.08	0.313	0.016	NA	0.07	NA	100.99
EHK11_ZnS3	0.047	33.62	63.83	3.24	0.373	0.018	NA	0.04	NA	101.17
EHK11_ZnS4	0.072	33.14	62.95	4.01	0.405	NA	NA	0.06	NA	100.64
EHK11_ZnS5	NA	33.46	64.40	3.41	0.084	NA	NA	0.09	NA	101.45
EHK11_ZnS6	NA	33.25	66.96	0.54	0.062	0.031	NA	0.07	NA	100.91
EHK11_ZnS7	NA	33.33	66.85	1.03	0.063	NA	NA	0.12	NA	101.39
EHK11_ZnS8	NA	33.36	67.53	0.28	0.033	0.030	NA	0.08	NA	101.32
EHK11_ZnS9	NA	32.64	58.22	8.12	0.237	NA	NA	0.07	NA	99.28
EHK11_ZnS10	NA	33.77	59.50	6.99	0.318	NA	NA	0.05	NA	100.63
EHK11_ZnS11	NA	33.62	64.66	2.96	0.124	NA	NA	0.19	NA	101.55
EHK11_ZnS12	NA	33.72	65.95	2.03	0.073	NA	NA	0.12	NA	101.89
EHK11_ZnS13	NA	30.20	66.89	0.66	0.158	NA	NA	0.16	NA	98.06
EHK11_ZnS14	NA	32.29	66.39	1.01	0.149	NA	NA	0.21	NA	100.05
EHK11_ZnS15	NA	33.14	66.68	0.76	0.065	NA	NA	0.20	NA	100.84
EHK11_ZnS16	NA	32.71	66.91	0.64	0.102	NA	NA	0.24	NA	100.60
EHK11_ZnS17	NA	33.05	67.22	0.38	0.058	NA	NA	0.21	NA	100.92
EHK11_ZnS18	NA	33.47	64.37	2.95	0.032	NA	NA	0.09	NA	100.91
EHK11_ZnS19	NA	33.33	66.77	0.65	0.122	NA	NA	0.10	NA	100.97
EHK11_ZnS20	NA	33.50	65.85	1.87	0.040	NA	NA	0.03	NA	101.29
EHK11_ZnS21	NA	33.31	63.91	3.13	0.050	NA	NA	0.06	NA	100.46
EHK11_ZnS22	NA	33.23	65.81	1.60	0.062	NA	NA	0.19	NA	100.89
EHK11_ZnS23	NA	33.11	66.64	0.83	0.181	NA	NA	0.19	NA	100.95
EHK11_ZnS24	NA	32.89	66.67	0.70	0.126	NA	NA	0.26	NA	100.65
EHK11_ZnS25	NA	32.82	65.48	1.79	0.125	NA	NA	0.21	NA	100.42
EHK11_ZnS26	NA	32.46	59.77	6.90	0.080	NA	NA	0.14	NA	99.36
EHK11_ZnS27	0.078	33.53	65.07	2.07	0.162	NA	NA	0.23	NA	101.14
EHK11_ZnS28	NA	29.83	66.38	0.38	0.042	NA	NA	0.29	NA	96.93
EHK11_ZnS29	0.024	33.77	55.12	10.69	0.271	NA	NA	0.06	NA	100.00
EHK11_ZnS30	0.060	33.47	59.57	6.46	0.375	0.010	NA	0.05	NA	100.05
EHK11_ZnS31	NA	33.55	59.26	7.10	0.368	NA	NA	0.10	NA	100.41
EHK11_ZnS32	NA	33.52	59.65	7.44	0.243	NA	NA	0.04	NA	100.90
EHK11_ZnS33	0.138	33.44	57.02	9.53	0.426	NA	NA	0.06	NA	100.61
EHK11_ZnS34	NA	33.33	65.44	1.15	0.105	NA	NA	0.21	NA	100.27
EHK11_ZnS35	0.022	32.29	65.73	0.51	0.619	0.077	NA	0.20	NA	99.46
EHK11_ZnS36	NA	33.28	66.30	0.91	0.126	NA	NA	0.18	NA	100.80
EHK11_ZnS37	NA	32.74	66.82	0.58	0.065	NA	NA	0.29	NA	100.49
EHK11_ZnS38	NA	32.78	67.94	0.12	0.018	NA	NA	0.44	NA	101.38
EHK11_ZnS39	NA	33.04	67.77	0.27	0.081	NA	NA	0.14	NA	101.33
EHK11_ZnS40	NA	33.26	66.81	0.90	0.051	NA	NA	0.23	NA	101.25
EHK11_ZnS41	NA	33.33	66.91	0.78	0.138	NA	NA	0.14	NA	101.30
EHK11_ZnS42	NA	33.30	67.97	0.18	0.041	NA	NA	0.16	NA	101.68
EHK11_ZnS43	NA	33.49	67.68	0.52	0.029	NA	NA	0.15	NA	101.90
EHK11_ZnS44	NA	33.19	67.21	0.24	0.280	NA	NA	0.20	NA	101.13
EHK11_ZnS45	0.505	33.14	67.13	0.49	0.099	NA	NA	0.31	NA	101.70
EHK11_ZnS46	NA	33.31	68.19	0.03	NA	NA	NA	0.23	NA	101.80
EHK11_ZnS47	NA	33.33	67.89	0.02	NA	NA	NA	0.40	NA	101.67

Table 9: Continued.

EMPA Bleiberg, unknown horizon [mass%]										
sample/analyses	**As**	**S**	**Zn**	**Fe**	**Pb**	**Ge**	**Cu**	**Cd**	**Tl**	**total**
EHK11_ZnS48	NA	33.11	68.30	0.01	NA	NA	NA	0.51	NA	101.94
EHK11_ZnS49	NA	33.41	68.13	0.11	NA	NA	NA	0.22	NA	101.87
EHK11_ZnS50	NA	32.74	67.29	0.17	0.068	NA	NA	0.45	NA	100.75
EHK11_ZnS51	NA	33.36	67.49	0.67	0.054	NA	NA	0.14	NA	101.75
EHK11_ZnS52	NA	32.24	67.08	1.01	0.130	NA	NA	0.24	NA	100.76
EHK11_ZnS53	NA	34.25	66.60	1.10	0.138	NA	NA	0.15	NA	102.26
EHK11_ZnS54	0.156	32.92	64.81	1.89	0.704	NA	NA	0.07	NA	100.55
EHK11_ZnS55	0.178	32.98	64.94	1.67	0.542	NA	NA	0.06	NA	100.38
EHK11_ZnS56	0.038	32.95	66.13	1.29	0.350	NA	NA	0.09	NA	100.86
EHK11_ZnS57	0.448	32.64	63.45	2.52	0.772	NA	NA	0.03	NA	99.86
EHK11_ZnS58	0.190	33.24	64.79	1.62	0.523	NA	NA	0.06	NA	100.43
EHK11_ZnS59	NA	33.31	65.65	2.32	0.091	NA	NA	0.15	NA	101.52
EHK11_ZnS60	0.032	33.12	65.89	1.55	0.373	NA	NA	0.07	NA	101.04
EHK11_ZnS61	0.017	30.81	66.72	0.98	0.167	NA	NA	0.15	NA	98.85
EHK11_ZnS62	NA	32.86	67.13	0.32	0.146	NA	NA	0.16	NA	100.63
EHK11_ZnS63	0.083	32.96	64.73	2.11	0.377	NA	NA	0.15	NA	100.43
EHK11_ZnS64	0.169	33.56	63.73	1.97	0.544	NA	NA	0.09	NA	100.07
EHK11_ZnS65	NA	33.24	67.83	0.17	0.206	NA	NA	0.31	NA	101.75
EHK11_ZnS66	NA	33.22	66.18	2.12	0.034	NA	NA	0.10	NA	101.67
EHK11_ZnS67	NA	33.51	68.39	0.04	NA	NA	NA	0.32	NA	102.26
EHK11_ZnS68	NA	33.31	67.59	0.37	0.064	NA	NA	0.27	NA	101.60
EHK11_ZnS69	NA	33.08	67.69	0.07	0.012	NA	NA	0.59	NA	101.44
EHK11_ZnS70	0.059	33.47	63.86	3.54	0.225	NA	NA	0.25	NA	101.41
EHK11_ZnS71	NA	33.48	67.18	0.50	0.088	NA	NA	0.17	NA	101.42
EHK11_ZnS72	NA	33.34	67.31	0.51	0.151	NA	NA	0.29	NA	101.60
EHK11_ZnS73	NA	31.33	67.33	0.64	0.194	NA	NA	0.37	NA	99.86
EHK11_ZnS74	NA	32.77	66.12	0.56	0.279	NA	NA	0.32	NA	100.05
EHK11_ZnS75	NA	32.82	66.14	0.56	0.281	NA	NA	0.32	NA	100.12
EHK23_ZnS4	NA	32.30	67.09	0.10	0.050	NA	NA	0.40	NA	99.94
EHK23_ZnS5	NA	32.32	67.05	0.02	NA	NA	NA	0.58	NA	99.97
EHK23_ZnS6	NA	32.11	67.68	0.02	NA	NA	NA	0.40	NA	100.21
EHK23_ZnS7	NA	32.37	67.48	0.02	0.022	NA	NA	0.57	NA	100.46
EHK23_ZnS8	NA	30.50	67.66	0.02	NA	NA	NA	0.65	NA	98.83
EHK23_ZnS9	NA	32.46	67.59	0.02	0.016	NA	NA	0.36	NA	100.45
EHK23_ZnS10	NA	32.70	67.41	0.03	0.025	NA	NA	0.58	NA	100.74
EHK23_ZnS11	NA	32.46	67.78	0.02	NA	NA	NA	0.17	NA	100.42
EHK23_ZnS12	NA	32.47	66.53	0.97	0.049	NA	NA	0.28	NA	100.29
EHK23_ZnS13	NA	32.43	66.53	0.79	0.076	NA	NA	0.25	NA	100.07
EHK23_ZnS14	NA	32.56	66.07	1.15	0.082	NA	NA	0.32	NA	100.18
EHK23_ZnS15	NA	32.35	67.81	0.19	0.030	NA	NA	0.20	NA	100.58
EHK23_ZnS17	NA	32.09	65.91	0.78	0.181	0.117	NA	0.23	NA	99.30
EHK23_ZnS18	NA	32.36	66.67	0.40	0.084	NA	NA	0.24	NA	99.77
EHK23_ZnS19	NA	32.39	66.52	0.21	0.071	NA	NA	0.12	NA	99.31
EHK23_ZnS20	NA	32.42	66.97	0.15	0.043	0.040	NA	0.16	NA	99.79
EHK23_ZnS21	NA	32.34	67.23	NA	NA	NA	NA	0.29	NA	99.86
EHK23_ZnS22	NA	32.23	66.84	0.03	0.027	NA	NA	0.32	NA	99.46

Table 9: Continued.

EMPA Bleiberg, unknown horizon [mass%]										
sample/analyses	**As**	**S**	**Zn**	**Fe**	**Pb**	**Ge**	**Cu**	**Cd**	**Tl**	**total**
EHK23_ZnS23	NA	32.40	67.07	0.01	NA	NA	NA	0.33	NA	99.81
EHK23_ZnS24	NA	32.13	66.66	0.02	0.081	NA	NA	0.35	NA	99.24
EHK23_ZnS25	NA	32.22	65.71	0.56	0.109	NA	NA	0.37	NA	98.96
EHK23_ZnS26	NA	32.37	66.73	0.46	0.306	NA	NA	0.15	NA	100.02
EHK23_ZnS27	NA	32.48	65.67	0.56	0.054	0.056	NA	0.18	NA	98.99
EHK23_ZnS28	NA	31.71	64.90	0.60	0.538	0.043	NA	0.24	NA	98.03
EHK23_ZnS29	NA	32.20	66.25	0.45	0.090	0.022	NA	0.30	NA	99.31
EHK23_ZnS30	NA	32.54	66.60	0.13	NA	NA	NA	0.17	NA	99.44
EHK23_ZnS31	NA	32.36	64.16	1.53	0.131	0.011	NA	0.12	NA	98.31
EHK23_ZnS32	NA	32.45	64.36	1.73	0.132	0.039	NA	0.15	NA	98.86
EHK23_ZnS33	NA	32.33	64.97	1.00	0.082	0.056	NA	0.27	NA	98.70
EHK23_ZnS34	NA	32.01	66.15	NA	0.065	NA	NA	0.29	NA	98.52
EHK23_ZnS35	NA	32.41	66.88	NA	0.035	NA	NA	0.28	NA	99.60
EHK23_ZnS36	NA	32.35	66.88	0.01	0.030	NA	NA	0.32	NA	99.59
EHK23_ZnS37	NA	32.25	66.91	0.02	0.020	NA	NA	0.23	NA	99.43
EHK23_ZnS38	NA	32.33	66.43	0.01	0.016	NA	NA	0.49	NA	99.28
EHK23_ZnS39	NA	32.35	66.53	0.02	0.058	0.018	NA	0.34	NA	99.32
EHK23_ZnS40	NA	32.58	66.61	0.02	0.053	NA	NA	0.20	NA	99.47
EHK23_ZnS41	0.025	32.12	65.29	1.49	0.145	NA	NA	0.20	NA	99.27
EHK23_ZnS42	NA	32.49	67.17	0.02	NA	NA	NA	0.23	NA	99.91
EHK23_ZnS43	NA	32.52	67.11	0.01	0.019	NA	NA	0.40	NA	100.07
EHK23_ZnS44	NA	32.55	67.01	NA	0.015	NA	NA	0.48	NA	100.05
EHK23_ZnS45	NA	32.43	67.00	NA	0.012	NA	NA	0.33	NA	99.78
EHK23_ZnS46	NA	32.50	66.53	0.01	NA	NA	NA	0.32	NA	99.35
EHK23_ZnS47	NA	32.43	66.89	0.01	NA	NA	NA	0.27	NA	99.60
EHK23_ZnS48	NA	32.15	63.51	1.02	0.140	0.022	NA	0.17	NA	97.02
EHK23_ZnS49	NA	31.90	64.64	1.44	0.071	0.066	NA	0.39	NA	98.51
EHK23_ZnS50	NA	32.27	65.47	0.22	0.066	NA	NA	0.40	NA	98.42
EHK23_ZnS51	NA	32.31	65.86	0.03	0.077	NA	NA	0.27	NA	98.55
EHK23_ZnS52	NA	32.56	66.92	NA	0.015	NA	NA	0.18	NA	99.68
EHK23_ZnS53	NA	32.17	66.39	0.01	0.056	NA	NA	0.29	NA	98.92
EHK23_ZnS54	NA	32.67	65.99	0.01	NA	NA	NA	0.58	NA	99.26
Blb122_1	NA	31.78	67.20	0.03	0.107	NA	NA	0.25	NA	99.37
Blb122_2	NA	31.36	67.24	0.05	0.151	NA	NA	0.36	NA	99.16
Blb122_3	NA	31.50	67.07	0.01	0.132	NA	NA	0.44	NA	99.16
Blb122_5	NA	31.13	66.40	0.03	0.201	NA	NA	0.40	NA	98.16
Blb122_6	NA	30.99	66.87	0.02	NA	NA	NA	0.33	NA	98.20
Blb122_7	NA	30.94	66.97	0.01	0.095	NA	NA	0.39	NA	98.41
Blb122_8	NA	31.07	66.81	NA	0.115	NA	NA	0.41	NA	98.41
Blb122_9	NA	31.12	65.97	0.02	0.243	NA	NA	0.43	NA	97.79
Blb122_10	NA	31.17	66.58	0.06	0.109	NA	NA	0.38	NA	98.30
Blb122_13	NA	31.68	65.82	0.02	0.179	NA	NA	0.52	NA	98.22
Blb122_14	0.512	31.39	65.63	0.10	0.987	0.048	NA	0.01	NA	98.68
Blb122_15	0.233	31.48	66.03	0.04	0.778	NA	NA	0.00	NA	98.56
Blb122_16	0.553	31.32	65.14	0.21	1.080	NA	NA	0.01	NA	98.31
Blb122_17	0.210	31.55	65.98	0.06	0.816	NA	NA	0.01	NA	98.63

Table 9: Continued.

EMPA Bleiberg, unknown horizon [mass%]										
sample/analyses	**As**	**S**	**Zn**	**Fe**	**Pb**	**Ge**	**Cu**	**Cd**	**Tl**	**total**
Blb122_18	0.270	31.46	65.80	0.12	0.823	NA	NA	0.01	NA	98.49
Blb122_19	NA	31.50	67.02	0.04	0.312	NA	NA	0.03	NA	98.90
Blb122_20	0.367	31.28	65.75	0.16	0.868	NA	NA	0.01	NA	98.43
Blb122_21	0.449	31.17	65.46	0.11	1.030	NA	NA	0.02	NA	98.24
Blb122_22	0.521	31.25	65.26	0.45	1.060	NA	NA	NA	NA	98.54
Blb122_23	0.517	31.12	65.11	0.57	1.040	NA	NA	NA	0.055	98.41
Blb122_24	NA	31.38	67.41	0.05	0.072	NA	NA	0.02	NA	98.93
Blb122_28	0.514	31.10	64.99	0.58	1.010	0.008	NA	NA	NA	98.20
Blb122_29	NA	30.90	66.90	0.04	0.242	NA	NA	0.07	NA	98.16
Blb122_30	NA	30.79	66.83	0.08	0.022	NA	NA	0.19	NA	97.91
Blb122_31	NA	30.96	66.48	0.04	0.273	NA	NA	0.10	NA	97.86
Blb122_32	0.237	30.77	65.59	0.12	0.503	0.018	NA	0.01	NA	97.25
Blb122_33	0.097	31.20	66.74	0.17	0.254	NA	NA	NA	NA	98.46
Blb122_34	0.458	31.02	64.86	0.79	1.050	NA	NA	NA	NA	98.18
Blb122_35	0.429	31.13	65.04	0.74	0.871	NA	NA	NA	NA	98.21
Blb122_36	0.283	31.04	65.81	0.70	0.555	NA	NA	NA	NA	98.39
Blb122_37	NA	31.17	67.25	0.12	0.130	NA	NA	0.01	NA	98.67
Blb122_38	NA	31.43	66.95	0.12	0.130	NA	NA	NA	NA	98.63
Blb122_39	0.113	31.04	66.65	0.12	0.250	NA	NA	0.02	NA	98.19
Blb122_40	0.475	30.95	64.98	0.37	1.060	NA	NA	0.00	NA	97.84
Blb122_41	0.075	31.08	66.28	0.10	0.240	NA	NA	0.02	NA	97.79
Blb122_42	0.353	30.54	65.33	0.36	1.050	NA	NA	0.01	NA	97.64
Blb122_44	NA	31.11	66.01	0.09	0.289	NA	NA	0.01	NA	97.50
Blb122_45	0.317	30.95	65.53	0.10	0.881	0.016	NA	0.02	NA	97.81
Blb122_46	0.073	30.76	66.38	0.06	0.481	NA	NA	0.01	NA	97.76
Blb122_47	0.169	30.83	65.99	0.09	0.586	NA	NA	0.01	NA	97.68
Blb122_48	0.466	30.92	65.29	0.22	0.993	NA	NA	0.02	NA	97.91
Blb122_49	0.622	30.70	64.58	0.43	1.070	0.057	NA	0.01	0.084	97.56
Blb122_50	NA	31.04	67.24	0.04	0.154	NA	NA	0.07	NA	98.55
Blb122_51	NA	31.04	67.35	0.04	0.099	NA	NA	0.05	NA	98.58
Blb122_52	NA	30.97	67.10	0.02	0.065	NA	NA	0.03	NA	98.19
Blb122_53	NA	31.21	66.97	0.02	0.122	NA	NA	0.37	NA	98.69
Blb122_54	NA	31.54	66.61	0.01	0.175	NA	NA	0.21	NA	98.55
Blb122_55	NA	29.16	67.39	NA	0.212	NA	NA	0.41	NA	97.19
Blb122_56	NA	31.17	67.25	0.06	0.051	NA	NA	0.05	NA	98.57
Blb122_57	NA	29.83	63.97	0.02	0.318	NA	NA	0.02	NA	94.16
Blb122_59	0.129	30.95	66.07	0.04	0.664	0.007	NA	0.01	NA	97.87
Blb122_60	0.108	30.76	66.04	0.03	0.676	NA	NA	0.02	NA	97.62
Blb122_61	0.060	30.48	65.88	0.04	0.545	NA	NA	0.02	NA	97.03
Blb122_62	0.110	30.44	66.44	0.03	0.488	NA	NA	0.01	NA	97.53
Blb122_64	0.214	30.41	65.68	0.04	0.500	NA	NA	0.01	NA	96.85
Blb122_65	0.149	30.53	65.94	0.04	0.487	0.034	NA	0.01	NA	97.18
Blb122_66	NA	30.89	67.09	0.04	0.147	NA	NA	0.02	NA	98.19
Blb122_68	0.140	30.43	65.99	0.04	0.309	NA	NA	NA	NA	96.91
Blb122_69	NA	30.80	67.37	0.06	0.058	NA	NA	0.01	NA	98.32
Blb122_70	NA	30.52	66.91	0.07	0.066	NA	NA	0.06	NA	97.63
Blb122_71	0.076	31.24	66.90	0.10	0.233	NA	NA	0.01	NA	98.55

Table 9: Continued.

EMPA Bleiberg, unknown horizon [mass%]										
sample/analyses	**As**	**S**	**Zn**	**Fe**	**Pb**	**Ge**	**Cu**	**Cd**	**Tl**	**total**
Blb122_72	NA	30.82	67.16	0.08	0.241	NA	NA	NA	NA	98.30
Blb122_73	0.593	30.34	64.94	0.19	1.220	NA	NA	0.00	NA	97.29
Blb122_74	0.490	30.52	65.03	0.22	1.400	NA	NA	0.01	NA	97.68
Blb122_75	NA	30.83	67.05	0.03	0.034	NA	NA	0.16	NA	98.10
Blb122_76	0.259	30.77	65.71	0.09	0.716	NA	NA	0.02	NA	97.56
Blb122_77	0.433	30.83	65.61	0.18	0.836	NA	NA	0.02	NA	97.91
Blb26_AS_1	NA	31.40	64.83	1.49	0.118	0.021	NA	0.04	NA	97.90
Blb26_AS_2	NA	31.50	65.39	0.77	0.122	0.101	NA	0.05	NA	97.94
Blb26_AS_3	NA	31.68	65.83	0.72	0.098	NA	NA	0.20	NA	98.53
Blb26_AS_4	NA	31.19	65.41	0.14	NA	NA	NA	0.34	NA	97.08
Blb26_AS_6	NA	32.00	65.47	0.40	0.017	NA	NA	0.20	NA	98.10
Blb26_AS_7	NA	31.59	64.86	0.63	0.187	0.082	NA	0.04	NA	97.39
Blb26_AS_8	NA	32.00	65.62	0.12	0.024	NA	NA	0.23	NA	97.99
Blb26_AS_9	NA	30.57	65.32	0.44	0.113	0.024	NA	0.14	NA	96.60
Blb26_AS_10	NA	32.00	67.69	0.05	NA	NA	NA	0.15	NA	99.89
Blb26_AS_12	NA	31.81	63.96	0.06	0.038	0.011	0.040	3.62	NA	99.54
Blb26_AS_13	NA	31.24	65.95	0.04	NA	NA	NA	0.10	NA	97.33
Blb26_AS_14	NA	31.67	65.98	0.11	0.013	NA	NA	0.16	NA	97.93
Blb26_AS_16	NA	31.78	65.91	0.13	0.070	NA	NA	0.17	NA	98.06
Blb26_AS_17	NA	33.10	63.99	0.23	0.037	0.017	NA	0.16	NA	97.53
Blb26_AS_18	NA	31.51	66.21	0.60	0.157	0.068	NA	0.04	NA	98.59
Blb26_AS_19	NA	32.29	66.62	0.11	NA	NA	NA	0.29	NA	99.31
Blb26_AS_22	NA	32.58	65.32	0.81	0.185	0.045	NA	0.03	NA	98.97
Blb26_AS_23	NA	32.71	66.15	0.73	0.194	0.009	NA	0.09	NA	99.88
Blb26_AS_24	0.055	32.25	65.87	1.10	0.187	NA	NA	0.03	NA	99.49
Blb26_AS_25	NA	32.50	65.27	0.48	0.034	0.083	NA	0.12	NA	98.48
Blb26_AS_26	NA	31.39	66.99	0.75	0.193	0.061	NA	0.06	NA	99.44
Blb26_AS_27	NA	32.83	65.72	0.73	0.122	0.061	NA	0.08	NA	99.54
Blb26_AS_28	NA	33.06	66.31	0.96	0.049	0.081	NA	0.11	NA	100.57
Blb26_AS_29	NA	31.80	68.62	0.63	0.166	0.043	NA	0.12	NA	101.38
Blb26_AS_30	0.020	33.00	68.94	0.52	0.110	0.029	NA	0.10	NA	102.73
Blb26_AS_31	NA	32.73	67.46	0.11	NA	NA	NA	0.34	NA	100.64
Blb26_AS_32	NA	32.73	69.59	0.04	NA	NA	NA	0.22	NA	102.60
Blb26_AS_33	NA	32.96	68.66	0.15	NA	NA	NA	0.19	NA	101.96
Blb26_AS_34	NA	32.73	69.87	0.04	NA	NA	NA	0.37	NA	103.04
Blb26_AS_35	NA	32.73	68.86	0.19	NA	NA	NA	0.22	NA	101.99
Blb26_AS_36	NA	32.59	69.51	0.06	0.065	NA	NA	0.27	NA	102.50
Blb26_AS_37	NA	32.71	68.59	0.17	NA	NA	NA	0.22	NA	101.69
Blb26_AS_38	NA	32.10	68.39	0.23	NA	NA	NA	0.22	NA	100.94
Blb26_AS_39	NA	33.22	67.26	0.12	NA	NA	NA	0.30	NA	100.90
Blb26_AS_40	NA	32.80	68.78	0.18	0.064	NA	NA	0.15	NA	101.98
Blb26_AS_41	NA	32.69	64.89	0.70	0.190	0.099	NA	0.03	NA	98.60
Blb26_AS_42	NA	32.86	64.81	0.73	0.117	0.038	NA	0.14	NA	98.69
Blb26_AS_43	NA	32.48	66.75	0.67	0.085	0.060	NA	0.07	NA	100.11
Blb26_AS_44	NA	32.75	67.28	0.04	NA	NA	NA	0.22	NA	100.28
Blb26_AS_45	NA	32.51	66.51	0.18	NA	NA	NA	0.06	NA	99.27

Table 9: Continued.

EMPA Bleiberg, unknown horizon [mass%]										
sample/analyses	**As**	**S**	**Zn**	**Fe**	**Pb**	**Ge**	**Cu**	**Cd**	**Tl**	**total**
Blb26_AS_46	NA	32.85	66.92	0.19	0.208	NA	NA	0.02	NA	100.19
Blb26_AS_47	NA	32.85	66.72	0.23	NA	NA	NA	0.07	NA	99.87
Blb26_AS_48	NA	33.02	66.86	0.09	0.153	NA	NA	0.05	NA	100.17
Blb26_AS_49	NA	32.99	66.69	0.04	NA	NA	NA	0.38	NA	100.10
Blb26_AS_50	NA	32.72	66.59	0.06	NA	NA	NA	0.27	NA	99.64
Blb26_AS_51	NA	32.89	66.05	0.74	0.088	0.048	NA	0.06	NA	99.88
Blb26_AS_52	NA	32.47	67.02	0.14	NA	NA	NA	0.33	NA	99.96
WS_Blb24_ZnS2	NA	32.94	67.20	0.67	0.013	NA	NA	0.26	NA	101.08
WS_Blb24_ZnS3	NA	32.74	69.27	0.08	NA	NA	NA	0.37	NA	102.46
WS_Blb24_ZnS4	NA	33.00	69.23	0.04	NA	NA	NA	0.27	NA	102.54
WS_Blb24_ZnS5	NA	32.90	67.99	0.07	NA	NA	NA	0.64	NA	101.60
WS_Blb24_ZnS6	NA	32.58	67.97	0.07	NA	NA	NA	0.51	NA	101.13
WS_Blb24_ZnS7	NA	32.83	68.77	0.09	0.028	NA	0.048	0.63	NA	102.40
WS_Blb24_ZnS8	NA	32.68	68.47	0.10	0.081	NA	0.072	0.90	NA	102.30
WS_Blb24_ZnS9	NA	32.70	68.53	0.15	NA	NA	NA	0.49	NA	101.87
WS_Blb24_ZnS10	NA	32.02	67.57	0.16	0.062	NA	NA	0.52	NA	100.35
WS_Blb24_ZnS11	NA	32.64	68.93	0.08	0.026	NA	NA	0.43	NA	102.11
WS_Blb24_ZnS12	NA	32.70	68.34	0.31	0.084	NA	NA	0.55	NA	101.99
WS_Blb24_ZnS13	NA	32.93	68.85	0.02	NA	NA	NA	0.32	NA	102.12
WS_Blb24_ZnS14	NA	33.05	65.30	0.07	NA	NA	NA	0.24	NA	98.66
WS_Blb24_ZnS15	NA	32.41	67.75	0.10	0.013	NA	NA	0.39	NA	100.66
WS_Blb24_ZnS16	NA	32.81	66.74	0.46	0.050	NA	NA	0.50	NA	100.57
WS_Blb24_ZnS17	NA	33.05	67.83	0.42	NA	NA	NA	0.20	NA	101.50
WS_Blb24_ZnS18	NA	32.61	67.81	0.55	0.020	NA	NA	0.49	NA	101.48
WS_Blb24_ZnS19	NA	32.64	68.83	0.23	NA	NA	NA	0.39	NA	102.10
WS_Blb24_ZnS20	NA	32.90	67.44	0.03	NA	NA	NA	0.68	NA	101.07
WS_Blb24_ZnS21	NA	32.86	68.88	0.07	NA	NA	NA	0.15	NA	101.95
WS_Blb24_ZnS22	NA	32.54	67.95	0.08	0.037	NA	0.018	0.48	NA	101.11
WS_Blb24_ZnS23	NA	32.49	67.28	0.11	0.155	NA	0.385	0.63	NA	101.05
WS_Blb24_ZnS24	NA	32.62	67.75	0.35	NA	NA	NA	0.23	NA	100.95
WS_Blb24_ZnS25	NA	32.66	66.40	0.38	0.128	NA	NA	0.56	NA	100.13
WS_Blb24_ZnS26	NA	31.48	65.04	0.05	0.106	NA	NA	0.58	NA	97.27
WS_Blb24_ZnS27	NA	32.54	67.16	0.04	0.230	NA	NA	0.57	NA	100.54
WS_Blb24_ZnS28	NA	32.63	68.67	0.16	0.040	NA	0.018	0.35	NA	101.87
WS_Blb24_ZnS29	NA	32.85	67.96	0.05	NA	NA	NA	0.21	NA	101.07
WS_Blb24_ZnS30	NA	32.69	66.98	NA	0.099	NA	0.010	0.35	NA	100.13
WS_Blb24_ZnS31	NA	32.67	67.12	0.08	0.298	NA	NA	0.49	NA	100.66
WS_Blb24_ZnS32	NA	32.72	67.21	0.04	0.207	NA	NA	0.50	NA	100.67
WS_Blb24_ZnS33	NA	32.97	67.31	0.01	0.039	NA	NA	0.30	NA	100.62
WS_Blb24_ZnS34	NA	33.20	67.94	0.04	0.047	NA	NA	0.17	NA	101.40
WS_Blb24_ZnS35	NA	31.93	60.98	0.05	4.770	NA	NA	0.54	NA	98.27
WS_Blb24_ZnS36	NA	32.53	65.87	0.03	0.222	NA	NA	0.48	NA	99.14
WS_Blb24_ZnS37	NA	32.49	66.30	0.03	0.097	NA	NA	0.51	NA	99.43
WS_Blb24_ZnS38	NA	32.04	65.26	0.05	0.489	NA	NA	0.72	NA	98.56
WS_Blb24_ZnS39	NA	33.39	67.92	0.26	0.047	NA	NA	0.27	NA	101.89
WS_Blb24_ZnS40	NA	32.62	68.13	0.03	0.066	NA	NA	0.46	NA	101.31

Table 9: Continued.

EMPA Bleiberg, unknown horizon [mass%]										
sample/analyses	**As**	**S**	**Zn**	**Fe**	**Pb**	**Ge**	**Cu**	**Cd**	**Tl**	**total**
WS_Blb24_ZnS41	NA	32.75	68.62	0.05	0.060	NA	NA	0.24	NA	101.72
WS_Blb24_ZnS42	NA	32.23	67.82	0.06	NA	NA	NA	0.28	NA	100.39
WS_Blb24_ZnS43	NA	32.90	67.56	0.09	NA	NA	0.041	0.28	NA	100.87
WS_Blb24_ZnS44	NA	32.52	68.26	0.12	NA	NA	NA	0.24	NA	101.15
WS_Blb24_ZnS45	NA	32.82	68.09	0.10	NA	NA	NA	0.66	NA	101.68
WS_Blb24_ZnS46	NA	32.95	68.90	0.42	NA	NA	0.030	0.25	NA	102.55
WS_Blb24_ZnS47	NA	32.77	67.69	0.25	NA	NA	NA	0.69	NA	101.41
WS_Blb24_ZnS48	NA	32.80	67.21	0.41	NA	NA	NA	0.66	NA	101.08
WS_Blb24_ZnS49	NA	33.04	68.55	0.22	0.022	NA	0.016	0.29	NA	102.13
WS_Blb24_ZnS50	NA	32.91	69.38	0.05	NA	NA	NA	0.43	NA	102.77
WS_Blb24_ZnS51	NA	32.83	69.32	0.05	NA	NA	NA	0.77	NA	102.97
WS_Blb24_ZnS52	NA	32.91	68.02	0.16	0.013	NA	NA	0.33	NA	101.43
WS_Blb24_ZnS53	NA	32.67	67.52	0.24	0.077	NA	NA	0.58	NA	101.08
WS_Blb24_ZnS54	NA	32.67	67.81	0.38	0.040	NA	NA	0.46	NA	101.37
WS_Blb24_ZnS55	NA	28.37	59.55	0.37	NA	NA	NA	0.45	NA	88.74
WS_Blb24_ZnS56	NA	33.13	69.33	0.12	NA	NA	NA	0.55	NA	103.13
WS_Blb24_ZnS57	NA	32.63	68.36	0.12	0.039	NA	NA	0.58	NA	101.73
WS_Blb24_ZnS58	NA	32.73	68.26	0.17	0.020	NA	NA	0.41	NA	101.60
WS_Blb24_ZnS59	NA	32.68	68.65	0.30	NA	NA	NA	0.68	NA	102.34
WS_Blb24_ZnS60	NA	32.84	68.81	0.23	NA	NA	NA	0.74	NA	102.62
WS_Blb24_ZnS61	NA	32.83	68.39	0.05	0.034	NA	NA	0.66	NA	101.97
WS_Blb24_ZnS62	NA	33.31	68.37	0.02	NA	NA	NA	0.51	NA	102.21
WS_Blb24_ZnS63	NA	32.79	68.15	0.01	NA	NA	NA	0.34	NA	101.29
WS_Blb24_ZnS64	NA	33.00	68.69	0.01	NA	NA	NA	0.37	NA	102.08
WS_Blb24_ZnS65	NA	32.81	69.19	0.01	NA	NA	NA	0.67	NA	102.68
WS_Blb24_ZnS66	NA	32.88	69.34	NA	0.018	NA	NA	0.69	NA	102.93
WS_Blb24_ZnS67	NA	33.00	68.15	0.02	0.028	NA	NA	0.75	NA	101.96
WS_Blb24_ZnS68	NA	32.64	68.33	0.01	0.033	NA	NA	0.64	NA	101.66
WS_Blb24_ZnS69	NA	32.85	68.96	0.02	NA	NA	NA	0.42	NA	102.26
WS_Blb24_ZnS70	NA	33.08	68.68	0.02	NA	NA	NA	0.65	NA	102.43
WS_Blb24_ZnS71	NA	32.69	68.59	0.01	NA	NA	NA	0.67	NA	101.96
WS_Blb24_ZnS72	NA	33.00	68.07	0.01	NA	NA	NA	0.60	NA	101.68
WS_Blb24_ZnS73	NA	33.02	68.67	NA	NA	NA	NA	0.25	NA	101.94
WS_Blb24_ZnS74	NA	32.91	68.01	0.02	NA	NA	NA	0.76	NA	101.70
WS_Blb24_ZnS75	NA	32.97	68.97	NA	0.012	NA	NA	0.49	NA	102.44

Table 10: EMP data of sphalerites from Mezica.

	EMPA Mezica, Moring [mass%]									
sample/analyses	**As**	**S**	**Zn**	**Fe**	**Pb**	**Ge**	**Cu**	**Cd**	**Tl**	**total**
Mz02b_1	NA	32.22	67.51	0.01	NA	NA	NA	0.34	NA	100.08
Mz02b_2	NA	32.26	67.69	0.01	NA	NA	NA	0.32	NA	100.28
Mz02b_3	NA	32.07	67.50	0.01	NA	NA	NA	0.25	NA	99.83
Mz02b_4	NA	32.25	67.60	0.01	NA	NA	NA	0.23	NA	100.10
Mz02b_5	NA	32.44	67.76	NA	NA	NA	NA	0.28	NA	100.48
Mz02b_6	NA	32.37	67.73	0.01	NA	NA	NA	0.35	NA	100.47
Mz02b_7	NA	32.34	67.79	NA	NA	NA	NA	0.32	NA	100.46
Mz02b_8	NA	32.13	68.13	0.01	NA	NA	NA	0.42	NA	100.70
Mz02b_9	NA	32.47	67.99	0.01	NA	NA	NA	0.13	NA	100.60
Mz02b_10	NA	31.99	67.61	0.01	NA	NA	NA	0.27	NA	99.88
Mz02b_11	NA	32.37	67.76	0.04	NA	NA	NA	0.25	NA	100.42
Mz02b_12	NA	32.38	67.43	0.02	0.014	NA	NA	0.25	NA	100.10
Mz02b_13	NA	32.38	67.55	0.01	NA	NA	NA	0.20	NA	100.14
Mz02b_14	NA	32.02	67.71	0.01	0.018	NA	NA	0.21	NA	99.97
Mz02b_15	NA	32.29	68.08	0.02	NA	NA	NA	0.19	NA	100.58
Mz02b_16	NA	32.38	67.59	0.01	NA	NA	NA	0.25	NA	100.24
Mz02b_17	NA	32.23	66.59	NA	NA	NA	NA	0.34	NA	99.16
Mz02b_18	NA	32.23	65.86	0.01	0.165	NA	0.282	1.22	NA	99.77
Mz02b_19	NA	31.50	64.71	0.02	0.092	NA	0.210	1.58	NA	98.11
Mz02b_20	NA	32.47	68.08	NA	NA	NA	NA	0.16	NA	100.71
Mz02b_21	NA	32.10	66.69	0.01	0.018	NA	NA	0.35	NA	99.16
Mz02b_22	NA	32.28	66.42	0.01	0.074	NA	0.188	0.49	NA	99.46
Mz02b_23	NA	32.57	65.24	0.02	0.252	NA	0.264	1.66	NA	100.00
Mz02b_24	NA	32.61	66.64	0.01	0.044	NA	0.174	0.49	NA	99.96
Mz02b_25	NA	32.55	67.06	NA	NA	NA	NA	0.51	NA	100.12
Mz02b_26	NA	32.61	66.99	0.01	NA	NA	NA	0.37	NA	99.97
Mz02b_27	NA	32.39	66.73	0.01	0.030	NA	0.042	0.36	NA	99.56
Mz02b_28	NA	32.52	67.58	NA	NA	NA	NA	0.31	NA	100.41
Mz02b_29	NA	32.37	67.51	0.01	NA	NA	NA	0.35	NA	100.24
Mz02b_30	NA	32.42	67.45	0.01	NA	NA	NA	0.30	NA	100.18
Mz02b_31	NA	32.51	67.39	0.01	0.016	NA	NA	0.32	NA	100.25
Mz02b_32	NA	32.43	66.84	0.01	0.055	NA	0.181	0.53	NA	100.05
Mz02b_34	NA	32.42	67.07	0.04	0.081	NA	0.158	0.50	NA	100.26
Mz02b_35	NA	32.31	66.86	0.04	0.090	NA	0.115	0.60	NA	100.01
Mz02b_36	NA	32.62	67.51	0.01	NA	NA	NA	0.22	NA	100.36
Mz02b_37	NA	32.24	66.40	0.02	0.092	NA	0.192	1.42	NA	100.36
Mz02b_38	NA	32.50	67.09	0.01	NA	NA	NA	0.38	NA	99.98
Mz02b_39	NA	32.44	67.06	NA	NA	NA	NA	0.38	NA	99.88
Mz02b_40	NA	32.49	67.32	NA	NA	NA	NA	0.23	NA	100.05
Mz02b_41	NA	31.65	66.53	0.02	0.103	NA	0.203	0.76	NA	99.27
Mz02b_42	NA	32.40	66.95	0.01	NA	NA	0.086	0.44	NA	99.88
Mz02b_43	NA	32.08	66.16	0.02	0.160	NA	0.242	1.46	NA	100.12
Mz02b_44	NA	32.04	66.04	0.01	0.092	NA	0.149	2.01	NA	100.34
Mz02b_45	NA	32.19	67.25	0.01	0.054	NA	NA	0.31	NA	99.81
Mz02b_46	NA	32.41	66.69	0.02	0.100	NA	0.259	1.02	NA	100.50
Mz02b_47	NA	32.44	67.28	NA	NA	NA	0.063	0.47	NA	100.25
Mz02b_48	NA	31.99	65.98	0.01	0.145	NA	0.400	1.48	NA	100.01

Table 10: Continued.

	EMPA Mezica, Moring [mass%]									
sample/analyses	**As**	**S**	**Zn**	**Fe**	**Pb**	**Ge**	**Cu**	**Cd**	**Tl**	**total**
Mz02b_49	NA	32.42	66.21	0.03	0.029	NA	0.120	1.92	NA	100.73
Mz02b_50	NA	32.30	65.96	0.02	0.076	NA	0.123	2.09	NA	100.57
Mz02b_51	NA	32.56	67.02	0.01	0.081	NA	0.165	0.49	NA	100.33
Mz02b_52	NA	32.29	67.00	0.01	0.014	NA	NA	0.39	NA	99.70
Mz02b_53	NA	32.36	67.21	NA	NA	NA	NA	0.39	NA	99.96
Mz02b_54	NA	32.48	67.27	0.01	0.013	NA	NA	0.33	NA	100.10
Mz02b_55	NA	33.20	67.39	NA	NA	NA	NA	0.14	NA	100.74
Mz02b_56	NA	32.51	67.31	NA	NA	NA	NA	0.30	NA	100.12
Mz02b_57	NA	32.31	66.23	0.01	NA	NA	0.085	1.48	NA	100.12
Mz02b_58	NA	30.61	67.70	NA	0.041	NA	0.109	0.43	NA	98.89
Mz02b_59	NA	29.23	68.93	0.02	0.023	NA	0.110	0.43	NA	98.74
Mz01.1_ZnS1	NA	32.87	67.50	NA	NA	NA	NA	0.39	NA	100.76
Mz01.1_ZnS2	NA	32.30	67.22	NA	NA	NA	NA	0.51	NA	100.03
Mz01.1_ZnS3	NA	32.76	65.81	0.02	0.088	NA	0.083	2.80	NA	101.57
Mz01.1_ZnS4	NA	32.37	67.40	0.01	0.031	NA	NA	0.37	NA	100.18
Mz01.1_ZnS5	NA	32.54	67.39	NA	NA	NA	NA	0.22	NA	100.15
Mz01.1_ZnS6	NA	31.90	64.62	0.01	0.066	NA	0.157	2.09	NA	98.84
Mz01.1_ZnS7	NA	32.75	67.79	0.01	NA	NA	NA	0.45	NA	100.99
Mz01.1_ZnS8	NA	32.50	67.22	0.02	NA	NA	NA	0.32	NA	100.06
Mz01.1_ZnS9	NA	32.36	67.18	NA	NA	NA	NA	0.32	NA	99.86
Mz01.1_ZnS10	NA	32.53	66.49	0.01	NA	NA	NA	0.31	NA	99.34
Mz01.1_ZnS11	NA	32.28	66.38	0.01	0.051	NA	NA	0.37	NA	99.09
Mz01.1_ZnS12	NA	32.39	65.70	NA	0.040	NA	NA	0.35	NA	98.48
Mz01.1_ZnS13	NA	32.15	66.04	NA	NA	NA	NA	0.38	NA	98.57
Mz01.1_ZnS14	NA	32.21	67.78	NA	NA	NA	NA	0.38	NA	100.37
Mz01.1_ZnS15	NA	32.29	67.57	NA	NA	NA	NA	0.41	NA	100.27
Mz01.1_ZnS16	NA	32.17	67.68	NA	0.013	NA	NA	0.44	NA	100.30
Mz01.1_ZnS17	NA	32.40	68.56	NA	0.013	NA	NA	0.22	NA	101.20
Mz01.1_ZnS18	NA	32.25	67.85	NA	NA	NA	NA	0.19	NA	100.30
Mz01.1_ZnS19	NA	32.52	67.06	0.01	NA	NA	0.015	0.43	NA	100.03
Mz01.1_ZnS20	NA	32.28	67.21	NA	NA	NA	NA	0.25	NA	99.75
Mz01.1_ZnS21	NA	32.47	67.73	NA	NA	NA	NA	0.14	NA	100.34
Mz01.1_ZnS22	NA	32.37	67.69	NA	NA	NA	NA	0.14	NA	100.20
Mz01.1_ZnS23	NA	32.15	66.61	NA	0.022	NA	0.180	0.58	NA	99.54
Mz01.1_ZnS24	NA	32.18	66.64	0.01	0.037	NA	0.031	0.62	NA	99.52
Mz01.1_ZnS25	NA	31.89	68.07	NA	NA	NA	NA	0.21	NA	100.17
Mz01.1_ZnS26	NA	31.57	68.37	NA	NA	NA	0.122	0.47	NA	100.53
Mz01.1_ZnS27	NA	32.41	67.90	NA	NA	NA	NA	0.34	NA	100.65
Mz01.1_ZnS28	NA	32.21	66.12	0.01	0.051	NA	0.182	0.84	NA	99.41
Mz01.1_ZnS29	NA	32.46	67.29	NA	NA	NA	NA	0.15	NA	99.90
Mz01.1_ZnS30	NA	32.33	68.24	NA	0.035	NA	0.081	0.36	NA	101.05
Mz01.1_ZnS31	NA	32.02	67.85	NA	0.103	NA	0.130	0.81	NA	100.91
Mz01.1_ZnS32	NA	32.36	68.20	0.02	NA	NA	NA	0.17	NA	100.76
Mz01.1_ZnS33	NA	31.79	65.08	0.02	0.554	NA	0.257	1.85	NA	99.55
Mz01.1_ZnS34	NA	31.86	65.94	0.02	0.544	NA	0.409	1.71	NA	100.48
Mz01.1_ZnS35	NA	32.33	68.62	NA	0.020	NA	NA	0.44	NA	101.41

Table 10: Continued.

	EMPA Mezica, Moring [mass%]									
sample/analyses	**As**	**S**	**Zn**	**Fe**	**Pb**	**Ge**	**Cu**	**Cd**	**Tl**	**total**
Mz01.1_ZnS36	NA	32.08	66.59	0.02	NA	NA	0.057	2.63	NA	101.37
Mz01.1_ZnS37	NA	31.91	65.44	0.01	0.342	NA	0.230	2.38	NA	100.32
Mz01.1_ZnS38	NA	32.23	67.63	NA	NA	NA	0.024	0.42	NA	100.30
Mz01.1_ZnS39	NA	32.38	68.39	NA	NA	NA	0.135	0.51	NA	101.42
Mz01.1_ZnS40	NA	32.33	66.70	0.02	0.054	NA	0.093	2.93	NA	102.13
Mz01.1_ZnS41	NA	31.04	64.96	0.02	0.022	NA	NA	0.17	NA	96.21
Mz01.1_ZnS42	NA	32.50	67.76	0.01	0.019	NA	NA	0.13	NA	100.42
Mz01.1_ZnS43	NA	32.25	67.36	0.02	NA	NA	NA	0.38	NA	100.01
Mz01.1_ZnS44	NA	32.34	67.66	0.01	NA	NA	NA	0.21	NA	100.22
Mz01.1_ZnS45	NA	31.98	65.99	NA	NA	NA	NA	0.19	NA	98.16
Mz01.1_ZnS46	NA	32.53	66.51	0.04	0.045	NA	NA	0.17	NA	99.29
Mz01.1_ZnS47	NA	32.34	65.76	NA	NA	NA	NA	0.31	NA	98.41
Mz01.1_ZnS48	NA	32.43	66.29	0.01	0.020	NA	NA	0.13	NA	98.88
Mz01.1_ZnS49	NA	32.40	66.40	0.01	NA	NA	NA	0.48	NA	99.29
Mz01.1_ZnS50	NA	32.24	67.71	NA	NA	NA	NA	0.43	NA	100.38
Mz01.1_ZnS51	NA	32.34	67.07	NA	0.049	NA	NA	0.45	NA	99.91
Mz01.1_ZnS52	NA	30.93	64.57	NA	NA	NA	NA	0.43	NA	95.93
Mz01.1_ZnS53	NA	32.39	67.48	NA	NA	NA	NA	0.33	NA	100.20
Mz01.1_ZnS54	NA	32.47	67.51	0.02	0.053	NA	0.033	0.87	NA	100.95
Mz01.1_ZnS55	NA	32.31	65.68	0.13	0.015	NA	NA	0.38	NA	98.51
Mz01.1_ZnS56	NA	32.72	64.93	0.02	0.053	NA	NA	0.20	NA	97.92
Mz01.1_ZnS57	NA	32.39	67.40	NA	NA	NA	NA	0.35	NA	100.14
Mz01.1_ZnS58	NA	32.39	67.45	NA	NA	NA	0.088	0.65	NA	100.58
Mz01.1_ZnS59	NA	32.11	65.71	0.02	0.375	NA	0.366	1.88	NA	100.46
Mz01.1_ZnS60	NA	32.36	66.82	NA	NA	NA	NA	0.43	NA	99.61
Mz01.1_ZnS61	NA	32.13	65.78	0.01	0.030	NA	0.065	0.71	NA	98.73
Mz01.1_ZnS62	NA	32.40	66.41	0.01	NA	NA	0.064	0.42	NA	99.31
Mz01.1_ZnS63	NA	32.11	67.49	NA	0.030	NA	0.036	0.58	NA	100.25
Mz08_ZnS1	NA	31.69	69.14	0.01	0.042	NA	NA	0.37	NA	101.25
Mz08_ZnS2	NA	31.66	68.97	NA	0.028	NA	NA	0.40	NA	101.06
Mz08_ZnS4	NA	31.67	68.28	NA	0.037	NA	NA	0.45	NA	100.44
Mz08_ZnS5	NA	31.61	67.74	0.01	0.048	NA	NA	0.51	NA	99.91
Mz08_ZnS6	NA	31.82	68.15	NA	0.034	NA	0.054	0.84	NA	100.90
Mz08_ZnS7	NA	31.38	68.01	0.01	0.051	NA	NA	0.66	NA	100.10
Mz08_ZnS8	NA	31.64	68.78	0.01	NA	NA	NA	0.36	NA	100.79
Mz08_ZnS9	NA	31.57	67.30	NA	0.013	NA	NA	0.26	NA	99.15
Mz08_ZnS12	NA	14.95	26.30	0.01	0.019	NA	NA	0.10	NA	41.38
Mz08_ZnS13	NA	31.32	67.26	NA	NA	NA	NA	0.29	NA	98.88
Mz08_ZnS14	NA	31.37	68.14	NA	0.046	NA	0.034	1.32	NA	100.91
Mz08_ZnS15	NA	31.50	69.43	NA	0.019	NA	0.011	1.05	NA	102.01
Mz08_ZnS16	0.046	31.41	69.65	NA	0.058	NA	0.051	1.08	NA	102.30
Mz08_ZnS17	NA	31.09	69.23	NA	0.024	NA	0.046	0.83	NA	101.22
Mz08_ZnS18	NA	31.42	69.01	NA	NA	NA	0.061	0.90	NA	101.39
Mz08_ZnS19	NA	31.70	68.70	NA	0.060	NA	0.035	1.19	NA	101.71
Mz08_ZnS20	NA	31.52	69.44	NA	0.081	NA	0.159	1.00	NA	102.20
Mz08_ZnS21	NA	31.36	69.00	NA	0.065	NA	0.112	0.94	NA	101.47

Table 10: Continued.

	EMPA Mezica, Moring [mass%]									
sample/analyses	**As**	**S**	**Zn**	**Fe**	**Pb**	**Ge**	**Cu**	**Cd**	**Tl**	**total**
Mz08_ZnS22	NA	31.85	69.33	0.01	0.020	NA	NA	0.52	NA	101.73
Mz08_ZnS23	NA	31.49	68.05	NA	0.041	NA	NA	1.06	NA	100.64
Mz08_ZnS24	NA	31.48	67.66	NA	0.061	NA	0.059	0.96	NA	100.22
Mz08_ZnS25	NA	31.69	69.86	NA	0.020	NA	NA	0.65	NA	102.22
Mz08_ZnS26	NA	31.59	69.64	NA	0.041	NA	NA	1.13	NA	102.41
Mz08_ZnS27	NA	31.48	69.43	NA	0.046	NA	0.020	0.92	NA	101.90
Mz08_ZnS28	NA	31.18	69.05	NA	NA	NA	0.017	1.01	NA	101.26
Mz08_ZnS30	NA	31.70	70.04	NA	NA	NA	NA	0.67	NA	102.41
Mz08_ZnS31	NA	31.59	70.52	0.06	NA	NA	NA	0.57	NA	102.74
Mz08_ZnS32	NA	28.00	66.73	0.01	0.045	NA	NA	0.42	NA	95.20
Mz08_ZnS33	NA	32.14	69.03	NA	0.057	NA	0.029	0.82	NA	102.07
Mz08_ZnS34	NA	31.43	69.48	NA	NA	NA	NA	0.71	NA	101.62
Mz08_ZnS35	NA	30.73	68.85	NA	0.035	NA	0.079	0.87	NA	100.56
Mz08_ZnS36	NA	31.64	69.78	NA	0.017	NA	0.011	0.76	NA	102.21
Mz08_ZnS37	NA	31.14	68.83	NA	NA	NA	NA	0.43	NA	100.40
Mz08_ZnS38	NA	19.73	35.17	0.45	2.910	NA	NA	0.24	NA	58.50
Mz08_ZnS40	NA	31.98	69.74	NA	0.021	NA	NA	0.47	NA	102.21
Mz08_ZnS41	NA	31.83	70.02	NA	NA	NA	NA	0.23	NA	102.08
Mz08_ZnS42	NA	31.49	68.87	0.03	NA	NA	NA	0.47	NA	100.86
Mz08_ZnS43	NA	32.03	68.10	NA	0.013	NA	NA	0.48	NA	100.63
Mz08_ZnS44	NA	31.64	69.13	NA	0.052	NA	NA	0.49	NA	101.32
Mz08_ZnS45	NA	31.61	70.28	NA	NA	NA	NA	0.28	NA	102.17
Mz08_ZnS46	NA	31.60	69.01	NA	0.058	NA	0.048	1.52	NA	102.24
Mz08_ZnS47	NA	31.90	69.30	NA	0.028	NA	0.022	0.99	NA	102.24
Mz08_ZnS48	NA	31.86	68.40	NA	0.037	NA	0.021	1.20	NA	101.52
Mz08_ZnS49	NA	31.67	69.18	0.01	0.080	NA	0.099	1.52	NA	102.57
Mz08_ZnS50	NA	31.74	70.10	NA	NA	NA	NA	0.71	NA	102.55
Mz08_ZnS51	NA	31.69	69.53	NA	0.068	NA	0.088	1.29	NA	102.67
Mz08_ZnS52	NA	31.66	68.52	NA	NA	NA	NA	1.75	NA	101.93
Mz08_ZnS53	NA	31.80	69.54	0.01	0.021	NA	NA	0.48	NA	101.87
Mz08_ZnS54	NA	31.37	69.91	0.05	NA	NA	NA	0.61	NA	101.94
Mz08_ZnS55	NA	31.74	69.84	0.07	NA	NA	NA	0.51	NA	102.16
Mz08_ZnS56	NA	31.74	67.86	NA	0.030	NA	NA	0.23	NA	99.86
Mz08_ZnS57	NA	31.40	68.25	NA	0.017	NA	NA	0.63	NA	100.30
Mz08_ZnS59	NA	31.91	69.81	0.01	0.044	NA	NA	0.45	NA	102.22
Mz08_ZnS60	NA	31.82	68.97	NA	NA	NA	NA	0.40	NA	101.19
Mz08_ZnS61	NA	31.70	68.64	NA	NA	NA	NA	0.43	NA	100.77
Mz08_ZnS62	NA	31.45	69.05	0.02	0.034	NA	NA	0.37	NA	100.93
Mz08_ZnS63	NA	32.27	69.05	0.01	0.019	NA	NA	0.52	NA	101.87
Mz08_ZnS64	NA	31.83	69.17	0.01	0.037	NA	NA	0.37	NA	101.42
Mz08_ZnS65	NA	31.93	68.71	NA	0.023	NA	0.049	1.22	NA	101.93
Mz08_ZnS66	NA	31.67	68.13	0.01	0.048	NA	0.028	1.23	NA	101.11
Mz08_ZnS67	NA	31.81	68.32	NA	0.031	NA	0.012	1.39	NA	101.56
Mz08_ZnS68	NA	31.75	69.41	NA	0.018	NA	0.058	1.31	NA	102.55
Mz08_ZnS69	NA	31.61	69.15	NA	0.016	NA	0.031	0.78	NA	101.59
Mz08_ZnS70	NA	31.97	69.36	0.01	0.024	NA	NA	0.42	NA	101.78
Mz08_ZnS71	NA	31.83	68.23	0.01	0.038	NA	NA	0.46	NA	100.57

Table 10: Continued.

	EMPA Mezica, Moring [mass%]									
sample/analyses	**As**	**S**	**Zn**	**Fe**	**Pb**	**Ge**	**Cu**	**Cd**	**Tl**	**total**
Mz08_ZnS72	NA	31.94	68.72	0.01	0.039	NA	NA	0.51	NA	101.22
Mz08_ZnS73	NA	31.67	68.49	NA	NA	NA	NA	1.75	NA	101.91
Mz08_ZnS74	NA	32.10	69.33	NA	0.019	NA	NA	0.39	NA	101.84
Mz08_ZnS75	NA	31.73	67.41	NA	0.024	NA	0.059	1.71	NA	100.94
Mz08_ZnS76	NA	29.57	61.72	0.01	5.310	NA	0.036	1.10	NA	97.74
Mz08_ZnS77	NA	31.46	67.12	NA	0.038	NA	NA	1.25	NA	99.87

Table 10: Continued.

	EMPA Mezica, Union [mass%]									
sample/analyses	**As**	**S**	**Zn**	**Fe**	**Pb**	**Ge**	**Cu**	**Cd**	**Tl**	**total**
Mz09_ZnS1	NA	32.97	69.36	NA	NA	NA	NA	0.45	NA	102.78
Mz09_ZnS2	NA	33.16	69.78	NA	0.017	NA	NA	0.20	NA	103.16
Mz09_ZnS3	NA	33.05	69.66	NA	NA	NA	NA	0.15	NA	102.87
Mz09_ZnS4	NA	32.76	68.50	NA	NA	NA	NA	0.42	NA	101.69
Mz09_ZnS5	NA	33.21	68.52	0.01	NA	NA	NA	0.39	NA	102.12
Mz09_ZnS6	NA	30.60	64.61	0.04	NA	NA	NA	0.25	NA	95.51
Mz09_ZnS7	NA	33.14	68.10	0.02	0.028	NA	NA	0.27	NA	101.56
Mz09_ZnS8	NA	33.12	68.41	NA	NA	NA	NA	0.47	NA	102.00
Mz09_ZnS9	NA	32.82	68.04	0.01	0.017	NA	NA	0.40	NA	101.28
Mz09_ZnS10	NA	32.89	67.77	0.01	NA	NA	NA	0.34	NA	101.01
Mz09_ZnS11	NA	33.09	68.66	NA	0.013	NA	NA	0.34	NA	102.11
Mz09_ZnS12	NA	33.14	68.55	NA	NA	NA	NA	0.41	NA	102.10
Mz09_ZnS13	NA	33.20	68.81	NA	NA	NA	NA	0.27	NA	102.29
Mz09_ZnS14	NA	33.13	68.49	NA	NA	NA	NA	0.19	NA	101.81
Mz09_ZnS15	NA	33.06	68.32	0.02	0.057	NA	0.055	0.68	NA	102.20
Mz09_ZnS16	NA	31.87	65.54	NA	0.021	NA	0.058	0.39	NA	97.88
Mz09_ZnS17	NA	33.00	69.11	0.01	NA	NA	NA	0.32	NA	102.43
Mz09_ZnS18	NA	33.22	68.40	0.01	NA	NA	NA	0.31	NA	101.94
Mz09_ZnS19	NA	32.94	68.44	NA	NA	NA	NA	0.38	NA	101.76
Mz09_ZnS20	NA	33.63	68.46	0.02	NA	NA	0.045	0.41	NA	102.57
Mz09_ZnS21	NA	32.28	66.96	0.02	NA	NA	NA	0.33	NA	99.59
Mz09_ZnS22	NA	33.07	68.00	0.01	NA	NA	NA	0.23	NA	101.31
Mz09_ZnS23	NA	32.98	68.87	0.02	NA	NA	NA	0.40	NA	102.27
Mz09_ZnS24	NA	33.07	67.77	NA	NA	NA	NA	0.34	NA	101.18
Mz09_ZnS25	NA	32.75	68.24	0.01	NA	NA	0.077	0.57	NA	101.65

Table 10: Continued.

	EMPA Mezica, Helena [mass%]									
sample/analyses	**As**	**S**	**Zn**	**Fe**	**Pb**	**Ge**	**Cu**	**Cd**	**Tl**	**total**
MzH01neu	NA	NA	NA	0.11	NA	NA	NA	0.65	NA	NA
MzH01_ZnS1	0.351	32.47	65.52	0.08	0.803	0.033	NA	0.35	NA	99.60
MzH01_ZnS2	0.041	32.93	67.02	0.04	0.240	0.011	NA	0.50	NA	100.79
MzH01_ZnS3	NA	33.29	67.45	NA	NA	NA	0.018	0.61	NA	101.37
MzH01_ZnS4	NA	32.97	67.27	NA	0.051	NA	0.030	0.76	NA	101.08
MzH01_ZnS5	0.096	32.26	65.39	0.04	1.630	NA	NA	0.39	NA	99.81
MzH01_ZnS6	0.021	32.83	66.90	0.02	0.083	NA	NA	0.63	NA	100.48
MzH01_ZnS7	0.029	32.94	66.94	0.08	0.077	NA	NA	0.63	NA	100.70
MzH01_ZnS8	NA	32.98	67.25	0.01	0.087	NA	NA	0.47	NA	100.80
MzH01_ZnS9	0.411	32.88	65.84	0.09	0.553	0.049	NA	0.35	NA	100.18
MzH01_ZnS10	0.108	32.99	66.55	0.08	0.238	0.026	NA	0.58	NA	100.58
MzH01_ZnS11	NA	33.08	67.50	NA	NA	NA	NA	0.41	NA	100.99
MzH01_ZnS12	0.010	33.06	67.54	NA	0.028	NA	NA	0.58	NA	101.22
MzH01_ZnS13	0.101	32.97	66.68	0.11	0.236	0.027	NA	0.66	NA	100.78
MzH01_ZnS14	0.087	33.18	66.52	0.14	0.177	0.026	NA	0.84	NA	100.96
MzH01_ZnS15	0.042	31.62	66.61	0.03	0.319	NA	NA	1.08	NA	99.70
MzH01_ZnS16	0.199	33.18	65.78	0.22	0.302	0.037	NA	1.11	NA	100.83
MzH01_ZnS17	0.204	32.91	65.54	0.39	0.356	0.050	NA	1.19	NA	100.64
MzH01_ZnS18	0.004	33.21	67.16	0.04	0.125	0.026	NA	0.78	NA	101.34
MzH01_ZnS19	0.055	33.03	66.75	0.17	0.127	0.031	NA	0.69	NA	100.86
MzH01_ZnS20	NA	33.35	67.35	0.03	NA	0.030	NA	0.33	NA	101.09
MzH01_ZnS21	NA	33.34	67.66	0.02	NA	NA	NA	0.26	NA	101.28
MzH01_ZnS22	NA	33.18	67.25	0.07	0.074	0.081	NA	0.44	NA	101.09
MzH01_ZnS23	0.004	33.29	67.57	NA	NA	NA	NA	0.42	NA	101.29
MzH01_ZnS24	0.017	33.26	67.31	NA	NA	NA	NA	0.66	NA	101.25
MzH01_ZnS25	NA	33.13	66.94	NA	NA	NA	NA	1.40	NA	101.47
MzH01_ZnS26	NA	33.14	67.70	0.00	NA	NA	NA	0.36	NA	101.20
MzH01_ZnS27	NA	33.33	67.44	NA	NA	NA	NA	0.44	NA	101.21
MzH01_ZnS28	NA	33.54	67.67	0.05	0.038	0.088	NA	0.13	NA	101.52
MzH01_ZnS29	0.041	33.01	66.67	0.11	0.071	NA	NA	0.85	NA	100.76
MzH01_ZnS30	0.255	33.04	65.33	0.35	0.416	0.087	NA	1.01	NA	100.49
MzH01_ZnS31	NA	33.05	66.90	0.03	0.050	NA	NA	0.64	NA	100.67
MzH01_ZnS32	NA	33.27	67.28	NA	NA	NA	NA	0.35	NA	100.90
MzH01_ZnS33	0.042	32.88	66.52	0.14	0.107	NA	NA	0.55	NA	100.25
MzH01_ZnS34	0.060	33.10	66.82	0.14	0.211	0.013	NA	0.62	NA	100.96
MzH01_ZnS35	NA	33.27	67.53	0.02	0.097	0.013	NA	0.44	NA	101.37
MzH01_ZnS36	0.086	33.12	66.80	0.11	0.184	NA	NA	0.56	NA	100.86
MzH01_ZnS37	0.082	32.79	66.74	0.14	0.132	NA	NA	0.62	NA	100.50

Table 10: Continued.

EMPA Mezica, Graben [mass%]										
sample/analyses	**As**	**S**	**Zn**	**Fe**	**Pb**	**Ge**	**Cu**	**Cd**	**Tl**	**total**
SF04_1	NA	32.57	66.70	0.02	0.055	NA	NA	0.12	NA	99.47
SF04_2	0.020	32.85	66.40	0.03	NA	NA	NA	0.17	NA	99.47
SF04_3	0.012	32.63	66.54	0.02	NA	0.012	NA	0.17	NA	99.37
SF04_4	NA	33.22	66.58	NA	NA	NA	NA	0.26	NA	100.06
SF04_5	0.195	33.09	65.65	0.22	0.189	0.073	NA	0.02	NA	99.44
SF04_6	0.162	32.50	65.26	0.44	0.201	0.071	NA	0.03	NA	98.67
SF04_7	0.180	33.44	65.74	0.19	0.087	0.041	NA	0.13	NA	99.81
SF04_8	0.118	32.93	65.38	0.04	0.292	0.019	NA	0.16	NA	98.94
SF04_9	0.128	32.96	65.39	0.03	0.242	NA	NA	0.19	NA	98.94
SF04_10	0.064	32.78	65.81	0.04	0.227	NA	NA	0.18	NA	99.10
SF04_11	0.117	32.65	64.94	0.04	0.225	0.026	0.009	0.41	NA	98.42
SF04_12	0.081	32.66	65.42	0.03	0.153	NA	NA	0.42	NA	98.76
SF04_13	0.076	32.76	64.82	0.03	0.216	0.009	0.007	0.37	NA	98.29
SF04_14	0.008	33.26	66.37	0.01	NA	NA	NA	0.33	NA	99.98
SF04_15	0.014	33.21	66.67	0.00	NA	NA	NA	0.11	NA	100.00
SF04_16	0.027	32.89	66.70	NA	NA	NA	NA	0.21	NA	99.83
SF04_17	NA	33.16	66.45	0.01	0.092	NA	NA	0.17	NA	99.88
SF04_18	NA	33.21	66.62	0.01	NA	0.009	NA	0.29	NA	100.13
SF04_19	NA	33.01	65.91	0.03	0.061	0.030	NA	0.23	NA	99.27
SF04_20	0.033	32.82	65.61	0.01	0.172	NA	NA	0.23	NA	98.88
SF04_21	0.024	33.03	65.44	0.03	0.152	0.029	0.008	0.31	NA	99.02
SF04_22	0.044	33.01	65.47	0.03	0.246	0.018	NA	0.24	NA	99.06
SF04_23	0.065	33.25	66.06	0.03	0.168	0.033	NA	0.21	NA	99.81
SF04_24	0.024	32.93	65.53	0.02	0.318	0.007	NA	0.17	NA	99.00
SF04_25	0.312	32.55	65.39	0.28	0.262	0.077	NA	NA	NA	98.87
SF04_26	0.156	32.46	64.96	0.37	0.206	0.036	NA	0.02	NA	98.20
SF04_27	0.143	32.86	65.42	0.28	0.133	0.031	NA	0.05	NA	98.93
SF04_28	NA	33.52	65.79	0.01	NA	NA	NA	0.29	NA	99.61
SF04_29	NA	33.18	65.71	0.01	NA	NA	NA	0.36	NA	99.26
SF04_30	NA	33.35	65.79	0.01	NA	NA	NA	0.37	NA	99.51
SF04_31	0.025	33.27	66.16	0.01	NA	0.007	NA	0.30	NA	99.78
SF04_32	0.098	32.87	65.39	0.03	0.334	0.010	NA	0.17	NA	98.90
SF04_33	0.050	32.91	65.71	0.03	0.282	NA	NA	0.22	NA	99.20
SF04_34	0.075	32.96	65.39	0.05	0.131	0.013	0.005	0.20	NA	98.82
SF04_35	0.035	32.85	65.54	0.02	0.195	NA	NA	0.39	NA	99.03
SF04_36	0.034	32.90	65.71	0.03	0.146	NA	NA	0.20	NA	99.02
SF04_37	NA	33.42	66.76	NA	NA	NA	NA	0.17	NA	100.35
SF04_38	0.008	33.66	66.42	0.01	NA	NA	NA	0.26	NA	100.36
SF04_39	NA	33.49	66.84	0.01	NA	NA	NA	0.19	NA	100.53
SF04_40	NA	33.35	66.37	NA	NA	NA	NA	0.14	NA	99.86
SF04_41	0.148	32.92	65.65	0.08	0.198	0.022	NA	0.10	NA	99.12
SF04_42	0.029	33.12	65.90	0.03	0.134	0.014	NA	0.21	NA	99.44
SF04_43	0.145	32.31	65.63	0.07	0.251	0.051	NA	0.15	NA	98.61
SF04_44	0.032	33.02	65.52	NA	NA	0.005	0.026	0.53	NA	99.14
SF04_45	0.250	32.39	64.52	0.11	0.345	0.057	NA	0.13	NA	97.81
SF04_46	0.018	33.29	65.86	0.02	NA	NA	NA	0.30	NA	99.48
SF04_47	NA	33.29	65.78	0.01	NA	NA	NA	0.30	NA	99.37

Table 10: Continued.

EMPA Mezica, Graben [mass%]										
sample/analyses	**As**	**S**	**Zn**	**Fe**	**Pb**	**Ge**	**Cu**	**Cd**	**Tl**	**total**
SF04_48	0.013	33.21	65.66	NA	NA	NA	NA	0.50	NA	99.38
SF04_49	NA	33.14	65.38	0.03	0.261	NA	NA	0.26	NA	99.07
SF04_50	0.243	32.99	64.32	0.54	0.236	0.027	NA	0.04	NA	98.40
SF04_51	0.050	32.87	65.68	0.04	0.204	0.019	NA	0.14	NA	99.00
SF04_52	0.019	32.94	65.18	0.01	0.170	0.030	NA	0.27	NA	98.62
SF03_1	0.125	32.87	67.14	0.04	0.398	0.027	NA	0.21	NA	100.81
SF03_2	0.021	32.96	67.25	0.01	0.198	NA	NA	0.33	NA	100.76
SF03_3	0.165	33.14	66.93	0.19	0.493	NA	NA	0.14	NA	101.06
SF03_4	0.084	33.04	67.21	0.02	0.306	NA	NA	0.22	NA	100.89
SF03_5	0.092	32.90	67.03	0.07	0.182	NA	NA	0.16	NA	100.43
SF03_6	0.015	33.00	67.54	0.04	0.062	NA	NA	0.10	NA	100.75
SF03_7	0.094	32.62	66.98	0.11	0.272	NA	NA	0.06	NA	100.14
SF03_8	0.051	32.61	67.22	0.07	0.248	NA	NA	0.12	NA	100.32
SF03_9	0.044	33.01	67.31	0.01	0.250	NA	NA	0.24	NA	100.86
SF03_10	0.025	32.73	67.32	0.01	0.303	NA	NA	0.22	NA	100.62
SF03_11	0.011	32.52	64.84	0.01	0.208	NA	NA	0.26	NA	97.85
SF03_12	0.101	33.01	67.30	0.05	0.345	NA	NA	0.24	NA	101.05
SF03_13	0.270	32.85	65.99	0.62	0.827	0.044	NA	0.06	NA	100.66
SF03_14	0.074	32.65	67.09	0.04	0.317	NA	NA	0.22	NA	100.39
SF03_15	0.087	33.02	67.40	0.03	0.337	NA	NA	0.26	NA	101.14
SF03_16	0.067	32.85	67.22	0.04	0.373	NA	NA	0.23	NA	100.78
SF03_17	0.131	32.22	66.64	0.08	0.511	0.068	NA	0.16	NA	99.80
SF03_18	0.064	32.52	67.30	0.01	0.254	NA	NA	0.29	NA	100.44
SF03_19	0.266	33.26	66.37	0.15	0.902	0.053	NA	0.04	NA	101.03
SF03_20	NA	31.92	67.05	0.02	0.243	NA	NA	0.24	NA	99.47
SF03_21	0.019	32.90	67.21	0.03	0.247	NA	NA	0.15	NA	100.56
SF03_22	0.027	33.06	67.32	0.02	0.159	NA	NA	0.11	NA	100.69
SF03_23	NA	33.01	67.48	0.05	NA	NA	NA	0.17	NA	100.71
SF03_24	0.060	32.97	66.98	0.05	0.262	NA	NA	0.04	NA	100.36
SF03_25	0.045	29.97	66.55	0.09	0.142	NA	NA	0.18	NA	96.97
SF03_26	0.096	32.50	65.44	0.02	0.366	NA	NA	0.37	NA	98.79
SF03_27	0.143	32.33	64.72	0.02	0.845	0.029	NA	0.53	NA	98.62
SF03_28	0.047	32.84	65.94	0.01	0.177	NA	NA	0.15	NA	99.16
SF03_29	0.038	32.56	65.86	0.02	0.272	NA	NA	0.15	NA	98.90
SF03_30	0.030	33.10	66.03	0.00	0.215	NA	NA	0.17	NA	99.54

Table 11: EMP data of ZnS from Topla.

	EMPA Topla [mass%]							
sample/analyses	**As**	**S**	**Zn**	**Fe**	**Pb**	**Ge**	**Cd**	**total**
Tp05_ZnS1	NA	31.94	65.70	0.33	0.212	NA	0.09	98.27
Tp05_ZnS2	NA	32.21	65.27	0.03	0.014	NA	0.11	97.64
Tp05_ZnS3	NA	31.67	65.35	0.09	NA	NA	0.14	97.25
Tp05_ZnS4	NA	32.10	66.39	0.14	0.086	NA	0.08	98.80
Tp05_ZnS5	NA	31.98	67.37	0.08	0.610	NA	0.05	100.09
Tp05_ZnS6	NA	32.11	66.94	0.02	NA	NA	0.09	99.17
Tp05_ZnS8	NA	30.99	62.74	0.08	NA	NA	0.11	93.92
Tp05_ZnS9	NA	32.23	67.04	0.05	0.025	NA	0.11	99.46
Tp05_ZnS11	NA	32.27	65.91	0.96	0.018	NA	0.10	99.25
Tp05_ZnS13	NA	31.91	64.13	0.10	0.032	NA	0.10	96.27
Tp05_ZnS14	NA	31.79	64.86	0.15	0.640	NA	0.19	97.63
Tp05_ZnS15	NA	32.25	66.85	0.16	0.427	NA	0.04	99.73
Tp05_ZnS16	NA	32.14	66.52	0.24	0.520	NA	0.02	99.44
Tp05_ZnS17	NA	32.08	66.04	0.44	0.098	NA	0.08	98.74
Tp05_ZnS18	NA	32.12	64.13	0.53	NA	NA	0.06	96.84
Tp05_ZnS19	NA	32.11	65.20	0.07	0.045	NA	0.22	97.64
Tp05_ZnS20	NA	30.47	61.59	0.31	NA	NA	0.07	92.45
Tp05_ZnS21	NA	31.88	65.39	0.10	NA	NA	0.15	97.53
Tp05_ZnS22	NA	32.05	66.06	0.30	0.252	NA	0.03	98.70
Tp05_ZnS23	NA	31.83	66.02	0.09	0.191	NA	0.03	98.16
Tp05_ZnS24	NA	32.65	67.01	0.14	0.085	NA	0.03	99.91
Tp05_ZnS25	NA	32.09	66.32	0.82	0.028	NA	0.19	99.44
Tp05_ZnS26	NA	32.16	66.63	0.90	0.059	NA	0.15	99.89
Tp05_ZnS29	NA	32.30	67.79	0.03	NA	NA	0.07	100.19
Tp05_ZnS30	NA	32.26	67.65	0.03	0.088	NA	0.10	100.13
Tp05_ZnS31	NA	32.19	65.63	0.37	0.072	NA	0.04	98.30
Tp05_ZnS32	NA	31.51	65.88	0.17	0.352	NA	0.08	97.98
Tp05_ZnS33	NA	30.46	67.06	0.05	NA	NA	0.26	97.83
Tp05_ZnS34	NA	32.12	67.59	0.04	NA	NA	0.09	99.85
Tp05_ZnS35	NA	32.33	66.42	0.11	0.014	NA	0.24	99.12
Tp05_ZnS36	NA	30.77	57.16	0.10	0.137	NA	0.06	88.23
Tp05_ZnS37	NA	32.38	66.31	0.55	0.033	NA	0.02	99.29
Tp05_ZnS38	NA	31.79	66.68	0.15	NA	NA	0.09	98.72
Tp05_ZnS39	NA	32.00	66.82	0.22	NA	NA	0.05	99.09
Tp05_ZnS40	NA	32.44	67.16	0.03	NA	NA	0.37	100.00
Tp05_ZnS41	NA	32.43	67.28	0.07	0.019	NA	0.12	99.92
Tp05_ZnS42	NA	32.17	67.29	0.39	0.155	NA	0.06	100.07
Tp05_ZnS43	NA	32.12	67.34	0.08	0.203	NA	0.13	99.88
Tp05_ZnS44	NA	32.34	67.74	0.02	0.033	NA	0.12	100.25
Tp05_ZnS45	NA	32.43	67.44	0.02	NA	NA	0.09	99.98
Tp05_ZnS46	NA	32.44	66.94	0.02	NA	NA	0.10	99.50
Tp05_ZnS47	NA	32.51	67.47	0.02	0.025	NA	0.14	100.17
Tp05_ZnS48	NA	31.74	67.00	0.05	NA	NA	0.21	99.00
Tp05_ZnS49	NA	29.77	66.47	0.07	0.094	NA	0.10	96.51
Tp05_ZnS50	NA	32.49	66.84	0.04	NA	NA	0.14	99.51
Tp05_ZnS51	NA	32.25	65.98	0.04	NA	NA	0.10	98.37
Tp05_ZnS52	NA	32.85	65.86	0.05	NA	NA	0.14	98.91

Table 11: Continued.

	EMPA Topla [mass%]							
sample/analyses	**As**	**S**	**Zn**	**Fe**	**Pb**	**Ge**	**Cd**	**total**
Tp06_ZnS1	NA	32.46	66.40	0.10	0.390	NA	0.09	99.43
Tp06_ZnS2	NA	32.51	65.85	0.19	0.444	NA	0.06	99.06
Tp06_ZnS3	NA	32.98	67.57	0.05	0.023	NA	0.34	100.96
Tp06_ZnS4	NA	32.48	66.04	0.18	0.541	NA	0.04	99.28
Tp06_ZnS5	NA	28.00	60.39	0.05	NA	NA	0.17	88.61
Tp06_ZnS6	NA	32.77	68.42	0.08	NA	NA	0.15	101.43
Tp06_ZnS7	NA	32.14	67.79	0.62	0.065	NA	0.05	100.66
Tp06_ZnS11	NA	32.85	68.63	0.13	NA	NA	0.16	101.77
Tp06_ZnS12	NA	32.73	68.46	0.42	NA	NA	0.17	101.78
Tp06_ZnS13	NA	32.99	66.83	0.41	NA	NA	0.26	100.49
Tp06_ZnS14	NA	32.62	66.88	0.40	0.311	NA	0.09	100.30
Tp06_ZnS15	NA	32.70	67.49	0.05	0.095	NA	0.27	100.60
Tp06_ZnS16	NA	32.65	67.42	0.11	0.029	NA	0.15	100.36
Tp06_ZnS17	NA	32.81	67.88	0.14	NA	NA	0.17	101.00
Tp06_ZnS19	NA	32.89	68.57	0.21	0.540	NA	0.03	102.24
Tp06_ZnS20	NA	32.77	68.91	0.42	NA	NA	0.06	102.17
Tp06_ZnS21	NA	32.97	69.50	0.49	0.053	NA	0.03	103.05
Tp06_ZnS22	NA	32.85	68.85	0.76	0.045	NA	0.03	102.53
Tp06_ZnS23	NA	32.86	68.92	0.18	0.382	NA	0.02	102.36
Tp06_ZnS24	NA	32.80	68.10	0.64	0.075	NA	0.05	101.67
Tp06_ZnS25	NA	32.91	68.13	0.63	0.097	NA	0.03	101.80
Tp06_ZnS26	NA	33.20	69.50	0.35	NA	NA	0.05	103.10
Tp06_ZnS27	NA	32.49	69.14	0.38	0.379	NA	0.02	102.41
Tp06_ZnS28	NA	32.95	68.43	0.65	NA	NA	0.08	102.11
Tp06_ZnS29	NA	33.02	68.08	0.63	0.090	NA	0.04	101.86
Tp06_ZnS30	NA	32.61	68.64	0.35	0.802	NA	0.05	102.45
Tp06_ZnS31	NA	32.94	69.02	0.40	0.200	NA	0.02	102.59
Tp06_ZnS32	NA	32.81	68.83	0.62	0.280	NA	0.03	102.57
Tp06_ZnS33	NA	33.04	68.17	0.42	NA	NA	0.03	101.67
Tp06_ZnS34	NA	33.07	68.53	0.35	0.026	NA	0.03	102.00
Tp06_ZnS35	NA	33.32	68.17	0.05	NA	NA	0.25	101.79
Tp06_ZnS37	NA	32.71	67.93	0.07	0.151	NA	0.26	101.12
Tp06_ZnS38	NA	32.85	67.83	0.02	NA	NA	0.18	100.89
Tp06_ZnS39	NA	33.54	63.99	0.03	NA	NA	0.17	97.75
Tp06_ZnS42	NA	32.99	68.69	0.01	NA	NA	0.27	101.96
Tp06_ZnS43	NA	32.75	68.45	0.03	0.083	NA	0.22	101.55
Tp06_ZnS44	NA	33.02	68.98	0.08	0.029	NA	0.17	102.28
Tp06_ZnS45	NA	33.06	68.90	0.17	NA	NA	0.22	102.36
Tp06_ZnS46	NA	33.03	69.06	0.05	0.040	NA	0.21	102.39
Tp06_ZnS47	NA	33.17	67.55	0.11	0.271	NA	0.12	101.22
Tp06_ZnS48	NA	32.75	68.08	0.05	NA	NA	0.11	101.00
Tp06_ZnS50	NA	32.81	67.66	0.20	0.620	NA	0.02	101.31
Tp06_ZnS52	NA	33.05	67.29	0.20	0.017	NA	0.15	100.71
Tp06_ZnS53	NA	32.93	68.35	0.12	0.277	NA	0.06	101.73
Tp06_ZnS54	NA	33.01	68.25	0.06	0.026	NA	0.15	101.51
Tp06_ZnS55	NA	31.87	66.87	0.13	0.055	NA	0.10	99.03
Tp06_ZnS56	NA	33.00	68.06	0.04	NA	NA	0.18	101.28
Tp06_ZnS57	NA	33.40	67.00	0.04	NA	NA	0.15	100.59

Table 11: Continued.

	EMPA Topla [mass%]							
sample/analyses	**As**	**S**	**Zn**	**Fe**	**Pb**	**Ge**	**Cd**	**total**
Tp06_ZnS58	NA	34.28	66.33	0.09	0.101	NA	0.17	100.97
Tp06_ZnS59	NA	32.67	68.91	0.12	0.028	NA	0.13	101.85
Tp06_ZnS60	NA	29.98	67.01	0.13	NA	NA	0.22	97.34
Tp06_ZnS61	NA	33.49	68.92	0.04	NA	NA	0.18	102.64
Tp06_ZnS62	NA	32.58	66.54	0.55	0.143	NA	0.23	100.04
1_Tp04_BSE1a	NA	32.54	66.08	0.50	0.590	NA	0.21	99.92
1_Tp04_BSE1a	NA	32.41	66.04	0.35	0.356	NA	0.10	99.25
3_Tp04_BSE1a	NA	32.45	66.52	0.25	0.129	NA	0.26	99.61
4_Tp04_BSE1a	NA	32.56	66.12	0.97	NA	NA	0.18	99.83
6_Tp04_BSE1a	NA	32.57	65.34	1.73	NA	NA	0.13	99.78
7_Tp04_BSE1a	NA	32.90	65.76	0.31	NA	NA	0.22	99.19
8_Tp04_BSE1a	NA	32.61	65.92	0.03	0.142	NA	0.18	98.88
9_Tp04_BSE1a	NA	32.56	65.44	0.01	0.126	NA	0.22	98.36
10_Tp04_BSE1a	NA	32.66	64.79	0.07	0.122	NA	0.26	97.89
12_Tp04_BSE1a	NA	33.14	65.72	0.03	NA	NA	0.28	99.17
13_Tp04_BSE1a	NA	32.67	65.89	NA	NA	NA	0.09	98.65
18_Tp04_BSE2b	NA	32.82	65.34	0.07	NA	NA	0.20	98.44
20_Tp04_BSE2b	NA	32.76	65.79	0.06	NA	NA	0.18	98.78
21_Tp04_BSE2a	NA	33.25	64.69	0.99	0.174	NA	0.04	99.15
22_Tp04_BSE3b	NA	31.96	64.32	0.05	0.125	NA	0.18	96.63
23_Tp04_BSE3b	NA	32.64	65.22	NA	NA	NA	0.18	98.04
24_Tp04_BSE3b	NA	32.75	64.98	0.02	0.177	NA	0.20	98.13
25_Tp04_BSE3b	NA	32.20	64.63	NA	NA	NA	0.21	97.04
26_Tp04_BSE3b	NA	32.68	65.28	0.04	0.330	NA	0.12	98.45
27_Tp04_BSE3b	0.027	32.61	64.89	0.03	NA	NA	0.19	97.74
28_Tp04_BSE3b	NA	32.60	65.28	0.04	0.187	NA	0.18	98.29
29_Tp04_BSE3a	NA	32.55	65.26	NA	NA	NA	0.19	97.99
30_Tp04_BSE3a	NA	32.73	63.93	0.03	NA	NA	0.13	96.83
31_Tp04_BSE4a	NA	33.08	64.58	0.12	0.139	NA	0.12	98.04
32_Tp04_BSE4a	0.025	32.52	64.75	0.02	NA	NA	0.23	97.55
33_Tp04_BSE4a	NA	31.20	63.78	0.03	0.128	NA	0.16	95.30
34_Tp04_BSE4a	NA	32.27	64.73	0.05	0.255	NA	0.19	97.49
36_Tp04_BSE4a	NA	32.13	63.84	0.05	NA	NA	0.27	96.29
37_Tp04_BSE4a	0.003	33.03	66.43	0.07	0.117	NA	0.20	99.85
BGR_Tp01_1	NA	32.85	66.72	0.05	NA	NA	0.23	99.85
BGR_Tp01_2	NA	33.05	66.52	0.04	0.024	NA	0.05	99.69
BGR_Tp01_3	NA	32.84	66.21	0.15	0.105	NA	0.11	99.41
BGR_Tp01_4	NA	33.08	66.40	0.09	0.071	NA	NA	99.64
BGR_Tp01_5	NA	32.75	65.76	0.11	0.048	NA	0.12	98.78
BGR_Tp01_6	NA	33.25	66.74	0.10	0.416	NA	0.06	100.56
BGR_Tp01_7	NA	32.96	66.31	0.25	NA	NA	0.05	99.57
BGR_Tp01_8	0.006	32.91	66.42	0.02	0.648	NA	0.07	100.07
BGR_Tp01_9	NA	33.29	67.07	0.05	0.080	NA	0.03	100.52
BGR_Tp01_10	NA	32.94	66.97	0.02	0.178	NA	0.05	100.16
BGR_Tp01_11	NA	32.81	66.57	0.32	0.058	NA	0.02	99.78
BGR_Tp01_12	NA	33.07	67.42	0.02	0.289	NA	0.08	100.87
BGR_Tp01_13	NA	33.16	66.73	0.06	NA	NA	0.19	100.14

Table 11: Continued.

	EMPA Topla [mass%]							
sample/analyses	**As**	**S**	**Zn**	**Fe**	**Pb**	**Ge**	**Cd**	**total**
BGR_Tp01_14	0.003	32.98	66.73	0.07	0.399	NA	0.04	100.22
BGR_Tp01_15	0.017	32.82	66.31	0.18	0.067	NA	0.04	99.44
BGR_Tp01_16	NA	32.87	66.91	0.04	0.036	NA	0.13	99.98
BGR_Tp01_17	0.003	31.60	65.26	0.05	0.092	NA	0.07	97.08
BGR_Tp01_18	0.012	33.02	66.37	0.16	0.196	NA	0.00	99.77
BGR_Tp01_19	NA	32.87	66.02	0.06	0.051	0.005	0.07	99.07
BGR_Tp01_20	NA	33.27	67.09	0.01	NA	NA	0.12	100.50
BGR_Tp01_21	0.007	32.57	65.29	0.28	0.716	0.028	0.01	98.90
BGR_Tp01_22	NA	32.91	67.18	0.02	NA	NA	0.09	100.20
BGR_Tp01_23	0.003	32.62	66.48	0.05	0.034	NA	0.20	99.39
BGR_Tp01_24	0.012	33.04	66.74	0.12	0.628	NA	0.01	100.55
Tp01_1	0.018	32.81	67.41	0.04	0.234	NA	0.06	100.57
Tp01_2	0.016	33.16	66.74	0.44	0.012	NA	0.05	100.41
Tp01_3	NA	32.99	66.99	0.02	NA	NA	0.27	100.27
Tp01_4	0.024	33.18	67.06	0.01	NA	NA	0.30	100.58
Tp01_5	NA	33.06	66.64	0.17	0.430	NA	0.03	100.33
Tp01_6	NA	33.16	66.14	0.08	0.100	NA	0.08	99.56
Tp01_7	NA	33.15	67.50	0.04	NA	NA	0.07	100.76
Tp01_8	NA	33.31	67.29	0.03	NA	NA	0.21	100.84
Tp01_9	NA	33.14	66.93	0.17	0.061	NA	0.05	100.35
Tp01_10	NA	33.16	66.85	0.29	NA	NA	0.05	100.35
Tp01_11	0.018	32.95	67.23	0.08	0.624	NA	0.06	100.97
Tp01_12	NA	32.94	66.43	0.11	0.779	NA	0.02	100.28
Tp01_13	0.031	33.11	67.39	0.06	0.023	NA	0.10	100.72
Tp01_14	NA	32.92	66.88	0.09	0.486	NA	0.08	100.46
Tp01_15	0.019	33.01	67.49	0.01	0.059	NA	0.09	100.68
Tp01_16	NA	33.26	67.39	0.03	0.354	NA	0.12	101.16
Tp01_17	0.013	33.14	67.14	0.13	0.025	NA	0.15	100.60
Tp01_18	NA	33.04	66.77	0.23	0.123	NA	0.07	100.24
Tp01_19	NA	33.02	67.04	0.12	0.030	NA	0.10	100.31
Tp01_20	NA	32.49	66.40	0.12	0.136	NA	0.04	99.19
Tp01_21	0.051	32.31	63.36	0.07	0.380	NA	0.10	96.27
Tp01_22	NA	33.10	66.62	0.04	0.038	NA	0.09	99.89
Tp01_24	NA	33.32	67.22	0.02	0.033	NA	0.20	100.79
Tp01_25	NA	32.70	65.63	0.07	NA	NA	0.26	98.65
Tp01_26	NA	32.93	66.19	0.05	0.037	NA	0.14	99.35
Tp01_27	NA	33.60	67.18	0.03	NA	NA	0.09	100.89
Tp01_28	NA	33.13	67.39	0.02	NA	NA	0.31	100.84
Tp01_29	NA	32.91	66.70	0.06	0.499	NA	0.07	100.24
Tp01_30	0.010	33.05	67.77	0.01	NA	NA	0.10	100.94
Tp01_31	0.020	32.95	67.86	0.02	NA	NA	0.10	100.94
Tp01_32	NA	32.92	67.97	0.01	NA	NA	0.12	101.02
Tp01_33	NA	32.38	66.97	0.12	0.114	NA	0.05	99.64
Tp01_34	0.019	33.25	67.45	0.01	NA	NA	0.18	100.90
Tp01_35	0.013	33.17	67.56	0.01	NA	NA	0.24	100.99
Tp01_36	NA	33.02	67.54	0.13	0.113	NA	0.02	100.82
Tp01_37	NA	33.10	67.04	0.74	0.007	NA	0.09	100.98
Tp01_39	NA	32.70	66.04	0.76	1.100	0.026	NA	100.62

Table 11: Continued.

	EMPA Topla [mass%]							
sample/analyses	**As**	**S**	**Zn**	**Fe**	**Pb**	**Ge**	**Cd**	**total**
Tp01_40	0.029	33.07	66.99	0.59	0.064	NA	0.12	100.86
Tp01_41	0.018	32.89	66.35	0.66	0.958	0.029	0.03	100.94
Tp01_42	NA	33.11	67.33	0.44	0.008	NA	0.23	101.12
Tp01_43	0.010	32.99	67.37	0.18	0.106	NA	0.14	100.79
Tp01_44	NA	33.53	66.55	0.18	0.068	NA	0.03	100.36
Tp01_45	NA	33.19	66.35	0.44	NA	NA	0.11	100.09
Tp01_46	NA	33.08	67.79	0.02	0.037	NA	0.13	101.06
Tp01_47	0.007	33.33	67.67	0.04	0.017	NA	0.08	101.14
Tp01_48	0.020	33.07	67.37	0.11	0.191	NA	0.08	100.85
Tp01_49	NA	32.55	66.63	0.33	0.645	NA	0.05	100.21
Tp01_50	NA	33.14	67.10	0.28	0.082	NA	0.07	100.67
Tp01_51	NA	33.00	66.92	0.02	NA	NA	0.08	100.02
Tp01_52	NA	33.06	66.91	0.01	NA	NA	0.10	100.08
Tp01_53	0.017	33.23	66.55	0.02	NA	NA	0.15	99.97
Tp01_54	0.006	33.03	66.82	0.05	NA	NA	0.10	100.01
Tp01_55	0.018	33.10	66.92	0.01	0.021	NA	0.32	100.39
Tp01_56	NA	NA	NA	NA	NA	NA	NA	NA
Tp01_40	0.029	33.07	66.99	0.59	0.064	NA	0.12	100.86
Tp01_41	0.018	32.89	66.35	0.66	0.958	0.029	0.03	100.94
Tp01_42	NA	33.11	67.33	0.44	0.008	NA	0.23	101.12
Tp01_43	0.010	32.99	67.37	0.18	0.106	NA	0.14	100.79
Tp01_44	NA	33.53	66.55	0.18	0.068	NA	0.03	100.36
Tp01_45	NA	33.19	66.35	0.44	NA	NA	0.11	100.09
Tp01_46	NA	33.08	67.79	0.02	0.037	NA	0.13	101.06
Tp01_47	0.007	33.33	67.67	0.04	0.017	NA	0.08	101.14
Tp01_48	0.020	33.07	67.37	0.11	0.191	NA	0.08	100.85
Tp01_49	NA	32.55	66.63	0.33	0.645	NA	0.05	100.21
Tp01_50	NA	33.14	67.10	0.28	0.082	NA	0.07	100.67
Tp01_51	NA	33.00	66.92	0.02	NA	NA	0.08	100.02
Tp01_52	NA	33.06	66.91	0.01	NA	NA	0.10	100.08
Tp01_53	0.017	33.23	66.55	0.02	NA	NA	0.15	99.97
Tp01_54	0.006	33.03	66.82	0.05	NA	NA	0.10	100.01
Tp01_55	0.018	33.10	66.92	0.01	0.021	NA	0.32	100.39

Table 12: EMP data of ZnS from other Pb-Zn deposits in the Drau Range (Erzkalk).

	EMPA Radnig [mass%]							
sample/analyses	**As**	**S**	**Zn**	**Fe**	**Pb**	**Ge**	**Cd**	**total**
EHK17_ZnS1	0.012	33.60	64.96	0.73	NA	0.049	0.12	99.47
EHK17_ZnS2	NA	33.68	65.55	0.89	0.050	0.027	0.13	100.33
EHK17_ZnS3	0.011	33.34	65.10	1.33	NA	0.049	0.16	99.99
EHK17_ZnS4	NA	33.36	67.60	0.05	0.038	0.014	0.20	101.27
EHK17_ZnS5	NA	33.67	67.59	0.14	NA	NA	0.21	101.61
EHK17_ZnS6	NA	33.36	67.40	0.30	NA	NA	0.21	101.27
EHK17_ZnS7	NA	33.34	67.71	0.05	NA	0.007	0.23	101.33
EHK17_ZnS8	NA	33.11	67.48	0.20	NA	NA	0.18	100.98
EHK17_ZnS9	NA	33.46	66.98	0.90	0.082	0.009	0.09	101.52
EHK17_ZnS10	NA	33.72	67.77	0.04	0.054	0.006	0.23	101.82
EHK17_ZnS11	NA	33.37	66.08	1.72	NA	0.033	0.16	101.37
EHK17_ZnS12	NA	33.52	67.26	0.45	NA	0.061	0.09	101.38
EHK17_ZnS13	NA	33.33	66.55	0.93	0.079	0.068	0.12	101.08
EHK17_ZnS14	NA	33.45	65.97	1.64	0.051	NA	0.18	101.29
EHK17_ZnS15	NA	33.24	67.20	0.26	0.232	0.024	0.05	101.00
EHK17_ZnS16	0.009	33.30	66.10	1.59	0.084	0.020	0.13	101.23
EHK17_ZnS17	0.010	33.40	66.43	1.36	0.066	0.026	0.19	101.48
EHK17_ZnS18	0.011	33.57	67.12	0.48	NA	0.056	0.10	101.34
EHK17_ZnS19	NA	33.63	66.82	0.96	NA	0.034	0.15	101.59
EHK17_ZnS20	NA	33.62	66.10	1.46	0.041	0.046	0.18	101.45
EHK17_ZnS21	NA	33.38	67.80	0.20	NA	0.014	0.05	101.44
EHK17_ZnS22	NA	33.81	66.21	1.49	NA	0.027	0.12	101.65
EHK17_ZnS23	NA	33.35	67.25	0.11	0.033	0.067	0.11	100.91
EHK17_ZnS24	NA	33.47	67.28	0.13	0.036	0.201	0.03	101.15
EHK17_ZnS25	NA	32.41	66.18	0.04	NA	0.019	0.17	98.82
EHK17_ZnS26	NA	33.11	66.76	0.07	NA	0.076	0.13	100.14
EHK17_ZnS27	NA	34.15	67.53	0.09	NA	0.071	0.11	101.95
EHK17_ZnS28	NA	33.59	66.54	0.10	NA	0.196	0.06	100.49
EHK17_ZnS29	NA	33.85	66.28	0.09	NA	0.241	0.05	100.51
EHK17_ZnS30	NA	33.74	65.98	0.12	NA	0.259	0.04	100.14
EHK17_ZnS31	NA	33.39	65.95	0.11	NA	0.114	0.08	99.64
EHK17_ZnS32	NA	33.33	67.18	0.15	NA	NA	0.27	100.92
EHK17_ZnS33	NA	33.49	67.55	0.04	NA	NA	0.25	101.33
EHK17_ZnS34	NA	33.42	67.30	0.04	0.027	0.008	0.25	101.04
EHK17_ZnS35	NA	33.47	67.41	0.26	NA	0.008	0.15	101.30
EHK17_ZnS36	NA	33.33	66.93	0.09	NA	0.022	0.10	100.47
EHK17_ZnS37	NA	32.95	65.43	0.08	0.036	0.069	0.12	98.68
EHK17_ZnS38	NA	32.90	66.36	0.21	NA	0.172	0.07	99.71
EHK17_ZnS39	NA	33.60	66.34	0.12	NA	0.127	0.09	100.27
EHK17_ZnS41	NA	33.51	66.19	0.15	NA	0.281	0.06	100.19
EHK17_ZnS42	NA	33.31	66.75	0.11	0.074	0.225	0.03	100.50
EHK17_ZnS43	NA	33.52	66.97	0.58	0.079	0.040	0.11	101.30
EHK17_ZnS44	NA	33.74	66.67	1.00	0.088	0.036	0.10	101.64
EHK17_ZnS45	0.010	33.78	67.71	0.05	NA	NA	0.15	101.70
EHK17_ZnS46	NA	33.67	67.93	0.01	NA	NA	0.12	101.74
EHK17_ZnS47	NA	33.27	65.98	1.57	NA	0.064	0.09	100.97
EHK17_ZnS48	NA	33.52	66.59	1.16	0.055	0.035	0.15	101.51
EHK17_ZnS49	0.004	33.52	66.24	1.57	0.064	0.036	0.10	101.53
EHK17_ZnS50	NA	32.88	66.24	0.22	NA	0.158	0.07	99.69

Table 12: Continued.

	EMPA Jauken [mass%]							
sample/analyses	**As**	**S**	**Zn**	**Fe**	**Pb**	**Ge**	**Cd**	**total**
1_MS391_JK5-9_BSE4_1	NA	32.53	63.96	0.22	NA	0.097	0.07	96.95
2_MS391_JK5-9_BSE4_1	NA	32.58	66.31	0.31	NA	0.152	0.04	99.46
3_MS391_JK5-9_BSE4_1	0.026	32.91	66.06	0.25	NA	0.159	0.04	99.55
4_MS391_JK5-9_BSE4_1	NA	32.36	66.16	0.21	0.126	0.139	0.05	99.06
5_MS391_JK5-9_BSE4_1	NA	32.87	65.88	0.19	NA	0.129	0.05	99.19
6_MS391_JK5-9_BSE4_1	NA	32.59	66.10	0.19	NA	0.122	0.04	99.07
7_MS391_JK5-9_BSE4_1	NA	32.77	65.98	0.19	NA	0.121	0.06	99.20
8_MS391_JK5-9_BSE4_1	NA	32.68	65.38	0.33	NA	0.150	0.03	98.69
9_MS391_JK5-9_BSE4_1	NA	32.66	65.87	0.59	0.126	0.041	0.08	99.39
10_MS391_JK5-9_BSE3_4	NA	32.72	65.77	0.28	NA	0.143	0.07	99.06
11_MS391_JK5-9_BSE3_4	NA	32.76	66.14	0.24	NA	0.140	0.06	99.43
12_MS391_JK5-9_BSE3_4	NA	32.72	66.17	0.22	NA	0.123	0.06	99.41
13_MS391_JK5-9_BSE3_4	NA	32.55	66.18	0.35	NA	0.162	0.05	99.45
14_MS391_JK5-9_BSE3_4	NA	32.81	66.24	0.30	0.125	0.153	0.05	99.67
15_MS391_JK5-9_BSE3_4	NA	32.60	66.72	0.27	0.228	0.014	NA	99.87
16_MS391_JK5-9_BSE4_6	NA	32.42	66.75	0.43	0.120	0.094	0.08	99.91
17_MS391_JK5-9_BSE4_6	NA	32.23	66.48	0.48	NA	0.038	0.06	99.37
18_MS391_JK5-9_BSE4_6	NA	32.71	64.71	2.17	0.130	0.076	0.10	99.92
19_MS391_JK5-9_BSE4_6	NA	32.55	66.28	0.60	NA	0.033	0.09	99.65
20_MS391_JK5-9_BSE4_6	NA	32.69	66.14	0.57	0.113	0.066	0.08	99.66
21_MS391_JK5-9_BSE4_6	0.046	32.71	65.88	0.51	NA	0.032	0.08	99.36
22_MS391_JK5-9_BSE5_8	NA	32.59	66.25	0.24	NA	0.079	0.09	99.34
23_MS391_JK5-9_BSE5_8	NA	32.59	65.12	1.49	NA	0.044	0.07	99.43
24_MS391_JK5-9_BSE5_8	NA	32.56	66.11	0.20	NA	0.135	0.06	99.15
25_MS391_JK5-9_BSE5_8	NA	32.75	66.13	0.22	0.167	0.180	0.07	99.51
26_MS391_JK5-9_BSE5_8	0.029	32.74	66.37	0.20	NA	0.147	0.06	99.66
27_MS391_JK5-9_BSE5_8	NA	32.69	66.70	0.15	NA	0.118	0.03	99.74
28_MS391_JK5-9_BSE5_8	0.037	32.71	66.35	0.78	0.119	0.072	0.07	100.15
29_MS391_JK5-9_BSE5_9	NA	32.47	66.37	0.70	0.161	0.060	0.08	99.84
30_MS391_JK5-9_BSE5_9	NA	32.65	65.72	0.24	0.114	0.128	0.06	98.93
31_MS391_JK5-9_BSE5_9	NA	32.98	66.19	0.27	NA	0.168	0.07	99.78
32_MS391_JK5-9_BSE5_9	NA	32.91	66.38	0.16	NA	0.165	0.07	99.76
33_MS391_JK5-9_BSE5_9	0.032	32.81	66.33	0.38	NA	0.218	0.05	99.87
34_MS391_JK5-9_BSE5_12	NA	32.88	65.84	0.50	NA	0.262	NA	99.60
35_MS391_JK5-9_BSE5_12	NA	32.79	65.92	0.34	NA	0.180	0.04	99.39
36_MS391_JK5-9_BSE5_12	NA	32.77	65.44	0.41	0.141	0.231	0.04	99.07
37_MS391_JK5-9_BSE5_12	NA	32.64	66.10	0.25	NA	0.107	0.07	99.24
39_MS391_JK5-9_BSE9_13	NA	32.90	66.21	0.32	0.118	0.246	0.05	99.88
40_MS391_JK5-9_BSE9_13	NA	32.88	65.79	0.43	NA	0.240	0.04	99.50
41_MS391_JK5-9_BSE9_13	NA	32.86	65.74	0.54	NA	0.205	0.03	99.47
42_MS391_JK5-9_BSE9_13	NA	32.77	65.64	0.56	NA	0.180	NA	99.22
43_MS391_JK5-9_BSE9_13	NA	32.92	65.26	0.61	NA	0.272	0.03	99.20
44_MS391_JK5-9_BSE9_13	NA	32.37	66.25	0.24	NA	0.074	0.07	99.11
45_MS391_JK5-9_BSE9_13	0.009	33.22	67.14	0.04	0.088	NA	0.01	100.50

Table 12: Continued.

	EMPA Windisch Bleiberg [mass%]							
sample/analyses	**As**	**S**	**Zn**	**Fe**	**Pb**	**Ge**	**Cd**	**total**
EHK16_1	NA	33.22	67.35	0.04	0.032	NA	0.06	100.69
EHK16_2	0.009	33.17	66.89	0.40	0.049	0.067	0.03	100.61
EHK16_3	NA	33.14	67.19	0.04	NA	NA	0.20	100.57
EHK16_4	NA	33.14	66.88	0.01	NA	NA	0.06	100.09
EHK16_5	0.003	33.35	66.86	0.14	0.038	0.060	0.05	100.51
EHK16_6	0.003	33.27	66.77	0.16	NA	0.039	0.11	100.35
EHK16_7	NA	33.32	67.00	0.02	0.039	NA	0.09	100.47
EHK16_8	0.020	33.09	66.63	0.18	0.157	0.017	0.19	100.29
EHK16_9	0.012	33.26	66.84	0.03	NA	0.005	0.12	100.27
EHK16_10	0.012	33.18	66.94	0.21	0.065	0.010	0.09	100.50
EHK16_11	0.015	33.23	66.55	0.28	0.057	0.005	0.19	100.34
EHK16_12	0.007	33.24	66.68	0.27	0.061	0.019	0.14	100.43
EHK16_13	0.037	33.17	66.35	0.34	0.239	0.011	0.12	100.26
EHK16_14	0.018	33.07	66.44	0.32	0.221	0.038	0.14	100.24
EHK16_15	0.003	33.25	67.17	0.07	0.041	NA	0.07	100.60
EHK16_16	0.035	33.16	66.45	0.31	0.122	NA	0.06	100.14
EHK16_17	0.007	32.74	66.56	0.19	0.177	0.017	0.13	99.83
EHK16_18	0.020	33.16	67.02	0.14	0.091	0.023	0.07	100.52
EHK16_19	0.011	32.92	66.96	0.17	0.146	0.016	0.06	100.28
EHK16_20	0.081	32.75	65.38	0.48	0.321	0.032	0.05	99.10
EHK16_21	NA	33.29	66.86	0.30	0.099	NA	0.08	100.63
EHK16_22	0.045	32.94	66.40	0.52	0.222	0.024	0.07	100.22
EHK16_23	0.029	32.92	66.33	0.76	0.169	0.011	0.14	100.36
EHK16_24	NA	33.43	67.24	0.07	NA	NA	0.14	100.88
EHK16_25	0.038	32.63	66.18	0.37	0.217	0.022	0.19	99.64
EHK16_26	0.019	32.80	66.34	0.32	0.144	NA	0.24	99.86
EHK16_27	NA	31.25	64.89	0.41	0.210	0.009	0.15	96.92
EHK16_28	0.009	32.81	66.00	0.47	0.213	0.008	0.23	99.75
EHK16_29	0.020	32.86	66.26	0.21	0.465	0.056	0.19	100.06
EHK16_30	NA	33.06	65.79	0.30	0.053	0.061	0.05	99.32
EHK16_31	NA	32.95	67.08	0.02	NA	NA	0.08	100.13
EHK16_32	0.004	33.48	66.63	0.05	NA	NA	0.10	100.27
EHK16_33	NA	32.95	65.77	0.09	NA	0.031	0.06	98.90
EHK16_34	NA	33.13	67.36	0.04	NA	NA	0.06	100.59
EHK16_35	NA	33.07	66.80	0.37	NA	0.082	0.04	100.36
EHK16_36	NA	32.98	67.51	0.08	NA	NA	0.09	100.67
EHK16_37	NA	33.05	66.74	0.41	0.080	0.076	0.03	100.39
EHK16_38	NA	33.06	66.93	0.21	NA	0.089	0.05	100.34
EHK16_39	0.004	32.76	66.25	0.08	0.065	NA	0.08	99.24
EHK16_40	NA	33.15	66.92	0.16	NA	0.063	0.04	100.34
EHK16_41	NA	32.93	67.66	0.02	NA	0.006	0.01	100.63

Table 12: Continued.

	EMPA Töplitsch [mass%]							
sample/analyses	**As**	**S**	**Zn**	**Fe**	**Pb**	**Ge**	**Cd**	**total**
Toe01neu_ZnS1	NA	32.74	67.79	0.03	NA	NA	0.00	100.56
Toe01neu_ZnS2	NA	32.86	67.80	0.03	NA	NA	0.08	100.77
Toe01neu_ZnS3	NA	32.39	68.04	0.02	0.025	NA	NA	100.48
Toe01neu_ZnS4	NA	32.32	67.84	0.03	NA	NA	0.07	100.26
Toe01neu_ZnS5	NA	33.14	67.75	0.21	NA	0.030	NA	101.13
Toe01neu_ZnS6	NA	32.87	67.78	0.17	NA	0.024	NA	100.84
Toe01neu_ZnS7	NA	33.16	68.08	0.01	NA	NA	0.02	101.26
Toe01neu_ZnS8	NA	32.31	67.65	0.08	0.057	NA	NA	100.09
Toe01neu_ZnS9	NA	32.78	67.83	0.09	0.030	0.012	0.01	100.75
Toe01neu_ZnS10	NA	32.63	67.78	0.19	0.039	0.012	NA	100.66
Toe01neu_ZnS11	NA	33.10	67.53	0.06	0.033	0.007	NA	100.73
Toe01neu_ZnS12	NA	32.99	67.45	0.01	NA	NA	0.02	100.47
Toe01neu_ZnS13	NA	32.39	67.40	0.06	0.045	0.067	NA	99.97
Toe01neu_ZnS14	NA	32.42	67.61	0.19	0.028	NA	NA	100.25
Toe01neu_ZnS15	NA	32.51	67.13	0.09	NA	NA	0.02	99.74
Toe01neu_ZnS16	NA	32.45	67.70	0.07	NA	NA	0.02	100.24
Toe01neu_ZnS17	NA	32.61	67.52	0.05	NA	NA	NA	100.18
Toe01neu_ZnS18	NA	31.88	67.81	0.01	NA	NA	0.14	99.84
Toe01neu_ZnS19	NA	32.45	67.00	0.15	NA	0.004	NA	99.61
Toe01neu_ZnS20	NA	32.92	66.99	0.01	NA	NA	0.12	100.04
Toe01neu_ZnS21	NA	32.44	67.11	0.01	NA	NA	0.01	99.57
Toe01neu_ZnS22	NA	32.56	66.89	0.02	0.048	NA	NA	99.52
Toe01neu_ZnS23	NA	32.81	67.38	0.01	NA	0.009	NA	100.20
Toe01neu_ZnS24	NA	32.45	67.28	0.05	NA	NA	0.01	99.78
Toe01neu_ZnS25	NA	32.48	66.80	0.14	NA	NA	NA	99.42
Toe01neu_ZnS26	NA	32.97	67.10	0.02	0.042	0.004	0.01	100.15
Toe01neu_ZnS27	NA	32.62	67.01	0.18	0.024	NA	NA	99.83
Toe01neu_ZnS28	NA	32.52	67.43	0.03	NA	NA	0.01	99.99
Toe01neu_ZnS29	NA	33.00	66.65	0.10	NA	NA	NA	99.75
Toe01neu_ZnS30	NA	32.71	66.58	0.02	0.043	NA	NA	99.36
Toe01neu_ZnS31	NA	32.95	66.96	0.05	NA	NA	0.01	99.97
Toe01neu_ZnS32	NA	32.91	66.91	0.09	NA	NA	0.01	99.92
Toe01neu_ZnS33	NA	32.82	66.86	0.01	NA	NA	0.03	99.72
Toe01neu_ZnS34	NA	33.11	66.96	0.03	NA	NA	0.03	100.13
Toe01neu_ZnS35	NA	33.13	66.85	0.01	NA	NA	0.01	100.00
Toe01neu_ZnS36	NA	32.78	66.46	0.10	0.030	NA	NA	99.37
Toe01neu_ZnS37	NA	32.54	66.77	0.04	NA	NA	0.03	99.38
Toe01neu_ZnS38	NA	33.18	66.70	0.01	NA	NA	0.03	99.92
Toe01neu_ZnS39	NA	32.64	66.71	0.16	0.024	0.011	NA	99.54
Toe01neu_ZnS40	NA	32.58	67.16	0.01	NA	NA	0.02	99.77
Toe01neu_ZnS41	NA	32.65	67.22	0.01	0.035	NA	NA	99.92
Toe01neu_ZnS42	NA	32.54	66.84	NA	0.034	NA	0.03	99.45
Toe01neu_ZnS43	NA	32.68	66.89	0.02	NA	NA	0.13	99.72
Toe01neu_ZnS44	NA	32.64	67.00	0.01	NA	NA	0.05	99.71
Toe01neu_ZnS45	NA	33.05	67.90	0.03	NA	NA	0.05	101.03
Toe01neu_ZnS46	NA	32.82	67.74	0.01	NA	0.008	0.11	100.69
Toe01neu_ZnS47	NA	32.53	67.67	0.02	0.079	NA	0.00	100.31
Toe01neu_ZnS48	NA	32.59	68.05	0.03	NA	NA	0.06	100.73

Table 12: Continued.

	EMPA Töplitsch [mass%]							
sample/analyses	**As**	**S**	**Zn**	**Fe**	**Pb**	**Ge**	**Cd**	**total**
Toe01neu_ZnS49	NA	33.07	67.68	0.01	NA	NA	0.02	100.78
Toe01neu_ZnS50	NA	32.90	68.04	0.04	NA	NA	NA	100.98
Toe01neu_ZnS51	NA	32.85	67.89	0.04	NA	0.008	0.02	100.81
Toe01neu_ZnS52	NA	32.99	67.78	0.03	NA	NA	0.04	100.84
Toe01neu_ZnS53	NA	32.83	67.93	0.03	NA	NA	0.03	100.82
Toe01neu_ZnS54	NA	33.02	67.69	0.04	NA	NA	0.02	100.77
Toe01neu_ZnS55	NA	32.59	66.69	NA	NA	NA	0.03	99.41
1_MS391_Toe02_BSE1	NA	32.79	66.41	NA	0.113	NA	0.06	99.39
2_MS391_Toe02_BSE1	NA	32.85	66.65	NA	0.140	NA	0.09	99.74
3_MS391_Toe02_BSE1	NA	32.45	66.42	NA	NA	NA	0.10	99.06
4_MS391_Toe02_BSE1	NA	32.92	66.39	0.24	NA	NA	NA	99.67
5_MS391_Toe02_BSE1	NA	32.52	66.24	0.02	NA	NA	0.06	98.92
6_MS391_Toe02_BSE1	NA	32.65	66.27	NA	NA	NA	NA	99.01
7_MS391_Toe02_BSE1	NA	32.87	65.86	0.03	NA	NA	0.04	98.92
8_MS391_Toe02_BSE1	NA	32.80	66.37	0.01	NA	NA	0.08	99.39
9_MS391_Toe02_BSE2	NA	32.99	66.55	0.01	NA	0.023	0.06	99.71
10_MS391_Toe02_BSE2	NA	32.60	66.41	NA	NA	NA	0.06	99.22
11_MS391_Toe02_BSE2	NA	32.89	66.43	0.02	NA	0.026	NA	99.45
12_MS391_Toe02_BSE2	NA	32.74	66.51	0.04	NA	0.028	NA	99.44
13_MS391_Toe02_BSE2	NA	33.09	66.47	0.08	NA	NA	NA	99.76
14_MS391_Toe02_BSE2	NA	32.90	66.97	NA	NA	NA	0.05	100.03
15_MS391_Toe02_BSE2	NA	32.82	67.28	0.02	NA	NA	0.09	100.29
16_MS391_Toe02_BSE3	NA	32.74	67.22	NA	NA	NA	0.06	100.06
17_MS391_Toe02_BSE3	NA	32.92	67.40	NA	0.124	NA	0.09	100.56
18_MS391_Toe02_BSE3	NA	32.98	67.02	NA	NA	NA	NA	100.10
19_MS391_Toe02_BSE3	NA	32.71	66.44	NA	NA	NA	0.10	99.34
20_MS391_Toe02_BSE3	NA	32.73	66.49	0.02	NA	NA	0.07	99.41
21_MS391_Toe02_BSE3	NA	32.91	66.46	NA	NA	NA	NA	99.50
22_MS391_Toe02_BSE3	NA	32.85	66.23	0.18	NA	NA	0.06	99.41
23_MS391_Toe02_BSE3	NA	32.75	66.22	0.01	NA	NA	0.07	99.16
24_MS391_Toe02_BSE3	NA	32.59	66.78	0.02	NA	NA	0.06	99.54
25_MS391_Toe02_BSE4	NA	32.68	66.32	0.14	0.145	NA	0.05	99.35
26_MS391_Toe02_BSE4	NA	33.02	66.44	NA	NA	NA	0.06	99.60
27_MS391_Toe02_BSE4	NA	32.66	66.21	0.02	NA	NA	0.11	99.15
28_MS391_Toe02_BSE4	NA	33.09	66.77	NA	NA	NA	NA	99.98
29_MS391_Toe02_BSE4	NA	32.97	66.90	0.03	0.129	NA	NA	100.06
30_MS391_Toe02_BSE4	NA	32.85	67.23	NA	NA	NA	NA	100.21
31_MS391_Toe02_BSE4	NA	33.40	67.29	NA	0.140	NA	0.04	100.90
32_MS391_Toe02_BSE4	NA	32.91	67.23	0.01	NA	NA	0.06	100.29
33_MS391_Toe02_BSE4	NA	32.15	67.19	NA	NA	NA	0.12	99.57
34_MS391_Toe02_BSE4	NA	32.66	67.06	0.04	NA	0.025	NA	99.86
35_MS391_Toe02_BSE5	NA	32.93	67.14	0.02	0.115	NA	0.06	100.28
36_MS391_Toe02_BSE5	NA	32.96	67.11	0.01	NA	NA	0.06	100.26
37_MS391_Toe02_BSE5	NA	32.85	67.18	0.03	NA	0.019	0.03	100.24
38_MS391_Toe02_BSE5	NA	32.73	66.56	NA	NA	NA	0.04	99.47
39_MS391_Toe02_BSE5	NA	32.92	66.94	NA	NA	NA	NA	100.01
40_MS391_Toe02_BSE5	NA	33.01	66.83	NA	0.142	NA	0.05	100.04

Table 12: Continued.

	EMPA Töplitsch [mass%]							
sample/analyses	**As**	**S**	**Zn**	**Fe**	**Pb**	**Ge**	**Cd**	**total**
41_MS391_Toe02_BSE5	NA	32.83	66.74	NA	NA	NA	0.05	99.74
42_MS391_Toe02_BSE5	NA	32.96	66.87	NA	NA	NA	0.06	100.01
43_MS391_Toe02_BSE5	NA	32.98	66.75	NA	0.136	NA	0.05	99.94
44_MS391_Toe02_BSE5	NA	32.96	66.62	0.03	NA	NA	0.06	99.79
45_MS391_Toe02_BSE5	NA	32.92	66.55	0.06	NA	NA	NA	99.60
46_MS391_Toe02_BSE5	NA	33.14	67.02	NA	NA	NA	NA	100.25
47_MS391_Toe02_BSE5	NA	32.80	67.22	0.09	NA	NA	0.07	100.25
48_MS391_Toe02_BSE5	NA	32.89	67.48	NA	NA	NA	0.04	100.46
49_MS391_Toe02_BSE5	NA	32.83	67.34	0.11	NA	NA	0.08	100.44
50_MS391_Toe02_BSE5	NA	NA	NA	NA	NA	NA	NA	NA

Table 13: EMP data of ZnS from other Alpine Pb-Zn occurrences.

	EMPA Zunderwand, Anisian [mass%]								
sample/analyses	**As**	**S**	**Zn**	**Fe**	**Pb**	**Ge**	**Cu**	**Cd**	**total**
Rd01.1_1	NA	33.05	67.22	0.06	NA	NA	NA	0.00	100.33
Rd01.1_2	NA	33.14	66.91	0.30	NA	NA	NA	0.01	100.36
Rd01.1_4	NA	33.08	67.24	0.09	NA	NA	NA	0.01	100.41
Rd01.1_5	NA	33.16	67.70	0.05	0.034	0.005	NA	NA	100.95
Rd01.1_6	NA	32.97	67.80	0.05	NA	NA	NA	0.01	100.83
Rd01.1_7	NA	33.07	67.62	0.05	NA	NA	NA	NA	100.74
Rd01.1_8	NA	33.20	67.83	0.09	0.081	NA	NA	0.01	101.20
Rd01.1_9	NA	32.73	67.36	0.08	0.036	NA	NA	NA	100.21
Rd01.1_10	NA	32.69	67.31	0.03	NA	NA	NA	0.00	100.03
Rd01.1_11	NA	32.75	67.07	0.04	0.027	NA	NA	0.00	99.89
Rd01.1_12	NA	32.86	67.65	0.03	0.036	NA	NA	0.00	100.59
Rd01.1_13	NA	32.97	67.46	0.09	NA	NA	NA	NA	100.52
Rd01.1_14	0.007	32.86	67.26	0.22	NA	NA	NA	NA	100.35
Rd01.1_15	NA	32.95	67.60	0.08	NA	NA	NA	0.01	100.63
Rd01.1_16	NA	32.97	67.80	0.06	0.030	NA	NA	NA	100.86

Table 13: Continued.

EMPA Raibl deposit, Wetterstein Fm. [mass%]									
sample/analyses	**As**	**S**	**Zn**	**Fe**	**Pb**	**Ge**	**Cu**	**Cd**	**total**
BGR_Ra1	0.002	32.13	67.23	0.01	0.028	NA	NA	0.65	100.05
BGR_Ra2	0.022	32.44	67.12	0.07	0.152	0.014	NA	0.13	99.94
BGR_Ra3	0.266	32.01	65.43	0.07	0.974	0.117	NA	0.00	98.87
BGR_Ra4	0.128	31.66	65.40	0.04	0.688	0.090	NA	0.03	98.04
BGR_Ra5	0.152	31.72	65.50	0.06	0.769	0.080	NA	0.06	98.34
BGR_Ra6	0.151	31.86	65.25	0.04	0.768	0.053	NA	0.03	98.15
BGR_Ra7	0.117	31.73	66.16	0.11	0.579	0.038	NA	0.06	98.79
BGR_Ra8	0.287	31.72	64.93	0.09	1.180	0.120	NA	0.01	98.34
BGR_Ra9	0.192	31.52	65.27	0.06	0.586	0.065	NA	0.16	97.85
BGR_Ra10	0.135	31.77	65.54	0.05	0.528	0.062	NA	0.06	98.14
BGR_Ra11	0.235	31.91	65.75	0.09	0.839	0.064	NA	0.03	98.91
BGR_Ra12	0.043	31.91	66.75	0.11	0.183	0.016	NA	0.11	99.13
BGR_Ra13	0.268	31.66	64.96	0.11	1.100	0.074	NA	0.01	98.18
BGR_Ra14	0.176	31.34	64.85	0.06	0.759	0.084	NA	0.03	97.30
BGR_Ra15	0.201	31.53	65.03	0.08	1.050	0.068	NA	0.02	97.98
BGR_Ra16	0.014	32.24	67.03	0.12	0.155	0.023	NA	0.09	99.67
BGR_Ra17	0.257	32.28	65.91		0.773	0.098	NA	0.01	99.44
BGR_Ra18	0.182	31.91	65.51	0.06	0.750	0.070	NA	0.05	98.53
BGR_Ra19	0.202	32.18	65.83	0.07	0.848	0.082	NA	0.03	99.24
BGR_Ra20	0.029	32.08	67.09	0.10	0.239	0.036	NA	0.14	99.71

Table 13: Continued.

EMPA Lafatsch deposit, Wetterstein Fm. [mass%]									
sample/analyses	**As**	**S**	**Zn**	**Fe**	**Pb**	**Ge**	**Cu**	**Cd**	**total**
BGR_La1	0.117	31.76	65.87	0.26	0.517	0.002	NA	0.16	98.69
BGR_La2	0.155	32.18	66.04	0.28	0.541	NA	NA	0.19	99.39
BGR_La3	0.128	31.95	66.12	0.24	0.565	0.001	NA	0.21	99.21
BGR_La4	0.124	31.83	66.13	0.22	0.491	NA	NA	0.19	98.99
BGR_La5	0.189	31.45	65.28	0.27	0.707	NA	NA	0.09	97.99
BGR_La6	0.193	31.97	65.70	0.22	0.755	0.005	NA	0.11	98.95
BGR_La7	0.193	31.99	65.80	0.24	0.751	NA	NA	0.10	99.07
BGR_La8	0.123	32.16	66.22	0.17	0.583	NA	NA	0.08	99.33
BGR_La9	0.085	32.18	66.76	0.15	0.359	NA	NA	0.10	99.63
BGR_La10	0.044	32.29	66.76	0.11	0.331	NA	NA	0.18	99.71
BGR_La11	0.091	32.09	66.69	0.17	0.375	0.012	NA	0.17	99.60
BGR_La12	0.139	32.14	66.21	0.12	0.701	NA	NA	0.12	99.43
BGR_La13	0.188	32.27	65.94	0.21	0.764	NA	NA	0.10	99.47
BGR_La14	0.206	32.12	65.87	0.24	0.702	0.003	NA	0.12	99.26
BGR_La15	0.157	32.19	66.36	0.16	0.531	NA	NA	0.05	99.44
BGR_La16	0.130	32.06	66.41	0.14	0.482	NA	NA	0.08	99.30
BGR_La17	0.167	31.98	66.21	0.16	0.572	NA	NA	0.03	99.12
BGR_La18	0.167	31.95	66.21	0.16	0.586	NA	NA	0.03	99.10
BGR_La19	0.137	31.72	65.32	0.10	0.555	NA	NA	0.51	98.34
BGR_La20	0.151	31.45	65.34	0.14	0.783	NA	NA	0.31	98.17
BGR_La21	0.095	31.87	66.16	0.15	0.275	NA	NA	0.40	98.95
BGR_La22	0.075	31.88	65.99	0.09	0.365	NA	NA	0.48	98.88
BGR_La23	0.041	31.90	66.91	0.14	0.113	NA	NA	0.48	99.58
BGR_La24	0.005	31.98	66.90	0.09	NA	NA	NA	0.75	99.73
BGR_La25	0.056	32.18	66.99	0.07	0.172	NA	NA	0.26	99.73
BGR_La26	0.041	32.36	66.90	0.07	0.140	NA	NA	0.39	99.91
BGR_La27	0.173	31.93	65.75	0.16	0.918	0.010	NA	0.13	99.07
BGR_La28	0.132	31.85	66.01	0.12	0.713	NA	NA	0.23	99.06
BGR_La29	0.104	32.12	66.26	0.13	0.571	NA	NA	0.04	99.22
BGR_La30	0.086	32.09	66.38	0.14	0.386	NA	NA	0.04	99.12
BGR_La31	0.121	31.74	65.88	0.17	0.575	NA	NA	0.12	98.61
BGR_La32	0.120	31.96	65.78	0.20	0.605	NA	NA	0.14	98.80
BGR_La33	0.122	32.06	66.06	0.22	0.554	NA	NA	0.16	99.18
BGR_La34	0.117	31.86	66.09	0.18	0.593	NA	NA	0.11	98.94
BGR_La35	0.018	32.98	67.35	0.01	NA	NA	0.039	0.83	101.22
BGR_La36	0.140	32.15	66.45	0.16	0.570	NA	NA	0.16	99.63
BGR_La37	0.072	32.18	66.74	0.10	0.367	0.002	NA	0.10	99.56
BGR_La38	0.115	32.31	66.47	0.18	0.551	NA	NA	0.08	99.70
BGR_La39	NA	33.31	67.79	0.18	NA	NA	NA	0.06	101.35
BGR_La40	0.005	33.24	67.66	0.09	0.018	NA	NA	0.11	101.12
BGR_La41	0.024	32.64	67.40	0.07	0.088	0.041	NA	0.11	100.38
BGR_La42	0.034	32.66	67.05	0.14	0.157	0.007	NA	0.66	100.71
BGR_La43	0.198	32.12	66.21	0.19	0.724	NA	NA	0.13	99.58
BGR_La44	0.155	32.01	66.01	0.16	0.618	NA	NA	0.12	99.08
BGR_La45	0.157	32.13	66.27	0.21	0.567	NA	NA	0.15	99.48
BGR_La46	0.100	31.95	66.33	0.09	0.490	NA	NA	0.12	99.08
BGR_La47	0.091	32.43	67.02	0.07	0.329	NA	NA	0.00	99.94

Table 13: Continued.

EMPA Lafatsch deposit, Wetterstein Fm. [mass%]									
sample/analyses	**As**	**S**	**Zn**	**Fe**	**Pb**	**Ge**	**Cu**	**Cd**	**total**
BGR_La48	0.051	32.51	67.15	0.09	0.186	0.006	NA	0.00	100.00
BGR_La49	0.050	32.28	67.03	0.14	0.135	0.008	NA	0.05	99.69
BGR_La50	NA	32.50	67.42	0.02	NA	NA	NA	0.05	99.99
BGR_La51	0.056	32.00	66.08	0.10	0.280	NA	NA	0.87	99.39
BGR_La52	0.015	32.04	66.53	0.09	0.102	NA	NA	0.88	99.65
BGR_La53	0.051	32.35	66.60	0.09	0.155	NA	NA	0.78	100.02
BGR_La54	0.011	32.28	67.09	0.02	0.269	NA	NA	0.46	100.14
BGR_La55	0.117	32.27	66.32	0.16	0.271	NA	NA	0.81	99.94
BGR_La56	0.044	32.20	66.78	0.10	0.191	NA	NA	0.61	99.92
BGR_La57	0.095	32.17	66.09	0.22	0.200	0.006	NA	0.95	99.73
BGR_La58	0.088	32.17	66.02	0.09	0.346	NA	NA	0.93	99.65
BGR_La59	NA	32.28	67.33	0.01	NA	NA	NA	0.29	99.91
BGR_La60	0.010	32.21	67.18	0.01	0.009	NA	NA	0.56	99.97
BGR_La61	0.009	32.21	67.14	0.02	0.019	NA	NA	0.71	100.11

Table 14: LA ICP-MS trace element data for ZnS in Blb26 (Bleiberg, Maxer Bänke).

	LA ICP-MS Blb26 [ppm]																		
analysis:	V^{51}	Mn^{55}	Fe^{57}	Co^{59}	Cu^{63}	Cu^{65}	Ga^{69}	Ga^{71}	As^{75}	Ag^{109}	Cd^{111}	In^{115}	Sn^{118}	W^{182}	Tl^{203}	Tl^{205}	Pb^{207}	Pb^{208}	Bi^{209}
Blb26_11	<d.l.	11.8	2471	0.091	<d.l.	<d.l.	1.34	1.39	422	0.172	1196	<d.l.	0.176	<d.l.	171	172	681	679	0.029
Blb26_12	<d.l.	10.2	657	0.082	<d.l.	<d.l.	3.02	2.99	91.3	0.206	1493	<d.l.	0.264	<d.l.	52.7	52.3	251	251	0.021
Blb26_13	0.823	11.5	1219	0.108	<d.l.	<d.l.	11.8	11.6	164	0.181	1216	<d.l.	0.315	<d.l.	84.1	84.5	402	400	0.033
Blb26_14	0.328	23.5	5957	0.186	<d.l.	<d.l.	3.23	3.44	665	0.242	609	<d.l.	0.172	<d.l.	252	264	1162	1219	0.024
Blb26_15	<d.l.	16.0	8741	0.197	0.264	0.181	4.71	4.63	821	0.884	711	<d.l.	0.142	<d.l.	285	285	1228	1279	0.027
Blb26_16	0.039	5.47	1115	0.071	1.46	1.36	5.85	5.96	157	6.13	2299	<d.l.	0.196	<d.l.	56.3	57.3	328	325	0.039
Blb26_17	0.089	14.3	3566	0.140	0.424	0.361	11.4	11.0	469	2.57	989	<d.l.	0.249	<d.l.	177	175	834	836	0.030
Blb26_18	0.034	13.1	4779	0.136	<d.l.	<d.l.	10.5	11.0	638	0.365	758	<d.l.	0.223	<d.l.	201	201	1029	1062	0.036
Blb26_19	0.060	11.7	6728	0.150	<d.l.	<d.l.	3.16	3.00	722	0.102	526	<d.l.	0.169	<d.l.	203	206.0	1130	1194	<d.l.
Blb26_20	<d.l.	3.22	108	0.037	<d.l.	<d.l.	0.656	0.748	6.85	1.57	2699	<d.l.	0.265	<d.l.	3.13	3.45	138	137	<d.l.
Blb26_21	<d.l.	2.17	105	0.044	<d.l.	<d.l.	<d.l.	<d.l.	7.20	<d.l.	1194	<d.l.	0.221	<d.l.	3.07	3.15	482	476	0.016
Blb26_22	<d.l.	3.76	137	0.050	<d.l.	<d.l.	0.442	0.406	16.7	0.383	2093	<d.l.	0.281	<d.l.	16.0	15.4	154	151	0.014
Blb26_23	<d.l.	6.53	1000	0.050	1.36	1.52	5.87	5.77	78.1	0.138	1827	0.076	0.753	<d.l.	38.3	38.3	224	224	<d.l.
Blb26_24	<d.l.	3.70	134	0.030	0.244	0.435	0.620	0.631	17.2	0.387	1859	<d.l.	0.245	<d.l.	15.2	15.2	146	145	0.018
Blb26_25	<d.l.	3.54	147	0.044	<d.l.	<d.l.	0.125	0.153	12.7	0.028	2015	<d.l.	0.178	<d.l.	6.34	6.12	182	180	<d.l.
Blb26_26	0.097	8.10	255	0.032	16.7	17.0	0.742	0.787	57.6	0.379	1144	0.059	0.562	<d.l.	25.0	24.9	405	402	0.028
Blb26_27	<d.l.	7.38	189	0.051	<d.l.	<d.l.	0.672	0.855	19.3	0.283	2762	<d.l.	0.118	<d.l.	6.46	6.52	119	116	0.034
Blb26_28	0.055	8.61	222	0.034	<d.l.	<d.l.	0.103	0.091	45.2	0.035	2080	<d.l.	0.191	<d.l.	15.9	15.9	196	193	0.033
Blb26_29	0.052	4.99	245	0.085	<d.l.	<d.l.	0.064	0.085	30.0	0.041	1907	<d.l.	0.273	<d.l.	13.9	13.6	152	151	0.036
Blb26_30	<d.l.	2.48	122	0.045	<d.l.	<d.l.	0.087	0.047	16.5	0.116	2311	<d.l.	0.247	<d.l.	14.2	14.0	161	159	0.027
Blb26_31	0.068	6.11	442	0.159	1.19	1.38	0.719	0.682	30.4	0.568	2535	<d.l.	0.285	<d.l.	7.95	7.92	234	233	0.039
Blb26_32	0.194	6.08	165	0.043	19.4	20.7	2.80	2.73	20.1	1.65	2258	0.277	1.62	<d.l.	13.9	14.1	148	145	0.042
Blb26_33	<d.l.	7.04	249	0.056	<d.l.	<d.l.	<d.l.	<d.l.	41.9	<d.l.	1000	<d.l.	0.180	<d.l.	30.0	30.2	254	252	0.032
Blb26_34	<d.l.	13.4	357	0.040	<d.l.	<d.l.	0.709	0.733	50.2	0.091	1391	<d.l.	0.199	<d.l.	22.4	22.6	236	233	0.027
Blb26_35	<d.l.	3.05	140	0.039	1.50	1.52	1.01	0.868	29.0	2.23	3156	<d.l.	0.236	<d.l.	9.21	9.39	248	244	0.031
Blb26_36	<d.l.	8.67	243	<d.l.	<d.l.	<d.l.	0.274	0.289	27.8	<d.l.	1915	<d.l.	0.179	<d.l.	12.1	12.2	137	132	<d.l.
Blb26_37	<d.l.	6.45	215	0.049	<d.l.	<d.l.	0.288	0.246	55.4	<d.l.	1799	<d.l.	0.167	<d.l.	14.0	14.5	263	260	0.041
Blb26_38	0.044	5.38	188	0.046	<d.l.	<d.l.	0.058	0.086	35.2	<d.l.	1294	<d.l.	0.186	<d.l.	12.6	12.7	150	146	0.017
Blb26_39	<d.l.	9.32	198	0.034	1.04	1.17	0.719	0.651	28.1	0.815	2227	<d.l.	0.272	<d.l.	19.0	18.9	224	220	0.025
Blb26_40	<d.l.	5.75	178	0.041	0.493	0.587	0.794	0.725	39.3	0.598	2034	<d.l.	0.298	<d.l.	12.7	12.6	300	299	<d.l.
Blb26_41	0.311	8.85	277	0.069	<d.l.	<d.l.	1.39	1.19	52.1	0.171	973	<d.l.	0.204	<d.l.	20.2	20.5	191	186	<d.l.
Blb26_42	<d.l.	4.19	192	0.042	<d.l.	<d.l.	0.861	0.904	25.3	0.432	1999	<d.l.	0.112	<d.l.	13.9	13.8	168	168	0.017
Blb26_43	<d.l.	11.7	290	0.033	<d.l.	<d.l.	0.995	0.926	45.7	0.140	1668	<d.l.	0.117	<d.l.	21.1	21.3	222	218	<d.l.
Blb26_44	0.044	10.8	291	0.031	<d.l.	<d.l.	0.806	0.831	36.6	0.098	1879	<d.l.	0.209	<d.l.	13.6	13.7	166	164	0.023
Blb26_45	<d.l.	8.31	303	0.065	<d.l.	<d.l.	0.388	0.418	52.5	0.045	1208	<d.l.	0.136	<d.l.	31.1	31.0	292	287	<d.l.
Blb26_46	<d.l.	4.67	158	0.036	<d.l.	<d.l.	0.573	0.505	15.8	0.141	2313	<d.l.	0.213	<d.l.	7.38	7.61	120	119	<d.l.
Blb26_47	<d.l.	7.39	225	0.035	0.433	0.404	0.559	0.520	23.4	0.132	1792	<d.l.	0.139	<d.l.	11.8	11.9	140	139	<d.l.
Blb26_48	<d.l.	10.2	280	0.059	1.88	1.82	0.447	0.506	53.0	0.071	1259	<d.l.	0.186	<d.l.	25.8	25.3	268	263	<d.l.
Blb26_49	<d.l.	9.77	360	0.057	2.58	2.31	0.509	0.459	75.4	0.084	1418	0.020	0.267	<d.l.	30.5	29.8	321	321	0.019
Blb26_50	0.055	12.9	395	0.142	0.674	0.357	0.266	0.229	126	0.071	1326	<d.l.	0.249	<d.l.	36.0	35.6	418	412	0.033
Blb26_51	<d.l.	7.71	436	0.046	1.40	1.67	0.737	0.766	84.3	0.137	1649	0.041	0.241	<d.l.	26.5	25.9	323	315	<d.l.
Blb26_52	<d.l.	7.54	356	0.049	5.78	6.15	1.15	1.33	39.5	0.354	1593	0.037	0.527	<d.l.	21.5	21.2	210	206	0.036
Blb26_53	<d.l.	7.07	523	0.091	3.39	3.03	1.86	1.78	48.6	0.241	1336	0.058	0.697	<d.l.	35.5	36.0	232	229	<d.l.
Blb26_54	<d.l.	6.26	227	0.075	2.50	2.66	1.23	1.24	41.0	0.111	1364	0.036	0.445	<d.l.	23.6	22.3	323	316	0.023
Blb26_55	0.038	6.11	267	0.041	1.86	2.01	1.36	1.34	51.9	0.196	1245	0.011	0.407	<d.l.	52.8	52.8	248	246	<d.l.
Blb26_56	<d.l.	9.43	300	0.043	<d.l.	<d.l.	0.487	0.467	59.0	0.044	1040	<d.l.	0.255	<d.l.	31.0	30.9	225	223	<d.l.
Blb26_57	0.336	11.8	671	0.205	1.05	1.19	5.16	5.17	82.4	0.139	1354	<d.l.	0.401	<d.l.	31.2	31.0	395	392	0.039
Blb26_58	0.049	9.78	345	0.040	0.308	0.325	1.18	1.12	80.9	<d.l.	981	<d.l.	0.331	<d.l.	39.1	38.8	324	322	0.032
Blb26_59	<d.l.	4.67	163	0.025	7.38	7.20	2.10	1.84	24.8	0.684	1821	0.136	1.00	<d.l.	16.4	16.4	283	281	<d.l.
Blb26_60	6.47	9.19	1312	0.509	4.45	4.46	8.29	8.05	83.7	0.074	601	0.014	2.35	<d.l.	137	134	441	444	0.055
Blb26_61	0.728	8.55	409	0.081	<d.l.	<d.l.	2.01	2.13	69.7	<d.l.	707	<d.l.	0.341	<d.l.	105	106	520	517	0.027
Blb26_62	<d.l.	21.9	422	<d.l.	0.613	0.723	0.695	0.663	123	0.136	1384	0.013	0.767	<d.l.	34.0	34.4	519	514	0.046
Blb26_63	0.058	15.0	227	0.022	5.16	5.41	0.961	0.946	56.3	0.575	1987	0.103	1.74	<d.l.	17.4	17.4	380	376	0.023
Blb26_64	<d.l.	14.3	831	0.047	0.602	0.636	6.83	6.94	205	0.024	547	<d.l.	0.572	<d.l.	101	101	498	501	0.026
Blb26_65	<d.l.	8.95	266	0.060	1.53	1.67	0.577	0.519	49.9	0.063	1118	<d.l.	0.366	<d.l.	31.3	32.3	292	287	0.016
Blb26_66	<d.l.	9.45	172	0.047	3.80	3.72	1.01	0.973	28.4	0.115	1776	0.035	0.792	<d.l.	9.24	9.07	475	471	0.057
Blb26_67	<d.l.	6.23	284	0.067	<d.l.	<d.l.	0.058	0.056	47.8	<d.l.	909	<d.l.	0.228	<d.l.	30.0	30.5	338	335	0.033
Blb26_68	<d.l.	9.67	403	0.050	4.16	4.12	1.06	1.06	76.2	0.070	1010	0.048	0.356	<d.l.	32.3	32.3	307	304	<d.l.
Blb26_69	<d.l.	2.39	114	0.069	6.98	6.89	1.98	2.08	19.1	1.61	2535	<d.l.	0.511	<d.l.	10.8	10.6	208	208	0.047
Blb26_70	0.107	7.80	279	0.083	6.27	6.33	3.53	3.38	16.0	0.450	2186	0.178	0.967	<d.l.	11.9	11.9	158	158	0.036

Table 15: LA ICP-MS trace element data for ZnS in WSBlb_29 (Bleiberg, 1st Raibl horizon).

	WS_Blb29 [ppm]																		
analysis:	V^{51}	Mn^{55}	Fe^{57}	Co^{59}	Cu^{63}	Cu^{65}	Ga^{69}	Ga^{71}	As^{75}	Ag^{109}	Cd^{111}	In^{115}	Sn^{118}	W^{182}	Tl^{203}	Tl^{205}	Pb^{207}	Pb^{208}	Bi^{209}
WSBlb29_1	<d.l.	25.7	10297	0.1	1.59	1.71	0.022	<d.l.	448	1.54	935	<d.l.	0.154	<d.l.	63.8	63.8	883	882	<d.l.
WSBlb29_2	<d.l.	17.2	6206	0.118	0.652	0.847	0.063	<d.l.	382	3.91	939	<d.l.	0.235	<d.l.	65.2	64.9	687	685	<d.l.
WSBlb29_3	0.102	6.84	3195	0.075	33.1	32.3	0.824	0.892	131	27.8	1561	<d.l.	0.415	<d.l.	31.4	31.1	392	391	0.027
WSBlb29_4	0.058	22.2	5666	0.186	0.36	0.615	0.207	0.2	372	5.15	830	<d.l.	0.327	<d.l.	70.9	70.2	557	549	0.02
WSBlb29_5	<d.l.	20.1	10294	0.143	<d.l.	<d.l.	0.03	0.052	584	0.666	1472	<d.l.	0.131	<d.l.	113	113	883	889	0.015
WSBlb29_6	0.093	14.6	3816	0.132	2.66	2.91	0.654	0.831	239	6.37	491	<d.l.	0.183	<d.l.	54.4	54.3	428	420	<d.l.
WSBlb29_7	0.245	9.38	3640	0.032	3.21	4.01	0.816	0.761	256	5.28	1042	<d.l.	0.152	<d.l.	59.2	59	476	470	<d.l.
WSBlb29_8	0.955	32.2	5812	0.09	3.28	3.49	0.569	0.464	288	4.61	888	<d.l.	0.256	<d.l.	61.7	61.3	513	512	<d.l.
WS_Blb29_8a	0.83	22.8	3718	0.077	1.82	2.07	0.288	0.268	250	2.78	906	<d.l.	0.094	<d.l.	62	61	452	445	<d.l.
WS_Blb29_9	0.217	11.5	5914	0.093	1.04	1.28	0.145	0.077	320	1.78	835	<d.l.	0.157	<d.l.	72.3	71.3	501	499	0.016
WS_Blb29_10	0.066	12.1	2922	0.115	2.98	3.19	0.756	0.69	148	11.4	938	<d.l.	0.183	<d.l.	41.3	41.3	315	311	<d.l.
WS_Blb29_11	<d.l.	7.22	2169	0.16	10.6	10.7	0.982	0.922	101	15.2	940	<d.l.	0.202	<d.l.	35.6	35.3	247	243	<d.l.
WS_Blb29_12	<d.l.	9.84	4374	0.109	0.68	0.727	0.321	0.292	192	1.87	780	0.009	0.285	<d.l.	43.9	43.9	391	385	0.028
WS_Blb29_13	1.44	52.7	3279	0.114	1.74	1.77	0.528	0.564	192	15.1	1031	<d.l.	0.266	<d.l.	48.3	49	356	349	<d.l.
WS_Blb29_14	2.05	16.6	4091	0.133	24.5	24.5	1.65	1.58	206	9.82	1109	<d.l.	0.181	<d.l.	46.8	46.5	403	401	<d.l.
WS_Blb29_15	0.321	20.9	5709	0.187	1.48	1.66	0.198	0.288	339	12.7	669	<d.l.	0.126	<d.l.	88.8	87.4	635	645	<d.l.
WS_Blb29_16	0.699	12.7	4462	0.129	3.23	3.21	0.341	0.314	307	3.18	787	<d.l.	0.185	<d.l.	69.6	69	552	542	<d.l.
WS_Blb29_17	0.765	24.5	3162	0.099	2.29	2.28	0.362	0.336	241	3.84	825	<d.l.	0.14	<d.l.	57.4	56.1	485	480	<d.l.
WS_Blb29_18	0.339	21.4	3771	0.107	1.66	1.64	0.145	0.182	303	2.85	752	<d.l.	0.136	<d.l.	75.1	75.4	559	560	<d.l.
WS_Blb29_19	0.259	18.1	4077	0.152	2.26	1.94	0.423	0.432	295	5.86	674	<d.l.	0.211	<d.l.	74.4	73	573	572	<d.l.
WS_Blb29_20	0.418	23.2	5186	0.113	1.98	2.01	0.172	0.178	321	2.71	706	<d.l.	0.073	<d.l.	73.6	74.5	575	577	<d.l.
WS_Blb29_21	1.41	27.9	3941	0.169	2.56	2.74	0.543	0.547	241	4.34	836	<d.l.	0.222	<d.l.	56.4	55.4	473	464	<d.l.
WS_Blb29_22	0.606	24.4	3743	0.105	3.34	3.45	0.355	0.389	254	4.64	833	<d.l.	0.262	<d.l.	60.6	61.7	513	507	0.021
WS_Blb29_23	1.05	19.1	3311	0.093	5.67	5.62	1.96	1.98	244	6.35	917	0.011	0.292	<d.l.	63.3	63.5	586	589	<d.l.
WS_Blb29_24	0.181	17.6	3791	0.122	1.94	2.44	0.368	0.39	300	2.95	762	<d.l.	0.253	<d.l.	71.4	71.4	545	539	0.025
WS_Blb29_25	0.049	13.5	3705	0.126	6.57	6.23	1.29	1.31	241	11.1	747	<d.l.	0.208	<d.l.	64.8	66.1	509	504	<d.l.
WS_Blb29_26	0.184	11.2	2888	0.124	4.98	4.49	1.93	2.08	189	12.2	716	<d.l.	0.371	<d.l.	51.5	51.4	434	426	0.025
WS_Blb29_27	0.568	30	453	<d.l.	1.74	1.93	26.3	27.5	12.5	1.43	2308	0.034	0.494	<d.l.	6.58	6.64	163	161	0.034
WS_Blb29_28	1.25	15.5	2268	0.171	11.9	11.3	1.04	1.1	369	21.6	957	<d.l.	0.368	<d.l.	82.8	82.6	754	749	0.019
WS_Blb29_29	0.424	17.6	2756	0.185	14.8	15.4	0.584	0.581	315	25	1058	<d.l.	0.425	<d.l.	81.3	81.4	678	675	<d.l.
WS_Blb29_30	1.01	15.8	2769	0.226	11.3	12	0.948	0.95	375	24	991	<d.l.	0.405	<d.l.	82.8	83.1	746	739	0.021
WS_Blb29_31	0.38	21.4	5353	0.236	0.478	<d.l.	0.461	0.347	259	10.1	671	<d.l.	0.403	<d.l.	92.1	91.7	666	649	0.025
WS_Blb29_32	0.849	39.4	1258	0.133	29.1	28	0.901	0.859	142	39.1	1296	<d.l.	0.298	<d.l.	46	45.8	364	357	0.028
WS_Blb29_33	0.912	23.4	8538	0.27	<d.l.	<d.l.	0.882	0.802	240	4.89	358	<d.l.	0.462	<d.l.	53.4	53.3	561	555	0.047
WS_Blb29_34	0.688	16	6581	0.164	12.5	12.2	0.631	0.729	405	16.1	1479	<d.l.	0.251	<d.l.	83.3	81.8	812	805	0.043
WS_Blb29_35	0.12	12.5	2395	0.109	35.5	33.9	1.33	1.46	273	27.6	1539	<d.l.	0.153	<d.l.	54.5	53.8	546	537	0.018
WS_Blb29_36	0.578	11.3	2986	0.092	11.2	11.8	0.394	0.397	381	10.9	1700	<d.l.	0.267	<d.l.	61.8	62	865	860	<d.l.
WS_Blb29_37	2.28	15.2	6772	0.209	10.3	10.4	0.767	0.727	389	14.6	1495	<d.l.	0.145	<d.l.	78.8	77.4	754	756	0.016
WS_Blb29_38	0.683	19.7	6233	0.12	8.64	8.56	0.306	0.283	454	10.8	1754	<d.l.	0.147	0.046	80.2	79.9	941	927	<d.l.
WS_Blb29_39	0.079	11.7	3204	0.152	23.9	22.3	0.212	0.196	420	38.7	1522	<d.l.	0.336	<d.l.	85.4	87.7	824	818	0.019
WS_Blb29_40	0.899	14.3	3495	0.162	16.8	17.2	0.685	0.628	420	24.9	1043	<d.l.	0.338	<d.l.	97.8	97.9	766	752	0.016
WS_Blb29_41	0.235	17.2	3927	0.123	7.96	7.52	0.435	0.471	422	27	1154	<d.l.	0.178	<d.l.	122	122	731	718	0.03
WS_Blb29_42	0.045	17.8	3806	0.132	21.5	20.8	0.6	0.608	323	57.4	1303	<d.l.	0.2	<d.l.	94.9	95.8	699	687	0.022
WS_Blb29_43	0.105	13.2	3351	0.116	2.72	2.59	0.875	0.773	322	34.2	1031	0.007	0.364	<d.l.	99.7	100	607	598	0.023
WS_Blb29_44	<d.l.	12.5	2101	0.126	<d.l.	<d.l.	28	30	79.1	0.872	927	<d.l.	0.205	<d.l.	16.8	17	386	379	0.043
WS_Blb29_45	1.43	33.1	16817	0.262	<d.l.	<d.l.	0.497	0.513	483	3.33	681	<d.l.	0.224	<d.l.	91.8	91.1	1145	1127	0.038
WS_Blb29_46	<d.l.	12.7	7863	0.137	<d.l.	<d.l.	0.046	0.073	83.9	1.46	1335	<d.l.	0.167	<d.l.	14.1	13.9	204	206	0.033
WS_Blb29_47	0.665	38.9	25606	0.379	<d.l.	<d.l.	0.172	0.219	428	0.779	195	<d.l.	0.221	<d.l.	81.3	80.1	905	892	0.028
WS_Blb29_48	<d.l.	4.97	631	0.052	<d.l.	<d.l.	0.418	0.433	21.1	7.49	2377	<d.l.	0.312	<d.l.	7.49	7.46	77.8	77	0.032
WS_Blb29_49	<d.l.	18.4	4542	0.12	<d.l.	<d.l.	<d.l.	<d.l.	216	6.55	1248	<d.l.	0.196	<d.l.	43.2	44	437	428	0.039
WS_Blb29_50	0.446	17.5	4348	0.16	18.1	18	0.722	0.639	375	48.5	1200	<d.l.	0.166	<d.l.	88.1	88.8	781	776	0.04
WS_Blb29_51	0.871	32.6	2196	0.218	26.3	26.1	0.478	0.53	180	49	1725	<d.l.	0.241	<d.l.	40.3	41.3	461	459	0.045
WS_Blb29_52	0.178	15.5	2498	0.11	13.4	13.4	0.445	0.509	405	24.3	980	<d.l.	0.155	<d.l.	78.8	79.3	833	828	<d.l.
WS_Blb29_53	1.47	12.5	1904	0.111	11.7	11.8	1.96	1.97	162	25.6	1044	<d.l.	0.4	<d.l.	48.2	47.2	358	354	0.012
WS_Blb29_54	0.138	16.4	1006	0.051	34.8	34.7	1.35	1.5	65.1	122	2618	<d.l.	0.183	<d.l.	13.2	13.3	189	187	0.025
WS_Blb29_55	0.228	30.5	5355	0.136	12.2	12	0.369	0.414	422	55	1364	<d.l.	0.178	<d.l.	102	103	713	704	0.024
WS_Blb29_56	0.233	21.5	2682	0.107	5.19	5.19	0.164	0.172	313	12.9	1506	<d.l.	0.199	<d.l.	56.2	56.3	651	649	0.027
WS_Blb29_57	<d.l.	18.1	4833	0.17	10.8	10.3	0.384	0.386	331	38.4	1203	<d.l.	0.237	<d.l.	89.8	90.3	608	594	0.031
WS_Blb29_58	0.466	28.6	3300	0.155	23.3	23.1	0.641	0.693	235	46.7	1573	<d.l.	0.238	<d.l.	72.3	71.7	436	428	0.021
WS_Blb29_59	0.933	21.5	1940	0.139	23.9	24.1	0.399	0.476	225	32.1	1235	<d.l.	0.259	<d.l.	55.3	55.3	508	500	0.042
WS_Blb29_60	0.633	16.2	2718	0.136	0.702	0.869	1.22	1.05	182	21.1	1079	<d.l.	0.393	<d.l.	61.1	61.4	299	295	0.06
WS_Blb29_61	0.411	19.7	4709	0.162	0.437	0.461	0.925	0.944	389	11.6	616	<d.l.	0.346	<d.l.	120	120	595	588	0.012
WS_Blb29_62	0.601	23	3608	0.186	0.693	0.786	0.271	0.232	382	17.6	984	<d.l.	0.278	<d.l.	112	112	570	553	0.019
WS_Blb29_63	0.771	34.7	8581	0.3	<d.l.	<d.l.	0.159	0.105	305	3.16	333	<d.l.	0.3	<d.l.	59.4	60.9	616	607	<d.l.
WS_Blb29_64	<d.l.	30.6	10943	0.21	<d.l.	<d.l.	<d.l.	<d.l.	768	3.69	349	<d.l.	0.549	<d.l.	207	209	1143	1127	0.038
WS_Blb29_65	0.141	16.3	3996	0.106	1.47	1.29	2	1.98	337	19	820	0.006	0.367	<d.l.	104	106	675	664	0.016
WS_Blb29_66	0.434	17.9	2680	0.115	3.8	4.23	1.94	2.29	288	24.1	866	<d.l.	276	<d.l.	97.5	97.8	621	621	<d.l.
WS_Blb29_67	<d.l.	11.4	3103	0.103	<d.l.	<d.l.	<d.l.	<d.l.	100	6.14	2145	<d.l.	0.466	<d.l.	22.6	22.6	358	349	0.019
WS_Blb29_68	0.446	18.6	13043	0.081	<d.l.	<d.l.	0.454	0.424	564	17.1	1390	<d.l.	0.314	<d.l.	132	132	945	933	<d.l.
WS_Blb29_69	<d.l.	12.2	3437	0.104	<d.l.	<d.l.	0.227	0.188	57.8	5.21	1605	0.008	0.288	<d.l.	17.3	17.4	161	160	0.014
WS_Blb29_70	<d.l.	26.2	7281	0.177	<d.l.	<d.l.	0.186	0.141	292	3.08	772	0.007	0.23	<d.l.	87.6	89.6	509	496	<d.l.

Table 16: Sulfur isotope data ($\delta^{34}S$, ‰) of sphalerite, galena and Fe-sulfides.

	$\delta^{34}S$ [‰]				$\delta^{34}S$ [‰]		
sample/origin	**ZnS**	**PbS**	**FeS_2**	**sample/origin**	**ZnS**	**PbS**	**FeS_2**
Blb17: Bleiberg, Maxer Bänke	-19.8	-24.4		**E14.2-4:** Bleiberg Revier Erlach	-24.5 -23.7	-29.0	
	-13.8 -21.5 -21.8 -14.5 -14.9 -15.0 -21.3 -13.4 -25.5 -26.0 -24.4 -16.2 -25.4 -1.5			**E14.3:** Bleiberg, Revier Erlach	-24.8 -22.0 -21.6		
				C6/14: Bleiberg 1st Raibl h.	-25.4 -26.3 -29.0	-29.8	
				Mz08: Mezica, Moring	-9.1 -10.8 -10.3		
Blb26: Bleiberg, Maxer Bänke	-18.6 -21.5 -19.8			**MzH01:** Mezica, Helena	-20.1 -18.0 -16.0 -15.2	-26.1 -24.6 -29.2	
EHK02: Bleiberg, Erzkalk	-18.2 -22.3 -6.6 -22.6 -4.6 -6.6	-25.1 -7.7	-21.8	**SF03:** Mezica, Graben	-15.7 -14.6 -15.6		-14.4 -18.7
				Tp01: Topla	-20.6 -21.7 -23.1		-23.9
WS_Blb07: Bleiberg, Erzkalk		-6.1		**Tp04:** Topla	-12.9 -9.8		-16.0
R8/2: Bleiberg, Crest Riedhardtscholle	-24.5 -4.1 -24.4 -7.0 -3.7		-24.5	**JK5-9:** Jauken	1.8 -1.6		
				Toe01: Töplitsch	-11.5 -13.2		
J10/4: Bleiberg, Crest Josefischolle	-27.2 -28.1 -24.7 -26.6 -27.8 -28.0 -24.6	-25.8		**Rd01.1:** Zunderwand (not D.R.)	0.5 0.2		
K2-2: Bleiberg, Crest Kalkscholle	-30.4 -27.6 -22.5						

Table 17: Results of the Pb isotope analysis of ZnS and PbS, according to the actual values of the NBS 981 standard.

sample/origin	ID	Min.	c. [ppm]	$^{206}Pb/^{204}Pb$ ±0.004%	$^{207}Pb/^{204}Pb$ ±0.004%	$^{208}Pb/^{204}Pb$ ±0.005%
EHK02 Bleiberg, Erzkalk	EHK02 ZnS-SB	Sp	18600	18.380	15.666	38.529
	EHK02 ZnS-xx	Sp	4080	18.381	15.668	38.535
	EHK02 PbS1	Gn	890000	18.379	15.667	38.529
	EHK02 PbS2	Gn	890000	18.378	15.665	38.254
J10.4 Bleiberg, Josefischolle (crest)	J10.4 ZnS-xx	Sp	683	18.3758	15.6742	38.5367
	J10.4 ZnS-SB	Sp	7600	18.3774	15.6751	38.5400
	J10.4 PbS	Gn	890000	18.3790	15.6745	38.5502
E14.6 Bleiberg, Erlach	E14.6 ZnS	Sp	5228	18.3906	15.6720	38.5243
	E14.6 PbS	Gn	890000	18.3917	15.6745	38.5269
C6.14 , Bleiberg 1st Raibl.h.	C6.14 ZnS	Sp	483	18.3902	15.6756	38.5402
Mz08 Mezica, Moring	Mz08 ZnS	Sp	2874	18.3704	15.6729	38.5339
	Mz08 PbS	Gn	890000	18.3683	15.6729	38.5322
MzH01 Mezica, Helena	MzH01 ZnS-SB	Sp	61150	18.4077	15.6697	38.5069
	MzH01 ZnS-xx	Sp	391	18.3966	15.6723	38.5136
	MzH01 PbS1	Gn	890000	18.4058	15.6715	38.5069
	MzH01 PbS2	Gn	890000	18.3966	15.6723	38.5136
JK5-9, Jauken	JK5-9 ZnS	Sp	144	18.4232	15.6765	38.5355
NBS981, Standard average composition (n = 8)				16.9418	15.4983	36.7224

Table 18: Rb-Sr data of sphalerites (+ pyrite) of samples from the western Bleiberg mine (J. Schneider, unpublished results).

Sample/ Origin	ID	Rb [ppm]	2σ [%]	Sr [ppm]	2σ [%]	$^{87}Rb/^{86}Sr$	2rs [ppm]	$^{87}Sr/^{86}Sr$	2rs [%]	$^{87}Sr/^{86}Sr$ t: 205 Ma	2σ [%]
C6.6 Bleiberg 1st Raibl h.	C6.6 Sp	0.112	1.28	0.081	1.11	4.0189	0.78	0.72060	0.011	0.709077	0.017
	C.6 Py	0.004	1.11	0.064	1.09	0.1941	0.80	0.70840	0.005	0.70783	0.005
C6.9 Bleiberg 1st Raibl h.	C6.9 Sp	0.413	1.47	0.613	1.09	1.9490	1.49	0.71408	0.002	0.70840	0.012
E14.2-2 Bleiberg Erlach	E14.2-2 Sp dunkel	0.764	1.33	0.155	1.09	14.2839	1.25	0.74963	0.005	0.70799	0.074
	E14.2-2 Sp hell	0.538	1.09	0.100	1.09	15.5994	0.76	0.75388	0.002	0.70841	0.0049
E14.2-7 Bleiberg Erlach	E14.2-7 Sp dunkel	0.643	1.33	0.119	1.09	15.6724	1.25	0.75413	0.005	0.70844	0.081
	E14.2-7 Sp hell	0.402	1.19	0.060	1.09	19.3783	0.98	0.76427	0.002	0.70778	0.078
E14.3 Bleiberg Erlach	E14.3 Sp	2.097	1.35	0.168	1.09	36.4308	1.28	0.81209	0.007	0.70589	0.192
E14.7-1 Bleiberg Erlach	E14.7-1 Sp	0.685	1.36	0.084	1.09	23.8570	1.29	0.77717	0.003	0.70762	0.127
J10.1 Bleiberg Josefisch.	J10.1 Sp hell	0.948	1.10	1.054	1.09	2.6055	0.78	0.71648	0.003	0.70888	0.009
J10.3 Bleiberg Josefisch.	J10.3 Sp dunkel	3.042	1.22	0.851	1.09	10.3786	1.43	0.73872	0.002	0.70847	0.061
J90 B Bleiberg Josefisch.	J90 B Sp	0.626	1.23	0.151	1.09	12.0670	1.65	0.74342	0.003	0.70825	0.082
R6.1 Bleiberg Riedhardts.	R6.1 Sp	1.000	1.19	0.348	1.09	8.3284	0.98	0.73266	0.003	0.70838	0.034
R11.1 Bleiberg Riedhardts.	R11.1 Sp	0.944	1.19	0.461	1.09	5.9294	0.85	0.72573	0.002	0.70845	0.021
R2-3 Bleiberg Riedhardts.	R2-3 Sp	0.319	1.08	8.623	1.10	0.1071	0.77	0.70884	0.006	0.70853	0.006
K2-2 Bleiberg Kalksch.	K2-2 Sp	0.998	1.44	0.298	1.09	9.6966	1.44	0.7329	0.015	0.70464	0.060